

This file is part of the following work:

**Beveridge, Tegan Louise (2022) *Bentonite geochronology and tephrostratigraphy for litho- and chronostratigraphic refinement of fossiliferous Campanian strata in western North America*. PhD Thesis, James Cook University.**

Access to this file is available from:

<https://doi.org/10.25903/293r%2D4g58>

Copyright © 2022 Tegan Louise Beveridge.

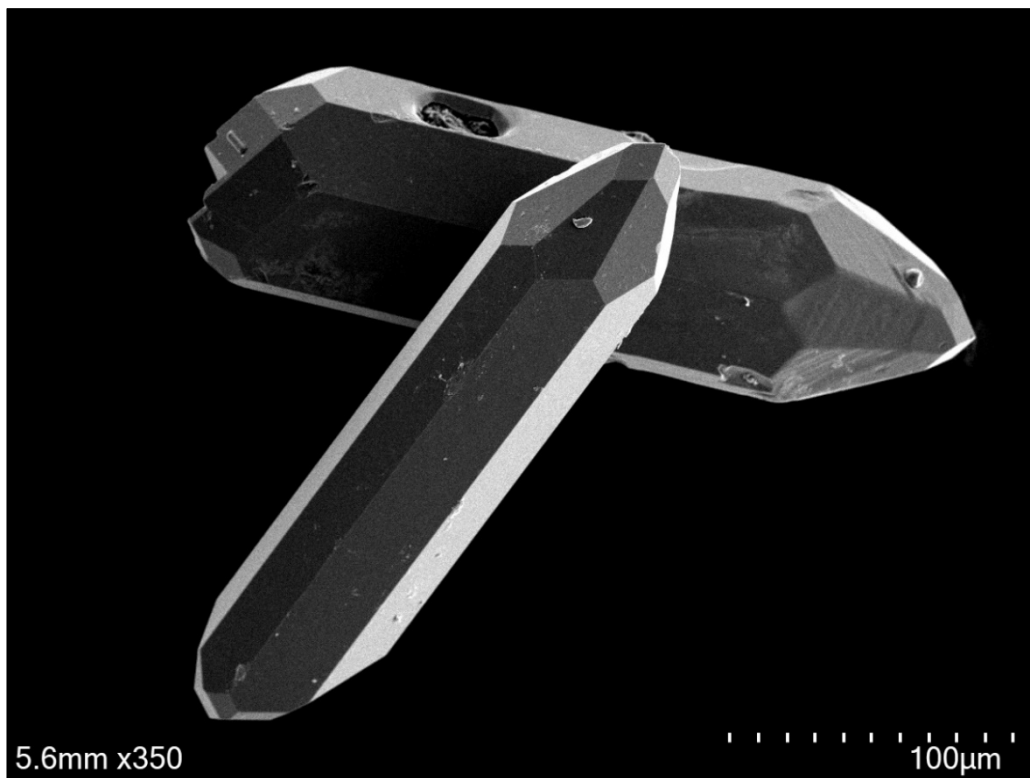
The author has certified to JCU that they have made a reasonable effort to gain permission and acknowledge the owners of any third party copyright material included in this document. If you believe that this is not the case, please email

[researchonline@jcu.edu.au](mailto:researchonline@jcu.edu.au)

Bentonite geochronology and tephrostratigraphy  
for litho- and chronostratigraphic refinement  
of fossiliferous Campanian strata in  
western North America

Thesis submitted by

Tegan Louise Beveridge



For the Degree of Doctor of Philosophy

College of Science and Engineering

James Cook University

(July 2022)



---

### Statement of Access

I, the undersigned author of this thesis, understand that James Cook University will make this thesis available for the use within the university library and allow access in other approved libraries after its submission and the specified embargo period has passed. All users consulting this thesis will have to sign the following statement:

*In consulting this thesis, I agree not to copy or closely paraphrase in whole or in part without written consent of the author, and to make proper public written acknowledgement for any assistance that I have obtained from it.*

Beyond this, I do not wish to place any restrictions on this thesis.

Tegan Beveridge

July 2022



---

### **Declaration**

I declare this is my own work. I have not submitted it in any form for another degree or diploma at any university or institution of tertiary education. Information derived from the published or unpublished work of others has been acknowledged in the text and a list of references is given.

Every reasonable effort has been made to gain permission and acknowledge the owners of copyrighted material. I would be happy to hear from any copyright owner who has accidentally been omitted or incorrectly acknowledged in this manuscript.

Tegan Beveridge

July 2022

---

## Acknowledgements

I acknowledge the Bindal and Wulgurukaba peoples as the Traditional Owners and Custodians of the lands on which I have lived and worked for many years and I wish to pay my respects to Aboriginal Elders, past and present. In the spirit of reconciliation, I am committed to honouring Australian Aboriginal and Torres Strait Islander peoples' unique cultural and spiritual relationships to the land, waters and seas, and their rich contributions to science and society.

There are so many individuals to be acknowledged and thanked for their support over the years. These collective contributions take the form of academic, technical, and personal support, without which this project could not have flourished.

Above all others, I thank Christopher Yule; my partner, my best friend. Over the course of my degree, you have celebrated every milestone and trudged through every hardship with me. Your companionship and emotional support have been and will continue to be indescribably valuable to me.

The success of any PhD project can be significantly attributed to the project advisors. I am deeply grateful to Eric Roberts for years of academic support and for facilitating opportunities that have advanced and shaped my career. Many thanks also to Carl Spandler, Maree Corkeron and Jan Huizenga for academic support and mentorship. You are all *sensational* geoscientists.

An enormous debt of gratitude is owed to Jahandar Ramezani for his patient tutelage in the fine art of precise science. I am grateful for the opportunity to have worked in the isotope laboratory at the Massachusetts Institute of Technology; an endeavor that was predominantly funded by the US National Science Foundation (grant number EAR1424892).

I have had the pleasure of working with a long list of geoscientists and paleontologists in the field and via academic collaborations. As a representative of these collaborators and for his involvement in work collated herein, I would like to thank Alan Titus of the Bureau of Land Management for valuable field support and many detailed manuscript edits. I would also like to thank my 2018 fieldwork partner Ashley Ferguson of Idaho State University.

Finally, many thanks go to the behind-the-scenes champions at James Cook University that provided critical technical support. To Judy Botting and Bec Steele, you have made the tedious and technical paperwork of a higher degree by research a breeze. Across the road, I am deeply grateful to those at the Advanced Analytical Centre, particularly Kevin Blake, Shane Askew, Yi Hu, and Huiqing (Jeffrey) Huang. Thank you for being patient with me and my unending stream of zircons.

---

### Statement of Contribution from Others

The candidate received financial support from the Australian Government Research Training Program (RTP scholarship) administered through James Cook University, and from the Economic Geology Research Center (EGRU) (W.C Lacy Scholarship). Research and travel were primarily funded by the U.S. National Science Foundation grant EAR1424892 (J. Ramezani / S.A. Bowring), which facilitated high-precision geochronology at the Massachusetts Institute of Technology.

Intellectual contributions are expressed below using the CRediT (Contributor Roles Taxonomy) scheme (see [credit.niso.org](http://credit.niso.org)) with additional comments in italics. Chapters Three to Six (inclusive) are either presently published or prepared for publication and a brief written statement of co-author contributions is included. Work presented here is primarily that of the candidate, whereby collaborator contributions supplemented and refined the quality of the research.

#### Chapter One

Eric Roberts: Supervision, Writing - Review & Editing

#### Chapter Two

Eric Roberts: Funding acquisition, Supervision, Writing - Review & Editing

Jahandar Ramezani: Funding acquisition, Project administration, Methodology [*guidance*]

#### Chapter Three

Eric Roberts: Supervision, Funding acquisition, Investigation [*field assistance*], Writing - Review & Editing

Jahandar Ramezani: Funding acquisition, Investigation [*geochronology: guidance*], Writing - Review & Editing

Alan Titus: Investigation [*field assistance*], Resources [*sample acquisition*], Data Curation, Writing - Review & Editing

Jeffrey Eaton: Writing - Review & Editing

Randall Irmis: Data Curation, Writing - Review & Editing

Joseph Sertich: Data Curation, Writing - Review & Editing, Writing - Original Draft [*partial contribution in Section 3.7.1*]

This published chapter is the primary work of the candidate in collaboration with the above co-authors. These contributors assisted with fieldwork, collation of fossil locality data, acquisition of high-precision U-Pb ages, and manuscript review and editing. The article was also refined based on helpful feedback from the journal editors and peer review.

---

**Chapter Four**

Eric Roberts: Supervision, Funding acquisition, Investigation [*field assistance*], Writing - Review & Editing

Jahandar Ramezani: Funding acquisition, Investigation [*geochronology: guidance and measurements*], Writing - Review & Editing

Alan Titus: Investigation [*field assistance*], Writing - Review & Editing

Joseph Sertich: Resources [*sample acquisition: IM1442*]

This publication-style chapter is the primary work of the candidate in collaboration with the above co-authors and will comprise the core of a future publication supplemented with fossil locality data from collaborators at the Utah Museum of Natural History, Denver Museum of Nature and Science, Raymond M. Alf Museum of Paleontology, The Bureau of Land Management (Kanab), and others. The work included herein was reviewed and edited by several co-authors, as described above.

**Chapter Five**

Eric Roberts: Supervision, Investigation [*field assistance*], Writing - Review & Editing

Alan Titus: Investigation [*field assistance*], Writing - Review & Editing

This published chapter is the primary work of the candidate in collaboration with the above co-authors. These contributors assisted with fieldwork and manuscript review and editing. The article was also refined based on helpful feedback from the journal editors and peer review.

**Chapter Six**

Eric Roberts: Conceptualization, Writing - Review & Editing

Carl Spandler: Supervision, Writing - Review & Editing

This publication-style chapter is the primary work of the candidate in collaboration with the above co-authors who provided helpful feedback and guidance. Investigation was also facilitated by Kevin Blake, Shane Askew, Yi Hu, and Huiqing (Jeffrey) Huang at the Advanced Analytical Centre at James Cook University.

**Chapter Seven**

Eric Roberts: Supervision, Writing - Review & Editing

---

## List of Publications

**Beveridge, T. L.,** Roberts, E. M., Ramezani, J., Titus, A. L., Eaton, J. G., Irmis, R. B., & Sertich, J. J. W. (2022). Refined geochronology and revised stratigraphic nomenclature of the Upper Cretaceous Wahweap Formation, Utah, U.S.A. and the age of early Campanian vertebrates from southern Laramidia. *Palaeogeography, Palaeoclimatology, Palaeoecology*, 591, 110876. doi.org/10.1016/j.palaeo.2022.110876

**Beveridge, T. L.,** Roberts, E. M., & Titus, A. L. (2020). Volcaniclastic member of the richly fossiliferous Kaiparowits Formation reveals new insights for regional correlation and tectonics in southern Utah during the latest Campanian. *Cretaceous Research*, 114, 104527. doi.org/10.1016/j.cretres.2020.104527

**Beveridge, T.** (2019). Multifaceted geochemical characterization for pre-Quaternary bentonite tephrostratigraphy [oral presentation; awarded best presentation]. GSA Earth Sciences Student Symposium, Brisbane. gesssq.org/2019

**Beveridge, T.L.,** Roberts, E.M., Ramezani, J., & Titus, A.L. (2019). New high-precision U-Pb geochronology for the Wahweap Formation, southern Utah, and implications for Late Cretaceous dinosaur evolution in North America [oral presentation]. Society of Vertebrate Paleontology 79<sup>th</sup> Annual Meeting, Brisbane. vertpalaeo.org/wp-content/uploads/2021/03/SVP-Program-book-v8\_w-covers.pdf

**Beveridge, T.L.,** Roberts, E.M., & Ramezani, J. (2018). High-resolution correlation and bentonite tephrochronology in the Campanian Western Interior Basin [poster presentation]. Goldschmidt, Boston. goldschmidtabstracts.info/2018/186.pdf

**Beveridge, T.L.,** Roberts, E.M., Ramezani, J., Eberth, D., Rogers, R.R., & Bowring, S. (2017). A new approach to correlating vertebrate faunas by combining high precision U-Pb geochronology with geochemical tephrostratigraphy: A case example from the Campanian Western Interior Basin [poster presentation]. Society of Vertebrate Paleontology 77<sup>th</sup> Annual Meeting, Calgary. vertpalaeo.org/wp-content/uploads/2021/03/SVP-2017-program-book-v6-Print-Ready-with-front-cover.pdf

*See Appendix A for more information.*

---

## Thesis Abstract

Litho- and chronostratigraphic context is critical for investigation of richly fossiliferous Campanian strata in western North America. These strata preserve perhaps the most diverse Cretaceous terrestrial ecosystems known from anywhere in the world and host numerous representatives of classic dinosaur clades such as Tyrannosaurs, Hadrosaurs, Ankylosaurs, and Ceratopsians. Reconstructions of these ecosystems rely on the spatio-temporal framework within which fossil localities are placed; however, the scope of recent palaeoecological studies has surpassed the resolution of supporting age and stratigraphic constraints. As such, this project was designed to refine the litho- and chronostratigraphic understanding of fossiliferous Campanian rocks, particularly those from southern Utah, to support continental-scale palaeoecological studies including hypothesized latitudinal endemism, tempos of biotic turnover, and pre-extinction diversity decline of dinosaurs and other faunal and floral groups.

Investigation of interbedded, devitrified volcanic ash beds (bentonites) constituted the core of this project. A high precision temporal framework was constructed using U-Pb geochronology of bentonite zircons via the chemical abrasion isotope dilution thermal ionization mass spectrometry (CA-ID-TIMS) approach. This thesis focused on the Campanian strata of southern Utah, namely the Wahweap and Kaiparowits formations, and this work fits within a broader project including temporal refinement of strata from Alberta to New Mexico. These data were used to construct Bayesian age-stratigraphic models for formation stratotype sections, which provides robust ages with appropriately propagated uncertainties for any stratigraphic level at one-meter increments throughout the modelled units.

Lithostratigraphic refinement included formal recognition and naming of seven previously described informal subdivisions of the Wahweap and Kaiparowits formations, and discovery and description of an entirely new member from the top of the Kaiparowits Formation. The new member names are, in ascending order, the Last Chance Creek, Reynolds Point, Coyote Point, and Pardner Canyon members of the Wahweap Formation, and the Tommy Canyon, The Blues, Powell Point, and Upper Valley members of the Kaiparowits Formation. Stratigraphic correlations of measured sections within the Kaiparowits Formation were refined by comparing high-precision type section bentonite ages with those from isolated sections, also using Bayesian age-stratigraphic models. This process included correlation of bentonite marker horizons and the formal recognition of six definable beds; the Star Seep, Horse Mountain, Death Ridge, Paria Hollow, Deadmans Corner, and Overlook bentonite beds. Finally, bentonite characterization and correlation (tephrostratigraphy) using zircon phenocrysts was demonstrated to be a viable tool for intra-formational and basin scale correlation. This technique can be applied to propagate high precision ages from dated type section bentonites with isolated outcrops to enhance the value of high-precision geochronology.

---

## Table of Contents

<b>Chapter One.....</b>	<b>1</b>
Preface.....	2
1.1 Project overview.....	3
1.2 The Western Interior Basin.....	4
1.3 Key Campanian strata.....	8
1.3.1 Belly River Group.....	8
1.3.2 Judith River Formation.....	9
1.3.3 Two Medicine Formation.....	11
1.3.4 Wahweap and Kaiparowits formations.....	11
1.3.5 Fruitland and Kirtland formations.....	12
1.4 Late Campanian biogeography.....	13
1.5 Research focus and thesis structure.....	15
<b>Chapter Two.....</b>	<b>17</b>
Preface.....	18
2.1 Introduction.....	19
2.2 Approach context.....	19
2.3 Bentonite sampling and preparation.....	21
2.3.1 Sample collection.....	21
2.3.2 Mineral separation.....	24
2.3.3 Zircon selection.....	24
2.4 Equipment preparation.....	26
2.4.1 Dissolution vessels and nano-capsules.....	26
2.4.2 Hex beakers.....	27
2.4.3 Sample beakers.....	28
2.4.4 Wash tubes.....	29
2.5 Laboratory procedures.....	29
2.5.1 Thermal annealing.....	30

---

2.5.2 Partial dissolution.....	30
2.5.3 Zircon rinse .....	31
2.5.4 Tracer spike and total dissolution.....	32
2.5.5 Chemical conversion.....	34
2.5.6 Anion exchange column chemistry – preparation .....	34
2.5.7 Anion exchange column chemistry – procedure .....	35
2.6 Machine operation.....	39
2.6.1 Load filaments.....	39
2.6.2 Loading mass spectrometer.....	40
2.6.3 Operating the mass spectrometer .....	41
2.7 Data reduction and uncertainties .....	45
2.7.1 Fractionation correction uncertainty ( $\alpha_{Pb}$ ).....	45
2.7.2 Common lead uncertainty ( $Pb_c$ ) .....	46
2.7.3 Oxygen isotope uncertainty ( $\delta^{18}O$ ).....	46
2.7.4 Initial thorium uncertainty ( $Th_i$ ).....	46
2.8 Summary of outcomes.....	47
2.9 Glossary.....	50
<b>Chapter Three .....</b>	<b>51</b>
Preface.....	52
Abstract .....	53
3.1 Introduction .....	54
3.2 Previous work.....	57
3.2.1 Lithostratigraphy .....	57
3.2.2 Chronostratigraphy.....	58
3.2.3 Paleontology.....	59
3.3 Lithostratigraphic nomenclature of the Wahweap Formation.....	61
3.3.1 Last Chance Creek Member .....	61
3.3.2 Reynolds Point Member.....	62
3.3.3 Coyote Point Member .....	62



---

3.3.4 Pardner Canyon Member .....	63
3.4 Materials and methods .....	63
3.4.1 Stratigraphy and field sampling .....	63
3.4.2 U-Pb LA-ICP-MS geochronology of sandstones .....	65
3.4.3 U-Pb CA-ID-TIMS geochronology of ash fall bentonites .....	65
3.4.4 U-Pb LA-ICP-MS geochronology of reworked bentonites .....	66
3.4.5 Comparison of U-Pb data .....	66
3.5 Geochronological results .....	67
3.5.1 Results: High-precision CA-ID-TIMS bentonite ages .....	67
3.5.2 Results: Reworked bentonite LA-ICP-MS ages .....	70
3.5.3 Results: Detrital zircon LA-ICP-MS ages .....	70
3.6 A new chronostratigraphic framework for the Wahweap Formation .....	72
3.6.1 Member boundaries and features .....	74
3.6.2 Upper and basal formation boundaries .....	75
3.6.3 Regional correlation .....	77
3.6.4 North American Land Mammal Ages .....	78
3.7 Improved chronostratigraphic constraint for fossil taxa .....	79
3.7.1 Spatio-temporal distribution of vertebrates .....	82
3.7.2 Age revision for key taxa .....	85
3.7.3 Long distance correlation of taxa: Tyrannosaurid case example .....	86
3.8 Conclusions .....	86
<b>Chapter Four .....</b>	<b>89</b>
Preface .....	90
Abstract .....	91
4.1 Introduction .....	92
4.2 Previous Work .....	95
4.2.1 Lithology and depositional environment .....	95
4.2.2 Stratigraphy and formation boundaries .....	97
4.2.3 Geochronology .....	100

---

4.2.4 Paleontology.....	102
4.3 Member Subdivision Nomenclature.....	103
4.3.1 Tommy Canyon Member .....	104
4.3.2 The Blues Member .....	105
4.3.3 Powell Point Member.....	105
4.4 Materials and Methods .....	106
4.4.1 Field techniques.....	106
4.4.2 Laboratory techniques .....	107
4.4.3 Bayesian age-stratigraphic model .....	108
4.4.4 Reference section calibration .....	109
4.5 Results .....	110
4.5.1 New high-precision geochronology .....	110
4.5.2 Revised intraformational correlation.....	111
4.6 Bentonite bed nomenclature.....	114
4.6.1 Horse Mountain Bentonite Bed.....	114
4.6.2 Paria Hollow Bentonite Bed.....	116
4.6.3 Deadmans Corner Bentonite Bed .....	116
4.6.4 Overlook Bentonite Bed.....	117
4.6.5 Informal bentonite horizons .....	117
4.7 Geologic Discussion.....	119
4.7.1 Refinement of stratigraphic correlations .....	119
4.7.2 Member boundary ages .....	121
4.7.3 Linear sediment accumulation rate estimates.....	122
4.7.4 Regional correlation .....	123
4.8 Paleontologic discussion .....	125
4.8.1 Guidelines for the application of new model ages .....	125
4.8.2 Examples of age refinement for fossil localities .....	128
4.9 Conclusions .....	129

---

<b>Chapter Five .....</b>	<b>131</b>
Preface.....	132
Abstract .....	133
5.1 Introduction.....	134
5.2 Previous work.....	136
5.2.1 Lithostratigraphy .....	136
5.2.2 Basal contact .....	136
5.2.3 Member subdivisions .....	137
5.2.4 Upper contact and the Table Cliff Syncline .....	138
5.2.5 Geochronology .....	140
5.3 Materials and methods .....	140
5.4 Sedimentological descriptions.....	142
5.4.1 Lithological descriptions .....	142
5.4.2 Mudstone mineralogy.....	145
5.4.3 Sandstone petrography .....	146
5.4.4 Concretions .....	148
5.5 Lithostratigraphy .....	150
5.5.1 The Upper Valley Member.....	150
5.5.2 Member field description .....	154
5.6 Detrital zircon geochronology.....	156
5.6.1 Maximum depositional age .....	156
5.6.2 Regional correlation .....	159
5.6.3 Detrital zircon provenance .....	160
5.7 Tectonic implications .....	162
5.8 Conclusions .....	165
<b>Chapter Six .....</b>	<b>167</b>
Preface.....	168
Abstract .....	169
6.1 Introduction.....	170

---

6.2 Background .....	173
6.2.1 Bentonite tephrostratigraphy .....	173
6.2.2 Previous bentonite characterization.....	173
6.2.3 Study areas .....	176
6.3 Experimental design.....	176
6.4 Fieldwork and sample preparation .....	178
6.4.1 Bentonite collection.....	178
6.4.2 Mineral separation.....	178
6.5 Characterization using zircon morphology .....	180
6.5.1 Zircon imaging procedure .....	182
6.5.2 Zircon morphology results .....	182
6.5.3 Morphology interpretation .....	184
6.6 Characterization using melt inclusions.....	189
6.6.1 Scanning electron microscopy procedure.....	189
6.6.2 Melt inclusion morphology results.....	192
6.6.3 Melt inclusion major element composition results.....	194
6.6.4 Melt inclusion interpretation .....	194
6.7 Characterization using zircon chemistry .....	196
6.7.1 Microbeam analysis procedure.....	197
6.7.2 Lu-Hf isotopic composition results .....	197
6.7.3 $\epsilon$ Hf interpretation .....	200
6.8 Discussion .....	204
6.8.1 Utility for bentonite tephrostratigraphy.....	204
6.8.2 Significance.....	206
6.8.3 Limitations .....	208
6.8.4 Implications.....	209
6.8.5 Formal bentonite beds .....	211
6.9 Conclusions .....	211

---

<b>Chapter Seven</b> .....	<b>213</b>
Preface.....	214
7.1 Summary of findings.....	215
7.1.1 Lithostratigraphic compilation and refinement .....	215
7.1.2 Bentonite identification and collection.....	215
7.1.3 High-precision bentonite geochronology .....	215
7.1.4 Refined stratigraphic correlations .....	218
7.1.5 Bentonite tephrostratigraphy .....	218
7.2 Implications of thesis outcomes .....	221
7.3 Recommendations for future work.....	222
<b>References</b> .....	<b>225</b>
<b>Appendix A</b> .....	<b>253</b>
<b>Appendix B</b> .....	<b>263</b>
<b>Appendix C</b> .....	<b>288</b>

---

## List of Figures

Fig. 1.1 Tectonic map of the Western Interior Basin .....	5
Fig. 1.2 General tectonic cross-section of western North America (Mesozoic).....	6
Fig. 1.3 Palaeogeography of western North America at <i>ca</i> 75 Ma .....	7
Fig. 1.4 Photographs of late Campanian exposures in northern and southern field areas .....	10
Fig. 1.5 Summary of work presented in this thesis .....	14
Fig. 2.1 Summary of the laboratory procedure for CA-ID-TIMS .....	20
Fig. 2.2 Examples of bentonite outcrops and more .....	22
Fig. 2.3 Demonstration of zircon morphological characteristics.....	25
Fig. 2.4 Various Teflon containers used in the Pb clean laboratory.....	27
Fig. 2.5 Photographs and schematic diagram of dissolution vessel components .....	28
Fig. 2.6 Examples of zircon internal textures and how they relate to ID-TIMS pre-treatment.....	30
Fig. 2.7 Anion exchange column chemistry carousel set up .....	36
Fig. 2.8 Schematic summary of chemical purification of uranium and lead.....	37
Fig. 2.9 Thermal ionisation mass spectrometer turret during a filament change .....	40
Fig. 2.10 IsoProbe displays during the analysis of lead and uranium .....	42
Fig. 2.11 Tripoli displays during the analysis of lead and uranium .....	43
Fig. 2.12 ET_Redux during the final stages of analysis or after completion .....	44
Fig. 2.13 Comparison of new high-precision CA-ID-TIMS ages (2017/2018) .....	49
Fig. 3.1 Simplified geological map of the Kaiparowits Plateau.....	55
Fig. 3.2 Large-scale palaeogeographic and physiographic maps and reconstructions .....	56
Fig. 3.3 Exposures of the Wahweap Formation on the southern Kaiparowits Plateau .....	62
Fig. 3.4 Correlated stratigraphic sections of the Wahweap Formation .....	64
Fig. 3.5 Plots of zircon $^{206}\text{Pb}/^{238}\text{U}$ dates with $2\sigma$ uncertainties.....	68
Fig. 3.6 Probability distribution plots of detrital zircon U-Pb dates.....	71
Fig. 3.7 U-Pb geochronology and Bayesian age-stratigraphic model for the Wahweap Formation .....	73
Fig. 3.8 Photographs of the pedogenic surface separating the Wahweap & Kaiparowits formations...	76
Fig. 3.9 Generalised temporal correlation of Campanian strata across the Western Interior .....	78

---

Fig. 3.10 Spatio-temporal distribution of Wahweap Formation fossil localities.....	83
Fig. 4.1 Paleogeography western North America (Laramidia) at <i>ca</i> 75 Ma.....	93
Fig. 4.2 Southern Utah physiographic areas illustrating outcropping Cretaceous strata.....	94
Fig. 4.3 Solid geology map of the study area across the Table Cliff and Kaiparowits plateaus .....	96
Fig. 4.4 Outcrop photos of the Kaiparowits Formation.....	98
Fig. 4.5 Bayesian age-stratigraphic model for the full Kaiparowits Formation .....	110
Fig. 4.6 Revised correlation of Kaiparowits Formation stratigraphic sections .....	112
Fig. 4.7 Bentonite photographs from the Kaiparowits Formation.....	115
Fig. 4.8 Comparison of stratigraphy and age models for The Blues Member (KBC vs KWC).....	120
Fig. 4.9 Regional correlation of Campanian strata across western North America .....	124
Fig. 5.1 Oblique-perspective Google Earth Pro imagery of the Kaiparowits Formation .....	135
Fig. 5.2 Geological map of the study area showing the Upper Valley Member type area.....	139
Fig. 5.3 Photographs of the new Kaiparowits Formation lithofacies (Sv and Gpm).....	145
Fig. 5.4 Summary of sandstone petrography in the Upper Valley Member.....	147
Fig. 5.5 Summary of carbonate nodules in the Upper Valley Member.....	149
Fig. 5.6 Correlated stratigraphic sections linking the Upper Valley Member to the KBC stratotype. ....	151
Fig. 5.7 The Upper Valley Member stratotype section .....	153
Fig. 5.8 Field photographs showcasing the new member .....	155
Fig. 5.9 Approximate age of Upper Valley Member strata.....	157
Fig. 5.10 Regional correlation across key fossil-bearing Campanian units .....	159
Fig. 5.11 Detrital zircon age spectra for five sandstones from the Upper Valley Member.....	161
Fig. 5.12 Simplified paleo-drainage interpretation of the southern Cordilleran foreland basin.....	164
Fig. 6.1 Summary of methodology.....	172
Fig. 6.2 Key localities relative to the <i>ca</i> 75 Ma paleogeography of western North America.....	175
Fig. 6.3 Sample localities in southern Utah.....	177
Fig. 6.4 Examples of bentonite outcrops and hand samples.....	181
Fig. 6.5 Zircon microphotographs.....	183
Fig. 6.6 SEM secondary electron imagery of loose zircons .....	185
Fig. 6.7 Pupin diagram highlighting the range of zircon forms observed in this study.....	186

---

Fig. 6.8 Summary data for zircon aspect ratio measurements.....	188
Fig. 6.9 Examples of zircon-hosted glass inclusion morphologies (ovoid and elongate) .....	190
Fig. 6.10 More examples of zircon-hosted glass inclusion morphologies (irregular and other).....	191
Fig. 6.11 Zircon-hosted glass inclusion total alkali versus silica (TAS) diagrams .....	192
Fig. 6.12 Zircon-hosted glass inclusion major element bivariate plots .....	193
Fig. 6.13 Demonstration of electron beam damage.....	195
Fig. 6.14 Summary of age vs $\epsilon\text{Hf}$ for bentonites in this study .....	199
Fig. 6.15 $\epsilon\text{Hf}$ signature for bentonites from southern Utah (correlation and distinction) .....	201
Fig. 6.16 $\epsilon\text{Hf}$ signature for contemporaneous bentonites from across the Western Interior .....	202
Fig. 6.17 Comparison of major element data for melt incls. and whole-rock bentonite samples .....	205
Fig. 6.18 Zircon from sample KP-07A with three 25 $\mu\text{m}$ ablation pits.....	207
Fig. 7.1 Litho- and chronostratigraphy of the Wahweap and Kaiparowits fms. prior to this study ....	216
Fig. 7.2 Updated and refined litho- and chronostratigraphy of the Wahweap and Kaiparowits fms. .	217
Fig. 7.3 Precise chronostratigraphic correlation of selected Campanian strata across Laramidia.....	219
Fig. 7.4 Precise correlation of the Dinosaur Park and Kaiparowits formations .....	220



---

## List of Tables

Table 2.1 Summary of bentonite ages generated during work at MIT .....	48
Table 3.1 Weighted mean U-Pb zircon ages for all Wahweap Formation samples .....	69
Table 3.2 Model ages for Wahweap Fm member boundaries generated using the new age model.....	75
Table 3.3 Shortlist of fossil localities from the Wahweap Formation.....	80
Table 4.1 New U-Pb CA-ID-TIMS zircon ages for the Kaiparowits Formation .....	107
Table 4.2 Compilation of age data used to make the new Kaiparowits age-stratigraphic model.....	109
Table 4.3 Model ages for Kaiparowits Fm member boundaries generated using the new age model	121
Table 4.4 Model and probable age ranges for portions of the Kaiparowits Formation.....	126
Table 4.5 Holotype locality information and revised ages for highlighted vertebrate species.....	127
Table 5.1 Lithofacies observed in the Upper Valley Member .....	143
Table 5.2 Facies associations observed in the Upper Valley Member .....	144
Table 5.3 Qualitative results of mudstone mineralogy determined using XRD analysis .....	146
Table 5.4 Summarized maximum depositional age data.....	158
Table 6.1 Sample summary including names, types, stratigraphic units, and regions .....	179
Table 6.2 Age and $\epsilon_{\text{Hf}}$ summary data for samples examined herein, listed in age order .....	198

# Chapter One

## Overview of fossiliferous Campanian strata of western North America



*Artwork by Raul Martin in Titus and Loewen (2013)*

**Preface**

This introductory chapter contextualizes the work included in this publication-based thesis by providing a broad overview of the geological setting and overarching research questions. This brief, unpublished chapter includes background information not described elsewhere that is helpful for situating each chapter within the known literature. This chapter also outlines the thesis structure and how each chapter relates to the broader research topic; a short summary of which is also included in the preface of each chapter.

## 1.1 Project overview

Upper Cretaceous strata from western North America host some of the richest and most diverse fossil records in the world (Russell, 1967; Sloan, 1969; Sahni, 1972; Horner, 1989; Sankey, 2001; Mallon *et al.*, 2012; Titus and Loewen, 2013). These rocks are exposed in a belt that covers a broad latitudinal range from Alaska to Mexico, which facilitates spatially detailed comparison of palaeo-ecosystems across a north to south transect of the continent. Paleontological research within these strata began over 130 years ago in northern regions and included the identification of iconic dinosaur fauna, while southern areas have generally been the subject of more recent detailed investigation. Over the decades, growing fossil collections illustrate an increasingly comprehensive portrayal of Late Cretaceous ecosystems represented within a suite of key, richly fossiliferous units. Increasingly, the focus of many investigations has shifted to understanding continental scale floral and faunal patterns such as latitudinal endemism vs cosmopolitanism, rates of biotic turnover, and diversity decline preceding the Cretaceous-Palaeogene extinction event (*e.g.*, Lehman, 1997, 2001; Gates *et al.*, 2010; Sampson *et al.*, 2010; Lucas *et al.*, 2016; Chiarenza *et al.*, 2019; Dean *et al.*, 2020; Condamine *et al.*, 2021; Maidment *et al.*, 2021). These concepts are founded on large compilations of spatially and temporally resolved fossil locality data, and the resolution of this data is reflected in the confidence of the broader concepts they support.

Chronostratigraphic resolution and correlation have been identified as one of several major limitations in testing continental-scale palaeoecological hypotheses (Sullivan and Lucas, 2006; Lucas *et al.*, 2016; Dean *et al.*, 2020). Existing temporal constraints comprise an ad hoc assortment of geochronology derived from various methods across decades of work including frequent recalibration of natural standards (*e.g.*, Deino and Potts, 1990; Renne *et al.*, 1998; Kuiper *et al.*, 2008; Phillips *et al.*, 2022). These data constitute the primary tool for basin scale correlation of strata and interbedded fossil material; however, continental palaeoecological investigations require correlation with better resolution than the existing chronostratigraphy can support (*e.g.*, Gates *et al.*, 2010 vs Lucas *et al.*, 2016). Biotic processes such as rates of evolution and extinction occur at timescales in the order of tens of thousands of years (*e.g.*, Mallon *et al.*, 2012), which is finer than the precision of existing radioisotopic constraints on Late Cretaceous strata in western North America. Investigation of evolutionary and palaeoecological processes requires a continental-scale high resolution temporal framework to precisely constrain rates of biotic turnover within a single field area and convincingly demonstrate synchronicity or diachroneity across distant regions (Ramezani *et al.*, in review).

The purpose of work compiled in this thesis and as part of a larger collaborative project (US NSF grant EAR1424892; Ramezani *et al.*, in review) was to refine the chronostratigraphic framework of Campanian fossil-bearing strata across western North America. The primary tool for this refinement was high precision U-Pb zircon geochronology using chemical abrasion isotope dilution thermal ionization mass spectrometry (CA-ID-TIMS; see Ch. 2). As in previous work, datable mineral

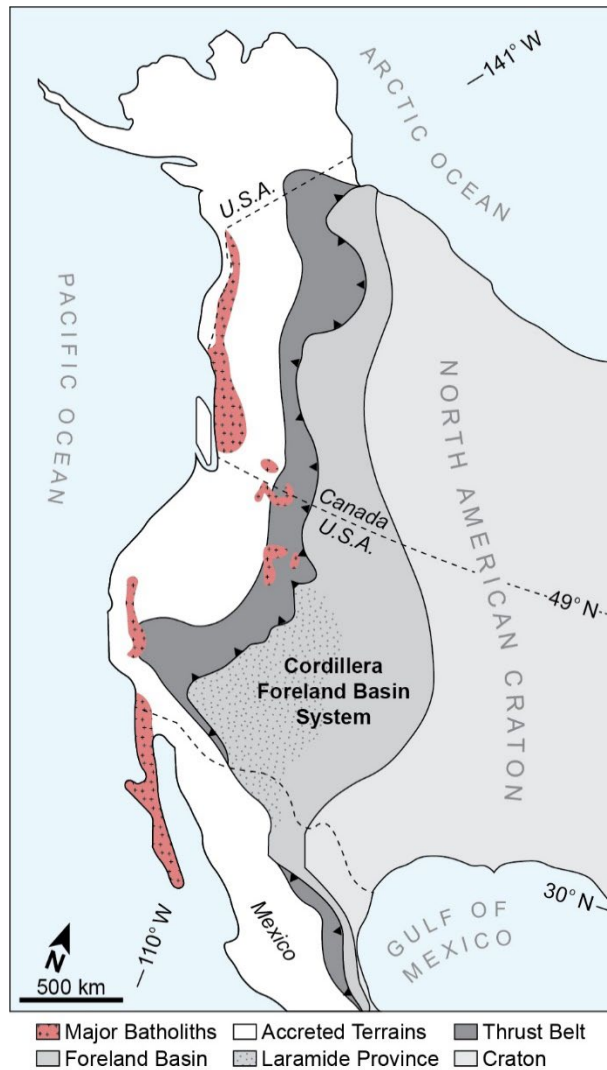
phenocrysts from weathered volcanogenic horizons (mostly bentonite) were used to obtain true depositional ages for Campanian strata from key fossil localities (see Ch. 3 and 4). Advantages of the geochronologic approach used in this project include; 1) greater precision and accuracy due to the application of an anthropogenic tracer solution rather than natural standards, and chemical pre-treatment that mitigates open system behavior (both only possible using zircon); 2) a unified approach to chronostratigraphic correlation across the basin whereby bentonite ages with internal uncertainties can be used to precisely correlate outcrops separated by tens to hundreds of kilometers; and 3) the application of a Bayesian algorithm (*i.e.*, Haslett and Parnell, 2008; Parnell *et al.*, 2008, 2011) to model the propagated uncertainty throughout a formation and more appropriately describe the precision with which any given horizon is constrained.

The construction of a new temporal framework also required detailed lithostratigraphy for the units under investigation. Work presented in this thesis focused on Campanian strata of the Kaiparowits Plateau and constitutes the southern Utah portion of the larger collaborative project. A comprehensive review of the Wahweap and Kaiparowits formations was corroborated by detailed fieldwork (see Ch. 3 and 4), which also led to the identification and formal description of an unrecognized 145 m of unique strata capping the Kaiparowits Formation (Upper Valley Member; see Ch. 5). A geochronology-based approach was employed to refine correlation of multiple measured sections throughout the Kaiparowits Formation using dated bentonite horizons (see Ch. 4), which was followed by a novel investigation of bentonite characterization methods for refined correlation (bentonite tephrostratigraphy [Ch.6]). These combined approaches were successfully applied to correlating bentonite horizons within the Kaiparowits Formation, as well as with bentonites from contemporaneous units to the north. The procedures are shown herein as viable new tools for correlation in any situation involving zircon-bearing interstratified volcanic products and may be used to propagate high-precision ages from dated outcrops to isolated areas.

Outcomes presented in this thesis have implications for continental scale models of late Cretaceous ecosystem dynamics. The detailed studies presented in each chapter lay the foundations for future palaeoecological studies by refining the context of fossil material from the study areas and by demonstrating a refined procedure for the development of temporal frameworks for fossil-bearing strata. To help contextualize the significance of these advancements, a summary of the broader context of the work is included in this chapter, particularly for topics relevant to but not explicitly discussed in the publication-form chapters. These include continental-scale basin dynamics, stratigraphy of coeval units, and continental-scale palaeoecological hypotheses.

## **1.2 The Western Interior Basin**

During the Cretaceous period, landform evolution in western North America was defined by a strongly convergent retro-arc foreland basin system featuring cordilleran thrusting and associated basin



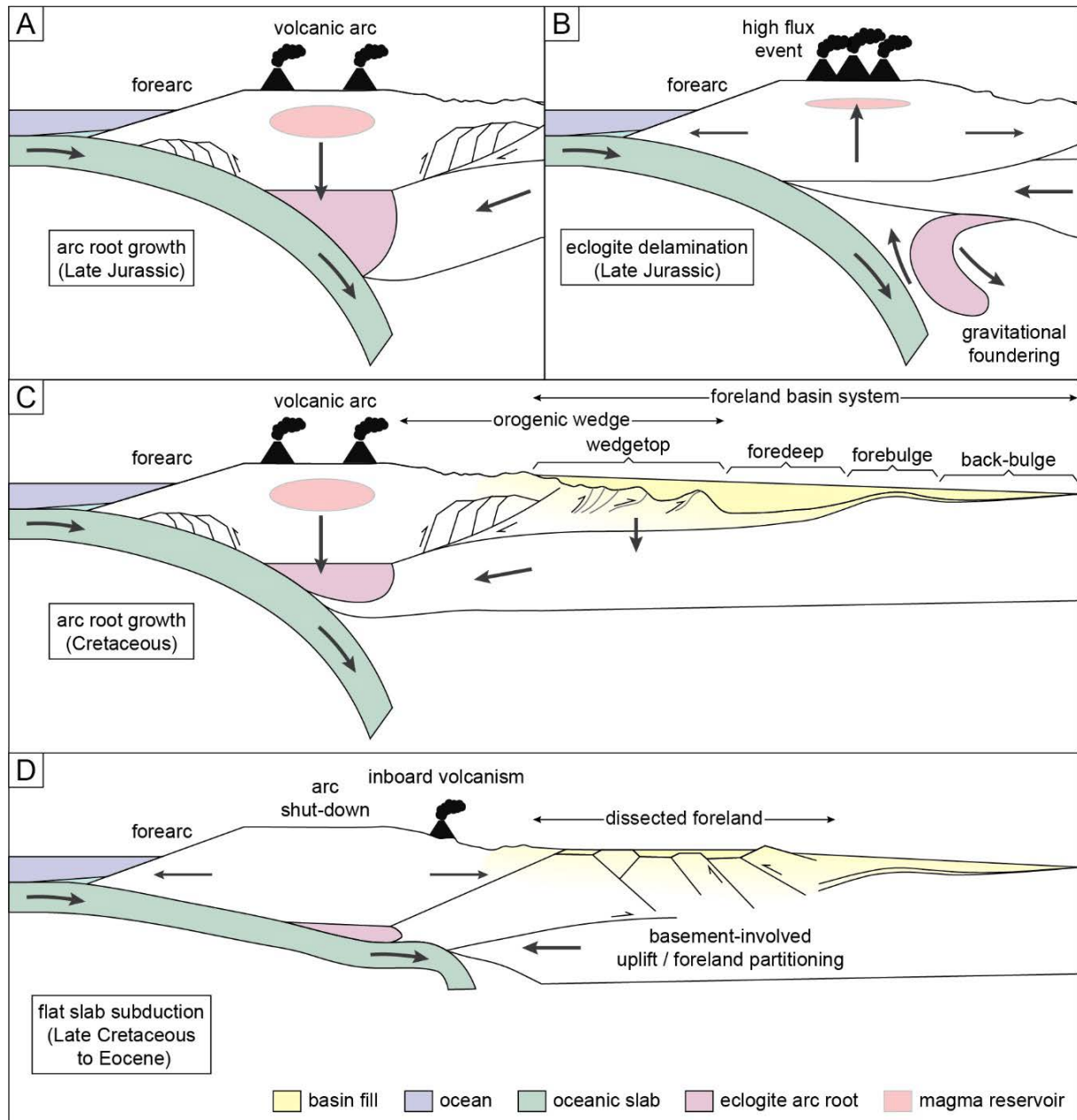
**Fig. 1.1** Tectonic map of the Cordillera Foreland Basin System / Western Interior Basin modified after DeCelles (2004).

temporal sense due to the restricted but palaeoecologically important window they represent.

A ribbon of alluvial and coastal plain environments spanned the eastern margin of Laramidia extending from Alaska to Mexico along the western flank of the retro-arc basin (e.g., Eberth and Hamblin, 1993; Rogers, 1998; Eberth *et al.*, 2004; Lucas *et al.*, 2006; Roberts, 2007; Fanti and Catuneanu, 2010; Fiorillo *et al.*, 2010; Seymour and Fielding, 2013; Rogers *et al.*, 2016; Adams *et al.*, 2017; Lehman *et al.*, 2019). These restricted terrestrial environments, which abutted the thrust belt to the west and the seaway to the east, are now well-exposed and present a rare and important opportunity for the reconstruction of Cretaceous non-marine ecosystems across a semi-continuous range of latitudes (Fig. 1.3). These strata also present an unmatched opportunity for the development and application of alluvial sequence stratigraphic models (e.g., Kauffman and Caldwell, 1993; Shanley and McCabe, 1995;

subsidence (Fig. 1.1) (Cross, 1986; DeCelles, 2004; DeCelles *et al.*, 2009). Subduction of the Farallon plate beneath the North America Plate resulted in an extensive continental arc system and the accretion of exotic terrains at the western margin (Fig. 1.2) (Dumitru, 1990; DeCelles, 2004). A compressional regime led to the development of a long-lived thrust belt behind the volcanic arc that was active from roughly the Late Jurassic (Kimmeridgian) to the Eocene (Ypresian) and crustal loading associated with this tectonic thickening resulted in a predominantly terrestrial foreland basin system referred to as the Cordilleran Foreland Basin or Western Interior Basin (Cross, 1986; DeCelles, 2004). A thick clastic sedimentary succession accumulated within the basin foredeep, interspersed with hiatuses associated with periods of tectonic quiescence or foreland uplift. Between *ca* 110 to 70 Ma, the basin was flooded by the epeiric Western Interior Seaway, temporarily separating North America into two subcontinents: Appalachia in the east and Laramidia in the west (cf. Sampson *et al.*, 2010). These subdivisions are generally used in both a spatial and vague





**Fig. 1.2** General tectonic cross-section (not to scale) of western North America during the late Mesozoic illustrating dynamic processes at the western plate boundary at the approximate latitude of Utah. Adapted from DeCelles and Giles (1996), DeCelles (2004), and DeCelles et al. (2009).

Rogers, 1998; Corbett *et al.*, 2011; Jinnah and Roberts, 2011; Seymour and Fielding, 2013; Rogers *et al.*, 2016). The strata appear as stacked and interfingering cycles of sea level transgressions and regressions reflected by marine deposits in the east, broadly transitioning through near-shore and coastal settings to alluvial plain environments in the west. Basin sediments were derived from the shedding highlands of the thrust belt and arc to the west and, in southern regions, from arc and uplifted terrains in the south (Eberth and Hamblin, 1993; Lawton *et al.*, 2003; Dickinson and Gehrels, 2008; Pecha *et al.*, 2018). Heterogeneous rates of subsidence across the basin reflect localized subsidence patterns as



**Fig. 1.3** Palaeogeography of western North America at approximately 75 Ma illustrating the location of key areas examined in the collaborative project. Inset shows the Cretaceous portion of the International Chronostratigraphic Chart (v2022/02; [stratigraphy.org](http://stratigraphy.org)) with the Campanian Stage highlighted in red for reference. Palaeogeographic reconstruction adapted from ©2013 Colorado Plateau Geosystems Inc.

evidenced by the significant discrepancy in thicknesses of contemporaneous packages in different parts of the basin (*cf.* Kaiparowits Formation vs Dinosaur Park Formation). Variations in the timing and magnitude of flexural loading across the basin is suspected based on patterns of spatio-temporal progression of the Bearpaw Seaway (the final transgression for the Western Interior Seaway) where



maximum flooding surfaces occur earlier in southern parts of Laramidia than in northern areas (see Roberts, 2007).

A transition from Sevier- to Laramide-style tectonics occurred in the latest Cretaceous during the final stages of the retro-arc foreland system, particularly in southern regions. At the western plate margin, the angle of the descending slab began to flatten, thought to be due to subduction of a comparably buoyant oceanic plateau (Cross and Pilger, 1979; Liu *et al.*, 2010). The impinging slab disrupted the arc regime causing volcanism at the arc (*e.g.*, Sierra Nevada and Idaho batholiths) to cease by or shortly after 80 Ma and migrate hundreds of kilometers inboard of the plate boundary (Coney and Reynolds, 1977; Dumitru, 1990). Around this time, the transition from Sevier to Laramide tectonics, equivalent to a shift from upper crustal thrusting to basement involved uplifts, resulted in partitioning of the foreland into isolated depositional centers punctuated by uplifted terrains (Fig. 1.2) (Coney and Reynolds, 1977; Bird, 1998; DeCelles, 2004). Foreland intermontane basins persisted within these uplifts into the Cenozoic.

### 1.3 Key Campanian strata

The collection of studies presented in this thesis pertain to richly fossiliferous Campanian strata from across western North America (Fig. 1.3). Rocks from southern Utah constitute the core of the work herein and several contemporaneous areas across Laramidia are directly relevant for correlation and comparison of strata their and interbedded biota (*e.g.*, Gates *et al.*, 2010; Ramezani *et al.*, in review).

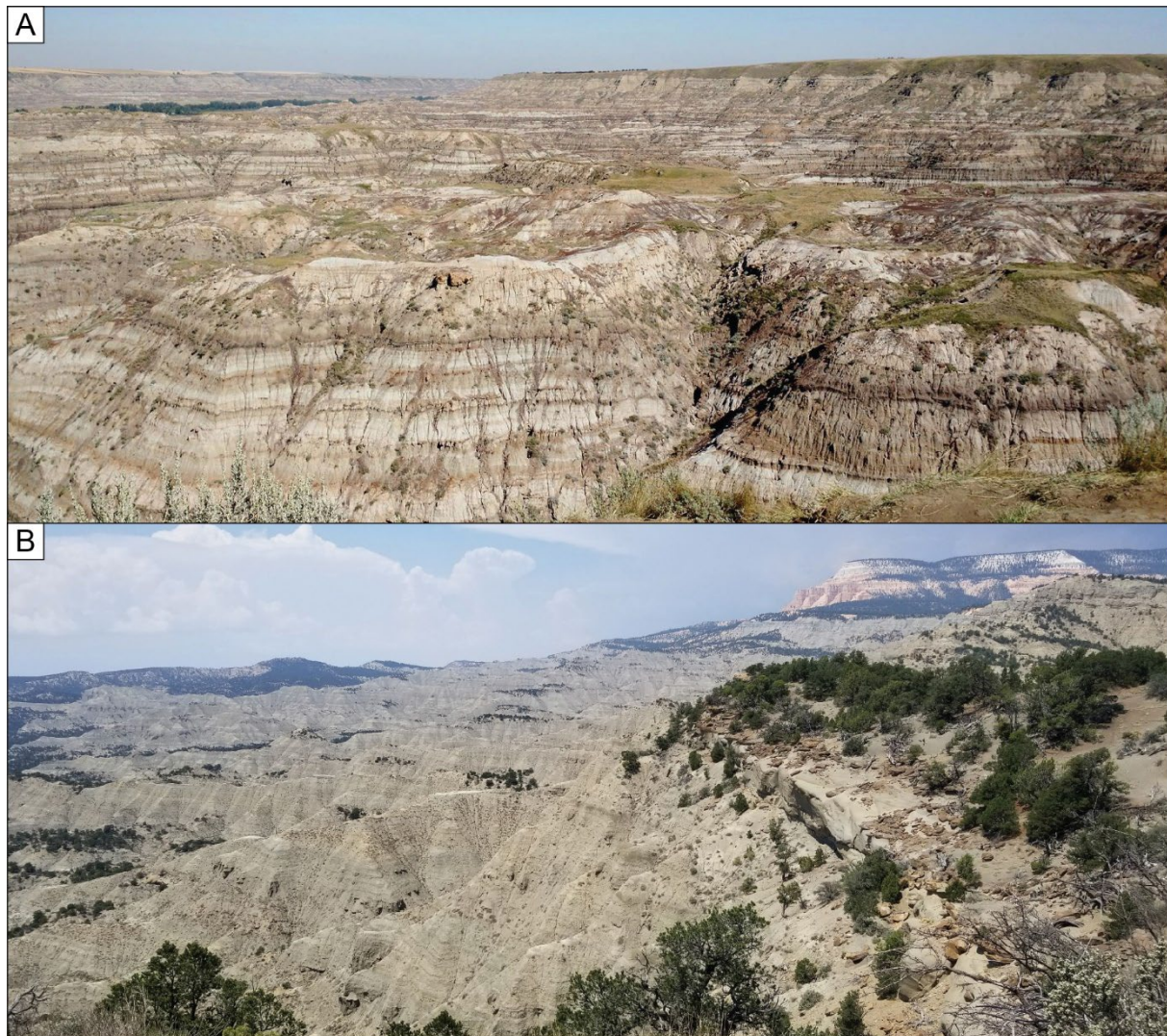
#### 1.3.1 Belly River Group

The Belly River Group outcrops primarily in central and southern Alberta and comprises, in ascending stratigraphic order, the Foremost, Oldman, and Dinosaur Park formations (Eberth and Hamblin, 1993; Eberth, 2005, 2015; Mallon *et al.*, 2012). These units represent a range of fluvial to estuarine environments that are capped by a transitional phase reflected by coastal swamps of the Lethbridge Coal Zone of the uppermost Dinosaur Park Formation, and conformably overlain by marine shales of the Bearpaw Formation. The group is underlain by the marine Pakowki Formation, and the Foremost Formation also contains two defined coal zones: the McKay and Taber at the base and top of the unit, respectively. Strata are exposed within coulees and palaeo-glacial valleys that incise the flat, prairie landscape, such as within Dinosaur Provincial Park where the Red Deer River valley creates broad exposures of late Campanian-aged rocks (Fig. 1.4). In this area, the Foremost (subsurface), Oldman, and Dinosaur Park formations are approximately 143, 53, and 80 m thick, respectively (Eberth and Hamblin, 1993). Further south, the Dinosaur Park Formation thins roughly proportional to thickening of the Oldman Formation, whereby Eberth and Hamblin (1993) suggest the two units represent interaction of separately sourced clastic wedges/lobes. The very fine to fine grained, lithic poor sandstones of the Oldman Formation are separated from the overlying fine to medium grained sandstones with relatively more abundant lithic fragments that characterize the Dinosaur Park Formation by a regionally extensive,

time-transgressive discontinuity, which becomes younger southward. The age of the Belly River Group is broadly constrained by marine and mammaliaform biostratigraphy as Campanian (Eberth, 1990, 2005; Eberth and Hamblin, 1993). Radiometric ages support a Campanian age and include (prior to this study) K-Ar and  $^{40}\text{Ar}/^{39}\text{Ar}$  bentonite ages reported by Thomas *et al.* (1990), Eberth and Deino (1992), Eberth *et al.* (1992), and Eberth (2005). These strata have been prospected for fossil material for over one hundred years and represent one of the best sampled and most diverse terrestrial biotas in the world with hundreds of articulated and associated dinosaur specimens and countless isolated elements and materials (Russell, 1969; Dodson, 1971; Farlow, 1976; Beland and Russell, 1978; Eberth, 1990; Eberth and Hamblin, 1993; Currie and Russell, 2005; MacDonald *et al.*, 2005; Mallon *et al.*, 2012; Brown *et al.*, 2013; van der Reest and Currie, 2017; Lowi-Merri and Evans, 2020).

### 1.3.2 Judith River Formation

The type area of the Judith River Formation is in north-central Montana mainly within the Upper Missouri River Breaks National Monument (Rogers, 1998; Rogers *et al.*, 2016). Exposures occur as sparsely vegetated badland-style slopes within coulees and larger river valleys. The unit is 177 m thick at the only complete measured section (91-JRT-8 of Rogers *et al.*, 2016) and is thickest in the western part of the type area where strata are predominantly non-marine. Detailed lithostratigraphic work by Rogers *et al.* (2016) included three key reference sections across the type area that captured the east-west and stacked lithological diversity represented by the formation and described four member subdivisions. The basal Parkman Sandstone Member disconformably overlies the Claggett Shale with an erosional boundary reflected by up to two meters of relief over short lateral distances. The member, which is *ca* 16 m thick at its type section in the west, composes tan and light gray, fine- to medium-grained shallow marine sandstones with varied cross-bedding. It is conformably overlain by the sandstone dominated terrestrial strata of the McClelland Ferry Member, which is *ca* 70 m thick at its type section and includes basal beds of lignite and abundant fluvial sandstones. The top of the McClelland Ferry Member is marked by a surface referred to as the mid-Judith discontinuity that reflects an abrupt shift in depositional character correlated to the transition from sea level regression to transgression.  $^{40}\text{Ar}/^{39}\text{Ar}$  ages constrain this surface to *ca* 76.2 Ma (Rogers *et al.*, 2016). Above the discontinuity, ~90 m of mud-rich alluvial and paralic strata including coals, organic-rich horizons and carbon drapes are referred to the Coal Ridge Member, which reflects a significant increase in sediment accumulation rates compared to members below the discontinuity. Towards the eastern edge of the type area, distinctive marine-shoreface sandstones that interfinger with the mud dominated facies of the Coal Ridge Member are delineated as the Woodhawk Member. This unit composes a series of three fourth-order sequences that backstep towards the west, marking the progression of the rising Bearpaw Seaway until eventually both the Coal Ridge and Woodhawk members are overlain by the fully marine Bearpaw Shale, marked by a laterally extensive bed of disarticulated marine invertebrate shells (Rogers *et al.*,



**Fig. 1.4** Exposures of late Campanian strata from northern and southern field areas. A) Belly River Group (Dinosaur Park Formation) within Dinosaur Provincial Park near the Red Deer River, southern Alberta. Strata are exposed in coulees and palaeo-glacial valleys that incise the flat, prairie landscape. B) Kaiparowits Formation within Grand Staircase – Escalante National Monument at The Blues area, southern Utah. Strata are exposed as steep, poorly consolidated slopes across rugged terrain.

2016). The Judith River Formation is closely associated with the middle and upper portions of the Two Medicine Formation that outcrops to the west but is separated by the Sweetgrass arch. Towards the north, strata equivalent to the Judith River Formation includes those of what is now the Belly River Group and although earlier studies tried to amalgamate the nomenclature of these closely comparable units (e.g., Stanton and Hatcher, 1905; McLean, 1977), complications across the international border convoluted the process and nomenclatural parity was abandoned (see Eberth and Hamblin, 1993; Hamblin and Abrahamson, 1996). Despite a long history of research within the Judith River Formation, relatively few radiometric ages have been acquired. The most recent ages (prior to the present study) were reported by Rogers *et al.* (2016) based on  $^{40}\text{Ar}/^{39}\text{Ar}$  geochronology, which solidified previous interpretations of a middle to late Campanian age for the unit. The Judith River Formation is most



famous for its paleontologic pedigree whereby some of the first skeletal dinosaur material formally described from North America were recovered from its strata. The upper portion of the unit (namely the Coal Ridge Member) has high vertebrate fossil richness (Sahni, 1972; Rogers *et al.*, 2016) and the mammaliaform assemblage from these strata constitute the type-fauna of the Judithian North American Land Mammal 'Age' (see Lillegraven and McKenna, 1986; Cifelli *et al.*, 2004). Furthermore, the Judith River Formation and correlative Two Medicine Formation constitute excellent examples for the development and application of Campanian sequence stratigraphic models (see Rogers, 1998; Rogers *et al.*, 2016).

### *1.3.3 Two Medicine Formation*

The Two Medicine Formation is exposed across a ~225 km north-south belt in northwestern Montana (Rogers *et al.*, 1993; Rogers, 1998; Foreman *et al.*, 2008). The middle and upper portions of the unit represent western correlatives of the Judith River Formation, separated by the Sweetgrass arch, while the lower Two Medicine Formation is of early Campanian age (see Rogers *et al.*, 1993; Ramezani *et al.*, in review). The unit is closely associated with the Elkhorn Mountain Volcanics (Roberts and Hendrix, 2000; Foreman *et al.*, 2008) and comprises volcanoclastic sandstones and variegated mudstones and siltstones that interfinger with the volcanic facies. Formal subdivisions have not been designated, although three lithofacies were described by Lorenz (1981) including a lower association composed of sandstone sheets that reflect distributary channels in a distal deltaic plain, a middle association represented by discontinuous, lenticular sandstone deposits, and an upper association that reflects shallow braided streams within an upper alluvial plain setting. The *ca* 600-meter-thick Two Medicine succession thins towards the east, with diachronous upper and basal boundaries (Rogers, 1990; Rogers *et al.*, 1993). It is underlain by nearshore sandstones of the Virgelle Formation and overlain by the Bearpaw Formation in the type area and by the Saint Mary River Formation further west (Rogers, 1990; Rogers *et al.*, 1993). Due to its proximity to the thrust belt, parts of the formation in the west are dissected by inboard thrust sheet migration resulting in isolated exposures that can be difficult to correlate to one another (Rogers, 1990). Abundant volcanogenic horizons throughout the Two Medicine Formation (over 19 unique bentonite beds; Foreman *et al.*, 2008) have facilitated radioisotopic dating that indicate a broad Campanian age for the formation with deposition lasting for over 6 Myrs (Rogers *et al.*, 1993; Foreman *et al.*, 2008). An abundant vertebrate assemblage collected over the last century is reported from the Two Medicine Formation, particularly from the upper portion, and the unit is most famous for excellently preserved dinosaur nests and hatchlings (*e.g.*, Horner and Makela, 1979; Horner, 1989; Horner *et al.*, 1992).

### *1.3.4 Wahweap and Kaiparowits formations*

The Wahweap and Kaiparowits formations from southern Utah are extensively exposed across the Kaiparowits and Table Cliff plateaus (Fig. 1.4) and less prominently across the Markagunt and

Paunsaugunt plateaus (Eaton, 1991; Roberts, 2007; Jinnah and Roberts, 2011; Biek *et al.*, 2015). These rocks are most intensely studied within and around the Grand Staircase – Escalante National Monument, a remote wilderness area that was officially protected in 1996 due to its wealth of natural resources including exquisite preservation of Cretaceous ecosystems (Titus *et al.*, 2005, 2016; Titus and Loewen, 2013). Together, the Wahweap and Kaiparowits formations include up to *ca* 1270 m of strata (prior to work included in this thesis) preserving terrestrial ecosystems that span much of the Campanian stage (Eaton, 1991; Roberts *et al.*, 2005; Roberts, 2007; Jinnah *et al.*, 2009; Jinnah and Roberts, 2011). These units are the subject of detailed investigation in this thesis; the Wahweap Formation is described in Chapter 3 and the Kaiparowits Formation is described in Chapters 4 and 5.

### *1.3.5 Fruitland and Kirtland formations*

Cretaceous strata of the San Juan Basin in northwest New Mexico include strongly time-transgressive stacked and interfingering marine, marginal marine, and terrestrial successions. Campanian rocks from this region include the terrestrial Fruitland and Kirtland formations, which are commonly studied in the western and central outcrop areas of the basin (Lucas *et al.*, 2006; Sullivan and Lucas, 2006). In these areas, the Fruitland Formation averages a thickness of approximately 90 m and is conformably underlain by the Pictured Cliffs Sandstone. It includes the Ne-nah-ne-zad Member, which comprises thick coals, carbonaceous shales, and interbedded channel sandstones, and the overlying sandstone dominated Fossil Forrest Member that contains thinner coals and less mudstone (Hunt and Lucas, 1992; Lucas *et al.*, 2006; Sullivan and Lucas, 2006). The Fruitland Formation is conformably overlain by the Kirtland Formation, whereby the boundary is marked by the first occurrence of ferruginous sandstones that characterize the Bisti Bed. The Kirtland Formation comprises up to *ca* 600 m of interbedded sandstone, siltstone, mudstone, coal, and shale, and includes three formal members: the Hunter Wash, Farmington, and De-na-zin members (Hunt and Lucas, 2003; Sullivan and Lucas, 2006). Although previously described at the member level, the Bisti Bed was defined as a subdivision of the Hunter Wash Member by Sullivan and Lucas (2003). The Kirtland Formation is unconformably overlain by the Ojo Alamo Formation. Previous radiometric ages for these units composed  $^{40}\text{Ar}/^{39}\text{Ar}$  sanidine dates reported by Fassett and Steiner (1997) and Fassett and Heizler (2017) in the context of constraining the magnetochron C33n-C32r reversal that was identified in these strata 328 m above the Huerfanito Bentonite Bed, which was used as a reference datum in those studies due to stratal diachroneity. These ages demonstrate a late Campanian age for the Fruitland and Kirtland formations including the fossiliferous intervals within the Fossil Forest / Hunter Wash and De-na-zin members (the Hunter Wash and Willow Wash local faunas, respectively; Sullivan and Lucas, 2003, 2006). Due to the unique fossil assemblage represented by these local faunas and their relative stratigraphic position above other North American vertebrate assemblage ‘ages’, Sullivan and Lucas (2003) proposed the ‘Kirtlandian’ land vertebrate ‘age’ (see also Sullivan and Lucas, 2006). This biochronologic unit differed from previously


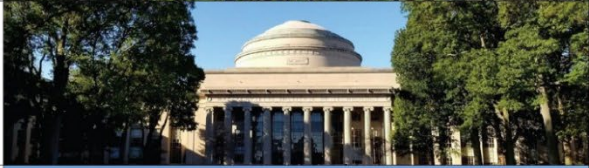




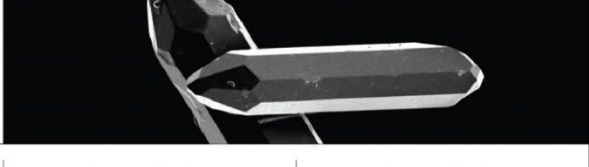
proposed land mammal ‘ages’ by incorporating large vertebrates (*i.e.*, dinosaurs) that were said to better define faunal assemblages that could be correlated across the continent.

#### 1.4 Late Campanian biogeography

The geographic distribution of dinosaurs across Laramidia during the late Campanian is inferred by some to reflect isolated speciation centers whereby large terrestrial fauna appear to have occupied limited geographic ranges (Russell, 1967; Sloan, 1969; Lehman, 1997, 2001; Sankey, 2001; Gates *et al.*, 2010, 2012; Sampson *et al.*, 2010, 2013a; Longrich, 2014; Williamson and Brusatte, 2014; Rivera-Sylva *et al.*, 2016; Dalman *et al.*, 2022). These isolated centers are interpreted from records of classic dinosaur clades whereby unique contemporaneous taxa at the species and genus level appear to show northern and southern endemism. Late Campanian ceratopsids have been studied in detail within this context and findings consistently support contemporaneous endemic centers across Laramidia with a potential boundary or transition in northern Utah/Colorado (Sampson *et al.*, 2010, 2013a; Longrich, 2014; Rivera-Sylva *et al.*, 2016; Dalman *et al.*, 2022). Detailed biogeographic analysis was conducted by Gates *et al.* (2010), which included a comprehensive review of material from six key localities across western North America. This statistical study identified highly divergent faunas for northern and southern zones separated by a transitional zone or a continuous latitudinal gradient. Given the absence of a physiographic barrier, many studies implicated a climatic gradient over the latitudinal range to explain the divergent faunas (Gates *et al.*, 2010; Sampson *et al.*, 2010; Burgener *et al.*, 2019, 2021).

The dinosaur endemism hypothesis is considered contentious by some based on several key concerns including, most relevant to this thesis, the resolution and accuracy of stratigraphic correlations. Several studies argue that the apparent endemism is an artefact derived from the comparison of time-transgressive strata across the Western Interior (*e.g.*, Sullivan and Lucas, 2006; Lucas *et al.*, 2016; Dean *et al.*, 2020). These authors suggest that uniformitarian rates of speciation explain the apparent diversity when distal faunas are considered diachronous. Available radiometric constraints used to support arguments for diachronous rather than endemic faunas were limited by the precision of these data, which is proportionally low compared to rates of biotic processes. The way in which age data were used in previous endemism investigations has also been questioned (*e.g.*, Lucas *et al.*, 2016; Dean *et al.*, 2020). The practice of time binning, whereby taxa are grouped into broad temporal brackets, has been proposed as oversimplistic for the investigation of fine scale processes such as rates of biotic turnover given also the complexities of taphonomic biases (Lucas *et al.*, 2016; Dean *et al.*, 2020). Temporally binning taxa using the age of their host stratigraphic units (*i.e.*, formation binning; Dean *et al.*, 2020) expands upon equal-interval time binning to recognize taphonomic influences; however, this approach still faces challenges regarding over-representation of temporal precision.

Overall, temporal clarity is a common theme in many continental scale, high-profile Late Cretaceous palaeoecological studies covering diverse perspectives (Gates *et al.*, 2010; Lucas *et al.*, 2016; Chiarenza

Context	Chapter One: Thesis Overview			
Method	Chapter Two: CA-ID-TIMS Methodology			
Publication	Chapter Three: Litho- and Chronostratigraphic Refinement of the Wahweap Fm			
Publication	Chapter Four: Litho- and Chronostratigraphic Refinement of the Kaiparowits Fm			
Publication	Chapter Five: New Volcaniclastic Member of the Kaiparowits Fm			
Publication	Chapter Six: Bentonite Tephrostratigraphy using Zircon Phenocrysts			
Context	Chapter Seven: Synthesis and Recommendations			
Compiled References		Appendix A: Collaborative Works	Appendix B: Extended Methods	Appendix C: Data Repository

**Fig. 1.5** Summary of work presented in this thesis with abbreviated chapter titles. Chapters One and Seven provide brief context for the thesis objectives and outcomes, Chapter Two composes a detailed methodology of the key approach, and Chapters Three through Six are presented as adapted research papers. References are compiled at the end of the main body of work, followed by appendices for collaborative work, extended methods, and raw data.

*et al.*, 2019; Dean *et al.*, 2020; Condamine *et al.*, 2021). Many of these tend to overlook or down-play the significance of temporal precision reflected within the large compilations of fossil locality data upon which the broader studies are founded. Continental scale studies are predisposed to employ coarse data groupings; however, these are undermined by the inherent juxtaposition between the rate of biotic processes under investigation and the resolution of ad-hoc, low precision temporal constraints presently available. The longevity of intervals of proposed endemism is also a vaguely or variously defined aspect of the ongoing discussion. Some authors appear to consider the period to cover the entire late Campanian

or even the entire Campanian, while others propose a short interval or short pulses of restricted dispersal (e.g., Longrich, 2014; Lucas *et al.*, 2016; Burgener *et al.*, 2021). A second phase of endemism in North America has also been proposed during the Maastrichtian (see Lehman, 1997, 2001; Sampson *et al.*, 2010; Vavrek and Larsson, 2010; Williamson and Brusatte, 2014), although this younger interval is not covered by work included in this thesis. The dinosaur endemism hypothesis is also plagued by other issues beyond the scope of this thesis such as biases pertaining to uneven collecting efforts, prevalence of exposures of particular intervals, excessive taxonomic delineation, and variable taphonomic factors (see Lucas *et al.*, 2016; Chiarenza *et al.*, 2019; Dean *et al.*, 2020; Maidment *et al.*, 2021; Ramezani *et al.*, in review); however, the focus of work presented herein is on refinement of stratigraphic correlations and the construction of a new temporal framework for Campanian strata from western North America.

### 1.5 Research focus and thesis structure

The focus of work presented herein is on closing this gap in the litho- and chronostratigraphic understanding of Campanian strata from western North America to facilitate future investigation of continental-scale palaeoecological hypotheses at a greater resolution than was previously possible. The work emphasizes temporal refinement and composes part of a larger project involving recalibration of strata from the Belly River Group in Alberta, the Two Medicine and Judith River formations in Montana, the Fruitland and Kirtland formations in New Mexico and, the focus of this thesis, the Wahweap and Kaiparowits formations in southern Utah. Objectives include:

- Compilation and re-examination of the lithostratigraphic understanding of the Wahweap and Kaiparowits formations
- Identification and collection of bentonite outcrops and samples
- High precision geochronology and characterization of bentonite samples
- Application of new age data for refined stratigraphic correlation and temporal constraint
- Investigation of bentonite characteristics to determine methods for correlation without reliance on high-precision ages

These objectives guided outcomes of the research and led to an improved understanding of the specific units examined herein, and to procedural refinements for stratigraphic correlation that can be implemented in similar instances anywhere. Work in this thesis is presented as a series of related publications with additional contextualizing works (see Fig. 1.5). The dominant theme through is the acquisition and presentation of new high-precision CA-ID-TIMS bentonite ages. This temporal refinement constitutes a significant improvement on previous age constraints that had become antiquated due to 1) technological advancements since their acquisition, 2) the ad-hoc patchwork of ages generated at different times using different approaches and recalibrations, and 3) comparably low spatial and temporal data density. New age data presented here constitute a significant improvement in precision and coverage, and internal consistency facilitated construction of high-resolution age-

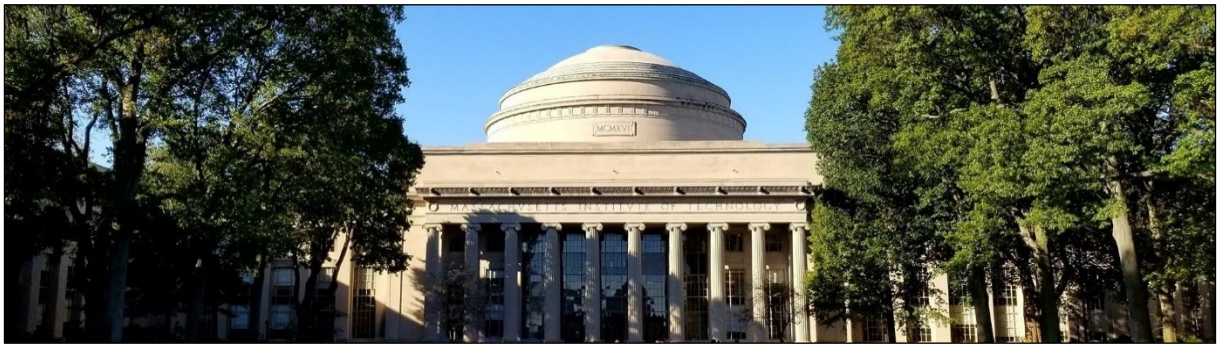


stratigraphic models. The Wahweap and Kaiparowits formations provided an excellent opportunity for stratigraphic refinement due to a fortunate combination of rapid sedimentation rate, sustained basin subsidence, biotic richness, and distribution of datable bentonite horizons that reflect an ideal scenario for the construction of meaningful high-resolution litho- and chronostratigraphic frameworks.

---

## Chapter Two

Chemical abrasion isotope dilution thermal ionization mass spectrometry at the Massachusetts Institute of Technology



*MIT, the Great Dome at Killian Court*

**Preface**

This chapter documents the detailed methodology employed for U-Pb zircon geochronology using CA-ID-TIMS at the Massachusetts Institute of Technology during 2017/2018. The purpose of including a detailed methodology is that the CA-ID-TIMS approach involves an elaborate laboratory component and, due to the exceptionally high precision of isotopic measurements, minor procedural variations can have statistically significant impacts on reported ages. The procedure was performed personally during a four-month research exchange to MIT in 2017 and an additional three-week visit in 2018. This chapter constitutes detailed approach notes on the methodology I employed and can be used for future replication by myself or others. I was trained in the procedure via one-on-one tutelage by Dr Jahandar Ramezani, coordinator for the isotope laboratory at MIT. This component of my project, including laboratory and travel expenses, was largely funded by a U.S. National Science Foundation grant [EAR1424892] awarded to J. Ramezani (on behalf of S. Bowring), and a scholarship [W.C. Lacy Scholarship] from James Cook University (see Statement of Contribution of Others, p. v). The text was edited for language and clarity by E. Roberts.

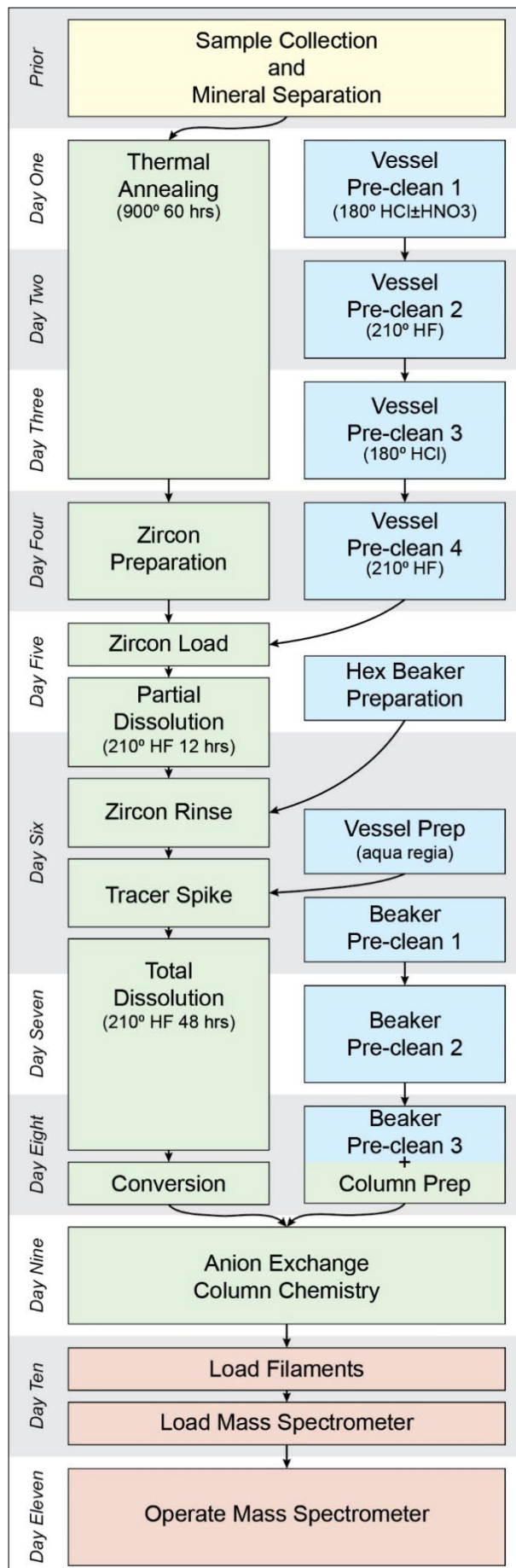
## 2.1 Introduction

Uranium-lead zircon geochronology using chemical abrasion isotope dilution thermal ionization mass spectrometry (CA-ID-TIMS) is currently the most precise radiometric dating approach available in geoscience. Analytical precision of this technique approaches 99.98% for Late Cretaceous volcanic zircon from bentonite in this study, which equates to an uncertainty of *ca* 20,000 years or better. This new caliber of high-precision geochronology approaches timescales comparable to palaeobiotic processes, such as rates of evolution and extinction, and thus facilitates the investigation of complex palaeoecological hypotheses (Bowring *et al.*, 2006; Chapter One).

High-precision geochronology reported in this thesis comprised part of a larger collaborative project that supported this PhD project to refine the temporal context of Campanian terrestrial ecosystems in western North America [NSF grant: EAR1424892]. This refinement was done by producing a stratigraphically arrayed framework of high-precision CA-ID-TIMS ages from several richly fossiliferous localities across the Western Interior spanning from Canada to New Mexico (presented in Ramezani *et al.*, in review, and in Chapters 3 and 4). As such, the framework facilitates direct comparison of coeval fossil-bearing strata from localities separated by up to 1500 km. Although a patchwork of less precise techniques has previously been employed to date and compare these strata, the novelty and advantage of the new approach herein was to generate data that was exactly comparable by executing the same procedure for the same isotopic system in the same laboratory. This deliberate and focused attention to replication reduced or eliminated biases that have previously hindered reliable basin-scale correlations. Due to substantial implications for experimental replicability, this chapter documents the detailed methodological approach to CA-ID-TIMS geochronology employed herein and for all samples investigated as part of this project.

## 2.2 Approach context

Before delving into the methods, it is important to consider why this approach was selected over other comparable geochronologic techniques. The first factor to consider is selection of the most appropriate radioisotopic system for the desired time interval (here, the Late Cretaceous). Ruling out radioisotopes with comparatively short (*e.g.*,  $^{14}\text{C}$ ) or long (*e.g.*,  $^{87}\text{Rb}$ ,  $^{147}\text{Sm}$ ) half-lives, the U-Th-Pb and K-Ar systems are most appropriate for these rocks. The U-Th-Pb system has triple merits over the K-Ar system; 1) U series decay constants are more precisely constrained (*i.e.*, Jaffey *et al.*, 1971); 2) co-occurring  $^{238}\text{U}$ - $^{206}\text{Pb}$  and  $^{235}\text{U}$ - $^{207}\text{Pb}$  decay chains facilitate an internal check for closed system behavior (concordance); and 3) U series geochronology most frequently uses zircon, which is a common accessory mineral in many rocks, is physically and chemically robust, has a high closure temperature, and naturally excludes Pb from its crystal lattice (Larson *et al.*, 1952; Davis *et al.*, 2003; Parrish and Noble, 2003; Bowring *et al.*, 2006). Analysis of the U-Th-Pb system in zircon can be conducted using a host of techniques, broadly separated into conventional (ID-TIMS) and microbeam (LA-ICP-MS,



SIMS, SHRIMP) (Bowring *et al.*, 2006). The advantage of microbeam techniques is that they are designed for the rapid analysis of small volumes of many individual grains. These functions mean that microbeam ages are relatively inexpensive to obtain; however, the analytical precision is generally limited to the realm of 0.1 - 1% uncertainty. The conventional ID-TIMS approach is nearly the opposite in these regards; the procedure is complex, time-consuming, and more destructive (uses the entire grain) meaning it is also comparatively expensive (~US\$500 per zircon). These restrictions are balanced by exceptional analytical precision, which is currently around an order of magnitude finer than ion microprobe techniques and nearly two orders of magnitude finer than laser ablation ICP-MS. The choice between conventional (ID-TIMS) and microbeam techniques is therefore synonymous with that for high or low precision.

Different geological scenarios necessitate varying levels of precision and thus, as discussed above, different geochronologic techniques. Richly fossiliferous Campanian-aged strata in western North America provide an excellent opportunity (perhaps the best in the world) for the application of high-precision geochronology due to the well-established geological and paleontological context, and an atypical abundance of interstratified primary volcanic material in the form of bentonite horizons (devitrified volcanic ash). The need for high-

**Fig. 2.1** Summary of the laboratory procedure for CA-ID-TIMS. Boxes are color-coded to sections where: Section 3 = yellow, Section 4 = Blue, Section 5 = Green, Section 6 = Red.

resolution constraint is tied to the scale of processes under investigation at these localities (*e.g.*, palaeobiotic distribution patterns and turnover). To address these concepts, uncertainty associated with the age of the strata should ideally be comparable to rates of the palaeoecological processes; therefore, high-precision CA-ID-TIMS is critically important in this scenario. Furthermore, the use of bentonite beds is key because these represent the true depositional age of strata given that volcanic ash is deposited in geologically insignificant timespans (Bowring *et al.*, 2006; Lowe, 2011). Conversely, lower precision microbeam techniques could be considered more appropriate by default in a situation with poor pre-existing temporal constraint, poor or absent primary volcanic material, and underdeveloped palaeoecological context. Indeed, in-situ approaches can be used to pre-screen grains for further high-precision geochronology via CA-ID-TIMS.

The use of high-precision CA-ID-TIMS geochronology is thus particularly well justified for this project and inclusion of a detailed procedural transcript is essential. At the level of precision achieved in this study, even minor procedural variation can result in a statistically significant divergence of results for the same bentonite horizons (J. Ramezani, per. com.). This exact scenario was encountered over the duration of the project where high-precision CA-ID-TIMS dates for a different but parallel project were generated for samples from Alberta using a comparable method in a different laboratory (see Eberth and Kanno, 2020). To ensure the geochronologic data from the two projects were compatible, one bentonite horizon (Bearpaw) was analysed in both laboratories using two portions of the exact same sample; however, the ages generated in each lab did not overlap in the first instance (J. Ramezani, per. com.). The discrepancy was rectified following minor procedural adjustments and this instance stands as an example of the complexity of comparing geochronological data including data generated using the same technique but with very slight procedural variation. As such a complete methodology is described here beginning with bentonite collection techniques through to data reduction (Fig. 2.1). A glossary is provided at the end of the chapter for clarity on abbreviations, acronyms and laboratory terminology.

## **2.3 Bentonite sampling and preparation**

### *2.3.1 Sample collection*

Bentonite collection methods are difficult to standardize due to variable preservation and differences in depositional styles. Some studies include outcrop descriptions and notes on lateral continuity, and some mention trenching outcrops to obtain fresh exposures (*e.g.*, Thomas *et al.*, 1990; Roberts *et al.*, 2005; Foreman *et al.*, 2008; Fanti, 2009; Jinnah *et al.*, 2009). Detailed collection methods are rarely described, but anecdotal experience shows that zircon populations and yield can be greatly affected by sampling techniques (Bowring *et al.* 2006; Chapter Six; E. Roberts, per.com.). The following five-step procedure is a generalization of the approach used in this study for the collection of Campanian bentonites from across western North America (Fig. 2.2).





**Fig. 2.2** Examples of bentonite outcrops and more. A) Bentonite collection site illustrating the trench and bench approach. B) Bentonite outcrop showing the classic popcorn weathering texture. C) Outcrop in panel B from a distance showing the texture/color change from mudstone to bentonite and the bench-forming nature of bentonite horizons (photograph looks down onto the bench that sits atop a ~20 m cliff). D) Accumulation of phenocrysts at the base of a bentonite horizon deposited in a shallow pond (pencil for scale). E) Bentonite hand sample (smectite chips) illustrating the common pistachio green color and waxy texture. F) Gypsum crystals collected from a bentonite outcrop (slightly rounded during post-collection transport).



1. Identify bentonite horizons
  - In badland-style outcrops, bentonite horizons are commonly identifiable on the landscape as weather-resistant benches with characteristic popcorn swelling textures. The color of bentonite exposures may vary depending on a host of factors including recent wetting but are generally gray to greenish-gray and exceptionally slick when wet. Beneath this friable, eroding surface material, 'fresh' in-situ bentonite may be present. Fresh bentonite is commonly rich pistachio green with a waxy luster, which signifies high purity smectite clay. Visible black flecks interpreted as fresh biotite mica are a good indicator of primary airfall bentonites (*i.e.*, minimal reworking). Check for gray/translucent grains of quartz, which may indicate reworking/incorporated detrital material. Diagenetic gypsum is also often associated with bentonite beds due to hydraulic impedance caused by the swelling clays, which typically leads to secondary precipitation of gypsum crystals (selenite) within cracks in the weathered portion of the bentonite.
2. Excavate a trench through the bentonite horizon to locate the best level from which to collect material
  - In many instances, the most reliable level is close to the base of the bentonite unit due to an upwards increasing likelihood of fluvial reworking. This is a guideline, and the unique characteristics of each outcrop should be observed in detail. Conversely, the basal few centimeters also have an increased likelihood of contamination, in this instance from comparatively larger volcanic detritus entrained during eruption. This material may not represent the true depositional age of the bentonite (*i.e.*, age of eruption); therefore, the absolute base of a bentonite horizon should also be avoided. Given sufficient thickness, avoid the first ~centimeter of the bentonite and sample from the next 20% of its total thickness. Note that this approach is not applicable in all situations.
3. Uncover a bench at the top of the desired interval
  - Once the optimal interval of the bentonite horizon from which to collect material has been identified, remove overburden to make a bench. Benching is not always possible depending on local terrain (*e.g.*, steep hills, cliffs). In these instances, clear the area of loose sediments and collect the targeted material by digging into the cut-face making sure not to dislodge undesired material that may contaminate the sample with younger or detrital material.
4. Collect bentonite material
  - Roughly 4 kgs of bentonite is typically sufficient; however, the required amount will vary depending on the size and abundance of zircon within the bentonite. Ensure the sample is clearly labelled and protected from contamination during transport and storage.
5. Record location and relevant details
  - Include GPS co-ordinates, photographs, rock description / depositional environment interpretation, stratigraphic height, bounding lithofacies and lateral extent.



### 2.3.2 Mineral separation

Mineral separation for the isolation of zircon from bentonite is similar to standard procedures for other rock types (thus, is not described in great detail here); however, because bentonite is typically >90% clay, specific additional steps are also applied.

1. Soak the bentonite sample overnight
  - Place approximately one kilogram of bentonite in a large beaker / jug, add water so that all material is covered, and leave it to soak overnight. Swelling clays in the sample will absorb the water and form a thick paste.
2. Blend the bentonite paste into a slurry
  - Homogenize the hydrated bentonite clay using a sediment blender. Add water until the resulting slurry is of similar viscosity to cream or less.
3. Gradually feed the bentonite slurry into an Ultrasonic Clay Separator (UCS)
  - The UCS apparatus designed by Hoke *et al.* (2014) disaggregates and decants the clay component of bentonite so that only clean phenocrysts remain. The process may take a day or two to complete and typically reduces the sample volume by >90%. See Hoke *et al.* (2014) for specific details.
4. Magnetic separation (if required)
  - Depending on the abundance of mica and other magnetically susceptible minerals in the crystalline separates from the previous step, conduct magnetic separation using a Frantz Isodynamic magnetic separator. Use two stages of separation both at 15° tilt or similar; first at 0.5 A to remove highly susceptible materials (*e.g.*, magnetite and magnetite-bearing micas), then at a higher field strength, usually 1.15 A, to remove biotite micas and similar.
5. High density liquid separation using methylene iodide (MEI)
  - Use high density liquid such as MEI (density = 3.32 g·mL<sup>-1</sup>) to separate zircon from the non-magnetic fraction. MEI is preferred over LST Heavy Liquid (water soluble lithium heteropolytungstates; density of 2.85 g·mL<sup>-1</sup>) because, although the former requires stricter safety procedures, its higher density more effectively discriminates between zircon (~4.7 g·cm<sup>-3</sup>) and the common accessory mineral apatite (~3.2 g·cm<sup>-3</sup>) (see also Appendix B.1).

### 2.3.3 Zircon selection

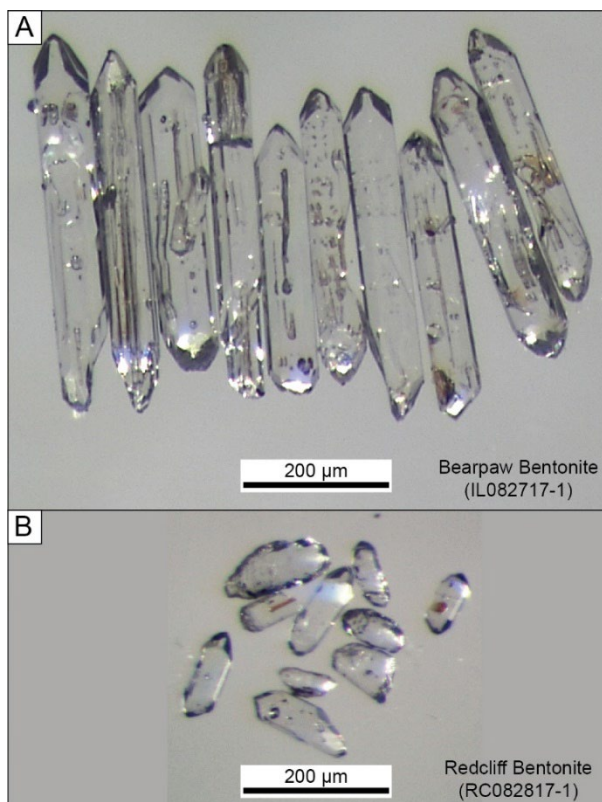
Due to the small number of analyses per sample used in the CA-ID-TIMS procedure (*i.e.*, typically less than a dozen), selection of zircon from the heavy mineral separates of bentonite samples is of particular importance. Several key morphological criteria are used to select a population of zircon that represents the true depositional age of the bentonite (Fig. 2.3):

- Well-developed habit (*i.e.*, clean crystal faces)
- High aspect ratio (5:1)

- Elongated glass (melt) inclusions orientated parallel to the crystallographic “C” axis

These characteristics have proven to be an effective metric for identification of the youngest zircon population (J. Ramezani, per. com.). These criteria are applied as follows and, due to the small sample size and high cost of analyses, particular care is taken to reduce the likelihood of zircon cross-contamination.

1. Clean the petri dish
  - To reduce the likelihood of sample cross-contamination, use a disposable 4 cm plastic petri dish. Flush the dish using compressed air and visually inspect it using a binocular microscope to check for loose grains.
2. Spread the heavy mineral separates in the dish
  - Fill the separates tube to the brim with ethanol and place the petri dish over the top then invert and remove tube. Add further ethanol to the petri dish (to ~2 mm depth) then swirl the dish gently to spread the material. This process results in subtle distributional patterns of zircon morphotypes. Add more ethanol as required.
3. Pick a target zircon population
  - Use purpose-made fine laboratory tweezers (sharpened further for precision picking) to gather the target population (n ~ 20) in a clear area of the dish based on the above morphological criteria.
4. Photograph the zircons
  - Use a fine tipped disposable pipette (washed with ethanol, inside and out) to transfer the selected population to a fresh dish (prepared as above). Position the crystals neatly using the tweezers and image the zircon population using a high-powered photomicroscope (e.g., Fig. 2.3). Rotate the stage and take photos at several lighting angles to better illustrate the crystal surfaces.
5. Prepare for thermal annealing



**Fig. 2.3** Zircon morphological characteristics. A) Example of desirable characteristics including high aspect ratio, good habit, and elongated glass (melt) inclusions. These grains consistently yielded precise and accurate dates. B) Example of sub-optimal morphologies (small, rounded, few inclusions) from grains that did not yield practically useful data.

- After the photographs have been taken, use the same disposable pipette to transfer the zircons to a clean quartz crucible (cleaned upside-down in a sonic bath and visually inspected using the microscope to check for zircon cross-contamination).

## 2.4 Equipment preparation

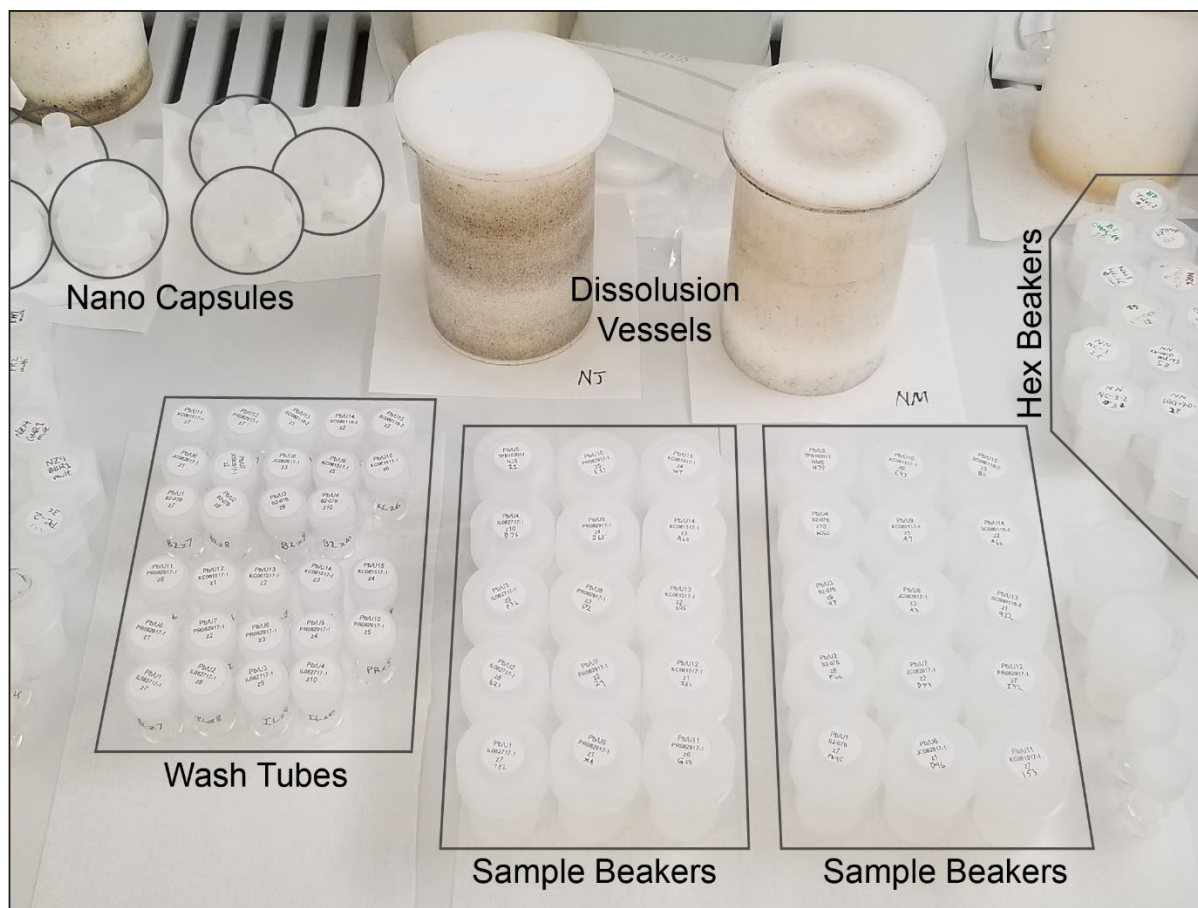
Contemporary high precision uranium-lead geochronology is reliant on the ability to measure isotopes, particularly those of lead, accurately at the picogram scale (1 picogram = 0.000000000001 grams), which requires reduction or elimination of lead contamination in the laboratory setting (Parrish and Noble, 2003; Bowring *et al.*, 2006; McLean *et al.*, 2011). As such, high-precision uranium-lead analyses using the CA-ID-TIMS approach can only be conducted in laboratories outfitted with high grade Pb clean rooms and associated procedures. All equipment used in the CA-ID-TIMS process must be thoroughly cleaned before each use. Most materials used in the clean laboratories are metal-free because: 1) most metal products contain some amount of lead that may contribute to contamination; and 2) the highly corrosive nature of the acids used in the process rapidly deteriorate metal equipment. Figure 2.4 shows the variety of polytetrafluoroethylene (Teflon) containers used in different steps in the process. Each are thoroughly cleaned before use.

### 2.4.1 Dissolution vessels and nano-capsules

The nano-capsules and dissolution vessel (Fig. 2.5) are used for zircon digestion and require a four-day pre-clean before use.

#### 1. HCl Pre-clean One

- Disassemble the vessel components on a laminar flow workbench in a fume hood within the Pb clean room
- Dispose of remaining acid (from previous cycle) and rinse components with MQ water to remove excess acid before placing them on durex squares
- Remove the caps of each nano-capsule using plastic forceps and place caps on parafilm
- Dispose of remaining acid from nano-capsules
- Add three drops of 6.2 M hydrochloric acid (HCl) to each nano-capsule and replace the caps
- Add ~7 mL of 6 M HCl ( $\pm$  5 drops of 14 M nitric acid [HNO<sub>3</sub>]) to the dissolution vessel
- Assemble the vessel components and transfer the sealed vessel to the oven room
- In the oven room fume hood, secure the vessel in its metal jacket
- Place the jacketed vessel in a 180°C oven overnight (minimum 8 hrs)
- Remove the metal jacket from the oven and let it cool for at least one hour
- Disassemble the metal jacket, wipe down the vessel with damp paper towel to remove metal contaminants, seal lid with parafilm and transfer to the clean lab atrium
- Remove the parafilm and clean the vessel again with MQ water and durex squares



**Fig. 2.4** Various Teflon containers used in the Pb clean laboratory including nano-capsules and dissolution vessels, sample beakers and hex beakers, and plastic wash tubes. All require pre-cleaning as per Section 2.4.

2. HF Pre-clean One
  - Repeat step 1 one using 29 M hydrofluoric acid (HF) in place of HCl and an oven temperature of 210°C instead of 180°C
3. HCl Pre-clean Two
  - Repeat stage one exactly (without HNO<sub>3</sub>)
4. HF Pre-clean Two
  - Repeat stage two exactly

#### 2.4.2 Hex beakers

These Teflon beakers (termed “hex” due to the hexagonal shaped lid) are used during the rinse stage where impurities leached from the zircon during partial dissolution are washed out. Since they will be exposed to minor contaminants during this process, the pre-clean is relatively minimal.

1. Fill the beakers and caps to the brim with MQ water
2. Dispose of the water and add ~1 mL of beaker cleaning 6 M HCl
3. Replace caps and flux overnight on a 50°C hotplate (minimum 3 hrs)
4. Dispose of acid appropriately before use

### 2.4.3 Sample beakers

These containers, also made of Teflon but approximately twice the size of the hex beakers, are used to collect the final uranium and lead components following chemical purification (*i.e.*, the final step before measurement). It is therefore important that these beakers are exceptionally clean. The cleaning process is similar to that for nano-capsules and includes three stages.

#### 1. HCl Beaker Pre-clean One

- Rinse the beakers and their caps with MQ water and clean inside each one with a wet durex square (pay particular attention to the cap screw)
- Rinse again with MQ water then fill beakers and caps to the brim with MQ water
- Dispose of water and immediately transfer the items to a laminar flow work bench in a fume hood holding the openings to the beakers and caps downward

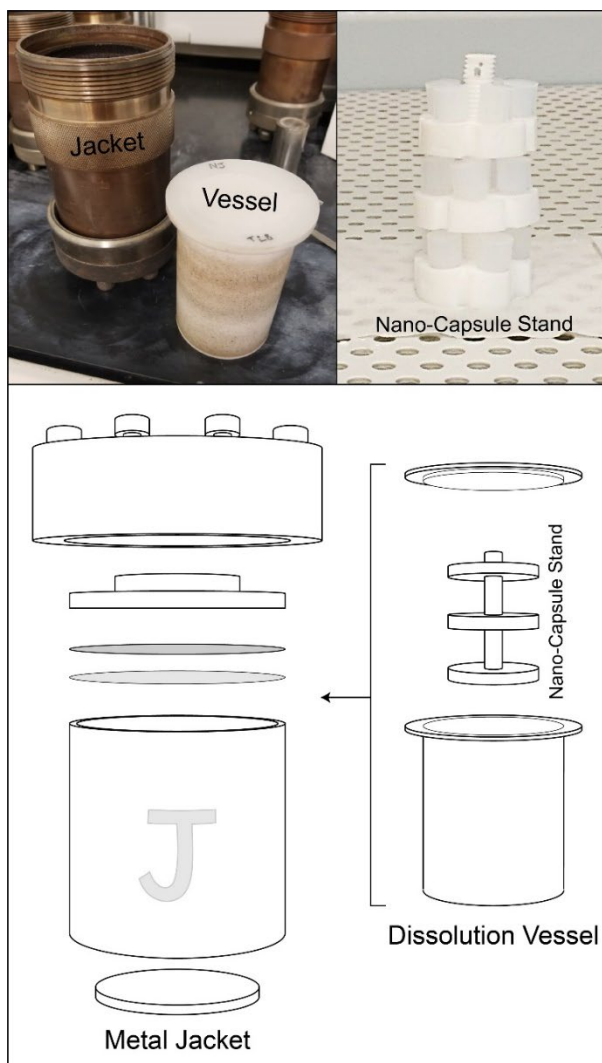
NB: Make sure beaker and cap pairs match, and place the items on a large durex square (helps with maneuverability)

- Add ~1 mL of beaker cleaning 6 M HCl to each beaker and replace caps
- Flux overnight on a 50°C hotplate inside the fume hood (minimum 6 hrs)
- Remove the beakers from the hotplate and rotate them to amass the acid condensate
- Dispose of the acid and place the items on a large durex square

#### 2. HF Beaker Pre-clean

- Add ~1 mL of beaker cleaning HF to each beaker and replace caps
- Flux overnight on a 50°C hotplate inside the fume hood (minimum 6 hrs)
- Remove the beakers from the hotplate and rotate them to amass the acid condensate
- Dispose of the acid and place the items on a large durex square

#### 3. HCl Beaker Pre-clean Two



**Fig. 2.5** Photographs and schematic diagram of dissolution vessel components including metal jacket and nano-capsule stand used to digest zircon at high temperature/pressure conditions in high-strength HF acid.



- Fill the beakers and caps to the brim with MQ water then discard the water (this ensures no plastic filings from the cap screws remain in the beakers)
- Add ~1 mL of beaker cleaning 6 M HCl to each beaker and replace caps
- Flux overnight on a 50°C hotplate inside the fume hood (minimum 6 hrs)
- Remove the beakers from the hotplate and rotate them to amass the acid condensate then dispose of the acid

#### 2.4.4 Wash tubes

These containers are small plastic sample vials that are used to collect additional chemical separates (washes) containing rare earth elements (REEs) and other dissolved components during chemical purification. Since these elements are less common in the environment than lead and will not be measured using the high precision thermal ionization mass spectrometer (TIMS), very little cleaning is necessary. Simply fill each tube with MQ water to rinse, then dispose of water.

### 2.5 Laboratory procedures

The intricate ID-TIMS laboratory procedure has evolved over seven decades of incremental advancements since its first iteration presented by Tilton *et al.* (1955). One of the most significant, relatively recent of which was development and refinement of the chemical abrasion zircon pre-treatment presented by Mattinson (2005). Even without pre-treatment, zircon is an exceptionally useful mineral for U-Pb geochronology because of its physical and chemical robustness; however, all radioisotope-bearing minerals are subject to radiation damage over geological timespans and this process affects the integrity of the crystalline lattice. In the case of zircon, the decay of uranium and thorium isotopes and their daughter products cause  $\alpha$ -particle damage (fission tracks, 10 to 20  $\mu\text{m}$ , ~100 atomic displacements) and alpha-recoil damage (30 to 40 nm, ~1000 atomic displacements; Ewing *et al.*, 2003). Compared to alpha decay, the effects of beta decay on the zircon crystal are negligible. Repeated alpha decay, such as the eight instances in the  $^{238}\text{U}$  chain, results in accumulated damage, particularly recoil damage at the site of the daughter nuclide (which constituted a particular challenge in the development of chemical abrasion techniques; see Mattinson, 2005). At a larger scale, interconnectivity of damage results in amorphous zones that facilitate migration and loss of radiogenic nuclides (*i.e.*, open system behavior / lead loss). More intense damage occurs in zones with comparably higher uranium and thorium concentrations (bright CL zones; Fig. 2.6).

Several pre-treatment techniques have been developed to mitigate the effects of lead loss in these radiation damaged zones. Prior to refinement of the chemical abrasion approach, mechanical abrasion was used to remove outer zones of damaged crystal (see Krogh, 1982). Although this method is suitably effective for zircons that crystallized with progressive enrichment of U, Th and REEs, it is not effective for internally damaged zones that result from comparatively complex crystallization histories (Fig. 2.6). With the revolution of chemical abrasion pre-treatment, open system behavior is virtually

resolved in all zircon including those with internal heterogeneity and the method is currently accepted as standard procedure for the effective preparation of zircons for high precision geochronology (Mattinson, 2005; Bowring *et al.*, 2006). As well as effectively mitigating lead loss in radiation damaged zones, chemical abrasion also removes other impurities that may contribute common lead such as glass (melt) and mineral inclusions (J. Ramezani, per. com.).

### 2.5.1 Thermal annealing

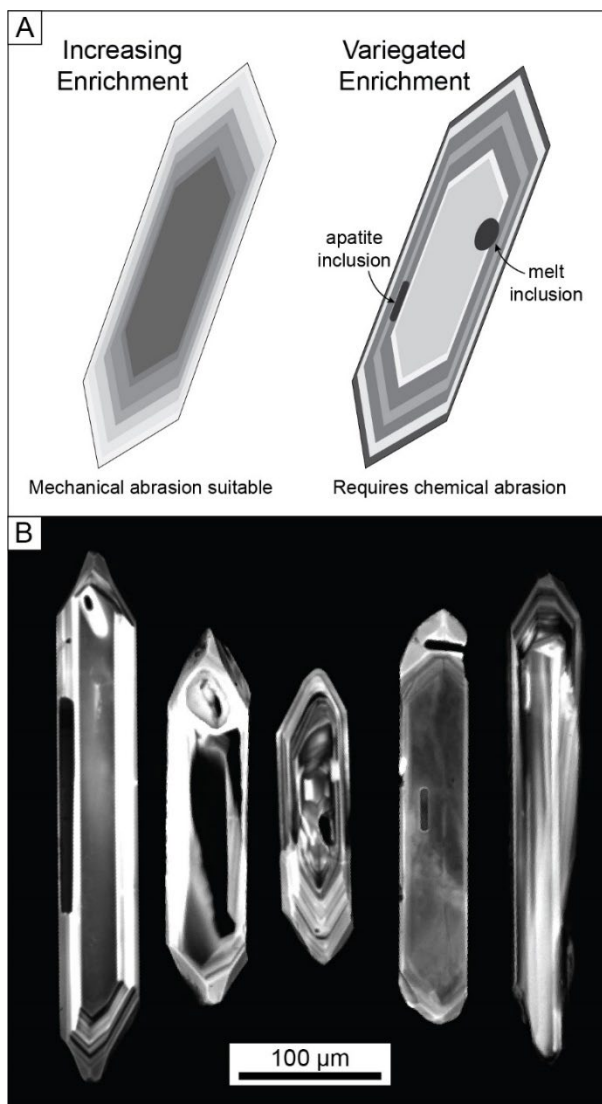
The first component of the two-part chemical abrasion procedure is to anneal zircons in preparation for partial dissolution. Thermal annealing protects isolated alpha-recoil-damaged radiogenic nuclide sites that otherwise have increased susceptibility to acid leaching (Mattinson, 2005). This protects the concordant radiogenic products and facilitates later removal of lead-loss affected amorphous zones.

1. Place quartz crucibles containing selected zircon from Section 2.3.3 in a furnace at 900°C for 60 hours ( $\pm 2$  hr)
2. After cooling, cover the crucibles with parafilm, place in a clean plastic container and transport to Pb clean room

### 2.5.2 Partial dissolution

Once the zircon grains have been prepared by thermal annealing, the radiation damaged zones (now microcrystalline zircon) are removed using high-strength acid at high temperature and pressure conditions within a dissolution vessel.

1. In the Pb clean room on the laminar flow workbench, prepare a mechanical pipette (set to 150  $\mu\text{L}$ ) by rinsing the disposable plastic tip with MQ water and 6 M HCl



**Fig. 2.6** Examples of zircon internal textures and how they relate to ID-TIMS pre-treatment. A) Schematic of zircons zones showing increasing and variegated enrichment represent by light and dark zones to reflect cathodoluminescent (CL) response. B) CL images of zircons from this study showing examples of internal heterogeneity such as glass (melt) inclusions and apatite mineral inclusions, as well as non-uniform oscillatory zoning, sector zoning and combinations.

2. Use the mechanical pipette to transfer zircons from the quartz crucible to a nano-capsule (all zircon from one sample can be placed in the same nano-capsule at this stage)  
**Note:** Nano-capsules and the dissolution vessel must be pre-cleaned according to Section 2.4.1.
3. Add 2 drops of 29 M HF to each nano-capsule (including those without zircon)
4. Add ~7 mL of moat HF to the dissolution vessel, assemble vessel components and transfer the sealed vessel to the oven room
5. In the oven room fume hood, secure the vessel in its metal jacket
6. Place the jacketed vessel in a 210°C oven for **exactly** 12 hours in which time the zircons will be partially dissolved  
**Note:** Consistent abrasion time is of utmost importance. Deliberate variation ( $\pm$  30 minutes) can be applied if needed for specific geological situations.
7. After 12 hours, remove the metal jacket from the oven and let it cool for at least one hour
8. Disassemble the metal jacket, wipe down the vessel with damp paper towel to remove metal contaminants, seal lid with parafilm and transfer to the clean lab atrium
9. Remove the parafilm and clean the vessel again with MQ water and durex squares

### 2.5.3 Zircon rinse

This phase involves cleaning zircons of their leachates, which include the dissolved components of radiation-damaged zones (areas of potential lead loss) and also dissolved melt and mineral inclusions (sources of common lead).

1. Preheat a hotplate to 42°C in a laminar flow workbench and prepare a transmitted light binocular microscope and sonic bath, all within the Pb clean room
2. Disassemble the dissolution vessel on the laminar flow workbench and dispose of the moat acid
3. Using plastic forceps, remove the cap of the zircon-bearing nano-capsules and empty the contents (zircon + leachates + HF acid) into a clean, labelled hex beaker (pre-cleaned following Section 2.4.2)
4. Add ~5 drops of concentrated HNO<sub>3</sub> to the hex beakers then use a transmitted light microscope to check that all zircons are present
5. Replace the hex beaker caps and flux on the hotplate at 42°C for one hour
6. At this time, also place a shallow dish of MQ water ( $\geq$ 5 mm depth) on the hotplate
7. While the hex beakers are fluxing, add 1 drop of concentrated HNO<sub>3</sub> and 3 drops of HCl to the nano-capsules that contained zircon during partial dissolution then replace the caps and leave the nano-capsule pucks aside within the workbench area until later  
**Note:** this ratio of acids creates aqua regia solution, which thoroughly cleans the leachates from the nano-capsules.



8. After one hour on the hotplate, transfer hex beakers to the shallow dish of warm water and place the dish within a sonic bath for one hour
  9. Prepare a mechanical pipette by rinsing the disposable plastic tip with MQ water and 6 M HCl
  10. After one hour in the sonic bath, remove the hex beakers and gently dry them
  11. Using a transmitted light microscope and the mechanical pipette, wash the zircons by moving them around using gentle jets from the pipette and ensure no droplets remain on the sides of the hex beaker
  12. Remove as much fluid as possible from the hex beakers and dispose of acid
  13. Placing the cap gently over the opening to reduce the likelihood of contamination, transfer hex beakers to the laminar flow workbench
  14. Add 10 drops of MQ water (blank checked) to each hex beaker and repeat the rinsing and fluid extraction process (steps 11-12)
  15. Return again to the workbench and add 10 drops of 6.2 M HCl to each hex beaker
  16. Repeat the hotplate and sonic bath steps (5-6, 8-13)
  17. Dispose of aqua regia solution from nano-capsules from step 7
  18. Add 10 drops of MQ water (blank checked) but this time, do **not** rinse and extract these fluids
  19. Using the microscope, carefully isolate single zircon crystals, extract them with as little fluid as possible and deposit them in individual nano-capsules, replacing nano-capsule caps as you progress
- Note:** set the mechanical pipette to 20  $\mu\text{L}$  for this step.

There should now be one clean zircon (with very little water and no acid) in each nano-capsule except one or two that are measured as a total procedural blank.

#### 2.5.4 Tracer spike and total dissolution

Spiking the nano-capsules with a calibrated uranium-lead tracer solution facilitates quantification of isotope ratios measured during analysis (Section 2.6.3). Unlike that of natural mineral standards, tracer solution isotopic composition can be defined by SI units, which facilitates robust uncertainty calculations (see Condon *et al.*, 2015; McLean *et al.*, 2015). EARTHTIME solutions used in the procedure described here contain a precisely calibrated mix of anthropogenic  $^{235}\text{U}$ ,  $^{233}\text{U}$ , and  $^{205}\text{Pb}$  (ET535), and these plus  $^{202}\text{Pb}$  (ET2535). Accurate spike weights are fundamental to the CA-ID-TIMS procedure, thus not a single drop of spike solution can be spilled, and exceptional care must be taken to avoid contamination of the spike solution (*i.e.*, do not touch the bottle tip to anything, do not reach over the exposed bottle tip etc.). Note also that due to the high sensitivity of the electronic balance, once the spiking process begins, the laboratory door must remain closed until completion. To allow time for the balance to equilibrate, turn it on several hours prior to spiking (*e.g.*, during step 8 of Section 2.5.3).

1. Prepare the laminar flow workbench by laying out durex cleaning pads and dampen them with MQ water to reduce any ambient static charge (droplets of tracer solution are so small that they can be easily deflected due to electrostatic interference)  
**Note:** Ensure all solutions required are full and ready to use (HF in particular).
2. Place two squares of parafilm adjacent to the workspace; one for the caps of the nano-capsules and another for the protective lid of the spike bottle
3. Retrieve the tracer solution (spike) bottle from the storage space at the back of the bench, carefully remove the parafilm from around the neck of the bottle and gently roll the bottle on the damp durex to remove any ambient static charge
4. With the protective lid in place, transfer the spike bottle to the electronic scales and gently close the Perspex door
5. While the balance is stabilizing, remove the cap from the first nano-capsule
6. Record the initial weight of the spike bottle on the laboratory records sheet as well as a specific dissolution sheet for the current zircon batch
7. Return the spike bottle to the workspace then set the bottle down and remove hands completely (this is to prevent the development of habitual short cuts that could result in contamination of the tracer solution spike bottle)
8. Remove the spike bottle cap and place it on parafilm, then add exactly two drops of the tracer solution to the nanocap  
**Note:** Be careful not to touch the tip of the dropper bottle on anything, including the rim of the nanocap.
9. Replace the protective lid on the spike bottle then set it down on the bench again (hands completely off) before transferring it to the electronic balance
10. While the balance is stabilizing, add 3 drops of 29 M HF to the nano-capsule and replace the cap, then rotate the nano-capsule puck and remove the cap of the next nano-capsule
11. Record the new spike bottle weight on the dissolution sheet then repeat steps 7-10 for each nano-capsule
12. Once all nano-capsules have been spiked, record the final weight of the spike bottle on the laboratory records sheet
13. Replace parafilm around the neck of the spike bottle and reassemble the dissolution vessel using ~7mL of moat HF
14. Transfer the sealed dissolution vessel to the oven room fume hood and secure the vessel in its metal jacket
15. Place the jacketed vessel in a 210°C oven for 48 hours in which time the zircons will be completely dissolved (the duration of this time is less strict than for partial dissolution)

### 2.5.5 Chemical conversion

After the zircon crystals have been completely digested by the hydrofluoric acid, the chemical components are in a hydrofluoric state. The resin used in Section 2.5.6 to isolate lead and uranium from other dissolved components is designed to react specifically with different strength hydrochloric acid conditions. It is therefore important to convert the chemical state of the dissolved zircon components from hydrofluoric to hydrochloric.

1. Remove the metal jacket from the oven and let it cool for at least one hour and preheat a hotplate in a laminar flow fume hood (in the Pb lab) to 50°C
2. Disassemble the metal jacket, wipe down the vessel with damp paper towel to remove metal contaminants, seal lid with parafilm and transfer to the clean lab atrium
3. Remove the parafilm and clean the vessel again with MQ water and durex squares
4. Disassemble the vessel components on a laminar flow workbench in a fume hood within the Pb clean room and dispose of moat HF acid
5. Transfer the nano-capsule pucks to the hotplate then remove the caps using plastic forceps and place these to the side on clean parafilm
6. Carefully cover the nano-capsule pucks with a plastic cover to reduce the likelihood of contamination

**Note:** be mindful of hand positioning; do not reach over open containers.

7. Leave the nano-capsule pucks on the 50°C hotplate for approximately one hour to evaporate HF from the nano-capsules (check for condensation droplets to ensure the sample is completely dry)
8. Once dry, add 3 drops of 6.2 M HCl to each nano-capsules, replacing the caps as you go, and remove the nano-capsule pucks from the hotplate
9. Reassemble the dissolution vessel using ~7mL of 6 M moat HCl and transfer the sealed vessel to the oven room
10. In the oven room fume hood, secure the vessel in its metal jacket and place the jacketed vessel in a 180°C oven overnight (minimum 8 hrs)
11. The next day (or 8 hrs later), repeat steps 1-7 to evaporate the HCl
12. Once dry, replace caps and remove from the hotplate and let cool for around 10 minutes
13. Add 2 drops of 3 M HCl to each nano-capsule and leave the nano-capsule pucks at the back of the laminar flow workbench ready for step 4 in Section 2.5.7.

### 2.5.6 Anion exchange column chemistry – preparation

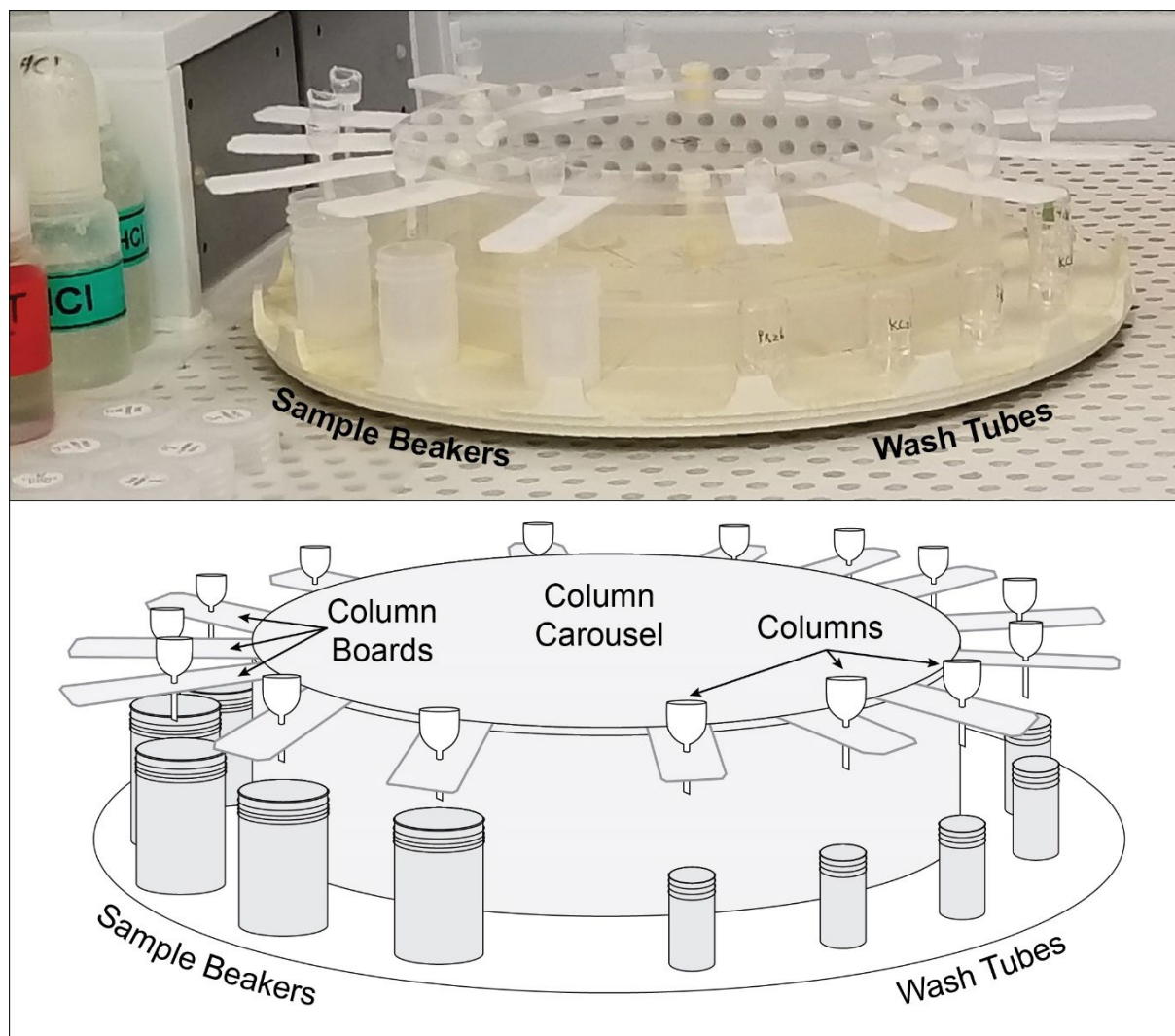
Purification of the dissolved chemical components of zircon samples is conducted in small (<1mL) plastic polymer funnels referred to as columns (Figs. 2.7 and 2.8). Like all other containers that come into contact with the samples, these columns and the resin that fills their tips must be thoroughly cleaned to reduce common lead contamination.

1. In the Pb clean lab, use plastic forceps to retrieve a column from the HNO<sub>3</sub> storage baths, handling it using the column board on which it is fitted
2. Rinse the column and board with MQ water twice, tapping gently between each wash
3. Transfer the rinsed column to the laminar flow workbench with the mouth of the column facing down
4. Over a collection dish, use a specific column cleaning MQ water bottle and touch the tip of the squirt bottle to the tip of the column and flush water back through the column neck to remove any contaminants (count five drops then repeat) and leave a small amount of water in the column to ensure no air bubbles remain in the neck
5. Add 3 to 5 drops of homogenized resin solution so that the neck of the column is completely filled but the reservoir has no more than 1mm depth of resin (Fig. 2.8)  
**Note:** If too much resin is added, use a clean mechanical pipette (prepared as previously) to remobilize the resin and remove the excess.
6. Hang the column by the board on the purpose-made column stand ensuring the tip does not interact with anything (be careful not to reach over the columns)
7. Repeat steps 1-6 for at least 15 columns (preparing extra columns is recommended)
8. Once the resin has settled and all water has drained through the columns, fill each column with beaker cleaning 6 M HCl, then cover the column stand and let the acid drain through entirely (~1 hr)
9. Fill each column with MQ water (blank checked), cover the column stand, and let the water drain through entirely (~1 hr) to reset the chemical state of the resin to neutral
10. Add 15 drops of 6.2 M HCl to each column, cover the column stand, and let the acid drain through entirely (~45 min) to remove any Pb contamination
11. Finally, add 15 drops of 0.1 M HCl to each column, cover the column stand, and let the acid drain through entirely (~45 min) to remove any U contamination

#### 2.5.7 Anion exchange column chemistry – procedure

This full day laboratory procedure involves several rounds of acid washes of varying molarity that changes the state of the resin mesh (AG1-X8 Anion Resin, Cl-form, 200-400 mesh) to selectively allow particular elements to pass through and be collected in batches (Fig. 2.8).

1. After column preparation (Section 2.5.6), add 8 drops of 3 M HCl to each column, cover the column stand, and let the acid drain through entirely (~30 min)
2. While the acid is draining through the column, prepare the wash tubes (Section 2.4.4) and the column carousel (Fig. 2.7) by wiping down all surfaces of the carousel with a damp duxex cleaning pad and placing parafilm patches on the collection platform to reduce the likelihood of the wash tubes moving during rotation



**Fig. 2.7** Anion exchange column chemistry carousel set up including schematic diagram. Represents transition from the wash elute to Pb elute (steps 16-17, Section 2.5.7).

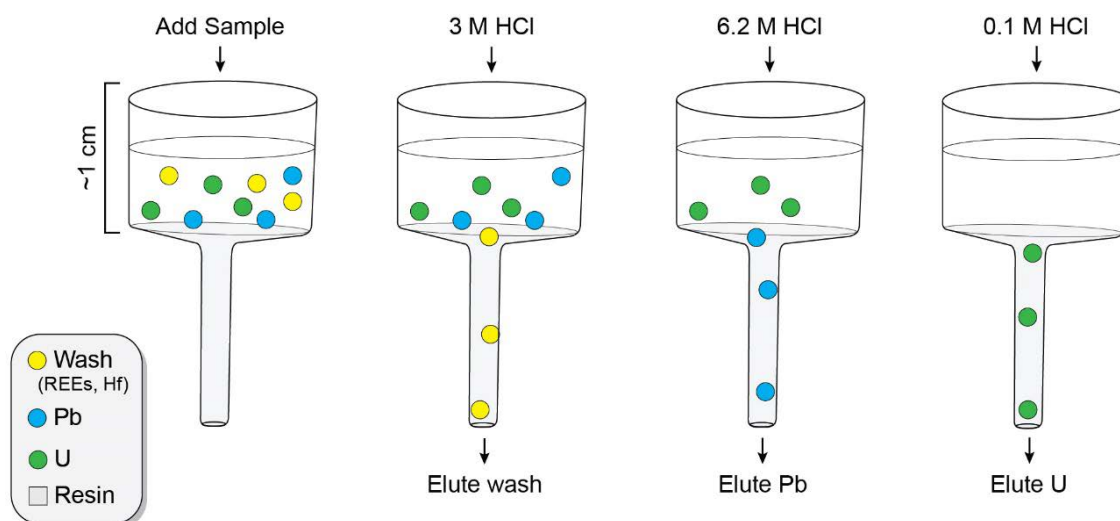
**Note:** If the REE washes are not to be collected, use durex squares in place of the parafilm.

- Once the pre-conditioning solution has completely drained from the columns, carefully transfer the columns to the carousel with the circle end of the column board facing out (ensure the tip of the column does not come into contact with anything and be careful not to reach over open containers)

**Note:** The boards should be loosely inserted into the carousel such that they can be easily removed with one hand.

At this point, take a moment to prepare the workspace and remove any unused equipment (including the now empty column stand). Place the pre-cleaned sample beakers (Section 2.4.3) nearby and retrieve the previously prepared nanocap pucks from the back of the workbench. Transfer of the dissolved zircon solutions from the nanocaps to the columns is a delicate process that requires maximum attention.

- Remove the cap of the first nano-capsule using plastic forceps and place it on clean parafilm



**Fig. 2.8** Schematic summary of chemical purification of uranium and lead using anion exchange column chemistry.

5. Hold the nano-capsule in your right hand using the plastic forceps then gently grip the circle end of the first column board using your left hand and remove it from the carousel (ensure the tip of the column does not come into contact with anything)
6. Without passing either hand over either open container, carefully cross hands and gently fit the nanocap into the mouth of the column by tilting both containers towards each other
7. When the two containers are fitted together, upturn the nanocap to transfer the contents into the column (be careful to move both hands in unison to ensure the containers remain together)
8. Gently tap the left-hand knuckle on the workbench to liberate the last of the liquid from the nano-capsule (again, ensure the tip of the column does not come into contact with anything)
9. Remove the nanocap and check that all of the liquid has been transferred to the column before returning it to the puck
10. Gently insert the column board circle-end-inward to the carousel and immediately place the labelled wash tube directly below the column neck (without touching the tip) and press the tube firmly down onto the parafilm for stability
11. Prepare the now empty nano-capsule for the next round of pre-cleaning by adding 3 drops of 6.2 M HCl and replacing the cap
12. Repeat steps 4-11 for each nano-capsule / column pair
13. Once all samples have been transferred, add 2 drops of 3 M HCl to each column and let the acid drain through entirely (~10 min) to elute the REEs, hafnium and other dissolved components (which are collected in the wash tubes)
14. Repeat step 13 twice more (total of 6 drops per column)

15. While the acid is draining, transfer prepared sample beakers (Section 2.4.3) to the workspace and assemble the dissolution vessel as part of the first pre-cleaning step for a future batch of zircons
16. Once the 3 M HCl has completely drained, gently tap the column boards to liberate the last drop of the wash component then remove and seal the wash tubes
17. Carefully position the labelled sample beakers below their corresponding columns (without touching the tip) and place the beaker caps open-side down on clean parafilm to the side of the workbench
18. Add 8 drops of 6.2 M HCl to each column and let the acid drain through entirely (~1 hr) to elute the Pb component
19. After this acid has completely drained, add 10 drops of 0.1 M HCl to each column and let the acid drain through entirely (~1 hr) to elute the U component  
**Note:** Both Pb and U components for each zircon are collected in the same sample beaker.
20. While the 0.1 M HCl is draining, preheat a hotplate in the laminar flow fume hood to 50°C
21. Once the solutions have completely drained from the columns, gently tap the column board to liberate the last drop
22. Carefully remove the sample beakers from the carousel (without touching the column tips) and add 1 drop of 0.05 M phosphoric acid (H<sub>3</sub>PO<sub>4</sub>) to each sample beaker (five beakers at a time is recommended)
14. Carefully transfer the sample beakers to the 50°C hotplate without reaching over the open containers and cover the beakers with a plastic cover to reduce the likelihood of contamination
23. Dry down the samples for approximately one hour, checking for condensation on the beaker sides  
**Note:** When the sample is completely dry, it should appear as a tiny black-brown dot at the bottom of the beaker.
24. While the samples are drying down, rinse the now empty columns in the same manner as for set up (Section 2.5.6, steps 2-4) and return the clean columns to their nitric acid storage bath
25. After the sample dry-down is completed, remove the sample beakers from the hotplate (without reaching over the open containers) and transfer them to the laminar flow workbench to cool for roughly 10 minutes
26. As soon as the beakers are cool enough to handle, replace the beaker caps and check that identification numbers on each beaker and cap match
27. Place the prepared sample beakers in a holder tray and within a thick plastic sample bag for transport



## 2.6 Machine operation

### 2.6.1 Load filaments

The isolated uranium and lead from dissolved zircon samples is transferred onto rhenium filament then immediately loaded into the thermal ionization mass spectrometer. The process of transferring the sample to the filament is conducted in a clean room laminar flow workbench in the same space that houses the TIMS machine.

1. Select previously prepared filaments (preparation method not described herein), avoiding those with warped or damaged prongs, and stand them in the purpose-made holding block (do not reach over the exposed filaments)
2. Prepare a micropipette by retrieving a pre-treated transfer tube from the storage bottle using clean forceps and fit it into a finger pipette bulb
3. Remove the cap of the sample beaker and (without reaching over the open container) place two separate droplets of silica gel solution into the cap
4. Draw up one of the droplets completely in the micropipette to rinse the inside of the tube then dispose of the silica solution drop on a durex cleaning pad
5. From the second droplet, draw up ~1cm of the solution in the tube and deposit it onto the sample within the beaker (look for the tiny black-brown dot)  
**Note:** It is sometimes best not to release the whole droplet so as to facilitate extra manipulation using surface tension.
6. Massage the sample for ~30 seconds by drawing up and releasing the silica solution repeatedly to encourage dissolution
7. Draw up the sample completely then dispense the droplet so that it hangs on the end of the pipette
8. Using this droplet, wipe down the walls of the beaker to ensure all of the sample is collected (be mindful to not reach over the open beaker)
9. Finally, draw up the droplet again and, without reaching over the filaments, dispense the droplet so that it hangs from the pipette and gently touch the droplet (but not the pipette) to the appropriate filament then dispose of the transfer tube
10. Record relevant details on a sample loading sheet and repeat steps 2-9 for each sample
11. Once all samples are loaded onto filaments, allow approximately 30 minutes for the silica solution to air dry
12. After air drying, use forceps to transfer filaments one at a time to a purpose made electrical box and fit the prongs gently into the receptacles



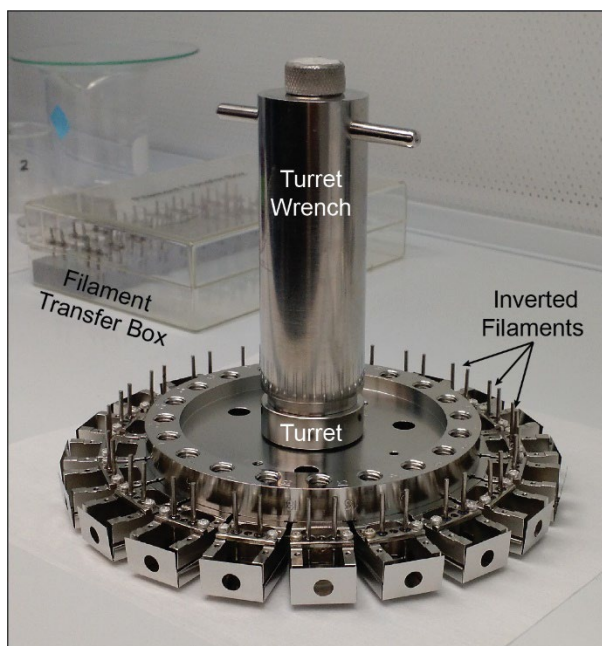
13. Steadily increase the amperage up to 2.7A OR until the sample glows red then immediately reduce again (after this process, the sample should appear as a smoked black spot on the filament)
14. Repeat steps 12 and 13 for each sample then carefully transfer the holding block into a clean sealed Perspex box for transport

### 2.6.2 Loading mass spectrometer

After the samples have been loaded onto the rhenium filaments and dried down, the filaments are loaded into the turret of the thermal ionization mass spectrometer (Fig. 2.9). The turret holds 20 samples at a time and samples are typically swapped out at least once a week (as needed).

1. Begin by equilibrating the vacuum in the source chamber of the TIMS machine to atmospheric pressure
  2. Break the chamber seal and swap the cold trap ensuring not to bump the cold finger as the heavy trap is removed
  3. Remove the turret using the specialized turret wrench and transfer to the adjacent clean room laminar flow workbench (Fig. 2.9)
  4. Remove used filaments in numerical order (note that adjacent filaments are not arranged numerically, *i.e.*, 1, 4, 7, 10, 13, 16, 19, 2, 5, 8 etc.)
- Note:** Do not remove the lab blank standard filament (position 20).
5. Load the new samples into the filament boxes in the correct numerical order
  6. Once all filaments are in place, hold the turret by the wrench handle and examine the underside to ensure all filaments are aligned with the slits in the metal boxes
  7. Load the turret back into the source chamber of the machine in reverse order (rotate the turret 360° while examining the filament connection point to check for misalignment)
  8. Before sealing the machine, ensure no dust has fallen into the source chamber or on the gasket and that no fingerprints are present anywhere inside the machine to ensure a high-quality vacuum can be achieved

**Note:** To further improve the seal, trace the gasket with a clean un-gloved finger to add natural oils but do not touch the metal of the chamber interior.



**Fig. 2.9** Thermal ionisation mass spectrometer turret (mechanism that holds filaments with dried sample material on them) during a filament change. Process is completed in a laminar flow work bench within the machine lab.

9. Restore the vacuum settings for the source chamber and allow the machine to pump down overnight (minimum 5 hours)
10. While machine is pumping down, input the sample metadata into the IonVantage software in preparation for analysis

### 2.6.3 Operating the mass spectrometer

The IsotopX X-62 thermal ionization mass spectrometer in the isotope laboratory at MIT is operated using IonVantage on a network connected desktop computer located within the clean room. The desktop computer can also be remotely accessed using third party software such as TeamViewer. To begin analysis of a new batch of samples, the machine must first be prepared and operated as follows.

1. Once the vacuum integrity in the source chamber of the machine has reached an acceptable level (overnight or ~5 hrs), fill the cold trap with ~4 L of liquid nitrogen, which (after 30 minutes) will improve the vacuum quality further by freezing any remaining particles in the source chamber onto the finger of the cold trap  
**Note:** The cold trap must be continuously maintained by adding liquid nitrogen once or twice per day for the entire operational period to ensure the entrapped particles are not released.
2. Using the IsoProbe window of IonVantage (Fig. 2.10) on the network linked desktop computer, check the source vacuum integrity and position the turret
3. Begin heating the first sample by increasing the current (Start Ramp button) until the temperature read-back reaches 1100°C
4. Check the source vacuum integrity again, then open the isolation valve that separates the source and analysis chambers
5. After entering operational parameters, run a peak center check to optimize the magnetic mass settings then complete an auto focus to set the ideal beam conditions
6. Repeat the peak center and adjust the high voltage setting if necessary
7. Check the counts per second (CPS) of the tracer Pb component ( $^{205}\text{Pb}$ ) and increase the current to achieve a stable ion beam if necessary
8. Return to the home window of IonVantage, select the appropriate sample and element (Pb) then press 'run' to begin analysis

Over the course of the lead isotope analysis, the ion counter will measure each selected isotope for a set period (~5-10 sec). The time taken to complete all selected isotopes is called a cycle. Depending on the methods set up, there are typically 14 to 16 cycles per block. If the ion beam decreases or becomes unstable, the current (and equivocally, the temperature) can be increased during inter-block calibrations. Depending on the sample size, tracer composition and ionization rate (beam intensity), among other factors, 10 to 12 blocks of lead measurements are typical, which takes approximately 3-4

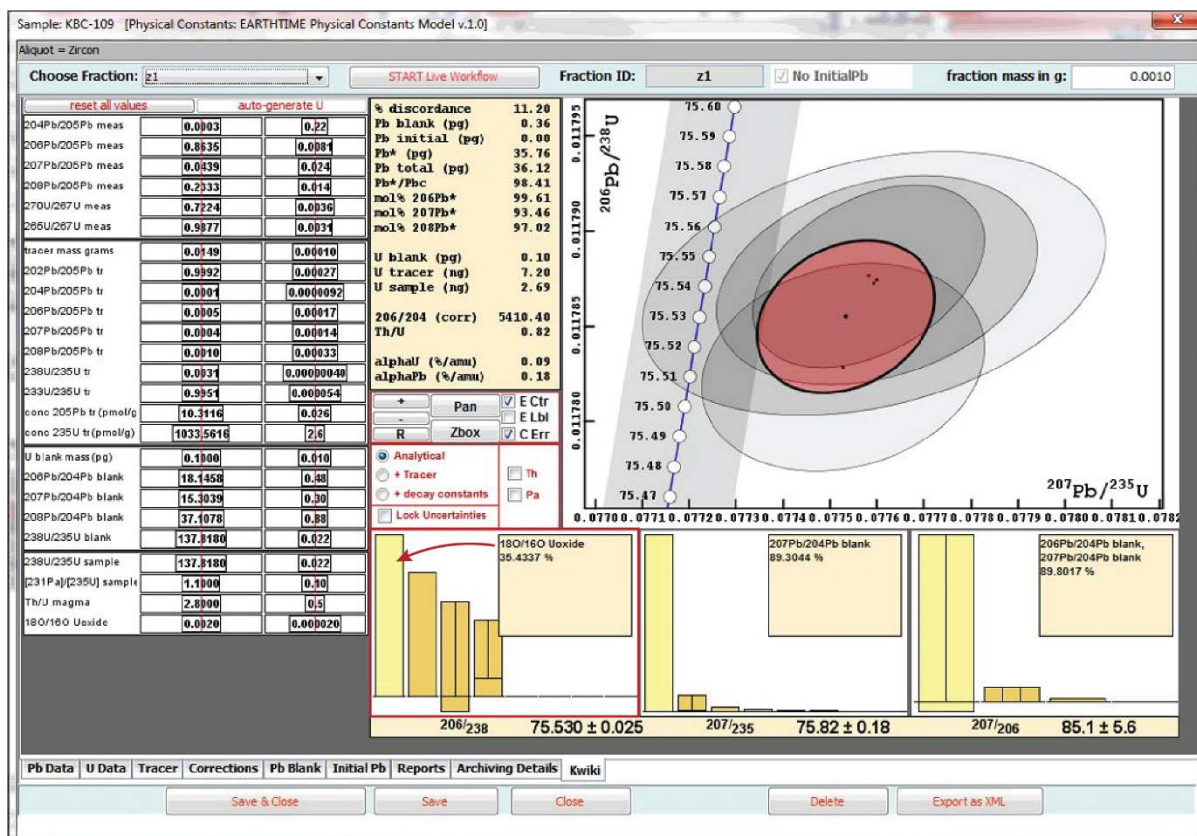


**Fig. 2.10** IsoProbe displays during the analysis of lead (top) and uranium (bottom). The measured isotopic masses are annotated in red where Pb isotopes are measured sequentially (separate peaks) with 14-16 cycles per block, and U isotopes are measured simultaneously (as oxides).





Fig. 2.11 Tripoli displays during the analysis of lead (top) and uranium (bottom). Trends and degree of scatter are used to advise operational conditions in real-time. For example, the first four blocks of the Pb analysis (top) show a strong fractionation trend and these data will not be used in calculating the sample date.



**Fig. 2.12** ET\_Redux during the final stages of analysis or after completion. The bar graph (highlighted within the red box) illustrates sources of uncertainty in the calculated  $^{206}\text{Pb}/^{238}\text{U}$  date and their proportional contribution to the overall uncertainty. In this example, the  $\delta^{18}\text{O}$  calculation uncertainty, which is often a negligible component, is the largest contributing factor (35.4%) due to the exceptionally high level of precision of this analysis.

hours. Over this time, the temperature of the filament may be increase up to  $\sim 1130^\circ\text{C}$ , after which point effectively all lead is ionized.

After the lead measurements have been completed, prepare the sample for uranium ionization.

9. In the IonVantage window, 'stop' the Pb measurement and record relevant notes
10. Proceed to change the operational parameters for the analysis of U isotopes (change CPS to volts, select appropriate display channels and adjust the magnetic mass)
11. Increase the current until the temperature read-back reaches  $1370^\circ\text{C}$
12. Conduct a peak center and adjust magnetic mass accordingly (auto focus is not required as the beam was focused for the same sample during measurement of Pb)
13. Check the beam intensity is appropriate and increase the current (hence temperature) if necessary
14. Return to the IonVantage home screen and select the appropriate sample and element (U) and press 'run' to begin analysis



Uranium has a high ionization potential within this temperature window; thus, all selected isotopes of uranium (as oxides) are measured simultaneously using faraday collectors. This means the beam intensity will falter much quicker compared to the lead analysis but can be adjusted at any time. The measurement of uranium isotopes typically takes less than 20 minutes and can contain 8 to 16 blocks. The maximum temperature for uranium ionization is ~1400°C.

Once all measurements are complete, immediately close the isolation valve, reduce the filament current to zero and restore the operational parameters to those of the lead measurements. Record relevant notes in IonVantage. Adjust the turret location using the digital control to position the next sample in place and repeat the measurement process for the next sample.

## 2.7 Data reduction and uncertainties

Data collected from the thermal ionization mass spectrometer is reduced and analysed in real-time while data collection is ongoing; an approach which is designed to facilitate dynamic analysis conditions (adjusting settings according to the observed ionization trends). Tripoli software is used to reduce the data by manually identifying fractionation trends and instability in the ion beam in real time (Fig. 2.11) (Bowring *et al.*, 2011). This data is then imported in a live workflow to ET\_Redux, which applies various mathematical corrections and calculates uncertainty (Fig. 2.12) (Bowring *et al.*, 2011). Procedures for data reduction and uncertainty calculation are also described by McLean *et al.* (2011, 2015).

Calculated uncertainties compiled in ET\_Redux are broken down into categories by percentage contribution to the overall uncertainty (Fig. 2.12). These values are used in the live workflow to establish the number analytical blocks required to optimize measurement precision. Uncertainty relating to the lead and uranium measurement can be reduced by stabilizing the ion beam and collecting further data. On the other hand, further measurements may not improve analytical precision if the largest source of uncertainty becomes the  $\alpha\text{Pb}$ , Pb blank,  $\delta^{18}\text{O}$  or  $\text{Th}_i$  calculation uncertainties, among others. The following are some of the most relevant uncertainties to monitor.

### 2.7.1 Fractionation correction uncertainty ( $\alpha\text{Pb}$ )

Fractionation of lead isotopes during ionization is mathematically corrected in ET\_Redux and the associated uncertainty of the calculation is called  $\alpha\text{Pb}$ . It is not uncommon that the  $\alpha\text{Pb}$  component of the overall uncertainty can constitute the largest factor when using the ET535 tracer solution because of the limited mass range covered by these isotopes. Where all other sources of uncertainty are anticipated to be comparatively small, the double spike ET2535 tracer solution can be used instead (Section 2.5.4) to reduce the impact of the  $\alpha\text{Pb}$  correction uncertainty. This double spike tracer solution includes  $^{202}\text{Pb}$ , which increases the isotopic range over which the correction factor is calculated, thus reducing uncertainty relating to the fractionation correction calculation.



### 2.7.2 Common lead uncertainty ( $Pb_c$ )

Given the present analytical capabilities of CA-ID-TIMS (including double spike tracer solutions), the primary restricting uncertainty is typically the laboratory lead blank, which is uncertainty relating to contamination of common lead ( $Pb_c$ ) during the laboratory procedure. The physical amount of  $Pb_c$  in any given measurement is usually in the range of 0.20 – 0.50 picograms. The impact of picogram scale increases in  $Pb_c$  depends on the size of the zircon crystal (estimated using  $Pb^*/Pb_c$ ; the radiogenic to common lead ratio). If the zircon is relatively large, marginally higher  $Pb_c$  is negligible; however, small samples (low  $Pb^*/Pb_c$ ) are more substantially impacted by  $Pb_c$  contamination. Caution during the laboratory procedure must be exercised to limit the introduction of contaminants (*i.e.*, high standard cleaning procedures, do not reach over open containers, etc.).

### 2.7.3 Oxygen isotope uncertainty ( $\delta^{18}O$ )

When the highest possible precision is neared, given current laboratory and analytical procedure, smaller sources of uncertainty begin to become proportionally significant. One such uncertainty is the  $\delta^{18}O$  correction uncertainty that arises from the measurement of uranium isotopes as oxides. Uranium isotopes measured during the TIMS procedure typically include  $^{233}U$  (anthropogenic spike isotope),  $^{235}U$  (mixed anthropogenic and natural) and  $^{238}U$  (natural); however, because the uranium is measured as oxides (two oxygens each), the actual isotopic weights measured are 265, 268 and 270 atomic mass units respectively, which assumes an oxygen isotopic composition of 100%  $^{16}O$ . Recalculating the ratio of uranium isotopes not measured or measured as the wrong isotope (*e.g.*,  $^{233}U + ^{16}O + ^{18}O$  measured as  $^{235}U + 2 \times ^{16}O$ ) is complex and relies on a regularly recalculated laboratory parameter of the  $\delta^{18}O$ . The  $^{18}O/^{16}O$  ratio that was used during the period of this study is  $0.00205 \pm 0.00002$  (J. Ramezani, per. comm.). This miniscule uncertainty propagates in the recalculation of uranium oxide isotopic masses causing typically negligible uncertainty unless all other sources of uncertainty are highly optimized.

### 2.7.4 Initial thorium uncertainty ( $Th_i$ )

Similar to  $\delta^{18}O$ , the initial Thorium ( $Th_i$ ) correction calculation is another source of uncertainty that is typically miniscule unless the highest precision currently possible is neared with the added rarity of unusually high thorium concentration in the zircon crystal. Correcting for initial thorium is a standard procedure in uranium-lead geochronology due to the intermediate daughter product  $^{230}Th$  present in the  $^{238}U - ^{206}Pb$  decay chain; however, uncertainty relating to this correction is only significant where other sources of uncertainty have been optimized (Schmitz and Bowring, 2001; Bowring *et al.*, 2006). Calculating the amount of Th initially present in zircon depends on the partitioning ratio between zircon and magma at the time of crystallization (Schärer, 1984). To accurately estimate the amount of non-radiogenic thorium present in the zircon at crystallization, the current  $^{230}Th$  composition of the sample is measured and the initial Th composition of the magma is estimated, then the two are correlated with a calculated coefficient. Two individual sources of uncertainty exist in this calculation: 1) the precision

of the coefficient and 2) uncertainty related to estimation of the initial magmatic Th composition. Uncertainty due to  $Th_i$  in TIMS data is commonly related to the latter of these two sources when the Th/U ratio measured during analysis is  $>1$ , which indicates an atypical magma composition that are not accounted for in the standard initial magmatic Th estimation.

## 2.8 Summary of outcomes

One hundred and thirty-one zircons from 20 different Campanian bentonites of the Western Interior were analysed with this method during my 2017 and 2018 visits. Eight entirely new ages were generated, two ages were generated for new samples of previously TIMS dated bentonite outcrops, and 21 zircon analyses supplemented five existing bentonite ages. Twenty-five zircon analyses from five further bentonite samples either didn't produce coherent ages or are yet to be finalized. Bentonite ages to which dates collected here contribute are listed in Table 2.1 and discussed in Chapters Three, Four and Six and in co-authored work (*e.g.*, Ramezani et al., in review).

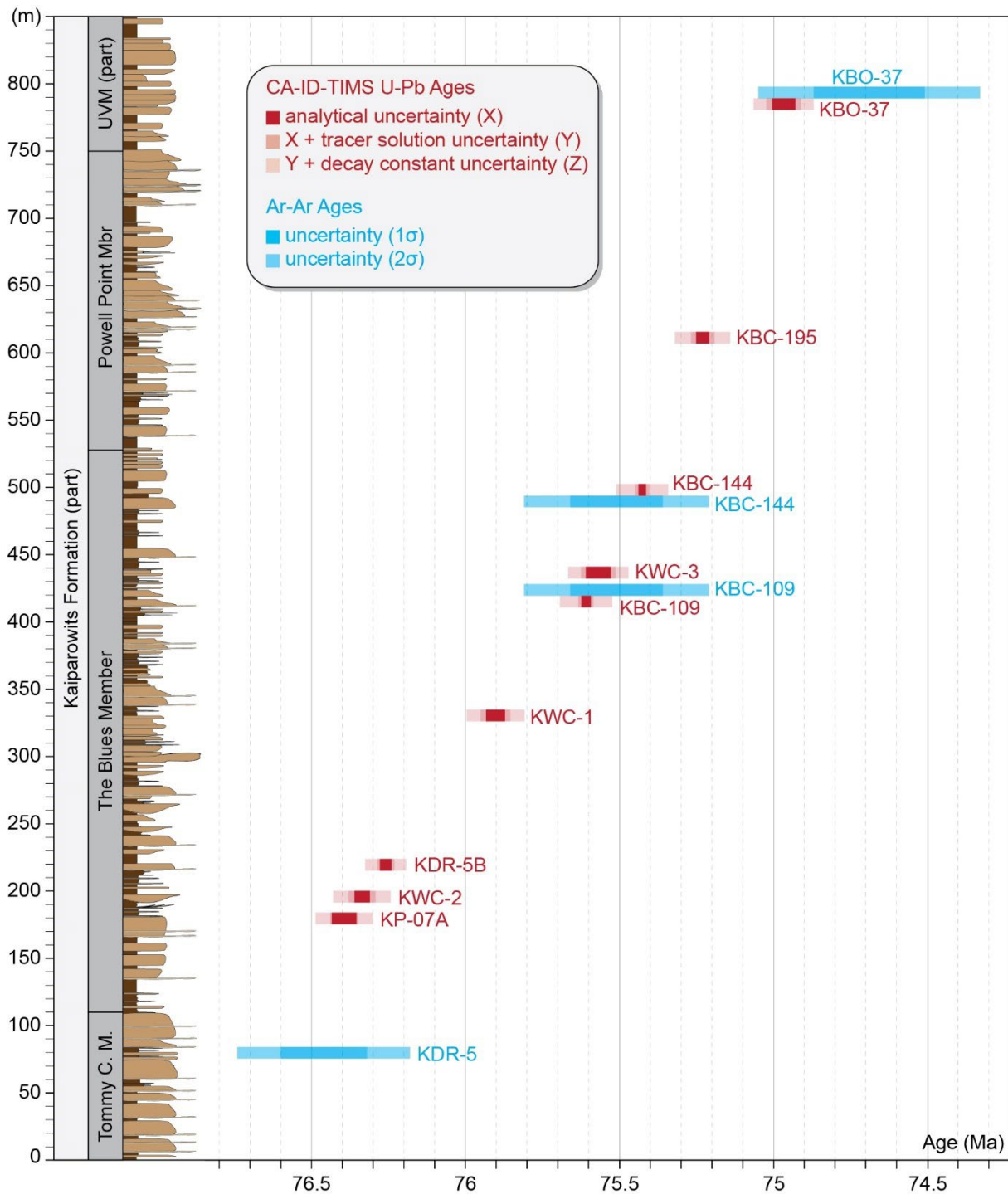
Precision of bentonite ages calculated here are on par with the forefront of current geochronologic techniques and were considerably improved from previous ages of the same units. Uncertainty was reported in the format of  $\pm X/Y/Z$  following Schoene *et al.* (2006), where X is the internal (analytical) uncertainty, Y incorporates tracer calibration uncertainty, and Z also includes the U series decay constants of Jaffey *et al.* (1971). Analytical uncertainty ranged from 0.02 to 0.05 % for bentonite ages reported here. Comparison of this new CA-ID-TIMS data for the Kaiparowits Formation in southern Utah with the previous  $^{40}\text{Ar}/^{39}\text{Ar}$  ages of Roberts *et al.* (2005; recalculated by Roberts, 2013) shows a considerable improvement in precision and accuracy (Fig. 2.13).

Significant refinements are made to the age and correlation of strata in the study areas based on data that are part of my contribution and other new ages generated from the project (*i.e.*, those of J. Ramezani; see co-authored works). These findings can be grouped into four general themes from broadest to most specific and summarized as follows. Firstly, new data demonstrate that richly fossiliferous Campanian strata separated by up to 1500 km were deposited contemporaneously (see Ramezani et al., in review). This finding contributes to discussion around dinosaur latitudinal endemism across the Western Interior during this time. The second finding was the discovery of bentonites from this study that are separated by up to 1500 km with statistically indistinguishable ages based on the internal (analytical) uncertainty ( $\sim 0.02\%$ ). This finding raises questions about bentonite correlation and synchronous, large-scale volcanism during the Campanian (see Chapter Six). The third theme regards stratigraphic refinement of the Kaiparowits Formation in particular. This unit is now one of the most tightly constrained successions in the world owing to nine new high-precision CA-ID-TIMS bentonite ages (Chapter Four and Ramezani et al., in review) and a novel, numerical approach to intraformational correlation presented in Chapter Four. Finally, age refinement of Campanian strata facilitates temporal calibration of fossil localities

**Table 2.1** Summary of bentonite ages from the candidate' s 2017 and 2018 work at the Massachusetts Institute of Technology.

Sample Name	Abbrev. Name	Stratigraphic Unit	Location	<sup>206</sup> Pb / <sup>238</sup> U Age (Ma)*	Uncertainty (Ma)			MSWD	n#			Publication / Chapter
					X	Y	Z		n <sub>m</sub>	n <sub>t</sub>	n <sub>c</sub>	
IL082717-1	IL	Dinosaur Park Fm	Alberta	74.27	0.017	0.026	0.084	0.47	7	>10	10	Ramezani <i>et al.</i>
KBO-37/KBO05056-1	KBO-37	Kaiparowits Fm	Utah	74.968	0.038	0.056	0.098	1.1	7	13	4	Chapter 4
KBC-195	KBC-195	Kaiparowits Fm	Utah	75.231	0.021	0.038	0.089	0.73	6	11	3	Ramezani <i>et al.</i>
KBC-144	KBC-144	Kaiparowits Fm	Utah	75.427	0.012	0.023	0.084	1.8	7	12	3	Ramezani <i>et al.</i>
KWC050316-3	KWC-3	Kaiparowits Fm	Utah	75.569	0.04	0.056	0.098	1.2	8	12	12	Chapter 4
KBC-109	KBC-109	Kaiparowits Fm	Utah	75.609	0.015	0.025	0.085	0.62	5	9	3	Ramezani <i>et al.</i>
KWC050316-1	KWC-1	Kaiparowits Fm	Utah	75.903	0.031	0.048	0.094	1.8	5	7	7	Chapter 4
KDR-5B/KDR050416-1	KDR-5B	Kaiparowits Fm	Utah	76.259	0.019	0.028	0.066	0.98	4	14	8	Chapter 4
PR082917-1	PR	Oldman Fm	Alberta	ca 76.3	(0.03%)^	-	-	-	3	11	11	N/A
NF082917-1	NF	Oldman Fm	Alberta	76.3ish	-	-	-	-	-	6	6	N/A
KWC050316-2	KWC-2	Kaiparowits Fm	Utah	76.336	0.025	0.044	0.093	0.92	9	10	10	Chapter 4
KP-07A	KP-07A	Kaiparowits Fm	Utah	76.394	0.04	0.045	0.093	0.6	5	5	5	Ramezani <i>et al.</i>
KC061517-1	KC	Judith River Fm	Montana	78.594	0.024	0.032	0.09	1.4	6	7	7	Ramezani <i>et al.</i>
B2-07B	B2-07B	Wahweap Fm	Utah	81.476	0.022	0.031	0.092	2.2	4	>10	10	Chapter 3
WLS-R-070818	WLS-R	Wahweap Fm	Utah	81.465	0.036	0.042	0.097	0.47	7	7	7	Chapter 3

*n*<sub>#</sub> = number of grains/analyses; *n*<sub>m</sub> = number of grains/analyses in weighted mean age; *n*<sub>t</sub> = total number of grains/analyses; *n*<sub>c</sub> = number of grains/analyses in my contribution. \* weighted mean age. MSWD = mean square of the weighted deviates. ^ Details omitted pending future publication.



**Fig. 2.13** Comparison of new high-precision CA-ID-TIMS ages (red, all  $2\sigma$ ) generated during the 2017/2018 research visits with previous  $^{40}\text{Ar}/^{39}\text{Ar}$  ages (blue) for the Kaiparowits Formation, southern Utah. Ages are plotted against the approximate stratigraphic level of the sampled bentonite outcrops (see Chapter Four). The new ages show considerably improved precision such that previously indistinguishable ages are easily separated using the analytical uncertainty of the CA-ID-TIMS ages. Note that direct comparison of these two datasets is tentative due to systematic difference in the analysis of each radioisotopic system. See Chapters 3 and 4 (and Ramezani et al., in review) for discussion.

including adjustments of up to (and exceeding) a million years, and robust, quantitative uncertainty for the first time (see Chapters Three and Four). This refinement has implication for direct comparison of fossil biota and investigations of diversification mechanisms (see Chapter Three). Together, these contributions answer the growing need for temporal refinement of Campanian strata in Western North America and the significance of these findings is explored throughout this thesis.

## 2.9 Glossary

*Blank checked:* solutions that are regularly analysed in isolation for U and Pb contamination

*Beaker cleaning solutions:* not blank checked for contamination; typically involved in cleaning and do not come into direct contact with sample material

*Moat solutions:* Similar to beaker cleaning; used in dissolution vessel to maintain an equilibrium inside and outside the nano-capsules

*Tracer solution:* Anthropogenic U and Pb isotopes in a precisely calibrated solution; added to samples in carefully measured amounts, which facilitates the calibration of isotopic ratios during analysis

*Total procedural blank:* Empty sample cell treated exactly as those containing samples throughout the entire laboratory process. Measured to check levels of procedural contamination.

*MQ (Milli-Q) water:* ultrapure (Type 1) water with virtually no dissolved or suspended contaminants. Refers to bulk MQ water unless otherwise stated as blank checked.

*Resin:* AG1-X8 Anion Resin, Cl-form, 200-400 mesh

*HCl:* Hydrochloric acid

*HF:* Hydrofluoric acid

*HNO<sub>3</sub>:* Nitric acid

*H<sub>3</sub>PO<sub>4</sub>:* Phosphoric acid

## Chapter Three

Refined geochronology and lithostratigraphy of the Upper Cretaceous Wahweap Formation, Utah, U.S.A. and the age of early Campanian vertebrates from southern Laramidia



*Wahweap Formation at Nipple Butte*



**Preface**

This is the first of three stratigraphy-focused chapters, which are presented in increasing stratigraphic order of Campanian units from southern Utah. As such, this work investigates the Wahweap Formation and includes two of the high-precision U-Pb ages reported in Chapter Two. The equivalent manuscript of this chapter was published in *Palaeogeography, Palaeoclimatology, Palaeoecology* in 2022 ([doi.org/10.1016/j.palaeo.2022.110876](https://doi.org/10.1016/j.palaeo.2022.110876)). The co-authored manuscript was adapted for inclusion in this thesis with only minor modifications. The Statement of Contribution of Others (p. v) outlines co-author contributions. I conducted and compiled all chrono- and lithostratigraphic work in the manuscript, which was edited for accuracy and language primarily by E. Roberts. Fossil locality details were provided by collaborating institutions including the Utah Museum of Natural History and Denver Museum of Nature and Science, and I conducted spatial and stratigraphic investigations and interpretations of this data. The only work that is not specifically my own is Section 3.7.1, which features notable contributions by J. Sertich that I summarize in the first and last paragraph of that section.

**Abstract**

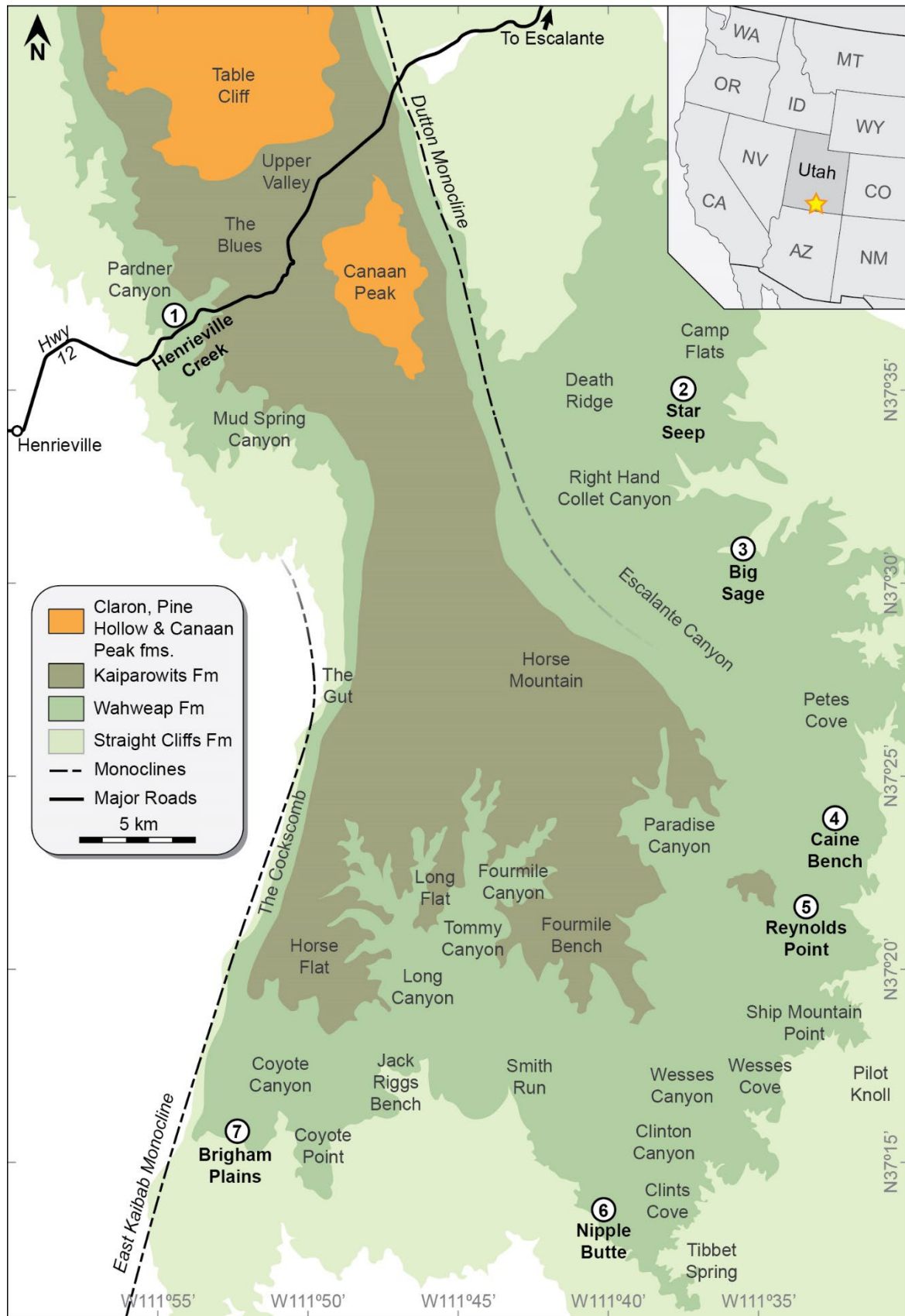
The Western Interior of North America preserves one of the most complete successions of Upper Cretaceous marine and non-marine strata in the world; among these, the Cenomanian-Campanian units of the Kaiparowits Plateau in southern Utah are a critical archive of terrestrial environments and biotas. This chapter presents new radioisotopic ages for the Campanian Wahweap Formation, along with lithostratigraphic revision, to improve the geological context of its fossil biota. The widely accepted informal stratigraphic subdivisions of the Wahweap Formation on the Kaiparowits Plateau are herein formalized and named the Last Chance Creek Member, Reynolds Point Member, Coyote Point Member, and Pardner Canyon Member (formerly the lower, middle, upper, and capping sandstone members respectively). Two high-precision U-Pb zircon ages were obtained from bentonites using CA-ID-TIMS, supported by five additional bentonite and detrital zircon LA-ICP-MS ages. Improved geochronology of the Star Seep bentonite from the base of the Reynolds Point Member via CA-ID-TIMS demonstrates that this important marker horizon is over a million years older than previously thought. A Bayesian age-stratigraphic model was constructed for the Wahweap Formation using the new geochronologic data, yielding statistically robust ages and associated uncertainties that quantifiably account for potential variations in sediment accumulation rate. The new chronostratigraphic framework places the lower and upper formation boundaries at  $82.17 \pm 1.47/-0.63$  Ma and  $77.29 \pm 0.72/-0.62$  Ma, respectively, thus constraining its age to the first half of the Campanian. Additionally, a holistic review of known vertebrate fossil localities from the Wahweap Formation was conducted to better understand their spatio-temporal distribution including revised ages for early members of iconic dinosaur lineages such as Tyrannosauridae, Hadrosauridae, and Centrosaurinae. Chrono- and lithostratigraphic refinement of the Wahweap Formation and its constituent biotic assemblages establishes an important reference for addressing questions of Campanian terrestrial palaeoecology and macroevolution, including dinosaur endemism and diversification throughout western North America.

### 3.1 Introduction

The Western Interior of North America preserves near-continuous successions of Upper Cretaceous strata deposited in a variety of settings ranging from alluvial and lacustrine to epicontinental marine (*e.g.*, Molenaar and Rice, 1988; Kauffman, 1985; Roberts and Kirschbaum, 1995; Miall *et al.*, 2008). These world-famous strata have been instrumental in developing global concepts of Cretaceous geochronology, biochronology, sequence stratigraphy, palaeoclimatology, and paleontology (*e.g.*, van Wagoner and Bertram, 1995; Lehman, 1997; Cifelli *et al.*, 2004; Cobban *et al.*, 2006; Fricke *et al.*, 2010; Sampson *et al.*, 2010; Loewen *et al.*, 2013a; Sewall and Fricke, 2013; Titus and Loewen, 2013; Voris *et al.*, 2020; Wilson *et al.*, 2020). Among these strata, the Upper Cretaceous succession of the Kaiparowits Plateau in southern Utah, U.S.A., preserves one of the most complete non-marine records in the Western Interior, and is remarkable for its abundant and diverse floral, invertebrate, and vertebrate fossil contents (*e.g.*, Titus and Loewen, 2013, and papers therein). These strata include the coastal to fluvial upper Turonian to Santonian Straight Cliffs Formation, fluvial lower to middle Campanian Wahweap Formation, and fluvial middle to upper Campanian Kaiparowits Formation. Fossils from these formations have been particularly important for developing recent hypotheses on the biogeographic distribution and macroevolution of Late Cretaceous dinosaurs and other non-marine tetrapods in western North America (*e.g.*, Sankey, 2001; Gates *et al.*, 2010; Sampson *et al.*, 2010; Loewen *et al.*, 2013a; Voris *et al.*, 2020). Rigorous investigation of these hypotheses of latitudinal endemism across Laramidia, the western of the two North American landmasses separated by the Western Interior Seaway during the Cretaceous (Fig. 3.2), requires temporally calibrated contemporaneous biota from both northern and southern localities (Sampson *et al.*, 2010).

Paleontological research in the Wahweap Formation in southern Utah over the last 30 years has documented a wealth of fossil taxa comprising significant Campanian non-marine assemblages from southern Laramidia (*e.g.*, Cifelli, 1990b, 1990c, 1990d; Eaton, 1991, 2002; Eaton *et al.*, 1999a, 1999b; Kirkland and DeBlieux, 2010; Gates *et al.*, 2011, 2014; Loewen *et al.*, 2013a; Titus and Loewen, 2013, and papers therein; Holroyd and Hutchison, 2016; Lund *et al.*, 2016a; Titus *et al.*, 2016). Indeed, because fossil exploration in the formation began relatively recently, compared to historic work from northern Laramidia, the paleontological significance of the Wahweap Formation is only now becoming more widely recognized. An exceptionally diverse micro-faunal assemblage and an ever-increasing collection of larger taxa from the formation, including some of the earliest known members of dominant Late Cretaceous dinosaur lineages such as Tyrannosauridae, Hadrosauridae, and Centrosaurinae (*e.g.*, Kirkland and DeBlieux, 2010; Loewen *et al.*, 2013a; Gates *et al.*, 2014; Lund *et al.*, 2016a), highlight the need to place these important fossils in a more refined temporal context.

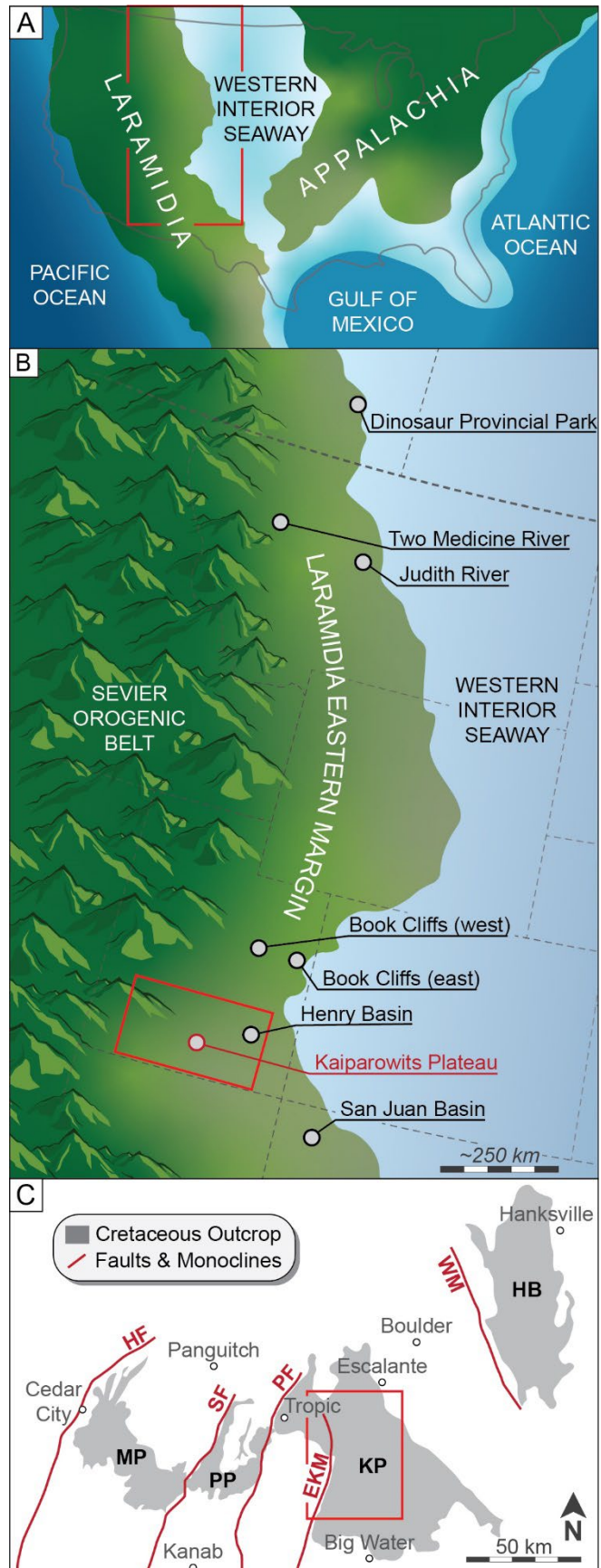
The lithostratigraphic framework for the Wahweap Formation proposed by Eaton (1991), including informal member subdivisions on the Kaiparowits Plateau, has proven to be widely accepted



**Fig. 3.1** Simplified geological map of the Kaiparowits Plateau, including field area names, compiled from various USGS 1:24,000 and the USGS 1:100,000 geological maps of the Escalante and Smoky Mountain 30' x 60' quadrangles by Doelling and Willis (2006, 2018). Numbers refer to measured stratigraphic sections in Figure 3.4.

and practical through repeated use in all subsequent sedimentological and paleontological studies. The age of the Wahweap Formation, indicated by Eaton (1991) as early Campanian based on mammal biostratigraphy, was later investigated by Jinnah *et al.* (2009) and Jinnah (2013) using  $^{40}\text{Ar}/^{39}\text{Ar}$  geochronology from two interstratified bentonite (weathered volcanic ash) beds. These, along with two U-Pb detrital zircon maximum depositional ages (Jinnah *et al.*, 2009) remain the only documented radioisotopic age constraints for the Wahweap Formation; however, subsequent magnetostratigraphic analysis (Albright and Titus, 2016) suggested that these early radioisotopic dates were erroneously young, leading to ambiguity about the formation's true age.

**Fig. 3.2** Large-scale palaeogeographic and physiographic maps illustrating the relative position of the Kaiparowits Plateau. A) Continental palaeogeography at ca 80 Ma illustrating western (Laramidia) and eastern (Appalachia) North America separated by the Western Interior Seaway (red box = panel B; adapted from Sampson *et al.*, 2010, and references therein). B) Interpreted palaeogeography of central-eastern Laramidia at ca 80 Ma illustrating the relative positions of key areas with early Campanian strata (see Fig. 3.9) (red box = panel C; adapted from Lehman, 1997, Jinnah *et al.*, 2009 and Titus *et al.*, 2013). C) Southern Utah physiographic regions illustrating the Markagunt (MP), Paunsaugunt (PP) and Kaiparowits (KP) plateaus and the Henry Basin (HB), partitioned by structural features including the Hurricane (HF), Sevier (SF) and Paunsaugunt (PF) faults and the East Kaibab (EKM) and Waterpocket (WM) monoclines (red box = Fig. 3.1) (adapted from Titus *et al.*, 2013).





The purpose of this study is to 1) formalize lithostratigraphic nomenclature for the Wahweap Formation; 2) provide new U-Pb zircon ages underpinned by high-precision chemical abrasion isotope dilution thermal ionization mass spectrometry (CA-ID-TIMS) for the Star Seep bentonite and supported by additional laser ablation inductively coupled plasma mass spectrometry (LA-ICP-MS) bentonite zircon and detrital zircon ages; 3) establish a well-resolved chronostratigraphic framework in the form of a Bayesian age-stratigraphic model for the formation; and 4) integrate the new temporal framework for the Wahweap Formation with its vertebrate fossil content.

Resolving the temporal framework of the Wahweap Formation and refining lithostratigraphic subdivisions within which paleontological specimens are placed provides much needed chronostratigraphic clarity. This can be used for subsequent palaeoecological and evolutionary studies and elucidates the age of key vertebrate taxa for understanding classic Campanian-Maastrichtian non-marine ecosystems from western North America. Furthermore, the present study advocates for best practice age reporting, specifically regarding the inclusion of uncertainty, which is often unreported and becomes statistically significant in studies that investigate geologically rapid evolutionary processes such as taxal turn-overs and diversification. Outcomes from this chapter support ongoing investigations of hypothesized Late Cretaceous latitudinal biotic distributions in North America and the driving mechanisms behind species diversification intervals leading to the ‘zenith of the dinosaurs’ (Sloan, 1976; Dodson, 1983; Clemens, 1986; Dodson and Tatarinov, 1990) in the Campanian and Maastrichtian.

### 3.2 Previous work

#### 3.2.1 Lithostratigraphy

The Wahweap Formation, first described by Gregory and Moore (1931) as the Wahweap Sandstone, is a 360 to 460-meter-thick fluvial succession comprising interbedded floodplain mudstones and channel sandstones. Peterson and Waldrop (1965) formally defined the unit as the Wahweap Formation, which was followed by more detailed sedimentological investigation by Peterson (1969), Eaton (1991), Little (1995), Pollock (1999), Simpson *et al.* (2008, 2014) and Jinnah and Roberts (2011). The Wahweap Formation is exposed in southern Utah, U.S.A., along the margins of the Markagunt and Paunsaugunt plateaus (Biek *et al.*, 2015) and extensively throughout the Kaiparowits Plateau (Fig. 3.1) and is also correlated to the Masuk and Tarantula Mesa Sandstone formations to the northeast in the nearby Henry Basin (Eaton, 1990; Corbett *et al.*, 2011; Jinnah, 2013; Lawton *et al.*, 2014a). These four physiographic regions were partitioned by the (west to east) Hurricane, Sevier, and Paunsaugunt faults, and the East Kaibab and Waterpocket monoclines (Fig. 3.2) (Titus *et al.*, 2013). Although all contain exposures of Upper Cretaceous strata, the Kaiparowits Plateau preserves the most numerous Wahweap Formation fossil localities of the four areas. This observed distribution potentially represents discovery bias due to the nature of exposures on the Kaiparowits Plateau as opposed to the heavily forested and inaccessible Markagunt and Paunsaugunt plateaus (the latter hosts rich microvertebrate localities, *e.g.*, Eaton, 1999;



Eaton and Cifelli, 2013; Titus *et al.*, 2016); however, it nevertheless highlights the need for targeted chronostratigraphic work on the heavily studied, fossiliferous Kaiparowits Plateau exposures east of the East Kaibab Monocline.

Two models for lithostratigraphic subdivision of the Wahweap Formation have previously been proposed. Eaton (1991) proposed the subdivisions of lower, middle, upper and capping members (informal) based largely on sand:mud ratios and changes in alluvial architecture observed on the Kaiparowits Plateau. Doelling (1997), on the other hand, described outcrops from the Markagunt and Paunsaugunt plateaus and did not delineate the lower three units of Eaton (1991); recommending instead only a lower and upper unit where Doelling's upper unit correlated to Eaton's capping sandstone. Discrepancies in sedimentary architecture of the lower portion of the formation across the three southern Utah plateaus and the Henry Basin succession are attributed to lateral facies change from proximal to distal floodplain environments (Corbett *et al.*, 2011; Jinnah and Roberts, 2011). Due to this lateral variation in sedimentological character, lithostratigraphic and geochronologic work in this chapter is generally restricted to strata across the Kaiparowits Plateau region.

### 3.2.2 Chronostratigraphy

The Wahweap Formation has previously been constrained as early to middle Campanian in age based on biostratigraphic and radioisotopic dating methods, additionally supported by magnetostratigraphic and sequence stratigraphic inferences (Eaton, 1991; Jinnah *et al.*, 2009; Jinnah and Roberts, 2011; Eaton and Cifelli, 2013; Albright and Titus, 2016). Detailed biostratigraphic efforts over the years include meticulous vertebrate microfossil work, particularly on mammaliaform assemblages, which suggested an early to middle Campanian age for the Wahweap Formation (Eaton, 1991, 1999, 2002; Eaton *et al.*, 1999a, 1999b; Eaton and Cifelli, 2013). Alluvial sequence stratigraphic studies of the Wahweap Formation have identified a sequence boundary at the top of the Coyote Point Member (formerly the upper member), inferred to reflect the globally recognized ~80 Ma sequence boundary (Lawton *et al.*, 2003; Jinnah and Roberts, 2011; Haq, 2014). Although these studies provided useful age control, independent radioisotopic geochronology is required to construct a robust chronostratigraphic framework for the Wahweap Formation at the resolution necessary for more detailed palaeoecological work. Despite their inherent intricacies (see Bowring *et al.*, 2006), radioisotopic chronometers provide the only means of arriving at a numerical age that can be globally correlated. Additionally, a biostratigraphically-independent geochronologic framework avoids circular interpretations when trying to simultaneously indicate age and infer biogeographic and macroevolutionary patterns from the same fossil assemblage (*e.g.*, Irmis *et al.*, 2010).

Jinnah *et al.* (2009) published the first radioisotopic age data for the Wahweap Formation, including an  $^{40}\text{Ar}/^{39}\text{Ar}$  bentonite age from ~40 m above the base of the formation in the Camp Flat area (Fig. 3.1), as well as two U-Pb detrital zircon maximum depositional ages generated using the sensitive

high resolution ion microprobe (SHRIMP) technique (Jinnah *et al.*, 2009). Using these data and other  $^{40}\text{Ar}/^{39}\text{Ar}$  ages from the overlying Kaiparowits Formation that provide minimum age constraint (Roberts *et al.*, 2005), Jinnah *et al.*, (2009) extrapolated a linear average sediment accumulation rate of between 8.4 and 13.1 cm/kyr for the Wahweap Formation. The initial bentonite age was later recalculated (Jinnah, 2013) using the revised age of the Fish Canyon Tuff sanidine standard of 28.2 Ma (Kuiper *et al.*, 2008). The recalculated bentonite age of  $80.6 \pm 0.6$  Ma ( $2\sigma$  internal error) was also accompanied by a second radioisotopically dated bentonite reportedly ten meters higher in section from the adjacent Star Seep area. The latter sample yielded an  $^{40}\text{Ar}/^{39}\text{Ar}$  age of  $79.9 \pm 0.6$  Ma. From this work, the Wahweap Formation was estimated to have been deposited between 81 and 77 Ma (Jinnah and Roberts, 2009; Jinnah, 2013).

The above two  $^{40}\text{Ar}/^{39}\text{Ar}$  bentonite ages remained for nearly a decade the only absolute constraints on the Wahweap Formation, whose abundance of well-preserved bentonites is significantly lower than that of the overlying Kaiparowits Formation. More recent magnetostratigraphic work by Albright and Titus (2016) identified a polarity reversal attributed to the C33r-C33n chron boundary 200 m stratigraphically higher than the upper bentonite of Jinnah (2013); however, both the reversal and the bentonite were thought to be  $\sim 79$  Ma given the then-current calibrations (GTS2012 – Ogg, 2012; Jinnah, 2013). To rectify this discrepancy, Albright and Titus (2016) revisited the calibration of the C33r-C33n reversal based on  $^{40}\text{Ar}/^{39}\text{Ar}$  geochronology of its reference section in the Elk Basin, Wyoming, and suggested a new age for this magnetochron boundary of 78.91 Ma, although this change was not adopted in GTS2020 (Gradstein *et al.*, 2020). Findings from Albright and Titus (2016) thus also highlighted the need for more robust of radioisotopic ages from the Wahweap Formation and across the Western Interior.

Chronostratigraphic divisions and nomenclature used in this study reflect globally recognized definitions described in GTS2020 (Gradstein *et al.*, 2020). Thus, the Campanian stage is constrained to between  $83.6 (\pm 0.2)$  Ma and  $72.1 (\pm 0.2)$  Ma, and further chronostratigraphic subdivision is not formally recognized (see Gale *et al.*, 2020). In North America, informal early, middle, and late Campanian subdivisions are common and although these constitute useful signposts, strict adherence to numerical boundary ages for these subdivisions represents a greater degree of confidence in these definitions than is currently appropriate. As such, the terms early and middle Campanian are used in this study to generally match a transition at *ca* 80.6 Ma indicated by the global first occurrence of *Baculites obtusus* in the marine realm (Cobban *et al.*, 2006; Gale *et al.*, 2020), although numerical ages are considered more relevant than the relative early and middle Campanian assignments.

### 3.2.3 Paleontology

Nearly one hundred aquatic and terrestrial vertebrate taxa have been recovered from the Wahweap Formation, making it one of the most diverse early to middle Campanian assemblages in North America

(Eaton, 1999; Eaton *et al.*, 1999a, 1999b; DeBlieux *et al.*, 2013; Titus and Loewen, 2013, and papers within; Titus *et al.*, 2016). These assemblages includes hadrosaurid, ceratopsid, and rare pachycephalosaurid and ankylosaurian ornithischian dinosaurs; tyrannosaurid and maniraptoran theropod dinosaurs; as well as numerous taxa of freshwater sharks and rays (chondrichthyans), bony fish (actinopterygians), lissamphibians (frogs, salamanders, and albanerpetontids), turtles, crocodyliforms, squamates (lizards), and many mammaliaforms (Cifelli, 1990b, 1990c, 1990d; Eaton, 1991, 2002; Eaton *et al.*, 1999a, 1999b; Kirkland and DeBlieux, 2010; Gates *et al.*, 2011, 2014; Brinkman *et al.*, 2013; DeBlieux *et al.*, 2013; Gardner *et al.*, 2013; Eaton and Cifelli, 2013; Irmis *et al.*, 2013; Kirkland *et al.*, 2013; Loewen *et al.*, 2013a, 2013b, 2013c; Rocek *et al.*, 2013; Holroyd and Hutchison, 2016; Lund *et al.*, 2016a; Titus *et al.*, 2016) (see Appendix C.3.1). Fossil material ranges from associated skeletons to isolated skeletal elements, teeth, osteoderms, fish scales, decapod crustacean claws, mollusk shells, petrified wood, leaves, and rare coprolites. Many of these smaller fossils occur commonly in micro- and mesovertebrate channel lag deposits in the lower three units of the formation (Jinnah and Roberts, 2011; DeBlieux *et al.*, 2013; Appendix C.3.1). Although relatively common in the overlying Kaiparowits Formation, articulated and associated remains in overbank mudstone deposits are less common in the Wahweap Formation (DeBlieux *et al.*, 2013), though this may be a stochastic sampling effect of fewer recorded vertebrate sites overall and increased reconnaissance efforts have begun to reveal more localities. A number of tetrapod trackways have been identified in the Wahweap Formation, particularly within strata at the boundary between the Last Chance Creek and Reynolds Point members (formerly lower and middle members), which predominantly preserve tridactyl impressions from hadrosaurs but also contain quadrupedal and smaller bipedal tracks possibly left by ceratopsians and theropods respectively (Hamblin and Foster, 2000; DeBlieux *et al.*, 2013).

Though the diverse faunal assemblage of the Wahweap Formation is known mostly from microsites (fragments <10 cm), and many taxa require more complete skeletal material for detailed identification and phylogenetic placement, notable macrofossils include early representatives of iconic latest Cretaceous dinosaur lineages such as the tyrannosaurid *Lythronax argestes* (Loewen *et al.*, 2013a), the centrosaurine ceratopsids *Diabloceratops eatoni* (Kirkland and DeBlieux, 2010) and *Machairoceratops cronusi* (Lund *et al.*, 2016a), and the hadrosaurids *Adelolophus hutchisoni* (Gates *et al.*, 2014), *Acristavus gagslarsoni* (Gates *et al.*, 2011) and two additional unnamed taxa (Gates *et al.*, 2014). These terrestrial large-bodied taxa, all described within the last decade, are part of critical early to middle Campanian assemblages from southern Laramidia including the potentially oldest known members of Tyrannosauridae, Hadrosauridae, and Ceratopsidae (Kirkland and DeBlieux, 2010; Loewen *et al.*, 2013a; Gates *et al.*, 2014; Holroyd and Hutchison, 2016; Voris *et al.*, 2020; Wilson *et al.*, 2020). As such, precise chronostratigraphic context of these biotic assemblages is a crucial component for continental-scale palaeoecological hypotheses around dinosaur diversification and endemism during the

Late Cretaceous (*e.g.*, Sankey, 2001; Gates *et al.*, 2010; Sampson *et al.*, 2010; Loewen *et al.*, 2013a; Voris *et al.*, 2020).

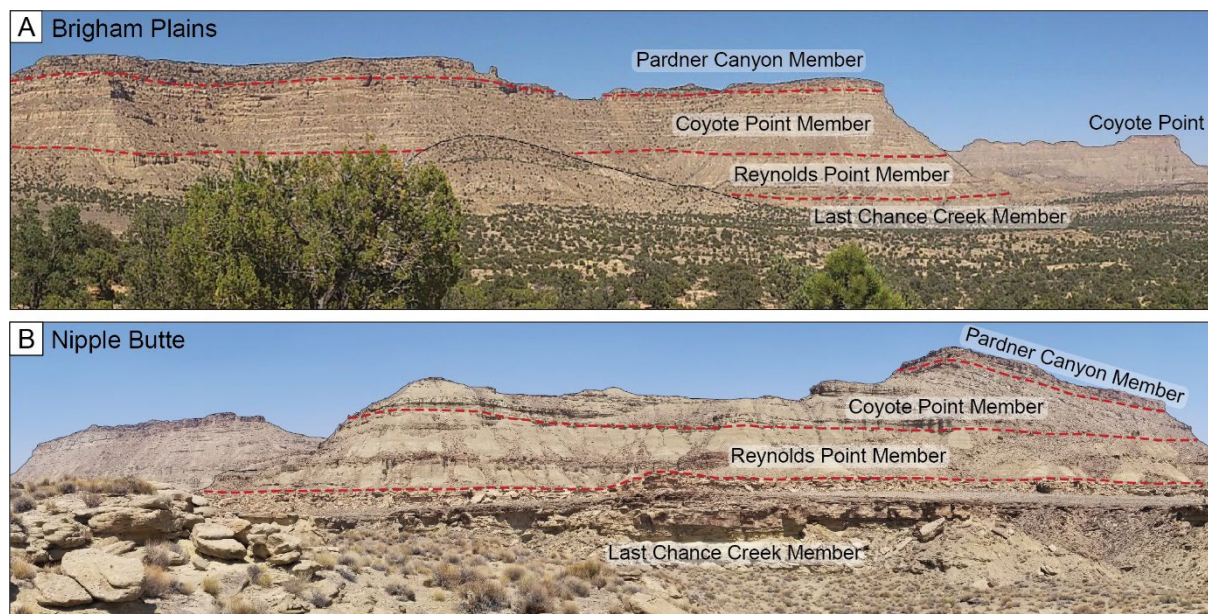
### 3.3 Lithostratigraphic nomenclature of the Wahweap Formation

Given the high degree of acceptance of the informal lithostratigraphic subdivisions specified for the Wahweap Formation by Eaton (1991), formal recognition is proposed for these members on the Kaiparowits Plateau following the guidelines of the International Commission on Stratigraphy and the North American Stratigraphic Code (see Oriel *et al.*, 2005). Formalization will significantly aid in clear and consistent reporting of fossil resources from the formation and simplify future stratigraphic studies. In place of the informal lower, middle, upper, and capping sandstone members of the Wahweap Formation on the Kaiparowits Plateau proposed by Eaton (1991), the present study suggests the names Last Chance Creek Member, Reynolds Point Member, Coyote Point Member, and Pardner Canyon Member, respectively. Examples of these formal subdivisions are annotated on field photographs from exposures on the southern Kaiparowits Plateau in Figure 3.3 and boundary ages are listed in Table 3.2. The application of the lower three formal members is seen as generally restricted to the Kaiparowits Plateau, whereas exposures on the Markagunt and Paunsaugunt plateaus should continue to be referred to as undifferentiated Wahweap Formation. The Pardner Canyon Member (previously capping sandstone member) is found extensively across all three plateaus (Biek *et al.*, 2015) and is confidently correlated with the Tarantula Mesa Sandstone in the Henry Basin (Eaton, 1990; Jinnah *et al.*, 2009; Corbett *et al.*, 2011). All four members of the Wahweap Formation have been described in detail by Eaton (1991), Jinnah and Roberts (2011) and many others; thus, the following descriptions are a synthesis of previous work paired with observations from the present study.

#### 3.3.1 Last Chance Creek Member

The Last Chance Creek Member (formerly the lower member) begins at the first major mudstone horizon above the Drip Tank Member of the Straight Cliffs Formation and is 65 m thick at the Reynolds Point lectostratotype section (Eaton, 1991; Jinnah and Roberts, 2011). The lower contact represents a notable depositional hiatus, identified by the coincidence of the C34n-C33r palaeomagnetic reversal boundary (Albright and Titus, 2016), and a sharp paraconformity across much of the Kaiparowits Plateau. The northward thinning Last Chance Creek Member ranges in thickness from 20 to 65 m and is mudstone dominated, although sandier in the north, and contains several laterally continuous single-story cross-bedded sandstone channel deposits including a distinctive bench-forming sandstone that caps the unit (Eaton, 1991; this study). The name Last Chance Creek is derived from the so-named watercourse adjacent to the Reynolds Point lectostratotype section measured by Eaton (1991) and proximal to the holotype locality of the ceratopsid dinosaur *Diabloceratops eatoni* (Kirkland and DeBlieux, 2010).





**Fig. 3.3** Exposures of the Wahweap Formation on the southern flank of the Kaiparowits Plateau where partial stratigraphic sections were measured at A) Brigham Plains, and B) Nipple Butte, illustrating the new member nomenclature.

### 3.3.2 Reynolds Point Member

The Reynolds Point Member (formerly the middle member) is 112 m thick at Reynolds Point and is commonly recessive above the Last Chance Creek Member, containing a higher proportion of floodplain deposits than the underlying member, and friable fine-grained sandstones occurring as isolated single-story channels (Eaton, 1991; Jinnah and Roberts, 2011). The boundary between the Reynolds Point Member and overlying Coyote Point Member is defined by Eaton (1991) as the base of a 20 m thick multi-story sandstone body, which Jinnah and Roberts (2011) describe as a gradational transition from the underlying mudstone dominated floodplain deposits of the Reynolds Point Member. The member name is derived from the Wahweap Formation lectostratotype section measured by Eaton (1991) at Reynolds Point in the Ship Mountain Point Quadrangle.

### 3.3.3 Coyote Point Member

The Coyote Point Member (formerly the upper member) comprises predominantly amalgamated tabular and lenticular sandstone deposits with a lesser proportion of fine-grained floodplain lithofacies across its 138 m thickness at Reynolds Point (Eaton, 1991; Jinnah and Roberts, 2011). Its fluvial floodplain depositional setting is inferred to have experienced some degree of marine influence near the base of the unit, possibly to the extent of estuarine development, as indicated by the presence of inclined heterolithic stratification, flaser bedding and possible brackish water invertebrate trace fossils (Jinnah and Roberts, 2011). The boundary between the Coyote Point Member and the overlying Pardner Canyon Member is marked by an undulatory erosional boundary incising into the Coyote Point Member by as

much as two meters of vertical relief, and the introduction of coarser, highly amalgamated sandstone and conglomerate facies (Eaton, 1991; Jinnah and Roberts, 2011). This member is named for Coyote Point, which is located in the Lower Coyote Spring quadrangle and contains excellent exposures of this stratigraphic interval.

#### *3.3.4 Pardner Canyon Member*

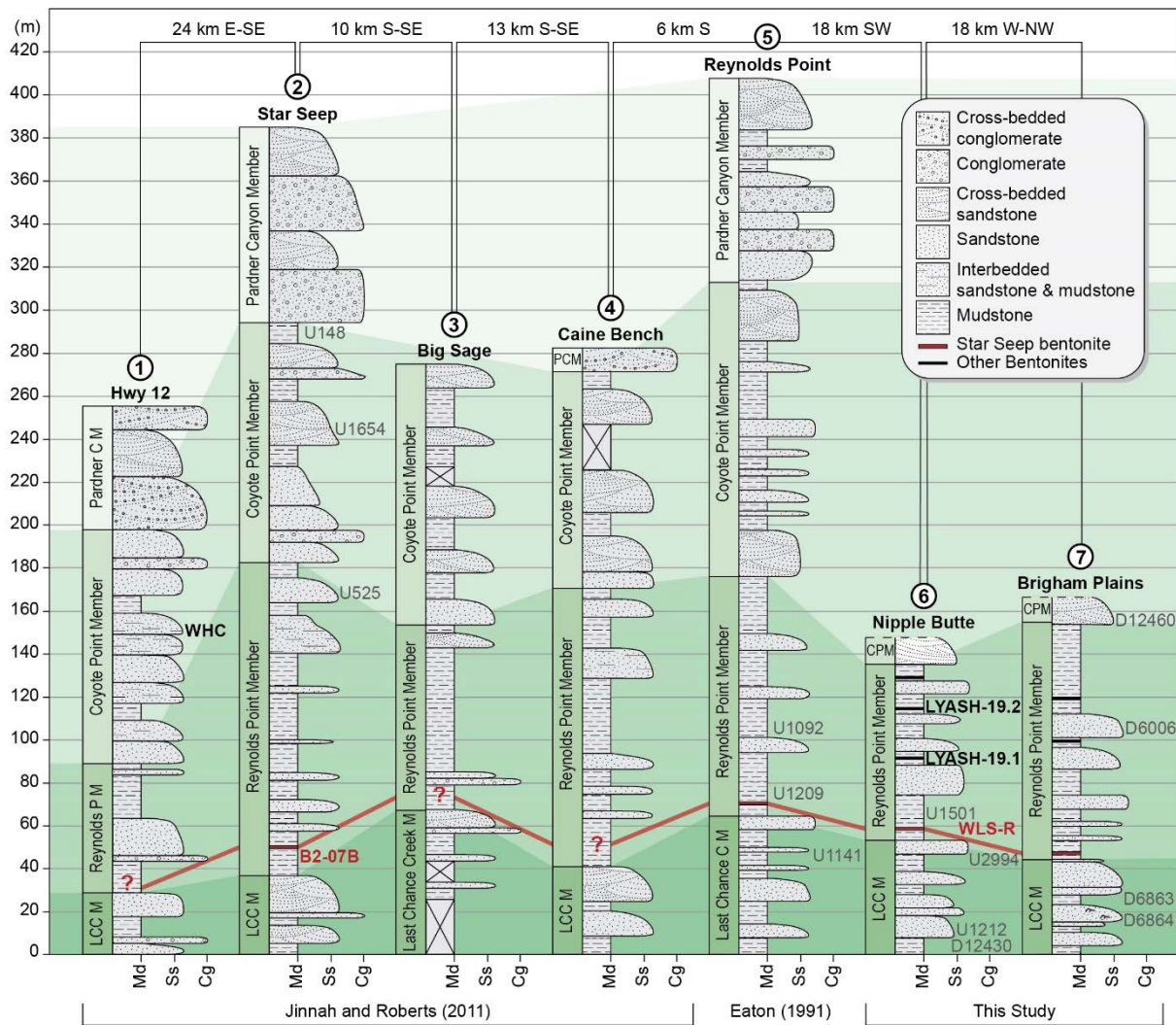
The Pardner Canyon Member is a regionally extensive, lithologically distinctive unit that reflects an abrupt change in sedimentological character (Pollock, 1999; Lawton *et al.*, 2003; Jinnah and Roberts, 2011). Varying in thickness across the Kaiparowits, Markagunt and Paunsaugunt plateaus to a maximum of ~140 m in the north, the Pardner Canyon Member is characterized by poorly sorted, cliff forming sandstones and conglomerates with thin, isolated mudstone lenses (Eaton, 1991; Pollock, 1999; Lawton *et al.*, 2003; Titus *et al.*, 2005; Jinnah and Roberts, 2011; Jinnah, 2013). As well as thickening towards the north, the Pardner Canyon Member also reportedly becomes coarser, where gravel conglomerates with clasts of chert and limestone occur more commonly in northern exposures on the Kaiparowits Plateau (Eaton, 1991; Lawton *et al.*, 2003; Jinnah and Roberts, 2011; Lawton *et al.*, 2014a). A dominance of planar-tabular bedforms at the base of the Pardner Canyon Member are indicative of a braided river depositional system, which grades to meander-style cross-bedded sandstones higher in the member (Eaton, 1991; Pollock, 1999; Jinnah and Roberts, 2011; Lawton *et al.*, 2014a). Changes in sedimentological character at the base of the member, along with other evidence, such as seismites and syn-sedimentary faulting, reflect renewed tectonic activity in the adjacent thrust belt and potential onset of intra-basin Laramide movement during the deposition of the Pardner Canyon Member (Little, 1995; Pollock, 1999; Lawton *et al.*, 2003; Hilbert-Wolf *et al.*, 2009; Tindall *et al.*, 2010; Lawton *et al.*, 2014a). The member name originates from Pardner Canyon in the Pine Lake and Henrieville quadrangles where this portion of the Wahweap Formation was measured by Eaton (1991).

### **3.4 Materials and methods**

#### *3.4.1 Stratigraphy and field sampling*

Previously studied exposures of the Wahweap Formation from across the Kaiparowits Plateau were revisited (*e.g.*, Eaton, 1991; Jinnah and Roberts, 2011), and two new localities were studied in detail. These two localities, Nipple Butte and Brigham Plains, are located on the southern flank of the Kaiparowits Plateau (Fig. 3.1, 3.3). These sites were selected for further investigation due to excellent exposures of the Wahweap Formation, proximity to important new vertebrate fossil sites, and the presence of bentonite horizons suitable for U-Pb dating and correlation. Investigation of these sites included decimeter-scale stratigraphic sections of the most fossiliferous intervals (Fig. 3.4) measured using a Jacob staff and clinometer, and collection of bentonite and sandstone samples. Sandstone samples for detrital zircon analysis were also collected from the cliffs adjacent to Highway 12 at





**Fig. 3.4** Correlated stratigraphic sections of the Wahweap Formation on the Kaiparowits Plateau including sections from Eaton (1991) and Jinnah and Roberts (2011), and the most fossiliferous interval of two new localities from the southern flank of the plateau measured herein. Locality ID abbreviations: D = DMNH Loc., U = UMNH VP Loc.; see Table 3.3 for details about fossil localities.

Henrieville Canyon and along Wahweap Creek at Horse Flats. An additional bentonite sample was collected from near the base of the Reynolds Point Member at Star Seep.

In situ vertebrate fossil sites cataloged by the Bureau of Land Management, Denver Museum of Nature and Science (DMNH), and Natural History Museum of Utah (UMNH) were documented using precise GPS coordinates (on file at their respective institution) and, where possible, correlated in the field to the nearest measured stratigraphic section. Other sites were plotted in Google Earth and attributed to either the lower, middle or upper portion of the lithostratigraphic members based on marker horizons (*e.g.*, bentonites, member boundaries) visible in Google Earth satellite imagery. Localities were also categorized based on their spatial distribution across the Kaiparowits Plateau and distance from the nearest vehicle access. Field areas across the Kaiparowits Plateau were grouped as follows: South-west = Brigham Plains, Coyote Canyon, Coyote Point; South-central = Nipple Butte, Tippet Springs, Clints

Cove; South-east = Clinton Canyon, Wesses Canyon, Wesses Cove, Ship Mountain Point, Pilots Knoll; Central = The Gut; North = Right Hand Collet Canyon, Star Seep, Camp Flat, Death Ridge (see Fig. 3.1). Distance from the nearest vehicle access was measured in Google Earth as direct map distance and results were characterized as: close = 0 - 249 m; moderately close = 250 - 499 m; moderately far = 500 - 749 m; far = 750 - 999 m; distal  $\geq$  1000 m.

#### 3.4.2 U-Pb LA-ICP-MS geochronology of sandstones

Detrital zircons were separated from five sandstone samples by standard mineral separation methods, including random-grain representative selection of all morphologies, and analyzed for U and Pb isotopes by LA-ICP-MS at the Advanced Analytical Centre at James Cook University as outlined in Beveridge *et al.* (2020). A Teledyne Analyte G2193 nm Excimer Laser with HeLex II Sample Cell was used to ablate 25 $\mu$ m pits in the zircons and liberated material was analyzed in a Thermo iCAP-RQ ICP-MS (see Todd *et al.*, 2019 and Huang *et al.*, 2021 for further details on laboratory procedures). Zircon mineral standards used included GJ1 (primary), and Plesovice and 91500 (secondary). All uranium-lead LA-ICP-MS data were reduced in the Iolite software package (iolite-software.com) and weighted mean ages were calculated using Isoplot (Ludwig, 2012). Complete data are given in Appendix C.3 (see also Beveridge *et al.*, 2022). Individual zircon grain ages with >5% discordance or >5%  $2\sigma$  propagated uncertainty (Y) were discarded. Maximum estimates of depositional ages were calculated, where appropriate, based on weighted mean  $^{206}\text{Pb}/^{238}\text{U}$  dates of the youngest population of overlapping analyses, and reported at a 95% confidence interval in the format  $\pm$  X/Y Ma, where X includes the internal uncertainty only and Y incorporates a calculated estimate of external reproducibility. Results are summarized in Table 3.1 and Figures 3.5 and 3.6.

#### 3.4.3 U-Pb CA-ID-TIMS geochronology of ash fall bentonites

High-precision U-Pb zircon analyses by the CA-ID-TIMS technique were conducted at the Massachusetts Institute of Technology Isotope Laboratory using procedures described in Ramezani *et al.* (2011). Bulk bentonite samples were processed in a sonic dismembrator device (Hoke *et al.*, 2014) designed to break apart and remove the clay component before heavy mineral separation by standard magnetic and high-density liquid separation techniques. The target zircon population of the two ash fall bentonites was selected under a binocular microscope according to a set of morphological criteria including faceted prismatic habit, high aspect ratio (1:5) and presence of elongated glass (melt) inclusions parallel to the crystallographic “C” axis. This selection approach has proven effective in screening reworked zircons (Ramezani *et al.*, 2011). Selected grains were pretreated by a chemical abrasion technique modified after Mattinson (2005), which involved thermal annealing at 900°C for 60 hours before partial dissolution in 28 M hydrofluoric acid at 210°C in a high-pressure digestion vessel for 12 hours. After thorough fluxing and rinsing to remove the leachates, the zircons were spiked with the EARTHTIME ET2535 mixed U-Pb tracer solution (Condon *et al.*, 2015; McLean *et al.*, 2015) and

completely dissolved in 28 M HF at 210°C for 48 hours. Chemically purified Pb and U via anion-exchange column chemistry were subsequently analyzed on an Isotopx X62 thermal ionization mass spectrometer with nine Faraday detectors and a Daly ion counting system. Data reduction and error propagation were conducted using Tripoli and ET\_Redux software (Bowring *et al.*, 2011; McLean *et al.*, 2011). Complete data are given in Appendix C.3.2 (see also Beveridge *et al.*, 2022). Bentonite ages are derived from the weighted mean  $^{206}\text{Pb}/^{238}\text{U}$  dates of the analyzed zircons after excluding visibly older analyses interpreted as xenocrystic or detrital; no zircon analyses from the young end of the age spectra were excluded from the weighted mean. Calculated age uncertainties are reported in the  $\pm X/Y/Z$  format, where X is the internal 95% confidence interval uncertainty in the absence of all external errors, Y incorporates X and the tracer calibration errors, and Z includes Y as well as the U decay constant uncertainties of Jaffey *et al.* (1971). Results are summarized in Table 3.1 and Figure 3.5.

#### 3.4.4 U-Pb LA-ICP-MS geochronology of reworked bentonites

Three additional bentonite samples from the Reynolds Point Member of the Wahweap Formation at Nipple Butte were also examined; however, each sample appeared to contain varying degrees of visibly detrital material, which suggested the horizons may have been partly reworked. Due to the increased likelihood of detrital incorporation, a mixed approach to dating these bentonites was employed. Zircon grains from these samples were selected using the same morphological criteria as for ash fall bentonites; however, the resulting grains were analyzed using the LA-ICP-MS approach and treated as maximum depositional ages. Complete data are given in Appendix C.3 (see also Beveridge *et al.*, 2022) and summarized in Table 3.1 and Figure 3.5.

#### 3.4.5 Comparison of U-Pb data

Within this study, and when comparing data from this study with others, consideration must be made with respect to the choice of uncertainties if meaningful comparisons are to be made between radioisotopic dates that resulted from different chronometers or produced by different techniques. In comparing U-Pb dates from different techniques (*i.e.*, LA-ICP-MS versus CA-ID-TIMS), the Y uncertainty should be used, whereas for comparing U-Pb and  $^{40}\text{Ar}/^{39}\text{Ar}$  dates, it is necessary to include decay constant uncertainties (Z). Previous investigations have also shown that mean ages from the same zircon crystals generated using CA-ID-TIMS and microbeam techniques (*i.e.*, LA-ICP-MS, and secondary ion mass spectrometry [SIMS]) may not always overlap within stated uncertainties (von Quadt *et al.*, 2014; Ickert *et al.*, 2015; Herriott *et al.*, 2019; Rasmussen *et al.*, 2021). Various factors are implicated in this possible bias (*e.g.*, untreated Pb loss, difficulty defining youngest population thresholds, use of mineral standards) and discrepancies in mean ages are not exclusively younger or older (*e.g.*, Herriott *et al.*, 2019; Rasmussen *et al.*, 2021); thus, it is possible that the LA-ICP-MS ages reported in the present study have additional geologic uncertainty not encapsulated by the reported internal (X) or propagated (Y) uncertainties. As well as being treated as MDAs due to the potential

incorporation of detrital material in samples chosen for LA-ICP-MS analysis in this study, it is recommended that these ages are used mindfully when comparing with ages generated using different techniques and/or chronometers.

#### 4.6 Bayesian age model

A quantitative chronostratigraphic model was constructed for the Wahweap Formation based on dated horizons from this study and their stratigraphic positions to calculate robust ages and uncertainty for any stratigraphic horizon of interest (*e.g.*, fossil localities, member boundaries). This was accomplished using the Compound Poisson-Gamma Bayesian statistical approach of Haslett and Parnell (2008) with a modified Markov chain Monte Carlo fitting algorithm included in the Bchronology R software package (Parnell *et al.*, 2008, 2011). By considering variable sediment accumulation rates using Poisson random variability, the Bchron statistical approach more appropriately propagates stratigraphic uncertainty (Haslett and Parnell, 2008; Parnell *et al.*, 2008, 2011; De Vleeschouwer and Parnell, 2014; Trayler *et al.*, 2020) compared to simple linear extrapolation, which assumes a constant sedimentation rate and thus falls short of realistic error propagation leading to overoptimistic uncertainty (De Vleeschouwer and Parnell, 2014). The Bayesian age-stratigraphic model is illustrated with a median (black line, Fig. 3.7), somewhat comparable to a linear model, and a 95% uncertainty envelope (blue shaded area, Fig. 3.7), which tends to balloon (*i.e.*, elevated stratigraphic age uncertainty) with distance from dated horizons.

The chronostratigraphic data produced in this study were modeled alongside the Reynolds Point lectostratotype section of Eaton (1991) and the Y uncertainties for both CA-ID-TIMS and LA-ICP-MS dates were used in the model construction. The graphical output of the model, shown in Figure 3.7, provides a useful tool for visualizing age-stratigraphic uncertainty, while the numerical output (Appendix C.3.5) lists a series of model ages represented by the median of predicted values and their 95% confidence level asymmetric uncertainties. All calculations were conducted in R Studio and relevant information including scripts can be found in Appendix C.3.3 and C.3.4.

### 3.5 Geochronological results

#### 3.5.1 Results: High-precision CA-ID-TIMS bentonite ages

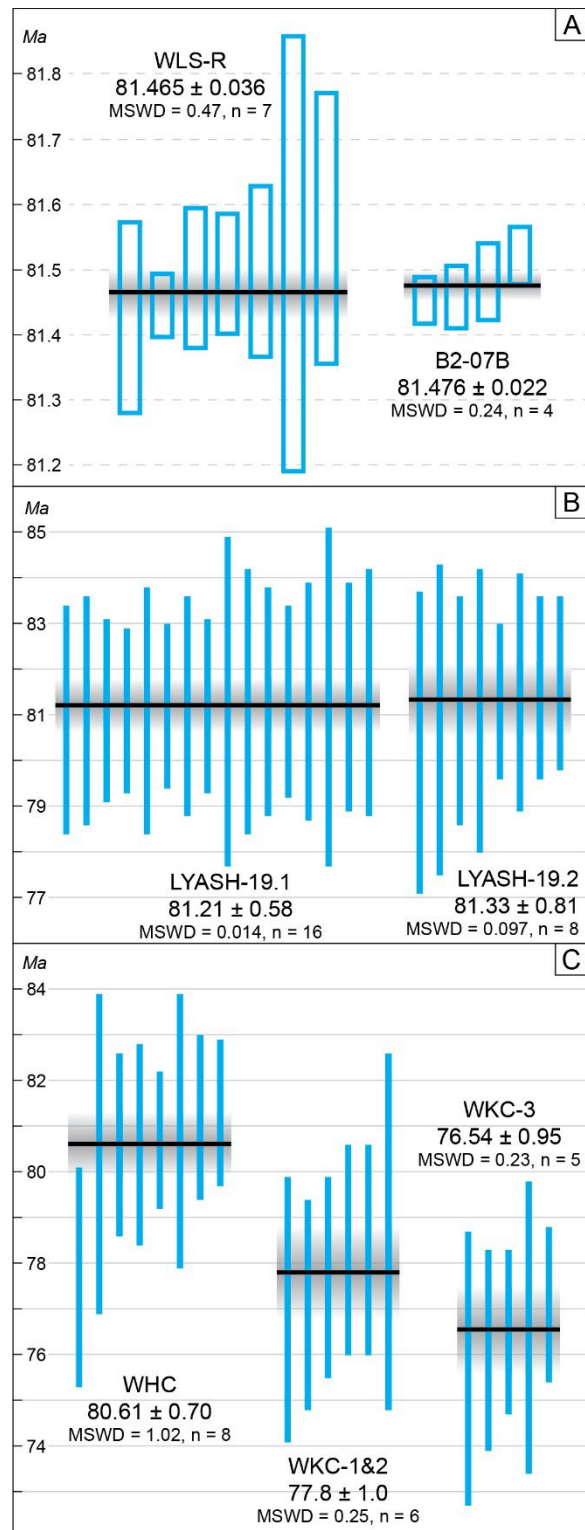
Two high-precision U-Pb ages are reported for the Wahweap Formation (Table 3.1, Fig. 3.5). The first sample (B2-07B) was collected from the same horizon as the previously dated  $^{40}\text{Ar}/^{39}\text{Ar}$  sample SS07-B (Jinnah, 2013) at Star Seep, 54 m above the base of the formation (Fig. 3.4). This bentonite, which is also presumably correlative with (or within  $\pm 5$  m of) bentonite CF05-B from Jinnah *et al.* (2009), is located near the base of the Reynolds Point Member ~10 m above a distinctive, laterally continuous sandstone that marks the top of the Last Chance Creek Member. The bentonite horizon is *ca* 20 cm thick, and the weathered outcrop shows characteristic popcorn swelling textures. Unweathered rock is yellowish-green in color with visible black flecks (biotite phenocrysts) and minimal translucent grains



(*e.g.*, quartz). New dating herein yielded a weighted mean  $^{206}\text{Pb}/^{238}\text{U}$  age of  $81.476 \pm 0.022/0.031/0.092$  Ma ( $2\sigma$ ) (MSWD = 2.2) based on four youngest overlapping zircon analyses. Besides a more than twenty-fold improvement in precision, this new age is  $1.6 \pm 0.6$  million years older than the previous  $^{40}\text{Ar}/^{39}\text{Ar}$  age of  $79.9 \pm 0.6$  Ma for the same bed, which is outside its reported ( $2\sigma$  internal) uncertainty (see Fig. 3.7). Similarly, it is  $0.9 \pm 0.6$  million years older than that of the correlative (or within  $\pm 5$  m) CF05-B bentonite ( $80.6 \pm 0.6$  Ma) (Jinnah *et al.*, 2009; Jinnah, 2013).

The second bentonite sample (WLS-R) was collected from Nipple Butte on the southern flank of the Kaiparowits Plateau and represents the first dated bentonite from the entire southern extent of the formation. The bentonite horizon is located 60 m above the base of the Wahweap Formation at Nipple Butte and, much like B2-07B from the northern field area, the WLS-R sample was collected  $\sim 5$  m above a distinctive, laterally continuous cross-bedded sandstone that marks the top of the Last Chance Creek Member. Characteristic swelling textures were also observed at this locality, and the *ca* 25 cm thick pistachio green horizon of unweathered material also exhibited visible black flecks and had a waxy smectite texture. This sample yielded a weighted mean  $^{206}\text{Pb}/^{238}\text{U}$  age of  $81.465 \pm 0.036/0.042/0.097$  Ma ( $2\sigma$ ) (MSWD = 0.47) based on all of its seven zircon analyses with no outliers.

Both high-precision CA-ID-TIMS bentonite ages are within analytical (X) uncertainty of each other, which supports field-based assessments that they represent the same bentonite horizon outcropping approximately  $\sim 38$  km apart. This



**Fig. 3.5** Plots of zircon  $^{206}\text{Pb}/^{238}\text{U}$  dates with  $2\sigma$  uncertainties (vertical bars) and their calculated weighted mean (horizontal bar) with a 95% error envelope (shaded band) for each sample. A) CA-ID-TIMS pure bentonite ages. B) LA-ICP-MS reworked bentonite ages. C) LA-ICP-MS detrital zircon maximum depositional ages.

**Table 3.1** Weighted mean U-Pb zircon ages for all samples analysed in this study (in stratigraphic order) including bentonite true ages and detrital zircon and bentonite maximum depositional ages. Additional data are not included here due to limited equivalency between CA-ID-TIMS and LA-ICP-MS datasets. Complete data are included in Appendix C.3.2.

Method / Age Type	Sample Name	Outcrop Area	Lithostratigraphic Member	Strat. Height* (m)	Weighted Mean Age					
					<sup>206</sup> Pb/ <sup>238</sup> U Age (Ma)	Error (2σ)^			MSWD	n#
						X	Y	Z		
	WKC-3	Horse Flat	lower Kaiparowits Fm	415	76.54	0.87	0.95	-	0.23	5
Detrital Zircon LA-ICP-MS / Maximum Depositional Age	WKC-1 & 2	Horse Flat	Pardner Canyon Member	405	77.8	0.93	1	-	0.25	6
	WHC	Hw12	Coyote Point Member	245	80.61	0.69	0.7	-	1.02	8
Bentonite LA-ICP-MS / Maximum Depositional Age	LYASH-19.2	Nipple Butte	Reynolds Point Member	148	81.33	0.72	0.81	-	0.097	8
	LYASH-19.1	Nipple Butte	Reynolds Point Member	117	81.21	0.53	0.58	-	0.014	16
Bentonite CA-ID-TIMS / True Depositional Age	WLS-R	Nipple Butte	Reynolds Point Member	72	81.465	0.036	0.042	0.097	0.47	7
	B2-07B	Star Seep	Reynolds Point Member	72	81.476	0.022	0.031	0.092	2.2	4

\* Meters above the base of the Wahweap Formation relative to Reynolds Point lectostratotype section of Eaton (1991)

^ Error for CA-ID-TIMS (X = analytical uncertainty in the absence of all external or systematic errors, Y = X plus U-Pb tracer calibration error, Z = Y plus U decay constant uncertainties) and LA-ICP-MS (X = internal uncertainty, Y = propagated uncertainty)

MSWD = mean square of weighted deviates

n# = number of analyses included in the calculated weighted mean age



widespread bentonite marker horizon is referred to as the Star Seep bentonite after the locality from which it was initially studied (Jinnah *et al.*, 2009; Jinnah, 2013) and it serves as a reliable tie point for correlating the Wahweap Formation across the Kaiparowits Plateau (*e.g.*, Fig. 3.4).

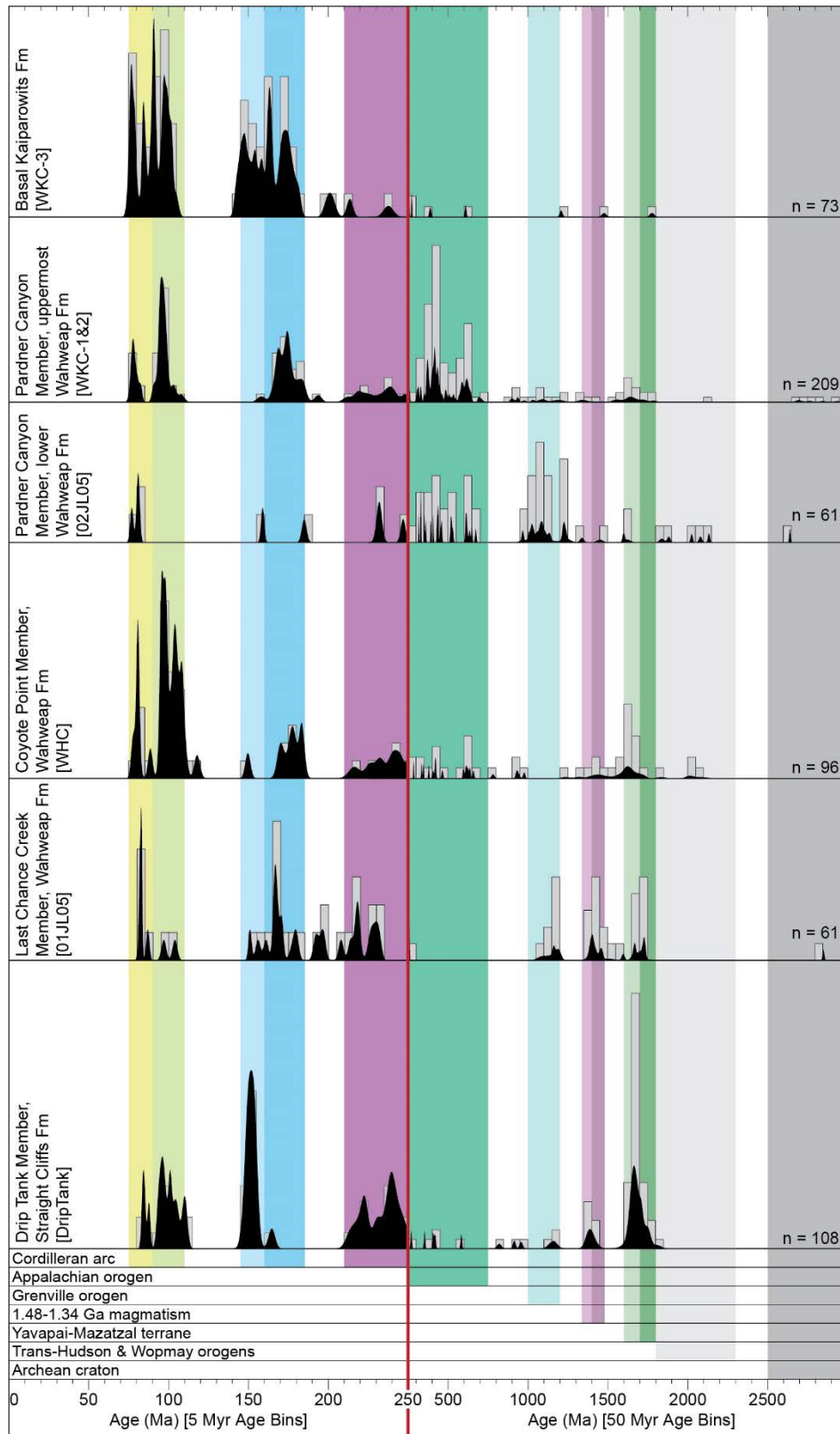
### 3.5.2 Results: Reworked bentonite LA-ICP-MS ages

Alongside high-precision CA-ID-TIMS geochronology for ash fall bentonites from the Wahweap Formation, this study also reports supporting  $^{206}\text{Pb}/^{238}\text{U}$  LA-ICP-MS ages for suspected reworked bentonite horizons that are interpreted as maximum depositional ages. Three such bentonite horizons were identified in the Reynolds Point Member of the Wahweap Formation at Nipple Butte and can also be observed in other stratigraphic sections (*e.g.*, Brigham Plains, Fig. 3.4). Samples were collected from 117 m (LYASH-19.1), 148 m (LYASH-19.2) and 163 m (LYASH-19.3) above the base of the formation at Nipple Butte.

Despite showing mineralogical evidence of some degree of detrital material, two of these three bentonite samples produced statistically coherent age populations within the uncertainties of the LA-ICP-MS analyses (Table 3.1, Fig. 3.5). The stratigraphically lowest reworked bentonite, LYASH-19.1, yielded a weighted mean age of  $81.21 \pm 0.53/0.58$  Ma ( $2\sigma$ ) (MSWD = 0.014) from a young population of 16 zircons. Based on crystal morphology and distribution of zircon ages, this bentonite age is considered a close approximation of the true depositional age. LYASH-19.2, which is 23 m stratigraphically higher than the previous sample, produced a weighted mean age of  $81.33 \pm 0.72/0.81$  Ma ( $2\sigma$ ) (MSWD = 0.097) from a young population of eight grains. Compared to the stratigraphically lower LYASH-19.1 and the CA-ID-TIMS dated Star Seep bentonite, the LYASH-19.2 results appear older than the expected age, probably due to incorporation of reworked zircons. The bentonite that showed the greatest degree of reworking (LYASH-19.3), did not yield a young coherent age population and therefore no depositional age can be calculated.

### 3.5.3 Results: Detrital zircon LA-ICP-MS ages

Additional age constraints for the Wahweap Formation were attained using five sandstone detrital zircon (DZ) samples from the Wahweap Formation, the underlying Straight Cliffs Formation, and the overlying Kaiparowits Formation. Maximum depositional ages (MDAs) for DZ samples were calculated using the weighted mean age of the youngest coherent population (YCP) (Table 3.1, Fig. 3.5). Sample “DripTank” from immediately below the Wahweap Formation at the top of the Drip Tank Member of the Straight Cliffs Formation did not yield a coherent young population, but the youngest single grain age was  $83.8 \pm 1.4/1.7$  Ma. A DZ sample was collected from cliffs adjacent to Highway 12 along Henrieville Canyon in the middle of the Coyote Point Member of the Wahweap Formation (~150 m above the base of the formation at this location, Fig. 3.4). This sample produced a MDA of  $80.61 \pm 0.69/0.70$  Ma (MSWD = 1.02) from a YCP of eight zircons. Three detrital zircon samples that bracket the top of the Wahweap



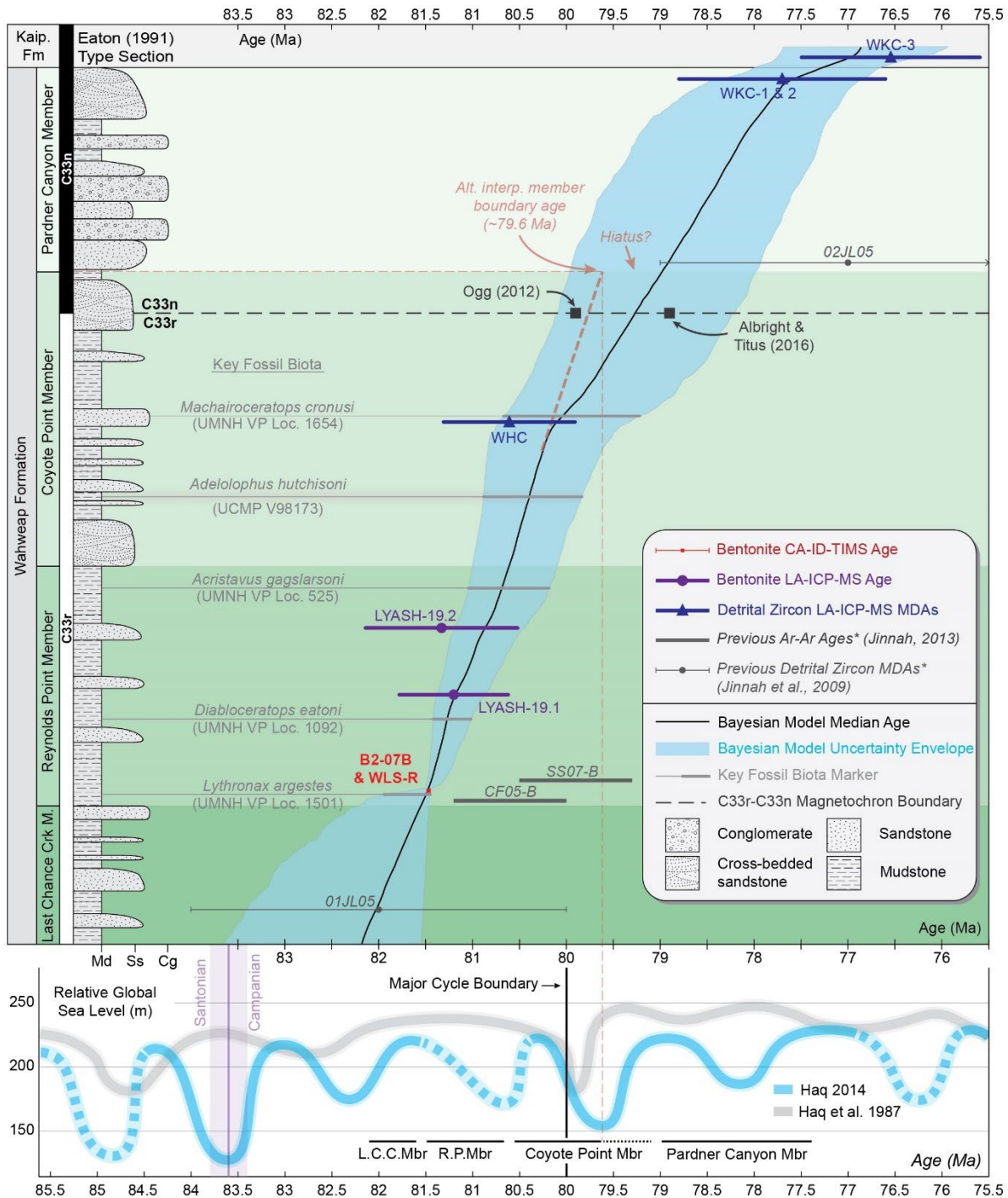
**Fig. 3.6** Probability distribution plots of detrital zircon U-Pb dates including samples 01JL05 and 02JL05 from Jinnah et al. (2009). Note the change in x-axis scale at the Permian-Triassic boundary, applied here to highlight significant discrepancies in Mesozoic zircon groups. Y-axis is scaled proportionally based on grain age frequency and number of grains per sample to facilitate direct comparison of modes and groups. Age groupings adapted from Laskowski et al. (2013) and references therein.

Formation were collected across a distinctive pedogenic surface inferred to be the top boundary of the Wahweap Formation at Horse Flats (Fig. 3.8). WKC-1 and WKC-2 consist of fine (to muddy) and medium grain quartz-arenite sandstones (respectively) from immediately below the pedogenic surface. Based on proximity and lithological similarity, these two samples were grouped together and this DZ suite produced a MDA of  $77.8 \pm 0.93/1.0$  Ma (MSWD = 0.25) calculated from a YCP of six grains. WKC-3, collected from a lithic arkose immediately above the pedogenic surface at the very base of the Kaiparowits Formation, yielded a MDA of  $76.54 \pm 0.87/0.95$  Ma (MSWD = 0.23) from five grains. Overall, the MDAs exhibit good correlation between their stratigraphic position and true depositional ages from bracketing ash fall bentonites, which is inferred to mean they reflect reasonable approximations of the depositional age.

The provenance of sandstones from the Wahweap Formation has been examined previously in great detail (*e.g.*, Dickinson and Gehrels, 2008; Larsen *et al.*, 2010; Dickinson *et al.*, 2012; Lawton and Bradford, 2011; Lawton *et al.*, 2014b), and was not the focus of this investigation; however, broad observations are reported here based on detrital zircon age spectra illustrated in Figure 3.6. For comparison, Figure 3.6 also includes two previous detrital zircon samples (01JL05, 02JL05) described by Jinnah *et al.* (2009). The four new samples highlight important trends in provenance, particularly across unconformities and formation boundaries (see Fig. 3.6). The single Drip Tank Member sample from immediately below the Wahweap Formation contains a notable mode at 151 Ma, a substantial Triassic cluster (14%), and major groups at *ca* 1.4 Ga and 1.7 Ga, the latter of which comprises 42% of the total grain count. Sample WHC from the Coyote Point Member of the Wahweap Formation is dominated by Cretaceous grain ages representing 39% of the total suite along with a broad group around 179 Ma and minor Paleozoic and Proterozoic groupings. Samples WKC-1&2 from the top of the Wahweap Formation in the Pardner Canyon Member contain Mesozoic groups with modes at 79 Ma, 96 Ma, 171 Ma and a minor suite of Triassic grains, as well as a major group of Paleozoic ages (36%). Sample WKC-3 from the base of the Kaiparowits Formation is best described as two dominant multi-modal groups; one from the Late Cretaceous and the other from the Middle to Late Jurassic. Interestingly, this sample contains only a handful of grains older than 200 Ma (<14%).

### 3.6 A new chronostratigraphic framework for the Wahweap Formation

Two new high-precision CA-ID-TIMS and five supporting LA-ICP-MS U-Pb zircon ages from a variety of stratigraphically well-constrained bentonites and sandstones form the basis of a new age model for the Wahweap Formation generated using a Bayesian statistical method. The age of the Wahweap Formation was found to range from approximately  $82.17 +1.5/-0.63$  Ma to  $77.29 +0.72/-0.62$  Ma, coinciding with the first half of the Campanian Stage (Table 3.2, Fig. 3.7). The new chronostratigraphic model indicates the base of the formation is *ca* 1.2 million years older than previous estimates (*i.e.*, Jinnah *et al.*, 2009; Jinnah, 2013) and provides objective age constraints on Wahweap fossil biota. The



**Fig. 3.7** U-Pb geochronology and Bayesian age-stratigraphic model for the Wahweap Formation against the Reynolds Point lectostratotype section of Eaton (1991) with global sea level curves (Haq et al., 1987, 2014) (NB: thickness of sea level curves does not reflect data precision). Due to lateral variation in unit thickness of the Wahweap Formation on the Kaiparowits Plateau, absolute stratigraphic height is not shown. Rock and vertebrate fossil specimens were stratigraphically correlated from their nearest measured section to the Reynolds Point lectostratotype section. Red dashed lines illustrate an alternate interpretation of the age of the Coyote Point – Pardner Canyon member boundary. \* Ages that were not used in the generation of the Bayesian model.

revised basal age confirms that the formation does indeed cover an interval of the early Campanian (*e.g.*, Eaton, 1991), contrary to the previous interpretation by Jinnah *et al.* (2009). Temporal extension of the Wahweap Formation means that strata of the combined Wahweap and overlying Kaiparowits formations (including the recently described Upper Valley Member of the Kaiparowits Formation; see Beveridge *et al.*, 2020), with a combined thickness of approx. 1.4 km, encompass nearly the entire Campanian stage.

### 3.6.1 Member boundaries and features

Model boundary ages of the newly formalized subdivisions of the Wahweap Formation reported in Table 3.2 are based on stratigraphic thicknesses at the lectostratotype section of Eaton (1991) measured at Reynolds Point in the Ship Mountain Point Quadrangle (Fig. 3.7). Member boundaries in the Wahweap Formation are generally considered isochronous across the Kaiparowits Plateau because the mechanisms that govern the alluvial architecture which defines the members are believed to act near synchronously across the immediate area (Jinnah and Roberts, 2011; Jinnah, 2013). The lower two boundaries appear to be simple and conformable; however, sedimentologic evidence indicates a significant depositional hiatus between the Coyote Point and Pardner Canyon members (Eaton, 1991; Jinnah and Roberts, 2011; this study); thus, the time interval represented by this boundary requires closer examination. The new Bayesian age model yields a member boundary age of *ca* 79.0 Ma with a large uncertainty window of approximately two million years resulting from sparsity and imprecision of constraining ages in this portion of the stratigraphy. The presence of a depositional hiatus in this broadly constrained section undoubtedly impacts the accuracy of the model age; although, the comparatively large uncertainty accommodates various interpretations for the age of the member boundary. For example, linear extrapolation of the sediment accumulation rate from the well-constrained Reynolds Point Member (~13 cm/kyr) suggests an older boundary age closer to ~79.6 Ma, which still falls within the error window of the chronostratigraphic model (see Fig. 3.7). This alternate interpretation has implications for sequence stratigraphic models of the Wahweap Formation as it aligns the depositional hiatus at the top of the Coyote Point Member with a global sea level minimum (*i.e.*, major sequence boundary; see Haq, 2014). The chronostratigraphic model herein further supports sequence stratigraphic interpretations discussed by Jinnah and Roberts (2011; and references within), although with slightly revised chronological constraint. Jinnah and Roberts (2011) discuss evidence of marine incursion close to the base of the Coyote Point Member, which the age model indicates is coincident with the preceding eustatic sea level maximum (Fig. 3.7). Future work may be able to revisit this interpretation using additional age constrains from the Coyote Point and Pardner Canyon members.

As well as implications for sequence stratigraphy, the age of the upper Coyote Point Member, including the alternate interpretation discussed above, is relevant to the C33r-C33n polarity reversal boundary identified by Albright and Titus (2016) at ~270 meters above the base of the Wahweap Formation. The



**Table 3.2** Model ages for member boundaries generated using the Bayesian age-stratigraphic model (Fig. 3.7, Appendix C.3.5). Note the asymmetrical uncertainty, which is related to the model's 95% confidence window.

Stratigraphic Level of Interest	Stratigraphic Height* (m)	Model Age (Ma)	2 $\sigma$ Uncertainty	
			+	-
Top of Wahweap Fm	410	77.29	0.72	0.62
Coyote Point – Pardner Canyon Mbr Boundary	313	79.00	0.98	0.99
Reynolds Point – Coyote Point Mbr Boundary	176	80.61	0.39	0.51
Last Chance Creek – Reynolds Point Mbr Boundary	65	81.55	0.62	0.09
Base of Wahweap Fm	0	82.17	1.47	0.63

\* Relative to Reynolds Point lectostratotype section of Eaton (1991).

C33r-C33n boundary was previously interpreted to occur at 79.9 Ma (GST2012 – Ogg, 2012) based on two  $^{40}\text{Ar}/^{39}\text{Ar}$  bentonite ages and linear extrapolation in the Elk Basin; however, Albright and Titus (2016) recalculated these  $^{40}\text{Ar}/^{39}\text{Ar}$  ages and report a revised magnetochron boundary age of 78.91 Ma. Interestingly, the model age at 270 meters above the base of the Wahweap Formation presented here (79.30 +1.05/-0.83 Ma at 293 m in the Reynolds Point lectostratotype section) is marginally closer to the Albright and Titus (2016) revised magnetochron boundary age, while the alternate interpretation discussed above aligns more closely with previous interpretations of the boundary age (*i.e.*, GST2012 – Ogg, 2012). Most importantly, both interpretations for the age of the C33r-C33n polarity reversal boundary fall within the uncertainty envelope of the age model and, given the uncertainty associated with the  $^{40}\text{Ar}/^{39}\text{Ar}$  ages from the Elk Basin that constrain the chron boundary, the two suggested ages are also probably within error of each other. Further investigation thus requires additional age constraints from the upper two members of the Wahweap Formation, which may lead to more definitive age assignment of the C33r-C33n polarity reversal boundary.

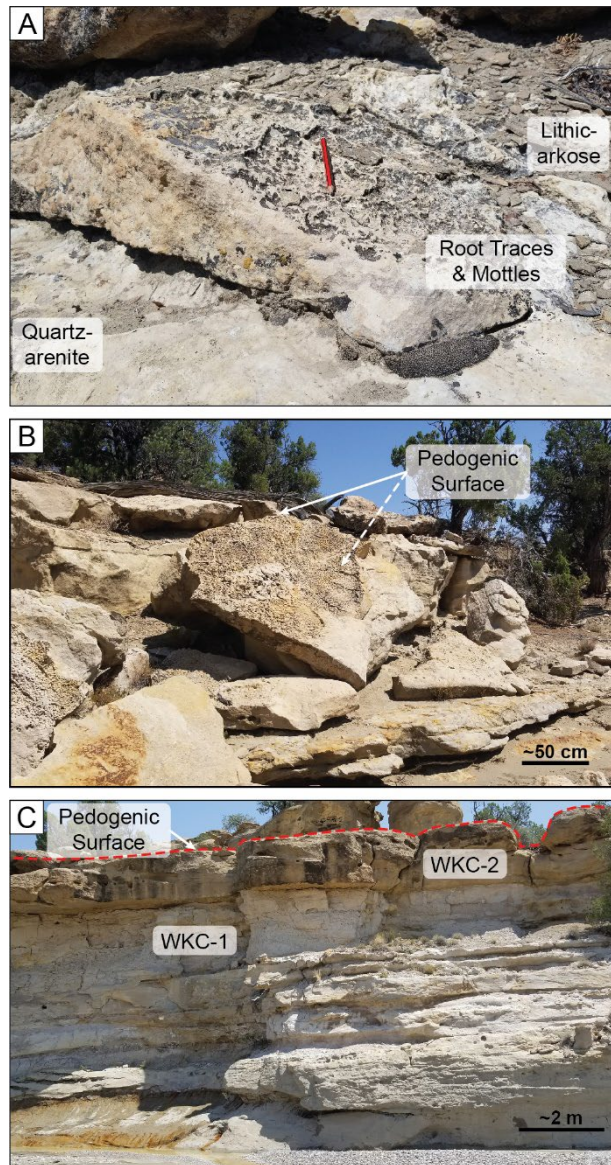
### 3.6.2 Upper and basal formation boundaries

The age of the upper boundary of the Wahweap Formation, 77.29 +0.72/-0.62 Ma, matches closely with previous estimates and, furthermore, the detrital zircon U-Pb data in this study provide useful insights into the nature of the contact. The upper boundary of the Wahweap Formation has been described in previous studies to be variously erosional and/or conformable with little clear consensus (Peterson, 1969; Eaton, 1991; Little, 1995; Pollock, 1999; Roberts, 2007; Jinnah and Roberts, 2011; Lawton *et al.*, 2014a). The most consistent description states that the contact is erosional across much of the Kaiparowits Plateau but locally gradational where continuous sections were measured (Jinnah and Roberts, 2011), which is interpreted as proximal to The Blues adjacent to Highway 12 and Henrieville Creek (Fig. 3.1). This description matches field observations closely. A pedogenic erosional surface with root traces and mottling observed in the present study at Horse Flat (Fig. 3.8) likely represents only a short hiatus, as indicated by the overlapping detrital zircon MDAs from the either side ( $\pm 5$  m) of the pedogenic surface (Fig. 3.5), although the large uncertainties of these MDAs preclude the exact quantification of this hiatus. Conversely, an immediate shift in sedimentology and provenance



across the surface is reflected by the sudden appearance of significant proportions of chert lithics and a large Late Jurassic zircon age group, as illustrated in Figures 3.6 and 3.8. Observation of an erosional surface separating visibly dissimilar sandstones (quartz arenite versus lithic arkose) that have distinct detrital zircon age spectra, supported by the inference that the duration of hiatus was minimal, suggests an abrupt change in sediment source, which marks the transition between the Wahweap and Kaiparowits formations. This interpretation also explains reports of a transitional zone of interfingering sandstones of varying provenance described elsewhere in the study area (Jinnah and Roberts, 2011; Lawton *et al.*, 2014a). As well as at the upper boundary of the Wahweap Formation, an abrupt change in sediment source is also noted across the unconformity at the Coyote Point – Pardner Canyon member boundary, evident most clearly by the sudden scarcity of Mesozoic grains when comparing data from this study and that of Jinnah *et al.* (2009) (Fig. 3.6).

Unlike that of the upper boundary, the age of the base of the Wahweap Formation demands a significant revision due to new chronostratigraphic data reported here. Previous estimates using  $^{40}\text{Ar}/^{39}\text{Ar}$  absolute ages and linear sediment accumulation rates estimated the base of the formation to occur at ~81 Ma (Jinnah, 2013). The new high-precision  $^{206}\text{Pb}/^{238}\text{U}$  CA-ID-TIMS age of ~81.47 Ma for the Star Seep bentonite (a combination of the overlapping B2-07B age of  $81.476 \pm 0.031[\text{Y}]$  Ma and the WLS-R age of  $81.465 \pm 0.042[\text{Y}]$  Ma), is significantly older (~0.9 to 1.6 Myr) than previous ages for what is



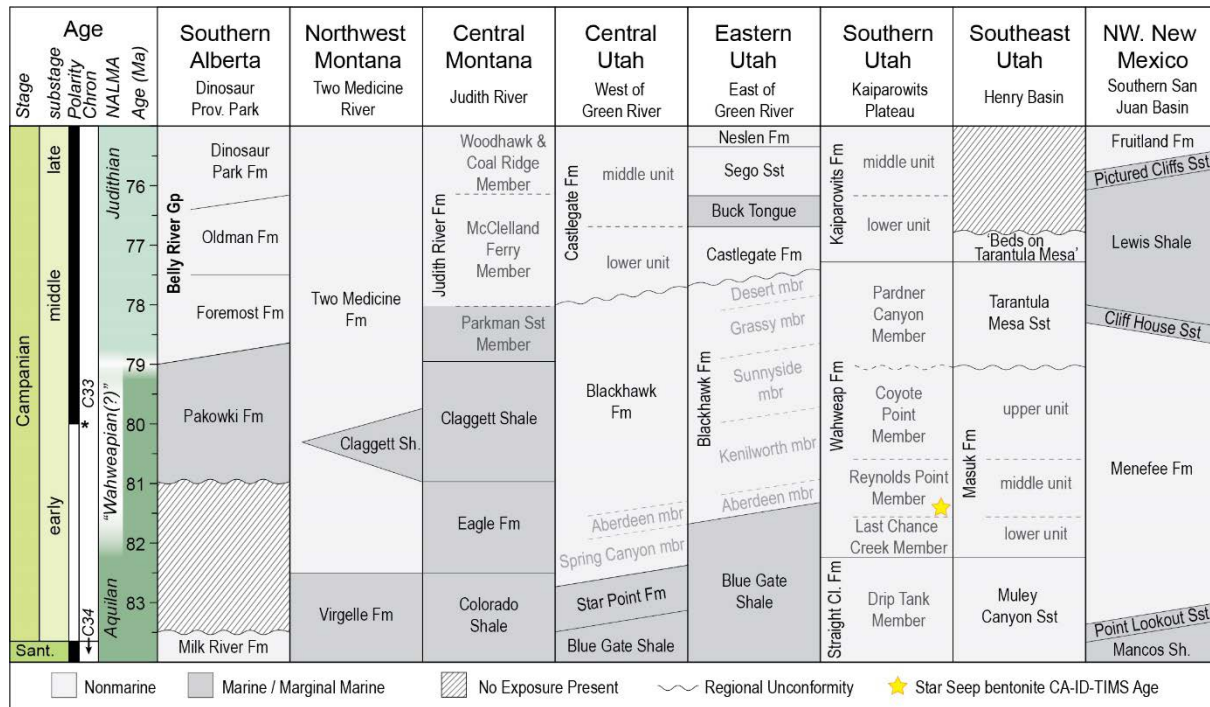
**Fig. 3.8** Annotated photographs of the pedogenic surface that separates the Wahweap and Kaiparowits formations at Horse Flat (see Fig. 3.1). A) Close-up showing a mottled surface with root traces separating Kaiparowits lithic arkose and Wahweap quartz arenite sandstones (pencil for scale). B) Displaced block of uppermost Wahweap Formation sandstone showing the texture of the boundary with the Kaiparowits Formation. C) Exposure illustrating sampled lithologies (WKC-3 collected above the dashed line) where the muddy, fine-grained sandstone WKC-1 would previously have been designated as the formation boundary.

interpreted to be the same horizon (SS07-B = 79.9 Ma, CF05-B = 80.6 Ma – Jinnah *et al.*, 2009; Jinnah, 2013). The new Bayesian model age for base of the Wahweap Formation is  $82.17 +1.47/-0.63$  Ma, which agrees well with detrital zircon MDAs from Jinnah *et al.* (2009) and with magnetostratigraphic data from Albright and Titus (2016); however, it is older than the MDA reported by Szwarc *et al.* (2015) for the underlying Drip Tank Member of the Straight Cliff Formation. Conversely, reinterpretation of the dataset from Szwarc *et al.* (2015) by removing single grain ages younger than the Star Seep bentonite age presented here yields a revised MDA for the Drip Tank Member of  $83.49 \pm 0.62$  Ma from five grains, which matches more closely with findings from this chapter and other studies (*e.g.*, Jinnah *et al.*, 2009; Albright and Titus, 2016) although further chronologic work on the Drip Tank Member is recommended.

### 3.6.3 Regional correlation

The revised age of the Wahweap Formation has significant implications for correlative units across the Western Interior. Current age estimates for presumed coeval units in the nearby Henry Basin, east of the Kaiparowits Plateau (Fig. 3.2), are based on constraints from the Wahweap Formation (Eaton, 1990; Corbett *et al.*, 2011; Seymour and Fielding, 2013; Lawton *et al.*, 2014a). Corresponding strata of the Henry Basin record coastal floodplain depositional environments, including the Masuk Formation and the Tarantula Mesa Sandstone which are believed to be equivalent to the Wahweap Formation's Last Chance Creek, Reynolds Point and Coyote Point members and the Pardner Canyon Member, respectively (Eaton, 1990; Corbett *et al.*, 2011). Assuming these units are indeed contemporaneous, the updated geochronology reported in this study also revises the chronology of the Henry Basin strata, as illustrated in Figure 3.9. Substantiating more formal correlation of the Kaiparowits Plateau and Henry Basin strata across the extensive gap in exposure between these areas would require future detailed lithostratigraphic work including adjustments to the unit hierarchy and, as such, is not considered further herein.

At a broader geographic scale, adjustments to the age of the Wahweap Formation also have implications for correlation across the Western Interior (Figs. 3.2 and 3.9). Most significantly, the findings support and expand upon those of Albright and Titus (2016) that the Last Chance Creek, Reynolds Point, and Coyote Point members are older than the richly fossiliferous Belly River Group in southern Alberta (Eberth, 2005, 2015) and Judith River Formation in central Montana (Foreman *et al.*, 2008; Rogers *et al.*, 2016). Campanian formations across western North America that are found to be partly or fully contemporaneous with the Wahweap Formation (including the Pardner Canyon Member) include: the Pakowki, Foremost and lower Oldman formations in southern Alberta (Payenberg *et al.*, 2002; Eberth, 2005, 2015); the Two Medicine Formation and Claggett Shale in northwest Montana (Foreman *et al.*, 2008; Rogers *et al.*, 2016); the Eagle Formation and Claggett Shale, as well as the



**Fig. 3.9** Generalized temporal correlation of lower to middle Campanian strata across the Western Interior (~north to south, left to right). Geochronologic framework was adapted from Payenberg *et al.* (2002), Cather (2004), Cifelli *et al.* (2004), Roberts *et al.* (2005), Foreman *et al.* (2008), Jinnah *et al.* (2009), Corbett *et al.* (2011), Seymour and Fielding (2013), Albright and Titus (2016), Eberth (2015), Rogers *et al.* (2016), Fassett and Hiesler (2017).

Parkman Sandstone and lower McClelland Ferry members of the Judith River Formation in central Montana (Rogers *et al.*, 2016); the Blue Gate Shale, Blackhawk and Castlegate formations in central and eastern Utah (Seymour and Fielding, 2013); the Menefee Formation, Cliff House Sandstone and Lewis Shale in southern exposures of the San Juan Basin in northwest New Mexico (Cather, 2004; Fassett and Hiesler, 2017), and the lower Aguja Formation in West Texas and northern Chihuahua/Coahuila (Lehman *et al.*, 2019). Higher resolution geochronological constraints are needed for many of these presumed coeval units as correlation of their fossil-bearing intervals is invaluable to our collective understanding of faunal and floral diversity across Laramidia during the Late Cretaceous.

### 3.6.4 North American Land Mammal Ages

Refinement of the age and basin-scale correlation of the Wahweap Formation enables re-examination of its relationship to the Late Cretaceous North American Land Mammal Ages (NALMA). The unique mammaliaform assemblage of the Wahweap Formation has proven difficult to place into the NALMA framework, with previous studies suggesting either Aquilan or Judithian affinity (Cifelli, 1990b, 1990c, 1990d, 2004; Eaton, 1991, 2002, 2006; Eaton and Cifelli, 2013; DeBlieux *et al.*, 2013). Based on a wealth of previous work focused on multituberculates and other microvertebrates, one hypothesis is that the Wahweap Formation contains both Aquilan and Judithian faunas that are mildly distinct from the



type faunas due to either latitudinal variation or incomplete description of the type faunal assemblage. In this scenario, the Aquilan assemblage is preserved low in the Wahweap Formation, with Judithian taxa occurring higher in the formation. Alternatively, the application of a unique early to middle Campanian biochronological assemblage may be appropriate; referred to by some authors as the “Wahweapian” (Jinnah *et al.*, 2009; Eaton and Cifelli, 2013; DeBlieux *et al.*, 2013).

Although NALMA biochronology provides useful temporal constraint by correlating similar vertebrate assemblages using shared index taxa, radioisotopic ages are helpful as independent age constraints for correlating between temporally and latitudinally varied assemblages. The NALMA framework was developed based on northern faunal assemblages; therefore, temporal variation is difficult to untangle from latitudinal variation of southern faunal assemblages without the use of radioisotopic ages. The Aquilan faunal assemblage is described from the upper strata of the Milk River Formation in southern Alberta (Lillegraven and McKenna, 1986; Cifelli *et al.*, 2004), which is estimated to be latest Santonian in age (~84.5 to 83.5 Ma; Payenberg *et al.*, 2002). The type Judithian is known from the middle Campanian (~75 to 79 Ma) Judith River Formation (Rogers *et al.*, 1993, 2016), specifically its uppermost strata (Lillegraven and McKenna, 1986; Cifelli *et al.*, 2004). Although Cifelli *et al.* (2004) infer the Aquilan – Judithian transition to occur at ~79 Ma, early Campanian faunal assemblages are not preserved at either type area. This means that the unique early Campanian assemblage found in the Wahweap Formation occupies a temporal gap in sampling between classic Aquilan and Judithian assemblages and may not simply be a southern variation of either. Alternatively, the widespread application of high-precision radiometric dating techniques that facilitates these finer-scale interpretations may render strict adherence to the NALMA framework and its defined temporal intervals somewhat obsolete. Rigorous reassessment of the utility of Late Cretaceous NALMA is recommended to investigate conceptual reform from a biochronologic-centered tool to potentially a spatio-temporal model.

### 3.7 Improved chronostratigraphic constraint for fossil taxa

A refined temporal framework for vertebrate fossil from the Wahweap Formation was produced by combining the new chronostratigraphic model with an updated record of localities from which in situ fossil material has been identified (Table 3.3, Fig. 3.10, Appendix C.3.1). This process was conducted to explore trends in biostratigraphic zonation, and new age constraints were generated for key taxa with pre-existing stratigraphic context. It should be noted that, although well-supported, stratigraphic correlation of fossil localities to their closest measured sections then again to the Reynolds Point lectostratotype for which the Bayesian age-stratigraphic model was created will introduce minor stratigraphic uncertainties in the locality ages. These uncertainties are predicted to be significantly smaller than the Bayesian age model error envelope and thus not considered further.

**Table 3.3** Shortlist of fossil localities from the Wahweap Formation with model ages calculated using the Bayesian age-stratigraphic model (Fig. 3.7, Appendix C.3.5). A complete list of fossil localities and their ages is included in Appendix C.3.1.

Museum Locality	Taxa Present (Specimen Numbers)	Area	Member	Approx. Height*	Model Age (Ma)**	2 $\sigma$ uncertainty +	-	Dist. from Road (m)^
UMNH VP Loc. 525	<i>Acristavus gaglarsoni</i> skull (UMNH VP 16607)	Star Seep	Reynolds Point Member	166	80.69	0.36	0.5	Moderately Close
UMNH VP Loc. 148	Centrosaurine frill (UMNH VP 9549)	Death Ridge	Coyote Point Member	313	79	0.98	0.99	Distal
UMNH VP Loc. 1092	<i>Diabloceratops eatoni</i> holotype, nearly complete skull (UMNH VP 16699)	Reynolds Point	Reynolds Point Member	105	81.27	0.15	0.26	Far
UMNH VP Loc. 1141	Centrosaurine frill (UMNH VP 20600)	Pilot Knoll	Last Chance Creek Member	45	81.74	1.04	0.25	Moderately Close
UMNH VP Loc. 1209	Hadrosaurid partial poscranial skeleton, partial turtle shell (UMNH VP 20213), <i>Melvius</i>	Wesses Canyon	Reynolds Point Member	70	81.49	0.37	0.04	Moderately Close
UMNH VP Loc. 1212	Hadrosaurid bonebed	Tibbet Springs	Last Chance Creek Member	10	82.08	1.4	0.55	Close
UMNH VP Loc. 1276	Hadrosaurid partial skeleton	The Gut	Coyote Point Member (base)	176	80.61	0.39	0.51	Close
UMNH VP Loc. 1501	<i>Lythronax argestes</i> holotype, partial skeleton (UMNH VP 20200)	Nipple Butte	Reynolds Point Member	70	81.49	0.37	0.04	Moderately Close
UMNH VP Loc. 1654	<i>Machairoceratops cronusi</i> holotype, partial skull (UMNH VP 20550)	Star Seep	Coyote Point Member	246	80.06	0.62	0.8	Distal
UMNH VP Loc. 2994	Centrosaurine partial skull (UMNH VP 16704)	Nipple Butte	Last Chance Creek Member	50	81.69	0.94	0.2	Close

Table 3.3 continued.

Museum Locality	Taxa Present (Specimen Numbers)	Area	Member	Approx. Height*	Model Age (Ma)**	2 $\sigma$ uncertainty		Dist. from Road (m)^
						+	-	
DMNH Locality 12445	Centrosaurinae gen. et sp. indet (isolated element)	Nipple Butte	Last Chance Creek Member	lower	82.17 to 81.98	1.47	0.46	Close
DMNH Locality 12430	Hadrosauridae gen. et sp. indet (articulated)	Nipple Butte	Last Chance Creek Member	lower	82.17 to 81.98	1.47	0.46	Close
DMNH Locality 12431	Hadrosauridae gen. et sp. indet (partially articulated)	Nipple Butte	Last Chance Creek Member	lower	82.17 to 81.98	1.47	0.46	Close
DMNH Locality 12463	Hadrosauridae gen. et sp. indet (disarticulated)	Coyote Point	Last Chance Creek Member	lower	82.17 to 81.98	1.47	0.46	Close
DMNH Locality 6864	Pachycephalosauridae gen. et sp. nov. (DMNH EPV.131000), hadrosauridae gen. et sp. indet (disarticulated)	Brigham Plains	Last Chance Creek Member	middle	81.98 to 81.64	1.33	0.16	Close
DMNH Locality 6863	Hadrosauridae gen. et sp. indet (partially articulated)	Brigham Plains	Last Chance Creek Member	middle	81.98 to 81.64	1.33	0.16	Close
DMNH Locality 6009	Hadrosauridae gen. et sp. indet (disarticulated)	Clints Cove	Last Chance Creek Member	middle	81.98 to 81.64	1.33	0.16	Moderately Far
DMNH Locality 6006	Hadrosauridae gen. et sp. indet (disarticulated)	Clints Cove	Reynolds Point Member	middle	81.44 to 80.69	0.05	0.5	Far
DMNH Locality 12460	Hadrosauridae gen. et sp. indet (disarticulated)	Coyote Point	Coyote Point Member	lower	80.69 to 80.58	0.36	0.52	Moderately Far

\* Relative to Reynolds Point lectostratotype section of Eaton (1991)

\*\* Median model age for stratigraphic level or age range for stratigraphic intervals

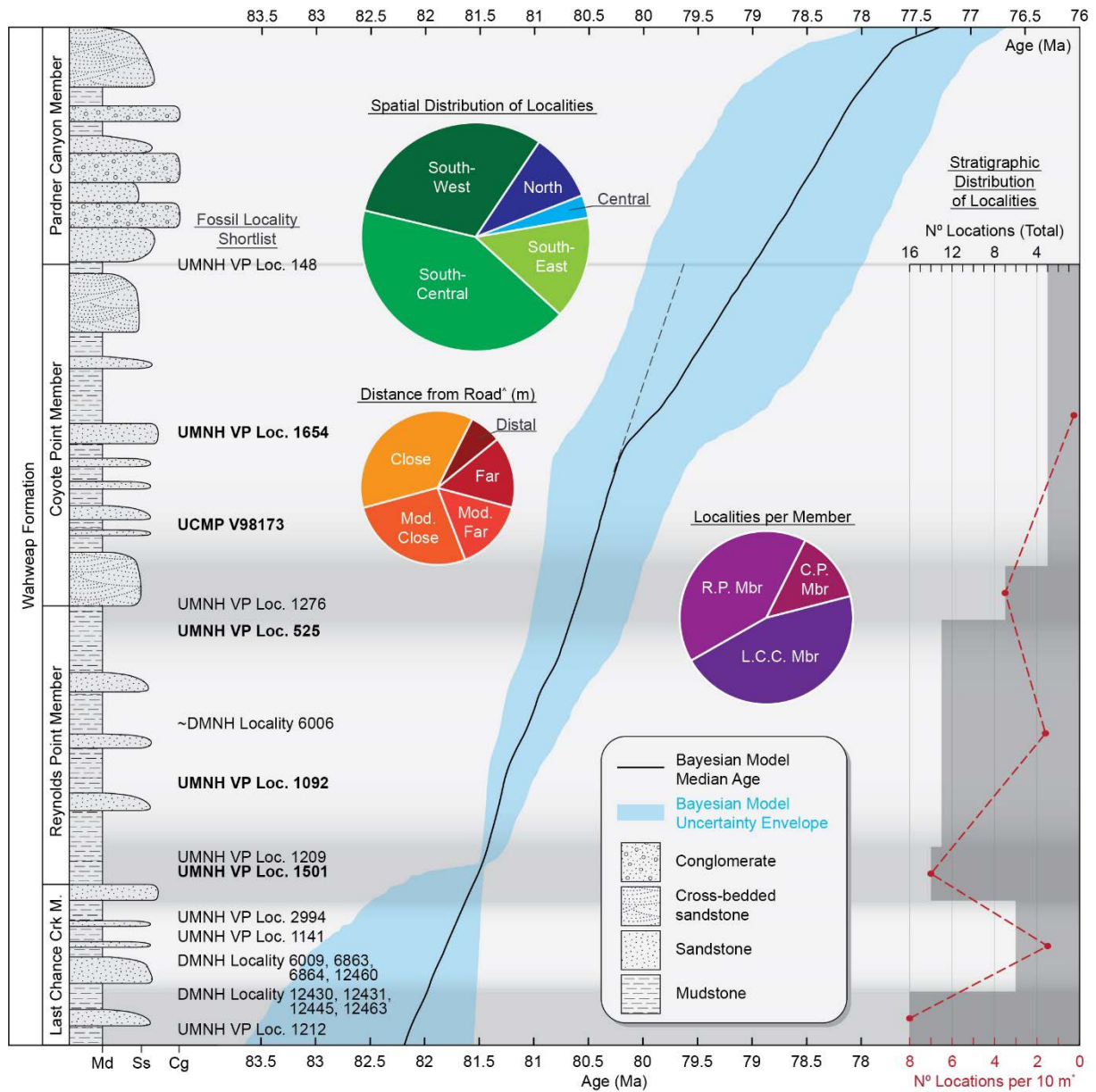
^ Direct map distance (close = 0 - 249 m; moderately close = 250 - 499 m; moderately far = 500 - 749 m; far = 750 - 999 m; distal  $\geq$  1000 m)



### 3.7.1 Spatio-temporal distribution of vertebrates

Accepting that the less accessible, cliff-forming nature of the Pardner Canyon Member has precluded the recovery of significant non-marine vertebrate assemblages, the fossiliferous portion of the Wahweap Formation is largely restricted to the Last Chance Creek, Reynolds Point, and Coyote Point members; a temporal interval of ~3.2 million years (82.17 +1.47/-0.63 Ma to 79.00 +0.98/-0.99 Ma) (Fig. 3.10, Table 3.3). Many similar stratigraphic intervals elsewhere in the Western Interior preserve multiple, biostratigraphically-defined local faunas, including the Fruitland and Kirtland formations of northwestern New Mexico (*e.g.*, Lucas *et al.*, 2006; Sullivan and Lucas, 2006), the Two Medicine and Judith River formations of Montana (*e.g.*, Horner *et al.*, 2001; Trexler, 2001; Mallon *et al.*, 2016), and the Aguja Formation of West Texas (*e.g.*, Lehman *et al.*, 2017, 2019). Investigations of well-preserved non-marine faunas from the Campanian infer turnover rates as rapid as 600 kyr (*e.g.*, Dinosaur Park Formation; Mallon *et al.*, 2012), although these estimates may be influenced by preservation potential and palaeoenvironmental preference (Cullen *et al.*, 2016). Based on these examples and a temporal range of ~3.2 million years for the fossiliferous portion of the Wahweap Formation, interpretation of a single, sympatric Wahweap fauna is almost certainly over-simplistic. Though sampling of the entire fossiliferous interval across the Kaiparowits Plateau and adjacent plateaus remains incomplete, at least a modest degree of biostratigraphic zonation within the Wahweap Formation is here noted.

Vertebrate fossils recovered from the Last Chance Creek Member (model age: 82.17 +1.47/-0.63 to 81.55 +0.62/-0.09 Ma) are largely disarticulated and durable remains from channel lag deposits. These isolated discoveries include baenid turtles, ceratopsians (*e.g.*, UMNH VP Loc. 20600, 2994, 1141; DMNH loc. 12445), and theropods (Table 3.3, Appendix C.3.1). Recent reconnaissance has recovered closely associated and even articulated remains in mudstone horizons largely concentrated in the lower two thirds of the member (model age: 82.17 +1.47/-0.63 to 81.76 +1.11/-0.27 Ma). This includes abundant hadrosaurid material (DMNH loc. 6863, 6864, 12430, 12431, 12463; UMNH VP Loc. 1212, 1253, 1263, 2020, 2923), a hadrosauroid skeleton (UMNH VP Loc. 2405), a pachycephalosaurid (DMNH loc. 6864), and several large crocodyliforms (UMNH VP Loc. 2587, 2999). Many of the vertebrates of the Last Chance Creek Member await full, detailed descriptions thus precluding comprehensive comparisons with other paracontemporaneous Western Interior assemblages; however, the overall composition compares closely with similar early Campanian units. This rapidly expanding Last Chance Creek Member vertebrate assemblage likely represents a unique temporal interval bridging the emerging records from the Santonian Deadhorse Coulee Member of the Milk River Formation (Evans *et al.*, 2013a), early Campanian Lower Shale Member of the Aguja Formation (Lehman *et al.*, 2019, Preito-Márquez *et al.*, 2019), and Allison Member of the Menefee Formation (Lucas *et al.*, 2005; McDonald and Wolf, 2018; McDonald *et al.*, 2021), although future geochronologic refinement of these units may influence faunal correlation.



**Fig. 3.10** Spatio-temporal distribution of fossil localities ( $n=60$ ). Full list of localities collated in this study can be found in Appendix C.3.1. <sup>^</sup> Direct map distance. \* Average stratigraphic distribution based on Reynold Point lectostratotype section. Member abbreviations: L.C.C. Mbr = Last Chance Creek Member; R.P. Mbr = Reynolds Point Member; C.P. Mbr = Coyote Point Member. See materials and methods for further detail.

Vertebrates from the Reynolds Point Member (model age:  $81.55 +0.62/-0.09$  to  $80.61 +0.39/-0.51$  Ma) are largely distributed throughout the section, mostly associated with channel lag deposits of durable skeletal material. Consisting nearly entirely of isolated remains, some specimens are exceptionally preserved, including the holotype skull of *Diabloceratops eatoni* (UMNH VP 16699), discovered in an indurated sandstone associated with a channel lag deposit (Kirkland and DeBlieux, 2010). Associated skeletal remains have also been recovered from mudstone horizons in the lower Reynolds Point Member, including the disarticulated and scattered skeleton of *Lythronax argestes* (UMNH VP 20200), and several hadrosaurids (*e.g.*, UMNH VP Loc. 1209). Due to the scattered

distribution of vertebrate remains throughout the Reynolds Point Member (Fig. 3.10), along with its still-expanding fossil record, identification of a specific faunal zone within the unit is problematic. Conversely, vertebrates from the lower portion of the Reynolds Point Member are roughly contemporaneous with the early Campanian Lower Shale Member of the Aguja Formation (Lehman *et al.*, 2019, Preito-Márquez *et al.*, 2019) and Allison Member of the Menefee Formation (Lucas *et al.*, 2005; McDonald and Wolfe, 2018), and possibly predate or partially overlap with the vertebrate assemblage from Lithofacies 3 of the Two Medicine Formation (Horner *et al.*, 2001).

The steep exposures of the Coyote Point Member are less intensely explored than the lower members of the Wahweap Formation; however, associated remains of dinosaurs have been recovered from this unit, including the holotype of the centrosaurine ceratopsian *Machairoceratops cronusi* (UMNH VP 20550; Lund *et al.*, 2016a) and hadrosaurids (*e.g.*, DMNH Loc. 12460) (Table 3.3, Appendix C.3.1). A recently identified, rich lag horizon in the upper two meters of the Coyote Point Member near Death Ridge, preserving hematite-encrusted vertebrate material, has already produced diagnostic remains of one dinosaur (Wahweap Centrosaurine C, UMNH VP 9549), in addition to abundant turtle and hadrosaurid remains, and less abundant crocodyliform and theropod material. The age of this horizon, dated to 79.03 +0.96/-1.00 Ma (Bayesian model age), or extrapolated to ~79.6 Ma based on sedimentation rates of the Reynolds Point Member, make this a significant fossiliferous interval for latitudinal comparisons with contemporaneous faunas. This includes northern faunas like those of the lower McClelland Ferry Member of the Judith River Formation (Mallon *et al.*, 2016) and the middle of Unit 3 of the Two Medicine Formation (Horner *et al.*, 2001). Increased sampling of this interval is necessary for more meaningful comparisons.

In summary, modest zonation of fossil localities is noted in herein including particularly rich zones in the lower two thirds of the Last Chance Creek Member, the lower levels of the Reynolds Point Member and in the uppermost Coyote Point Member (Fig. 3.10). The majority of fossil localities from the Wahweap Formation are situated within 500 m of a vehicle-accessible road, chiefly because access roads in the southern field areas, which encompass 87% of localities listed in this study, utilize benched areas above the steep cliff-forming Drip Tank sandstones. Despite increased accessibility to the Last Chance Creek and Reynolds Point members due to lower topographic relief and thus proximity of these exposures to roads, collection bias does not entirely explain locality distribution patterns. This is evident by the observed reduction or absence of localities in the middle to upper portion of the Last Chance Creek Member, despite abundant exposures of these levels close to roads. Increased preservation at the boundary between juxtaposing lithofacies (*e.g.*, channel sandstones at the top of the Last Chance Creek Member to the floodplain deposits of the Reynolds Point Member) may be implicated in the observed locality distribution patterns; however, detailed lithologic and taphonomic investigation is required to investigate these hypotheses further. Nevertheless, improved chronostratigraphic constraint is useful for comparing the modest faunal zones noted here with those from across the Western Interior.

### 3.7.2 Age revision for key taxa

The new high-precision U-Pb age for the Star Seep bentonite of ~81.47 Ma at the base of the Reynolds Point Member significantly improves the accuracy and precision of the inferred age of several well-known taxa including *Diabloceratops eatoni*, an early member of Ceratopsidae (Kirkland and DeBlieux, 2010; Wilson *et al.*, 2020) and *Lythronax argestes*, one of the oldest described members of Tyrannosauridae in North America (Loewen *et al.*, 2013a; Voris *et al.* 2020). As well as bearing significance in basin-scale paleontological discussion, these two taxa are ideal for discussing the revised ages because the holotype specimen of each originated from localities that were correlated with high confidence to the Reynolds Point lectostratotype section, thus the estimated ages are considered highly robust.

The holotype specimen of *Diabloceratops eatoni* was collected from a typical channel lag deposit in the Reynolds Point Member 105 m above the base of the Wahweap Formation (UMNH VP Loc. 1092) (Kirkland and DeBlieux, 2010). The age of the specimen was originally estimated to be 79.9 Ma based on  $^{40}\text{Ar}/^{39}\text{Ar}$  geochronology (Jinnah *et al.*, 2009; Kirkland and DeBlieux, 2010). Lithostratigraphic information included with the description of *D. eatoni* was indispensable in recalculating the age of the specimen. Based on the stratigraphic measurements, location description and field photographs provided by Kirkland and DeBlieux (2010), the present study was able to identify the exact level from which the specimen was recovered and place it with high confidence in the new chronostratigraphic model. This produced a revised age of 81.27  $\pm$  0.15/-0.26 Ma for *D. eatoni*, which is 1.4 million years older than previously thought and includes quantified uncertainty. Furthermore, this revised age indicates that *Diabloceratops* is the oldest known centrosaurine, providing a key minimum age constraint for the timing of the diversification of Ceratopsidae.

Vertebrate locality UMNH VP Loc. 1501 from which the holotype *Lythronax argestes* specimen was recovered is located two meters below the Star Seep bentonite at Nipple Butte (Loewen *et al.*, 2013a; this study). Due to this serendipitous proximity, the high-precision U-Pb age of 81.465  $\pm$  0.036/0.042/0.097 Ma (WLS-R) tightly constrains this interval of the Bayesian age model resulting in an estimated age of 81.49  $\pm$  0.37/-0.04 Ma for the *L. argestes* holotype. This model age is up to 1.6 million years older and considerably more precise than previous estimates and, furthermore, is exceptionally robust because factors such as variable sediment accumulation rates are accounted for in the Bayesian statistical approach and quantified as a component of the propagated uncertainty. This revised age for *L. argestes* (along with *Dynamoterror dynastes*, McDonald *et al.*, 2018) provides a minimum age constraint for initial tyrannosaurid diversification given that *L. argestes* is the oldest known well-dated tyrannosaurid (Loewen *et al.*, 2013a; Voris *et al.*, 2020). Specifically, this even older age supports the hypothesis that tyrannosaurids diversified during a time interval that witnessed particularly high sea levels in the Western Interior (Loewen *et al.*, 2013a).

### 3.7.3 Long distance correlation of taxa: Tyrannosaurid case example

Application of radioisotopic ages to the fossil record is of critical importance for comparing near-contemporaneous faunas, particularly across large distances; however, in doing so, the uncertainty of a radioisotopic age is just as important as the age itself. An excellent example of the utility of high-precision geochronology for distinguishing between near-contemporaneous taxa involves the holotype specimens of three of the currently oldest described tyrannosaurid dinosaurs from North America; *Lythronax argestes*, *Dynamoterror dynastes*, and *Thanatotheristes degrootorum* (Loewen *et al.*, 2013a; McDonald *et al.*, 2018; Voris *et al.*, 2020). The recently described *T. degrootorum* from the Foremost Formation in Alberta, is reported to be “slightly” younger than *L. argestes* from the Wahweap Formation (Voris *et al.*, 2020), although the age uncertainty is not reported and does not appear to have been considered. The age of the holotype specimen of *T. degrootorum* was reported as “~79.5 Ma” based on a bentonite in the Taber Coal Zone, although the origin and precision of this bentonite age is ambiguous. Considering the probable uncertainty of this data and the known uncertainty associated with the previous age of *L. argestes* (79.9 to 80.6 Ma  $\pm$  0.6 [2 $\sigma$ ]), the two tyrannosaurs were statistically indistinguishable in age prior to new chronostratigraphic data presented herein; therefore, when *T. degrootorum* was first described, the specimen could have been considered contemporaneous with *L. argestes*, which would have significant implications for latitudinal endemism hypotheses. Conversely, the revised temporal framework for the Wahweap Formation developed herein ratifies the original statement that *T. degrootorum* is indeed quantitatively younger than *L. argestes* by approximately two million years (according to currently available data).

Reporting the limitations of available geochronologic constraint when describing new taxa reduces the likelihood of miscommunication around faunal correlations which are difficult to rectify in later work. For example, the age of the holotype specimen for *D. dynastes* from the upper Allison Member of the Menefee Formation in New Mexico (McDonald *et al.*, 2018) remains poorly constrained due to a sparsity of dated horizons and the time-transgressive nature of Upper Cretaceous strata in the area and, as such, this specimen cannot (currently) be temporally distinguished from either *L. argestes* or *T. degrootorum*. The way in which the age of this specimen (*D. dynastes*; McDonald *et al.*, 2018) was reported is commendably appropriate as the available chronostratigraphic data was listed and the precision was not overstated, which allows future chronostratigraphic revisions to refine the age without needing to dispute previous erroneous interpretations. These examples not only highlight the importance of the origin and uncertainty of radioisotopic ages, but also the need for higher precision chronostratigraphic data across the Upper Cretaceous strata of the Western Interior.

## 3.8 Conclusions

This study proposes revised stratigraphic nomenclature and a robust new age model for the Wahweap Formation based on U-Pb geochronology that emphasizes quantitative uncertainty and provides



comprehensive stratigraphic context for most of the archived fossil localities from the formation on the Kaiparowits Plateau. Formal recognition of members of the Wahweap Formation is intended to provide nomenclatural clarity in future work. These newly named units include, in ascending stratigraphic order, the Last Chance Creek Member, Reynolds Point Member, Coyote Point Member, and Pardner Canyon Member. These supplant the informal lower, middle, upper, and capping sandstone ‘member’ names of Eaton (1991). Member definitions and descriptions are primarily built upon the seminal work of Eaton (1991) and later work by Jinnah and Roberts (2011), with member boundary ages refined herein. Future regional lithostratigraphic work paired with high-precision geochronology for strata of the Markagunt and Paunsaguant Plateaus and in the Henry Basin is necessary to refine precise correlations between potentially correlative strata.

The central component of this study was the development of a new age-stratigraphic model for the Wahweap Formation that was developed using new U-Pb zircon ages and the application of Bayesian statistical modelling. The age of the base of the Wahweap Formation was determined to be *ca* 1.2 million years older than previously thought, and the total duration of the formation is suggested to span  $82.17 \pm 1.47$ – $0.63$  Ma to  $77.29 \pm 0.72$ – $0.62$  Ma. This study also compiled and stratigraphically calibrated most of the known vertebrate fossil localities discovered throughout the formation over the last 25 years. This calibrated list was used to investigate spatio-temporal trends and provide age estimates with objective uncertainties for Wahweap biota. Spatio-temporal investigation indicates that most fossil localities are situated within Last Chance Creek and Reynolds Point member strata. Whether this is due to biotic zonation or preservation bias is uncertain; however, these findings allude to the possibility of discrete faunal zonation within the formation. The second trend noted was the abundance of vertebrate localities in southern field areas (Brigham Plains to Caine Bench) compared to northern exposures on the plateau. Identification of these trends highlights possible biases and should guide future fossil exploration within the Wahweap Formation. Age calibration of currently known localities as well as future discoveries using the age model herein aids in faunal comparisons with contemporaneous biota elsewhere.

---





## Chapter Four

High-resolution stratigraphic correlation within the Kaiparowits Formation, southern Utah, U.S.A., and implications for late Campanian biota from southern Laramidia



*Kaiparowits Formation at The Blues*

**Preface**

This is the second of three stratigraphy-focused chapters, which are presented in increasing stratigraphic order of Campanian units from southern Utah. It involves refinement of the Kaiparowits Formation, which directly overlies the Wahweap Formation discussed in Chapter Three. Litho- and chronostratigraphic refinement in this chapter is founded on high-precision U-Pb ages reported in Chapter Two. Five such ages are presented here, and these were implemented in tandem with four others that are included in a co-authored publication (Ramezani et al., in review).

This chapter is presented in the form of a manuscript for publication; although, at the time of thesis submission, it is yet to be submitted to a scientific journal pending further collaborator contributions. Contributors to the work presented herein include E. Roberts, J. Ramezani, and A. Titus, who provided field and technical support, and edits for accuracy and language. Future work will include the adaption of this chapter for publication with the addition of an extensive fossil locality dataset (comparable to but larger than that of Chapter Three) compiled through collaboration with the Utah Museum of Natural History (R. Irmis, M. Loewen, J. Eaton, C. Levitt-Bussian, T. Birthisel), Denver Museum of Nature and Science (J. Sertich, S. Mccracken, N. Toth, I. Miller), Raymond M. Alf Museum of Paleontology (A. Farke), the Bureau of Land Management (Kanab), and others.

**Abstract**

The Kaiparowits Formation in southern Utah hosts a thick and richly fossiliferous succession of upper Campanian terrestrial strata that preserves a complex palaeoecological tapestry from the peak of non-avian dinosaur diversity. Recent high-precision geochronology demonstrates the paleontological significance of this unit in the broader North American context as a critical southern equivalent to the intensely studied Dinosaur Park Formation in Alberta. The purpose of this chapter was to expand upon dating in the Kaiparowits Formation to facilitate precise correlation of fossil biota within the formation and with other important late Campanian terrestrial ecosystems across the Western Interior. Robust intraformational correlation was conducted using five new high-precision bentonite ages from key reference sections in conjunction with the four published ages that constrain the type section. An expanded Bayesian age-stratigraphic model was used to tie the new ages to the well-constrained type section and hence calibrate the relative level of key reference sections to which remote fossil localities can be correlated. In line with recent work in the underlying early to middle Campanian Wahweap Formation, three new lithostratigraphic members for the Kaiparowits Formation were described to formally replace the previous lower, middle, and upper informal unit subdivisions. These are the Tommy Canyon Member, The Blues Member, and Powell Point Member, respectively, which are overlain by the previously named Upper Valley Member. These litho- and chronostratigraphic refinements facilitate robust temporal calibration of fossil localities from the Kaiparowits Formation across the Table Cliff and Kaiparowits plateaus, as demonstrated here by a study of ten holotype descriptions of vertebrate species known from the formation. Future work will include age-stratigraphic calibration of a comprehensive list of fossil localities (vertebrate macrofossils, mammalian microfossils, botanical fossils, invertebrates, and more), which can be used to pursue increasingly more complex palaeoecological investigations within the Kaiparowits Formation and across late Campanian terrestrial strata of western North America.

## 4.1 Introduction

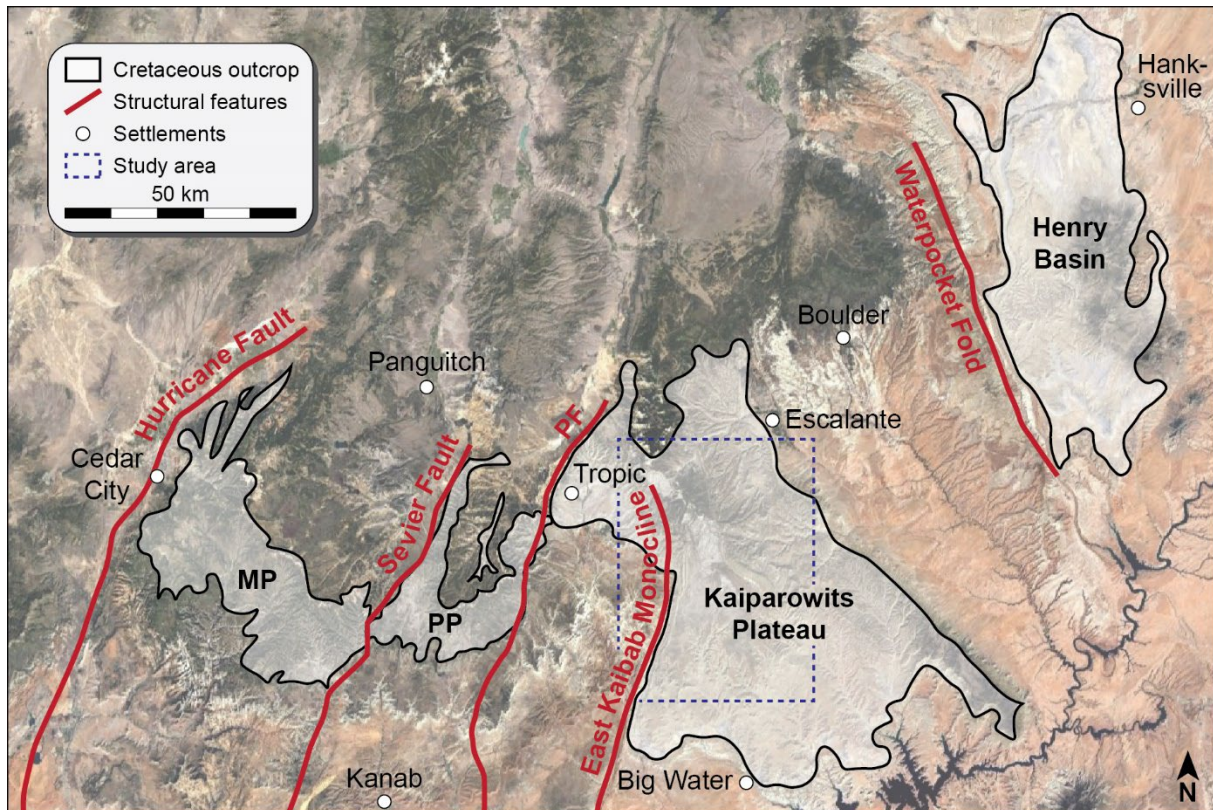
Fossil biota from western North America studied in their geologic and chronologic context form the entire basis of our understanding of drivers of both terrestrial biogeography and evolution during the peak of global dinosaur diversity in the Late Cretaceous (*e.g.*, Lehman, 1997; Gates and Sampson, 2007; Gates *et al.*, 2010; Sampson *et al.*, 2010, 2013a; Mallon *et al.*, 2012; Loewen *et al.*, 2013a; Leslie *et al.*, 2018; Chiarenza *et al.*, 2019; Voris *et al.*, 2020; Wilson *et al.*, 2020; Condamine *et al.*, 2021). Preserved ecosystems from Laramidia, the western of two Cretaceous landmasses in North America separated by the Western Interior Seaway (Sampson *et al.*, 2010), are represented by some of the most extensive, richly fossiliferous continental deposits from this, or any other part of the Mesozoic Era. This presents a unique opportunity to investigate the dynamic Campanian biosphere in greater detail. Several key localities from across the coastal and alluvial plains of eastern Laramidia have been crucial to these reconstructions including, but not limited to, Dinosaur Provincial Park and the surrounding Red Deer River badlands in Alberta, the Two Medicine River and Judith River areas in Montana, the Kaiparowits Plateau and adjacent plateaus in Utah, the San Juan Basin in New Mexico, and Big Bend National Park in West Texas (Fig. 4.1; Lehman, 1989; Eberth and Hamblin, 1993; Rogers *et al.*, 1993, 2016; Roberts *et al.*, 2005, 2013; Roberts, 2007; Mallon *et al.*, 2012; Fassett and Heizler, 2017; Leslie *et al.*, 2018; Ramezani *et al.*, in review).

The Kaiparowits Plateau in southern Utah (Fig. 4.2) holds particular promise as a representative from southern Laramidia for the reconstruction of ecological and evolutionary patterns during the Late Cretaceous. This is because the plateau hosts a remarkably continuous and incredibly thick package of fossiliferous strata with interbedded bentonite horizons (weathered volcanic ash beds) throughout most of the Campanian (Roberts *et al.*, 2005, 2013; Jinnah *et al.*, 2009; Jinnah, 2013; Beveridge *et al.*, 2020 [Ch.5], 2022 [Ch.3]; Ramezani *et al.*, in review). This stratigraphic interval is represented by the Wahweap and Kaiparowits formations, which have a combined thickness of 1,415 m with only one confidently identified depositional hiatus of statistical significance (Roberts, 2007; Jinnah and Roberts, 2011; Beveridge *et al.*, 2020 [Ch.5], 2022 [Ch.3]) and preserve a rich, diverse fossil record including dinosaurs, mammals, crocs, turtles, nesting sites, abundant flora, insect traces, and more (see Titus and Loewen, 2013, and papers therein; also Zanno and Sampson, 2005; Roberts and Tapanila, 2006; Gates and Sampson, 2007; Sampson *et al.*, 2010; Carr *et al.*, 2011; Zanno *et al.*, 2011; Sampson *et al.*, 2013b; Lively, 2015; Lund *et al.*, 2016b; Atterholt *et al.*, 2018; Wiersma and Irmis, 2018; Maccracken *et al.*, 2019, 2021, 2022; Titus *et al.*, 2021; Ferguson and Tapanila, 2022). The richness of this fauna and its palaeogeographic position within the central to southern portion of the eastern palaeomargin of Laramidia (Fig. 4.1) makes the Kaiparowits Plateau a critical location to assess spatio-temporal dependent hypotheses relating to dinosaur palaeoecology, palaeobiogeography and diversification patterns (*e.g.*, Gates *et al.*, 2010; Sampson *et al.*, 2010, 2013a; Loewen *et al.*, 2013a).



*Fig. 4.1 Palaeogeography western North America (Laramidia) at ca 75 Ma illustrating the relative location of Campanian field areas in this study (red), the broader CA-ID-TIMS study (orange), and other areas of interest (yellow). Palaeogeographic reconstruction adapted from ©2013 Colorado Plateau Geosystems Inc.*





**Fig. 4.2** Southern Utah physiographic areas illustrating the extent of outcropping Cretaceous strata on the Markagunt Plateau (MP), Paunsaugunt Plateau (PP), Kaiparowits Plateau and Henry Basin, and delineating structural features (PR = Paunsaugunt Fault) overlain on Google Earth Pro imagery. Adapted from Titus *et al.* (2016).

Addressing these complex hypotheses in detail, particularly across areas separated by hundreds to over a thousand kilometers, requires high-resolution chronostratigraphic context derived from a series of tightly correlated stratigraphic sections with precise radioisotopic age control (*e.g.*, Ramezani *et al.*, in review). Recent geochronologic refinement for Campanian strata from the Kaiparowits Plateau has significantly improved temporal constraint with the addition of six high-precision U-Pb bentonite zircon ages and Bayesian age-stratigraphic modeling (Beveridge *et al.*, 2022 [Ch.3]; Ramezani *et al.*, in review). From this work, the stratotype sections of the Kaiparowits and Wahweap formations are now constrained within a high-precision temporal framework; however, improved intraformational correlation of fossil localities to the well-dated type sections is necessary to facilitate reliable comparison of biota at a local and basin scale. Lithological correlation of outcrop exposures is challenging in the Kaiparowits Formation because it is characterized by laterally discontinuous fluvial-floodplain lithofacies and has been dissected by variable post-depositional structural and erosional landscape complexities into a series of discontinuous outcrop areas. To overcome these obstacles, the abundant bentonite horizons found throughout the Kaiparowits Formation were investigated using a modified tephrostratigraphic approach to calibrate the stratigraphic positions of isolated exposures and fossil localities relative to the well-dated stratotype section.

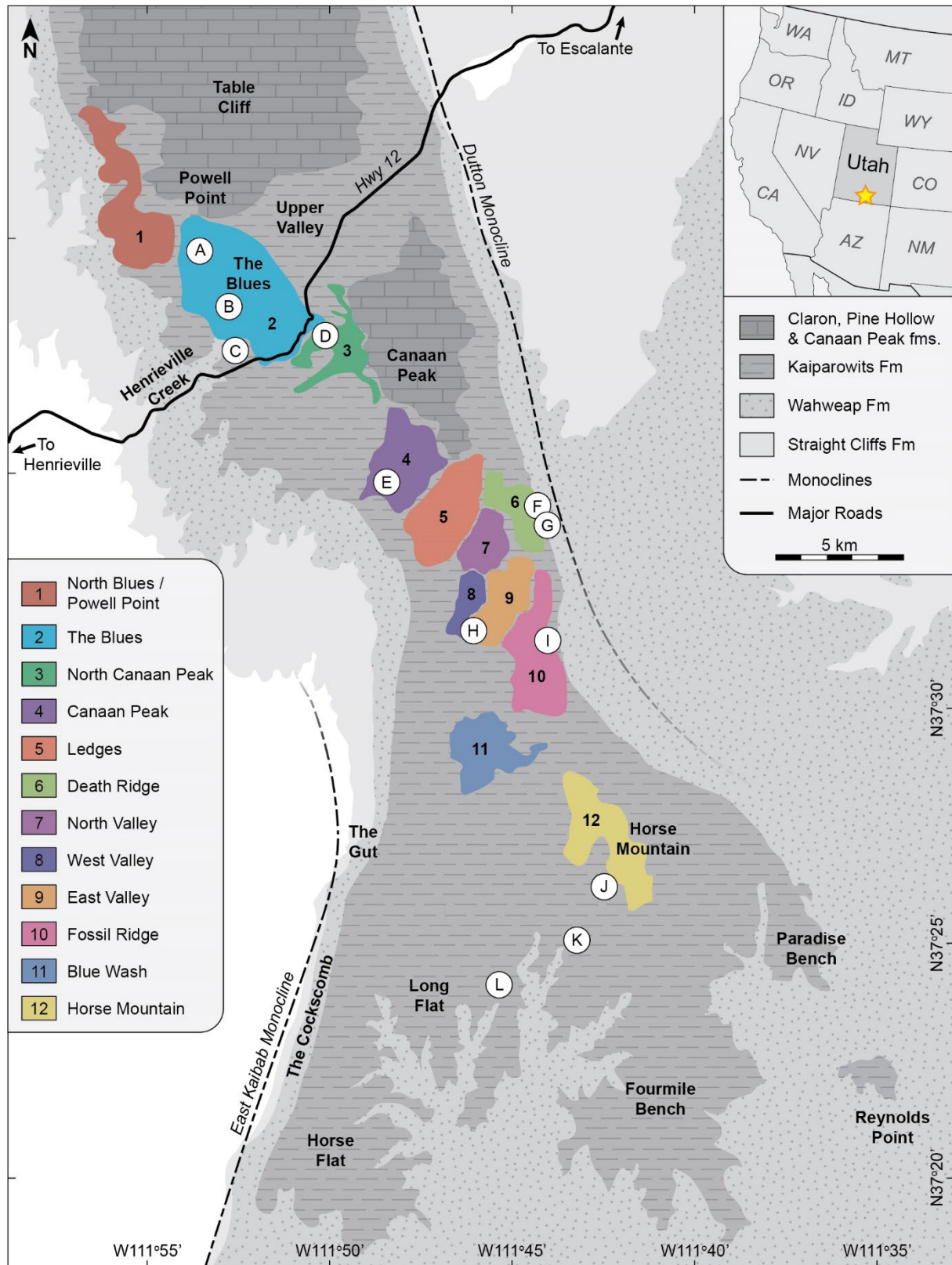
The goal of this study was to improve intraformational correlation of stratigraphic sections and key fossil localities throughout the outcrop extent of the Kaiparowits Formation on the Table Cliff and Kaiparowits plateaus. This was accomplished via: 1) refined lithostratigraphy of the Kaiparowits Formation based on detailed fieldwork, which included formal recognition and description of three new members (in addition to the previously named Upper Valley Member) and four formal bentonite beds; 2) expansion of the Bayesian age-stratigraphic model for the Kaiparowits Formation after Ramezani *et al.* (in review) to include the Upper Valley Member and associated data from Beveridge *et al.* (2020 [Ch.5]); 3) measurement of five new high-precision U-Pb zircon ages from bentonites in remote reference sections; 4) numerical calibration of the stratigraphic level of reference sections using the new high-precision bentonite ages and the modified type section age-stratigraphic model; and 5) a comprehensive age-stratigraphic review of major fossil localities from across the Kaiparowits Formation, a simplified version of which is included in this thesis. Calibrating the age of fossil localities from the formation will aid in future palaeoenvironmental reconstruction and identification of local biotic and evolutionary trends. This work is also expected to facilitate correlation of biota from southern Laramidia to coeval northern localities for the purpose of investigating hypothesized latitudinally distinct biotic distribution and diversification patterns during the Campanian in western North America.

## 4.2 Previous Work

### 4.2.1 Lithology and depositional environment

The Kaiparowits Formation in southern Utah is characterized as a thick alluvial succession dominated by fluvial-floodplain deposition (Lohrengel, 1969; Eaton, 1991; Little, 1995; Lawton *et al.*, 2003; Roberts, 2007; Titus *et al.*, 2005, 2013). Although the formation appears dominantly fine-grained from a distance, the poorly indurated sandstones and mudstones are, on average, proportionally equivalent (Eaton, 1991; Roberts, 2007). The formation is extensively exposed across the Kaiparowits and Table Cliff plateaus and in isolated pockets across the Paunsaugunt Plateau (Biek *et al.*, 2015). Exposures of Kaiparowits-like strata on the Markagunt Plateau (*e.g.*, friable sandstones, freshwater shark and ray teeth etc.), which were initially thought to correlate to the Kaiparowits Formation, were later suggested to represent the underlying Wahweap Formation (Eaton *et al.*, 2001); however, this remains unresolved (Biek *et al.*, 2015, Titus *et al.*, 2016).

Lithofacies from the Kaiparowits Formation suggest a rapidly subsiding fluvial-floodplain system with abundant pond deposits and meandering to anastomosing style suspended load channel systems (Eaton, 1991; Little, 1995; Roberts, 2007; Roberts *et al.*, 2013; Titus *et al.*, 2013). Weakly developed hydromorphic soils commonly associated with floodplain deposits in the formation indicate relatively warm, wet palaeoenvironmental conditions with seasonal or periodic aridity, and varying proximity to major channels belts (Roberts, 2007; Foreman *et al.*, 2015; Crystal *et al.*, 2019; Burgener



**Fig. 4.3** Solid geology map of the study area across the Table Cliff and Kaiparowits plateaus illustrating specific field areas (colored/numbered) and the locations of measured sections (bases; denoted by letters, see Fig. 4.6). Compiled from various USGS 1:24,000 geological maps and the USGS 1:100,000 geological map of the Escalante and Smoky Mountain 30' x 60' quadrangles by Doelling and Willis (2006, 2018).



*et al.*, 2019; Yamamura *et al.*, 2021). Recent investigations into palaeohydrological systems of the Kaiparowits Formation have revealed the presence of discrete components that include seasonal runoff of isotopically light waters from high-altitude sources (Sevier Mountains) to the west of the basin, in addition to local precipitation derived more directly from the Western Interior Seaway (Foreman *et al.*, 2015; Yamamura *et al.*, 2021). In addition, these authors and others (*i.e.*, Crystal *et al.*, 2019) have demonstrated that the Kaiparowits Formation experienced climate-driven monsoonal precipitation that led to pulsed flooding of these fluvial systems, which may be reflected by the presence of storm-event-related shell beds (Roberts *et al.*, 2008).

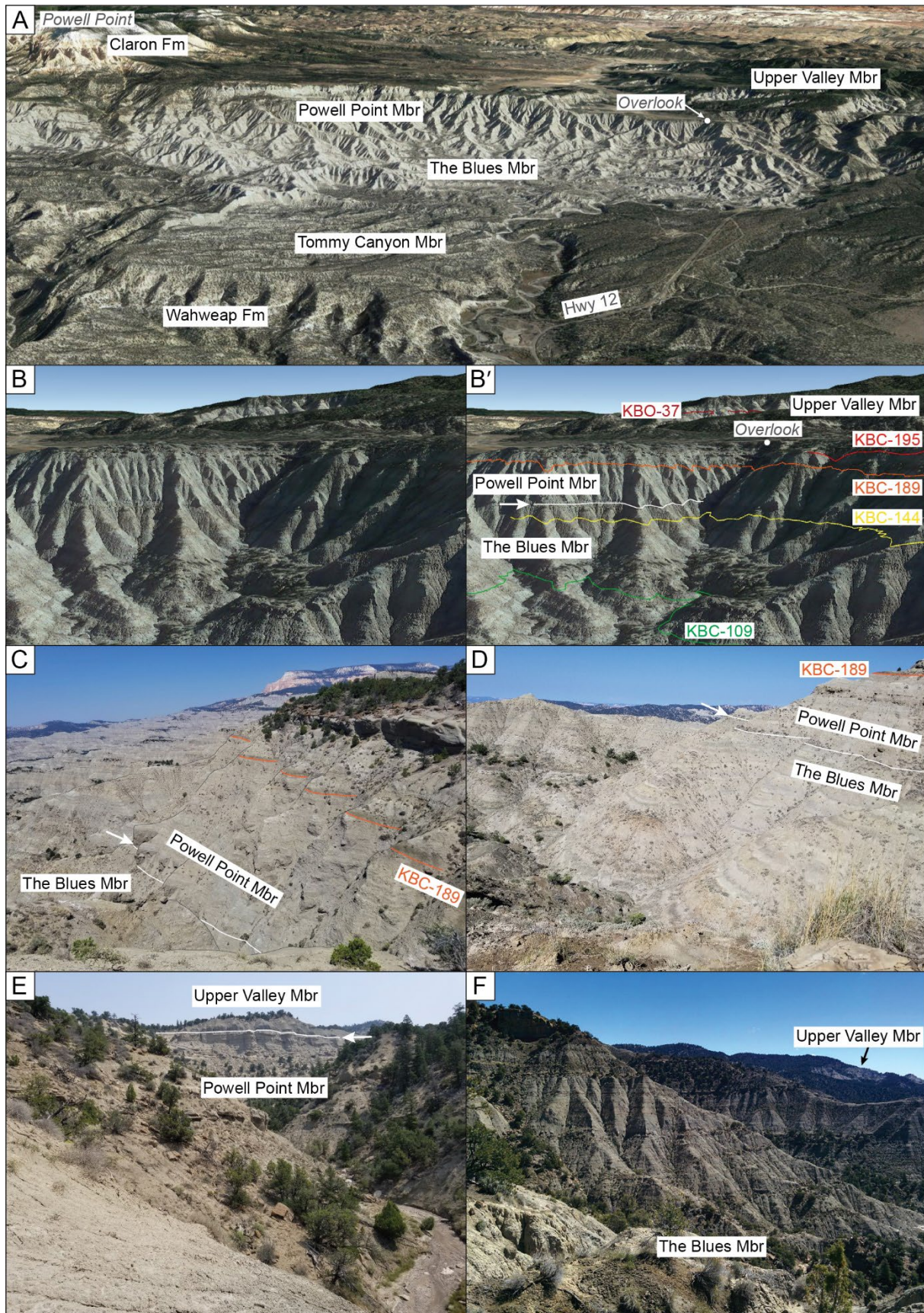
Though the poorly indurated nature of sandstones from the formation impedes detailed descriptions of sedimentary architecture (Eaton, 1991), Little (1995), Roberts (2007), and Beveridge *et al.* (2020 [Ch.5]) provide comprehensive insights. Roberts (2007) describe nine facies associations with the most common being sandy mudstone (FA8), carbonaceous mudstone (FA9) and minor tabular and lenticular sandstone (FA5). From this work, Roberts (2007) suggested that the alluvial architecture in the formation was controlled primarily by tectonics and is also strongly influenced by climate (*i.e.*, monsoon precipitation) and sea level (see also Lawton *et al.*, 2003; Lawton and Bradford, 2011). Despite wet, lush palaeoenvironmental conditions, coal is notably rare in the formation, which Roberts (2007) attributes to atypically high sediment accumulation rates that are lithologically evident in the abundance of preserved floodplain deposits including crevasse splays, common poorly developed soils, root traces, burrows and insect nests (Roberts and Tapanila, 2006).

Although dominantly alluvial, evidence of marine influence (*e.g.*, tidal channels) has been identified in the lower portion of The Blues Member (previously middle unit), particularly between 120 - 320 m, with the highest concentration of such lithofacies occurring at ~180 m (Lohrengel, 1969; Roberts, 2007; Roberts *et al.*, 2008). This includes clay/carbon draped foresets, lenticular and flaser bedding, the trace fossil *Teredolites*, and bryozoans encrusting unionoid mollusks (Roberts, 2007). Although these elements are typically associated with tidal influence or estuarine development, maximum transgression of the palaeoshoreline at that time was still tens of kilometers to the east, thus suggesting relatively distal incursion of brackish water conditions on a low-relief alluvial plain with both high-elevation upland and locally derived hydrologic sources (*e.g.*, Foreman *et al.*, 2015; Crystal *et al.*, 2019).

#### 4.2.2 Stratigraphy and formation boundaries

The Kaiparowits Formation lectostratotype (principal reference) section designated by Roberts (2007) (the KBC section) makes use of the accessible, continuous exposures in The Blues along Highway 12 (Figs. 4.3 and 4.4). The stratigraphy of the formation has been incrementally refined based on these exposures over the last 90 years since the formation was named by Gregory and Moore (1931), who measured an incomplete section from the lower part of the formation but did not designate a stratotype.





**Fig. 4.4** Outcrop photos of the Kaiparowits Formation. A) Google Earth Pro image of The Blues area annotated with the members of the Kaiparowits Formation and other formations/landmarks. (continued)



The first complete section (Lohrengel, 1969) reported a thickness of *ca* 840 m from The Blues, which was later extended to 855 m (Eaton, 1991), then to 860 m in the near-continuous KBC lectostratotype (Roberts, 2007). Measurements in The Blues provide an excellent foundation for understanding the Kaiparowits Formation stratigraphy; however, this locality in the northern part of the Kaiparowits Plateau is separated from central and southern exposures by structural and geographic complications (*i.e.*, the East Kaibab and Dutton monoclines, and Canaan Peak), thus restricting stratigraphic correlation by means of lateral continuity. For example, ~145 m of additional, recently identified Kaiparowits-style strata on the northwestern flank of Canaan Peak (~2 km east-southeast of The Blues overlook) was found stratigraphically higher than the previously interpreted upper boundary of the formation (Beveridge *et al.*, 2020 [Ch.5]). This work led to the extension of the Kaiparowits Formation to a total of 1005 m and included a principal reference section of the therein described Upper Valley Member. Furthermore, the formation is reportedly thickest proximal to Canaan Peak (Eaton, 1991; Beveridge *et al.*, 2020 [Ch.5]) thinning northwards due to tilting and erosion prior to deposition of the Canaan Peak Formation. This may indicate that future work on Canaan Peak could yield new insight into the uppermost strata of the formation.

The basal contact of the Kaiparowits Formation with the underlying Pardner Canyon Member (previously called the capping sandstone member; see Beveridge *et al.*, 2022 [Ch.3]) of the Wahweap Formation is generally conformable but is typically marked by an undulatory erosional surface (~15 m of relief) (Peterson, 1969; Eaton, 1991; Lawton *et al.*, 2003; Roberts, 2007; Lawton and Bradford, 2011; Roberts *et al.*, 2013; Beveridge *et al.*, 2022 [Ch.3]). This surface is interpreted to represent a brief depositional hiatus, as indicated by pedogenic features such as mottling and root traces noted at some localities, and fluvial scours at others (Lawton and Bradford, 2011; Beveridge *et al.*, 2022 [Ch.3]). Where the transition is gradational or ambiguous, previous studies have marked the base of the Kaiparowits Formation as the first occurrence of laterally continuous fine-grained beds (Eaton, 1991; Little, 1995; Lawton *et al.*, 2003; Roberts, 2007; Roberts *et al.*, 2013); however, interfingering of Wahweap-style quartz arenite and Kaiparowits-style lithic arkose sandstones is also observed, which may be a useful, more specific identification tool (Lawton *et al.*, 2003; Beveridge *et al.*, 2022 [Ch.3]). Thus, the first occurrence of abundant black chert grains visible in hand sample (indicating a transition

---

**Fig. 4.4 (continued)** B) Google Earth Pro image of The Blues and Powell Point members at the tourist overlook (Powell Point Vista) with the Upper Valley Member in the background B') annotated copy showing the member boundary and bentonite marker horizons. C) Photograph taken near the tourist overlook illustrating features shown in panel B. D) Photograph illustrating a more gradational example of The Blues – Powell Point member contact close to Highway 12. E) Photograph taken from the KBU-C sample site with the Powell Point Member in the foreground and the lower portion of the Upper Valley Member in the distance. F) Photograph of the excellent exposures of The Blues Member in the Canaan Peak area (KWC section) with pale outcrops of the Upper Valley Member in the background.



to chert-rich lithic arkose) is here considered the most suitable criteria for identifying the base of the Kaiparowits Formation. The shift from quartzose to feldspatholithic petrofacies identified by Lawton *et al.* (2003) was reported to occur tens of meters above the formation's base, although this inference was built upon the previous boundary definition (*i.e.*, first laterally continuous mudstone), thus it is here considered that the relevant findings from Lawton *et al.* (2003) and Beveridge *et al.* (2022 [Ch.3]) concur. This interpretation links the definition of the formation boundary to a change in sedimentary provenance related to palaeo-drainage rearrangement and tectonism in the thrust belt (Lawton *et al.*, 2003; Lawton and Bradford, 2011; Beveridge *et al.*, 2022 [Ch.3]).

The upper contact of the Kaiparowits Formation with the overlying Canaan Peak Formation has been the subject of recent revision. The boundary was originally considered to be unconformable, indicated by a sharp lithologic change from blue-gray sandstone to crimson conglomerates and a subtle angular offset (Bowers, 1972; Eaton, 1991; Lawton *et al.*, 2003; Roberts, 2007; Larsen *et al.*, 2010; Roberts *et al.*, 2013); however, recent recognition of the Upper Valley Member as a capping unit of the Kaiparowits Formation reported evidence of interfingering lithofacies between the two formations (Beveridge *et al.*, 2020 [Ch.5]). The formation was found to be *ca* 145 m thicker than previously thought, likely due to slumping obscuring the stratigraphy below Powell Point. Features such as minor incision and extra-formational conglomerates interbedded with Kaiparowits-style lithotypes were used to suggest that the lithological transition to the overlying Canaan Peak Formation is at least partly gradational and the unconformity between formations represents far less time than previously thought. This hypothesis, which may imply syn-depositional deformation and erosion to account for the angular offset between the two formations noted elsewhere (*i.e.*, closer to Powell Point in the north), is yet to be examined in detail and has implications for the onset of peak Laramide uplift (Beveridge *et al.*, 2020 [Ch.5]).

#### 4.2.3 Geochronology

The first age constraints for the Kaiparowits Formation were based on terrestrial biostratigraphy and comparison with similar units in the north. Unlike contemporaneous units elsewhere in the Western Interior, the terrestrial strata of the Kaiparowits Formation are not bounded by marine units, which limited early biostratigraphic-based age assessment of the formation due to the absence of typical marine index fossils (Lohrengel, 1969). Nevertheless, numerous studies of terrestrial vertebrates, particularly mammaliaforms, indicate a (middle to late) Campanian age, equivalent to the Judithian NALMA (Eaton and Cifelli, 1988, 2013; Cifelli, 1990a, 1990c; Eaton, 1991, 1999, 2002; Eaton *et al.*, 1999a, 1999b; Cifelli *et al.*, 2004). Although Lohrengel (1969) described a Maastrichtian palynomorph assemblage, Bowers (1972) and Eaton (1991) strongly contested this interpretation, proposing that the formation could be no younger than Campanian.

Over the last two decades, radioisotopic dating has been the focus of geochronologic refinement of the Kaiparowits Formation and is facilitated by abundant interbedded bentonite horizons (weathered volcanic ash; *i.e.*, Roberts *et al.*, 2005, 2013; Ramezani *et al.*, in review; this study). Findings from these radioisotopic studies support biostratigraphic inferences of a (middle to) late Campanian age for the Kaiparowits Formation. The first radioisotopic ages for the formation were four  $^{40}\text{Ar}/^{39}\text{Ar}$  bentonite sanidine ages reported by Roberts *et al.* (2005), which were later recalculated by Roberts *et al.* (2013) based on revision of the Fish Canyon Tuff standard (see Kuiper *et al.*, 2008). The initial study calculated a sediment accumulation rate of *ca* 41 cm/kyr and noted exceptional bentonite preservation and implied a relationship with the abundance of paludal environments in the formation. Along with revision of  $^{40}\text{Ar}/^{39}\text{Ar}$  geochronology, Roberts *et al.* (2013) reported the first high-precision U-Pb bentonite zircon age for the Kaiparowits Formation generated using the chemical abrasion isotope dilution thermal ionization mass spectrometry (CA-ID-TIMS) approach (KP-07,  $76.264 \pm 0.046/0.062/0.10$  Ma). Finding from this study were supported by magnetostratigraphic work by Albright and Titus (2016) that concluded the lower half of the formation was referable to magnetochron C33n.

Following this work on radiometric bentonite ages, as well as several detrital zircon U-Pb studies (*e.g.*, Larson *et al.*, 2010; Lawton and Bradford, 2011; Beveridge *et al.*, 2020 [Ch.5]), a recent basin-scale study by Ramezani *et al.* (in review) presented a series high-precision  $^{206}\text{Pb}/^{238}\text{U}$  zircon ages from Campanian localities across the Western Interior including four stratigraphically arrayed bentonites from the Kaiparowits Formation. These new ages were generated using CA-ID-TIMS methods and yielded internal precision nearing 99.98%. The work was further supported by the development of Bayesian age-stratigraphic modeling of type sections for the richly fossiliferous Dinosaur Park and Kaiparowits formations, which demonstrated the two to be exact temporal correlatives despite being spatially separated by up to 1500 km. This high-resolution temporal framework provides the foundation upon which this thesis chapter builds.

Due to the high-resolution nature of the temporal framework refined throughout this study, clear and detailed geochronological reporting is of utmost importance. Campanian chronostratigraphic boundary definitions followed here were those defined by Gale *et al.* (2020) of  $83.7 \pm 0.5$  Ma and  $72.2 \pm 0.2$  Ma for the basal and upper boundaries respectively (see GTS2020, Gradstein *et al.*, 2020). Due to continued revision of these chronostratigraphic boundary definitions, it is recommended that numerical age data in this study are treated more preferably than relative terms where possible and should include an indication of the uncertainty (*e.g.*, “a model age of  $75.34 +0.06/-0.08$  Ma” vs “late Campanian”). Furthermore, substages of the Campanian are not currently formal, thus strict adherence to numerical substage boundary ages was here avoided. Sources of uncertainty must be considered when comparing  $^{206}\text{Pb}/^{238}\text{U}$  ages generated in this study with other ages generated using different methods and mineral systems (see Bowring *et al.*, 2006; Schoene *et al.*, 2006), whereas only the internal error is required for

direct comparison with other CA-ID-TIMS ages, particularly those of Beveridge *et al.* (2022 [Ch.3]) and Ramezani *et al.* (in review).

#### 4.2.4 Paleontology

The Kaiparowits Formation preserves a record of rich and diverse Campanian ecosystems that represent a key southern equivalent to rigorously studied areas in Montana and Alberta. Paleontological interest in the Kaiparowits began in the 1980's with meticulous mammaliaform biochronology (Eaton and Cifelli, 1988, 2013; Cifelli, 1990a, 1990c; Eaton, 1991, 1999, 2002; Eaton *et al.*, 1999a, 1999b), which identified a Judithian affinity and highlighted the Kaiparowits Plateau as an area of rich fossil preservation. Since this time, the Kaiparowits fossil record has continued to expand in volume and diversity and now incorporates members of Ceratopsidae, Tyrannosauridae, Hadrosauridae, Ankylosauridae, Troodontidae, Caenagnathidae, Avisauridae, and possibly Pachycephalosauridae, and a multitude of taxa and materials representing crocodyliforms, turtles, freshwater sharks and rays, bony fish, salamanders, frogs, lizards, snakes, mammals, plants, insects and other invertebrates (Zanno and Sampson, 2005; Roberts and Tapanila, 2006; Gates and Sampson, 2007; Sampson *et al.*, 2010; Carr *et al.*, 2011; Zanno *et al.*, 2011, 2013; Brinkman *et al.*, 2013; Evans *et al.*, 2013b; Gardner *et al.*, 2013; Gates *et al.*, 2013; Hutchison *et al.*, 2013; Irmis *et al.*, 2013; Kirkland *et al.*, 2013; Loewen *et al.*, 2013b, 2013c; Miller *et al.*, 2013; Nydam, 2013; Roček *et al.*, 2013; Sampson *et al.*, 2013a, 2013b; Tapanila and Roberts, 2013; Wiersma and Loewen, 2013; Lively, 2015; Lund *et al.*, 2016b; Atterholt *et al.*, 2018; Wiersma and Irmis, 2018; Maccracken *et al.*, 2019, 2021, 2022; Titus *et al.*, 2021; Ferguson and Tapanila, 2022). Materials include isolated, associated, and articulated skeletal elements, teeth, osteoderms, eggshell, fish scales, mollusk shells, floral imprints, petrified wood, charcoal, rare coprolites, and trace fossils. Most localities are known from the middle portion of the formation (upper Tommy Canyon Member to lower Powell Point Member), which may reflect preferable taphonomic conditions in the mudstone dominated Blues Member or possibly an artefact of collection strategy in the extensive and more accessible terrain formed by these lithotypes.

The Kaiparowits floral assemblage is dominated by angiosperms (flowering plants) and includes ferns and gymnosperms among other morphotypes, represented by thousands of specimens of leaves, seeds, fruits, and flowers (Miller *et al.*, 2013; Maccracken *et al.*, 2019, 2021, 2022). This sizable collection also facilitates the study of Campanian insects, complementary to ichnological work on social insect nests (Roberts and Tapanila, 2006; Maccracken *et al.*, 2019, 2021, 2022). Together with trace fossils and invertebrates (Tapanila and Roberts, 2013), these constitute the most detailed and definitive palaeobiotic evidence for high biodiversity in a wet, warm floodplain setting, and contribute to a broader understanding of biogeographic patterns across Laramidia during the Campanian (see also Titus and Loewen, 2013 and references therein).

Several classic dinosaur lineages are represented in the Kaiparowits Formation including Ceratopsidae, Hadrosauridae, Ankylosauridae, and Tyrannosauridae (Zanno and Sampson, 2005; Gates and Sampson, 2007; Sampson *et al.*, 2010; Carr *et al.*, 2011; Zanno *et al.*, 2011; Sampson *et al.*, 2013b; Lund *et al.*, 2016b; Wiersma and Irmis, 2018). Comparison of these taxa with northern correlatives shows comparable representation at the family level but reveals a disparate record of genus and species. For example, ceratopsids from the Kaiparowits Formation include the chasmosaurines *Utahceratops gettyi* and *Kosmoceratops richardsoni* and the centrosaurine *Nasutoceratops titusi*, which are distinguished from the coeval chasmosaurines *Chasmosaurus belli*, *Chasmosaurus russelli* and *Vagaceratops irvinensis*, and the centrosaurines *Centrosaurus apertus* and *Styracosaurus albertensis* from the Dinosaur Park Formation, Alberta (Mallon *et al.*, 2012). This apparent lack of overlap in latitudinal distribution of large terrestrial vertebrates is interpreted to reflect dinosaur endemism whereby northern and southern parts of Laramidia developed unique coeval faunas during the late Campanian (Lehman, 1997, 2001; Gates *et al.*, 2010; Sampson *et al.*, 2010, 2013a). This hypothesis has been challenged on the grounds of miscorrelation of diachronous successions (*e.g.*, Sullivan and Lucas, 2006; Lucas *et al.*, 2016); however, recent temporal refinement across western North America (Ramezani *et al.*, in review) demonstrate that the fossiliferous intervals of key units from Alberta to Utah are exactly contemporaneous. With this improved chronostratigraphic framework, it is now possible to provide more robustly supported arguments around late Campanian faunal endemism.

#### 4.3 Member Subdivision Nomenclature

Due to its exceptional thickness, informal subdivisions of the Kaiparowits Formation are widely used to help identify the stratigraphic interval for features of interest such as fossil localities. Broad changes in alluvial architecture throughout the Kaiparowits Formation were first noted by Little (1995) and subsequently characterized in detail by Roberts (2007) as three informal subdivisions: the lower, middle, and upper units. These units have been widely adopted in subsequent sedimentological and paleontological studies, especially due to the need to separate the exceptionally thick formation (1005 m) into, smaller, more convenient units. More recently, Beveridge *et al.* (2020 [Ch.5]) described and formally recognized the volcanoclastic-dominated Upper Valley Member of the Kaiparowits Formation, which predominantly consists of previously unrecognized strata. This work, as well as formal recognition of members in the underlying Wahweap Formation (Beveridge *et al.* 2022 [Ch.3]), prompted the revision and formal recognition of the lower three units of the Kaiparowits Formation.

Although the current naming scheme is widely used, relative nomenclature such as lower, middle, and upper units can result in unintuitive locality descriptions, particularly when compounding these relative terms. For example, holotype and assigned specimens described by Sampson *et al.* (2010) were reported to “occur in the upper portion of the lower unit and the lower portion of the middle unit”, and the holotype *Akainacephalus johnsoni* was recorded by Wiersma and Irmis (2018) from a locality

“within the lower portion of the middle unit of the upper Campanian Kaiparowits Formation”. These examples highlight the need for updated lithostratigraphic nomenclature to support the wealth of paleontological work conducted throughout the richly fossiliferous formation. Thus, this study proposes recognition of the three informal units as formal members of the Kaiparowits Formation. The new names are the Tommy Canyon Member (replacing the lower unit), The Blues Member (replacing the middle unit), and the Powell Point Member (replacing the upper unit), which are in addition to the recently defined Upper Valley Member that caps the formation (Figs. 4.4 and 4.6; Beveridge *et al.*, 2020 [Ch.5]). The lithostratigraphy of the Kaiparowits Formation, including its subdivisions, has been described in detail previously; therefore, the following descriptions constitute an expanded summary of prior work following the facies associations described by Roberts (2007) and supported by additional observations herein.

#### 4.3.1 Tommy Canyon Member

The Tommy Canyon Member (previously the lower unit) is the lower of two channel-dominated units in the Kaiparowits Formation where sandstone channel complexes (FA3, FA4) constitute roughly three times as much of its 90 to 110 m thickness as overbank mudstones (FA8, FA9) (Little, 1995; Lawton *et al.*, 2003; Roberts, 2007). Alluvial architecture of the member dominantly reflects closely spaced single story major tabular sandstones (FA3) with common lateral accretion macroforms (Eaton, 1991; Lawton *et al.*, 2003; Roberts, 2007). These river systems are interpreted to have drained longitudinally towards the north, parallel to the foredeep axis (Goldstrand, 1992; Lawton *et al.*, 2003; Roberts, 2007). Small (<0.5 cm) isolated chert and limestone pebbles occur in the lowest ~ 50 m of the member and constitute the only significant component of extra-formational clasts in the lower three members of the formation (Eaton, 1991; Roberts, 2007; Beveridge *et al.*, 2020 [Ch.5]), with the exception of rare large pebbles throughout the formation associated with carbonized logs with roots suggesting long-distance rafting in root balls. Fossil occurrence is notably rare in the lower two-thirds of the member compared to the upper third. The base of the Tommy Canyon Member is most reliably described as the first occurrence chert-rich lithic arkose sandstones above the quartz-arenites of the Pardner Canyon Member of the Wahweap Formation (Beveridge *et al.*, 2022 [Ch.3]), and the top boundary is denoted by the first instance of widespread over-bank deposits greater than 10 m in thickness (Roberts, 2007). Variegated red and purple mudstones that occur in the Tommy Canyon Member but nowhere else in the Kaiparowits Formation indicate at least a slightly higher degree of aridity in the depositional system than in other members, which may help explain the paucity of fossils in its lower portion. The name of the member is derived from Tommy Canyon in the Horse Mountain Quadrangle, found between the KFL principal reference section and the KFMB additional reference section, both of which illustrate detailed records of the member interval. The Tommy Canyon Member is also represented in the KFR section at Fossil Ridge, albeit sparsely, and in the KBC lectostratotype section in The Blues.



### 4.3.2 *The Blues Member*

The Blues Member (previously the middle unit) is a 440 to 510 m thick mudstone-dominated interval (~95 to 550 m above the base of the formation) that is well exposed in The Blues area where the Kaiparowits Formation lectostratotype section was measured (Fig. 4.4; Roberts, 2007). The member was named for The Blues area (see Pine Lake and Upper Valley quadrangles) and, as such, 'The' is generally capitalized and included in the formal name of this unit. It is the thickest of the four Kaiparowits Formation subdivisions and represents stereotypical strata of the formation. Due to the muddy and highly friable nature of sandstones and mudstones alike, The Blues Member forms poorly consolidated steep-sloped badlands (Gregory and Moore, 1931; Lohrengel, 1969; Eaton, 1991). Although the member has the visual appearance of consisting nearly entirely of blue-gray and yellow-green overbank deposits, channel sandstones are nearly as common. Most channel deposits occur as isolate major lenticular (FA4) and minor single-story tabular and lenticular sandstones (FA5) and record a shift to eastward-flowing transverse, anastomosing river systems, which may be linked to early Laramide uplifts northwest or west of the study area (Roberts, 2007). Fine-grained lithofacies are dominated by sandy (FA8) and carbonaceous (FA9) mudstones, while finely laminated calcareous siltstones (FA6) are also present and can be used as laterally continuous marker horizons. Interpreted as a combination of palaeoenvironmental-driven preservation bias and greater unit thickness, seven of at least ten unique bentonite horizons (Fig. 4.6) reported from the formation are found within The Blues Member (Roberts *et al.*, 2005, 2013; Roberts, 2007; this study). Evidence of tidal influence is also reported from the lower portion of the member (ca 120-320 m) (Roberts, 2007). The Blues Member hosts the richest concentration of fossil localities in the Kaiparowits Formation, and by extension, in southern Utah, particularly between 150 to 400 m above the base of the formation (Roberts, 2007). The majority of lithostratigraphic measurements from the formation describe portions of The Blues Member including portions or the entirety of nine of the twelve measured sections and eight of the nine CA-ID-TIMS dated bentonite outcrops (Fig. 4.6). The KBC section constitutes the principal reference for The Blues Member, and the unit is also represented in eight additional sections throughout the study area including the KWC section, which is an important reference on the southern flank of Canaan Peak at the headwaters of Wahweap Creek. The top of the member is defined as the base of a set of continuous, easily identifiable amalgamated multistory channel complexes that crops out as cliffs above the steep, friable badlands of The Blues Member (Roberts, 2007). This contact can be observed beneath the overlook along Highway 12 at the top of The Blues area.

### 4.3.3 *Powell Point Member*

The ~200-meter-thick Powell Point Member (previously the upper unit) represents an upward coarsening package of amalgamated sandstone channel complexes (FA3) and overbank mudstones (FA8, FA9) that is architecturally similar to the Tommy Canyon Member (Little; 1995; Lawton *et al.*,

2003; Roberts, 2007), although with a marginally higher proportion of overbank deposits near the base of the member (~2:1 sand to mud, recalculated herein based on changes implemented in Beveridge *et al.*, 2020 [Ch.5]). The Powell Point Member is named after the iconic peak that overlooks The Blues, which is also proximal to the portion of the lectostratotype section that best represents the member. It is characterized by a series of heavily incised and amalgamated multistory major tabular sandstones (FA3) with lesser overbank mudstones (FAs 8 and 9) (Eaton, 1991; Roberts, 2007). Fossil localities are notably scarce in the member, which may be attributed to collection bias because of the cliff-forming nature of outcrops (Eaton, 1991), or to reduced preservation within the higher-energy palaeoenvironments commonly represented in the member. The uppermost ~110 m of the Powell Point Member (650-750 m above the base of the formation) constitute a thick package of amalgamated multistory sandstones (FA3) and intraformational conglomerates (FA1) with massive (>3 m) soft sediment deformation bands (Roberts, 2007; Beveridge *et al.*, 2020 [Ch.5]). For clarity, the mud-dominated uppermost ~100 m of the ‘upper unit’ described by Roberts (2007) (~750 to 860 m above the base of the formation) was reassigned to the Upper Valley Member by Beveridge *et al.* (2020 [Ch.5]). As such, the revised thickness of the ‘upper unit’, now Powell Point Member, is ~200 m (~550 to 750 m above the base of the formation), while the Upper Valley Member is 255 m thick (750 to 1005 m above the base of the formation). A distinctive change in slope characterized by a sharp transition to a bentonitic mudstone interval above thick multistory amalgamated sandstones marks the contact between the Powell Point Member and the overlying Upper Valley Member (Beveridge *et al.*, 2020 [Ch.5]).

#### 4.4 Materials and Methods

##### 4.4.1 Field techniques

Selected stratigraphic sections across the outcrop extent of the Kaiparowits Formation originally published in Roberts (2007), Roberts *et al.* (2013), Beveridge *et al.* (2020 [Ch.5]) and Titus *et al.* (2021) were revisited in this study with a focus on resampling and lateral tracing of bentonite marker horizons to establish more precise correlations between outcrop areas. In some cases, this led to recalibration of existing sections and their correlations (*e.g.*, KDR sections), and measurement of additional stratigraphic sections (*i.e.*, KWC, KLF) using a Jacob Staff and Brunton Compass. Coordinates are reported in WGS84. The uppermost Wahweap Creek area south of Canaan Peak (KWC section) was the primary focus of new stratigraphic investigations and bentonite sampling presented here. New ash fall bentonite samples were collected for dating from three areas: Canaan Peak (upper Wahweap Creek; KWC), Death Ridge (KDR-1), and East Valley (KBW) (see Figs. 4.3, 4.5-4.7). Collection of samples was conducted with care to avoid contamination with detrital material using the trench, bench and collect approach described as follows. Upon identification of a prospective ash fall bentonite, a trench was excavated to identify the best layer from which to collect material. The basal ~5% thickness was avoided to reduce likelihood of including detritus that may not be representative of the eruption age, while the upper layers

**Table 4.1** U-Pb CA-ID-TIMS zircon ages presented herein. All bentonites are from The Blues Member.

Sample	Location	$^{206}\text{Pb}/^{238}\text{U}$ Age (Ma)	Error (2 $\sigma$ ) <sup>^</sup>			MSWD	n <sup>#</sup>	Calculated Strat. Level (m) <sup>*</sup>	Error (m) <sup>**</sup>	
			X	Y	Z				+	-
KWC-3	Canaan Peak	75.569	0.04	0.056	0.098	1.2	8	437	24	21
IM1442	East Valley	75.659	0.036	0.054	0.097	0.86	6	406	16	17
KWC-1	Canaan Peak	75.903	0.031	0.048	0.094	1.8	5	331	15	15
KDR-5B	Death Ridge	76.259	0.019	0.028	0.066	0.98	4	220	9	9
KWC-2	Canaan Peak	76.336	0.025	0.044	0.093	0.92	9	196	14	13

MSWD mean square of weighted deviates, n<sup>#</sup> number of analyses included in the weighted mean

<sup>^</sup> Error: X = analytical uncertainty in the absence of all external or systematic errors, Y = X plus U-Pb tracer calibration uncertainty, Z = Y plus U decay constant uncertainty

<sup>\*</sup> compared to the Bayesian age-stratigraphic model for the KBC/KBU type section

<sup>\*\*</sup> stratigraphic error based on correlation of maximum and minimum bentonite age (Y uncertainty)

were also treated with caution due to an upwards increasing likelihood of reworking. Once the ideal layer was identified, the overlying material was removed to form a bench from which to collect the bentonite material. Approximately four kilograms of bentonite was collected for each sample. Bentonite collection technique has significant implications for experimental reproducibility (see Ch. 2 and 6).

#### 4.4.2 Laboratory techniques

Ash fall bentonite samples were prepared at the Massachusetts Institute of Technology (MIT) alongside similar samples from Campanian strata across the Western Interior (see Beveridge *et al.*, 2022 [Ch.3], Ramezani *et al.*, in review, and Ch. 2). The crystalline component of the bentonites was isolated from the bulk clay material using the ultrasonic separation technique described by Hoke *et al.* (2014). Standard heavy mineral separation was conducted using magnetic and high-density liquid separation. Zircons were hand-picked from the heavy mineral separates using a binocular microscope. Criteria used to select a population of zircons inferred to be representative of the eruptive age include: 1) high aspect ratio; 2) natural crystalline habit; and 3) elongated glass (melt) inclusions aligned with the crystallographic “C” axis (see Ramezani *et al.*, 2011 and Ch. 2).

Chemical abrasion isotope dilution thermal ionization mass spectrometry (CA-ID-TIMS) was conducted at MIT using methods described in Ramezani *et al.* (2011) adapted from the chemical abrasion approach of Mattinson (2005) (see Ch. 2). Selected grains were thermally annealed at 900°C for 60 hours before partial dissolution in 28 M hydrofluoric acid (HF) at 210°C for 12 hours in a digestion vessel. After thorough rinsing and fluxing, ET2535 EARTHTIME tracer solution was added (Condon *et al.*, 2015; McLean *et al.*, 2015) and the grains were fully dissolved in 28 M HF over 48 hours at 210°C. Anion

exchange column chemistry was used to isolate the U and Pb components, which were then analysed in an Isotopx X62 thermal ionization mass spectrometer with a Daly ion counting system and 12 Faraday detectors. Data were handled in Tripoli and ET\_Redux for reduction and error propagation (Bowring *et al.*, 2011; McLean *et al.*, 2011, 2015; Condon *et al.*, 2015). Weighted mean ages for each bentonite were calculated excluding older grain ages that were interpreted as inherited or detrital and no young grain ages were excluded. Uncertainty is reported in  $\pm X/Y/Z$  format following Schoene *et al.* (2006) where X represents the internal 95% uncertainty in the absence of any external factors, Y includes X and the tracer solution calibration errors, and Z incorporates Y and the uranium decay uncertainties of Jaffey *et al.* (1971). Full data are given in Appendix C.4.1 and summarized in Table 4.1 and Figure 4.5.

#### 4.4.3 Bayesian age-stratigraphic model

An expanded Bayesian age-stratigraphic model was constructed for the Kaiparowits Formation based on the data and approach of Ramezani *et al.* (in review), extended to include the Upper Valley Member using the detrital zircon LA-ICP-MS maximum depositional ages of Beveridge *et al.* (2020 [Ch.5]) and one additional bentonite single grain age reported here (Table 4.2). The KBO-37 bentonite was originally dated using  $^{40}\text{Ar}/^{39}\text{Ar}$  geochronology (Roberts *et al.*, 2005), although Beveridge *et al.* (2020 [Ch.5]) noted potential reworking of the horizon causing ambiguity over its true age. From this same bentonite outcrop, a suite of zircons was analysed using the CA-ID-TIMS U-Pb approach described herein, which yielded a population with a weighted mean age of  $74.968 \pm 0.038/0.056/0.098$  Ma (MSWD 1.1) from seven grains, with one young outlier grain age of  $73.90 \pm 0.17$  Ma. Based on the detrital zircon maximum depositional ages of Beveridge *et al.* (2020 [Ch.5]), this youngest grain is interpreted as the best-fit depositional age for the KBO-37 bentonite and was used to further constrain the Upper Valley Member. A second age-stratigraphic model was constructed for the KWC section using refined stratigraphic measurements and the three newly dated bentonites from that area (Fig. 4.8).

The Kaiparowits Formation age models in this study were constructed using a Compound Poisson-Gamma Bayesian statistical approach with a modified Markov chain Monte Carlo fitting algorithm in R Studio using the Bchronology package (Haslett and Parnell, 2008; Parnell *et al.*, 2008; 2011). The model was generated for a stratigraphic section based on combination of the KBC lectostratotype of Roberts (2007) and the Upper Valley Member composite stratotype of Beveridge *et al.* (2020 [Ch.5]), which is here informally referred to as the KBC/KBU type section. Model ages were generated at one-meter increments throughout the formation. From 100,000 iterations at each meter level, the median value represents the model age and an asymmetric 95% confidence window represents the spread of predicted values (recorded as asymmetric +/-). Complete data and scripts are included in Appendix C.4. Due to the combined application of  $^{206}\text{Pb}/^{238}\text{U}$  ages generated using both CA-ID-TIMS and LA-ICP-MS approaches in construction of the models, the Y uncertainty of each data type was employed (*e.g.*, see Beveridge *et al.*, 2022 [Ch.3]). The primary advantage of the Bayesian age-stratigraphic approach

**Table 4.2** *Compilation of data used in construction of the Kaiparowits type section age-stratigraphic model herein.*

Sample Name	Stratigraphic level (m)*	<sup>206</sup> Pb/ <sup>238</sup> U Age (Ma)	Uncertainty (Y)	Data Type**	Data Source
KBU-W	1010	73.1	1.2	DZ MDA	Beveridge <i>et al.</i> (2020)
KBU-O	930	73.2	1.4	DZ MDA	Beveridge <i>et al.</i> (2020)
KBU-F	800	73.68	0.81	DZ MDA	Beveridge <i>et al.</i> (2020)
KBO-37	790	73.9	0.17	Single Grain Age	This study
KBU-V	765	73.68	0.66	DZ MDA	Beveridge <i>et al.</i> (2020)
KBU-S	730	75.2	1.4	DZ MDA	Beveridge <i>et al.</i> (2020)
KBC-195	612	75.231	0.038	Bentonite TDA	Ramezani <i>et al.</i> (in review)
KBC-144	498	75.427	0.023	Bentonite TDA	Ramezani <i>et al.</i> (in review)
KBC-109	420	75.609	0.025	Bentonite TDA	Ramezani <i>et al.</i> (in review)
KP-07A	180	76.394	0.045	Bentonite TDA	Ramezani <i>et al.</i> (in review)
Top Wahweap Fm	0	77.29	0.72	Model age	Beveridge <i>et al.</i> (2022)

*Abbreviations: DZ = detrital zircon; MDA = maximum depositional age; TDA = true depositional age*

*\* above the base of the Kaiparowits Formation*

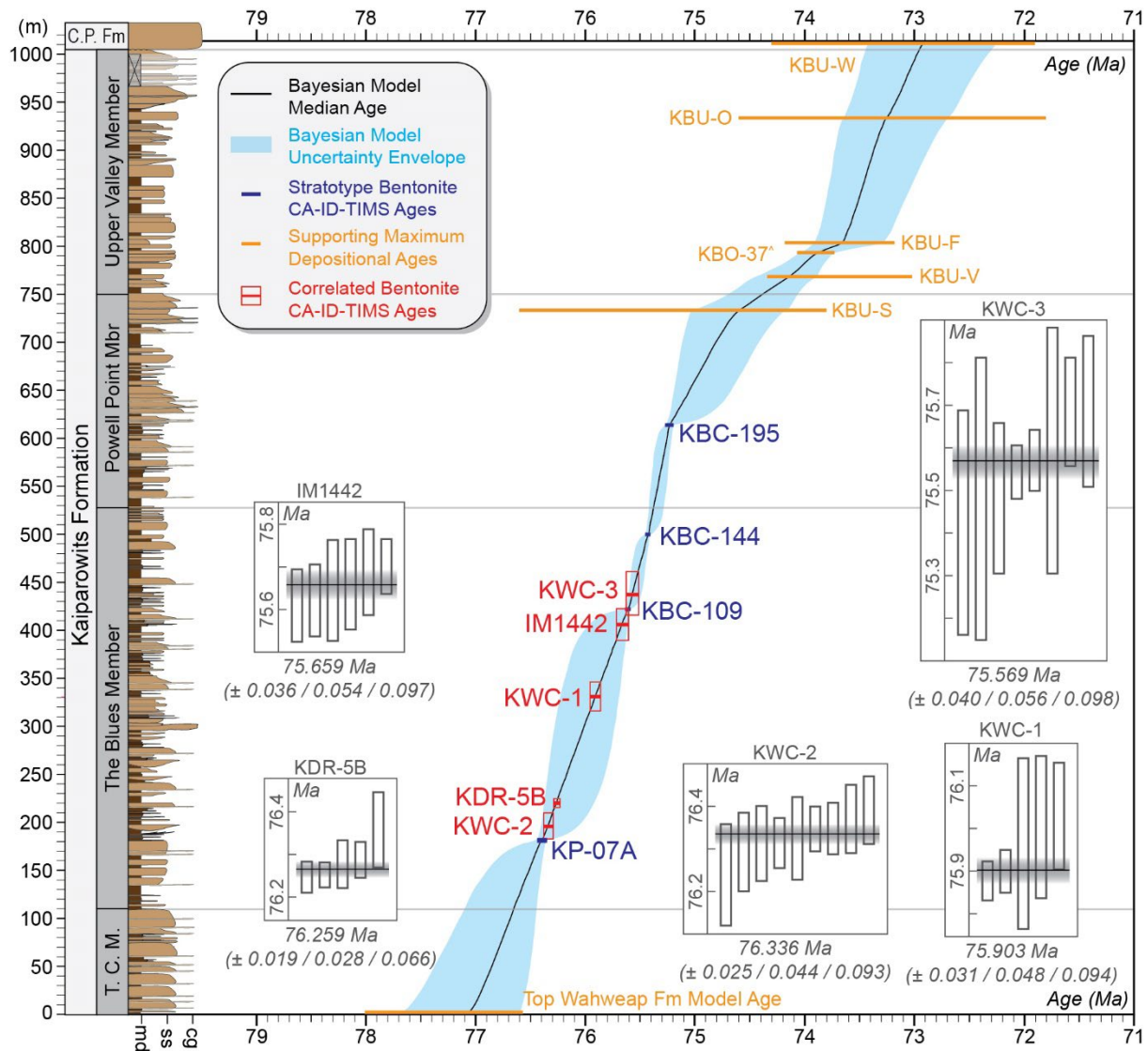
*\*\* DZ MDAs measured using LA-ICP-MS; Bentonite TDAs and the single grain age measured using CA-ID-TIMS; Model age generated using Bayesian modeling of CA-ID-TIMS and LA-ICP-MS dates from the underlying Wahweap Formation (see Beveridge *et al.*, 2022)*

compared to simple linear extrapolation is the use of random variability to model sediment accumulation rates, which leads to more appropriate error propagation (Haslett and Parnell, 2008; Parnell *et al.*, 2008, 2011; De Vleeschouwer and Parnell, 2014; Trayler *et al.*, 2020).

#### 4.4.4 Reference section calibration

Kaiparowits Formation reference sections were calibrated against the well-dated KBC/KBU type section by matching high-precision bentonite ages from the reference sections with the type section age-stratigraphic model (Table 4.1, Fig. 4.5). The weighted mean age of each bentonite dated in this study was matched with a meter-level type-section model age, which yielded a correlated stratigraphic level relative to the base of the formation in the type section. An approximation of stratigraphic uncertainty was included as the range of model ages covered by the bentonite age Y uncertainty (same uncertainty used in model generation). The calculated bentonite levels relative to the base of the formation were used as robust tie-points to calibrate the level of reference sections relative to KBC/KBU type section and minor adjustments were made to support lithologic correlation generally within the stratigraphic uncertainty associated with the bentonite ages (Fig. 4.6). Note that the Bayesian age model uncertainty (95% confidence window) was not considered in the stratigraphic uncertainty approximated here, although this is not anticipated to incur substantial undefined uncertainty due to tight age constraint in the portion of the formation where most measured stratigraphic sections occur (The Blues Member).





**Fig. 4.5** Bayesian age-stratigraphic model for the full Kaiparowits Formation generated from published data (Beveridge *et al.*, 2020, 2022; Ramezani *et al.*, in review) and the KBO-37 single grain age. Five bentonites dated in this study (not used in construction of the model) are shown in red, illustrating their correlated stratigraphic position and stratigraphic uncertainty (red boxes). Inset are plots of zircon grain ages with  $2\sigma$  uncertainties (vertical bars) and their calculated weighted mean (horizontal bar) with a 95% error envelope (shaded band) for each sample dated herein.

## 4.5 Results

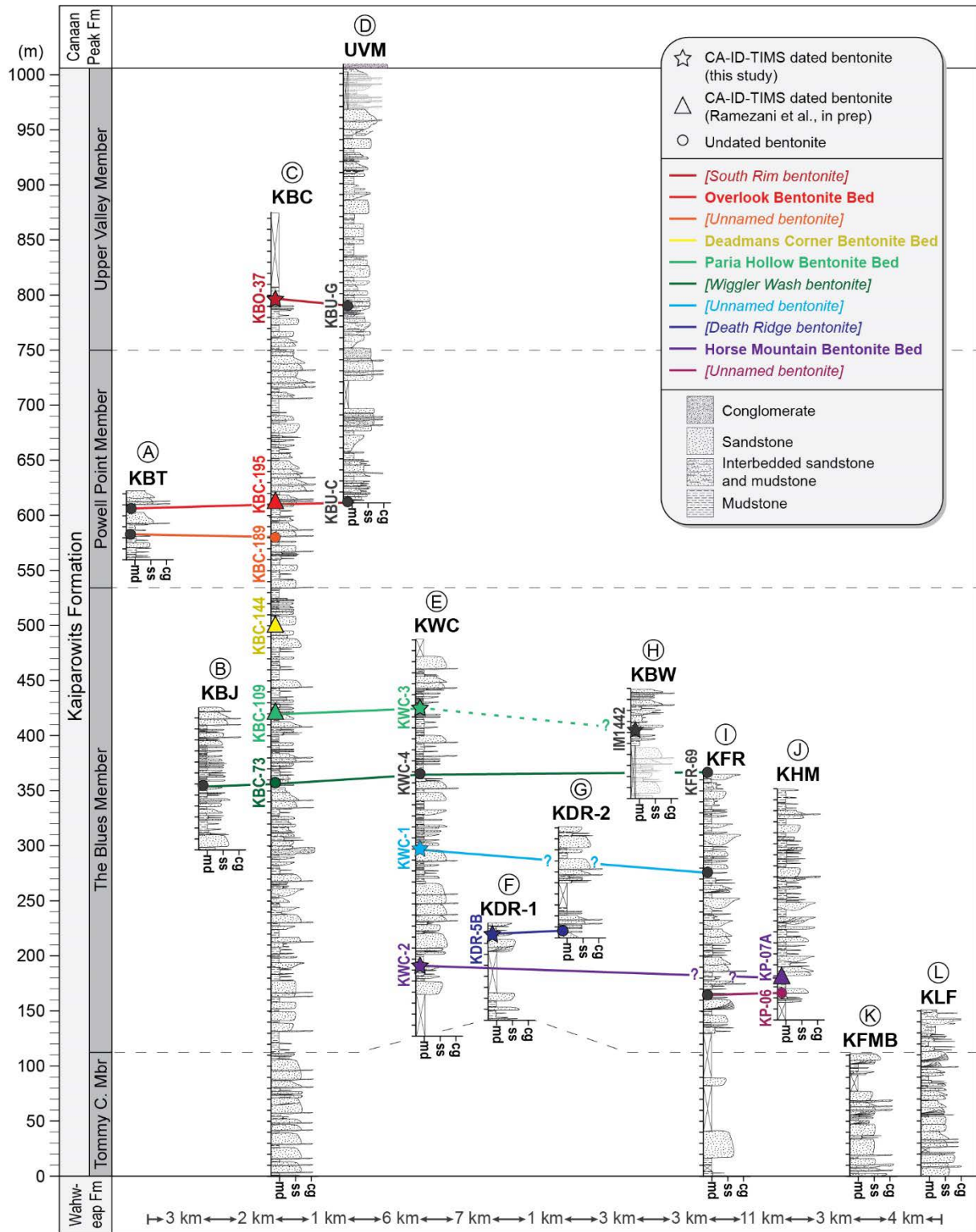
### 4.5.1 New high-precision geochronology

Five new high-precision  $^{206}\text{Pb}/^{238}\text{U}$  bentonite ages from multiple reference sections are presented here (Table 4.1). CA-ID-TIMS geochronology conducted in this study was executed in tandem with that of Ramezani *et al.* (in review) and Beveridge *et al.* (2022 [Ch.3]), which facilitates reliable comparison of data between these studies. Three bentonites were collected from the Canaan Peak area at approximately 62 m (KWC-2), 170 m (KWC-1), and 300 m (KWC-3) above the base of the KWC section. The lowest

bentonite, KWC-2, produced an age of  $76.336 \pm 0.025/0.044/0.093$  Ma (MSWD 0.92) from nine zircons, which is statistically indistinguishable from the age of the KP-07A bentonite of Ramezani et al. (in review) as their internal uncertainties (X) overlap. The middle bentonite from the Canaan Peak area, KWC-1, produced an age of  $75.903 \pm 0.031/0.048/0.094$  Ma (MSWD 1.8) from five zircons. The uppermost bentonite from the Canaan Peak area, KWC-3, produced an age of  $75.569 \pm 0.04/0.056/0.098$  Ma (MSWD 1.2) from eight zircon and is statistically indistinguishable from the age of the KBC-109 bentonite of Ramezani et al. (in review). One bentonite (IM1442) was collected from the East Valley area at approximately 60 m above the base of the KBW section. This sample produced an age of  $75.659 \pm 0.036/0.054/0.097$  Ma (MSWD 0.86) from six zircons. Based on the internal uncertainty (X), the age of IM1442 marginally overlaps with that of KBC-109 (Ramezani et al., in review), but is older than KWC-3. The final bentonite (KDR-5B) was collected from the Death Ridge area 80 m above the base of the KDR-1 section. This sample produced an age of  $76.263 \pm 0.019/0.028/0.086$  Ma (MSWD 1.9) from five zircons, which is similar to but younger than KWC-2 and KP-07A (Ramezani et al., in review) based on the internal uncertainty (X). As mentioned in Section 4.3, a single grain age of  $73.90 \pm 0.17$  Ma is reported for sample KBO-37 from the KBC section within the Upper Valley Member.

#### 4.5.2 Revised intraformational correlation

Correlated levels for bentonites dated in this study relative to the KBC/KBU type section were determined by matching their high-precision ages with an age-equivalent meter interval from the Bayesian age-stratigraphic model presented herein (Fig. 4.5, Table 4.1). Undated bentonites were also correlated or recalibrated in this study for many sections (where possible) by walking out these units between sections, or more commonly by tracing these horizons via Google Earth Pro. The five dated bentonites in this study were collected from three key reference sections. The closest of these to the KBC/KBU type section is the KWC section at Canaan Peak (uppermost Wahweap Creek). The three dated bentonites from this section correlate to the following levels above the base of the Kaiparowits Formation: KWC-2 =  $196 \pm 14/-13$  m, KWC-1 =  $331 \pm 15/-15$  m, and KWC-3 =  $437 \pm 24/-21$  m. The next reference section (KBW) is in East Valley, ~15 km southeast of The Blues area, contains the IM1442 bentonite, which correlates to  $406 \pm 16/-17$  m above the base of the formation. Finally, the KDR-1 reference section at Death Ridge, ~15 km east-southeast of The Blues area, is constrained by the age of the KDR-5B bentonite, which corresponds to  $220 \pm 9/-9$  m above the base of the formation relative to the KBC/KBU type section. Based on these calibrated bentonite levels, the relative stratigraphic positions of local measured sections reported by Roberts *et al.* (2013), Beveridge *et al.* (2020 [Ch.5]), and Titus *et al.* (2021) were refined, and one section (KWC) was remeasured (and extended) in this study and stratigraphically adjusted based on the suite of newly dated bentonites. The following is a summary of the stratigraphic recalibration of sections, from northwest to southeast across the Table Cliff



**Fig. 4.6** Revised correlation of Kaiparowits Formation stratigraphic sections. Adjustments were based on age-supported tephrostratigraphy of ten unique bentonite horizons. Sections are from Roberts (2007, 2013), Beveridge et al. (2020), Titus et al., (2021), and this study (i.e., significant adaption to KWC).

and Kaiparowits plateaus (Fig. 4.6). All stratigraphic levels below represent meters above the base of the Kaiparowits Formation unless otherwise stated.

Four measured sections are known from The Blues area in the northwestern portion of the field area. The KBT section (base GPS: 37°39'37.1", -111°53'44.8") covers an interval of ~63 m of the Powell Point Member and contains two undated bentonites that were correlated to similarly spaced bentonite outcrops in the KBC section (KBC-189 and KBC-195) using Google Earth imagery. The section begins at *ca* 555 m and little to no change was made herein. The KBJ section (base GPS: 37°38'37.2", -111°52'20.9") consists of ~130 m of strata from the middle portion of The Blues Member and includes one undated bentonite that is qualitatively correlated (via Google Earth Pro and outcrop characteristics) to the KBC-73 bentonite in the KBC section. The base of the section was previously inferred to occur at *ca* 280 m. A minor upwards shift to *ca* 295 m is here proposed. Stratigraphic correlation between the KBC (base GPS: 37°37'30.9", -111°53'14.9") and KBU (base GPS: 37°37'47.4", -111°50'14.9") sections remain unchanged from Beveridge *et al.* (2020 [Ch.5]), where the sections are reliably tied by the KBC-195/KBU-C bentonite pair and KBO-37/KBU-G bentonite pair based on outcrop characteristics (see Ch.6) and tracing these beds in the field and using Google Earth imagery.

The KWC section was the subject of significant expansion and refinement in this study. The original section from Roberts *et al.* (2013) covered ~98 m of strata beginning at *ca* 410 m. The section was here remeasured (base GPS: 37°34'23.9", -111°48'38.5"), beginning lower and finishing higher, for a total thickness of 360 m through much of The Blues Member in the headwater tributaries of Wahweap Creek at Canaan Peak. Three dated bentonites (KWC-2, KWC-1, KWC-3) now facilitate excellent temporal and stratigraphic calibration of this section (see also Fig. 4.8). The newly calibrated level of 127 m for the base of the section is significantly lower than previously thought, even when considering the additional 262 m of measured strata.

The KDR-1 section (GPS: *ca* 37°33'40", -111°44'10") also required close re-examination. The section covers an interval of ~88 m of what was previously thought to be the lower unit (now Tommy Canyon Member). The new high-precision KDR-5B bentonite age was found to correlate to a level of 220 +9/-9 m in the KBC/KBU type section; however, this finding conflicts significantly with the original interpretation by Roberts (2007), who believed that the tree-covered sandstone bench and covered interval at the base of the section corresponded to the Wahweap Formation contact. Reevaluation herein suggests that the major sandstone bench at the base of the section is most likely the top of the Tommy Canyon Member, meaning that the base of the KDR-1 section occurs at *ca* 120 - 140 m. The KDR-2 section consists of ~101 m of strata and is correlated to the top of the KDR-1 section by the KDR-5B bentonite; thus, it has been adjusted in kind to a revised level of *ca* 216 m.

Finally, four sections are known from the southern portion of the field area. The KFR section (base GPS: 37°31'14.8", -111°43'40.9") begins at the base of the formation covering an interval of ~365 m throughout mostly covered section in the Tommy Canyon Member and into a well-exposed section of The Blues Member. It contains three undated bentonites (including KFR-69) and was not

stratigraphically recalibrated in this study. The KHM section (base GPS: 37°25'30.7", -111°42'26.3") consists of ~210 m of strata through The Blues Member. The base of the section was originally placed at ~152 m and a minor downward shift to *ca* 142 m is here suggested based on the new dating. The KFMB section (base GPS: 37°24'16.2", -111°43'38.5") begins at the base of the formation and constitutes a complete 110-meter-thick record of the Tommy Canyon Member. The KLF section (Titus *et al.*, 2021) also begins at the base of the formation and comprises ~150 m of strata through the Tommy Canyon Member and the lowermost portion of The Blues Member.

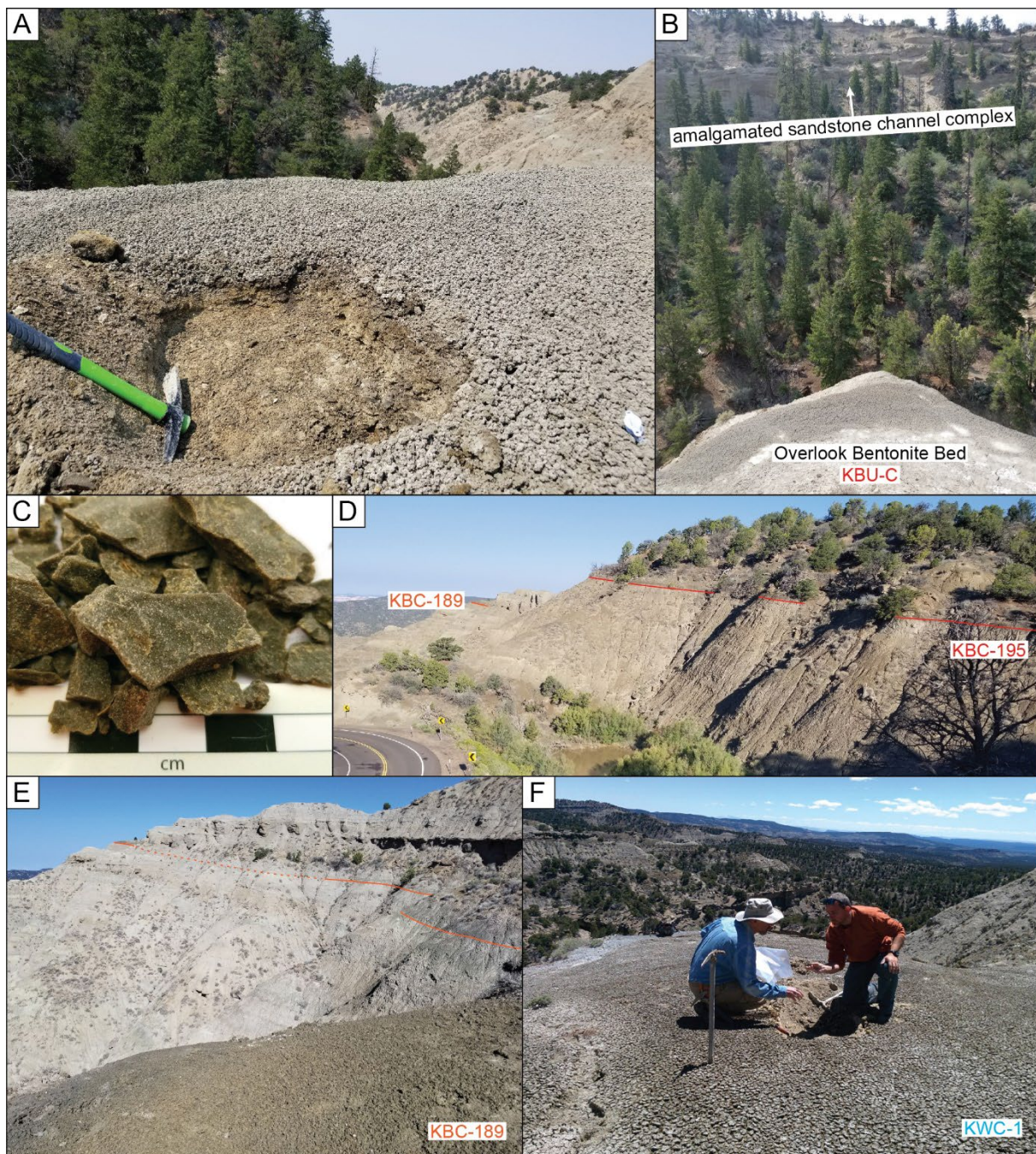
#### 4.6 Bentonite bed nomenclature

Bentonite marker beds have been and will continue to be fundamental to stratigraphic correlation (*i.e.*, tephrostratigraphy) in the Kaiparowits Formation (*e.g.*, Figs. 4.6 and 4.7). These units are exceptionally abundant in the formation, particularly in The Blues Member, and ten unique beds were confidently identified in this study. Of these, four are sufficiently documented at present to be formally described, while the remaining six are partly described here, but require future investigation to confirm inferred correlations. Criteria for formal recognition in this work includes a CA-ID-TIMS age and clear stratigraphic distinction. To provide a firm basis for future investigation, formal bentonite beds were characterized from a specific outcrop locality then these attributes were used to assign additional outcrops and correlate the unit across the formation. It is important to highlight that assignment of a bentonite outcrop to a named bed should be supported by lithologic or age observations, not purely stratigraphic level. The exception to this guideline is where other well-dated and well-characterized bentonite outcrops occur in the same section, facilitating reliable correlation of the unknown outcrop.

##### 4.6.1 Horse Mountain Bentonite Bed

The Horse Mountain Bentonite Bed is defined by sample KP-07A (also KP-7, KP-07, or KP-07B in other works), the lowest dated bentonite sample from the Kaiparowits Formation. It occurs 180 m above the base of the formation in the KHM section at Horse Mountain (GPS: 37°26'11.9", -111°41'51.8") and was dated to be  $76.394 \pm 0.040/0.045/0.093$  Ma (Ramezani *et al.*, in review). It appears in outcrop as a gray to greenish gray prominent low-lying platform that, like other named bentonite beds in this study, exhibits typical bentonite swelling textures (popcorn weathering). The horizon is easily traceable for up to a kilometer in either direction, or further with more rigorous scouting. The crystalline component contains plentiful vitreous to adamantine zircon, generally ranging in length from 120 to 500  $\mu\text{m}$  with an average length to width ratio of 5:1, and frequently display unbroken double terminations with well-defined habit. An atypical abundance of clean, subhedral to euhedral titanite was also noted in the heavy mineral separates compared to other bentonites from the Kaiparowits Formation. The unit is named after Horse Mountain within the Horse Mountain quadrangle where it is defined. Sample KWC-2 (KWC section) is confidently assigned to the Horse Mountain Bentonite Bed based on overlapping CA-ID-





**Fig. 4.7** Bentonite photographs from the Kaiparowits Formation. A) Excavated pit at the collection site of KBU-C (Overlook Bentonite Bed) showing popcorn swelling textures with pistachio green smectite claystone beneath. B) Same location as panel A illustrating outcrop appearance and stratigraphic distance below the amalgamated sandstones of the upper Powell Point Member. C) Close-up photo of waxy, pistachio green bentonite fragments (KBC-D, Overlook Bentonite Bed). D) Thin, traceable horizon of the Overlook Bentonite Bed. E) Discontinuous but laterally reoccurring bentonite horizon with a bench showing popcorn swelling textures. F) A broad, well-formed bentonite bench in the KWC section showing excavation in search of a suitable sampling level.

TIMS ages and similarities in their outcrop appearance and phenocrysts. The Horse Mountain Bentonite Bed has not yet been documented in the Kaiparowits Formation lectostratotype section (KBC), which

is not surprising as this stratigraphic level in The Blues area forms a broad vegetated bench along Henrieville Creek where exposures are poor. The source of the protolithic volcanic ash for this bentonite and others from the formation is interpreted to have been several hundred kilometers to the south or southeast (see Ch. 6), although a specific volcanic center cannot currently be implicated. The age of the Horse Mountain Bentonite Bed is statistically indistinguishable from that of several northern Laramidian bentonites based on internal uncertainties ( $\sim 0.05\%$ ) including ST1-03 ( $76.329 \pm 0.035/0.043/0.092$  Ma) from the Judith River Formation and JC082817-1 ( $76.354 \pm 0.057/0.061/0.1$  Ma) from the Dinosaur Park Formation (Ramezani et al., in review). These contemporaneous occurrences may constitute evidence of a single far-reaching eruption event or possibly synchronous volcanism across Laramidia, although these hypotheses require more detailed examination (see Ch. 6).

#### 4.6.2 Paria Hollow Bentonite Bed

The Paria Hollow Bentonite Bed is represented by sample KBC-109, which was collected 420 m above the base of the formation in The Blues area (GPS:  $37^{\circ}37'46.8''$ ,  $-111^{\circ}51'18.7''$ ) and was dated to be  $75.609 \pm 0.015/0.025/0.085$  Ma (Ramezani et al., in review). The bentonite is a relatively thin but laterally extensive bentonite marker bed that can be identified at several localities across The Blues area and further. The crystalline component contains vitreous zircon ranging in length from 63 to 258  $\mu\text{m}$ , averaging *ca* 155  $\mu\text{m}$  with a length to width ratio of 4:1. Zircons contain a mix of glass melt inclusions and apatite mineral inclusions. The unit is named after Paria Hollow, which is immediately northwest of the type locality in the Upper Valley quadrangle. Bentonite sample KWC-3 (KWC section) is assigned to the Paria Hollow Bentonite Bed based on high-precision ages with overlapping analytical uncertainties and similar measured stratigraphic levels (Figs. 4.5, 4.6, and 4.8). The age of bentonite sample IM1442 (KBW section) marginally overlaps with the Paria Hollow Bentonite Bed type-outcrop KBC-109 but not with the confidently assigned KWC-3 sample. IM1442 is the only bentonite identified from the KBW section and constitutes a locally extensive marker horizon in the East Valley, West Valley and Fossil Ridge areas. As such, sample IM1442 is tentatively correlated to the Paria Hollow Bentonite Bed, but further investigation is required to confirm this. The age of the Paria Hollow Bentonite Bed overlaps within  $\sim 0.02\%$  internal uncertainty with the Plateau tuff in southern Alberta (CD082717-1;  $75.639 \pm 0.025/0.032/0.087$  Ma; Ramezani et al., in review), again suggesting either the presence of widespread ash fall units, or coeval volcanic centers in different parts of Laramidia.

#### 4.6.3 Deadmans Corner Bentonite Bed

The Deadmans Corner Bentonite Bed is characterized by sample KBC-144 from 498 m above the base of the formation in The Blues area (GPS;  $37^{\circ}37'59.9''$ ,  $-111^{\circ}50'51.3''$ ) and was dated to be  $75.427 \pm 0.012/0.023/0.084$  Ma (Ramezani et al., in review). The internal precision of this age (0.016%) is the finest from the collective CA-ID-TIMS geochronology project (*e.g.*, Beveridge *et al.*, 2022 [Ch.3]; Ramezani et al., in review) probably due to the larger average size and well-preserved condition of



zircon from this sample. Zircon phenocrysts range from 236 to 520  $\mu\text{m}$  in length, averaging 366  $\mu\text{m}$ , with a length to width ratio of 5:1. An atypical abundance of apatite mineral inclusions was also noted within the zircons. The unit is named after a locally renowned section of Highway 12 in the Upper Valley quadrangle immediately adjacent to the type locality. The stratigraphic position of the Deadmans Corner Bentonite Bed near the top of The Blues Member constitutes a bottleneck of the stratigraphic record, where ~85 m of strata, including the level of KBC-144, are only represented in the KBC lectostratotype. As such, there are currently no correlative bentonite outcrops of the Deadmans Corner Bentonite Bed known across the Kaiparowits and Table Cliff plateaus. Furthermore, unlike the Horse Mountain and Paria Hollow bentonite beds, no temporally correlative bentonites have been identified from across the Western Interior.

#### 4.6.4 Overlook Bentonite Bed

The Overlook Bentonite Bed is represented by sample KBC-195, which is the stratigraphically highest reliably CA-ID-TIMS dated bentonite from the Kaiparowits Formation with an age of  $75.231 \pm 0.021/0.038/0.089$  Ma (Ramezani et al., in review). It occurs 612 m above the base of the formation (lower Powell Point Member; GPS:  $37^{\circ}38'12.7''$ ,  $-111^{\circ}50'41.7''$ ) near The Blues tourist overlook (Powell Point Vista) after which the bed is named. The bentonite crops out below a vegetated sandstone bench, is generally thin (~20 cm), and is laterally traceable for tens of meters before passing into steep cliffs. The crystalline component contains characteristic acicular zircon with vitreous to adamantine luster, well preserved crystal faces, an aspect ratio of 6:1, and an average length of 183  $\mu\text{m}$  (ranging from 62 to 326  $\mu\text{m}$ ). Glass and mineral inclusions are significantly less common than in other bentonite zircons from the formation. Sample KBU-C from Beveridge *et al.* (2020 [Ch.5]) was collected one kilometer southeast of the type outcrop and is correlated based on similar zircon morphology and tracing of lateral continuity using a combination of fieldwork and satellite imagery (Google Earth Pro). A second unnamed outcrop in the KBT section is also correlated to the Overlook Bentonite Bed. This correlation is based on stratigraphic level and the presence of a second underlying bentonite, which together match the KBC-195 and underlying KBC-189 bentonites in the KBC section (Fig. 4.6). The age of the Overlook Bentonite Bed also matches other dated bentonites from across the Western Interior (~0.03 internal uncertainty) including PPF1-03 from the Judith River area ( $75.219 \pm 0.031/0.046/0.093$  Ma) and 90TMT-590-U60 ( $75.259 \pm 0.027/0.034/0.087$  Ma) and a currently unpublished bentonite from the Two Medicine River area (Ramezani et al., in review).

#### 4.6.5 Informal bentonite horizons

At least six other unique bentonite horizons were identified in the Kaiparowits Formation (Fig. 4.6). Description of these as informal bentonites is valuable because they constitute important local marker horizons for correlation, and aid in accurate stratigraphic placement of fossil localities. Each horizon is described in ascending stratigraphic order and includes an indication of confidence in the recorded

interpretations. Note that although ten horizons are distinguished herein, it is highly likely that there are more unique bentonites within the Kaiparowits Formation.

The lowest unique bentonite horizon is represented by an outcrop labeled KP-06 from the KHM section at Horse Mountain. This horizon occurs at *ca* 165 m, approximately 15 m below the Horse Mountain Bentonite Bed. A bentonite outcrop in the nearby KFR section occurs at a similar level and may correlate to either the Horse Mountain Bentonite Bed or the KP-06 horizon. Above the Horse Mountain Bentonite Bed, the KDR-5B bentonite is interpreted as unique based on the younger CA-ID-TIMS age of  $76.259 \pm 0.019/0.028/0.066$  Ma (this study); although the stratigraphic level of the section in which the KDR-5B bentonite occurs (KDR-1) remains somewhat ambiguous. Due to its probable distinction from other named beds, it is informally referred to as the Death Ridge bentonite, and is correlated to an outcrop in the nearby KDR-2 section and may also correlate to one of several unmarked bentonites that occur in the KHM section above the Horse Mountain Bentonite Bed type location.

The KWC-1 bentonite (KWC section) yielded a CA-ID-TIMS age of  $75.903 \pm 0.031/0.048/0.094$  Ma, which is unique within the formation. This bed is expressed as a well-defined bench atop a steep slope and is laterally traceable for ~65 m in either direction. It occurs at 170 m above the base of the KWC section, which correlates to 331 +15/-15 m above the base of the formation. Based on its stratigraphic position, this bed presents represents an important marker horizon in the middle of The Blues Member, although correlated outcrops have thus far only been observed in the KFR section. Seventy meters stratigraphically above this bed, an undated outcrop (KWC-4) presents as a prominent bench-forming unit traceable across large distances with characteristically small, rare zircons phenocrysts. This bed correlates to KBC-73 (KBC section), based on outcrop characteristics and similar stratigraphic levels, and together they are informally referred to as the Wiggler Wash bentonite, which may also be represented in the KBJ and KFR sections.

A distinct bentonite horizon (KBC-189) forms a prominent bench *ca* 30 m below the Overlook Bentonite Bed that can be traced discontinuously across The Blues area. An unlabeled outcrop in the KBT section is correlated to this bentonite bed. The stratigraphically highest distinguishable bentonite horizon described here is represented by sample KBO-37 from South Rim. It occurs 790 m above the base of the formation (KBC section) as a broad, gently sloping bench at the top of sandstone cliffs, and features abundant secondary gypsum and splintered carbonate nodule material that is characteristic of the Upper Valley Member (Beveridge *et al.*, 2020 [Ch.5]). Geochronologic data for the KBO-37 sample (or equivalent) was difficult to interpret and reworking is possible (Beveridge *et al.*, 2020 [Ch.5]). Nevertheless, the bed is informally referred to as the South Rim bentonite. Similar outcrops are found across the South Rim although the horizon is often obscured by forest, overburden, slumps, and pre-Canaan Peak Formation erosion. Some outcrops in the Upper Valley Member type area (northern Canaan Peak) also correlate to the South Rim bentonite (*e.g.*, KBU-G, KBU-H).

## 4.7 Geologic Discussion

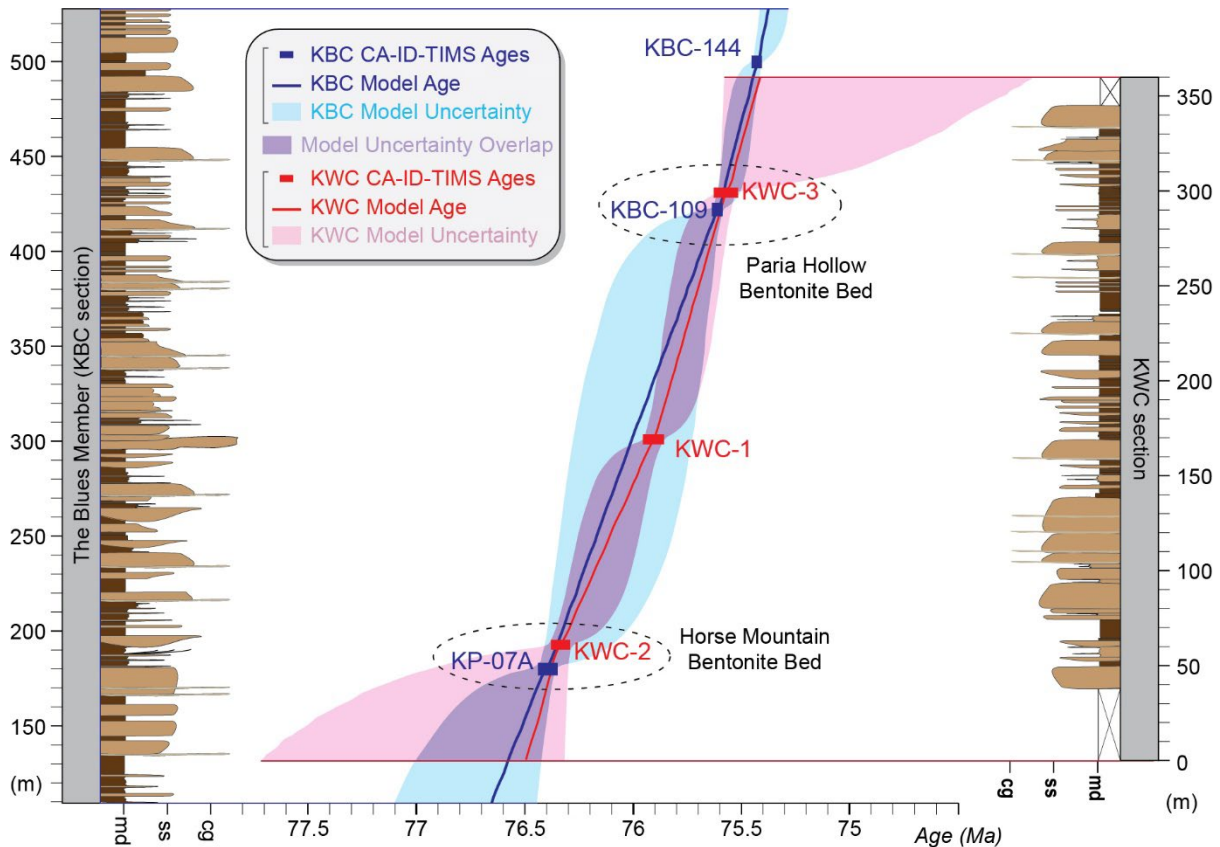
Five new high-precision CA-ID-TIMS bentonite ages from key Kaiparowits reference sections were used to develop robust stratigraphic correlation throughout the Kaiparowits Formation. The combined high-precision ages from this study and those of Ramezani *et al.* (in review) make the Kaiparowits Formation potentially one of the most precisely dated alluvial sedimentary successions in the world at the time of publication. From these nine high-precision bentonite ages, four were used to generate a Bayesian age-stratigraphic model for the KBC/KBU type section (Fig. 4.5) after the approach of Ramezani *et al.* (in review) and extended to include the Upper Valley Member and data of Beveridge *et al.* (2020 [Ch.5]). The five new high-precision ages presented here were also used to calibrate the stratigraphic level of these bentonites relative to the base of the formation and, thus, refine the correlated level of several key reference sections. Findings from this work yield new insights into various geologic characteristics of the formation.

### 4.7.1 Refinement of stratigraphic correlations

Reliable stratigraphic correlation is important for robust temporal constraint of fossil localities; however, several factors hinder correlation in the Kaiparowits Formation across the Table Cliff and Kaiparowits plateaus. Lithological correlation is considerably impacted by 1) lateral discontinuity of lithofacies, 2) geographic isolation of the lectostratotype and reference sections, and 3) large, covered intervals (*e.g.*, the densely forested Canaan Peak) and structural complications relating to the Dutton and East Kaibab monoclines that bound exposures of the formation to the east and west, respectively. Thick, relatively monotonous lithologic packages with few traceable horizons are common elements of rapidly subsiding floodplain environments where alluvial architecture is dominated by isolated single-story sandstone channels within extensive overbank mudstones. As such, even closely spaced reference sections may be difficult or impossible to correlate precisely (outside of member boundaries) based on facies and lithostratigraphy alone. This observation highlights the need for detailed examination of marker horizons, such as bentonites.

Bentonite marker horizons are an exceptionally useful tool for stratigraphic correlation because any given unit represents a regionally extensive isochron. They may be as laterally discontinuous as other lithotypes because preservation of bentonite horizons in the Kaiparowits Formation is generally dependent on depositional environment (*i.e.*, shallow, still-water environments such as ponds and small lakes; Roberts *et al.*, 2005, Roberts, 2007); however, isolated bentonite pockets may be correlated to one another using less direct inferences. Previously, stratigraphic level was the most widely used attribute for correlation of bentonite outcrops in situations comparable to those examined in this study. This level-matching approach can be highly effective, particularly if bentonites are present but relatively uncommon; however, the Kaiparowits Formation boasts exceptional abundance of bentonite beds and bentonitic mudstones, which limits the reliability of this approach. In this study, a numeric adaption of





**Fig. 4.8** Comparison of stratigraphy and age models for The Blues Member from the KBC principal reference section and equivalent KWC reference section. Meters are from the base of each section, dates are shown with  $Y$  uncertainty, and the same vertical scale is used for both sections.

tephrostratigraphy was employed to calibrate reference section levels by comparing high-precision bentonite ages against the type section age-stratigraphic model. This approach facilitated quantitative calibration of bentonite stratigraphic levels including an approximation of stratigraphic uncertainty (Fig. 4.5, Table 4.1), which led to recalibration of reference sections across the plateau.

Stratigraphic refinement of several key sections is outlined herein and illustrated in Figure 4.6. One of the important adjustments was to the KDR-1 and KDR-2 sections, which includes the KDR-5B bentonite previously used for age constraint of the formation. Findings indicate the section most likely begins at the base of The Blues Member rather than the base of the formation and further work is recommended to verify this inference. The second significant adjustment was to the KWC section whereby its expansion and refinement aids in and was aided by stratigraphic correlation of three dated bentonites. These outcrops (KWC-2, 1 and 3, lowest to highest) help tie the KBC type section with southern outcrop areas, particularly because two of the three ages are statistically indistinguishable from others across the formation (Figs. 4.5, 4.6 and 4.8). The matching sets include outcrops of the Paria Hollow and Horse Mountain bentonite beds, which supported stratigraphic calibration of the level of the KP-07A bentonite relative to the base of the formation (see Fig. 4.8). These outcomes demonstrate the

**Table 4.3** Model ages for member boundaries calculated using the type section Bayesian age-stratigraphic model (Fig. 4.5) assuming no temporally significant depositional hiatus are present.

Stratigraphic Level of Interest	Stratigraphic Level (m) *	Model Age (Ma)	2 $\sigma$ Uncertainty	
			+	-
Top of Kaiparowits Formation	1005	72.94	0.49	0.66
Top of Powell Point Member	750	74.35	0.31	0.30
Top of The Blues Member	550	75.34	0.06	0.08
Top of Tommy Canyon Member	110	76.64	0.45	0.20
Base of Kaiparowits Formation	0	77.06	0.62	0.47

\* relative to the base of the Kaiparowits Formation

success of stratigraphic calibration using high-precision bentonite ages in the Kaiparowits Formation. On the other hand, the effectiveness of this approach is limited by the cost and complexity of analyses, restricting its use to a handful of samples. Other avenues for bentonite tephrostratigraphy include lithologic description and geochemical characterization of bentonite horizons (*e.g.*, Thomas *et al.*, 1990; Foreman *et al.*, 2008; Fanti, 2009; Ch. 6) and of their phenocrysts, although these approaches are yet to be proven as effective as high-precision geochronology.

#### 4.7.2 Member boundary ages

Based on the KBC/KBU type-section age-stratigraphic model, calculated ages and uncertainty for any stratigraphic level at one-meter intervals throughout the formation are provided including member boundary ages (Table 4.3). The base of the Kaiparowits Formation was found to be 77.06 +0.62/-0.47 Ma, which is older than, but within error of the boundary age reported by Roberts *et al.* (2005, 2013). The results are slightly younger than but overlap with the model age of the top of the Wahweap Formation (Beveridge *et al.*, 2022 [Ch.3]) and is essentially the same as that of Ramezani *et al.* (in review). An age of 76.64 +0.45/-0.20 Ma was calculated for the top of the Tommy Canyon Member, which overlaps with the basal Tommy Canyon Member age due to a sparsity of precise age constraint and exceptionally rapid sediment accumulation rates. The top of The Blues Member is very well constrained with an age of 75.34 +0.06/-0.08 Ma due to closely spaced, highly precise bentonite ages in this portion of the formation.

The lower and upper boundaries of the Upper Valley Member were previously discussed by Beveridge *et al.* (2020 [Ch.5]) based on approximate linear extrapolation of detrital zircon ages generated from volcanoclastic sandstones. Although the interval is generally described as richly volcanoclastic, ash fall bentonites are rare. As such, the present study employed detrital zircon maximum depositional ages and one new CA-ID-TIMS single grain age from the member (KBO-37) within the Bayesian age-stratigraphic model to produce refined boundary ages with quantified uncertainty. The Powell Point - Upper Valley Member contact model age is 74.35 +0.31/-0.30 Ma and the top of the Kaiparowits Formation is 72.94 +0.49/-0.66 Ma. Both ages are slightly older but within error of ages

reported by Beveridge *et al.* (2020 [Ch.5]) and show a significant improvement in precision. Furthermore, the top boundary age marginally overlaps with the age of the Campanian-Maastrichtian stage boundary ( $72.2 \pm 0.2$  Ma; Gale *et al.*, 2020). Despite this refinement, temporal constraint in the Upper Valley Member remains poor, as reflected by the comparatively large uncertainty envelope and slightly more erratic median age curve. Unidentified sedimentological features such as hiatuses, sudden changes in deposition styles, and similar, may not be well represented by the median age but are accounted for by the broad uncertainty window. Furthermore, the use of the KBO-37 single grain age rather than the weighted mean age of the population is tentative. As such, future fine detail geochronologic work in the Upper Valley Member, including magnetostratigraphy, would be highly beneficial.

#### 4.7.3 Linear sediment accumulation rate estimates

One of the most remarkable geologic characteristics of the Kaiparowits Formation is the exceptionally rapid rate of subsidence. This is lithologically evident in the preservation of thick overbank successions and related lithotypes and recorded numerically via radioisotopic dating of its abundant bentonites (Roberts *et al.*, 2005, 2013; Roberts, 2007; Beveridge *et al.*, 2020 [Ch.5]; Ramezani *et al.*, in review). Roberts *et al.* (2005) first report an average rock accumulation rate of 41 cm/kyr across the formation based on  $^{40}\text{Ar}/^{39}\text{Ar}$  geochronology, with slightly higher rates in the upper portion compared to the lower. After recalculation of these  $^{40}\text{Ar}/^{39}\text{Ar}$  ages, Roberts *et al.* (2013) suggested even higher maximum rates for parts of the formation. These sediment accumulation rates and others like them have been historically important in stratigraphic studies for age estimates and interpretations of preserved environments. The rates are calculated using simple linear extrapolation, meaning they are calculated from the difference of two attributes, here the stratigraphic level and absolute age, between two points. Many studies report undecompressed sediment accumulation rates which do not account for heterogeneous compaction during lithification; thus, these rates generally reflect subsidence but are not an exact measurement. The terms undecompressed sediment and rock are used interchangeably here in reference to accumulation rates. Similarly, the term linear is used to mean the average across a designated range, which may incorporate heterogeneous rates across subsections of the interval. Linear rock accumulation rates presented here were framed in the context of utility of such values relative to Bayesian models.

Given the expanded thickness of the Kaiparowits Formation to 1005 m over a total duration of *ca* 4.12 Myrs, an average rock accumulation rate of 24.4 cm/kyr was calculated, which is more subdued than previous estimates but at the same order of magnitude. Despite this difference, previously established paleoenvironmental interpretations for the formation remain unchanged due to substantial lithological evidence. The amalgamated-sandstone-dominated Tommy Canyon and Powell Point members demonstrate rates of 26.2 and 20.2 cm/kyr, respectively, based on linear accumulation between the boundary points. This reflects their lithological similarities and an implied relationship with reduced

subsidence during these time intervals. The mudstone-dominated Blues Member demonstrates a higher rock accumulation rate of 33.8 cm/kyr, which is more closely comparable to the average rates estimated previously (*i.e.*, Roberts *et al.*, 2005, 2013) and may also be causally related to the observed change in lithofacies to overbank mudstone dominated. Average rock accumulation rates in the Upper Valley Member were found to be the slowest in the formation at 18.1 cm/kyr although, due to comparatively poor age constraint, future litho- and chronostratigraphic work may refine this value and influence inferred rates in the Powell Point Member.

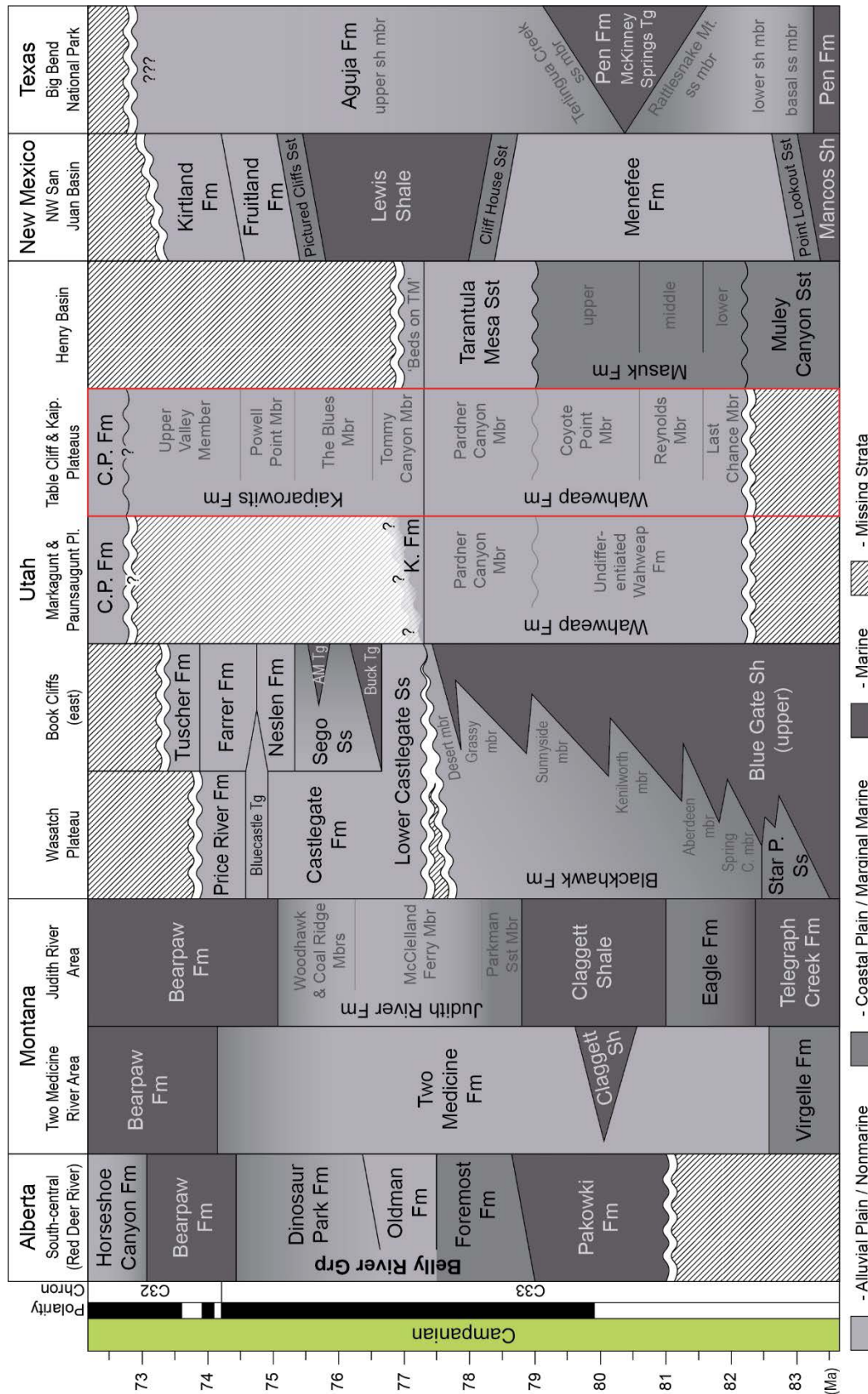
Accumulation rates between member boundary points was found to be generally slower than those calculated between bentonites. The highest member accumulation rate (33.8 cm/kyr for The Blues Member) closely reflects the inter-bentonite rate calculated between horizons that generally bracket this interval (*i.e.*, KP-07A to KBC-144 = 30.6 cm/kyr); however, is slower than other inter-bentonite rates from the formation (*i.e.*, KBC-109 to KBC-144 = 42.9 cm/kyr and KBC-144 to KBC-195 = 58.2 cm/kyr; comparable to rates of Roberts *et al.*, 2013). Seemingly more rapid rock accumulation rates between closely spaced bentonites may represent coarsely heterogeneous subsidence or compaction, or a combination of both. Regardless of the explanation, these examples highlight the utility of Bayesian age-stratigraphic modeling to represent variable sediment accumulation and compaction behaviors (through the use of modeled uncertainty) and, inversely, the limitations of linear extrapolation. Linear extrapolation was found to be particularly unsuitable for the Kaiparowits Formation, where minor changes to input data resulted in significant discrepancies, raising the question of which other well-dated sedimentary successions around the world would benefit from Bayesian age-stratigraphic models.

#### 4.7.4 Regional correlation

Revised ages for bentonites from the Kaiparowits Formation presented here and in Ramezani *et al.* (in review) provide the opportunity for refined correlation of the formation with other units across the Western Interior (Fig. 4.9). Ramezani *et al.* (in review) discussed the precise correlation of the Kaiparowits and Dinosaur Park formations, which are separated by ~1500 km but were found to be exact temporal correlatives. Specifically, the Dinosaur Park Formation was demonstrated to be contemporaneous with The Blues and Powell Point members (and possibly the lowermost Upper Valley Member) of the Kaiparowits Formation. Ramezani *et al.* (in review) also presented refined correlation with the Two Medicine and Judith River formations in Montana and Fruitland and Kirtland formations in New Mexico. With the expansion of the age-stratigraphic model herein to include data from the Upper Valley Member, the present study supports the findings of Beveridge *et al.* (2020 [Ch. 5]) that the Upper Valley Member is temporally correlative with the Kirtland Formation of the San Juan Basin, based also on the new bentonite ages from New Mexico presented in Ramezani *et al.* (in review).

Correlation of Kaiparowits Formation bentonites with others from across the Western Interior also yields insights into the final transgression of the Western Interior Seaway. Roberts (2007) reported





**Fig. 4.9** Regional correlation of Campanian strata across key localities from western North America. Timescale is of Gale et al. (2020). Chronostratigraphic data from Lehman (1989), Eaton (1990), Eberth and Hamblin (1993), Rowe et al. (1992), Rogers et al. (1993, 2016), Payenberg et al. (2002), Cather (2004), Jinnah et al. (2009), Corbett et al. (2011), Seymour and Fielding (2013), Cullen et al. (2016), Fassett and Heizler (2017), Leslie et al. (2018), Pecha et al. (2018), Eberth and Kamo (2020), Prieto-Márquez et al. (2019), and Ramezani et al. (in review).

indicators of brackish-water incursion in the lower portion of The Blues Member (120-320 m) and, using the  $^{40}\text{Ar}/^{39}\text{Ar}$  geochronology of Roberts et al. (2005), suggested that this interval temporally aligned with the maximum transgression of the Bearpaw Seaway as it is found in the San Juan Basin. This



inference was based on the then-current  $^{40}\text{Ar}/^{39}\text{Ar}$  age for the Huerfanito Bentonite Bed that is interstratified with marine shales indicative of maximum transgression in the area (Fassett and Steiner, 1997; Fassett *et al.*, 1997). The Huerfanito Bentonite Bed  $^{40}\text{Ar}/^{39}\text{Ar}$  age has since been redated by Fassett and Heizler (2017) to  $76.26 \pm 0.34$  Ma, which is notably older than previously thought; however, in kind redating of Kaiparowits Formation bentonites herein and in Ramezani *et al.* (in review) indicate the maximum transgression in these two areas was indeed contemporaneous. The stratigraphic level of the KP-07A bentonite (180 m above the base of the formation) coincides with the densest concentration of tidally influenced facies reported by Roberts (2007), and the age of this bentonite ( $76.394 \pm 0.040/0.045/0.093$  Ma; Ramezani *et al.*, in review) overlaps with the revised Huerfanito Bentonite Bed age of Fassett and Heizler (2017). Furthermore, this study shows that strata between 120 and 320 meters above the base of the Kaiparowits Formation ranges in age from  $76.61 +0.44/-0.18$  Ma to  $75.94 +0.30/-0.23$  Ma. This refined correlation has implications for unravelling the hypothesized time-transgressive nature and mechanisms of the final sea level transgression across the Western Interior.

## 4.8 Paleontologic discussion

### 4.8.1 Guidelines for the application of new model ages

The approach to temporal constraint for fossil localities developed herein is based on the new Bayesian age-stratigraphic model and includes robust error propagation for the first time in the Kaiparowits Formation. The strength of this approach is that it facilitates consideration of the certainty with which taxa can be temporally distinguished. Defining temporal precision becomes particularly relevant for richly fossiliferous successions studied in the context of processes that occur at timescales comparable to the magnitude of analytical uncertainty (*e.g.*, biotic turnover and diversification; tens of thousands of years). Radioisotopic ages are often cited without uncertainties and linear extrapolation rarely, if ever, incorporates propagation of uncertainty with stratigraphic distance from the dated horizons. Uncertainties generated based on the Bayesian age model herein may appear comparable to or larger than in previous work; however, they incorporate uncertainty associated with variable sedimentation rates to produce more realistic error envelopes for any stratigraphic level throughout the formation and facilitates significantly more reliable fossil correlation.

The model age of a stratigraphic level of interest (*e.g.*, fossil locality) can be reported in two general formats. The first is an exact ‘model age’ generated from a measured meter level and reported with asymmetric uncertainty. For example, the RUQ locality was reported to occur *ca* 138.5 m above the base of the formation (Titus *et al.*, 2021); thus, the model age is here reported as *ca*  $76.55 +0.41/-0.13$  Ma (see Fig. 4.5 and Appendix C.4.4). Note that since the stratigraphic level was reported as an approximation, the age is also reported as such (denoted as *ca*, abbreviated from *circa* to mean of/at approximately).

**Table 4.4** Model and probable age ranges for portions of the Kaiparowits Formation.

Member	Portion	Stratigraphic Interval (m) *	Model Age Range (Ma)	Probable Age Range (Ma) (95% confidence)
Kaiparowits Formation (entire)	0	0-1005	ca 77.06 to 72.94	77.68 to 72.28
Upper Valley Member	0	750-1005	ca 74.35 to 72.94	74.65 to 72.28
	(entire)	550-750	ca 75.34 to 74.35	75.40 to 74.05
	upper	684-750	ca 74.87 to 74.35	75.14 to 74.05
Powell Point Member	middle	617-684	ca 75.20 to 74.87	75.24 to 74.49
	lower	550-617	ca 75.34 to 75.20	75.40 to 74.98
	(entire)	110-550	ca 76.64 to 75.34	77.09 to 75.26
	upper	404-550	ca 75.67 to 75.34	75.96 to 75.26
The Blues Member	middle	257-404	ca 76.14 to 75.67	76.33 to 75.62
	lower	110-257	ca 76.64 to 76.14	77.09 to 75.80
	(entire)	0-110	ca 77.06 to 76.64	77.68 to 76.44
	upper	74-110	ca 76.77 to 76.64	77.25 to 76.44
Tommy Canyon Member	middle	37-74	ca 76.89 to 76.77	77.43 to 76.47
	lower	0-37	ca 77.06 to 76.89	77.68 to 76.52

\* based on the KBC/KBU type section used in construction of the Bayesian age-stratigraphic model

The second age format uses the interval within which or over which a locality or multiple localities occur to produce an age range. There is a subtle distinction between age reporting for one locality within an interval and multiple localities over an interval, and this may be reflected in the way the age range is presented (Table 4.4). The ‘model age range’ format is based on the median model age at the base and top of a specified interval and does not include an indication of the uncertainty. As such, it should be reported as an approximation (*i.e.*, ‘ca’) and may be appropriate for general statements including the age of one locality within an interval. The ‘probable age range’ format incorporates the modelled uncertainty at the base and top of a specified interval and can be used for more specific descriptions including the exact temporal range of a specific taxon or assemblage known from localities that occur within a measured interval. As an example of these formats, the most fossiliferous portion of the Kaiparowits Formation could be reported as the upper Tommy Canyon Member and lower two thirds of The Blues Member, which equates to a model age range of ‘ca 76.77 to 75.67 Ma’. Alternatively, the fossiliferous interval may be presented as occurring between 150 and 400 m (Roberts, 2007) and presented as a probable age range written as ‘between 76.88 and 75.62 Ma’. For exact description of a taxon’s temporal range, the measured level of the first and last appearance should be used to generate a probable age range so that the precision of this calculated range is incorporated. Since first and last appearance datums exhibit spatio-temporal heterogeneity at geologically fine timescales (Landing *et al.*, 2013), the temporal range of a taxon in one area may not be applicable on a continental scale and should probably be constructed independently for each spatially distinct field area.

**Table 4.5** Holotype locality information and revised ages for highlighted vertebrate species from the Kaiparowits Formation.

Taxa	Specimen Number	Holotype Definition	Field Area	Strat. Level	Stratigraphic Description	Host Lithology	Cited Age	Refined Age
<i>Akainacephalus johnsoni</i>	UMNH VP 20202	Wiersma and Irmis (2018)	Horse Mountain	190 m	Within 1 m of KP-07A	crevasse splay sandstone	late Campanian	76.39 +0.05/-0.07 Ma
<i>Arvinachelys goldeni</i>	UMNH VP 21151	Lively (2015)	Horse Mountain	ca 170 m	The Blues Member	-	Between 76.46 ± 0.14 & 75.97 ± 0.14 Ma	ca 76.44 +0.25/-0.06 Ma
<i>Gryposaurus monumentensis</i>	RAM 6797	Gates and Sampson (2007)	-	-	The Blues Member	point bar deposit	late Campanian	ca 76.64 to 75.34 Ma
<i>Hagryphus giganteus</i>	UMNH VP 12765	Zanno and Sampson (2005)	The Blues	-	-	fine-grained ss channel deposit	Between 76 and 75 Ma	ca 77.06 to 72.94 Ma
<i>Kosmoceratops richardsoni</i>	UMNH VP 17000	Sampson <i>et al.</i> (2010)	-	-	upper Tommy Canyon Mbr, lower Blues Mbr	-	late Campanian	Between 77.25 and 75.80 Ma
<i>Mirarce eatoni</i>	UCMP 139500	Atterholt <i>et al.</i> (2018)	-	-	-	-	76-74.1 Ma	ca 77.06 to 72.94 Ma
<i>Nasutoceratops titusi</i>	UMNH VP 16800	Sampson <i>et al.</i> (2013a)	-	ca 250-320 m	The Blues Member	-	Between ca 75.51 and 75.97 Ma	ca 76.16 to 75.94 Ma
<i>Talos sampsoni</i>	UMNH VP 19479	Zanno <i>et al.</i> (2011)	The Blues	ca 260 m	middle Blues Member	light greenish gray silt/fine ss unit	late Campanian	ca 76.13 +0.20/-0.33 Ma
<i>Teratophoneus curriei</i>	BYU 8120/9396 (etc)	Carr <i>et al.</i> (2011)	-	-	-	-	late Campanian	ca 77.06 to 72.94 Ma
<i>Utahceratops gettyi</i>	UMNH VP 16784	Sampson <i>et al.</i> (2010)	-	-	upper Tommy Canyon Mbr, lower Blues Mbr	-	late Campanian	Between 77.25 and 75.80 Ma

#### 4.8.2 Examples of age refinement for fossil localities

The new approach for fossil locality age calibration presented herein was demonstrated using a selection of key holotype localities and will be applied to a comprehensive locality list in future work. Locality data for ten unique vertebrates from the Kaiparowits Formation were collated from the systematic paleontology of their holotype specimens (Table 4.5). Some descriptions included comprehensive locality information while others provided a broader overview, and this level of detail was translated to the precision of the revised age assignments herein.

The stratigraphically best constrained holotype specimen investigated here is that of the ankylosaurid *Akainacephalus johnsoni* reported by Wiersma and Irmis (2018). The holotype specimen (UMNH VP 20202) was recovered from UMNH VP Locality 1109 (“HMG Quarry”) at *ca* 190 m above the base of the formation in the Horse Mountain area. It was said to occur within approximately one meter of the KP-07(A) bentonite; thus, the locality can be revised to 181 m based on the new age-calibrated type section. This level yields a tightly constrained model age of 76.39 +0.05/-0.07 Ma. Other holotype specimen localities with measured levels include those of the troodontid dinosaur *Talos sampsoni* at *ca* 260 m (Zanno *et al.*, 2011) and the baenid turtle *Arvinachelys goldeni* reported as occurring *ca* 170 m above the base of the formation (Lively, 2015). These levels yield model ages of *ca* 76.13 +0.20/-0.33 Ma and *ca* 76.44 +0.25/-0.06 Ma, respectively, although inconsistencies were identified in the locality information; these will be examined in future work.

Stratigraphic ranges are commonly reported either to represent a range of multiple occurrences, reflect stratigraphic uncertainty, or occasionally to protect the confidentiality of a site. Some ranges are based on meter intervals such as for the basal centrosaurine ceratopsid *Nasutoceratops titusi* from between *ca* 250 to 320 m (Sampson *et al.*, 2013a) or *ca* 200 to 350 m (Lund *et al.*, 2016b), which equate to model age ranges of *ca* 76.16 to 75.94 Ma and *ca* 76.32 to 75.84 Ma, respectively. Other stratigraphic ranges are reported more generally as portions of subunits such as for the holotype and referred specimens of two chasmosaurine ceratopsids described by Sampson *et al.* (2010); *Utahceratops gettyi* and *Kosmoceratops richardsoni*. These were said to occur within what is now the upper Tommy Canyon and lower Blues members, which equates to a model age range of *ca* 76.77 to 76.14 Ma. In the broadest sense, some sites are referred only to a member (*e.g.*, the hadrosaurine hadrosaurid *Gryposaurus monumentensis*, Gates and Sampson, 2007; The Blues Member, *ca* 76.64 to 75.34 Ma) or the *ca* 77.06 to 72.94 Ma Kaiparowits Formation in general (*e.g.*, the tyrannosaurid *Teratophoneus curriei*, Carr *et al.*, 2011; the avisaurid *Mirarce eatoni*, Atterholt *et al.*, 2018; and the oviraptorosaur *Hagryphus giganteus*, Zanno and Sampson, 2005).

The holotype specimens of fossil biota investigated here represent only a small portion of the wealth of material known from the Kaiparowits Formation. Future work will aim to compile a comprehensive list of Kaiparowits fossil localities then apply and expand upon the approaches discussed

herein to provide improved age and stratigraphic constraint. This project will be achieved through collaboration with institutions including the Natural History Museum of Utah (UMNH), Denver Museum of Nature and Science (DMNS), Raymond M. Alf Museum of Paleontology, and Bureau of Land Management (Paria River District). Outcomes will contribute to the investigation of intraformational and basin scale biotic trends for topics ranging from faunal turnover to latitudinal endemism.

#### 4.9 Conclusions

This study of the Kaiparowits Formation elevates previous informal units to formal members, formalizes several bentonite marker beds, presented five new high-precision bentonite ages, established a Bayesian age-stratigraphic model for the full formation, and places important fossil localities from across the formation into greater stratigraphic and temporal context. The five new U-Pb CA-ID-TIMS bentonite ages from key reference sections complement four previously published matching ages that constrain the type section (*i.e.*, Ramezani et al., in review). An expanded Bayesian age-stratigraphic model for the type section was built upon and supersedes the model of Ramezani et al. (in review) and includes the Upper Valley Member. Formalized member-level lithostratigraphic subdivisions were also described where the lower, middle, and upper informal units of Roberts (2007) are superseded by the Tommy Canyon Member, The Blues Member, and Powell Point Member respectively. These new member names bring the Kaiparowits Formation in line with the underlying Wahweap Formation and are expected to aid in clear expression of type locality descriptions in futures studies including systematic paleontology, as well as for future lithostratigraphic work. Ten unique bentonite horizons were stratigraphically calibrated, four of which were formally recognized as the Horse Mountain Bentonite Bed, Paria Hollow Bentonite Bed, Deadmans Corner Bentonite Bed, and Overlook Bentonite Bed. Implications of the refined litho- and chronostratigraphic framework for the Kaiparowits Formation developed herein include precise correlation of fossil biota within the formation and across contemporaneous Campanian terrestrial strata of the Western Interior to support the investigation of complex hypotheses around biogeographic distribution and palaeoenvironmental relationships during the peak of non-avian dinosaur diversity.

---





## Chapter Five

Volcaniclastic member of the richly fossiliferous Kaiparowits Formation reveals new insights for regional correlation and tectonics in southern Utah during the latest Campanian



*Upper Valley Member Stratotype Area*

**Preface**

This is the final of three stratigraphy-focused chapters, which are presented in increasing stratigraphic order of Campanian unit from southern Utah. This chapter builds upon formalized subdivisions of the Kaiparowits Formation discussed in Chapter Four with a focus on the newly recognized Upper Valley Member that caps the Campanian succession. This work was published in *Cretaceous Research* in 2020 ([doi.org/10.1016/j.cretres.2020.104527](https://doi.org/10.1016/j.cretres.2020.104527)) and is included herein with minor adaptations to reflect the nomenclature presented in Chapter Four. The Statement of Contribution of Others (p. v) outlines co-author contributions. I conducted and compiled all lithostratigraphic work presented in the manuscript, which was edited for accuracy and language by E. Roberts and A. Titus.

**Abstract**

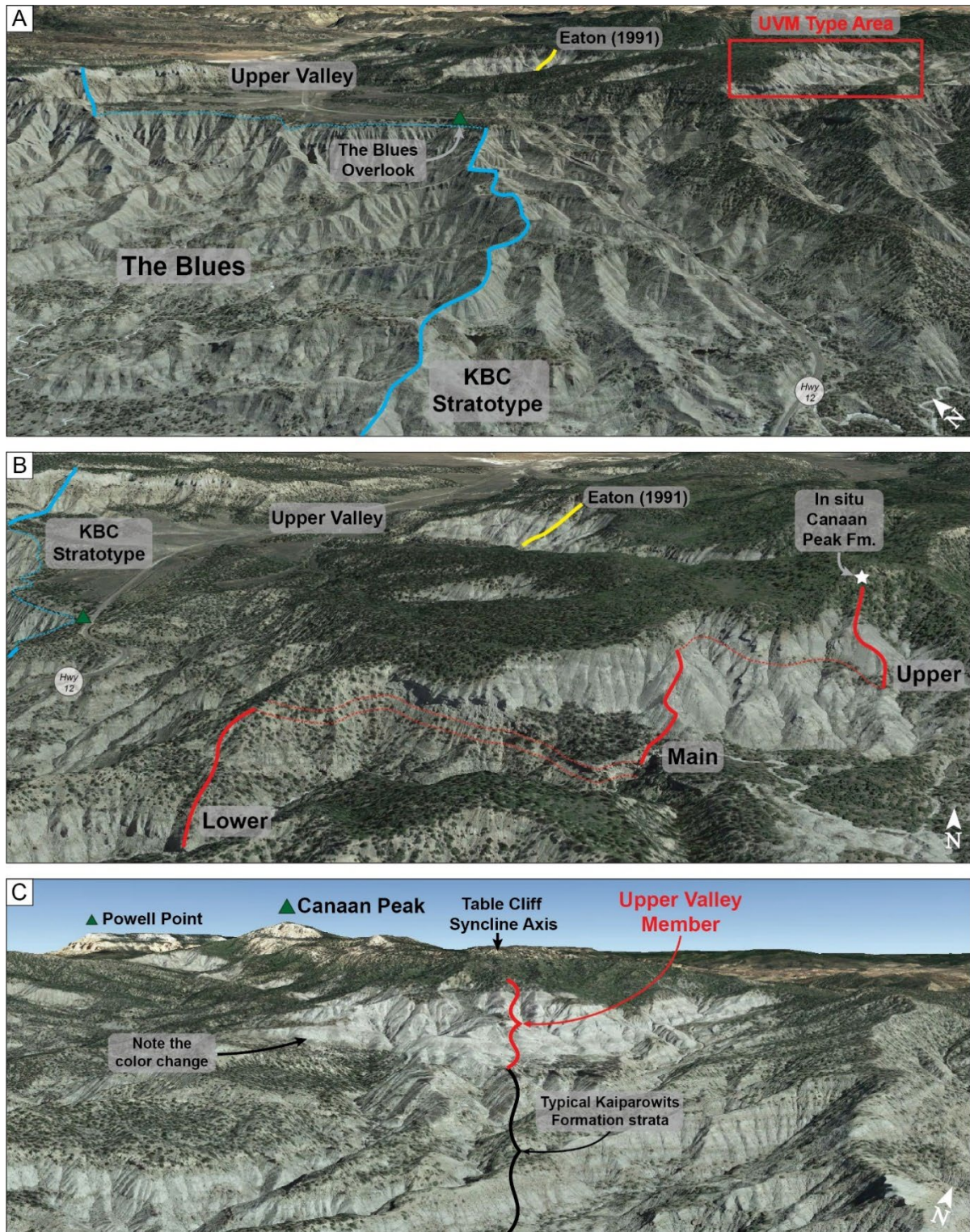
Lithostratigraphic investigation of the richly fossiliferous Kaiparowits Formation in southern Utah reveals the presence of a previously unidentified stratigraphic unit herein named the Upper Valley Member. The 255-m-thick Upper Valley Member is latest Campanian to earliest Maastrichtian in age and records a significant sedimentological change in the Kaiparowits Formation. This change is illustrated in the member by a significant increase in near syn-sedimentary aged zircons, coincident with the introduction of white, volcaniclastic sandstones, as well as a paucity of Jurassic grains, which dominate the provenance of the rest of the formation. The source of the late Campanian volcaniclastic material, including near syn-sedimentary zircons, is most likely from nearby volcanic centers within the Laramide porphyry copper province to the south of the Kaiparowits Plateau in the Mogollon region. Measured sections reported here stratigraphically expand the Kaiparowits Formation to a total of 1005 m and find that the upper boundary of the formation is largely gradational with the overlying Canaan Peak Formation. Lithological changes documented in this study are interpreted to signify a sedimentological response to proximal magmatism and emerging uplifts within the Cordilleran foreland basin during early Laramide orogenesis, which resulted in palaeo-drainage rearrangement in southern Laramidia in the latest Campanian. The fossil-bearing Upper Valley Member can be correlated regionally to the Kirtland, Tuscher and Bearpaw formations and other latest Campanian – and possibly early Maastrichtian – units across western North America and represents the capping member one of the most continuous terrestrial records of the Campanian biosphere found anywhere in the world.

## 5.1 Introduction

The richly fossiliferous Kaiparowits Formation in southern Utah preserves a highly resolved temporal and stratigraphic record of mid-to-late Campanian strata of the proximal Cordilleran Foreland Basin in southern Laramidia. Although the reportedly 860-meter-thick succession is renowned for its diverse and abundant assemblages of fossil vertebrates, plants, invertebrates and trace fossils, recent advances in understanding the sedimentary architecture, mineralogy, age and depositional settings of the formation highlight its importance as a keystone for palaeoenvironmental reconstruction of the southern Cordilleran foreland basin. The Kaiparowits Formation conformably overlies the early to middle Campanian age Wahweap Formation (Eaton, 1991; Jinnah and Roberts, 2011), and continues a remarkably complete terrestrial sedimentary record throughout the Campanian. The upper contact of the Kaiparowits Formation is a truncating low angle unconformity with the overlying Canaan Peak Formation (Bowers, 1972; Eaton, 1991; Roberts, 2007). Previous dating of Kaiparowits bentonite beds (devitrified volcanic ash) indicate the formation is mid- to late Campanian in age (Roberts *et al.*, 2005, 2013). Several studies including Lohrengel (1969) and Eaton (1991) describe the thickness of the Kaiparowits Formation to be greatest in the vicinity of Canaan Peak, close to the axis of the Table Cliff syncline; however, the lectostratotype section reported by Roberts (2007) was measured in The Blues area below Powell Point, located northwest of Canaan Peak. This section terminates in a covered interval and Roberts (2007) inferred the contact with the overlying Canaan Peak Formation to lie 70 m above the uppermost exposed Kaiparowits Formation strata below Powell Point. Conversely, Eaton (1991) reported exposed Kaiparowits Formation strata through to the top of a similarly thick section measured ~2.2 km southeast of that in Roberts (2007). Efforts to identify and estimate the true thickness of the formation over the last few decades have been confounded by the presence of numerous large slumps, landslide blocks and scree obscuring most of the accessible outcrop area of the uppermost Kaiparowits Formation.

To resolve stratigraphic discrepancies in upper parts of the formation, satellite imagery of the region was investigated to identify areas with better exposure of the top of the Kaiparowits Formation. The quality and resolution of publicly available satellite imagery, particularly in Google Earth, have significantly improved in recent years making this a valuable tool for remote investigation of the Kaiparowits Plateau, where large wilderness areas with limited ground access provide logistical challenges to standard pedestrian fieldwork. Through Google Earth analysis, it became clear that large tracts of well-exposed Kaiparowits Formation strata occur at elevations considerably higher than expected given the approximate top contact estimated by Roberts (2007) and Eaton (1991) (Fig. 5.1). Indeed, even in this preliminary remote sensing exercise, it appeared that a previously unrecognized stratigraphic interval existed between the prior established top of the Kaiparowits Formation and the base of the overlying Canaan Peak Formation. This interval was readily recognizable by its distinctive outcrop patterns and colors (pale-gray hues vs. blue-gray of the rest of the Kaiparowits Formation).





**Fig. 5.1** Oblique-perspective Google Earth Pro imagery of the Kaiparowits Formation. A) Location of the Upper Valley Member type area (red box) relative to the KBC lectostratotype of Roberts (2007) (blue) and top of the measured section of Eaton (1991) (yellow). B) Close-up of the Upper Valley Member type area showing the measured sections reported herein (red) and previous measured sections (blue and yellow). C) An example of the pale strata of the Upper Valley Member clearly distinguishable from other Kaiparowits Formation units in the vicinity of Canaan Peak looking north-northwest along the axis of the Table Cliff syncline. NB: use of a scale bar is not suitable due to oblique perspective of the images.

Subsequent fieldwork confirmed the initial diagnosis made in Google Earth that a previously unrecognized stratigraphic interval, distinctive enough to be given member status, exists in the uppermost Kaiparowits Formation. A composite measured section was assembled as the stratotype for the new member. Accompanying detailed sedimentological descriptions and interpretations establish the provenance and mode of sedimentation, while detrital zircon U-Pb ages presented here gives the Kaiparowits Formation a significant age extension to approximately the Campanian-Maastrichtian boundary. The identification of a new, distinctive stratigraphic interval in the upper Kaiparowits Formation, here named the Upper Valley Member, has major implications for understanding not only Campanian terrestrial biome evolution, but also large-scale magmatism and tectonism in North America during the Late Cretaceous relating to partitioning of the southern section of the Cordilleran Foreland Basin by Laramide orogenesis.

## 5.2 Previous work

### 5.2.1 Lithostratigraphy

The Kaiparowits Formation in southern Utah is primarily exposed on the Kaiparowits Plateau and occurs largely within Grand Staircase-Escalante National Monument and Dixie National Forest. Isolated exposures of the lower part of the formation are also found along the western margin of the Paunsaugunt Plateau (Biek *et al.*, 2015). The formation was first described in The Blues field area below Powell Point by Gregory and Moore (1931) who noted poorly consolidated drab arkosic sandstones and shales with poor lateral continuity. This early study reported an approximate thickness of 610 m but did not designate a stratotype section. The remote area remained relatively unstudied and underexplored for another four decades until palynological investigations by Lohrengel (1969) reported similar lithofacies and provided the first measured section of the formation, suggesting a thickness of 838 m in The Blues area. Eaton (1991) later revised the thickness of the Kaiparowits Formation to 855 m and significantly refined biostratigraphic age constraints on the formation. Sedimentological and stratigraphic analysis of the formation was completed by Roberts (2007), who provided detailed evidence in support of the informal subdivision of the Kaiparowits Formation into the lower, middle and upper units based on gradational changes in fluvial architecture. Furthermore, Roberts (2007) proposed a single complete lectostratotype of 860 m for the formation, designated “KBC” in The Blues area.

### 5.2.2 Basal contact

The boundary between the Kaiparowits and Wahweap formations is disconformable, but difficult to identify in the field due to local gradational changes in lithofacies and mineralogy from the Pardner Canyon Member of the Wahweap Formation to the Tommy Canyon Member of the Kaiparowits Formation (Lohrengel, 1969; Little, 1995; Chapter Three). Where the contact is readily apparent, the erosional surface undulates considerably over short distances (Eaton, 1991; Roberts, 2007). The 15-meter stratigraphic variation of the contact described by Eaton (1991) may explain discrepancies in total



stratigraphic thickness of the formation reported by various authors. The key tool used by Roberts (2007) to identify the boundary was the first occurrence of a laterally continuous mudstone.

### 5.2.3 Member subdivisions

Informal subdivision of the Kaiparowits Formation into the lower, middle and upper units proposed by Roberts (2007) has been widely applied in subsequent sedimentological and paleontological studies and formal nomenclature was presented in Chapter Four. The Tommy Canyon Member (lower unit of Roberts, 2007) is characterized by a high proportion of channel deposits compared with overbank facies resulting in a roughly 3:1 sandstone to mudstone ratio (Roberts, 2007). The roughly 100-meter-thick unit is dominated by tabular sandstones with a prevailing east-northeast palaeocurrent orientation (Roberts, 2007; Lawton and Bradford, 2011). Identifiable vertebrate fossils are uncommon in the lower two thirds of the unit; however, the upper third is slightly more productive (Roberts, 2007; Sampson *et al.*, 2013b).

The Blues Member of the Kaiparowits Formation (middle unit of Roberts, 2007) is characterized by extensive overbank deposits resulting in an overall higher proportion of mudstone than sandstone (55:45 respectively). This unit dominates exposures in The Blues field area in the form of steeply incised badlands. The unit is reported to range in thickness from 440 to 510 m, thinning towards the north (Eaton 1991; Roberts 2007). Average palaeocurrent data from The Blues Member reflects a subtle change in orientation towards the east and are marginally less uniform than that of the underlying Tommy Canyon Member (Roberts, 2007; Lawton and Bradford, 2011). This change is believed to reflect renewed tectonism related to the Laramide-style East Kaibab uplift which may also contribute to the minor dispersion observed. The Blues Member hosts the best fossil preservation in the Kaiparowits Formation and is known for producing numerous specimens of terrestrial vertebrates including members of Ceratopsidae, Ankylosauridae, Hadrosauridae, Tyrannosauridae and more (Gates and Sampson, 2007; Sampson *et al.*, 2010, 2013a; Carr *et al.*, 2011; Zanno *et al.*, 2011; Wiersma and Irmis, 2018) as well as numerous freshwater turtles, crocodylians, fish, invertebrates, plants and mammals (Eaton and Cifelli, 1988; Gates *et al.*, 2010; Getty *et al.*, 2010; Irmis *et al.*, 2013; Miller *et al.*, 2013; Sampson *et al.*, 2013b; Tapanila and Roberts, 2013).

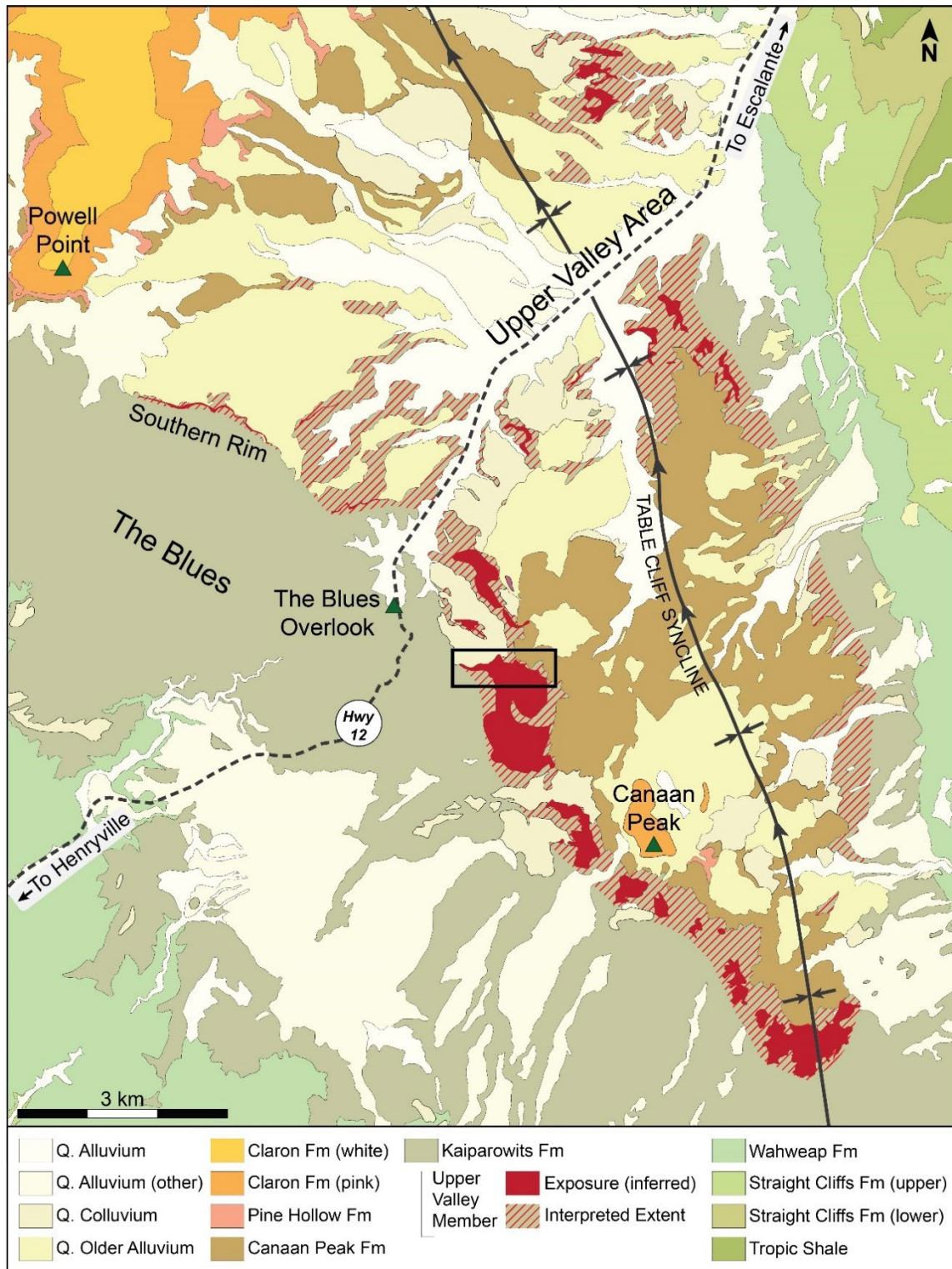
The sedimentological character of the Powell Point Member of the Kaiparowits Formation (upper unit of Roberts, 2007) grades back to a sandstone dominated alluvial architecture comparable to that of the Tommy Canyon Member, exhibiting a sandstone to mudstone ratio of 3:2 (Roberts, 2007). The 300 to 350-meter-thick interval is characterized by comparatively well indurated multistory channel complexes outcropping as cliffs atop the well exposed, mud-dominated Blues Member. Roberts (2007) reported the palaeocurrent direction in the Powell Point Member to swing further south with an overall south-easterly orientation also reflecting a higher degree of dispersion; however, Lawton and Bradford (2011) measured a prevailing easterly orientation. Diagnostic fossils are not widely reported from the

member, possibly resulting from rapid recycling rates and high energy of the stream systems represented by the dominance of stacked sandstone channels. Furthermore, there may also be some degree of collection bias due to the dominance of highly inaccessible cliff-forming sandstone in this interval and distance away from roads (Roberts, 2007; Roberts *et al.*, 2013).

Reported lithological descriptions of the Powell Point Member, particularly the topmost interval, are of specific interest to this study. Roberts (2007) describe the lower two thirds of the unit to consist of stacked and incised major tabular sandstones with common bands of soft sediment deformation (~3 m thick) interpreted to reflect possible syn-depositional seismicity. This ~200-meter-thick interval crops out as a laterally extensive amalgamated sandstone channel complex. The topmost ~100 m of the unit described by Roberts (2007) are reportedly mud dominated and largely covered by colluvium in the type section, providing minimal insight into the sedimentology of the top of the formation. The most detailed description of the uppermost Kaiparowits Formation is given by Lohrengel (1969) who identified the top 16% of the 838-meter stratigraphic section measured in that study (equating to ~135 m) as “dominantly bentonitic mudstone, clean quartz sandstone and bentonite”. Considerable volcanic activity proximal to the formation was inferred by Lohrengel (1969) based on the high bentonite content of the interval.

#### 5.2.4 Upper contact and the Table Cliff Syncline

The nature of the upper contact of the Kaiparowits Formation with the overlying Canaan Peak Formation is somewhat ambiguous due to cover, slumping and deformation associated with the formation of the Table Cliff syncline. The contact is commonly reported in literature as a sharp erosional surface between the two highly contrasting formations reflecting a subtle angular unconformity (Bowers, 1972; Eaton, 1991; Roberts, 2007). An interval of folding and erosion related to the Table Cliff syncline is inferred to have occurred after deposition of the Kaiparowits Formation but prior to deposition of the Canaan Peak Formation (Bowers, 1972; Eaton, 1991). The degree of folding prior to deposition of the Canaan Peak Formation is estimated to be between 10° to 15° at the eastern end of the Table Cliff Plateau on the downward limb of the Dutton monocline based on angular discordance between the two formations (Bowers, 1972). At the western end of the Table Cliff Plateau along the Southern Rim (below Powell Point), the erosional surface is difficult to identify but was interpreted to represent a significant erosional boundary (Bowers, 1972; Eaton, 1991; Roberts, 2007). In the vicinity of Canaan Peak, proximal to the area of maximum down-warping of the Table Cliff syncline, Lohrengel (1969) and Eaton (1991) indicated thickening of the Kaiparowits Formation, but no published stratigraphic sections or descriptions of this interval are recorded from this area. This disparity is presumably related to the relative inaccessibility of the area as well as extensive slumping reported by Lohrengel (1969) and remotely observed in this study.



**Fig. 5.2** Geological map of the study area showing the Upper Valley Member type area (black box). Adapted from USGS 1:24,000 geologic maps of the Upper Valley, Pine Lake, Henryville and Canaan Peak quadrangles (Bowers, 1973a; 1973b, 1975, 1981) and 1:100,000 interim geologic map of the Escalante 300 x 600 quadrangle (Doelling and Willis, 2018). The Upper Valley Member inferred exposure was determined using Google Earth imagery (based on color and texture), of which several locations were ground-truthed in accessible locations. The interpreted extent of the member was established based on the approximate stratigraphic height of strata within the previously mapped Kaiparowits Formation.



### 5.2.5 Geochronology

Originally assigned a Maastrichtian age based on vertebrate faunas and palynology (Lohrengel 1967), Eaton and Cifelli (1988) and Eaton (1991) among others studied micro-vertebrates from the formation to revise the age of the Kaiparowits Formation to be no younger than Campanian, equating to a Judithian land mammal age. The first absolute dating was conducted by Roberts *et al.* (2005) using  $^{40}\text{Ar}/^{39}\text{Ar}$  isotopes from sanidine phenocrysts of four interstratified bentonite (weathered volcanic ash) horizons, confirming a mid-to-late Campanian age. Revision of the Fish Canyon Tuff standard by Kuiper *et al.* (2008) prompted the adjustment of these ages, as reported by Roberts *et al.* (2013), such that the Kaiparowits Formation is currently estimated to range from 76.6 to 74.5 Ma.

The age of the upper boundary of the Kaiparowits Formation is of particular relevance to the timing and duration of the erosional event between the Kaiparowits and Canaan Peak formations. The stratigraphically highest dated bentonite (KBO-37) yielded an  $^{40}\text{Ar}/^{39}\text{Ar}$  age of  $74.69 \pm 0.36$  Ma ( $2\sigma$ ), occurring at 790 m above the base of the Kaiparowits Formation (Roberts *et al.*, 2005, 2013). The age of the Canaan Peak Formation remains ambiguous due to poor representation of macrofossils and absence of bentonites or young detrital zircon grains (Eaton, 1991; Larsen *et al.*, 2010). Palynomorph data from Bowers (1972) indicate the lower boundary of the Canaan Peak Formation is Campanian in age and argues that reworking of the plant material is unlikely. In contrast, Eaton (1991) identified that the duration of the significant folding and erosion event that separates the two formations must have been exceedingly rapid if both the upper Kaiparowits and lower Canaan Peak formations are both late Campanian in age, and instead suggested a Maastrichtian age for the latter unit.

Also relevant to this study, Lawton and Bradford (2011) conducted a detrital zircon (DZ) U-Pb study of the Kaiparowits Formation examining the youngest single grains and youngest coherent population (YCP) weighted mean ages of various sandstones. The purpose of this part of their work was to compare DZ ages to the  $^{40}\text{Ar}/^{39}\text{Ar}$  ages of Roberts *et al.* (2005) to test the accuracy of maximum depositional ages (MDAs) in the formation. The investigation of youngest zircon grains and populations yielded insightful results including identifying loss of daughter isotope in some grains (lead loss) that resulted in a small population of unreasonably young single grain ages. Lawton and Bradford (2011) acknowledged the issue of lead loss in some grains and surmised that youngest coherent population MDAs (excluding the anomalously young grains) were close to the expected age based on previous  $^{40}\text{Ar}/^{39}\text{Ar}$  ages although slightly older on average.

## 5.3 Materials and methods

Preliminary observations were conducted using Google Earth Pro software to remotely examine the extent of the newly identified unit and explore for suitable field sampling areas. Likely outcrops of the new unit were visually identified based on color and texture of the exposures and a subset of these exposures were later ground-truthed during 2018 and 2019 fieldwork. Findings were mapped using

USGS geological maps (Bowers, 1973a, 1973b, 1975, 1981) as illustrated in Figure 5.2. The most suitable exposure of the new stratigraphic interval, discovered via Google Earth, was targeted for detailed field studies. This locality (approx. 37°37'55" N, 111°49'40" W, WGS84) is situated approx. 1.5 to 2 km southeast of The Blues Overlook in the vicinity of a headwater tributary of Henryville Creek (Figs. 5.1, 5.2) and is here designated the type area for the proposed Upper Valley Member.

A detailed decimeter-scale stratigraphic section through the Upper Valley Member was measured in the type area using a Jacob Staff and clinometer. The type section for the member began at the top of a distinctive sandstone marker horizon at 37°37'52.4" N, 111°49'43.2" W (WGS84). This distinctive unit can be traced laterally into the Kaiparowits Formation KBC type section in The Blues. Detailed sedimentological descriptions were made in the field and a variety of samples were collected including details such as GPS location, stratigraphic position and lithofacies (Appendix C.5.2). Sandstones throughout the new unit were sampled for framework petrography and detrital zircon geochronology; mudstones were sampled for clay mineralogy; and carbonate concretions collected for stable isotope and diagenesis investigations.

Sandstone and concretion descriptions were derived both in the field and using a petrographic microscope. Sandstone grain counts were conducted using transmitted light microscopy on 30 µm thin sections based on methods described in Lawton *et al.* (2003). Powdered mudstone samples were analysed for clay mineralogy using XRD analysis (USGS method) at the CARF lab, Queensland University of Technology. Semi-quantitative bulk geochemistry of carbonate concretions was analysed by energy dispersive spectroscopy (EDS) using a Hitachi SU5000 field emission scanning electron microscope (SEM) at the Advanced Analytical Centre (AAC), James Cook University. Oxygen and carbon isotope composition of concretions were determined using a gas bench coupled with a continuous flow Thermo Delta-V isotope ratio mass spectrometer at the AAC and results are reported as  $\delta^{18}\text{O}$  and  $\delta^{13}\text{C}$  in ‰ (VPDB). The isotopic composition of concretion-forming fluids was calculated using the temperature-dependent fractionation equation of Kim and O'Neil (1997):

$$1000\ln\alpha = 18.03 \times (10^3 T^{-1}) - 32.42$$

$$\text{where } \alpha = (1000 + \delta^{18}\text{O}_{\text{calcite}}) \div (1000 + \delta^{18}\text{O}_{\text{water}})$$

Where T is temperature in kelvin. A temperature approximation of 23°C was used based on work by Foreman *et al.* (2015) and references within.

Detrital zircon samples were collected for five sandstone units throughout the member type area for U-Pb geochronology (Appendix C.5). Laser ablation inductively coupled plasma mass spectrometry (LA ICP MS) was conducted using a Teledyne Analyte G2193 nm Excimer Laser with HeLex II Sample Cell and a Thermo iCAP-RQ ICP-MS at the AAC (as per. Todd *et al.*, 2019). All uranium-lead laser ablation ICP-MS data was reduced and handled in Iolite (iolite-software.com) and Isoplot (Ludwig,

2012) respectively. Individual zircon grain ages with > 5% discordance or > 5%  $2\sigma$  analytical uncertainty were not included in this study.

## 5.4 Sedimentological descriptions

### 5.4.1 Lithological descriptions

Facies analysis of the Upper Valley Member described here builds upon detailed work by Roberts (2007). Of the fourteen lithofacies previously described from the Kaiparowits Formation, eight were observed in the member and an additional two are described here: massive white sandstone (Sv) and clast-supported pebble conglomerate (Gpm) (Table 5.1). Facies associations in the Upper Valley Member mirror the observed lithological change where five of the nine FAs designated by Roberts (2007) were identified and an additional two are here described (Table 5.2). The two new FAs (FA10 volcaniclastic sandstone and FA11 extra-formational conglomerate) are described and interpreted as follows (Fig. 5.3).

#### 4.1.1 FA10 – Volcaniclastic sandstone description

FA10 is very common in the Upper Valley Member and is characterized by massive white sandstones (Sv) with subordinate green variants of muddy sandstones (Sf). Minor bentonitic claystones (Sb) with various proportions of reworked material are also present; however, pure bentonites are rare. FA10 is a distinguishing FA unique to the Upper Valley Member and is observed as isolated lenses (< 1 m) to massive tabular to lenticular sandstone horizons (> 8 m) with interbedded green muddy sandstones and smectite-rich mudstones. FA10 was observed slightly more commonly in the lower half of the member than the upper half. The most identifiable feature of FA10 sandstones is their pale color with common dark grains. Elsewhere in the formation, dark grains in sandstone are typically chert; however, in the massive white sandstone (Sv) from FA10, which is entirely restricted to the Upper Valley Member, dark grains are often large biotite phenocrysts. The lighter overall color of the sandstone, together with the additional biotite grains, results in a salt and pepper texture distinct from other parts of the Kaiparowits Formation.

#### 4.1.2 FA10 – Volcaniclastic sandstone interpretation

The volcaniclastic sandstone is interpreted to represent periods of high volcanic activity proximal to the formation. This hypothesis matches interpretations by Lohrengel (1969) who described the uppermost strata of the Kaiparowits Formation as exceptionally volcaniclastic rich. A combination of two scenarios is proposed: 1) volcanogenic material may have been transported aurally to the floodplain and subsequently reworked by river systems, and/or 2) rivers sourced and reworked the volcanic ash and other pyroclastic material from active volcanic terrain on the edge of the basin, transporting the volcaniclastic material a short distance before deposition on the floodplain. The closest volcanic terrains active during the late Campanian were likely in southern Arizona to northern Sonora in the Mogollon

**Table 5.1** Lithofacies observed in the Upper Valley Member adapted from Roberts (2007). “Occurrence” refers to the prevalence of each lithofacies within the member. See Roberts (2007) for detailed descriptions of previously described lithofacies.

Lithofacies	Description	Occurrence
<b>Lithofacies Unique to the Upper Valley Member</b>		
Gpm	Clast-supported pebble conglomerate; typically pebble size clasts (1-3 cm) in a medium to coarse sand matrix. Clasts, including chert, volcanics, and quartzite, are all highly rounded. Occurs as fine lenses beginning at ~955 m.	Rare
Sv	Massive white sandstone; typically medium to coarse grained, pale color with clean calcite cement (effervesces). Commonly contains large biotite phenocrysts. Occurs as thin lenses to thick tabular horizons. Occurs throughout the member but is generally more common in the lower half.	Very Common
<b>Previously Described Lithofacies</b>		
St	Trough cross-bedded sandstone	Occasional
Sr	Ripple cross-laminated sandstone	Occasional
Sh	Horizontally stratified sandstone	Occasional
Sf	Massive to slightly laminated muddy sandstones	Common
Fl	Finely laminated sandstone, siltstone and claystone with very small ripples	Rare
Fc	Massive to laminated carbonaceous mudstone	Common
Fb	Bentonitic claystone	Common
C	Coal stringers	Rare

region from an area collectively termed the Laramide porphyry copper province (Roberts *et al.*, 2005; Lawton and Bradford, 2011; Pecha *et al.*, 2018). Palaeocurrent data in the Upper Valley Member is poor to absent due to the highly friable nature of the rocks; however, Lawton and Bradford (2011) hypothesized northward palaeo-rivers transecting the region during the latest Campanian. Palaeoclimate modelling also supports northward palaeo-wind directions (Fricke *et al.*, 2010); therefore, both reworked aerial and direct fluvial derivation of volcaniclastic material are hypothetically plausible. A combination of both mechanisms is likely, although a dominantly fluvial transport mechanism is suspected based on the scarcity of primary ashfall deposits (pure bentonites) compared to the rest of the Kaiparowits Formation and generally low bentonite abundance in neighboring sub-basins.

#### 4.1.3 FA11 – Extra-formational conglomerate description

Beds of clast-supported pebble conglomerates and associated tan sandstones in the uppermost 50 m of the Kaiparowits Formation are designated FA11. The extra-formational conglomerate (Gpm) that typifies this association is composed mostly of well-rounded, pebble sized, extra-formational clasts,

**Table 5.2** Facies associations observed in the Upper Valley Member adapted from Roberts (2007). \* FAs unique to the member. “Occurrence” refers to the prevalence of each FA within the member. See Roberts (2007) for detailed descriptions of previously described FAs.

	Facies association	Facies	Interpretation of depositional environment	Occurrence
FA3	Major tabular sandstone	St, Sp, Sh, Sr	Dominantly meandering fluvial channels	Occasional
FA5	Minor tabular and lenticular sandstone	St, Sp, Sh, Sr	Crevasse splays and crevasse channels	Common
FA6	Finely laminated, calcareous siltstone	Fl, Sr	Shallow lakes	Rare
FA8	Sandy mudstone	Fb, Sf, Fl, Sh, C	Floodbasin ponds, lakes and weakly developed palaeosols	Very Common
FA9	Carbonaceous mudstone	Fc, C	Backswamps and oxbow lakes	Common
FA10*	Volcaniclastic-rich sandstone	Sv, Sf, Sb	Fluvial channels and floodplain deposits overwhelmed with volcaniclastic material	Very Common
FA11*	Extra-formational conglomerate	Gpm, St, Sr, Sp, Sv	Fluvial channel lags with reduced basin accommodation	Rare

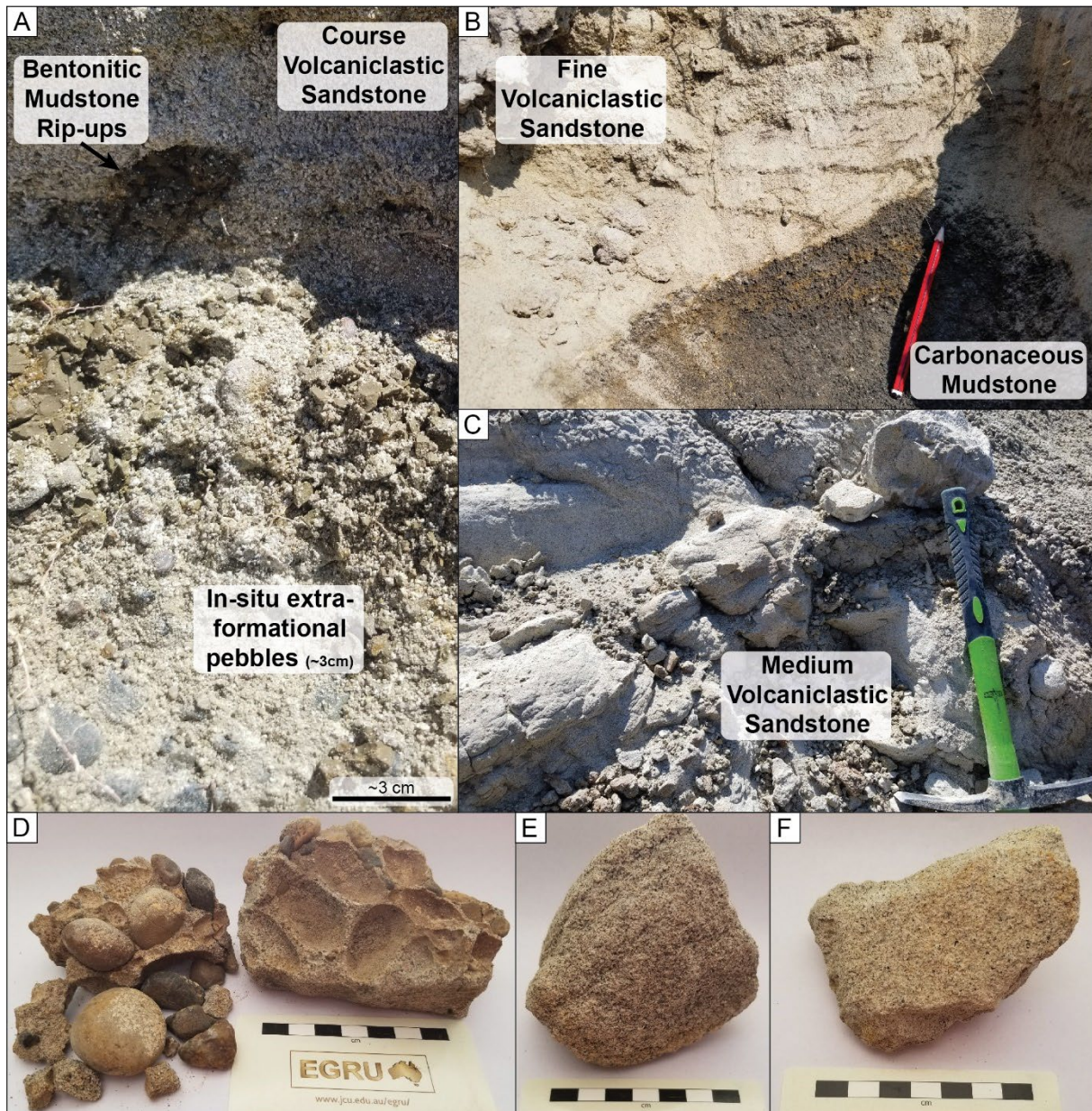
including quartzite, chert and volcanics, in a coarse sandstone matrix. These clast types vary but are essentially the same as those found in the overlying Canaan Peak Formation. FA11 also contains subordinate beds of various sandstone lithofacies including St, Sr and Sh. Units from FA11 first appear at 955 m as isolated lenses typically < 10 cm with pebble-sized clasts within coarse white sandstone.

Higher in section, bed thickness and clast size increases. Excavating fresh surfaces of this unit was difficult due to the friable nature of the rocks coupled with the abundance of large, hard clasts; however, it is clear that this FA is packaged between typical Kaiparowits facies in the Upper Valley Member.

#### 4.1.3 FA11 – Extra-formational conglomerate interpretation

Introduction of the extra-formational conglomerate FA high in section is interpreted to represent a gradational transition from low-gradient, floodplain fluvial environments seen in the Kaiparowits Formation (Roberts, 2007) to the high-gradient braided stream lithotypes of the Canaan Peak Formation (Schmitt *et al.*, 1991). The depositional environment reflected in FA11 represents gravel bars associated with bed load rivers. Interbedding of this conglomeratic FA with other typical Kaiparowits Formation lithotypes demonstrates, for the first time, a gradational transition between the Kaiparowits and Canaan Peak formations.





**Fig. 5.3** Photographs of the massive white sandstone (*Sv*) and clast-supported pebble conglomerate (*Gpm*) lithofacies in typical, highly friable exposures of the Upper Valley Member and in hand sample. A) Cross-sectional view of the first occurrence of the pebble conglomerate at ca 955 m. B and C) Fine and medium grained examples of the massive white sandstone in-situ. D) Hand sample example of the extra-formational pebble conglomerate. E and F) Course and medium grained hand samples of the massive white sandstone (KBU-F and KBU-V respectively).

#### 5.4.2 Mudstone mineralogy

Samples for clay mineralogy were selected from three types of mudstones commonly found in the Upper Valley Member: carbonaceous, green and bentonitic. Qualitative results are shown in Table 5.3 alongside legacy data from Roberts (2007). Mudstones in the Upper Valley Member closely resemble those from the rest of the Kaiparowits Formation featuring high abundance of smectite clay and

**Table 5.3** Qualitative results of mudstone mineralogy determined using XRD analysis including legacy data from Roberts (2007) for comparison. Symbols: mineral weight percent < 5% = ±, 5-15% = ✓, 15-30% = ✓✓, >30% = ✓✓✓. Carb. = Carbonaceous.

Mineral	Roberts 2007				This Study		
	Green Mudstone	Standard Mudstone	Carb. Mudstone	Lacustrine Mudstone	Carb. Mudstone	Green Mudstone	Bentonitic Mudstone
Quartz	✓	✓	✓✓	✓	✓✓✓	✓✓✓	✓✓
K-feldspar	±	±	±	±	✓	✓	±
Plagioclase	±	±	±	-	±	±	±
Calcite	-	-	-	±	±	✓	±
Dolomite	±	±	-	✓✓	±	✓	-
Smectite	✓✓✓	✓✓✓	✓✓✓	✓✓✓	✓✓✓	✓✓	✓✓✓
Mica	✓✓	✓✓	✓✓	✓✓	±	±	-
Kaolinite	✓	✓	±	✓	±	±	-
Chlorite	✓	✓	±	±	±	-	-

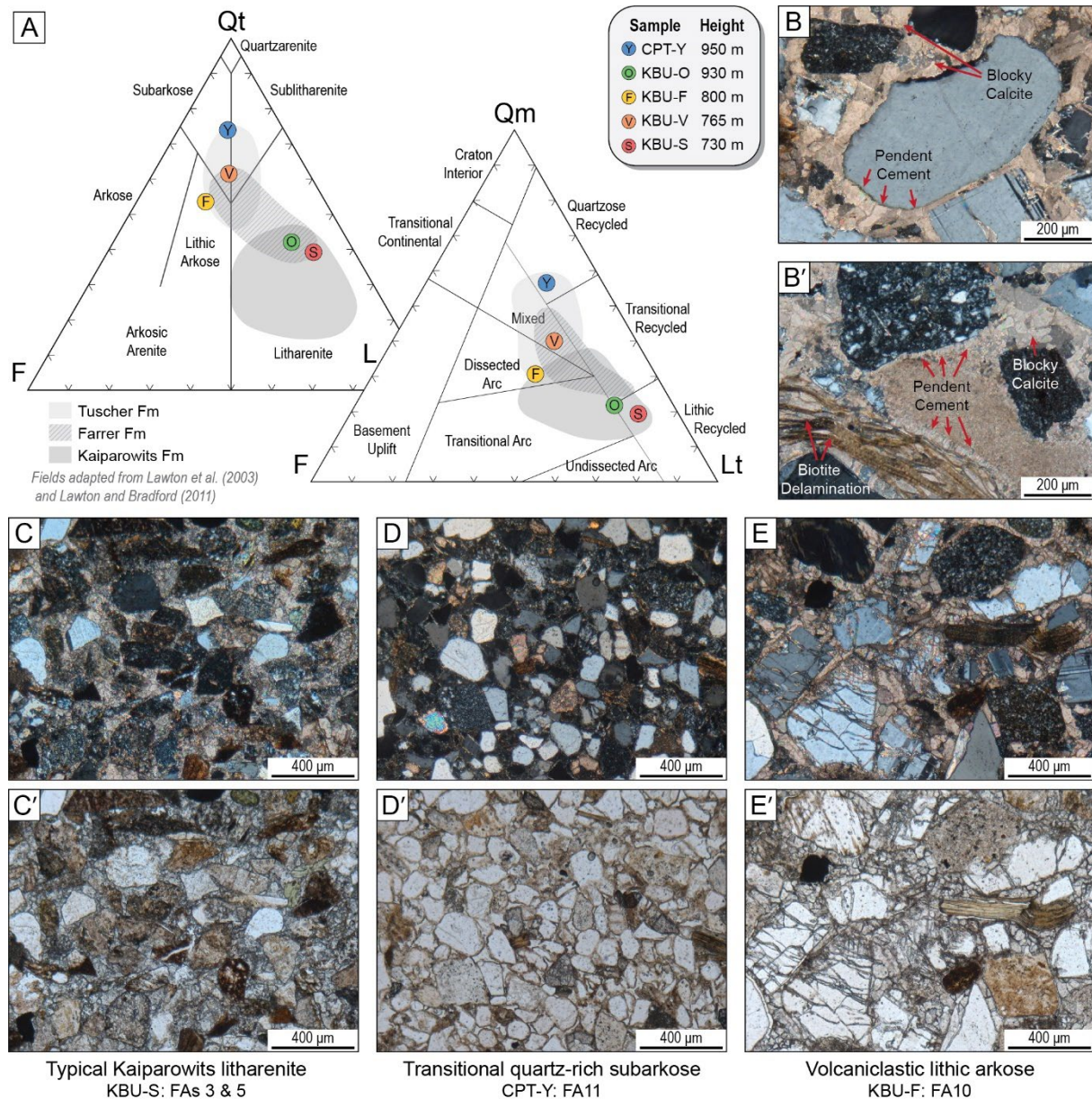
subordinate proportions of mica, illite and kaolinite. The considerable proportion of smectite clay compared to kaolinite and other forms is indicative of relatively rapid burial in an environment frequently subjected to volcaniclastic input. Pedogenic signatures in the Upper Valley Member are typically poorly expressed including weakly developed palaeosol features and small caliche (pedogenic carbonate nodules), along with occasional root traces. Overall, the mudstone mineralogy of the member generally reflects similar characteristics to the other members of the Kaiparowits Formation. It is important to note that the two datasets shown here are not directly comparable as values from Roberts (2007) were measured from the <4 µm fraction whereas this study reports values for >4 µm fractions, which explains the higher concentration of quartz and feldspar in the latter. Nevertheless, general comparisons between the two datasets remain valid.

#### 5.4.3 Sandstone petrography

The five sandstone thin sections examined here represent a variety of common Upper Valley Member lithologies including sandstones from facies associations 3, 5, 10 and 11. Sandstone compositions observed in this study were compared to data from other units of the Kaiparowits Formation and coeval units from Lawton *et al.* (2003) and Lawton and Bradford (2011). Results are summarized in Figure 5.4 and Appendix C.5.3.

Kaiparowits Formation sandstones are typified as litharenites by Lawton *et al.* (2003) and Lawton and Bradford (2011), and a sample from the top of the Powell Point Member at 730 m (KBU-





**Fig. 5.4** Sandstone petrographic summary. A) Point count data displayed in ternary diagrams based on parameters in Lawton et al. (2003). Lithology and provenance fields for each formation were adapted from Lawton et al. (2003) and Lawton and Bradford (2011). B) Cross polar microphotographs of clean calcite cement in a volcaniclastic sandstone (FA10) showing evidence for blocky calcite and subtle pendent cements. C) Cross and plane polar examples of a typical Kaiparowits litharenite (FAs 3 & 5). D) Cross and plane polar examples of a subarkose from the extra-formational conglomerate facies association (FA11). E) Cross and plane polar examples of a lithic arkose from the volcaniclastic sandstone facies association (FA10).

S) in this study matches this assessment. A typical Kaiparowits sandstone found high in the Upper Valley Member at 930 m (KBU-O) also showed a similar composition. These samples feature high proportions of lithic grains (23% and 30% L), particularly volcanic fragments, and fall generally in the lithic recycled provenance field.

In contrast, samples studied from the lower and middle part of the Upper Valley Member out of the massive white sandstone lithofacies (Sv) (KBU-V and KBU-F) illustrate a notable change in sedimentology of the Kaiparowits Formation. Both samples contain < 20% lithic grains (L), up to 5% biotite, and between 20 to 30% feldspar, plotting as subarkose and lithic arkose, respectively. These lie outside of the general provenance range of Kaiparowits Formation sandstones documented by Lawton *et al.* (2003), instead representing a mixed to dissected arc signature (Fig. 5.4).

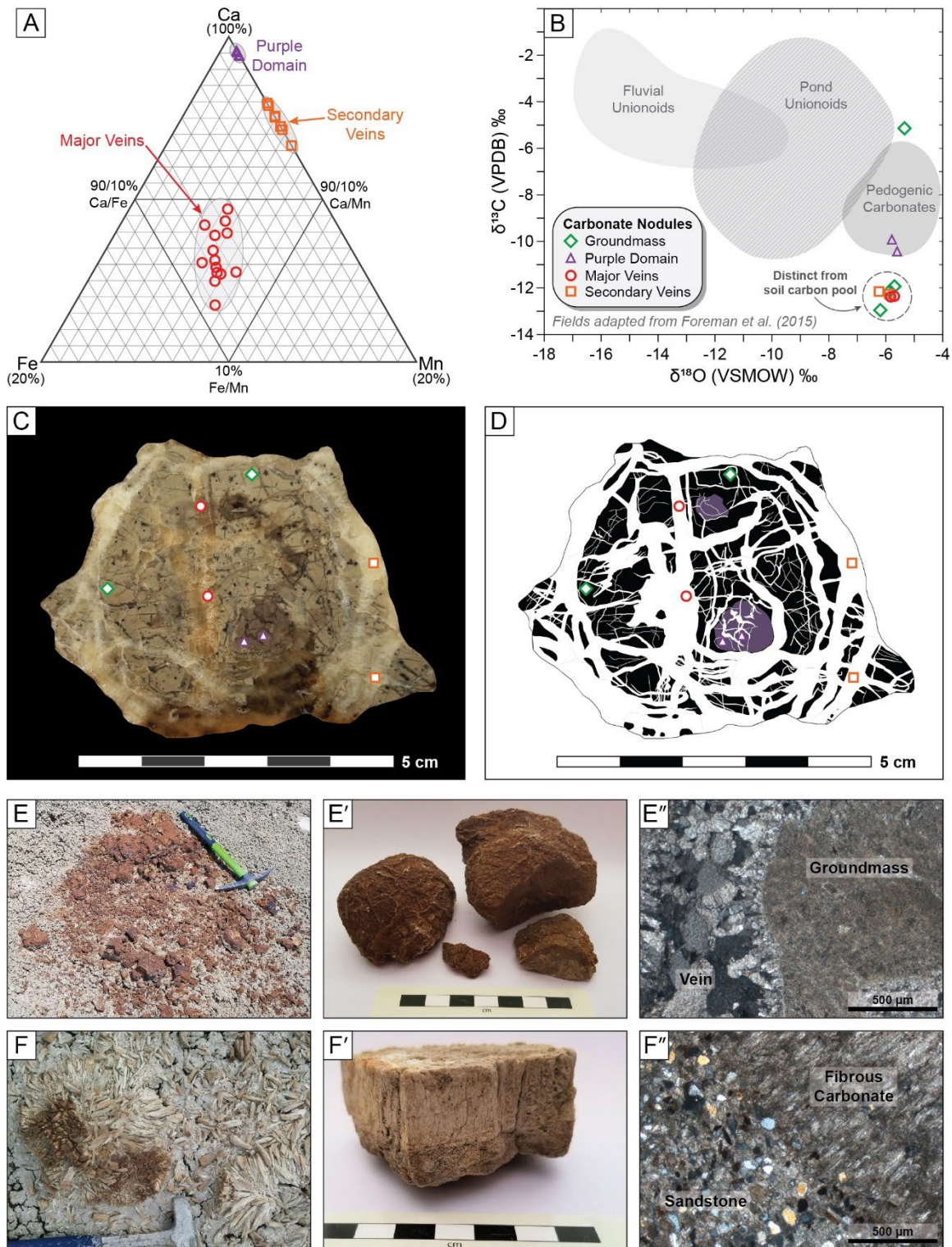
The highest sandstone examined in this study (CPT-Y, 950 m) from a sandstone lens within FA11 (extra-formational conglomerate), also had distinctly different petrology. This sample differs from typical Kaiparowits samples and other Upper Valley Member samples in that it contained a much higher percentage of monocrystalline quartz and total quartz and, unlike all other samples in this study, lacked calcite cement. This sample is classified as a subarkose with a quartzose recycled derivation.

#### 5.4.4 Concretions

One of the most apparent sedimentological differences between the lower members of the Kaiparowits Formation and the proposed Upper Valley Member is related to concretion development. Specifically, fibrous concretions and septarian nodules (Fig. 5.5) are ubiquitous in many parts of the member but are totally absent from the rest of the formation. Typical sandstone concretions of the lower, middle and upper Kaiparowits Formation, composed of Fe-oxides and Fe-sulfides (Roberts and Chan, 2010), are present in the Upper Valley Member, but they are less apparent or abundant than the fibrous concretions and septarian nodules unique to this member. Fibrous carbonate concretions are commonly observed to occur at the boundary between sandstone and mudstone strata and typically displace the host material, wedging apart the bounding rocks. The fibrous texture of these concretions is distinct from septarian nodules and other concretion types in the Kaiparowits Formation and isolated fragments can, at a glance, be mistaken for fossil wood. These fibrous concretions are not observed to occur in the same cluster as septarian nodules.

Septarian nodules are commonly found to contain multiple generations of infilled and barren fractures and are generally spherical despite the fractured and poorly consolidated nature of many concretions. Amber to milky colored calcite veins in these carbonate concretions occasionally exhibit comb-tooth growth textures and euhedral crystal faces in larger veins and cavities. Septarian nodules were observed in a variety of rock types and were found to incorporate the host material. The KBU-M nodule sample studied in detail (Fig. 5.5) was found to contain a purple domain interpreted as an incorporated pedogenic carbonate nodule (caliche) that may have facilitated nucleation of the later septarian concretion. Septarian nodules in the member tend to occur in clusters with poor lateral continuity although the cause of this clustering is not readily apparent. Nodule clusters were observed in one location to be closely associated with a bonebed, where it caused significant post-depositional displacement and breakage of fossilized crocodylian bones.





**Fig. 5.5** Summary of carbonate nodules in the Upper Valley Member. A) Major cation composition of calcite zones within a septarian nodule illustrating discrete phases of concretion formation. B) Oxygen and carbon isotope composition of calcite zones within a septarian nodule compared to data from Foreman et al. (2015). C) Septarian nodule (KBU-M) showing extensive crosscutting calcite veins. Stable isotope sampling locations are indicated (see key in panel B). D) Schematic of a septarian nodule highlighting extensive veining and two purple domains interpreted as incorporated pedogenic carbonate nodules (caliche). E) Septarian nodules in outcrop, hand sample and thin section. F) Fibrous concretions in outcrop, hand sample and thin section.



Semi-quantitative geochemistry of the septarian nodules revealed distinct cation compositions for each domain of calcite (Fig. 5.5, Appendix C.5.4). Chemically distinct calcite veins (amber major veins vs milky secondary veins) are indicative of discrete generations of carbonate mineralization, suggestive of multiple episodes of concretion formation. Geochemically distinct calcite phases in a single concretion also indicates that nodules probably did not experienced later diagenesis; therefore, stable isotopic values should accurately reflect the mineralizing fluid.

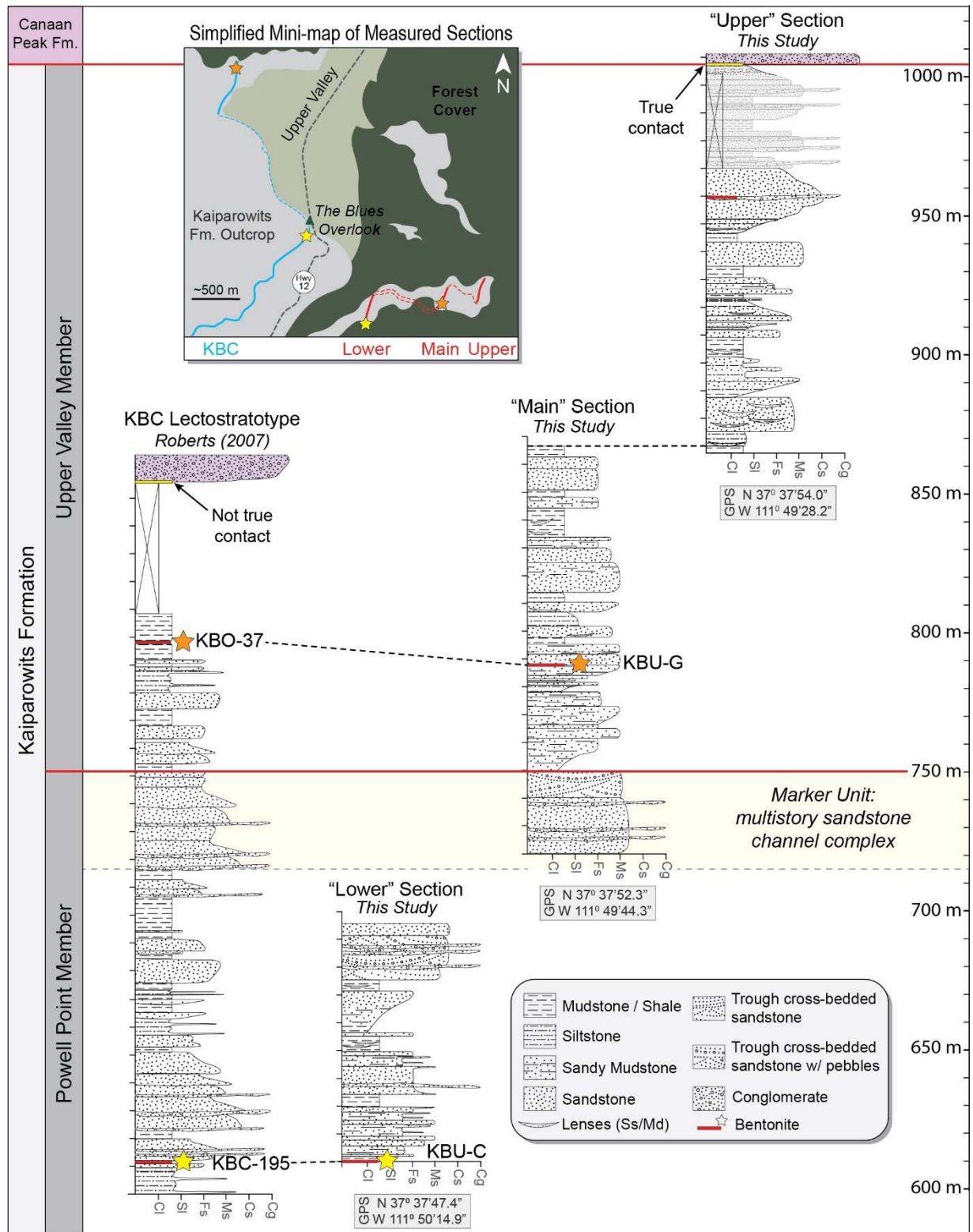
Stable isotope data from Upper Valley Member septarian nodules were compared to Kaiparowits Formation pedogenic carbonates and unionoids from Foreman *et al.* (2015) (Fig. 5.5, Appendix C.5.5). The  $\delta^{18}\text{O}$  values of the mineralizing fluids (calculated using the calcite fractionation equation of Kim and O'Neil, 1997) indicate a strong similarity between all samples in this study with a range of -5.9 to -6.8 ‰ (VSMOW). This range coincides with values reported in Foreman *et al.* (2015) for local meteoric precipitation, suggesting that fluids may have been sourced from low elevation rain relatively close to the continental seaway based on precipitation-dependent fractionation models (Fricke *et al.* 2010; Foreman *et al.* 2015). This is interpreted to indicate that nodule formation occurred before final seaway regression, early in the diagenetic history of the unit. The  $\delta^{13}\text{C}$  values measured in this study show a higher degree of dispersion than the  $\delta^{18}\text{O}$  results. Two data points match the soil carbon pool described by Foreman *et al.* (2015). These two sub-samples were collected from material interpreted as an incorporated pedogenic nodule. Aside from one significant outlier, the remaining seven data points cluster tightly between -11.8 and -12.8 ‰ (VPDB); notably different to the pedogenic carbonates.

In summary, septarian nodules from the Upper Valley Member are interpreted to have formed from local meteoric water prior to uplift-related seaway regression (based on  $\delta^{18}\text{O}$  values), but not at the surface as pedogenic carbonates (based on  $\delta^{13}\text{C}$  values). The characteristic fractures of the septarian nodules may be associated with wetting and drying during concretion formation. Coupled with evidence of chemically distinct calcite phases, this is interpreted to represent short-term water table fluctuations that point towards climatic seasonality in the area during the latest Campanian to early Maastrichtian. Combining all factors, septarian nodules in the Upper Valley Member are interpreted to have formed in the shallow subsurface shortly (in geological terms) after host rock deposition.

## 5.5 Lithostratigraphy

### 5.5.1 The Upper Valley Member

This study proposes the formal establishment of a new member of the Kaiparowits Formation, defined herein as the Upper Valley Member. A change in lithological character at the top of the Kaiparowits Formation has been noted by previous workers including Lohrengel (1969) and Roberts (2007); however, the presence of a definable member was not recognized due to cover and poor exposure of the top of the Kaiparowits Formation in its type area. Indeed, the more extensive but remote outcrops of the

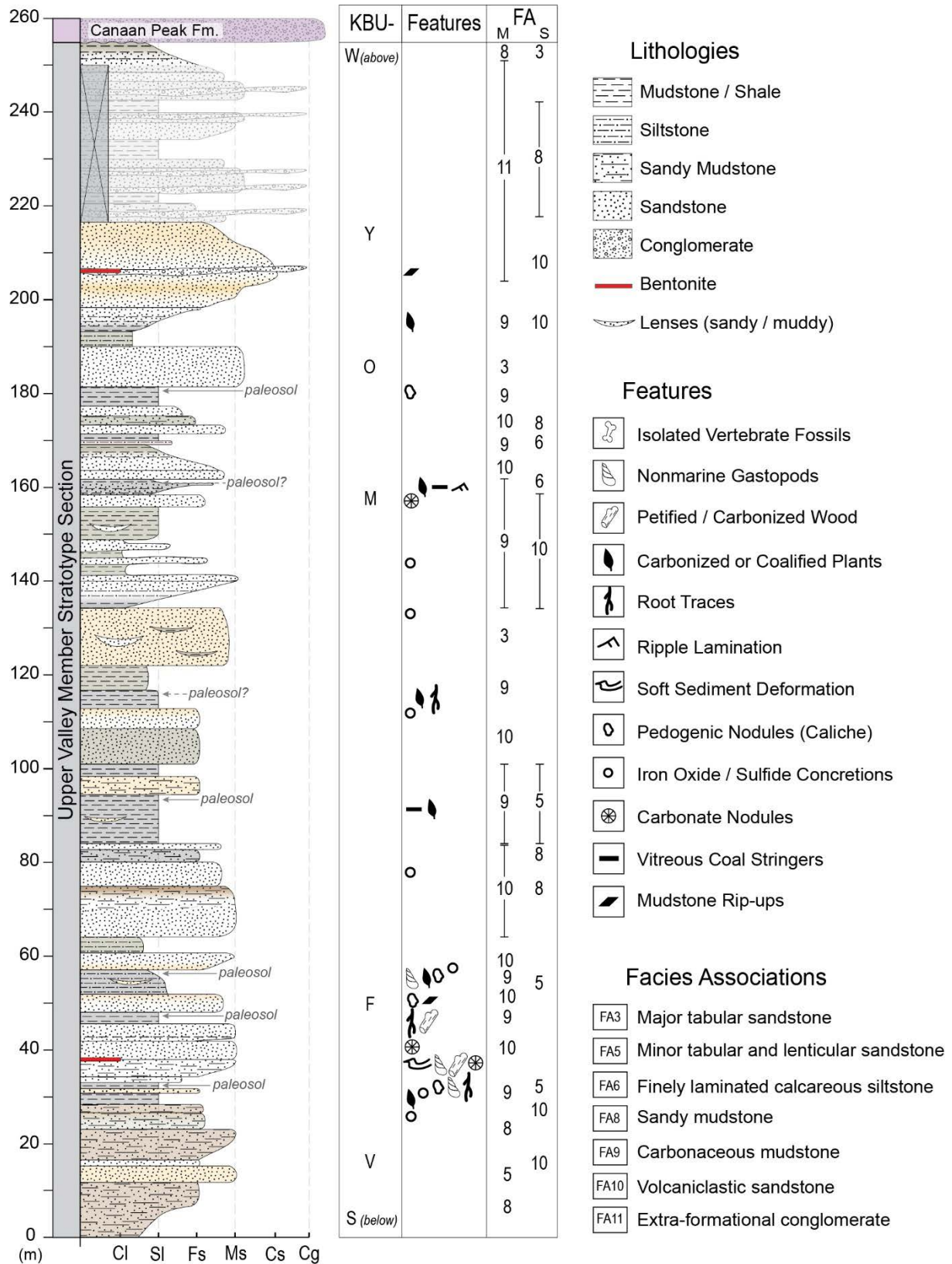


**Fig. 5.6** Correlated stratigraphic sections linking the Upper Valley Member type area to the KBC lectostratotype in The Blues area. Three measured sections reported here, titled Lower, Main and Upper, were measured in the vicinity of a headwater tributary of Henryville Creek. The KBC section was adapted from Roberts (2007). The inset mini-map shows the relative location of each measured section where the dashed line shows correlation between closely related sections and paired bentonite marker horizons are indicated with color-coordinated stars (see also Fig. 5.1). Latitude and longitude GPS data are reported in WGS84.

uppermost Kaiparowits Formation are found within isolated exposures on the heavily forested western flanks of Canaan Peak, which remained largely unstudied until now. Member status is merited for the uppermost strata of the Kaiparowits Formation based on the distinct transition in lithological character that is observed between this new capping unit and the underlying Powell Point Member as well as with the overlying Canaan Peak Formation. The name “Upper Valley” is derived from the mapped region where the unit crops out to the north and south of Highway 12 (Figs. 5.1, 5.2). The regional expression of the Upper Valley Member extends from the southeast flank of Powell Point to the southern flank of Canaan Peak (~15 km) and eastward from the top of The Blues for about 6 km through Upper Valley. It is mostly eroded or poorly exposed to the northside of Upper Valley between Powell Point and the Dutton monocline; however, it is reasonably well exposed in places along the south side of Highway 12 in Upper Valley. The thickest and best exposures of the unit are found in exceptional, isolated exposures hidden within Ponderosa pine forests on the west side of Canaan Peak. The type area for the Upper Valley Member is located approximately 1.5 km southeast of The Blues Overlook on Highway 12 on the northwest flank of Canaan Peak (Fig. 5.1, 5.2). Correlated stratigraphic sections link the Upper Valley Member type section, which begins at 37°37'52.8"N, 111°49'43.2"W (WGS84), to the KBC lectostratotype section of Roberts (2007) (Figs. 5.6, 5.7).

The basal contact of the Upper Valley Member with the Powell Point Member lies directly above a laterally extensive amalgamated sandstone channel complex that defines the top of the latter unit (Figs. 5.6, 5.8). This ~45-meter-thick multistory sandstone complex is a regionally extensive marker horizon. The basal facies of the Upper Valley Member are defined by pale gray-green mudstones that appear to conformably overlie the major sandstone unit at approximately 750 m above the base of the formation. The contact is easily recognized in satellite photos, which show a distinct color change from blueish-gray hues of the Powell Point Member to pale gray hues of the Upper Valley Member (Fig. 5.1). The uppermost 110 m the KBC stratotype section that was previously defined by Roberts (2007) as part of the upper unit of the Kaiparowits Formation, consisting of a mostly covered interval, was reassigned to the Upper Valley Member thus reducing the thickness of Roberts' (2007) upper unit to *ca* 220 m. The measured thickness of the Upper Valley Member is 255 m, which brings the revised total thickness of the Kaiparowits Formation to 1005 m (Figs. 5.6, 5.7).

The top contact of the Upper Valley Member with the overlying Canaan Peak Formation is somewhat less conspicuous because of scree covering the boundary in most places. The formation contact has previously been described as a significant erosional unconformity with a subtle angular offset due to pre-Canaan Peak Formation development of the Table Cliff syncline (Bowers, 1972; Little, 1995; Roberts, 2007). This study finds that the top of the Upper Valley Member of the Kaiparowits Formation exhibits a surprising gradational transition into the Canaan Peak Formation. An erosional disconformity does mark the contact in the Upper Valley Member type area (Fig. 5.8); however, the bedding relationships provide little clear evidence of an angular unconformity. The presence of a series



**Fig. 5.7** The Upper Valley Member stratotype section composed of a compilation of the “Main” and “Upper” sections in Figure 5.6. Additional information includes stratigraphic height of key samples, notable features and the approximate extent of major and subordinate facies associations.



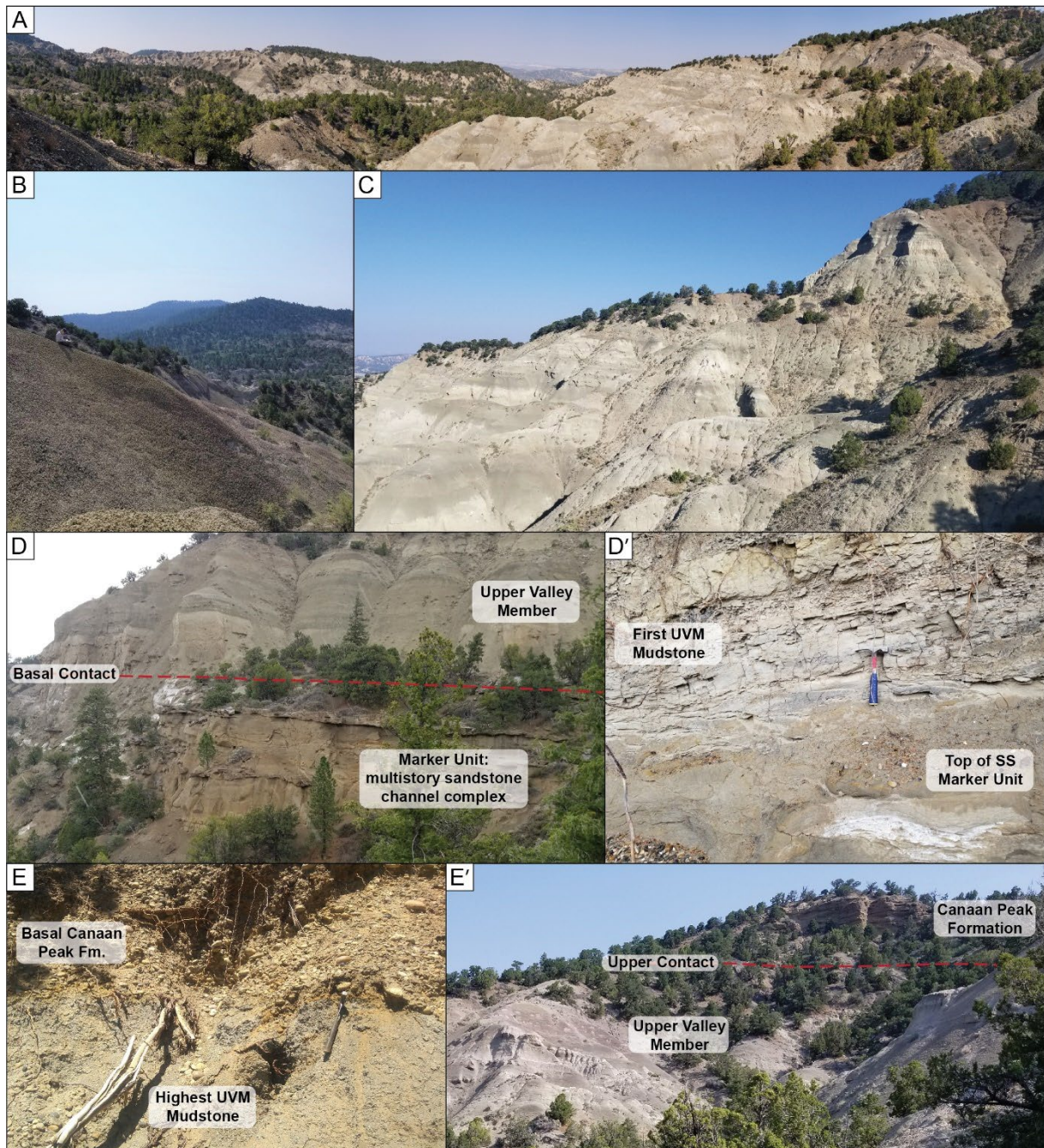
of thin (10 - 70 cm), Canaan Peak-like pebble conglomerate lenses (FA11) that interfinger with typical Kaiparowits mudstone and sandstone facies within the top 50 m of the Upper Valley Member is considered highly significant. These previously undocumented lenses, which have similar compositions and textures to the much thicker and coarser-grained conglomerates of the Canaan Peak Formation, demonstrate the gradational nature of the Kaiparowits-Canaan Peak transition, and also show that the tectonic and sedimentological regimes of Canaan Peak time actually initiated during deposition of the Upper Valley Member. This transition zone at the top of the Upper Valley Member also displays a distinctive shift in detrital zircon provenance and sandstone petrography that begins at approximately 955 m above the base of the formation and continues all the way up to the erosional contact with the Canaan Peak Formation. It remains unclear whether or not angular discordance between the two formations is present in the member type area but because of the gradational nature of the contact it seems more likely that this boundary represents a minor disconformity rather than a major tectonic angular unconformity.

#### 5.5.2 Member field description

The Upper Valley Member of the Kaiparowits Formation in its type locality is generally characterized by massive, muddy sandstones interspersed with sandy, bentonitic and organic-rich mudstones. Strata from the member are typically poorly indurated and friable, requiring considerable excavation to reveal fresh surfaces for observation. Slumping was noted both in the field and using satellite imagery, particularly in exposures below Powell Point and southeast of Canaan Peak. The member has a generally lighter color (pale gray) compared to the rest of the Kaiparowits Formation making it easily recognizable from a distance (Fig. 5.8) and in satellite imagery (Fig. 5.1). The surface expression of the strata is comparable to the middle Kaiparowits Formation in that both are characterized by highly dissected badland topography showing distinctive bedding and prominent bentonitic mudstone units. This unit is recessive above the massive sandstone at the top of the Powell Point Member, and appears to be mud-dominated from afar, although closer inspection reveals a higher proportion of poorly cemented sandstone than mudstone at a 3:2 ratio.

The depositional environment of the Upper Valley Member is interpreted to have been a wet, warm fluvial floodplain system with oxbow ponds and small lakes transected by suspended load, meandering or anastomosing rivers. The high abundance of carbonized plant fragments and organic-rich mudstones suggest a well vegetated ecosystem consistent with the findings of Miller *et al.* (2013) for the rest of the Kaiparowits Formation. The presence of numerous microfossils with aquatic and terrestrial vertebrate and invertebrate fragments, teeth and shells, isolated macro-vertebrate bones and rare macro-vertebrate bonebeds throughout the member indicate similarly productive ecosystems to those documented in the rest of the Kaiparowits Formation (*e.g.*, Eaton and Cifelli, 1988; Gates and Sampson, 2007; Gates *et al.*, 2010; Getty *et al.*, 2010; Sampson *et al.*, 2010, 2013a, 2013b; Carr *et al.*, 2011; Zanno





**Fig. 5.8** Field photographs showcasing the new member. A) Panoramic photo of the Upper Valley Member type area. B) Common volcanic-rich mudstones that have shrink and swell “popcorn” weathered textures but do not represent pure bentonite. C) General outcrop of the Upper Valley Member showing the steeply incised, highly friable nature of the strata and periodic palaeosol (dark) horizons. D) Basal contact of the Upper Valley Member with the underlying Powell Point Member from a distance and closeup. E) Contact between the Upper Valley Member of the Kaiparowits Formation and the overlying Canaan Peak Formation closeup and from a distance.

*et al.*, 2011; Miller *et al.*, 2013; Wiersma and Irmis, 2018). Although a detailed survey of the paleontology of this unit was not conducted as part of this study, the presence of diagnostic ceratopsian, hadrosaur and theropod dinosaur bones was noted, along with abundant turtle shell, crocodilian bones and fish teeth. Mollusks are also abundant, including both gastropods and bivalves. It is difficult to

estimate the richness of fossils in this unit, but it appears to be comparable to other parts of the formation. A wet palaeolandscape is also indicated by the presence of iron-sulfide-replaced organic matter (typically wood) as well as iron concretions and sandstone stains (Roberts and Chan, 2010). Weakly developed palaeosol horizons observed throughout the member at frequent intervals show similar features to those observed in the lower units of the Kaiparowits Formation (*e.g.*, Roberts, 2007) including small pedogenic carbonate nodules (caliche) and poorly established soil profiles that document some degree of seasonality in precipitation. Along with typical floodplain deposits such as emergent ponds and oxbow lakes, it appears as though larger lacustrine deposits developed higher up in the member which may indicate changes in drainage on the palaeolandscape.

The presence of lateral accretion elements associated with channel sandstones suggest that meandering style, suspended load rivers were present (Roberts, 2007). In addition, many channel sandstones contained a significant component of volcaniclastic detritus (*e.g.* euhedral biotite phenocrysts) while many of the mudstones in the member are highly bentonitic, indicative of significant input of volcanic ash into the depo-system. Despite a considerable amount of volcanogenic material observed in the member, pure bentonite horizons (devitrified volcanic ash beds) are puzzlingly rare. Another unique feature observed in the member were abundant carbonate nodules. Although iron oxide and pyrite concretions were also present, medium to large carbonate concretions of fibrous and septarian variants were far more common and are unique to the Upper Valley Member, which likely reflects a change in the depositional system. The exact mechanism for the change in concretion types remains unknown but, nevertheless, they provided a useful tool for identifying strata from the Upper Valley Member.

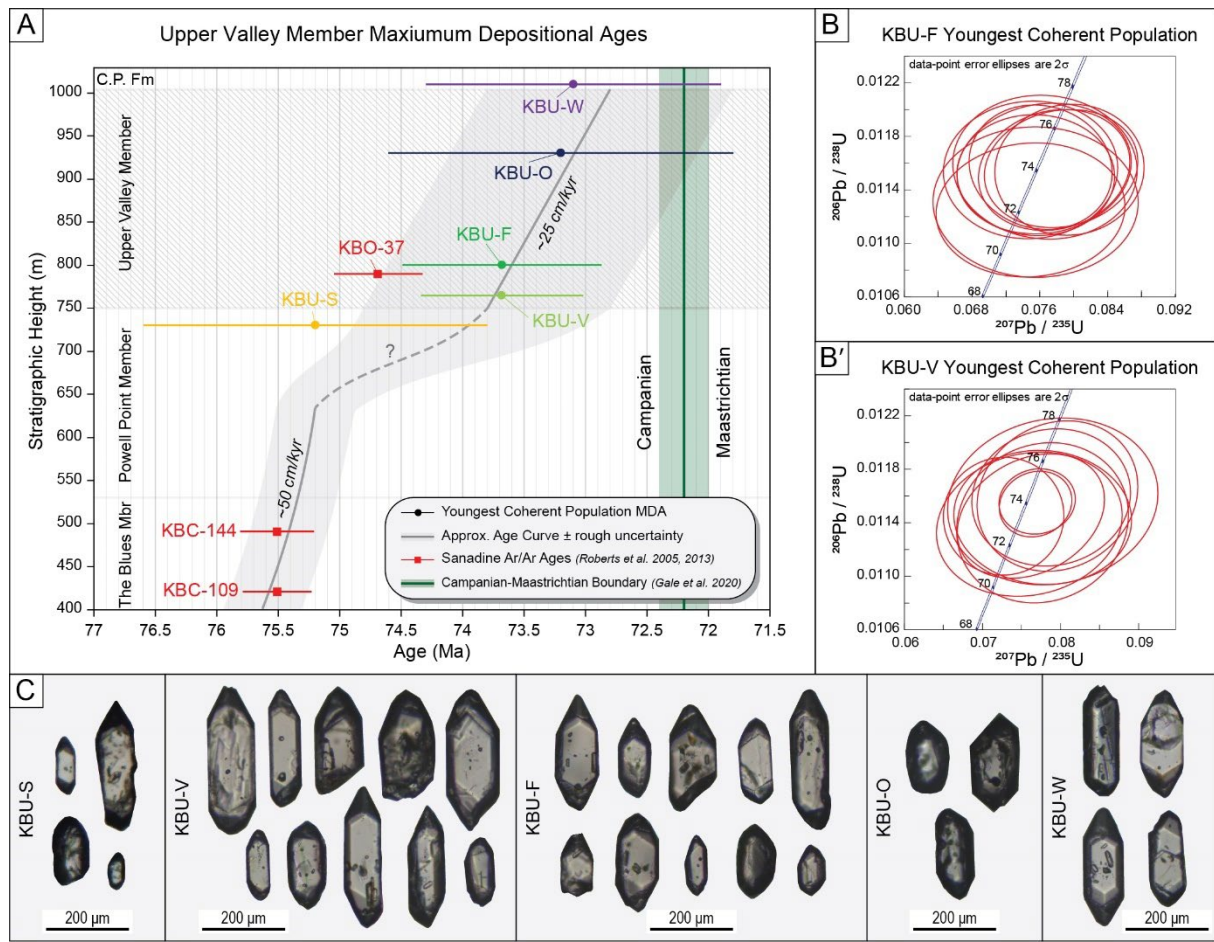
## 5.6 Detrital zircon geochronology

### 5.6.1 Maximum depositional age

The maximum depositional age (MDA) of the Upper Valley Member was constrained using detrital zircon analysis of five sandstone samples from the member type area. The only existing temporal constraint in the member is a  $^{40}\text{Ar}/^{39}\text{Ar}$  absolute age from a single bentonite at 790 m above the base of the formation (KBO-37, Roberts *et al.* 2005, 2013). Unpublished high-precision U-Pb TIMS data for this bentonite suggests subtle reworking of the ash horizon (J. Ramezani, per. com.); therefore, this  $^{40}\text{Ar}/^{39}\text{Ar}$  age is here treated as a maximum depositional age.

All detrital zircon age data in this study were subjected to criteria including high degree of concordance (95%) and analytical certainty (95% at  $2\sigma$ ) to reduce the impact of lead loss affected grains, an issue previously identified by Lawton and Bradford (2011). Data reduction using the 5% criteria (above), as opposed to the more commonly employed 10% discordance cut-off, had minimal impact on the youngest single grain age and youngest coherent population (YCP) weighted mean age for three of





**Fig. 5.9** Approximate age of Upper Valley Member strata based on detrital zircon U-Pb maximum depositional ages (MDAs) determined using youngest coherent populations (YCPs). A) Estimated age curve for the Upper Valley Member, approximating the basal and upper contacts at 73.8 and 72.8 Ma respectively within a  $\sim 1$  Myr margin. B) Concordia diagrams of the youngest grain ages from the two volcanoclastic sandstones (KBU-F and KBU-V) illustrating highly clustered, highly concordant ages. C) Transmitted plane-polar light microphotographs of zircon grains that contributed to the YCP weighted mean age for each sample (stratigraphic order left to right) illustrating excellent crystal features in many of the youngest grains, particularly those from the two volcanoclastic sandstones KBU-V and KBU-F. [Note: Although a refined version of this data was presented in Chapter Four, the version presented here is consistent with Beveridge et al. (2020) published in *Cretaceous Research*].

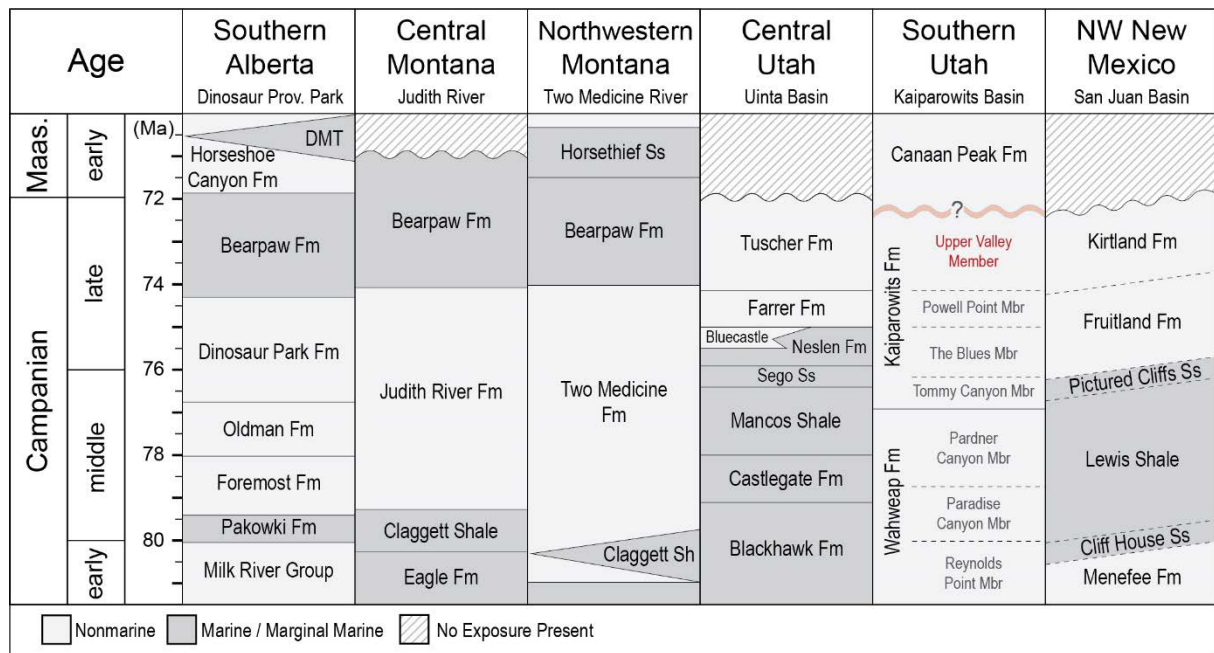
the five samples in this study (Appendix C.5.6). The YCP ages of the other two sandstones (KBU-V and KBU-F), both of which were dominated by Campanian grains, were older by as much as a million years when calculated using the 5% criteria as compared to 10%. This means that either those two samples exhibited a very subtle degree of lead loss which was subsequently addressed by using tighter vetting criteria, or the member may be even younger than suggested by the MDA's reported here. Interestingly, no anomalously young grains were present after vetting with the 5% criteria, meaning the youngest single grain in each sample contributed to the YCP weighted mean age. This finding is a good indicator that the lead loss problem noted by Lawton and Bradford (2011) has been effectively addressed in this study.

**Table 5.4** Summarized maximum depositional age data. All data shown here exclude grain ages with >5% discordance and >5%  $2\sigma$  analytical uncertainty. The number of grains ( $n$ ) in the youngest coherent population was capped at ten grains where no clear break was observed. All error is reported at  $2\sigma$  uncertainty. Stratigraphic height is reported as meters above the base of the Kaiparowits Formation.

Sample	Strat. Height	Youngest Single Grain	Youngest Coherent Population		
Name	(m)	Age (Ma)	Weighted Mean Age (Ma)	n	MSWD
KBU-W	1010	72.3 $\pm$ 2.0	73.1 $\pm$ 1.2	4	0.43
KBU-O	930	72.6 $\pm$ 2.0	73.2 $\pm$ 1.4	3	0.51
KBU-F	800	72.1 $\pm$ 2.6	73.68 $\pm$ 0.81	10	0.3
KBU-V	765	73.0 $\pm$ 2.8	73.68 $\pm$ 0.66	10	0.19
KBU-S	730	74.3 $\pm$ 3.3	75.2 $\pm$ 1.4	4	0.15

The temporal range of the Upper Valley Member was approximated based on MDAs that were calculated using YCP weighted mean ages, where each YCP age consisted of at least 3 and no more than 10 grain ages (Fig. 5.9, Table 5.4). The basal and upper contacts of the Upper Valley Member are approximated to be 73.8 and 72.8 Ma respectively, albeit within a rough confidence of around 1 Myr. It is important to note that this approximation using detrital zircon MDAs is here used only as an estimate of the depositional age; more precise approaches such as U-Pb TIMS dating or magnetostratigraphy are required to confirm the accuracy of this interpretation.

The most significant implication of these findings concerns the stratigraphic placement of the Campanian-Maastrichtian stage boundary within strata of the Kaiparowits Plateau. As illustrated in Figure 5.9, the Campanian-Maastrichtian boundary occurs at  $72.2 \pm 0.2$  Ma (Gale *et al.*, 2020). Based on maximum depositional ages and uncertainties reported here, it is possible that the boundary between these two significant geochronological stages is preserved in the strata of the Upper Valley Member. Conversely, if the stage boundary is not within the member and since lithostratigraphic interpretations in this study suggest the contact between the Kaiparowits and Canaan Peak Formations is largely gradational, the stage boundary may instead be preserved in the basal strata of the Canaan Peak Formation. If this is so, a late Campanian age for the basal Canaan Peak Formation proposed by Bowers (1972) may be plausible, thus explaining the reported presence of unworked Campanian palynomorphs in that unit (Bowers, 1972). In either situation, this study highlights that, between the Wahweap, Kaiparowits and Canaan Peak formations, the Kaiparowits Plateau contains a nearly continuous record of strata throughout the entire Campanian stage and, indeed, one of the most continuous fossiliferous Campanian-age terrestrial successions in the world. These framework detrital zircon ages suggest that future chronostratigraphic work on the Kaiparowits Formation holds great promise for establishing even finer-scale temporal resolution of this part of the stratigraphy.



**Fig. 5.10** Regional correlation across key fossil-bearing Campanian units in the Cordilleran foreland basin. The temporal gap between the Kaiparowits and Canaan Peak formations is here represented as a lower order unconformity based on the largely gradational transition between the units representing little to no missing time. Geochronological framework is based on works by Roberts et al. (2005, 2013), Lawton and Bradford (2011), Fassett and Heizler (2017) and Pecha et al. (2018). [Note: Although a refined version of this data was presented in Chapter Four, the version presented here is consistent with Beveridge et al. (2020) published in *Cretaceous Research*].

### 5.6.2 Regional correlation

Correlation of the Upper Valley Member with contemporaneous units in adjacent sub-basins highlights the importance of documenting this new member of the Kaiparowits Formation. Based on the latest Campanian age assigned to the Upper Valley Member, temporally comparative terrestrial units include the Tuscher Formation in central Utah and the Kirtland Formation in the western portions of the San Juan Basin in north-western New Mexico (Fig. 5.10). Farther afield, the Upper Valley Member is broadly contemporaneous with the marine Bearpaw Formation in central and north-western Montana and across southern Alberta (Fig. 5.10). The age of the Upper Valley Member of the Kaiparowits Formation is generally consistent with the concept of a “Kirtlandian” “land vertebrate age”, which was originally proposed by Sullivan and Lucas (2006) to fill a temporal gap between the Judithian and Edmontonian land mammal ages. Little is yet known about the taxonomy of vertebrate fossils from this interval, and careful exploration of these strata for new fossils is necessary to test the utility of the previously proposed “Kirtlandian” land mammal age.

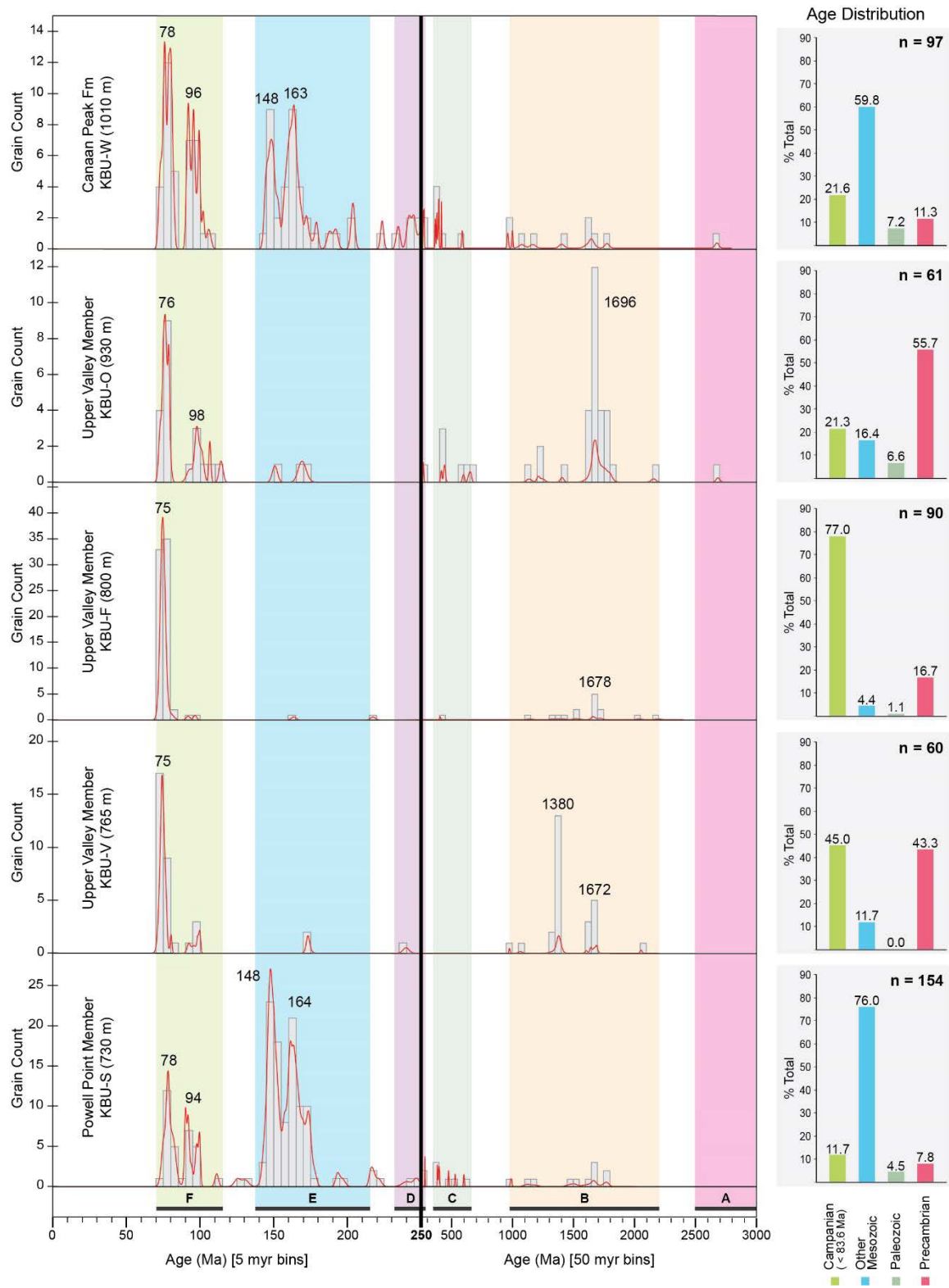


### 5.6.3 Detrital zircon provenance

Detrital zircon (DZ) age data were also used to investigate the provenance of strata from the Upper Valley Member (Fig. 5.11). Overall, the data show a high degree of variation between all samples in this study. Kolmogorov-Smirnov quantitative comparison found that none of the five samples are statistically similar, which implies that there was a considerable degree of drainage and source variation (Appendix C.5.7). Distinct shifts in detrital zircon provenance were observed across the basal and upper boundaries of Upper Valley Member, which reflects sedimentological change and signposts regional tectonic events.

Detrital zircon data from the amalgamated multistory sandstone channel complex (KBU-S) immediately below the Upper Valley Member is comparable to other DZ suites from the Powell Point Member of the Kaiparowits Formation. The age spectrum closely resembles that of the upper Kaiparowits Formation sample 04JL05 from Larsen *et al.* (2010), which was described as having a transitional to lithic recycled source from an arc dominated terrain with minor influence from the Sevier orogenic belt (Lawton and Bradford, 2011). Findings herein agree with previous interpretations for the Powell Point Member inferred to have a southwest to western sediment source.

The detrital zircon age spectra from Upper Valley Member sandstones are dominated by Campanian grains and, for the first time in the formation, show a distinct absence or under-representation of the Jurassic population. The high proportion of near syn-sedimentary aged grains is interpreted to represent flooding of the depositional system with volcaniclastic material that completely overwhelmed the sediment supply for parts of the member. The source of Campanian grains in the Kaiparowits Formation and adjacent sub-basins is tentatively attributed to the Laramide porphyry copper province (LPCP) in the Mogollon region of southern Arizona, southwestern New Mexico and northern Sonora (Roberts *et al.*, 2005; Lawton and Bradford, 2011; Pecha *et al.*, 2018). This region of intra-continental volcanism, which initiated during the Campanian, is located to the south of the Kaiparowits Plateau and is proposed as the primary source terrain for the Upper Valley Member. A specific terrain within the LPCP is difficult to identify, although previous studies have suggested the Tarahumara assemblage in Sonora as the source of aerially-derived Campanian volcanic grains throughout southern Laramidia (Lawton and Bradford, 2011). Considering that the volcaniclastic material from the Upper Valley Member is interpreted as dominantly fluvially derived, the Tarahumara assemblage may not be the source for these strata due to the Border Rift system divide that would have impeded fluvial transport across this physiographic feature and may also have supplied Jurassic-aged grains (Fig. 5.12) (Lawton and Bradford, 2011; Pecha *et al.*, 2018). Western source terrains within the Sevier Orogenic Belt and the Cordilleran arc probably did not contribute significantly to strata in the member as indicated by the absence of notable Jurassic, Paleozoic and Mesoproterozoic (Grenville) zircon populations (*e.g.*, Dickinson *et al.*, 2012). Conversely, the stratigraphically highest sample from



**Fig. 5.11** Detrital zircon age spectra for five sandstones from the Upper Valley Member type area including below the base of the member (KBU-S) and above the member at the base of the Canaan Peak Formation (KBU-W). Populations are labelled A to F (i.e., Lawton and Bradford, 2011) and color coded generally according to the International Chronostratigraphic Chart. Grain age distribution is presented in four groupings: Campanian (< 83.6 Ma), Mesozoic (excluding the former grouping), Paleozoic and Precambrian. Note that the x-axis scale changes at the Permian-Triassic boundary (251.9 Ma) to highlight younger populations.

the Upper Valley Member shows a slightly broader spectrum of ages which is interpreted to indicate a degree of mixing of sources between volcaniclastic dominated and other terrains up-section.

A prominent Jurassic population is reported in coeval strata in adjacent sub-basins including the Farrer and Tuscher formations in the Uinta Basin (Lawton and Bradford, 2011) and the Fruitland and Kirtland formations in the San Juan Basin (Pecha *et al.*, 2018). The paucity of Jurassic grains in the Upper Valley Member compared to coeval units indicates that the source terrain for the member is largely unique to that of adjacent sub-basins, most closely resembling that of the Kirtland Formation reported by Pecha *et al.* (2018), which was interpreted to have a Mogollon derivation (Reference subset M of Dickinson *et al.*, 2012). Proterozoic grains with peaks around 1675 Ma and 1380 Ma in all Upper Valley Member samples are attributed to the Yavapai-Mazatzal provinces (~1.8 - 1.6 Ga) and a ~1.4 Ga magmatic province; both of which occur south of the study area (Lawton and Bradford, 2011; Laskowski *et al.*, 2013; Pecha *et al.*, 2018).

The DZ age spectrum for the basal Canaan Peak Formation (KBU-W) represents a marked change from the underlying Upper Valley Member but is strikingly similar to the rest of the Kaiparowits Formation (Lawton and Bradford, 2011). The sandstone sample from the basal Canaan Peak Formation illustrates a significant resurgence in the Jurassic grain population where Mesozoic ages, other than Campanian, constitute the majority of total grain ages at 60%. The detrital zircon age spectra reported here is unique to that of the Canaan Peak Formation sample 05JL05 (220 m above base of C.P. Fm.) reported by Larsen *et al.* (2010) and is unlike any other latest Campanian to Maastrichtian units from either Lawton and Bradford (2011) or Pecha *et al.* (2018). The sediment source for the basal Canaan Peak Formation is interpreted to be either similar to that of Powell Point Member of the Kaiparowits Formation (arc-dominated with some degree of input from the Sevier Orogenic Belt) or alternatively from recycling of strata comparable to the Powell Point Member caused by shedding from local uplifts (Roberts, 2007; Larsen *et al.*, 2010). In either case, the source is also mixed with far travelled polymictic clasts, which may also contribute a Sevier DZ signature to the spectrum (Schmitt *et al.*, 1991).

### **5.7 Tectonic implications**

Strata from the Upper Valley Member document a significant provenance shift and change in sedimentology within the Kaiparowits Formation. This change is highlighted by the total absence of the previously dominant Jurassic zircon population, a subtle increase in Proterozoic grains, and flooding of the zircon spectra by near syn-sedimentary latest Campanian grains, which is coincident with the introduction of distinctive, white volcaniclastic sandstones. These changes are interpreted to reflect some degree of palaeo-drainage rearrangement related to the combined intensification of proximal volcanism and emergence of Laramide uplifts which ultimately partitioned the southern portion of the Cordilleran Foreland Basin into isolated, internally draining sub-basins beginning around this time (Fig. 5.12).

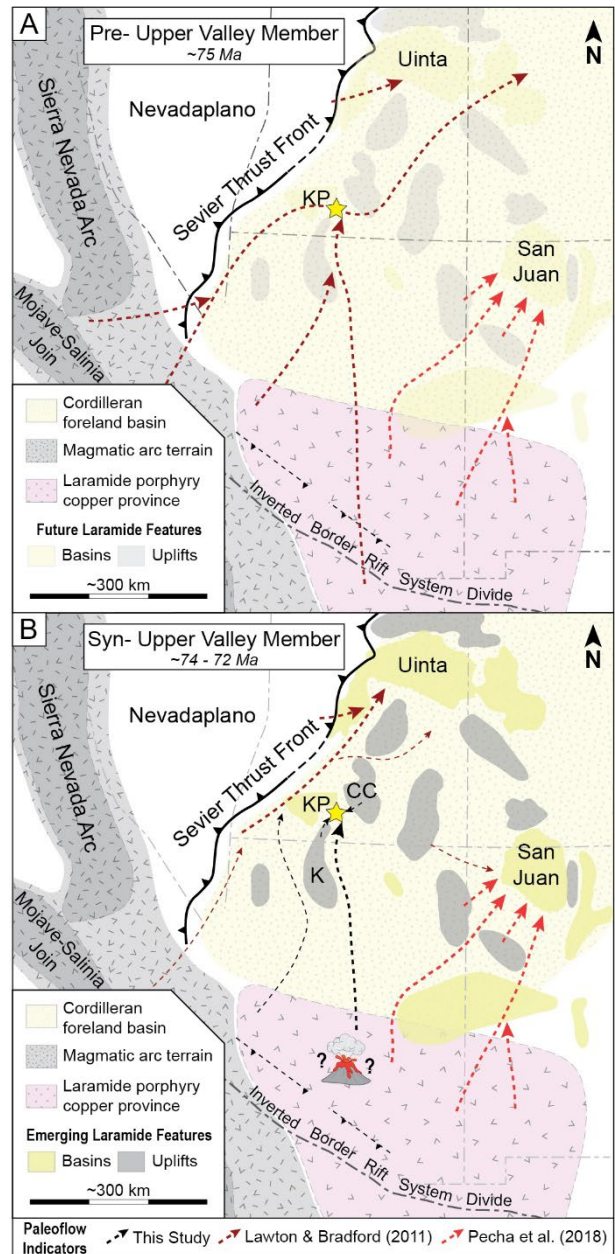
The sharp sedimentological and provenance changes at the base of the Upper Valley Member indicates either missing time, represented by an unconformity, or a sudden change in sediment source caused by a significant tectonic event. Although Bowers (1972) reported a possible unconformity at the approximate level of the base of the Upper Valley Member, no other studies, including this one, find lithological evidence (*e.g.*, an erosional surface) indicating a significant depositional break. On the other hand, maximum depositional ages for upper Kaiparowits Formation sandstones reported herein suggest that a short hiatus or unconformity between the Powell Point and Upper Valley members is plausible (Fig. 5.9). Finer temporal constraint and further field observations are required to examine this possibility.

The rapid shut-off of Jurassic sediment sources is particularly interesting for late Campanian strata from this area. A substantial Jurassic zircon population typifies the rest of the Kaiparowits Formation provenance and has been reported from most other sedimentary units of this age in southern Laramida (*e.g.*, Jinnah *et al.*, 2009; Larsen *et al.*, 2010; Lawton and Bradford, 2011; Dickinson *et al.*, 2012; Pecha *et al.*, 2018). This suggests that a drainage change was initiated at this time that diverted previous river systems from long-lived arc or Sevier sources away from the Kaiparowits Basin (Fig. 5.12) in favor of a highly localized sediment source. During deposition of the lower part of the Upper Valley Member, it appears as though drainage into the basin was restricted almost entirely to a localized source area inferred to have been within the LPCP in the Mogollon region directly south of the study area. An increase in Jurassic and other grain ages higher in the Upper Valley Member, illustrated by a broader spectrum of grain ages in Figure 5.11 (KBU-O), is interpreted to represent either a return to previous drainage patterns or a transition to sediment recycling from local uplifts as proposed for coeval strata in adjacent basins (Lawton and Bradford, 2011; Pecha *et al.*, 2018).

The cause of the shift in sedimentology and provenance in the Upper Valley Member is unclear; however, the suspected cause is a rearrangement in basin drainage due to the emergence of Laramide-related uplifts and initiation of basin partitioning related to Laramide orogenesis in the latest Campanian combined with the escalation of proximal volcanism. Abrupt onset of volcanism without other palaeo-drainage changes is, at first glance, the simplest explanation; however, it does not account for the counterintuitive increase in Proterozoic zircons despite the significant decrease in Jurassic grains. This leads us to consider that the change in sedimentology may have been a combination of magmatic and tectonic factors. Streams flowing out of arc and Sevier source terrains from which Jurassic, Paleozoic and Mesoproterozoic (Grenville) aged grains were previously sourced, were cut off from the area during deposition of the Upper Valley Member potentially due to local uplifts such as the Kaibab and Circle Cliffs uplifts. These emerging physiographic features may have deflected western and southwestern sources away from the actively depositing region of the Kaiparowits Basin as illustrated in Figure 5.12 which shows these streams to be redirected along the edge of the Sevier thrust front in a northward flow direction.

Reintroduction of a broader spectrum of grain ages up-section, including Jurassic grains, is interpreted to represent either reconnection of Sevier and arc sources to the basin or early initiation of sediment shedding from emerging uplift blocks proximal to the Upper Valley Member. Local unroofing of basement-involved uplifts has been suggested for provenance shifts in the coeval Kirtland Formation in the San Juan Basin to the east (Pecha *et al.*, 2018) and Tuscher Formation in the Uinta Basin to the north (Lawton and Bradford, 2011). Local sediment shedding during the latest Campanian in this area may explain the striking similarity between the basal Canaan Peak Formation DZ spectra (KBU-W) and that of the Powell Point Member of the Kaiparowits Formation (KBU-S); both of which showed matching peaks at 78, 95, 148 and 164 Ma.

Subtle palaeo-drainage rearrangement and the interpreted southern sediment source for the Upper Valley Member have implications for understanding the network of river systems across the palaeo-landscape of the southern Cordilleran foreland basin. Drainage patterns across the south-western corner of the Cordilleran Foreland Basin (present day Arizona) during the mid to late Campanian are reported as both generally eastward and northward by various authors. Lawton and Bradford (2011) argue a northward-trending system connected the Mogollon region to the Kaiparowits Formation, which carried on northwards to supply sediment to the Uinta Basin. On the other hand, eastward to north-eastern oriented rivers connecting the Cordilleran arc and adjacent terrains to the San Juan Basin were



**Fig. 5.12** Simplified palaeo-drainage interpretation of the southern Cordilleran foreland basin during the latest Campanian illustrating a subtle rearrangement during deposition of the Upper Valley Member. Palaeo-flow indicators were adapted from Lawton and Bradford (2011) (dark red) and Pecha *et al.* (2018) (light red) with minor changes. Palaeogeographic features adapted from Pecha *et al.* (2018) and references within. Abbreviations: KP = Kaiparowits, K = Kaibab, CC = Circle Cliffs. Study area is indicated by the gold star.



proposed by Wernicke (2011) and Pecha *et al.* (2018), although the latter study does identify the reduction of Sevier sources after 73 Ma. These varying palaeo-flow orientations within coeval strata from the San Juan, Kaiparowits and Uinta sub-basins may represent some form of radially distributive pattern; however, intersecting east-west and north-south rivers in the south-western corner of the foreland basin cannot exist synchronously. Data presented herein provides strong evidence for southerly sourced fluvial systems in the southwestern corner of the Cordilleran Foreland Basin during the latest Campanian as indicated most convincingly by the presence of near syn-sedimentary volcaniclastic material in the Upper Valley Member that was sourced from the LPCP within the Mogollon region. Whether this represents the prevailing flow orientation for the region throughout the Campanian is unclear; however, this confirms that a shift in source terrain for strata from the San Juan Basin noted by Pecha *et al.* (2018) most likely occurred earlier than previously reported.

## 5.8 Conclusions

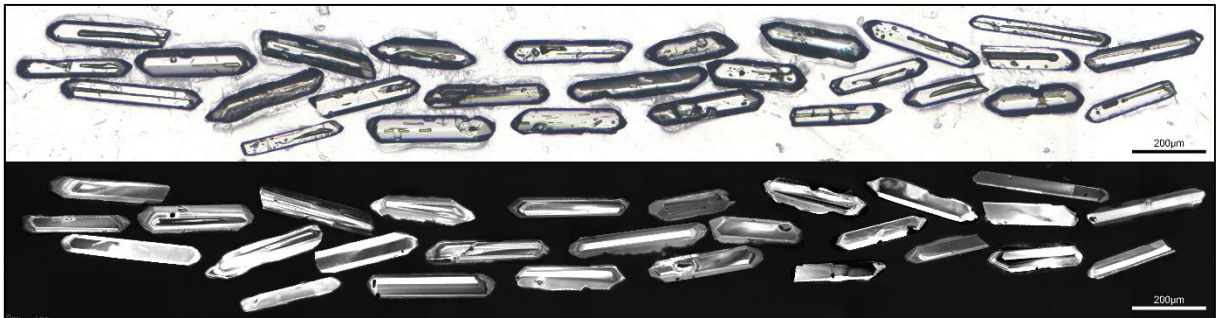
The uppermost strata of the Kaiparowits Formation were herein described and identified as a new lithological unit termed the Upper Valley Member. This investigation clarifies longstanding issues and discrepancies noted in the stratigraphy of the uppermost Kaiparowits Formation in previous studies. It is surprising that a 255-meter-thick, sedimentologically distinct unit has remained unrecognized until now in such a closely scrutinized area. This is attributed to the remote nature of Upper Valley Member outcrops and the prevalence of scree and slumping that commonly obscures the upper boundary. Initial suspicion of the new member resulted from examination of publicly available Google Earth satellite imagery, which prompted detailed sedimentological and geochronological analyses that provided the necessary support for the introduction of this lithostratigraphic unit. Palaeo-drainage rearrangement in the Cordilleran foreland basin and renewed tectonism relating to Laramide orogenesis is suspected to have played a role in the sedimentological change observed in the Upper Valley Member. This finding makes the Kaiparowits Plateau an excellent example from which to study stratigraphic records of basin partitioning processes. The identification of previously unstudied latest Campanian strata at the top of the Kaiparowits Formation has implications for regional stratigraphic correlation, possible land vertebrate “ages” and the placement of the Campanian-Maastrichtian stage boundary in southern Utah. Paleontological resources, including dinosaurs, await discovery within this previously unrecognized sedimentary unit from southern Laramidia. Addition of the Upper Valley Member to the Kaiparowits Formation extends the completeness of the Campanian stratigraphic and paleontological record of the Kaiparowits Basin to nearly the entire stage, making it one of the most continuous records of Campanian terrestrial biosphere found in a single section anywhere in the world.

---



## Chapter Six

A multifaceted approach to bentonite  
tephrostratigraphy in Campanian strata of  
western North America



*Zircon phenocrysts from bentonite ES080216-2*

**Preface**

This constitutes the final data chapter of my thesis and was designed to provide a novel extension to previous work herein. Throughout Chapters Three, Four, and Five, the utility of volcanogenic horizons for litho- and chronostratigraphic refinement were clearly demonstrated; however, correlation of these units was largely dependent on high-precision geochronology. This chapter applies the ages reported in Chapters Two through Five to investigate novel uses for interbedded volcanic material for stratigraphic correlation. The work is presented as a long-format research article although may be considered a pilot study for future (postdoctoral) research. All analyses and data reduction were completed personally with technical aid from staff at the Advanced Analytical Centre at JCU (K. Blake, S. Askew, Y. Hu, H. Huang). Editing and academic guidance was provided by C. Spandler and E. Roberts. Note that age data for some samples are considered confidential awaiting future publication (not yet specified).

*Institutional abbreviations:* MIT Massachusetts Institute of Technology, JCU James Cook University, AAC Advanced Analytical Centre

**Abstract**

This study investigated approaches to bentonite tephrostratigraphy for richly fossiliferous Campanian strata of western North America with the intention of establishing a protocol that is simple, effective, and broadly accessible. These approaches were based on characterization of zircon phenocrysts for 28 bentonite samples including zircon morphology description, melt inclusion morphology/major element composition, and Lu-Hf isotopic ratios. To guide the study, an effective approach was defined as 1) able to distinguish between bentonites known to be unique, 2) one that consistently produces matching signatures for bentonites known (or suspected) to match, and 3) supports correlations made using high-precision U-Pb ages. All characterization methods yielded useful broad insights into the source of the volcanogenic material including the first direct measurement of major element compositions for the Campanian magmatic sources from which the studied bentonites were generated. The most successful technique for bentonite tephrostratigraphy was comparison of zircon  $\epsilon\text{Hf}$  signatures, as this approach demonstrated the capacity to distinguish between different bentonite horizons and it produced matching signatures for correlated samples. Interestingly,  $\epsilon\text{Hf}$  data did not support correlation of bentonites with statistically indistinguishable high-precision ages that were separated by up to 1500 km, suggesting these instances represent multiple near-synchronous volcanic centers active and contributing ash deposits across western North America during the Campanian. More broadly, correlation of bentonite outcrops using bentonite tephrostratigraphy helps to establish refined litho- and chrono-stratigraphic frameworks within which fossil biota may be placed, facilitating the investigation of complex palaeoecological concepts.



## 6.1 Introduction

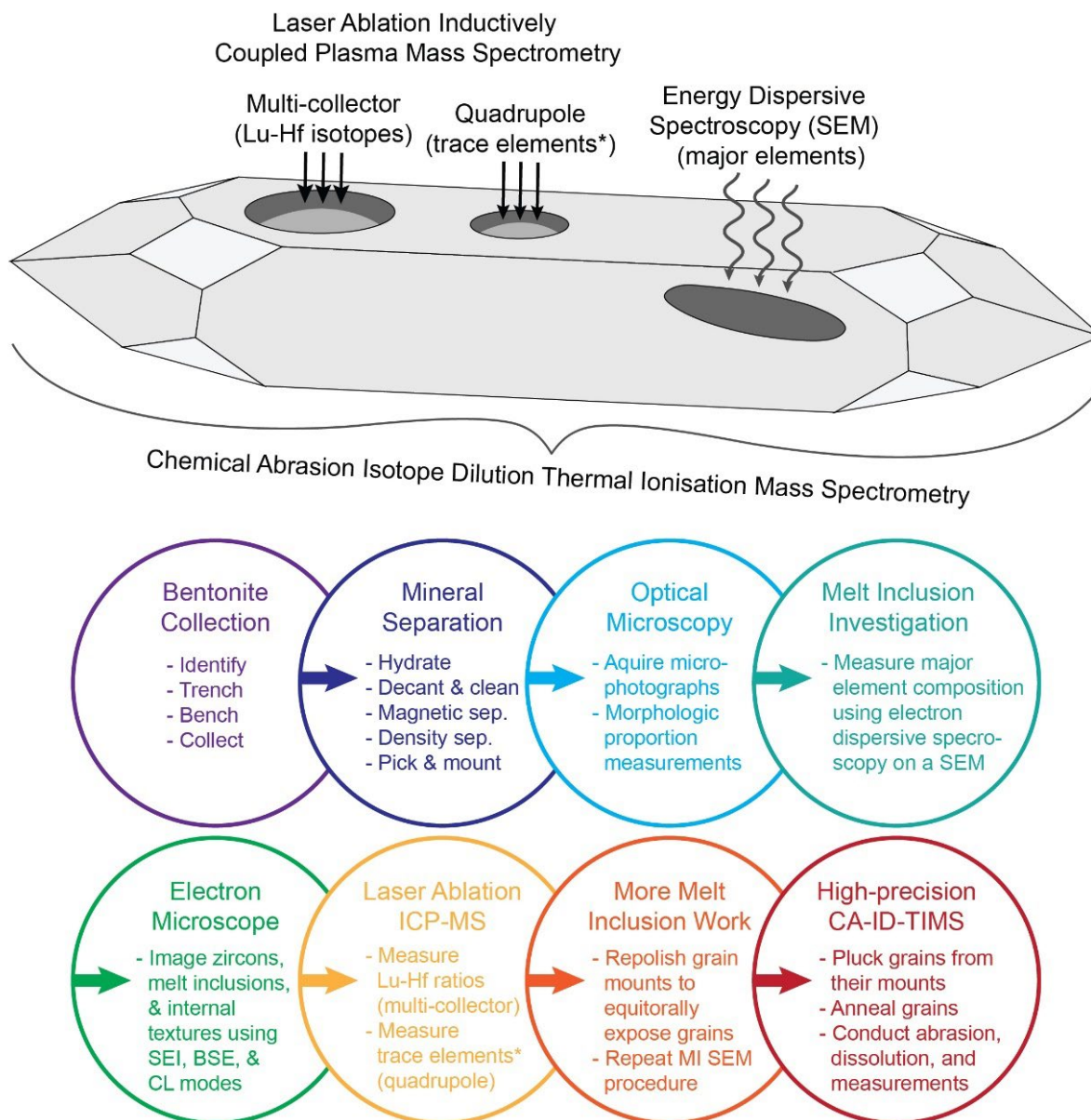
Campanian bentonite horizons across western North America have proven to be fundamental in calibrating a high-resolution temporal framework for the richly fossiliferous strata with which they are interbedded (*e.g.*, Rogers *et al.*, 1993, 2016; Thomas *et al.*, 1990; Fassett *et al.*, 1997; Payenberg *et al.*, 2002; Roberts *et al.*, 2005, 2013; Foreman *et al.*, 2008; Jinnah *et al.*, 2009; Jinnah, 2013; Fassett and Heizler, 2017; Eberth and Kamo, 2020; Beveridge *et al.*, 2022 [Ch.3], in prep [Ch.4]; Ramezani *et al.*, in review). These radiometric ages facilitate spatio-temporal comparison of strata and biota across the length of the Laramidian continent and facilitate investigation of complex palaeoecological processes (*e.g.*, Gates and Sampson, 2007; Gates *et al.*, 2010; Sampson *et al.*, 2010; Loewen *et al.*, 2013a). The most recent generation of bentonite ages achieve precision in the realm of tens of thousands of years through the application of chemical abrasion isotope dilution thermal ionization mass spectrometry (CA-ID-TIMS) to generate zircon  $^{206}\text{Pb}/^{238}\text{U}$  ages with internal uncertainty reaching *ca* 0.02% (Eberth and Kamo, 2020; Beveridge *et al.*, 2022 [Ch.3], in prep [Ch.4]; Ramezani *et al.*, in review). This approach is shown to be highly effective for temporal calibration of fossiliferous strata and, furthermore, for stratigraphic refinement in successions with abundant bentonite horizons (Beveridge *et al.*, in prep [Ch.4]). The key limitation of high-precision geochronology, other than requiring interstratified volcanogenic material, is the cost and time commitment required for analysis, thus reducing the accessibility of this technique for widespread application in non-geochronology specific projects.

Bentonite horizons provide excellent opportunities for stratigraphic correlation and refinement due to their isochronous and laterally extensive / reoccurring nature (Lowe, 2011; Thomas *et al.*, 1990; Foreman *et al.*, 2008; Beveridge *et al.*, in prep [Ch.4]). Although correlation of distinctive bentonite units between distant stratigraphic sections can be confidently accomplished through high-precision dating at both section localities (*e.g.*, Beveridge *et al.* in prep [Ch.4]), the cost and time commitment required for this method generally make other approaches preferable. More commonly, stratigraphic studies rely on matching patterns of bentonite occurrences like bar codes between measured sections that are assumed to be laterally correlative to one another and supplementing these interpretations with tracing of horizons where possible (*i.e.*, Roberts *et al.*, 2013). The limitation of this approach is that it is difficult to check for miscorrelation that may arise when calibrating sections with abundant bentonites especially because these horizons tend to be discontinuous due to preservation biases in some environments/sections (Roberts, 2007; Beveridge *et al.*, in prep [Ch.4]). For instance, in one section, there may be multiple bentonites preserved in the same section because it represents a long-lived ponded-floodplain environment (proximal to the main fluvial channel system) conducive to preservation, whereas in a correlative high-energy fluvial channel facies or in distal, subaerial exposed floodplain environment typified by pedogenic processes, bentonite preservation is less likely, leading to significant potential for miscorrelation. Moreover, there may be considerable differences in post-depositional compaction between these different facies types, leading to variable thickness

measurements; hence basing bentonite correlation purely on stratigraphic thickness and position, also has potential for miscorrelations.

To overcome issues with lithostratigraphic bentonite correlation, several studies have investigated the potential for correlation of Campanian bentonite horizons using geochemical characterization (*e.g.*, Thomas *et al.*, 1990; Lerbekmo, 2002; Foreman *et al.*, 2008; Fanti, 2009). These studies have shown significant potential; however, the overall effectiveness of whole-rock bentonite characterization in these previous studies has been strongly limited by chemical alteration associated with devitrification and diagenesis. Specifically, the breakdown of primary volcanic ash into stable, clay minerals (smectite) significantly limits that potential of these approaches for tephrostratigraphy and interpretation of the source volcano(s). In Quaternary geology, widespread correlation using tephra is common practice and relies heavily on geochemical characterization of glassy groundmass (see Lowe, 2011). In rocks older than a few million years, devitrification of volcanic glasses limits reliable tephrostratigraphy using the groundmass; however, some studies have shown promise in correlation using phenocrysts, which generally maintain their original compositions (*e.g.*, Thomas *et al.*, 1990). These approaches have included characterization phenocryst element and isotopic compositions (*e.g.*, Haynes *et al.*, 1995; Samson *et al.*, 1995; Huff, 2008) and, rarely, element compositions of melt inclusions in common phenocryst such as quartz (*e.g.*, Delano *et al.*, 1995; Nairn *et al.*, 2004; Borisova *et al.*, 2008). Other than for U-Pb geochronology, no previous studies have used zircon from bentonites for tephrostratigraphy.

The purpose of this study was to investigate new approaches to bentonite tephrostratigraphy (characterization and correlation) and to develop a protocol for bentonite correlation that facilitates correlation of precisely dated bentonite samples from well-constrained type sections to remote or isolated reference sections without the necessity of additional dating or reliance on “bar-code” lithostratigraphy. Methods selected for investigation focused on characterization of zircon phenocrysts from bentonites, which avoids challenges relating to devitrification and diagenesis identified in previous whole-rock studies (*i.e.*, Thomas *et al.*, 1990; Foreman *et al.*, 2008). Furthermore, zircon grains are routinely isolated from bentonite heavy mineral separates for U-Pb geochronology making the approach herein easy to include within the dating workflow (Fig. 6.1). Zircon characterization methods investigated herein included morphological description of grains, a new approach for geochemical ‘fingerprinting’ using glass melt inclusions trapped within the zircons, and microbeam analysis of trace element and Lu-Hf isotopic compositions from the zircon itself. All bentonite investigated in this study were previously dated using the CA-ID-TIMS approach described by Ramezani *et al.* (2011) and herein in Chapter 2 (see also Beveridge *et al.*, 2022 [Ch.3], in prep [Ch.4], Ramezani *et al.*, in review) as part of a basin-scale project to develop a high-resolution temporal framework for fossiliferous Campanian strata from western North America. Pre-existing bentonite ages were required to guide the study and



**Fig. 6.1** Summary of methodology. Schematic of analytical approaches used to characterize zircon from bentonites (top) and a flow chart of the approach affixed within the U-Pb dating protocol (bottom) \* trace element composition discussed elsewhere.

validate findings; however, future expansion of this work would aim to match unknown bentonite samples with characterized type-section bentonites without the use of high-precision ages, thus facilitating the propagation of age data to remote outcrops. The approach developed in this study may be applied to comparable geologic situations elsewhere for lithostratigraphic correlation, contributing to refinement of the temporal and geologic context of extinct biota and ecosystems globally. Furthermore, future expansion and deeper interpretation of the geochemical dataset presented herein may contribute to a refined understanding of highly explosive volcanism in North America during the Late Cretaceous.

## 6.2 Background

### 6.2.1 Bentonite tephrostratigraphy

The term ‘tephra’ refers to fragmented, unconsolidated, explosively erupted volcanic products including fall deposits and unconsolidated pyroclastic deposits and may comprise ash (<2 mm grain sizes), lapilli (2-64 mm), and/or blocks and bombs (>64 mm) (see Lowe, 2011). Tephra deposits can be extremely widespread, blanketing landscapes in discrete layers of pyroclastic material that, if identified in basin successions, can provide ideal horizons for dating, correlation, and reconstruction of the source and type of ancient volcanic activity. Over time, glassy volcanic material in the tephra deposits break down to smectite clays either from environmental weathering or subsurface diagenesis. This is particularly pronounced in thin, distal tephra deposits composed almost exclusively of ash-sized particles, which are altered relatively rapidly to form distinctive swelling clay beds typically referred to as bentonites. Resistant mineral phenocrysts from these horizons, which are presumed to have crystallized during or immediately prior to the eruption, facilitate accurate radioisotopic age dating. Furthermore, the distinctive physical characteristics of bentonites make them excellent marker horizons for stratigraphic correlation, particularly in discontinuous outcrop belts or structurally complex regions (*e.g.*, Thomas *et al.* 1990; Rogers *et al.*, 1993, 2016; Roberts *et al.*, 2013). Correlation of bentonite beds may be built on lateral tracing, radioisotopic ages, or in some cases, lithologic, petrographic, and geochemical characterization (*e.g.*, Thomas *et al.*, 1990; Foreman *et al.*, 2008; Fanti, 2009; this study). Characterization of bentonites for the purpose of stratigraphic correlation is herein referred to as bentonite tephrostratigraphy based on definitions by Lowe (2011).

The field of tephrostratigraphy involves the utilization of widespread tephra deposits (or, in this case, bentonites) for stratigraphic correlation and age control, and may involve description, characterization, and dating of the horizons (see Lowe, 2011). Although the term tephrochronology may elsewhere be used interchangeably with tephrostratigraphy, the term (*sensu stricto*) concerns transferal of age information to connect and synchronize successions; thus, the distinction is relevant herein. In this sense, the present study aims to develop methods for tephrostratigraphy (characterization and stratigraphic correlation), which will facilitate future tephrochronology (age transferal from dated to non-dated outcrops).

### 6.2.2 Previous bentonite characterization

Bentonites interbedded with Campanian strata in western North America have received considerable attention for their geochronologic applications (*e.g.*, Thomas *et al.*, 1990; Rogers *et al.*, 1993, 2016; Fassett *et al.*, 1997; Payenberg *et al.*, 2002; Roberts *et al.*, 2005, 2013; Foreman *et al.*, 2008; Jinnah *et al.*, 2009; Jinnah, 2013; Fassett and Heizler, 2017; Eberth and Kamo, 2020; Beveridge *et al.*, 2022 [Ch.3], in prep [Ch.4]; Ramezani *et al.*, in review), but comparatively few studies have investigated their geochemical composition and potential for long-distance correlation via tephrostratigraphy. Previous

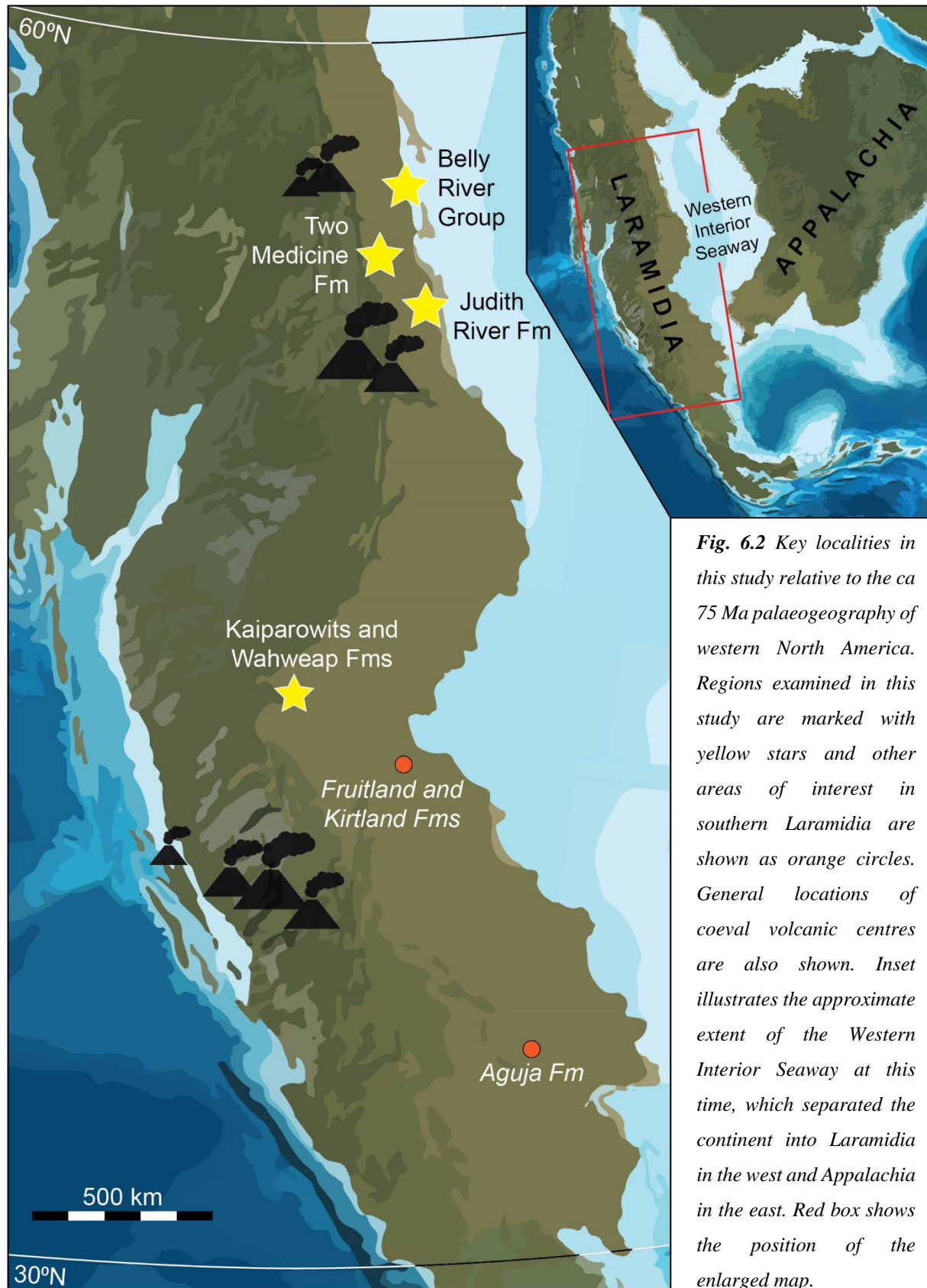
studies of Late Cretaceous bentonites in Montana and Alberta have used whole-rock geochemistry (major and trace element composition determined using X-ray fluorescence spectroscopy; XRF) as a tool for characterization and correlation (Thomas *et al.*, 1990; Foreman *et al.*, 2008; Fanti, 2009). Element mobility due to bentonite alteration was recognized as a barrier to classification in these whole-rock studies and the adopted schemes were built upon immobile trace elements and multi-step discriminant analysis.

Thomas *et al.* (1990) provided one of the first and most detailed multi-disciplinary characterizations of a Campanian bentonite from western North America including meticulous lithostratigraphic, chronologic, and geochemical descriptions of the Plateau bentonite (tuff) from Dinosaur Provincial Park in southern Alberta. The premise for regional correlation using bentonite geochemistry posed in that study was that outcrops must yield reproducible radioisotopic ages and be geochemically and petrographically distinguishable. Whole-rock trace element data from eight samples of the Plateau tuff were used to characterize the chemical variability of the horizon, then principal component and factor analysis was used to compare this horizon with stratigraphically higher and lower bentonites. Ratios of immobile trace elements were used to indicate a rhyodacitic to rhyolitic parent magma composition of a volcanic arc tectonic setting inferred to reflect a subaerial, Plinian eruptive center. The exact source was tentatively suggested to be a volcanic center represented by the Elkhorn Mountain Volcanics in present-day Montana. Although the authors were cautiously optimistic about whole-rock trace element characterization, this approach was complicated due to chemical alteration of volcanogenic material during devitrification and diagenesis. The study found that the clearest compositional distinction was provided by phenocrysts, specifically feldspar microprobe data.

This early work was subsequently expanded upon by Foreman *et al.* (2008) for a series of bentonites from the Two Medicine Formation in Montana. This work refined the approach of Thomas *et al.* (1990) by collecting and characterizing a dataset of 27 samples across four different horizons then applying a stepwise analysis (to three of the four horizons), which yielded two discriminant functions based on seven immobile trace elements (Zr, Sc, V, Cr, U, Ga, and Th). Cross-validation was conducted using samples excluded from discriminant function determination and found that the approach was consistently accurate. A range of magma compositions was inferred from the trace element data including rhyolitic, rhyodacitic, dacitic, trachyandesitic and trachytic. The Elkhorn Mountain Volcanics and Adel Mountain Volcanics were identified as likely source terrains.

Following procedural developments by Thomas *et al.* (1990) and Foreman *et al.* (2008), an applied study of bentonite characterization was conducted by Fanti (2009) in which the composition 21 unique bentonites from Alberta were compared. These horizons were generally younger than those of the previous studies (latest Campanian through Maastrichtian), and chemical alteration of the whole-rock samples constituted a more pronounced issue in this work since an investigation of geochemical





**Fig. 6.2** Key localities in this study relative to the ca 75 Ma palaeogeography of western North America. Regions examined in this study are marked with yellow stars and other areas of interest in southern Laramidia are shown as orange circles. General locations of coeval volcanic centres are also shown. Inset illustrates the approximate extent of the Western Interior Seaway at this time, which separated the continent into Laramidia in the west and Appalachia in the east. Red box shows the position of the enlarged map.

reproducibility was not included. Although comparison of these samples and data from published literature was limited in this work, Fanti (2009) inferred a predominantly trachyandesitic and rhyolitic

magma composition for the bentonites and suggested these were the product of multiple sources representative of volcanic arc to within-plate volcanism during this time.

These initial studies were intended to serve as foundations for later, broader application; however, the limitations of this work appear to have hindered widespread uptake. Poor uptake may be due to the heavy reliance on multi-step trace element discriminant functions to overcome issues with whole-rock alteration that convoluted the process of correlating strata. Furthermore, the successful multi-factor discriminant analyses demonstrated by Foreman *et al.* (2008) was based on a small trial of three unique bentonites, whereas distinction between all Two Medicine bentonite beds (>19) mentioned in that study would require an increasingly complex approach to statistically quantify distinctions between additional samples. Nonetheless, these studies provided the foundation for further development of bentonite tephrostratigraphy including the framework for this study, which investigates a suite of new approaches aimed at simplifying the approach and avoiding issues associated with alteration and weathering.

### 6.2.3 Study areas

Samples examined in this study represent bentonites from fossiliferous Campanian strata spanning a latitudinal range of nearly 1500 km in western North America. During the Cretaceous, North America was divided into two landmasses by the Western Interior Seaway, referred to as Appalachia in the east and Laramidia in the west (Sampson *et al.*, 2010; Fig. 6.2). Campanian terrestrial strata representing a ribbon of coastal plain environments spanned the length of Laramidia and can be broadly separated into northern and southern regions. Northern localities are represented in this study by the Oldman and Dinosaur Park formations of the Belly River Group in southern Alberta (Eberth and Hamblin, 1993), and by the Two Medicine and Judith River formations in north-western and central Montana (Rogers *et al.*, 1993, 2016), respectively. Key Campanian localities from southern Laramidia include the Wahweap and Kaiparowits formations in southern Utah (Eaton, 1991; Roberts, 2007; Jinnah and Roberts, 2011; Beveridge *et al.*, 2022 [Ch.3], in prep [Ch.4]), examined herein, and the Fruitland and Kirtland formations of northwest New Mexico (Fassett and Hiesler, 2017) and the Aguja Formation of West Texas (Lehman *et al.*, 2019), not considered in this study (see Chapter 1 for lithostratigraphic summaries). Due to exceptional exposure of the Kaiparowits Formation's type section and multiple, well constrained reference sections, samples from this area form the core of the study supported by a suite of northern samples. The distribution of samples from the Kaiparowits Formation type section in The Blues and those of isolated outcrops is illustrated in Figure 6.3.

## 6.3 Experimental design

Procedures for bentonite tephrostratigraphy based on zircon characterization were developed to test three specific questions that guide the scope of the work and the following discussion. Firstly, can these



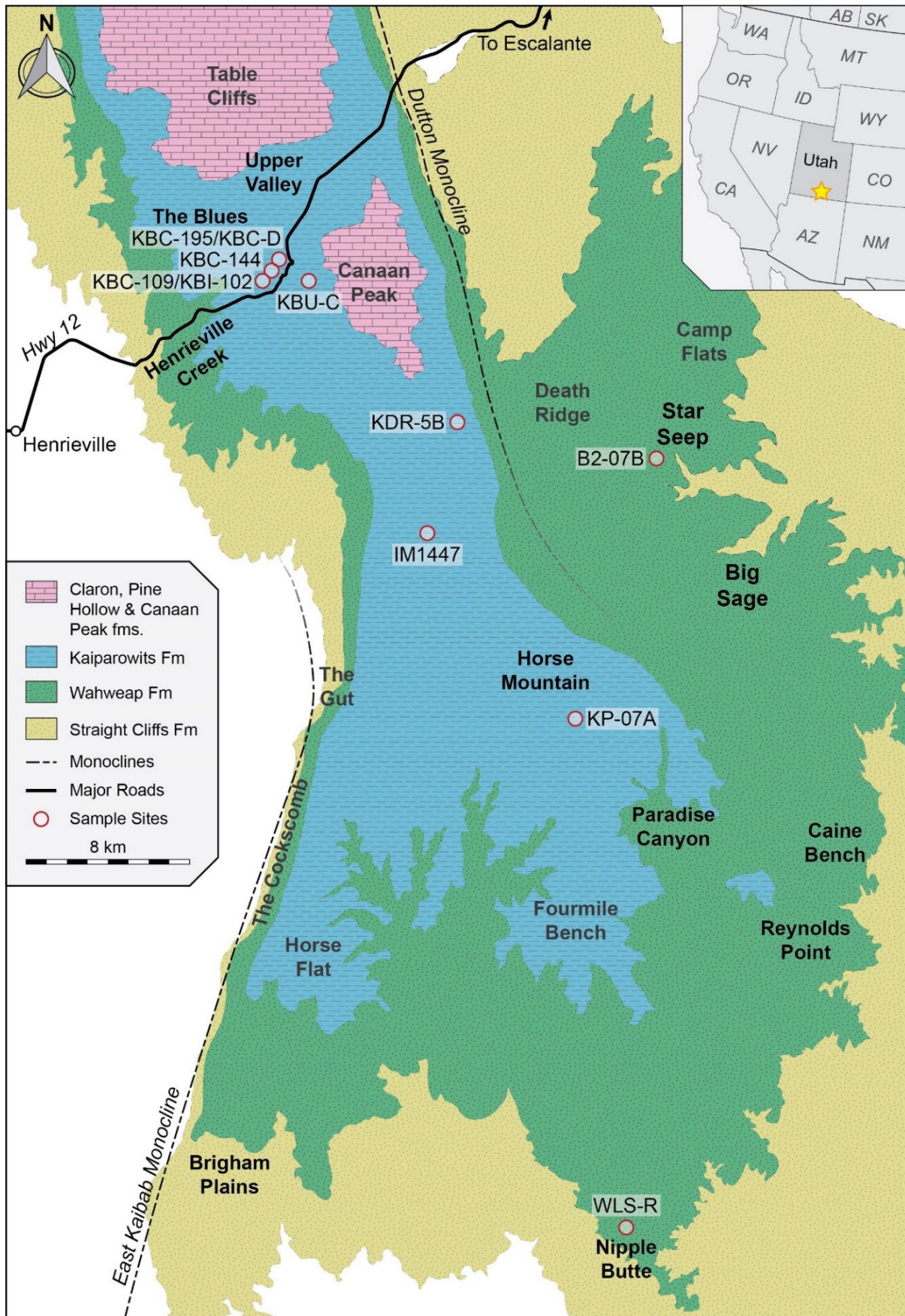


Fig. 6.3 Sample localities in southern Utah illustrating field relationships between type section samples and those from isolated outcrops. Note that some locations are generalized for confidentiality.

new tephrostratigraphic methods distinguish between unique bentonite horizons represented by successive beds within a stratigraphic framework? In other words, are the ‘fingerprints’ created for different bentonites in close succession unique enough from one another for reliable correlation and distinction? To test this question, three sequential bentonites from the Kaiparowits Formation stratotype section were examined as the primary example. These horizons are known to be unique and constitute formally named lithostratigraphic units (the Paria Hollow, Deadmans Corner and Overlook bentonite beds). The second goal was to ensure that bentonite beds produce the same ‘fingerprint’ using these methods across their lateral extent, which enables reliable long-distance correlations. A series of bentonite samples from across the Kaiparowits Plateau representing three named beds were examined as primary examples (Overlook and Paria Hollow bentonite beds from the Kaiparowits Formation and the Star Seep bentonite from the Wahweap Formation). The third goal was to determine if well-dated bentonites of the same age (overlapping U-Pb zircon CA-ID-TIMS ages at *ca* 0.03% uncertainty) from up to 1500 km apart could be confidently correlated to the same volcanic event, or if coeval Campanian bentonites across western North America are from different but synchronous volcanic centers. This research question was examined using three sets of bentonite samples with statistically indistinguishable CA-ID-TIMS ages that occur between *ca* 76.3 and 75.1 Ma across northern and southern Laramidia.

## 6.4 Fieldwork and sample preparation

### 6.4.1 Bentonite collection

Bentonite samples (Table 6.1) were collected using the approach outlined in Chapter Two (Section 2.3.1). Pure ash fall bentonites were identified in outcrop as greenish-gray weather-resistant platforms often atop steep slopes (Fig. 6.4). These outcrops showed characteristic ‘popcorn’ swelling textures and were exceptionally slick when wet. Hand samples were characterized as pistachio to olive green clays with waxy texture and luster. A hand lens was used to check for detrital material (*i.e.*, sandy grains) and look for fresh, flaky black spots (*i.e.*, biotite). Once an optimal outcrop was located, a trench was excavated to dissect the unit and identify the best interval from which to collect material. The top of the optimal horizon was exposed to form a bench and material was collected from the bench with care to avoid contamination from overburden. Between approximately one to five kilograms of material was collected for each sample and relevant details were recorded (*e.g.*, GPS, lithologic description, bounding lithologies, lateral continuity).

### 6.4.2 Mineral separation

Mineral separation was conducted at both MIT and JCU using parallel procedures and discrepancies were considered negligible. Bentonite samples were first re-hydrated and pulsed to form a slurry then agitated and decanted to remove the clay fraction. At MIT, this was achieved using an ultrasonic clay separator apparatus (Hoke *et al.*, 2014), whereas samples processed at JCU were decanted manually. The remaining crystalline fraction (~2 and 10% pre-processed mass) was further reduced using a Frantz

**Table 6.1** Sample summary including names, types, stratigraphic units, and regions.

Full Sample Name	Abbrev. Name	Sample Type	General Horizon Name	Stratigraphic Unit	Region
IL082717-1	IL	Bentonite	Bearpaw tuff	Bearpaw Formation	Southern Alberta
Plateau	Plateau	Bentonite	Plateau tuff	Dinosaur Park Formation, Belly River Group	Southern Alberta
NF082917-1	NF	Bentonite	Nesmo tuff	Oldman Formation, Belly River Group	Southern Alberta
PR082917-1	PR	Bentonite	Double bentonite	Oldman Formation, Belly River Group	Southern Alberta
FS082717-1	FS	Bentonite	Fieldstation tuff	Oldman Formation, Belly River Group	Southern Alberta
ES080216-2	ES	Bentonite	(Eyre Site)	Two Medicine Formation	Northwestern Montana
DVMT-1	DVMT-1	Crystal tuff	-	Two Medicine Formation	Northwestern Montana
LSB-1-14	LSB	Bentonite	(Landslide Butte)	Two Medicine Formation	Northwestern Montana
EMC080216-1	EMC	Bentonite	(Egg Mountain Camp)	Two Medicine Formation	Northwestern Montana
Hadro Hill	HH	Bentonite	Hadro Hill bentonite	Two Medicine Formation	Northwestern Montana
PPF2-17	PPF	Bentonite	(Powerplant Ferry)	Judith River Formation	Central Montana
ST1-03	ST1	Bentonite	Stafford Ferry bentonite	Judith River Formation	Central Montana
KC061517-1	KC	Bentonite	(Kennedy Coulee)	Judith River Formation	Central Montana
KBU-F-050818	KBU-F	Sandstone	-	Upper Valley Member, Kaiparowits Formation	Southern Utah
KBU-H-050818	KBU-H	Crystal tuff	-	Upper Valley Member, Kaiparowits Formation	Southern Utah
KBU-I-050818	KBU-I	Crystal tuff	-	Upper Valley Member, Kaiparowits Formation	Southern Utah
KBU-V-090818	KBU-V	Sandstone	-	Upper Valley Member, Kaiparowits Formation	Southern Utah
KBC-195	KBC-195	Bentonite	Overlook Bentonite Bed	Powell Point Member, Kaiparowits Formation	Southern Utah
KBC-D-030818	KBC-D	Bentonite	Overlook Bentonite Bed	Powell Point Member, Kaiparowits Formation	Southern Utah
KBU-C-300718	KBU-C	Bentonite	Overlook Bentonite Bed	Powell Point Member, Kaiparowits Formation	Southern Utah
KBC-144	KBC-144	Bentonite	Deadmans Corner Bentonite Bed	The Blues Member, Kaiparowits Formation	Southern Utah
KBC-109	KBC-109	Bentonite	Paria Hollow Bentonite Bed	The Blues Member, Kaiparowits Formation	Southern Utah



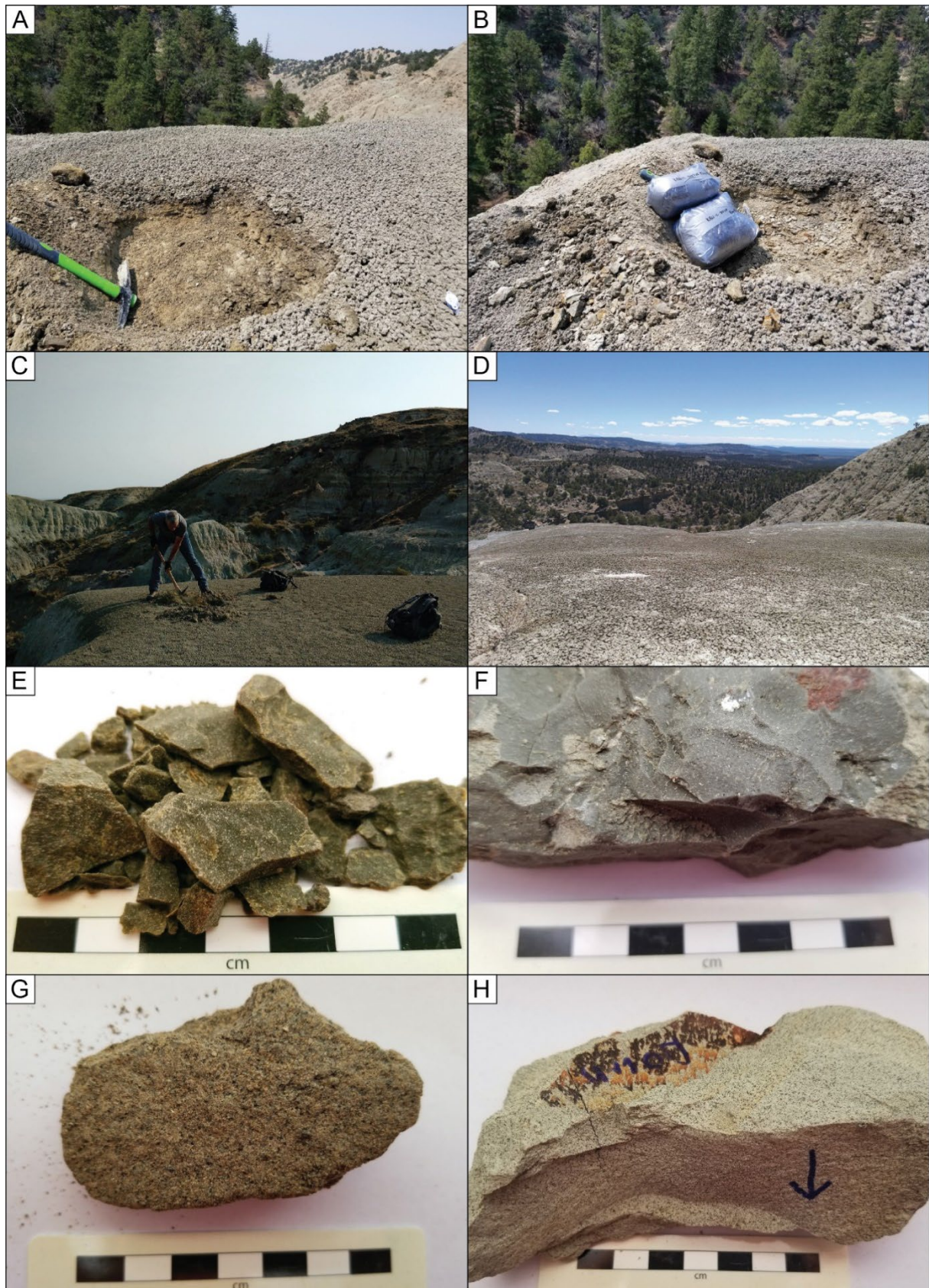
*Table 6.1 Continued.*

Full Sample Name	Abbrev. Name	Sample Type	General Horizon Name	Stratigraphic Unit	Region
KBI-102	KBI-102	Bentonite	Paria Hollow Bentonite Bed	The Blues Member, Kaiparowits Formation	Southern Utah
IM1442	IM1442	Bentonite	Paria Hollow Bentonite Bed	The Blues Member, Kaiparowits Formation	Southern Utah
KDR-5B	KDR-5B	Bentonite	Death Ridge Bentonite Bed	The Blues Member, Kaiparowits Formation	Southern Utah
KP-07A	KP-07A	Bentonite	Horse Mountain Bentonite Bed	The Blues Member, Kaiparowits Formation	Southern Utah
B2-07B	B2-07B	Bentonite	Star Seep Bentonite Bed	Reynolds Point Member, Wahweap Formation	Southern Utah
WLS-R-070818	WLS-R	Bentonite	Star Seep Bentonite Bed	Reynolds Point Member, Wahweap Formation	Southern Utah

Isodynamic Magnetic Separator and high-density liquid separation (methylene iodide at MIT and hot lithium heteropolytungstates at JCU; see Appendix B.1 for extended methods). The resulting non-magnetic heavy mineral fraction typically contained a mix of zircon, apatite, titanite and other accessory minerals. Zircon were selected for analysis from this fraction based on a set of morphological criteria including 1) acicular morphology with high aspect ratios, 2) well-developed crystal faces including doubly terminated grains, and 3) elongate glass melt inclusions parallel to the long crystal axis (see Corfu *et al.*, 2003; Ramezani *et al.*, 2011; Chapter Two, Section 2.3.3). Ideally 60 grains were selected for each sample, although less grains were retrieved from mineral separates that had been previously used for geochronology (~20-30 grains). Grains were hand-picked in ethanol using a binocular microscope and mounted in epoxy. Polishing was conducted in several phases. In the first instance, mounts were polished only until most grains were exposed. This was done to reduce the likelihood of losing grains via plucking and to ensure there was enough crystal for all analyses. Later, mounts were polished again so that zircons were equatorially exposed (roughly half depth) with less sensitivity towards unintentional grain loss and a stronger focus on exposing internal features.

### 6.5 Characterization using zircon morphology

Systematic description of zircon crystal morphology has been investigated for rock classification most notably by Pupin (1980) who developed a typology method based on the arrangement of prismatic (*e.g.*, {110} and {100}) and pyramidal (*e.g.*, {211} and {101}) faces (see also Benisek and Finger, 1993; Vavra, 1993; Corfu *et al.*, 2003; Belousova *et al.*, 2006). The study inferred that the development of pyramids is influenced by the chemical composition of the crystallizing medium, notably the aluminium over alkaline ratio, and prisms are influenced by the temperature of the medium, although this was contested by Benisek and Finger (1993) who suggested chemical factors were also responsible for prism development (generally, high  $U = \{110\}$  dominant; low  $U = \{100\}$  dominant). Water content was also



**Fig. 6.4** Examples of bentonite outcrops and hand samples. A) Excavated pit for sample collection illustrating the transition from weathered surface material to consolidated bentonite claystone beneath (tool ~35 cm long; KBU-C, southern Utah). B) Sample bags illustrating the typical volume of material to collected. (*continued*)



said to influence zircon growth, where water-poor magmas result in early growth and water-rich magmas show ongoing growth. The approach of Pupin (1980) for genetic classification proposed distinction between granitic rocks from three broad sources; 1) crustal or mainly crustal derived (~autochthonous), 2) hybrid crustal and mantle derived (calc-alkaline, sub-alkaline), and 3) mantle or mainly mantle derived (alkaline, tholeiitic). These categories were somewhat based on inferred zircon morphological evolution, and Vavra (1993) argued that constraining grain evolution to two degrees of freedom is oversimplistic when the system calls for at least three. Although Pupin (1980) specifically did not discuss crystal elongation, a systematic review of zircon textures by Corfu *et al.* (2003) indicated that zircon length to width ratios reflect crystallization rate, where elongate/acicular grains represent rapid crystal growth. The concepts of crystal proportions and, to some extent, pyramidal and prismatic typology were applied herein to characterize zircons from bentonite horizons for the primary purpose of sample correlation/distinction, but also to provide general comments on their magmatic origin.

### 6.5.1 Zircon imaging procedure

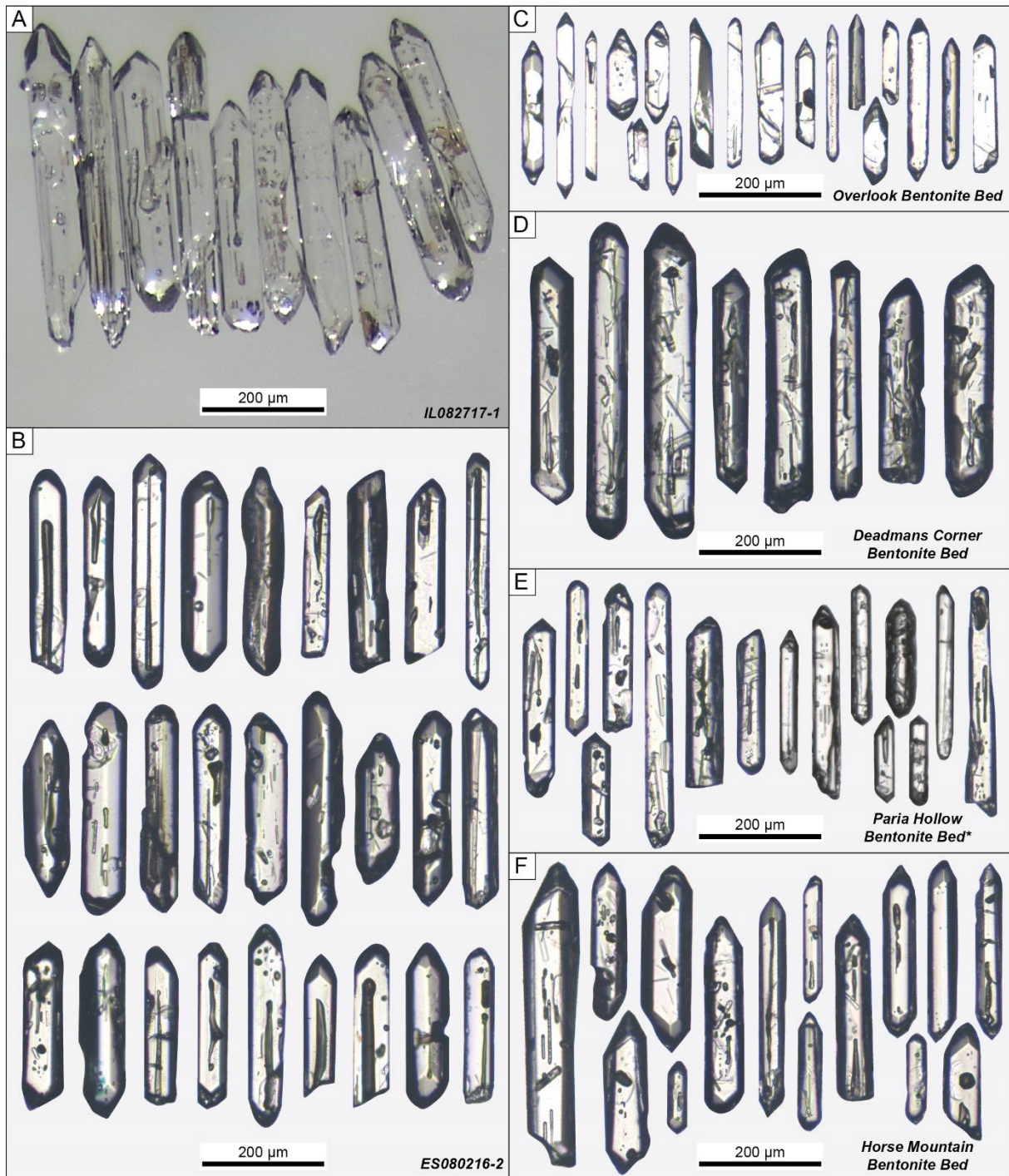
Zircon morphology was primarily examined using a Leica DMRXP optical microscope and scale-calibrated transmitted and reflected light microphotographs (Fig. 6.5). Length, width, and cross-sectional area for each grain was measured from these microphotographs using ImageJ (Fiji) image processing software (see Appendix B.2 for extended methods). Scanning electron microscope (SEM) imagery was also used for morphological characterization. A representative selection of loose grains was positioned on a carbon tape puck using an optical microscope then platinum coated before imaging using secondary electron imagery (SEI) on a Hitachi SU5000 field emission SEM at the AAC, JCU. Detailed zircon descriptions for each sample can be found in Appendix C.6.4, which includes general comments on appearance, morphology, the presence of melt and mineral inclusions, and internal textures described from cathodoluminescent (CL) images acquired in a later procedure (Section 6.6.1). Grain maps compiled in Adobe Illustrator are included in Appendix C.6.3.

### 6.5.2 Zircon morphology results

Based on observations and measurements of over 1150 zircons from 26 samples, bentonite zircons in this study were found to be nearly exclusively elongate and commonly acicular with good to excellent terminations and ubiquitous well-developed crystal faces. The length over width ratio averages for samples ranged from 3.0 to 6.1 and the grain length averages ranged from 128 to 366  $\mu\text{m}$ . Figure 6.5

---

**Fig. 6.4 (continued)** C, D) Typical bench-like outcrops of a bentonite showing swelling textures and dark weathered coloration (PR, southern Alberta, and KWC-1, southern Utah). E-H) Specimen hand samples including; E) ideal bentonite with pistachio-green, waxy smectite claystone and visible euhedral phenocrysts of biotite, F) olive-green, waxy smectite claystone with finer phenocrysts, G) Phenocryst-rich 'crystal tuff' with minor bentonite claystone, and H) Phenocryst-rich 'crystal tuff' with groundmass that appears glassy and welded.



**Fig. 6.5** Zircon microphotographs illustrating acicular grains with frequent melt and mineral inclusions commonly observed in this study. A) Loose grains of the Bearpaw tuff (IL082717-1). B-F) Mounted and polished zircons in transmitted light (sample/unit name in corners). Panel B includes every zircon selected for analysis for that sample while panels C-D, which represent the four named bentonite beds from the Kaiparowits Formation presented in stratigraphic order, includes a selection of the analysed grains (from multiple samples where appropriate).

illustrates the appearance of zircons from this study in transmitted light (both loose and mounted/polished grains) and demonstrates similarities and discrepancies between unique samples. SEM-SEI for a selection of loose grains is shown in Figure 6.6 to illustrate the variety of crystal

morphologies encountered in this study. Crystal forms were assigned according to the typology of Pupin (1980) and described in terms of dominant prism and pyramidal forms. Based on the SEM imagery and anecdotal observations, zircons from this study range from {100} to {110} dominant prism forms but typically present with roughly equal preference ( $\{100\} \approx \{110\}$ ). Pyramidal forms ranged from equal dominance of {101} and {211} through to strongly {211} dominant. Although not imaged with SEM, rare instances of the purely {211} pyramidal form were observed during mineral separation / zircon selection. Internal textures described from CL imagery did not appear to show systematic variation; homogenous grains and zones were common in all samples although many other textures were also noted (see Appendix C.6.3 and C.6.4). Melt and mineral inclusions were observed to be more abundant in zircon from some samples and also, in some instances, to be zonally distributed (*i.e.*, apatite inclusions in outer zones and melt inclusions in inner zones).

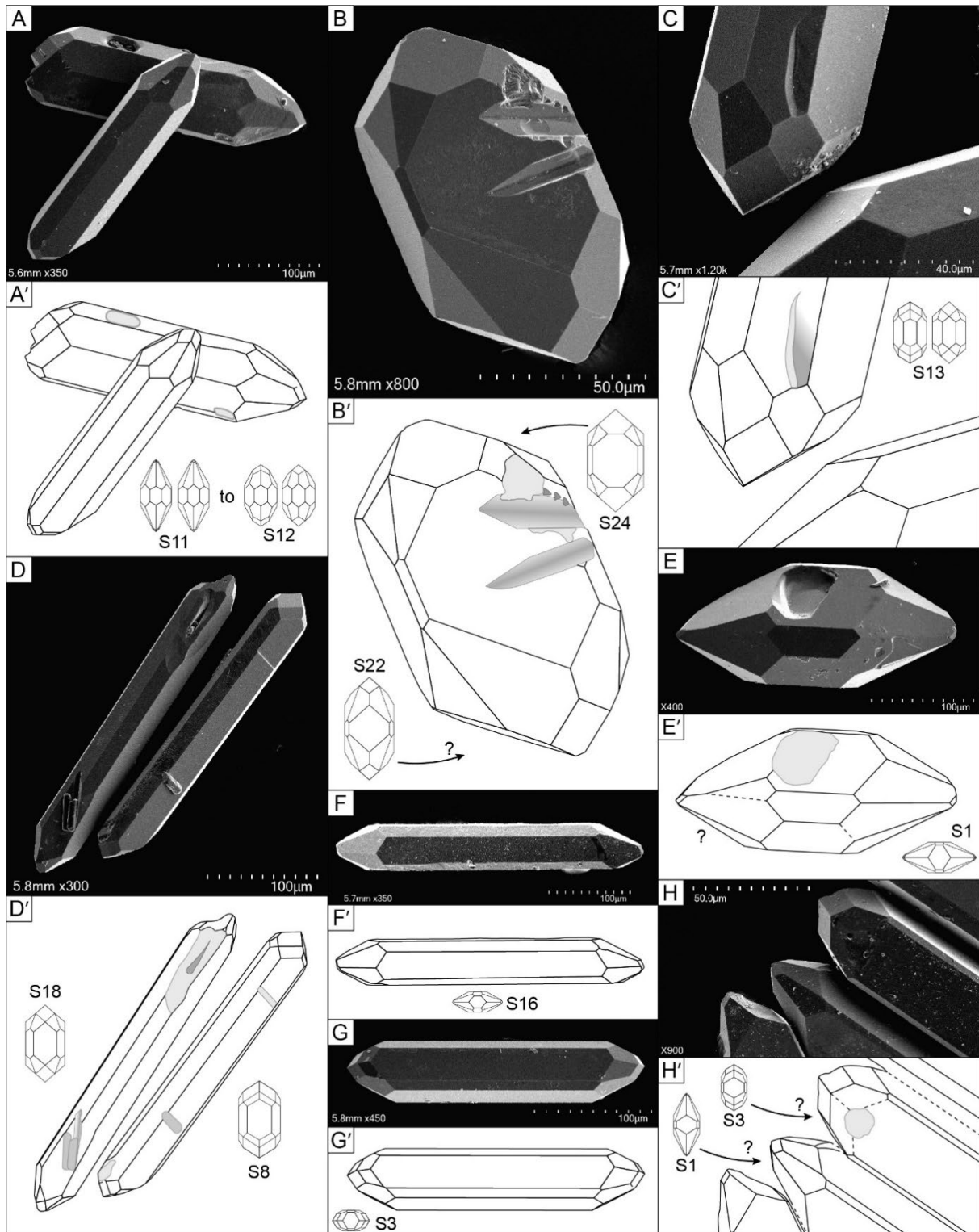
Outside of the bentonite samples detailed above, two samples described as crystal tuffs from the Upper Valley Member, Kaiparowits Formation (KBU-I, KBU-H), featured grains that were generally less needle-like, with length/width values averaging  $\sim 3$ , although the average length differed significantly (grains from KBU-I were 50% longer on average than those of KBU-H). The morphology of zircons from volcanoclastic sandstones KBU-F and KBU-V from the Upper Valley Member were not examined quantitatively; however, qualitative assessment found the youngest grain population of these samples to be closely comparable to the interbedded crystal tuffs (clean/transparent, similarly stout with good crystal faces and infrequent, blobby melt inclusions).

### 6.5.3 Morphology interpretation

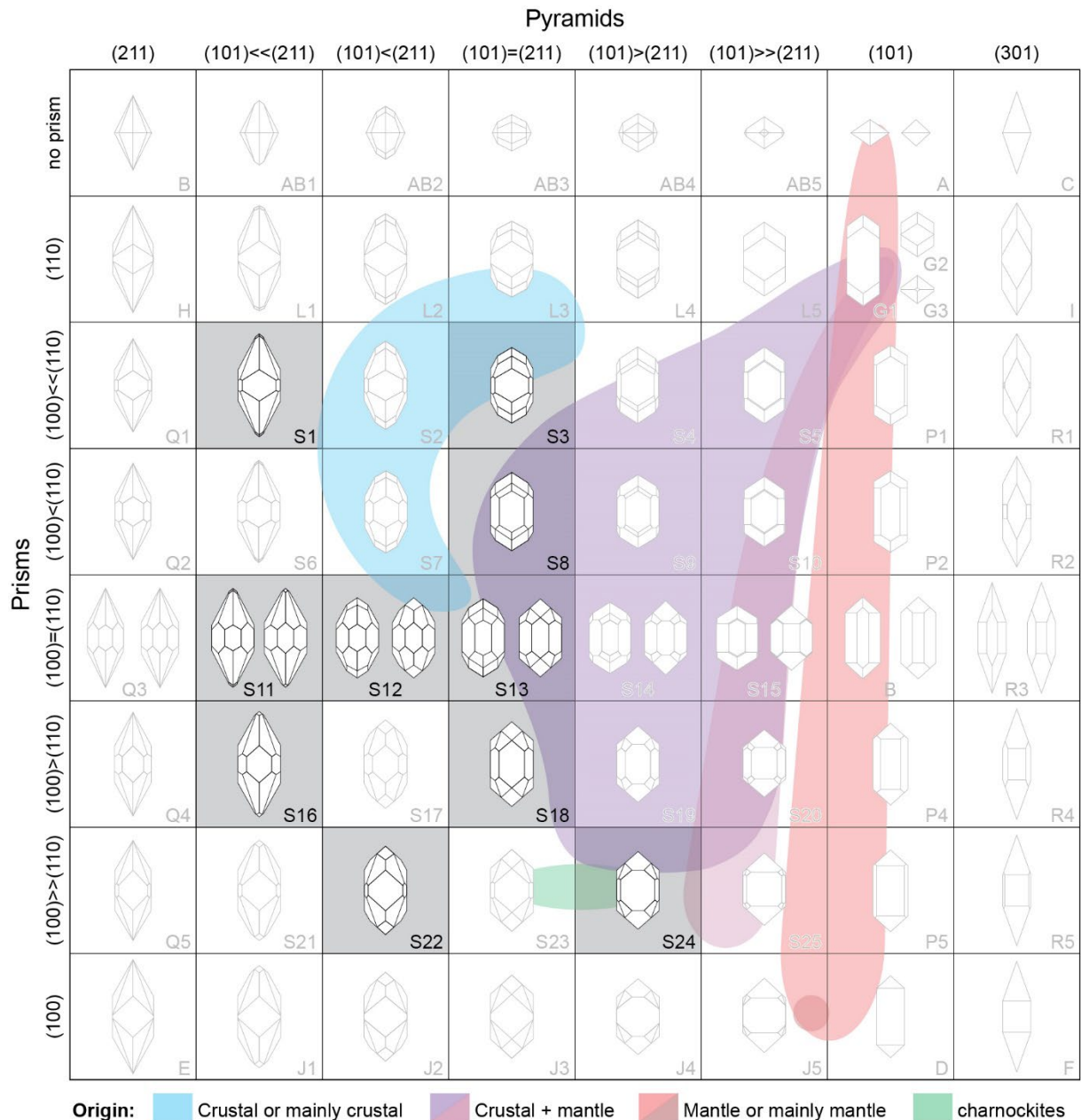
Zircon morphologies in this study suggest a volcanic origin, as would be expected given derivation from bentonites (devitrified volcanic ash). Elongate, needle-like forms observed here support interpretation of high crystallization rate (Corfu *et al.*, 2003) as would be associated with volcanism. The prevalence of captured melt and mineral inclusions is also interpreted to indicate rapid crystallization. It is yet undetermined whether zircons crystallized in a shallow crustal reservoir for geologically definable periods (*i.e.*, magmatic residency) or whether crystallization was more closely associated with an eruption event. Future examination of internal textures may shed light on this concept, which has implications for high precision geochronology and the identification of cryptic inheritance.

Broad inferences about the origin of zircon in this study may also be deduced from the prismatic and pyramidal forms observed (Fig. 6.7). Pupin (1980) proposed that pyramidal forms relate to the relative abundance of aluminium versus alkaline elements within the crystallizing medium. Observations herein show a dominance of the {211} pyramidal form, which may reflect higher abundance of Al with respect to Na+K within the parent magma. Prism forms range between {100} and {110} dominant, thus do little to constrain the possible temperature of the crystallizing medium (Pupin, 1980) or U / trace element variations (Benisek and Finger, 1993).





**Fig. 6.6** SEM secondary electron imagery of loose zircons illustrating excellent crystal forms for a selection of grains (various samples including KP-07A and Plateau) accompanied by schematic outlines. Typology of Pupin (1980) are inset. Prism forms range from  $\{100\}$  to  $\{110\}$  dominant and pyramidal forms range from roughly equal  $\{101\}$  to  $\{211\}$  expression to strongly  $\{211\}$  dominant. Some zircons show different forms at each termination. Evidence of mineral intergrowths/extruding inclusions are shown in panels B and D and gouges/voids are shown most readily in panels A and E.



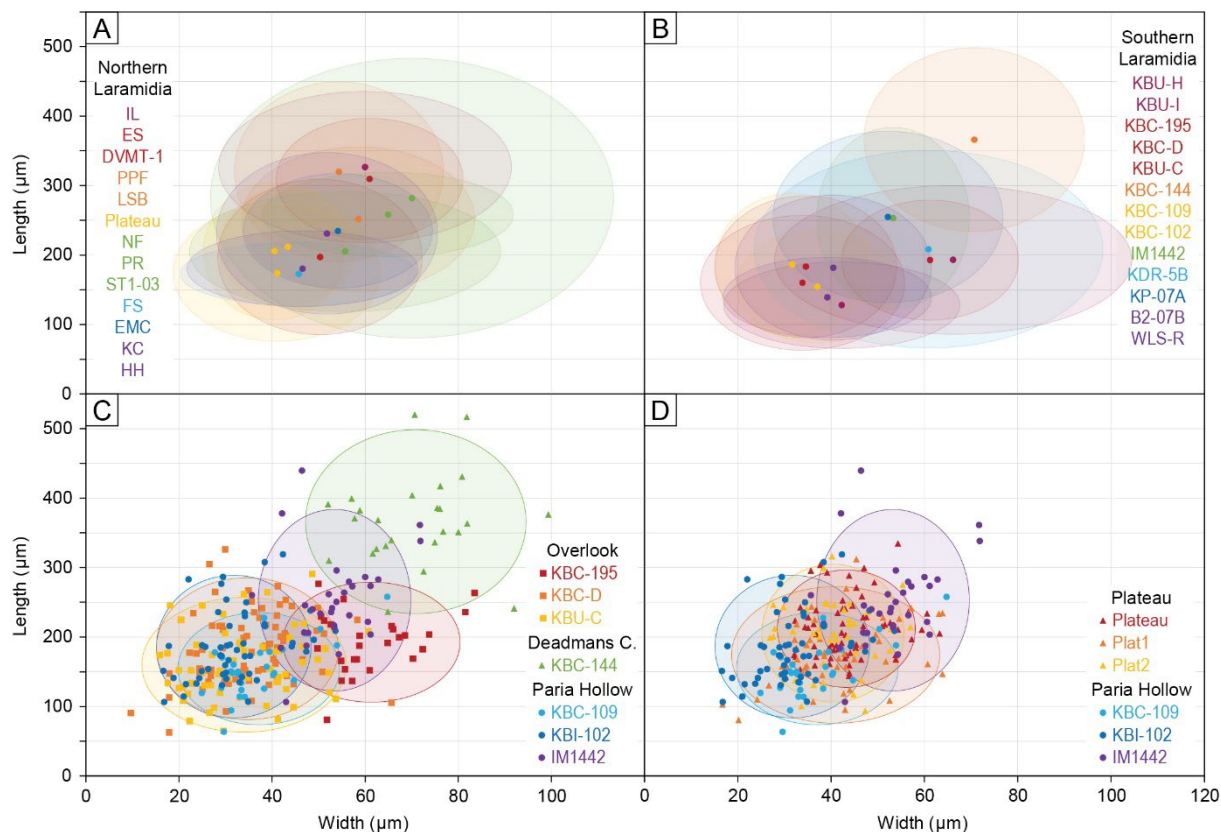
**Fig. 6.7** Pupin diagram highlighting the range of zircon forms observed in this study. Adapted from Pupin (1980) augmented with magmatic source inferences therein. Prism forms are distributed across the {100} to {110} range, whereas pyramidal forms show a preference for {211} dominance. The range of forms observed herein does not fall specifically within crustal or mixed source domains, although it is clearly distinct from the mantle sourced domain.

Zircon morphology was found to have limited applicability as a stand-alone method for correlation and/or distinction of bentonite samples discussed herein. Systematic morphological variation between samples was generally not obvious and was quantitatively unsupported in nearly all instances (Figs. 6.5 and 6.8); thus, the method did not pass the qualifying hypothesis of being capable of distinguishing between unique bentonites. Selected grains shown in Figure 6.5 demonstrate that the average appearance of zircons may differ between stratigraphically arrayed samples, but the range of

proportions within each sample, illustrated as the error envelopes in Figure 6.8, broadly overlap with most samples examined herein. As such, the second and third research questions cannot be robustly investigated, which means that although samples from the Plateau tuff in Alberta and the Paria Hollow Bentonite Bed in Utah appear similar in size and proportions (Fig. 6.8), this doesn't necessarily support correlation of these units as a single, wide-spread ash bed.

Although the zircon morphological characterization approach was found to be mostly ineffective for bentonite tephrostratigraphy, some results yielded useful insights that may lead to future improvements. Examination of the Overlook, Deadmans Corner, and Paria Hollow bentonite beds from the Kaiparowits Formation showed some promise for sample distinction. These beds were represented by four samples with very similar morphologic measurements (the 'main cluster') and three with distinct measurements, one from each bed (Figs. 6.5 and 6.8). The first example of distinct measurements is most likely geologically driven where zircons from the Deadmans Corner Bentonite Bed (KBC-144) were found to have a similar average length/width ratio (5.3) to the main cluster (see Fig. 6.8) but averaged roughly twice the size. This was supported by qualitative descriptions that report generally large grains with exceptionally abundant apatite mineral inclusions compared to most samples (Appendix C.6.4). Thus, zircon morphology can be used for tephrostratigraphy in this specific example to distinguish the Deadmans Corner Bentonite Bed (KBC-144) from bentonite horizons stratigraphically above (Overlook) and below (Paria Hollow).

Other causes of distinctive zircon morphology are more ambiguous. Within the Paria Hollow Bentonite Bed, two attributed samples produce consistent measurements (KBC-109, KBI-102), but IM1442 was found to be subtly distinct. The average morphologic proportions of this sample were similar to the main cluster, but grains were *ca* 45% larger on average. This observation may indicate that IM1442 does not belong to the Paria Hollow Bentonite Bed or that grain size may be highly sensitive to distance from the source or to environmental factors during deposition, but it is also possible that the reported grain size may be biased by sample handling procedures. Introduced bias is the leading suspect in the third distinction noted in this example; that of samples from the Overlook Bentonite Bed. Although the replicate sample of the type outcrop (KBC-D) and the laterally correlated sample KBU-C yielded similar measurements from clear, inclusion-poor, acicular zircons, those from the original type sample (KBC-195) were described as generally less elongated (average length/width = 3.2) and were often fractured and/or turbid with uncommon to rare crystal faces (Appendix C.6.4). Morphological bias was probably introduced in the selection of the subset of zircon from KBC-195 studied here because subsets of zircon from the heavy separates for this sample had previously been removed for other, unrelated analysis on several occasions; thus, it is possible the clearest, inclusion-poor, acicular grains had already been removed from the finite pool of zircon for that sample due to the application of selection criteria (see Section 6.4.2). This finding is somewhat unsurprising but may lead to more careful consideration of sample treatment in the future.



**Fig. 6.8** Summary data for zircon aspect ratio measurements. A-B) Samples from northern and southern field areas, respectively, in approximate stratigraphic order (matching color ramp with groups for coeval units) illustrating average proportions for each sample with an uncertainty envelope of two standard deviations. The data show generally similar aspect ratios although with large overlaps and no clear stratigraphic trend. C) Length and width data for samples pertaining to three unique but closely spaced bentonite beds. Individual data points are shown with error ellipses for each sample (see panel B). Four samples constitute a main cluster while three have marginally more distinguishable ranges. D) Length and width data for samples pertaining to the coeval Plateau tuff from Alberta and Paria Hollow Bentonite Bed from Utah. Individual data points are shown with error ellipses for each sample (see panels A and B). The data overlap significantly, although this is also seen for samples known to be unique from one another. Note the consistent axis scale.

Further examples show that the impact of previous zircon selection and removal on morphological measurements depends on the abundance of grains that demonstrate the targeted morphology. Sample KP-07A of the Horse Mountain Bentonite Bed (Kaiparowits Formation) underwent several rounds of zircon selection and removal prior to this study; however, the grains examined here are relatively large (average 255  $\mu\text{m}$ ) and elongated (average length/width = 5.0). On the other hand, the Plateau bentonite from the Dinosaur Park Formation, Alberta, was re-collected specifically for this study and zircons were selected in three consecutive sessions that yielded subtly decreasing average lengths (212, 206, 174  $\mu\text{m}$ , respectively); a minor but possibly meaningful trend.



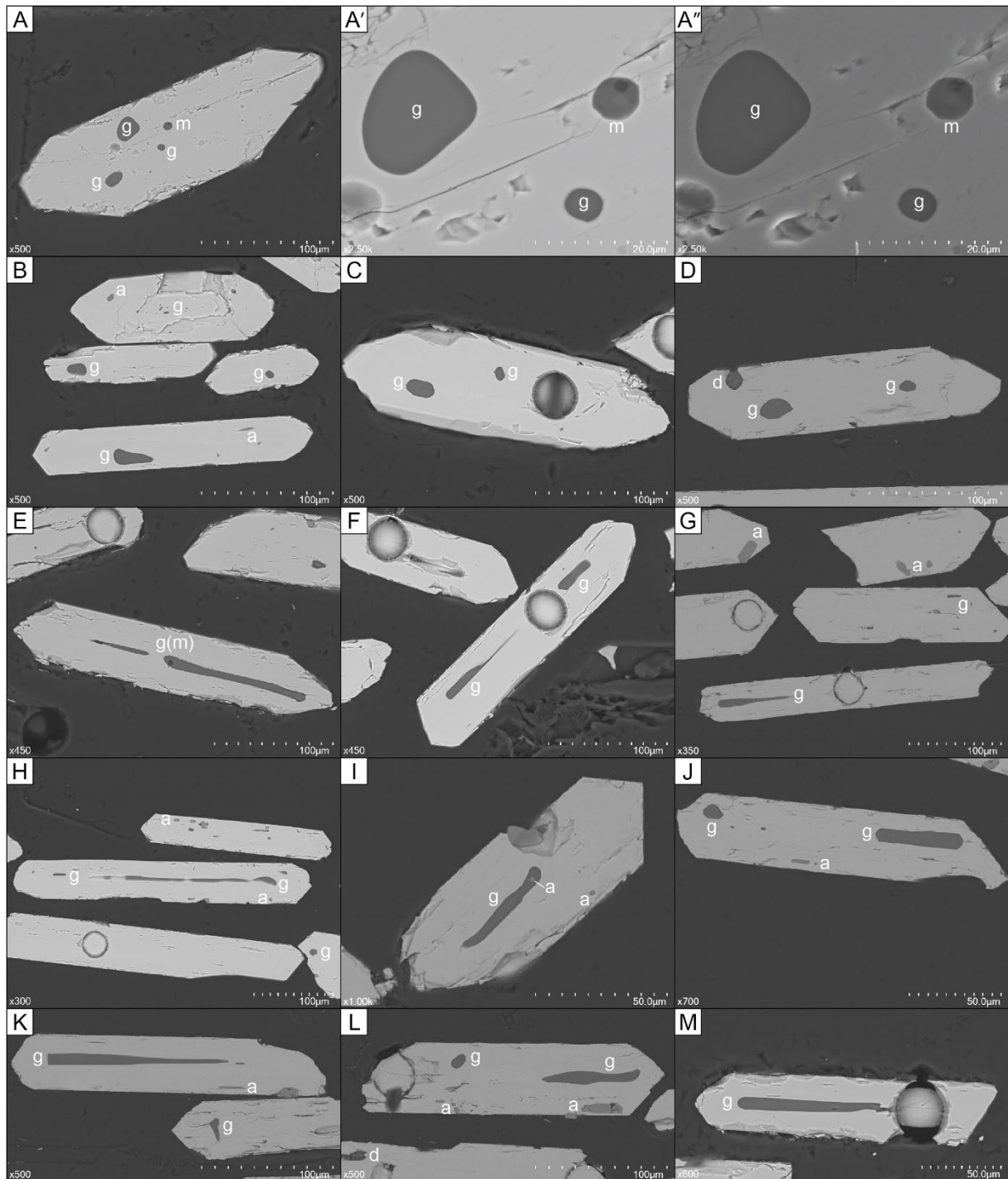
## 6.6 Characterization using melt inclusions

Melt inclusions in magmatic zircon are generally common but rarely examined in detail (Thomas *et al.*, 2003; Gudelius *et al.*, 2020), particularly those from rapidly cooled systems. Chemical characterization of melt inclusions is generally used to establish and investigate magmatic conditions in complex, slow-cooling systems to delineate chemically and temporally distinct phases (Sobolev, 1996; Spandler *et al.*, 2000; Thomas *et al.*, 2003; Gudelius *et al.*, 2020), although early work on zircon hosted inclusions incorporated provenance investigations for detrital samples (Chupin *et al.*, 1998). Melt inclusions provide a direct proxy for parent magma composition at the time of host mineral crystallization and can occur as either homogenous glass or multiphase crystalline inclusions (both with or without vapor bubbles) depending on the rate of cooling (Thomas *et al.*, 2003). In a review of zircon-hosted melt inclusions, Thomas *et al.* (2003) described them to be generally as small as  $\sim 2 \mu\text{m}$  to as large as can be contained within the host mineral, and commonly ovoid to irregularly shaped to occasionally negative-crystal-shaped. Glass inclusions may appear clear or light brown in transmitted light, while crystalline inclusions are typically dark and require homogenization prior to chemical analysis. The microscale size of melt inclusions necessitates microbeam techniques for measurement of their major and trace element composition, typically via electron microprobe but also using secondary ion mass spectrometry (SIMS) and laser ablation inductively coupled plasma mass spectrometry (LA-ICP-MS) (*e.g.*, Morgan and London, 1996; Sobolev, 1996; Chupin *et al.*, 1998; Spandler *et al.*, 2000; Humphreys *et al.*, 2006; Lowe, 2011; Gudelius *et al.*, 2020). Due to the pseudo-stability of glass inclusions (primary or homogenized), electron beam exposure may cause permanent damage in the form of element migration that can impact analytical outcomes if not properly considered (Morgan and London, 1996; Humphreys *et al.*, 2006).

### 6.6.1 Scanning electron microscopy procedure

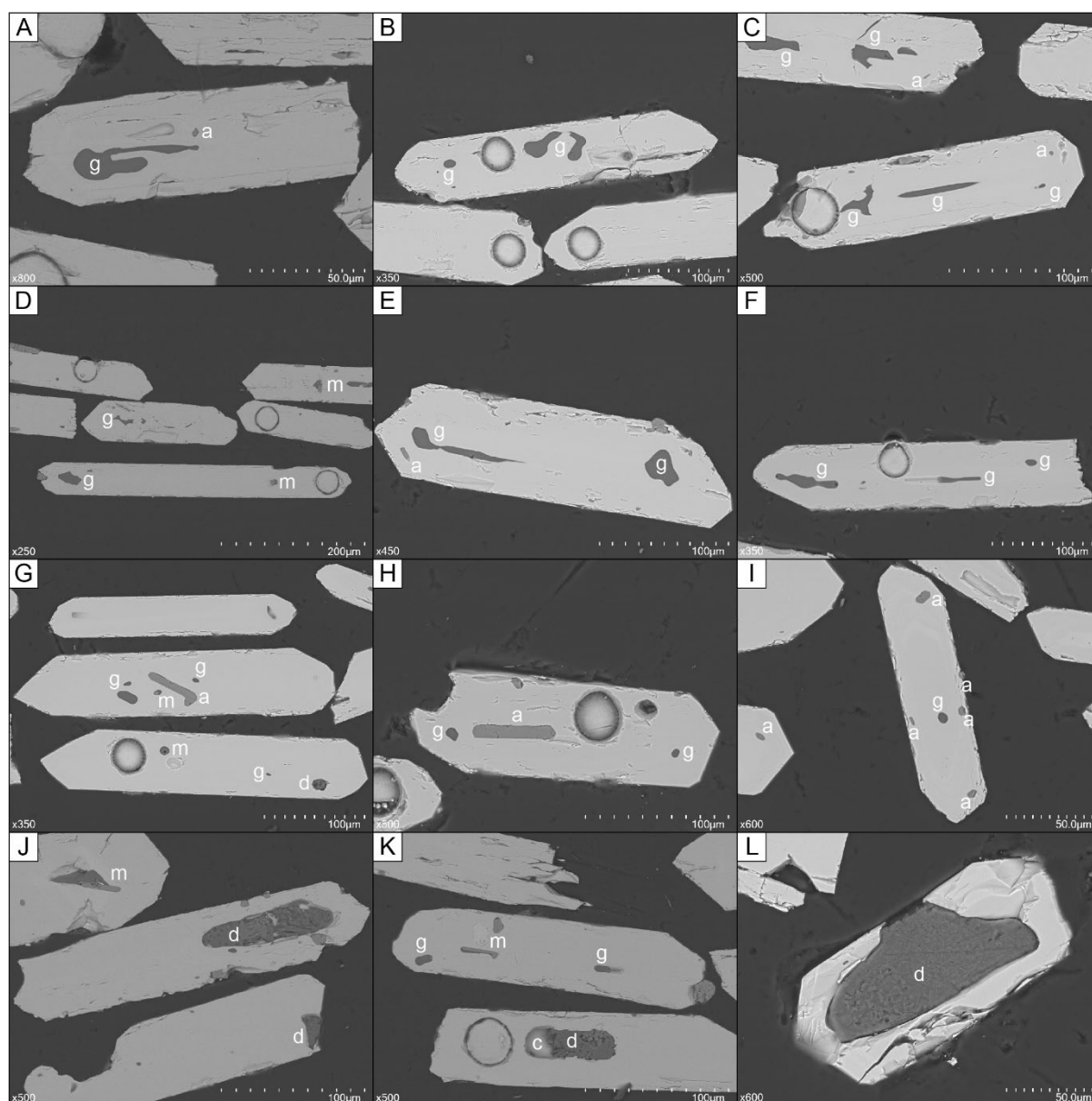
Zircon-hosted melt inclusions were examined herein via general morphological descriptions and major element compositional measurements. The zircon mounts (see Section 6.4.2) were carbon coated and analysed using a Hitachi SU5000 field emission SEM at the AAC, JCU. Backscattered electron mode (BSE) was used to identify inclusions within the host zircons based on comparative emission strength as well as compositional and surface textures (secondary electron mode) (see Fig. 6.9). This screening was used to broadly distinguish between homogenous glass, devitrified glass, multi-phase, and mineral inclusions. Following brief electron beam exposure during identification, the major element composition of each inclusion was measured using quantitative energy dispersive spectroscopy (EDS) with 20 second count times (plus *ca* 6% deadtime) using an acceleration voltage of 15 kV and calibrated according to internal laboratory standards. Although a glass standard was not used in this work, measurements were checked against the stoichiometric composition of the host zircons and apatite inclusions. The size of the analysis window was adjusted depending on inclusion size and shape (Figs. 6.9 and 6.10) and limited to no less than  $\sim 1 \mu\text{m}$  width to reduce the extent of electron beam damage. This damage was also reduced





**Fig. 6.9** Examples of zircon-hosted glass inclusion morphologies imaged in BSE mode. A) ovoid melt inclusions, A') higher magnification of panel A, A'') same area as panel A' in SEI mode to illustrate smooth surface textures of the inclusions. B-D) ovoid morphologies. E-M) elongate morphologies. Inclusion annotation: g = glass, a = apatite, d = devitrified, m = multi-phase.

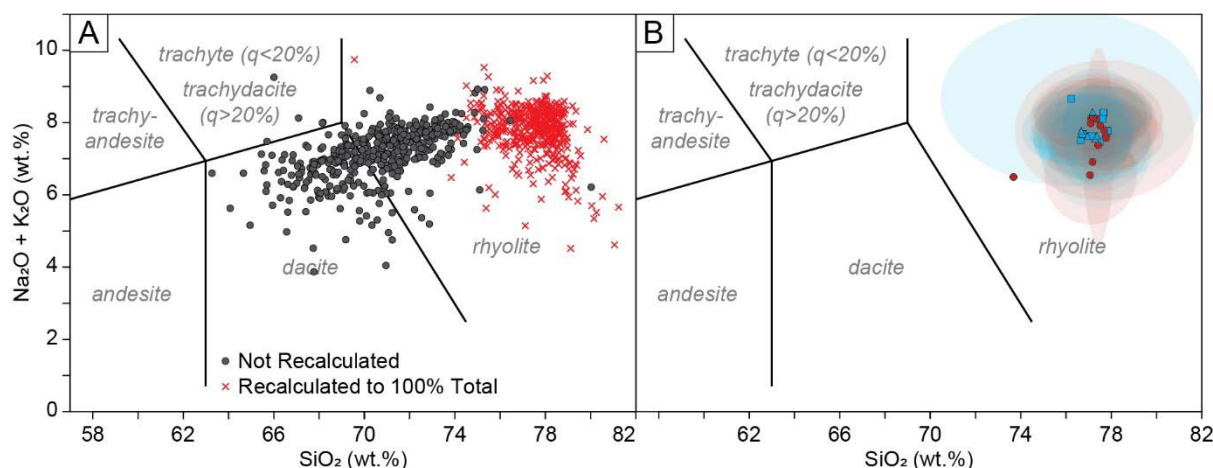
by imaging the inclusions and host zircons (BSE and CL) after compositional analysis rather than before. After all SEM work was completed, the grain mounts were gently polished to remove the carbon coat. Following later analyses (LA-ICP-MS; Section 6.7.1), the zircon mounts were repolished to expose grains approximately equatorially and thus also expose larger inclusions deeper within the crystals. The



**Fig. 6.10** More examples of zircon-hosted glass inclusion morphologies imaged in BSE mode. A-F) irregular morphologies. G-I) apatite mineral inclusions. J-L) devitrified melt inclusions. Inclusion annotation: g = glass, a = apatite, d = devitrified, m = multi-phase, c = cavity.

melt inclusion methodology described above was then applied to the repolished mounts.

The major element data were reduced and handled in Microsoft Excel and details of data reduction procedures are included in Appendix B.4. The most novel of these procedures was recalculation of melt inclusion composition to account for analysis that marginally overlapped with the host zircon, which was necessary due to the generally small size of the inclusions. This recalculation was conducted using the stoichiometric composition of zircon and the measured zirconium concentration (wt.%) assuming this component would be undetectable in a purely glass analysis given the limits of the analytical approach (Appendix B.4).

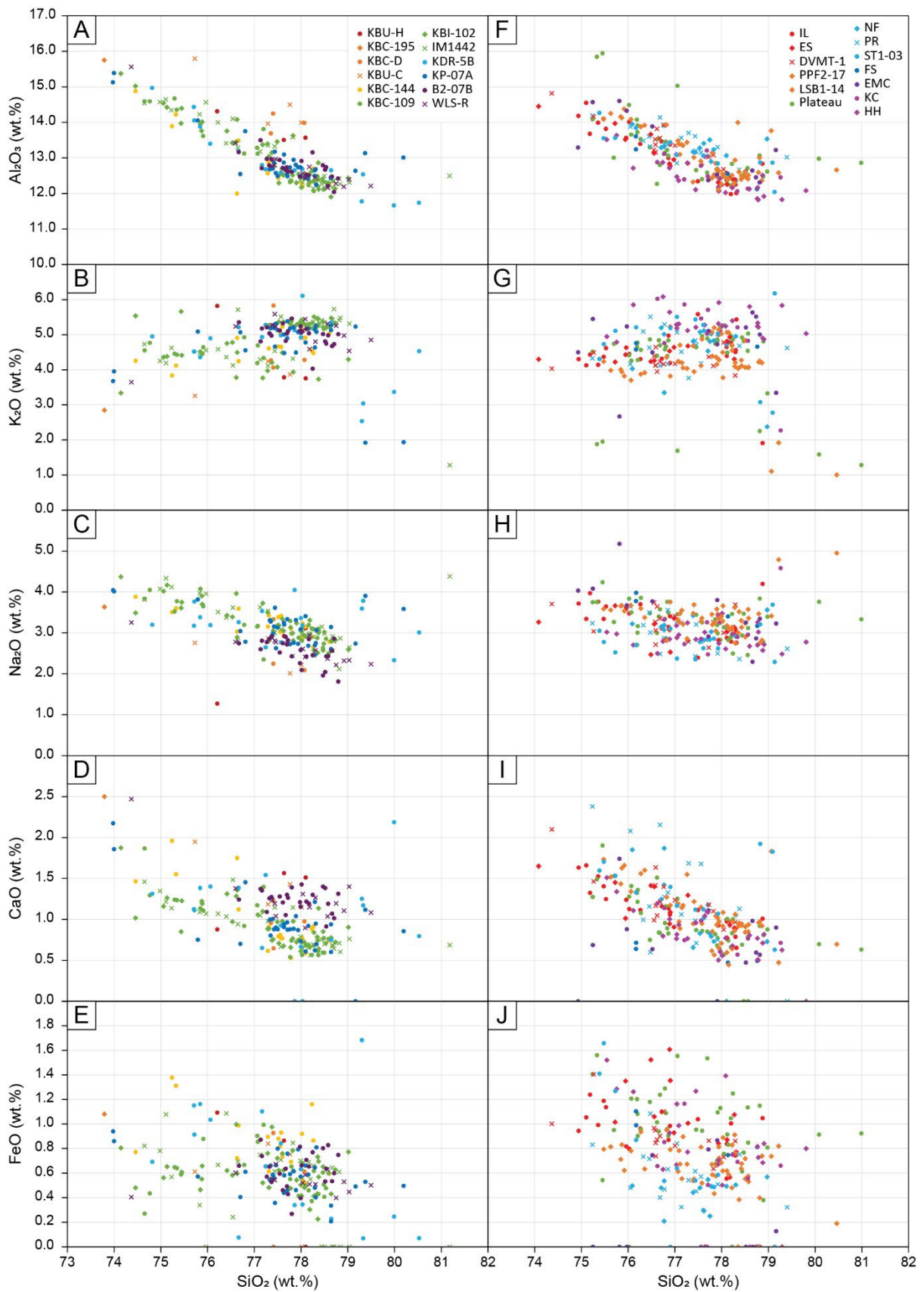


**Fig. 6.11** Zircon-hosted glass inclusion total alkali versus silica (TAS) diagrams. A) All melt inclusion data points before and after recalculation to anhydrous composition (100% total) as per Le Bas et al. (1986). B) TAS diagram illustrating the average composition of samples with two standard deviation error ellipses. All samples reflect a rhyolitic magma composition; samples from northern areas are shown in blue (Alberta = triangles, Montana = squares) and those from the south (Utah) are shown as red circles.

### 6.6.2 Melt inclusion morphology results

Melt inclusion morphology was examined to infer broad generalizations about the inclusions rather than to characterize specific samples. The dominant type observed in this study were glassy inclusions, which were observed to be texturally smooth, homogenous domains of contrasting compositional response (darker than the surrounding zircon in BSE; Figs. 6.9 and 6.10). Outer zones of the host zircons were found to be either barren or contain only very small glass inclusions ( $< 2 \mu\text{m}^2$ ). Considerably larger inclusions were found in the cores of some grains, including exposed areas up to  $ca 840 \mu\text{m}^2$ ; although, inclusions of this size were exceedingly rare, and the average was roughly an order of magnitude smaller or less. Since most inclusions were not exposed equatorially, the size of the exposed areas was not examined in detail. Typical glass inclusion morphologies observed in this study fell into three groupings: elongate, ovoid, and irregular (Figs. 6.9 and 6.10). Backscattered electron imagery cannot confirm whether ovoid and elongate inclusions represent the same morphology shown in perpendicular orientations; however, transmitted light microphotographs show that elongated inclusions are strongly aligned with the long crystal axis and that ovoid inclusions can occur in isolation (Appendix C.6.3).

Other types of inclusions observed in this study included glassy inclusions with vapor bubbles, devitrified inclusions (partly or wholly turned to clay), and multi-phase melt inclusions; all of which were far less common than pure glass inclusions. Multi-phase inclusions typically contained a small portion of glass, one or multiple vapor bubbles and accessory-type phases; most commonly apatite and occasionally titanite. No fully crystalline multi-phase inclusions were observed. Mineral inclusions were dominantly apatite and rarely titanite, feldspars, quartz, and iron-oxide minerals. Apatite inclusions were



**Fig. 6.12** Zircon-hosted glass inclusion major element bivariate plots. A-E) Southern Laramidia samples. F-J) Northern Laramidia samples. Although many of the bivariate relationships show correlated trends, distinction between bentonite samples is difficult without further statistical treatment.



generally spindly and randomly orientated in most samples. Some samples (particularly B2-07B) showed zoned patterns where glass inclusions were found in the core of grains and apatite was more common in the peripheries (Fig. 6.10). Impressions of apatite and other minerals were also observed on the outside surface of some zircon grains (Fig. 6.6).

#### 6.6.3 Melt inclusion major element composition results

A total of 435 viable analyses were collected for the major element composition of zircon-hosted glass inclusions from 25 bentonite samples. All sample compositions broadly overlap and plot as a tight cluster in the rhyolite field on a total alkali versus silica (TAS) diagram when recalculated to a total weight of 100%, as recommended by Le Bas *et al.* (1986). Recalculation based on total weight percent was observed to reduce data scatter, as illustrated in Figure 6.11. Most major elements were observed to show inverse correlation with silica content except potassium, which was independent of or slightly increased with increasing silica (Fig. 6.12). Total iron was also observed to be mostly independent of silica content and generally constituted a small contribution to the total oxides (<1.5 wt.%). Compositional distinction of samples from within and between field areas was difficult to quantify due to significant data overlap, although some samples showed a greater degree of clustering than others.

#### 6.6.4 Melt inclusion interpretation

Data from, and observations of melt inclusions in this study confirm that the zircon in these bentonites are of volcanic origin, as expected. Rapid cooling / crystallization associated with eruptive volcanism is inferred from 1) the frequency of inclusions in the studied zircons, 2) a clear dominance of single-phase glassy inclusions, and 3) the commonality of elongate inclusion morphologies (see Thomas *et al.*, 2003). Instances of either slightly less rapid cooling or proportionally higher volatile content may be inferred by the uncommon occurrence of vapor bubbles within glassy inclusions. Mineral phases in the equally uncommon multi-phase inclusions were dominated by apatite ( $\pm$  titanite), which are unlikely to have precipitated from the trapped melt as daughter crystals, and probably represent trapped minerals from the parent magma that were co-crystallizing with zircon. This interpretation could be further tested using homogenization experiments that were otherwise unnecessary in this investigation due to the dominance of glassy inclusions (already homogenous).

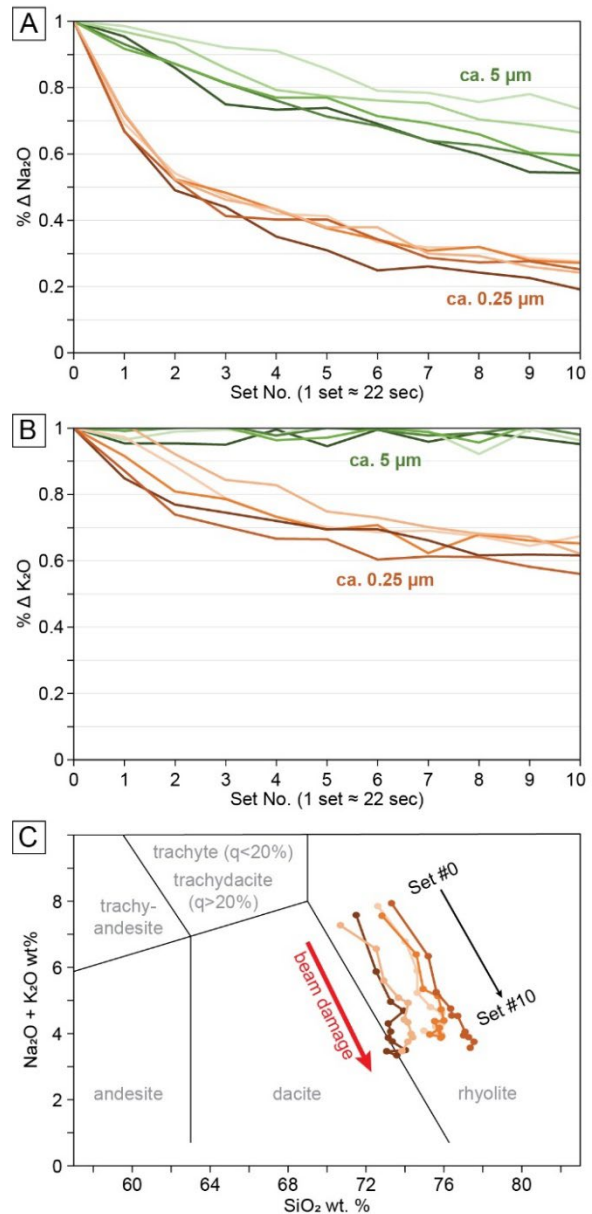
The major element composition of glass inclusions in this study also reflects a far-travelled volcanic ash protolith. Silica content across all samples was generally high and consistently averaged ~77% (wt.) when data were recalculated to 100% totals, as recommended for TAS classification (Le Bas *et al.*, 1986; see also Lowe, 2011). These values, plotted against total alkali content (ca. 6-8 wt. %) strongly indicate a rhyolitic parent magma (Fig. 6.11). This finding supports inferences that the volcanic sources of bentonites in this study were highly explosive (high silica content; Plinian-style), producing far-travelled volcanic ash up to hundreds of kilometers from the basin margins into depositional settings. This data represents the first direct measurement of the parent magma major element composition for



these bentonites and is a considerable improvement in this respect from previous whole-rock bentonite analyses that were impeded by chemical alteration (*e.g.*, Foreman *et al.*, 2008; Fanti, 2009). These studies instead used the trace element composition of the whole-rock bentonite samples and although this approach may have also been useful for glass inclusion characterization in the present study, most of the inclusions examined here were too small given the methods available at the time of investigation. Future work may explore this option in more detail.

Characterization of bentonite beds using the major element composition of zircon-hosted glass inclusions is a novel approach that applies tephrostratigraphic methods to ancient, devitrified tephra deposits (bentonites). Results in this study demonstrate significant potential, particularly for better characterization of parent magmas; however, as with zircon morphology, the procedure applied here had difficulties in distinguishing between different bentonite beds and requires additional refinements. Future use of glass standards (*e.g.*, NIST610/612) may help to delineate analytical precision from natural variability in parent magma compositions. The spread of the data herein may represent genuine geologically driven variation such as temporally heterogeneous melt entrapment or cryptic zircon inheritance, or it may be an artifact of the approach that could be addressed and mitigated in future work.

Two major trends were noted during data reduction: one roughly parallel to the silica saturation/oversaturation field boundary (trachydacite/dacite) on the TAS diagram, and the other roughly parallel to the dacite-rhyolite field



**Fig. 6.13** Demonstration of electron beam damage. Comparison of the change in sodium (A) and potassium (B) across sequential analysis (20 seconds each plus deadtime) illustrating the difference in element migration for comparably high (*ca.* 0.25 μm; orange) and low (*ca.* 5 μm; green) beam intensity. Data represent the change in composition relative to the first of eleven analyses. C) TAS diagram representation of electron beam damage observed for analyses at *ca.* 0.25 μm illustrating the rhyolite/dacite-boundary-parallel trend.

boundary. The first of these primarily reflects variation in SiO<sub>2</sub> content, which was found to be closely dependent on the total weight percent of each analysis and was significantly reduced when data were recalculated based on 100% totals (as recommended by Le Bas *et al.*, 1986). Inclusions that yielded less than 85% total oxides were not used; however, an unaccounted portion of 15% is still considerably higher than could be attributed to volatile content alone. Due to the application of EDS that matches spectral peaks to a complete catalogue of element data (rather than wavelength dispersive spectroscopy (WDS) using an electron microprobe that requires a defined list of less than a dozen common elements) the missing component is unlikely to constitute an unmeasured oxide. The most probable explanation may be heterogeneous surface textures/level. Slightly embayed inclusions may return lower totals, given that the electron beam is focused at the surface of the host zircon and may explain why this issue appears specific to the present study. Anecdotal observations support this hypothesis although detailed investigation is yet to be conducted. Future work may also investigate polishing techniques to mitigate glass inclusion embayment.

The second data distributional trend, oriented roughly parallel to the dacite-rhyolite field boundary, may reflect subtle electron beam damage. With the knowledge that electron beam exposure may cause element migration (Humphreys *et al.*, 2006), tests were undertaken herein to generalize the scope of damage possible based on the applied methodology. This testing involved eleven repeated analyses using two beam diameters, which include: 1) the optimal analysis size (>5 µm window) and 2) an exceedingly small analysis size (~0.25 µm window). Five areas for each beam size were selected from inclusions across three similar samples. Results from this testing are illustrated in Figure 6.13. Clearly prolonged exposure at high beam intensities (small analytical area) caused significant migration of sodium and, to a lesser extent, potassium. These correspond to a proportional increase in silicon (and aluminium), thus producing a rhyolite/dacite-boundary-parallel trend. Although this data represents only a demonstration of beam damage and lacks the rigor of an in-depth beam damage investigation, it shows that precautions implemented in the main method (including maximizing the analytical area) are probably sufficient for beam damage mitigation to the extent relevant for the present study. For future, more rigorous work, a consistent analytical area may be employed where possible or, if this is not possible due to inclusion size/morphology, data may be grouped by the analytical area applied so that potential introduced biases may be investigated.

### **6.7 Characterization using zircon chemistry**

Zircon constitutes a primary sink for U, Th, Hf, and the REE budget of magmatic systems (Hoskin and Schaltegger, 2003) and thus preserve a geochemical signature of their source that can be used to characterize samples. Due to practically identical geochemical behavior, Hf readily substitutes for Zr in zircon up to ~2 wt.% (Hoskin and Schaltegger, 2003; Kinny and Maas, 2003), which facilitates investigation of Lu-Hf systematics for parent magma source determination. Zircon trace element

composition is also frequently used for these purposes and can yield insights into fractionation processes and rock classification (Belousova *et al.*, 2002; Hoskin and Schaltegger, 2003). Both Lu-Hf isotopic composition and trace element composition in zircon are commonly determined using laser ablation inductively coupled plasma mass spectrometry (LA-ICP-MS) for in situ analysis of relatively small analytical volumes (Halliday *et al.*, 1995; Kinny and Maas, 2003; Belousova *et al.*, 2006) although solution ICP-MS and TIMS, and in situ SIMS may also be used (Patchett and Tatsumoto, 1980; Kinny *et al.*, 1991; Blichert-Toft and Albarede, 1997).

#### 6.7.1 Microbeam analysis procedure

Zircon grains were analysed for Lu-Hf isotope ratios (and trace element composition) via laser ablation inductively coupled plasma mass spectrometry (LA-ICP-MS) at the AAC, JCU, adapted from the approach of Kemp *et al.* (2009) and Tucker *et al.* (2016). In situ ablation was conducted using a Teledyne Analyte G2193 nm Excimer Laser with HeLex II Sample Cell with spot sizes of 40  $\mu\text{m}$  and 25  $\mu\text{m}$  for Lu-Hf isotopes and trace elements, respectively. Preliminary examination of the trace element data is promising, and generally reflects similar findings as other characterization methods herein in the context of bentonite correlation; however, due to time constraints, this avenue of investigation remains a topic for future investigation.

Lu-Hf isotopes were measured across two consecutive days using a Finnegan Neptune multi-collector mass spectrometer calibrated against Mudtank (primary) and Plesovice (secondary) zircon standards. A maximum of 15 grains were analysed per sample unless otherwise specified. Data were handled in Microsoft Excel using the  $^{176}\text{Lu}$  decay constant of Söderlund *et al.* (2004) and the CHUR  $^{176}\text{Lu}/^{177}\text{Hf}$  and  $^{176}\text{Hf}/^{177}\text{Hf}$  ratios of Bouvier *et al.* (2008). The weighted mean  $\epsilon\text{Hf}$  value for each sample was derived in the first instance from all overlapping analysis. This result was used for 11 of the 28 samples. Where the MSWD of the initial weighted mean was greater than three (possibly indicating multiple grain populations), data were visually inspected for outliers. Thirteen samples were refined using this approach, four of which still produced weighted means with  $\text{MSWD} > 3$ . Four of the 17 first instance weighted means with  $\text{MSWD} > 3$  did not show obvious outliers; thus, the original data were retained.

#### 6.7.2 Lu-Hf isotopic composition results

A total of 367 viable analyses were obtained for the Lu-Hf isotopic composition of zircons from 28 bentonite samples (Table 6.2). The weighted mean  $\epsilon\text{Hf}$  values generally cover a broad negative range, with one positive exception. Figure 6.14 illustrates weighted mean  $\epsilon\text{Hf}$  versus age (both with uncertainty) for all samples in this study, and specifically of the most data-dense interval between 74 and 77 Ma. The  $\epsilon\text{Hf}$  values of samples from Utah appear to generally decrease over time; although, several less negative samples demonstrate significant up-section heterogeneity. A convincing time-

**Table 6.2** Age and  $\epsilon\text{Hf}$  summary data for samples examined herein, listed in age order.

Sample	Age (Ma)			$\epsilon\text{Hf}$ Summary				
	$^{206}\text{Pb}/^{238}\text{U}$	Error*	Ref.	Weighted mean	Error	MSWD	$n_m$	$n_e$
KBU-F	73.68	0.81	5	-15.03	0.45	2.1	14	0
KBU-H	74.80	0.17	5	-14.19	0.25	1.4	9	11
KBU-I	74.80	0.17	5	-14.94	0.19	1.1	9	6
KBU-V	73.68	0.66	5	-15.22	0.37	0.45	8	3
IL	74.27	0.017	2	-16.55	0.5	2.9	7	8
ES	ca 74.4	(con)	1	-16.5	1.1	14	15	0
DVMT-1	~74.5	N/A	1	-14.76	0.38	1.4	14	1
PPF	75.22	0.031	2	-16.29	0.41	1.9	15	0
KBC-195	75.23	0.021	2	-13.04	0.41	2	15	0
KBC-D	75.23	0.021	4	-13.98	0.29	2.7	14	1
KBU-C	75.23	0.021	4	-13.33	0.2	1.15	9	2
LSB	ca 75.2	(con)	1	-16.98	0.39	1.7	15	0
KBC-144	75.43	0.012	2	-2.13	0.41	2	15	0
KBC-109	75.61	0.015	2	-7.57	0.6	6.8	9	0
KBI-102	75.61	0.015	4	-7.82	0.62	5.5	9	4
Plateau	75.64	0.025	2	-4.02	0.36	3.7	14	1
IM1442	75.66	0.036	4	-7.95	0.28	2.2	15	0
KDR-5B	76.26	0.019	4	-11.65	0.21	1.3	12	3
NF	~76.3	N/A	1	-21.13	0.98	9.6	13	2
PR	ca 76.3	(con)	1	-20.2	1.1	11.9	14	4
ST1	76.33	0.035	2	-21.09	0.71	4.3	12	3
KP-07A	76.39	0.04	2	-9.92	0.31	2.3	13	2
FS	76.72	0.02	2	-1.62	0.17	1.14	15	1
EMC	ca 78.0	(con)	1	2.69	0.38	2.7	10	5
KC	78.59	0.024	2	-2.83	0.58	3.6	15	1
HH	ca 78.6	(con)	1	-2.78	0.27	2	13	2
B2-07B	81.48	0.024	3	-6.18	0.23	1.3	10	5
WLS-R	81.47	0.036	3	-6.27	0.49	1.8	5	2

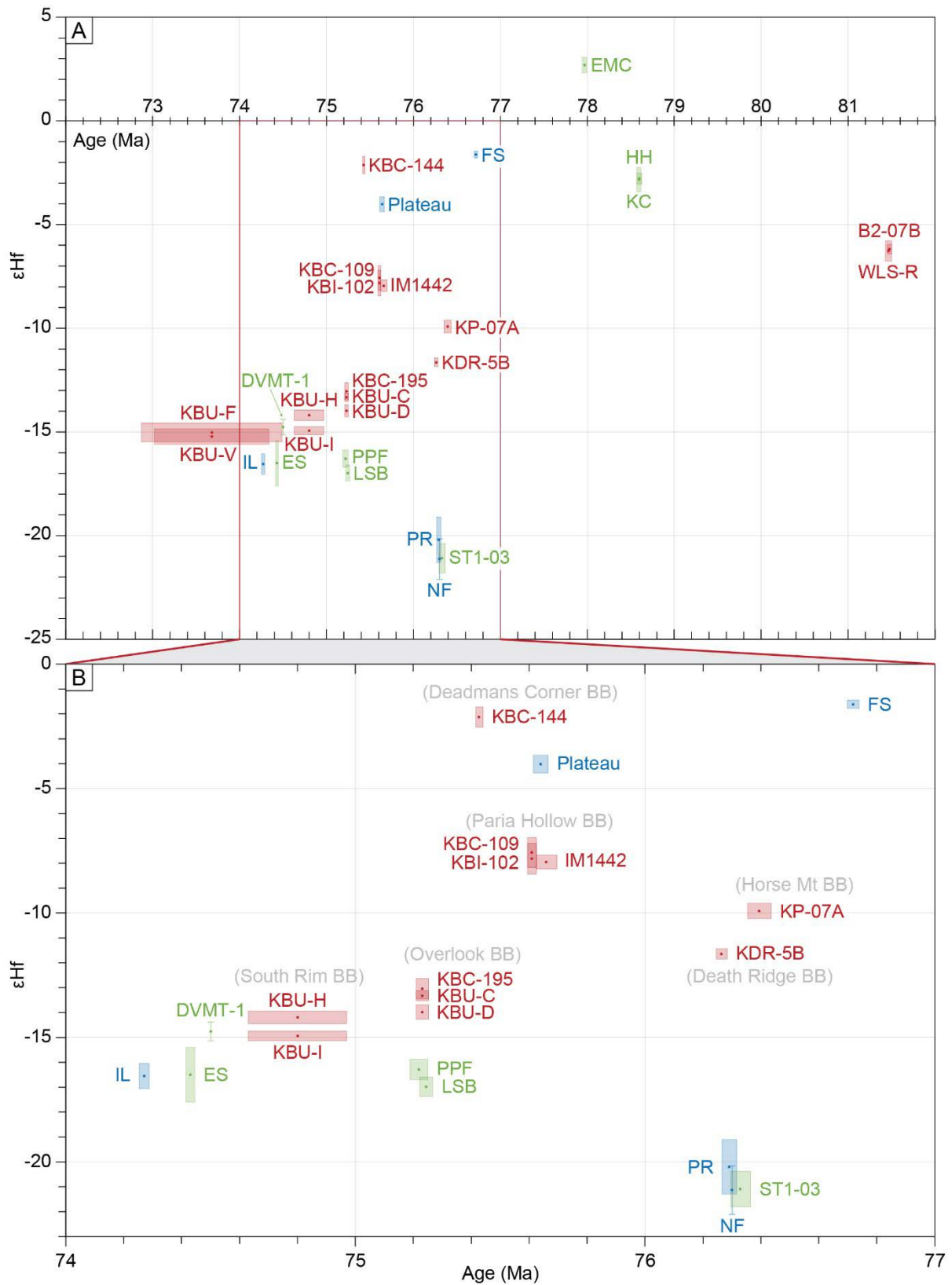
All ages except KBU-F, KBU-H, KBU-I, and KBU-V were generated using CA-ID TIMS. Exceptions were generated using LA-ICP-MS. The age of some samples was inferred (~) from confident correlation with a dated horizon.

\* Error for CA-ID-TIMS ages use the internal uncertainty while LA-ICP-MS ages use the propagated uncertainty (both  $2\sigma$ ).

Ref. = Reference; 1 not yet published (con = confidential), 2 Ramezani et al. (in review), 3 Beveridge et al. (2022 [Ch.3]), 4 Beveridge et al. (in prep [Ch.4]), 5 Beveridge et al. (2020 [Ch.5]).

MSWD = mean square of weighted deviates,  $n_m$  = number of analyses in the weighted mean,  $n_e$  = number of analyses excluded from the weighted mean.

dependent trend was not observed across samples from northern Laramidia. Several instances of contemporaneous bentonites recorded  $\epsilon\text{Hf}$  values that are either identical, closely comparable, or entirely distinct. Most commonly, contemporaneous bentonites from the same region (*i.e.*, northern or southern Laramidia) frequently yielded significantly overlapping  $\epsilon\text{Hf}$  weighted means (*e.g.*, B2-07B and



**Fig. 6.14** Summary of age ( $X$  uncertainty) versus  $\epsilon_{\text{Hf}}$  for bentonites in this study. A) All samples. B) Expansion of the most densely populated interval (74-77 Ma). Samples from Utah are shown in red, Montana in green and Alberta in blue. BB = bentonite bed (Utah only).



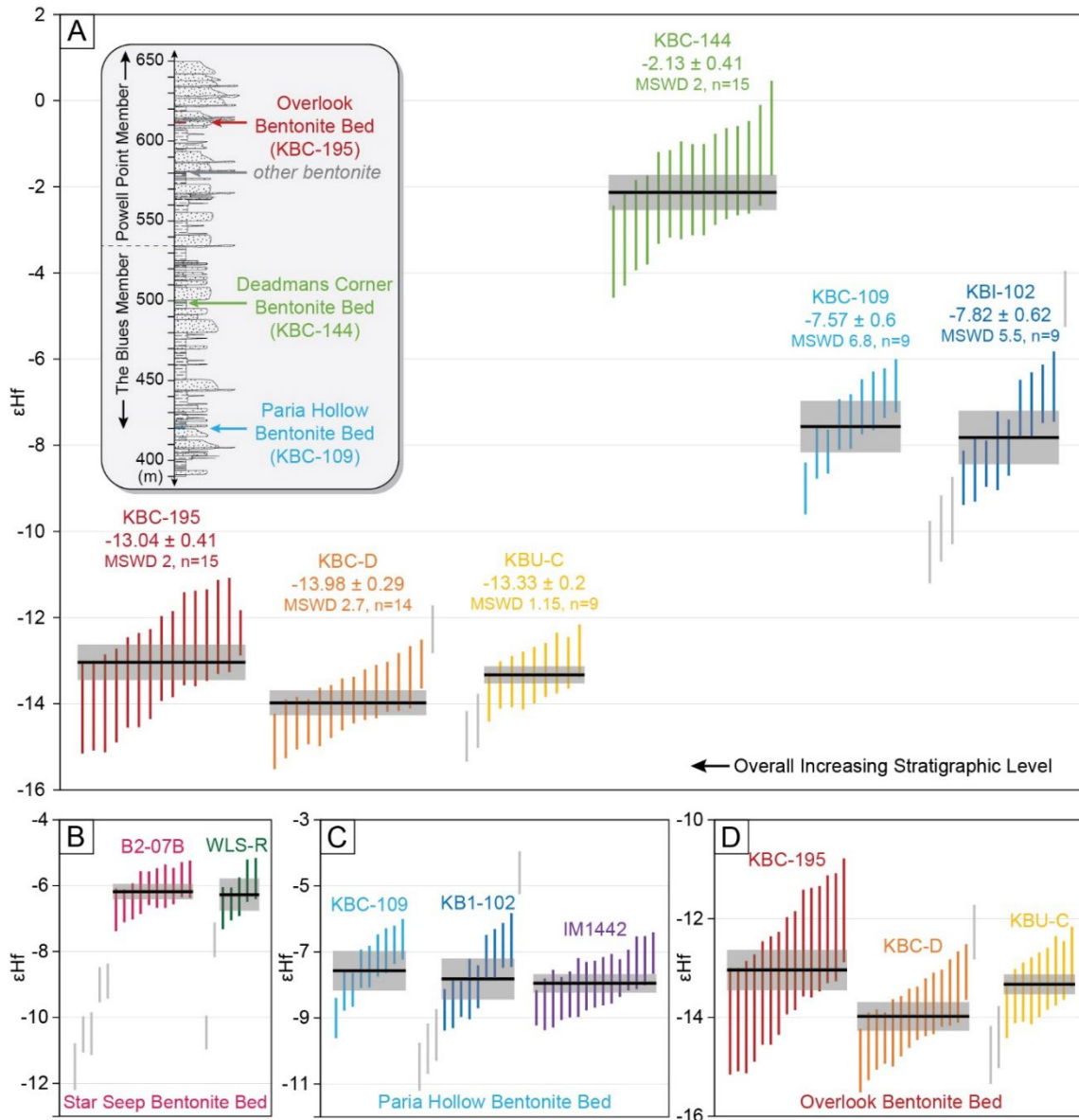
WLS-R; KC and HH). Occasionally, presumed correlative bentonites from the same region did not yield overlapping  $\epsilon\text{Hf}$  weighted means, although individual grain data overlap considerably (*i.e.*, KBU-C, KBC-D, and KBC-195; KBU-H and KBU-I). There are no instances of overlapping  $\epsilon\text{Hf}$  weighted means for contemporaneous bentonites from southern and northern Laramidia.

### 6.7.3 $\epsilon\text{Hf}$ interpretation

The  $\epsilon\text{Hf}$  signature of zircon was found to be an effective tool for characterization of bentonites in this study, on par with and complementary to precise U-Pb geochronology. The  $\epsilon\text{Hf}$  signature of analysed zircons demonstrate that these beds were sourced from magmas enriched in Hf relative to the bulk silicate earth, as demonstrated by the prevalence of negative  $\epsilon\text{Hf}$  values, sometimes strongly negative ( $<-20$ ). This finding reflects an intracontinental setting for parent magma generation involving melting and assimilation of continental crust, which is consistent with a shift in magmatism at this time (post-80 Ma) from arc magmatism at the western plate margin to eastward migrating volcanic centers, particularly in southern areas (*e.g.*, Coney and Reynolds, 1977; Dumitru, 1990; Lageson *et al.*, 2001). The isotopic data records high diversity from a geologically brief interval within the Campanian, interpreted to reflect a variety of discrete and geochemically evolving magmatic centers across Laramidia, from north to south.

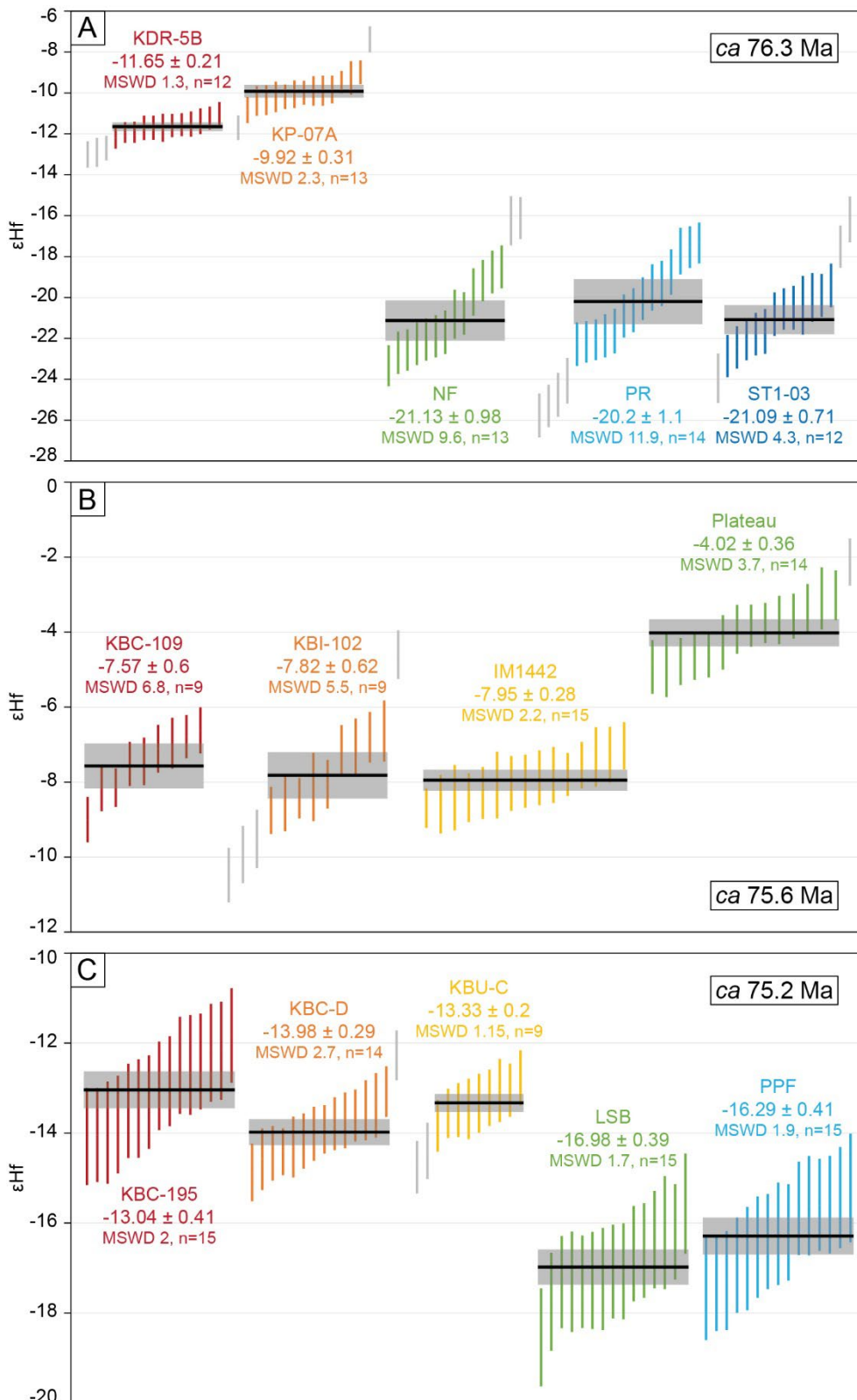
Zircon Lu-Hf systematics were successfully applied to bentonite characterization to investigate all three research questions put forward for consideration in this study (Fig. 6.15 and 6.16). Weighted mean  $\epsilon\text{Hf}$  values for bentonite samples were found to be precise enough to distinguish between different horizons in this study. The primary case example was for three stratigraphically closely spaced bentonite beds in the KBC section of the Kaiparowits Formation, southern Utah (Fig. 6.15). The KBC-109 and KBI-102 samples from the Paria Hollow Bentonite Bed (Beveridge *et al.*, in prep [Ch.4]) yielded a weighted mean  $\epsilon\text{Hf}$  range of -7.82 to -7.57 ( $\pm 0.6$ ). Seventy-eight meters above this bed, the weighted mean for the Deadmans Corner Bentonite Bed, represented by KBC-144, was  $-2.3 \pm 0.41$ . The overlying Overlook Bentonite Bed, which is 114 m above the Deadmans Corner Bentonite Bed, is represented by samples KBC-195, KBC-D, and KBU-C. These samples yielded a weighted mean  $\epsilon\text{Hf}$  range of -13.98 to -13.04 ( $\pm 0.4$ ). These results demonstrate that zircon  $\epsilon\text{Hf}$  tephrostratigraphic method is capable of distinguishing between different bentonite beds, including those in close stratigraphic succession. In the northern field areas, bentonite samples with clearly different ages did not ubiquitously demonstrate distinguishable  $\epsilon\text{Hf}$  signatures (samples LSB, PPF, ES and IL yielded  $\epsilon\text{Hf}$  of *ca* -16.5), meaning that this approach may not always be as successful as demonstrated by the primary example from the Kaiparowits Plateau.

Results demonstrate that the  $\epsilon\text{Hf}$  signature of zircons from bentonite samples is consistent across the lateral extent of these horizons, supporting a positive outcome for the second goal of this study.



**Fig. 6.15**  $\epsilon_{\text{Hf}}$  signature for bentonites from southern Utah demonstrating correlation and distinction. A) Example of bentonites known to be unique (known from the same stratigraphic succession, and their presumed correlatives) distinguishable based on  $\epsilon_{\text{Hf}}$  weighted means and single grain values. Inset illustrates the relative position of the bentonite beds within the KBC lectostratotype section of Roberts (2007). B-D) Examples of bentonites suspected to be correlative pairs/sets based on age and stratigraphic relationships demonstrating matching  $\epsilon_{\text{Hf}}$  signatures.

Specifically, the examined groupings show matching weighted mean  $\epsilon_{\text{Hf}}$  values, thus confirming that this approach is suitable for correlation of bentonite beds across broad areas (Fig. 6.15; see also Fig. 6.3). The first set of samples tested for correlation was the B2-07B and WLS-R bentonite pair, which were previously correlated based on matching stratigraphic levels and overlapping CA-ID-TIMS ages from both localities (Beveridge *et al.*, 2022 [Ch.3]). The essentially identical  $\epsilon_{\text{Hf}}$  signatures for these two samples are definitive support for the approach. The second set of samples represent the Paria Hollow Bentonite Bed in the Kaiparowits Formation, which includes samples KBC-109 (type locality),



**Fig. 6.16**  $\epsilon_{\text{Hf}}$  signature for contemporaneous bentonites from across the Western Interior. A) Samples with overlapping high-precision ages at ca 76.3 Ma. B) Samples with overlapping high-precision ages at ca 75.6 Ma. C) Samples with overlapping high-precision ages at ca 75.2 Ma. Warm colors (red, orange, yellow) represent samples from southern Laramidia, and cool colors (green, light blue, dark blue) represent samples from northern Laramidia.

KBI-102 (proximal to the type locality) and IM1442 (ca. 13 km SE of the type locality). Prior to this study, the latter sample was only tentatively correlated to the Paria Hollow Bentonite Bed based on marginally overlapping internal uncertainties for high-precision ages (Beveridge *et al.*, in prep [Ch.4]). The  $\epsilon_{\text{Hf}}$  signature of all three samples was found to match closely, supporting correlation of IM1442 with the Paria Hollow Bentonite Bed. The third set of samples are those assigned to the Overlook Bentonite Bed, which includes samples KBC-195 (type locality), KBC-D (a recollection from the type locality), and KBU-C (ca. 1 km SE in the next valley). The latter outcrop was correlated based on lateral continuity and marks the base of the KBU Lower section of Beveridge *et al.* (2020 [Ch.5]), tying the recently defined Upper Valley Member to the now formalized Powell Point Member (both Kaiparowits Formation). Interestingly, the weighted mean  $\epsilon_{\text{Hf}}$  values of KBC-195 and KBU-C overlap, supporting correlation of the more isolated outcrop to the type locality; however, the weighted mean for KBC-D is slightly more negative than the other two. Despite this distinction, which may be related to sampling bias (see Section 6.5.3) or data reduction, the range of values for individual grains (Fig. 6.15) broadly overlaps across the three samples and provides support for the inference that all three localities are correlatives representing the Overlook Bentonite Bed.

The third and final research question involved the investigation of Campanian bentonites from across Laramidia that yielded statistically indistinguishable CA-ID-TIMS ages in previous studies (Fig. 6.16). The working hypothesis was that bentonites from different areas, sometimes up to ~1500 km apart, may have originated from the same volcanic source, thus explaining the exactly coeval ages. The first set of samples examined for this test were those dated to *ca* 76.3 Ma including KP-07A and KDR-5B from Utah, ST1-03 from Montana, and PR and NF from Alberta. Importantly, the two Utah samples do not overlap in age with each other and are thought to represent different horizons; however, both overlap in age with the northern samples. Both the weighted mean and individual grain  $\epsilon_{\text{Hf}}$  values for this grouping show a clear distinction between the northern and southern samples. Furthermore, the weighted mean  $\epsilon_{\text{Hf}}$  indicates the two Utah samples are also chemically distinct from one another, supporting distinction of these as separate bentonite beds that reflect different volcanic events. The second set of samples in this test occur at *ca* 75.6 Ma, consisting of those from the Paria Hollow Bentonite Bed in Utah (KBC-109, KBI-102, and IM1442) and the Plateau tuff (bentonite) from Alberta. Again, the northern and southern samples are distinguishable in both the weighted mean and individual grain  $\epsilon_{\text{Hf}}$  values. The third set of contemporaneous bentonites occur at *ca* 75.2 Ma and includes the Overlook Bentonite Bed samples (KBC-195, KBC-D, KBU-C) from Utah and the PPF and LSB samples from Montana. Yet again, the same pattern emerges where northern and southern counterparts are distinguishable from one another using both the weighted mean and individual grain  $\epsilon_{\text{Hf}}$  values. These findings clearly demonstrate that apparently synchronous bentonites from northern and southern Laramidia originate from distinct, contemporaneously active volcanic sources on multiple occasions within 1.2 Myrs in the late Campanian.

## 6.8 Discussion

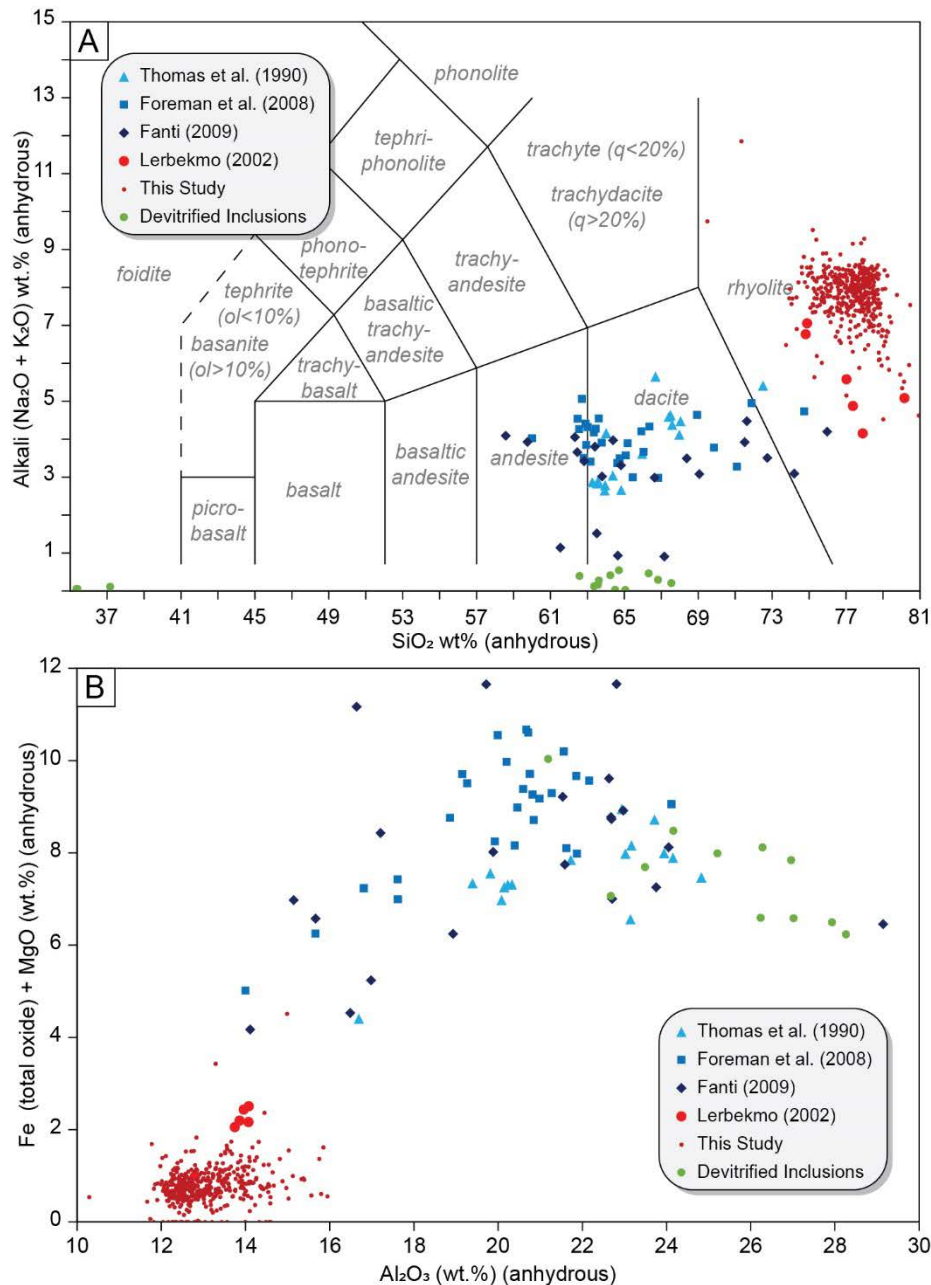
### 6.8.1 Utility for bentonite tephrostratigraphy

This investigation tested methods of zircon characterization for the application of bentonite tephrostratigraphy using samples from the Campanian strata of western North America. Overall results were mixed although all methods yielded useful basic information about the origin of the zircons. Qualitative descriptions were the most helpful aspect of the morphology characterization approach, where particular attributes were useful in some instances such as unusually large size (*e.g.*, KBC-144) or the specific abundance or absence of melt and mineral inclusions (*e.g.*, KBC-144, Overlook Bentonite Bed samples). Melt inclusion major element composition was demonstrated to be a promising approach for bentonite tephrostratigraphy, although further work is needed to refine the procedure so that meaningful distinctions can be made. By far the most useful technique for sample correlation and distinction was the application of zircon Lu-Hf systematics. The  $\epsilon_{\text{Hf}}$  signature of samples known to be unique often reflected this difference where, for example, every set of bentonites known to be unique from the Utah field area yielded distinguishable weighted mean  $\epsilon_{\text{Hf}}$  values, although the crystal tuffs (KBU-H, KBU-I) and volcanoclastic sandstones (KBU-F, KBU-V) yielded similar values to the closest bentonite (Overlook Bentonite Bed). Samples from the northern study areas that represent at least three different bentonite beds between the ages of 74 and 75.5 Ma yielded comparable  $\epsilon_{\text{Hf}}$  signatures (IL, ES, DVMT-1, PPF, LSB); thus, zircon  $\epsilon_{\text{Hf}}$  tephrostratigraphy may need to be supplemented by other means in these strata (*e.g.*, basic location/lithostratigraphic data).

Distinction between samples known to represent different bentonite beds was the first of the three guiding hypotheses applied in this study and was satisfied using zircon  $\epsilon_{\text{Hf}}$  signatures. The second hypothesis was that samples of the same bentonite bed over a lateral range would produce the same ‘fingerprint’. This null statement was supported by all methods and specifically by the Lu-Hf approach, which is most relevant since it was the only method to convincingly pass the qualifying first test. The third and final research question was whether characterization methods in this study support attribution of synchronous bentonite samples to the same volcanic center despite being collected from localities up to 1500 km apart. Zircon  $\epsilon_{\text{Hf}}$  signatures clearly and consistently demonstrated that every example of contemporaneous bentonites separated across the northern and southern areas were sourced from different volcanic events. More locally, the  $\epsilon_{\text{Hf}}$  signatures of contemporaneous samples within the same area (northern or southern) were generally found to match, which implicates a common magmatic source within each region.

Findings herein demonstrate that zircon characterization for bentonite tephrostratigraphy is at least equally as successful as previous whole-rock studies (*e.g.*, Thomas *et al.*, 1990; Foreman *et al.*, 2008; Fanti, 2009). The most apparent advantage of zircon characterization is that due to the chemical





**Fig. 6.17** Comparison of major element data for melt inclusions (this study) and whole-rock bentonite samples (Thomas et al., 1990; Lerbekmo, 2002; Foreman et al., 2008; Fanti, 2009). All data were recalculated to 100% totals as per Le Bas et al. (1986).

and physical robustness of zircon, data in this study were not considerably affected by chemical alteration that is inherited during devitrification of fresh tephra to bentonite clays. This advantage is most apparent when comparing the major element composition from whole-rock bentonite studies with melt inclusion data herein, as illustrated in Figure 6.17. The fresh glasses definitively plot as rhyolite, as represented by zircon-hosted inclusions (herein) and several fresh tephra samples from the exceptionally thick Dorothy Bentonite (late Campanian, southern Alberta) reported by Lerbekmo (2002). Devitrified inclusions show significantly lower silica and near absent alkalis (Na + K) and are therefore unrepresentative of natural silicate melt compositions. Whole-rock bentonite samples from Thomas *et*

*al.* (1990), Foreman *et al.* (2008) and Fanti (2009) show similar silica content to devitrified inclusions although with a higher alkali component, which may be attributed to the influence of feldspar phenocrysts. Furthermore, aluminium, iron and magnesium concentrations were considerably higher and less consistent in the devitrified samples compared to fresh glasses. These shortcomings in bentonite whole-rock data were readily recognized by the authors of those studies. Immobile trace element composition combined with statistical discriminant functions were used to overcome issues with alteration for the sake of bentonite correlation (Thomas *et al.*, 1990; Foreman *et al.*, 2008). On the other hand, the reliability of previous source rock determinations is debatable since parent magma types for samples from those studies does not match those herein for replicate samples of the same outcrops (*e.g.*, Plateau, Hardro Hill/HH, Landslide Butte/LSB). Nevertheless, rigorous statistical treatment for characterization and distinction of bentonites was a core strength of earlier studies and could be incorporated in future zircon characterization work.

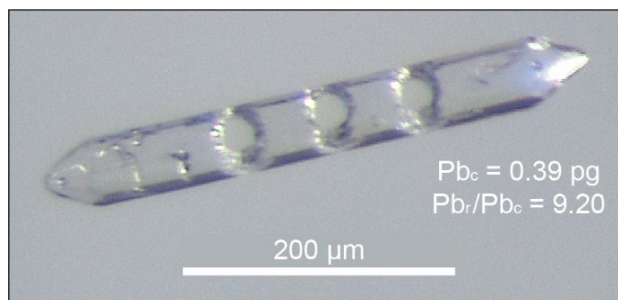
A less conspicuous advantage of zircon characterization over whole-rock bentonite studies reflects the impact of phenocrysts. Although Foreman *et al.* (2008) suggested that bentonite geochemical signatures should be laterally consistent (when comparing immobile elements), this hypothesis does not account for variation in the proportion of phenocrysts, which is known to decrease with distance from a volcanic source. On the other hand, zircon geochemistry is hypothetically consistent regardless of the size or abundance of grains (which may or may not depend on distance from the source). Both studies are limited by reworking, although detrital or inherited zircons may be less obvious; therefore, multiple zircon characterization methods are useful for data validation.

### 6.8.2 Significance

The purpose of investigating bentonite tephrostratigraphy in the context of this project was to develop an accessible and effective method for correlation of temporally well-constrained type section outcrops with isolated, undated outcrops. This approach to correlation would facilitate propagation of high-precision ages across a broader field extent without the need for excessive geochronologic work, thus aiding in stratigraphic refinement and improved temporal and geologic context for strata and interbedded fossils. The bentonite characterization techniques examined in this study were generally presented in order of increasing cost / decreasing accessibility. Although the most readily available techniques (*e.g.*, zircon morphology comparisons, which require only mineral separation and a microscope) were inconclusive at this stage of development, characterization using zircon Lu-Hf isotopic compositions was clearly effective and is relatively fast and cheap, particularly compared to CA-ID-TIMS geochronology. Zircon  $\epsilon_{\text{Hf}}$  signatures also offer more precise distinction between bentonite beds than microbeam (*e.g.*, via LA-ICP-MS) U-Pb ages in isolation. The most effective approach to identifying the stratigraphic level of an unknown bentonite sample, other than via high-precision geochronology, is therefore to compare its zircon Lu-Hf isotopic composition with those of previously characterized type-

section bentonites. In lieu of CA-ID-TIMS ages, preliminary microbeam U-Pb ages and/or basic lithostratigraphic correlation can be used in the first instance to ascertain imprecise but generally accurate bentonite levels, which can then be refined using the zircon Lu-Hf tephrostratigraphic approach presented here for precise correlation.

Characterization of type-section bentonite outcrops is therefore significant for both the assembly of temporal frameworks and for providing foundations for bentonite tephrostratigraphy. As such, it is pertinent to consider whether the characterization methods presented herein can be applied within the workflow of CA-ID-TIMS geochronology, as opposed to dating and characterizing different subsets of zircon. This would improve data quality assurance and facilitate internal checks as well as reducing the overall time needed for investigation. Although uncommon, it is possible to elute and analyze Hf isotopes (and trace elements) from the remaining aliquot following U-Pb elution for CA-ID-TIMS (see Hf ion-exchange column chemistry methods in Appendix B.3). This approach requires little to no procedural interference prior to U-Pb dating; however, comparison of solution ICP-MS data (type section samples) and laser ablation ICP-MS data (unknown samples) may require careful calibration. Alternatively, some laboratories commonly opt to mount and screen zircons prior to CA-ID-TIMS analysis, particularly when a detrital/inherited component is known or suspected. Screening includes equatorially exposing mounted grains, then collecting cathodoluminescent imagery and preliminary microbeam U-Pb ages. The primary concern in this approach is the reduction in analytical volume, which leads to proportionally higher common Pb contamination (represented as a smaller radiogenic over common lead ratio) and thus less precise ages. To test whether prior screening is of concern to samples examined in this study, grains from sample KP-07A were subjected to equatorial polishing and laser ablation analyses prior to dated using CA-ID-TIMS geochronology. Figure 6.18 shows one of five grains from KP-07A post-screening prior to dating. All five grains were previously polished and had at least one ablation pit and all were included in the weighted mean age for this sample. This age ( $76.394 \pm 0.040/0.045/0.093$  Ma, MSWD = 0.6, n = 5) was presented in Ramezani et al. (in review) as one of four key ages from the Kaiparowits Formation. This demonstrates that the size of the zircons examined herein is sufficient to accommodate destructive analyses prior to CA-ID-TIMS geochronology without significant impacts on precision, although it is noted that this may not be appropriate for all samples.



**Fig. 6.18** Zircon from sample KP-07A with three 25  $\mu\text{m}$  ablation pits imaged prior to CA-ID-TIMS analysis. Weighted mean age for this sample reflects a precision of 0.05% (n=5), demonstrating that individual crystals can be subjected to the full spectrum of analysis presented herein and produce adequately precise ages provided they are of sufficient

### 6.8.3 Limitations

Procedures for bentonite tephrostratigraphy examined here can distinguish between samples that originated from different volcanic events and correlate those probably from the same source; however, more specific distinction between different, closely spaced eruptions from the same, stable volcanic center (*e.g.*, stacked but distinct bentonites) is less clear-cut. The relevance of these finer-scale distinctions depends on the longevity of the volcanic source since multiple eruption events within the analytical uncertainty of high-precision U-Pb dates makes little difference to reliable correlation of marker beds. On the other hand, if a stable volcanic source inputs ash into basin successions for millions of years without significant parent magma variation, distinction between the resulting bentonites is relevant and may be difficult using methods other than high-precision U-Pb dating.

Examples from this study illustrate how tephrostratigraphy is reliant on parent magma variation. The three bentonite horizons from the KBC section of the Kaiparowits Formation, Utah, show morphological and geochemical distinctions that facilitated correlation of type section and outlier samples. This implies that the Paria Hollow, Deadmans Corner and Overlook bentonite beds were sourced from either; 1) different volcanic centers, 2) the same volcanic center with an evolving chemical signature across ~200,000-year major eruption intervals, or 3) a combination of both. Specifically, the parent magma of the Overlook Bentonite Bed may be genetically related to that of the Paria Hollow Bentonite Bed, although representing a greater degree of crustal assimilation (based on  $\epsilon\text{Hf}$  results), and Deadmans Corner Bentonite Bed may be sourced from a unique volcanic center. On the other hand, they may be from three distinct sources. In the northern study areas (Alberta and Montana), a set of five samples (IL, ES, DVMT-1, PPF, LSB) representing at least three unique bentonites (based on U-Pb ages) show nearly identical characteristics other than their ages, which might represent repeated eruptions from the same, stable volcanic center. This is a reasonable assumption given the spatial proximity and temporal range of less than 1.5 Myr for these samples.

Similarities between samples can also relate to limited data resolution or poor geologic sensitivity of a characteristic. For example, zircons associated with rapid crystallization during volcanic episodes reflect archetypal acicular morphologies that are easy to distinguish from detrital, metamorphic, and slow-forming igneous crystals; however, subpopulations are not readily distinguishable from one another. The spread of morphological proportion measurements illustrated herein demonstrates that zircon morphology is not sensitive enough to magmatic conditions to distinguish between bentonite samples in this study, although selection bias may also play a role. The lack of distinction between samples using melt inclusion major element composition may also reflect similarities between magmas capable of generating far-travelled ashes presumably from highly explosive volcanism with less sensitivity to minor differences, low analytical precision notwithstanding. Data resolution may also be improved with future procedural refinements.

#### 6.8.4 Implications

Although the source of the volcanogenic material examined in this study was not a key focus, zircon  $\epsilon\text{Hf}$  signatures coupled with high-precision ages demonstrate interesting large-scale implications. The Elkhorn Mountain Volcanics ( $\pm$  Adel Mountain Volcanics) have previously been inferred as the primary source of volcanogenic material in the Two Medicine and Judith River formations and Belly River Group in the northern field areas (Thomas *et al.*, 1990; Rogers *et al.*, 1993, 2016; Roberts and Hendrix, 2000; Foreman *et al.*, 2008), and tentatively implied for bentonites much further south in the Wahweap and Kaiparowits formations from Utah (Roberts *et al.*, 2005; Foreman *et al.*, 2008; Jinnah *et al.*, 2009). A recent basin-scale high-precision geochronology project found numerous instances of bentonite samples from both these northern and southern areas with statistically indistinguishable U-Pb zircon ages (internal uncertainty of  $\sim 0.02$  to  $0.05\%$ ) (Beveridge *et al.*, 2022 [Ch.3], in prep [Ch.4]; Ramezani *et al.*, in review). This new age constraint appears to support the idea that the Elkhorn Mountains constituted a large, central source for volcanic ash products across Laramidia, although it is difficult to reconcile this ash dispersal hypothesis with palaeoclimate and palaeowind reconstructions that demonstrate prevailing westerlies (*e.g.*, Fricke *et al.*, 2010; Sewall and Fricke, 2013).

Despite numerous examples of apparently synchronous bentonites, the  $\epsilon\text{Hf}$  data presented herein does not support a single, central locus for volcanism as an explanation for abundant interstratified ashes across the Campanian strata of western North America. Three instances of ‘synchronous’ bentonites from northern and southern Laramidia all yielded clearly distinguishable  $\epsilon\text{Hf}$  signatures between different areas and matching signatures for coeval samples from the same area (Fig. 6.14-6.16). This confirms that the ‘synchronous’ bentonites do not represent the exact same eruption event contributing material to northern and southern areas. It appears unlikely that they represent successive eruptions from a single, rapidly varying magmatic source, although further investigation is required to definitively exclude this scenario. It is here suggested that while the previously assigned Elkhorn Mountain source for northern bentonites is likely, southern bentonites of the same age were more likely derived from volcanism predominantly on the southern and western margins of the basin in present-day southern Arizona/New Mexico and northern Sonora, and southern Nevada and California. Cross-continental contributions may still have occurred (*e.g.*, ash from northern volcanoes in southern strata), although probably not synchronously in both areas, which is consistent with proposed westerly palaeowind patterns.

Regardless of the exact volcanic centers, the occurrence of multiple instances of apparently synchronous eruptions in northern and southern Laramidia within an interval of less than 1.5 Myrs provides the opportunity to consider large-scale volcanic arc dynamics by proxy of these distal tephra deposits (*e.g.*, Allen *et al.*, 2022). This temporal resolution is founded on CA-ID-TIMS geochronology, and it is difficult to argue that the apparent synchronicity is an artefact of low precision, especially since



there are long, definable intervals between each synchronous set. Interestingly, only one other bentonite occurs in this 1.5 Myr period that is not attributed to one of the synchronous groupings (KBC-144). Synchronous (or near synchronous) episodes of volcanism across Laramidia may represent pulses of activity at a scale of hundreds of thousands of years (*e.g.*, Allen *et al.*, 2022). Volcanic arc cyclicality at the scale of tens of millions of years is well documented (*e.g.*, DeCelles *et al.*, 2009; Paterson and Ducea, 2015; Martinez-Ardila *et al.*, 2019), whereby volcanic cycles are related to tectonic processes. An emerging body of work also supports shorter term (100 kyr) compositional variations and apparent flair ups in volcanic arc systems (Jellinek *et al.*, 2004; Schindlbeck *et al.*, 2018; Allen *et al.*, 2022). These patterns have been tentatively attributed to changing conditions and geometry of magmatic systems such as in response to short-term crustal loading (*e.g.*, glaciers, epicontinental seaways).

The scale and probable frequency of eruptions that produced the far-travelled deposits examined herein may also be useful to consider since the horizons preserved within terrestrial basin strata may represent only larger events (Allen *et al.*, 2022). The magnitude of an eruption (*e.g.*, volcanic explosivity index; Newhall and Self, 1982) is difficult to determine based on distal bentonite horizons since criteria, such as the true volume of ejecta, are nearly impossible to determine. Ash dispersal at the scale of hundreds of kilometers is likely particularly for the southern localities given the closest known volcanic centers. High silica content determined from glass inclusions herein (77% SiO<sub>2</sub>, anhydrous) is also consistent with highly explosive volcanism; thus, bentonites from this study probably reflect eruptions at a Plinian to ultra-Plinian scale, which agrees with the inferences of Thomas *et al.* (1990) regarding the Plateau tuff. Possible cyclicality in eruptions such as these may be temporally distinguishable based on the resolution of the CA-ID-TIMS ages for bentonite examined herein (12 to 40 kyr internal uncertainty). Further investigation is recommended to determine whether apparently synchronous Campanian volcanism across Laramidia may reflect short term (100 kyr scale) magmatic cyclicality.

Whether or not ‘synchronous’ bentonites were derived from the same volcanic eruption, long-distance stratigraphic correlation based on matching high-precision ages still provides robust and invaluable tie-points between northern and southern field areas. Despite many of these horizons probably not originating from the same eruption, it is incredibly useful to know that, for example, the stratigraphic level of the Plateau tuff in Alberta and Paria Hollow Bentonite Bed in Utah are temporally equivalent. This utility will probably remain largely unchanged regardless of future revisions to ages with even greater precision since the current uncertainty nears the timescale of relevant sedimentological processes such as the tempo of palaeolandscape evolution. It is nevertheless significant that the εHf data herein shows that these bentonites are unique so that findings from studies of outcrops in one area are not erroneously applied to another (*e.g.*, the Plateau tuff outcrop cannot be attributed to / renamed the Paria Hollow Bentonite Bed). Confirmation of multiple sources of synchronous Campanian volcanism across western North America also contributes to palaeoenvironmental reconstructions and palaeoecological hypothesis whereby there is no evidence that northern and southern Laramidia were

separated by a central area of volcanism or related unfavorable biotic conditions. Rather, the opposite may be conceivable, whereby northern and southern fossiliferous localities may coincide with zones of frequent tephra input and the intermediary zone may reflect poorly fossiliferous and tephra-starved strata. Findings regarding bentonite origin and distribution may also support future spatio-temporal taphonomic investigation of the abundant and diverse late Campanian biota preserved in strata interbedded with the bentonites studied herein (see Roberts *et al.*, 2013).

#### 6.8.5 Formal bentonite beds

Recent work on Campanian strata of southern Utah, particularly the Kaiparowits Formation, included the formal recognition of four bentonite beds; the Horse Mountain, Paria Hollow, Deadmans Corner, and Overlook bentonite beds (Beveridge *et al.*, in prep [Ch.4]). Detailed description of these important marker horizons supports intra-formational stratigraphic correlation and hence correlation of fossil material across outcrop exposures. Bentonite characterization herein supports previous litho- and chronostratigraphic correlations within formations; thus, solidifying previously tenuous inferences and supporting formal recognition of another two bentonite beds. The first of these is the Star Seep Bentonite Bed from the Wahweap Formation, southern Utah, which is represented by a ~20-centimeter-thick interval approximately five meters above the base of the Reynolds Point Member, dated to *ca* 81.47 Ma (Jinnah *et al.*, 2009; Jinnah, 2013; Beveridge *et al.*, 2022 [Ch.3]). Correlation of two outcrops represented by samples B2-07B and WLS-R is strongly supported by sample characterization herein including matching  $\epsilon_{\text{Hf}}$  weighted mean values of  $-6.18 \pm 0.23$  and  $-6.27 \pm 0.49$  and close similarities in zircon morphological descriptions (see Appendix C.6.4). The name Star Seep Bentonite Bed (previously Star Seep bentonite) was derived from where the horizon (or possibly a close correlative of it) was first described by Jinnah *et al.* (2009) in the Carcass Canyon quadrangle. The second formal bentonite described here is the Death Ridge Bentonite Bed, which previously yielded an age of *ca* 76.26 Ma from sample KDR-5B (KDR-5 elsewhere) collected from the Death Ridge area (Roberts *et al.*, 2005; Beveridge *et al.*, in prep [Ch.4]). This age was only marginally distinguishable from that of the Horse Mountain Bentonite Bed; however, the  $\epsilon_{\text{Hf}}$  weighted mean values presented herein supports distinction of these units and validates the Death Ridge Bentonite Bed as a unique horizon.

## 6.9 Conclusions

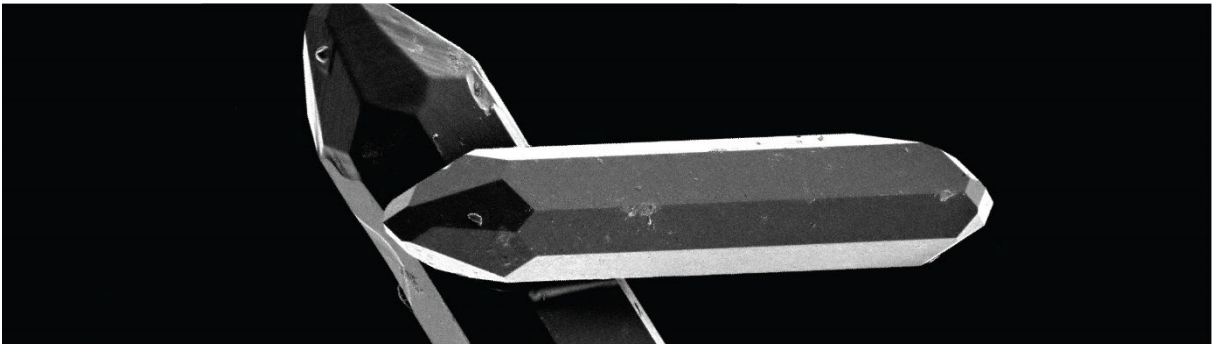
This study investigated methods for bentonite tephrostratigraphy using zircon characteristics and found that the  $\epsilon_{\text{Hf}}$  signature of zircon was the most effective tool for bentonite correlation and distinction, although other approaches were promising and yielded useful, broader insights. The  $\epsilon_{\text{Hf}}$  approach was demonstrated to be capable of distinguishing between samples known to be unique and produced matching signatures for samples known or suspected of being correlative. On the other hand, rather than supporting correlation based on high-precision U-Pb ages, the zircon  $\epsilon_{\text{Hf}}$  signatures for coeval samples separated by up to 1500 km were found to be unique in all three instances. This finding indicates that

despite matching ages, these bentonite groups do not represent the same eruption, although it cannot be confirmed whether they originate from the same volcanic center. Interpretation of these results leans towards a model of widely distributed, highly explosive volcanism across Laramidia during the late Campanian, rather than a single, central locus of major volcanism contributing volcanogenic material to surrounding basin depocenters. Regardless of their provenance, bentonites with statistically indistinguishable high-precision ages still provide excellent marker horizons across Laramidia with the caveat that other geochemical data from coeval outcrops in the north and south cannot necessarily be equated. Recommendations for extensions to this study include; 1) refinement of the melt inclusion procedure to include analysis via wavelength dispersive spectroscopy (WDS) electron microprobe analysis calibrated more precisely using glass standards; 2) investigation of whether solution geochemical characterization following zircon dissolution and U-Pb elution yields similar results to microbeam pre-screening techniques; 3) exploration of multi-factor analysis and statistical quantification of sample distinction; and 4) expansion of the investigation into volcanic sources of the bentonites and examination of spatio-temporal trends in highly-explosive late Campanian volcanism in western North America.

---

# Chapter Seven

## Synthesis and recommendations



*SEM secondary electron image of zircon phenocrysts*

**Preface**

This summary chapter synthesizes outcomes of this publication-based thesis in the context of the overarching research questions and outlines potential directions for future work that stem from this thesis. This brief, unpublished chapter also includes information presented in a co-authored work to which the candidate contributed significantly (see Ramezani *et al.*, in review), that provides a summary of the larger project within which this thesis is included and highlights the broader implications of the thesis outcomes.



## 7.1 Summary of findings

The purpose of this thesis was to improve the litho- and chronostratigraphic framework of richly fossiliferous Campanian strata in western North America, particularly those from southern Utah. This was achieved primarily through the investigation of bentonite horizons including high-precision geochronology and correlation. Objectives outlined in the introduction of this thesis (Ch.1) were address throughout Chapters Three to Six and are summarized as follows.

### 7.1.1 Lithostratigraphic compilation and refinement

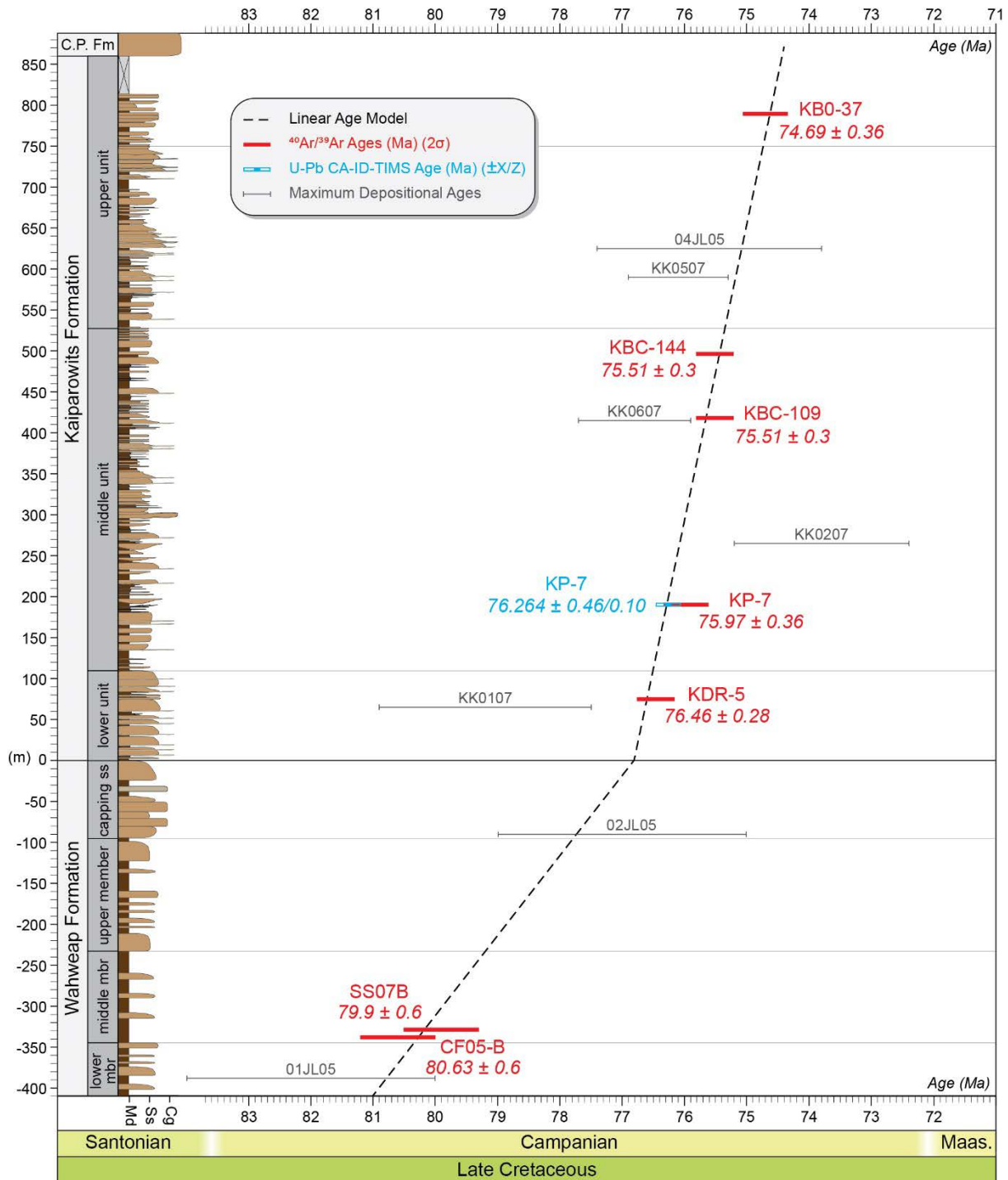
Detailed lithostratigraphic descriptions of the Wahweap and Kaiparowits formations were presented in Chapters Three, Four, and Five. Field observations as part of this project supported previous studies, particularly those of Eaton (1991), Roberts (2007) and Jinnah and Roberts (2011) and justified the formal recognition of established informal stratigraphic subdivisions (Figs. 7.1 and 7.2). New formalized member names include the Last Chance Creek, Reynolds Point, Coyote Point, and Pardner Canyon members of the Wahweap Formation (previously lower, middle, upper, and capping sandstone members, respectively; Eaton, 1991), and the Tommy Canyon, The Blues, and Powell Point members of the Kaiparowits Formation (previously the lower, middle, and upper units, respectively; Roberts, 2007). The main deviation from previous work was the identification of 145 m of strata above the previously inferred top boundary and hence the description and formal recognition of another new member of the Kaiparowits Formation, the Upper Valley Member (Beveridge *et al.*, 2020 [Ch.5]). This addition expanded the total thickness of the Kaiparowits Formation to 1005 m, as illustrated in Figure 7.2.

### 7.1.2 Bentonite identification and collection

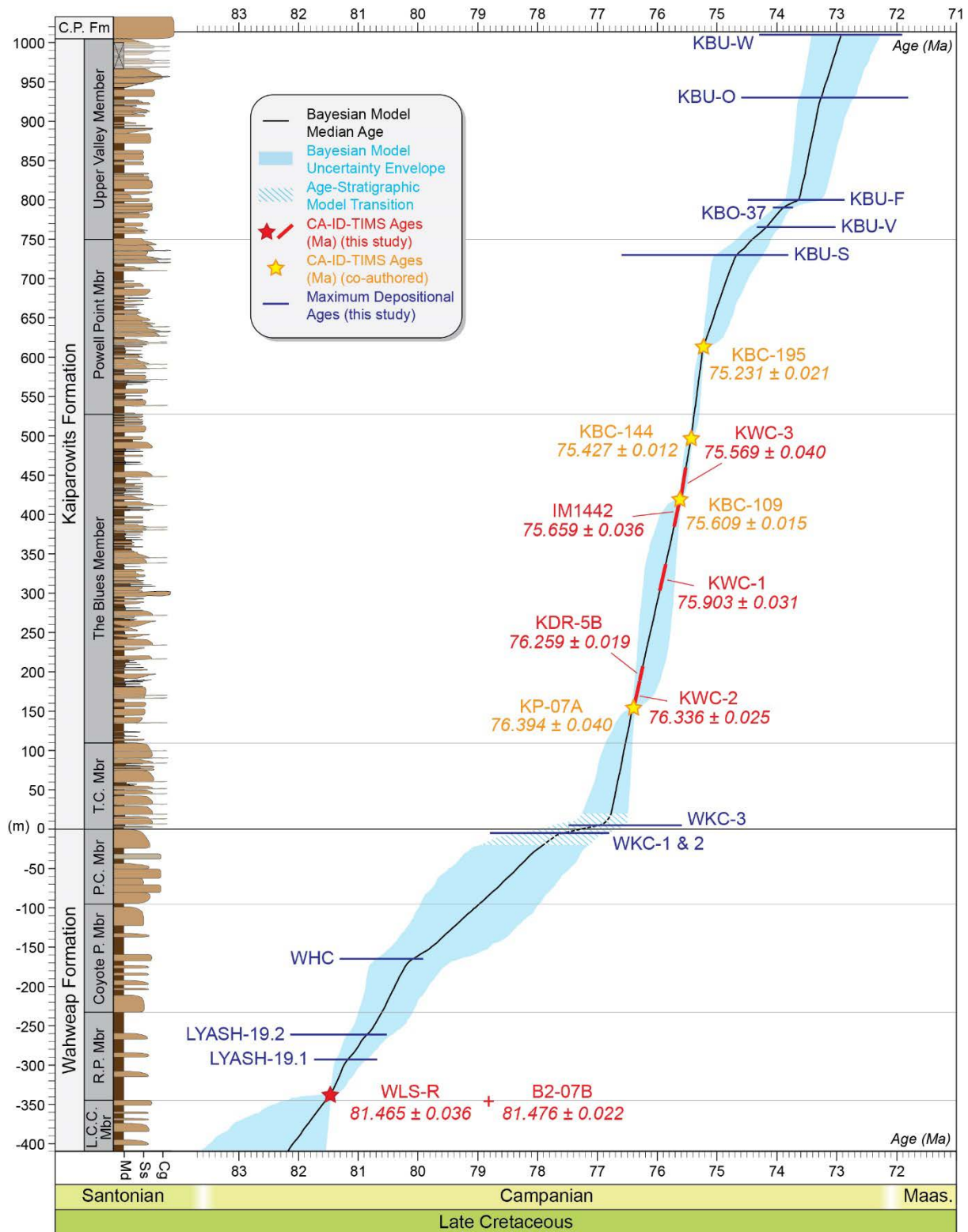
A total of 32 bentonite samples were examined in this study, including 19 from the Wahweap and Kaiparowits formations. Thirteen unique horizons were confidently identified from these units (ten from the Kaiparowits Formation and three from the Wahweap Formation) and six were described and formally recognized as the Star Seep, Horse Mountain, Death Ridge, Paria Hollow, Deadmans Corner, and Overlook bentonite beds. Field and remote horizon tracing (*i.e.*, walking out horizons and tracing them in Google Earth Pro) supported outcrop-to-outcrop correlation in several instances and expanded the known extend of key horizons.

### 7.1.3 High-precision bentonite geochronology

As part of work contributing to this thesis, the author analysed a total of 106 zircons via the CA-ID-TIMS approach contributing to 15 new high-precision bentonite ages from the Kaiparowits, Wahweap, Bearpaw, Dinosaur Park, Oldman, and Two Medicine formations. Of these, seven bentonite ages are exclusive to the first authored work included herein (Ch. 3 and 4). With a total of nine high-precision bentonite ages (Beveridge *et al.*, in prep [Ch.4]; Ramezani *et al.*, in review), the Kaiparowits Formation



**Fig. 7.1** Litho- and chronostratigraphy of Campanian units from the Kaiparowits Plateau prior to contributions presented in this thesis. Lithostratigraphic columns are from Eaton (1991) and Roberts (2007), and age data are from Roberts et al. (2005, 2013), Jinnah et al. (2009), Larsen et al. (2010), Jinnah (2013), and Lawton and Bradford (2013).



**Fig. 7.2** A summary of litho- and chronostratigraphic refinements for Campanian units from the Kaiparowits Plateau presented herein including formal member subdivisions, 146 m of new strata (see Upper Valley Member), and 11 new CA-ID-TIMS ages. These high precision ages are shown as stars (and red intervals on the model) because the X and Y uncertainties are small and otherwise not easily visible at this scale.

now has the best constrained temporal framework of any Campanian unit in western North America (Fig. 7.2). Together with the refined framework for the underlying Wahweap Formation presented herein (Beveridge *et al.*, 2022 [Ch.3]), strata of the Kaiparowits and Table Cliff plateaus include a 1415-meter-thick near-continuous record of the Campanian stage, barring one temporally substantive hiatus between the Coyote Point and Pardner Canyon members of the Wahweap Formation. Bayesian age-stratigraphic modeling (*i.e.*, Haslett and Parnell, 2008; Parnell *et al.*, 2008, 2011) was used to provide ages with propagated uncertainty at one-meter intervals throughout several stratotype sections. As demonstrated herein, these model ages can be applied to the fossil record using the stratigraphic level (or interval) of localities relative to modeled stratotype sections to produce robust ages for individual specimens. Age models were generated for the Kaiparowits, Wahweap, Dinosaur Park, and Judith River formations and constitute the first models of this kind for Laramidian strata (see Beveridge *et al.*, 2022 [Ch.3], in prep [Ch.4], Ramezani *et al.*, in review).

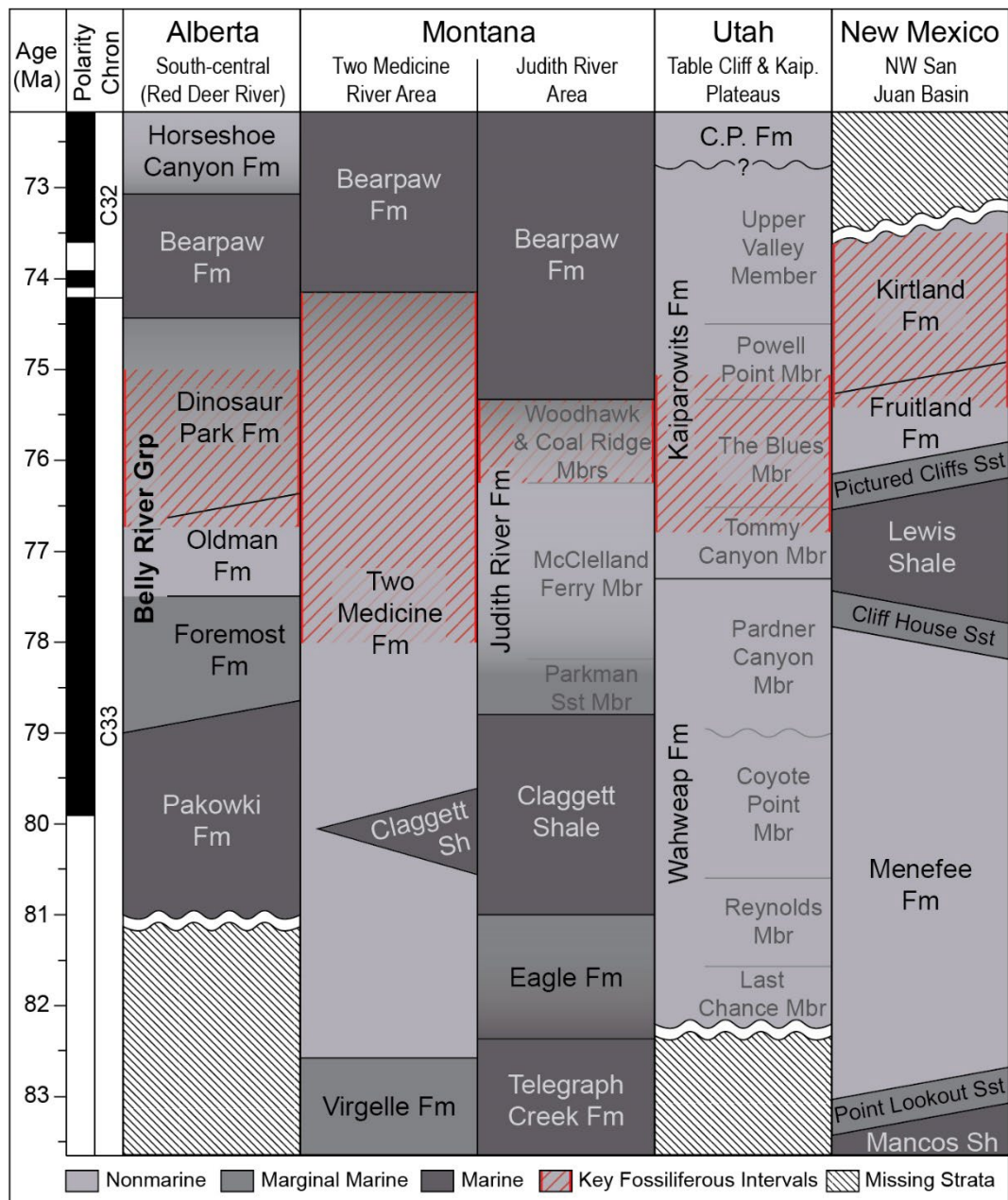
#### 7.1.4 Refined stratigraphic correlations

Measured stratigraphic sections of the Kaiparowits Formation were re-examined and their correlations to the stratotype section were refined using the age-stratigraphic model and new high-precision bentonite ages from isolated sections. Most significantly, the KWC section in the Canaan Peak area was expanded upon and tightly constrained using three new ages and a separate age model, and the level of the KDR sections were significantly adjusted (see Ch.4). Stratigraphic correlation using bentonite ages proved to be an extremely effective tool for stratigraphic packages characterized by otherwise discontinuous lithofacies and across intermittent exposures. On the other hand, broader application of this approach is limited by the cost of analysis whereby age data with the resolution to distinguish between closely spaced bentonite beds (*i.e.*, CA-ID-TIMS) may cost upwards of US \$3000 per sample (US \$500 per analysis, minimum 6 analyses) and requires an existing framework of ages for the stratotype section. Nevertheless, stratigraphic correlation using high-precision bentonite ages in tandem with stratotype section age models is here considered the most reliable approach currently available.

#### 7.1.5 Bentonite tephrostratigraphy

Following successful demonstration of the utility of bentonite ages for stratigraphic correlation, new and improved methods for bentonite tephrostratigraphy (characterization and correlation) were investigated based on morphological and geochemical measurements of zircon phenocrysts (see Ch.6). The objective was to develop an approach that could reliably correlate dated stratotype section bentonite beds with isolated, undated bentonite outcrops to expand the utility of the high-precision ages and reduce future repeated analysis of the same bentonite bed. Results found that zircon Lu-Hf isotopic signatures could be used to distinguish between samples known to be unique and provided matching signatures for samples known (or suspected) to be correlative. This data also found that bentonites separated by up to 1500 km that had yielded statistically indistinguishable high-precision ages were geochemically unique

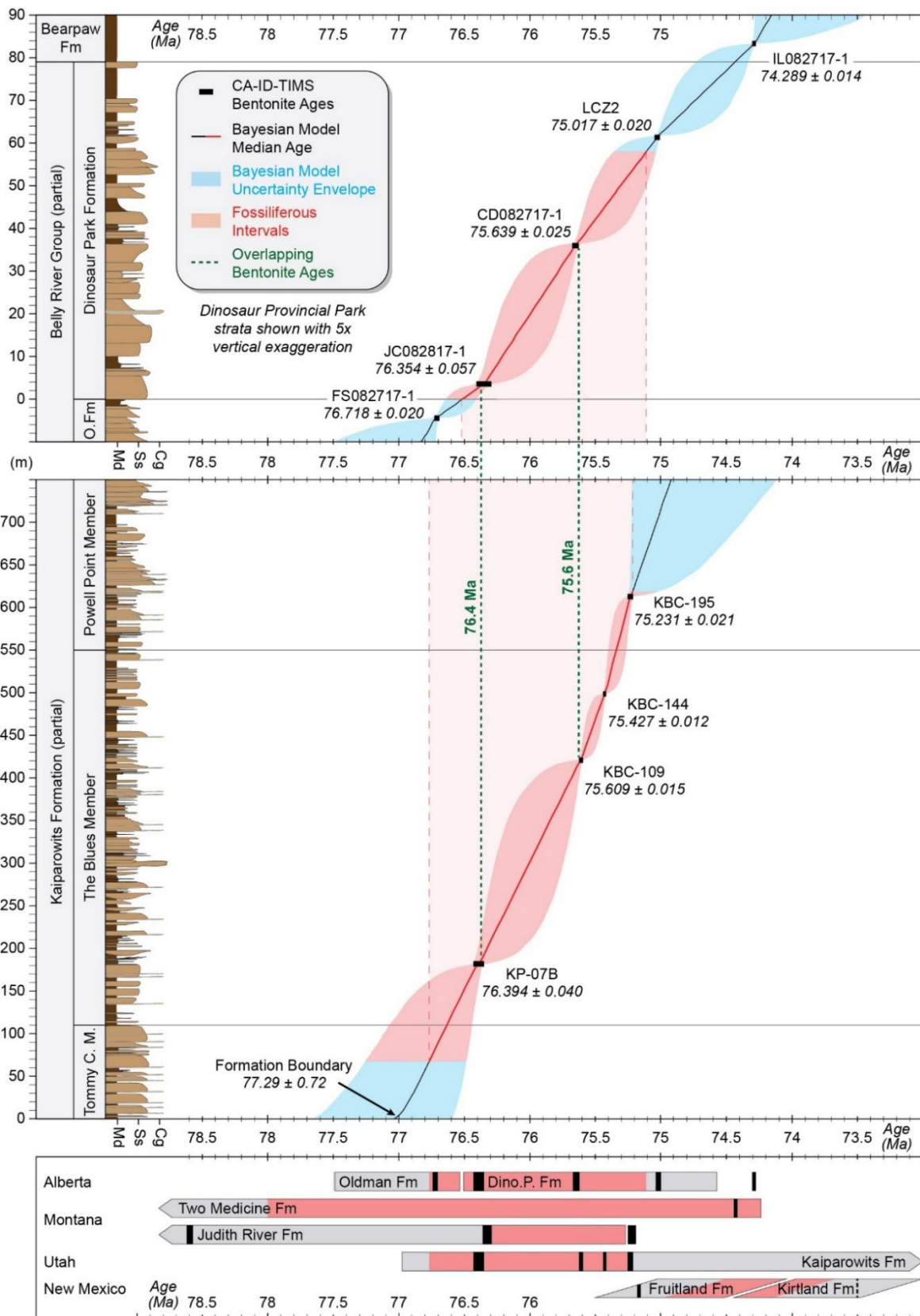




**Fig. 7.3** Precise chronostratigraphic correlation of selected Campanian strata across western North America. Key fossiliferous intervals of late Campanian age are highlighted (red stripes) illustrating precise correlation between several localities, although the most fossiliferous interval in the San Juan Basin appears to occur later than elsewhere across Laramidia. Adapted from Ramezani *et al.* (in review).

from one another, demonstrating that the contemporaneous volcanogenic products were not sourced from the same large-scale eruption event. It is most likely that the several recorded instances of apparently synchronous bentonites across nearly 1500 km reflect widespread coeval volcanism across Laramidia. Other approaches to bentonite tephrostratigraphy (*e.g.*, zircon morphology, glass inclusion composition) showed promising results and, with future procedural refinement, may contribute to an understanding of highly explosive Campanian volcanism in western North America by proxy of bentonites interbedded in basin strata.





**Fig. 7.4** Precise correlation of the Dinosaur Park Formation (Alberta) and the Kaiparowits Formation (Utah). The new Bayesian age-stratigraphic models facilitate exact correlation of strata and interbedded fossil material across ca 1500 km. Adapted from Ramezani et al. (in review). [Note: The candidate was heavily involved in data acquisition and modelling for both the Kaiparowits Formation and Belly River Group bentonites; see Ch.2].

## 7.2 Implications of thesis outcomes

Temporal refinement presented herein and in coauthored work indicates that stratigraphic diachroneity is not the cause of apparent biogeographic patterns of endemism across Laramidia during the late Campanian (Figs. 7.3 and 7.4). Synchronicity of key fossiliferous intervals between suspected northern and southern endemic centers is most explicitly demonstrated in Figure 7.4, which compares the age-stratigraphic models for the Dinosaur Park and Kaiparowits formations from Alberta and Utah, respectively (see also Ramezani *et al.*, in review). The most fossiliferous intervals of these units are near-perfectly aligned (within error) and there are also two instances of exactly coeval bentonite ages. Discrete faunal zones within each formation can now be compared to one another with greater resolution to more precisely examine spatio-temporal relationships of coeval taxa across western North America.

Although the results clearly demonstrate synchronicity of several key localities, the most fossiliferous late Campanian strata in the San Juan Basin were shown to be distinguishably younger than those of the Dinosaur Park, Judith River, and Kaiparowits formations. This finding is consistent with some of the arguments presented by Sullivan and Lucas (2006) and Lucas *et al.* (2016), which were dominantly founded on observations from the San Juan succession (*i.e.*, faunal diachroneity evident from the San Juan perspective is validated by the new high-precision ages). This means that the addition of data from the Kaiparowits Formation provided a critical southern representative, without which there is less clear evidence for a southern endemic center synchronous with northern equivalents. Inclusion of additional southern areas (*e.g.*, Aguja Formation, West Texas) may further elucidate late Campanian biogeographic trends and facilitate investigation of proposed faunal gradients versus defined endemic centers (*cf.* Gates *et al.*, 2010). The overall outcome is the validation of many perspectives, which demonstrates the complexity of the latitudinal endemism hypothesis and how refinement of foundational datasets is critical for the advancement of palaeoecological hypotheses (*cf.* Maidment *et al.*, 2021).

Refined temporal (and lithostratigraphic) frameworks for key fossiliferous strata of Campanian age are anticipated to facilitate improved precision and accuracy in future palaeoecological investigations. As demonstrated in Chapters 3 and 4, individual fossil localities can be assigned a robust age (including uncertainty) based on their stratigraphic level relative to age-stratigraphic type section models. These robust ages can be used to refine first and last appearance datums and, in turn, the temporal range of individual taxon, which can be implemented in time-calibrated phylogenetic analyses and for the investigation of biotic turnover rates / faunal zones. This work may also contribute to investigation of inferred diversity decline preceding the Cretaceous-Palaeogene extinction event (*e.g.*, Chiarenza *et al.*, 2019; Condamine *et al.*, 2021) since the development of a database of robust first and last appearance ages overcomes time-binning challenges highlighted as one of several obstacles to precise interpretation of temporally dependent trends (Lucas *et al.*, 2016; Dean *et al.*, 2020).

### 7.3 Recommendations for future work

Significant refinement to the age of fossiliferous Campanian strata across western North America has helped to close a critical gap in the dinosaur endemism hypothesis and enables renewed focus on other aspects of the concept. These include examination of taphonomic biases (*e.g.*, lithotypes, environments, subsidence rates, diagenesis), and ensuring spatio-temporally representative collection efforts across Laramidia (*e.g.*, reducing collection biases relating to prevalence and accessibility of particular intervals). Future work may incorporate other contemporaneous strata to increase latitudinal representation and examine distribution in greater detail as opposed to simple northern and southern endemic centers. For example, approximately coeval strata of the Aguja Formation in West Texas (Big Bend National Park) would provide a far southern datapoint and, although less fossiliferous, strata from the Unita Basin near Green River / Book Cliffs in central Utah and in the Big Horn Basin in Wyoming may provide a critical central link. Ultimately, a spatio-temporal “heat map” of taxa occurrences across Laramidia may prove to be a robust tool for investigating large scale biogeographic trends.

Improvements to the geologic context of fossiliferous strata presented herein has also opened new avenues for investigation. These may include:

- Expansion of spatial and temporal coverage of high-precision U-Pb bentonite zircon ages using the same CA-ID-TIMS approach applied in this project (*e.g.*, contemporaneous, overlying and underlying units)
- The development of age-stratigraphic models for other Campanian units across Laramidia (Two Medicine Formation, Fruitland/Kirtland formations, Aguja Formation in West Texas)
- Expansion of the high-resolution age models into Maastrichtian strata (*e.g.*, Eberth and Kamo, 2020) to cover the entire interval leading to and following the apparent peak in biotic diversity in the Campanian and through to the Cretaceous-Palaeogene extinction event
- A large-scale campaign to place fossil localities from across Laramidia into better stratigraphic context based on the new age models (*e.g.*, Beveridge *et al.*, 2022 [Ch.3])
- Re-examination of unit relationships (*e.g.*, Upper Valley Member and the overlying Canaan Peak Formation; correlation of the Wahweap Formation and its constituents with the Masuk Formation and Tarantula Mesa Sandstone in the Henry Basin)
- Further procedural refinement and application of bentonite tephrostratigraphy in other units to correlate dated and undated bentonites enabling propagation of high-precision ages (particularly useful in dissected terrain such as western strata of the Two Medicine Formation)
- Investigation of highly explosive volcanism in western North America (and elsewhere) by proxy of bentonites in sedimentary successions, which are particularly frequent in Campanian strata

across Laramidia (implications for understanding subduction mechanics via identification of high flux events)

- Investigation of magmatic residency times for zircons erupted and emplaced as volcanic ash based on geochemical diversity within a supposedly coeval grain population and their glass inclusions
  - Potential procedural developments in CA-ID-TIMS using glass inclusion composition to refine the initial thorium coefficient for individual samples, which may result in a reduction in the calculated uncertainty in instances of very low Pb blanks and other sources of uncertainty
-





## References

## References

---

- Adams, G., Fielding, C. R., & Oboh-Ikuenobe, F. E. (2017). Stratigraphy and depositional environments of the Mesaverde Group in the northern Bighorn Basin of Wyoming. *Palaeogeography, Palaeoclimatology, Palaeoecology*, 485, 486-503. doi.org/10.1016/j.palaeo.2017.07.005
- Albright, L. B. & Titus, A. L. (2016). Magnetostratigraphy of Upper Cretaceous strata in Grand Staircase-Escalante National Monument, southern Utah: The Santonian-Campanian Stage boundary, reassessment of the C33N/C33R magnetochron boundary, and implications for regional sedimentation patterns within the Sevier Foreland Basin. *Cretaceous Research*, 63, 77-94. doi.org/10.1016/j.cretres.2016.03.004
- Allen, S., Lee, C.-T., & Minisini, D. (2022). Temporal variations in the composition of Cretaceous Cordilleran arc volcanism through a high-frequency record of bentonites. *Earth and Planetary Science Letters*, 584. doi.org/10.1016/j.epsl.2022.117470
- Atterholt, J., Hutchison, J. H., & O'Connor, J. K. (2018). The most complete enantiornithine from North America and a phylogenetic analysis of the Avisauridae. *PeerJ*, 6, e5910. doi.org/10.7717/peerj.5910
- Beland, P. & Russell, D. A. (1978). Palaeoecology of Dinosaur-Provincial-Park (Cretaceous), Alberta, Interpreted from Distribution of Articulated Vertebrate Remains. *Canadian Journal of Earth Sciences*, 15(6), 1012-1024. doi.org/10.1139/e78-109
- Belousova, E. A., Griffin, W. L., & O'Reilly, S. Y. (2006). Zircon crystal morphology, trace element signatures and Hf isotope composition as a tool for petrogenetic modelling; examples from Eastern Australian Granitoids. *Journal of Petrology*, 47(2), 329-353. doi.org/10.1093/petrology/egi077
- Belousova, E. A., Griffin, W. L., O'Reilly, S. Y., & Fisher, N. I. (2002). Igneous zircon; trace element composition as an indicator of source rock type. *Contributions to Mineralogy and Petrology*, 143(5), 602-622. doi.org/10.1007/s00410-002-0364-7
- Benisek, A. & Finger, F. (1993). Factors controlling the development of prism faces in granite zircons: a microprobe study. *Contributions to Mineralogy and Petrology*, 114(4), 441-451. doi.org/10.1007/BF00321749
- Beveridge, T. L., Roberts, E. M., & Titus, A. L. (2020). Volcaniclastic member of the richly fossiliferous Kaiparowits Formation reveals new insights for regional correlation and tectonics in southern Utah during the latest Campanian. *Cretaceous Research*, 114, 104527. doi.org/10.1016/j.cretres.2020.104527
- Beveridge, T. L., Roberts, E. M., Ramezani, J., Titus, A. L., Eaton, J. G., Irmis, R. B., & Sertich, J. J. W. (2022). Refined geochronology and revised stratigraphic nomenclature of the Upper Cretaceous Wahweap Formation, Utah, U.S.A. and the age of early Campanian vertebrates from southern Laramidia. *Palaeogeography, Palaeoclimatology, Palaeoecology*, 591, 110876. doi.org/10.1016/j.palaeo.2022.110876
- Biek, R. F., Rowley, P. D., Anderson, J. J., Maldonado, F., Moore, D. W., Hacker, D. B., Eaton, J. G., Hereford, R., Sable, E. G., Filkorn, H. F., & Matyasik, B. (2015). Geologic map of the Panguitch 30' x 60' quadrangle, Garfield, Iron, and Kane Counties, Utah. Utah Geological Survey, Map 270DM, scale 1:62,500.

## References

---

- Bird, P. (1998). Kinematic history of the Laramide orogeny in latitudes 35°-49°N, western United States. *Tectonics*, 17(5), 780-801. doi.org/10.1029/98TC02698
- Blichert-Toft, J. & Albarede, F. (1997). The Lu-Hf isotope geochemistry of chondrites and the evolution of the mantle-crust system. *Earth and Planetary Science Letters*, 148(1-2), 243-258. doi.org/10.1016/S0012-821X(97)00040-X
- Borisova, A. Y., Freydier, R., Polvé, M., Salvi, S., Candaudap, F., & Aigouy, T. (2008). In Situ Multi-Element Analysis of the Mount Pinatubo Quartz-Hosted Melt Inclusions by NIR Femtosecond Laser Ablation-Inductively Coupled Plasma-Mass Spectrometry. *Geostandards and Geoanalytical Research*, 32(2), 209-229. doi.org/10.1111/j.1751-908X.2008.00882.x
- Bouvier, A., Vervoort, J. D., & Patchett, P. J. (2008). The Lu-Hf and Sm-Nd isotopic composition of CHUR; constraints from unequilibrated chondrites and implications for the bulk composition of terrestrial planets. *Earth and Planetary Science Letters*, 273(1-2), 48-57. doi.org/10.1016/j.epsl.2008.06.010
- Bowers, W. E. (1972). The Canaan Peak, Pine Hollow, and Wasatch formations in the Table Cliff region, Garfield County, Utah. U.S. *Geological Survey Bulletin*, 1331-B, 1-39.
- Bowers, W. E. (1973a). Geologic map and coal resources of the Upper Valley quadrangle, Garfield County, Utah. U.S. Geological Survey, Coal Investigations Map C-60, scale 1:24,000.
- Bowers, W. E. (1973b). Geologic map and coal resources of the Pine Lake quadrangle, Garfield County, Utah. U.S. Geological Survey, Coal Investigations Map C-66, scale 1:24,000.
- Bowers, W. E. (1975). Geologic map and coal resources of the Henrieville quadrangle, Garfield and Kane Counties, Utah. U.S. Geological Survey, Coal Investigations Map C-74, scale 1:24,000.
- Bowers, W. E. (1981). Geologic map and coal deposits of the Canaan Peak quadrangle, Garfield and Kane Counties, Utah. U.S. Geological Survey, Coal Investigations Map C-90, scale 1:24,000.
- Bowring, S. A., Schoene, B., Crowley, J. L., Ramezani, J., & Condon, D. J. (2006). High-precision U-Pb zircon geochronology and the stratigraphic record: Progress and promise. *Paleontological Society Papers*, 11, 23-43. doi.org/10.1017/S1089332600001339
- Bowring, J. F., McLean, N. M., & Bowring, S. A. (2011). Engineering cyber infrastructure for U-Pb geochronology: Tripoli and U-Pb\_Redux. *Geochemistry Geophysics Geosystems*, 12(6). doi.org/10.1029/2010GC003479
- Brinkman, D. B., Newbrey, M. G., Neuman, A. G., & Eaton, J. G. (2013). Freshwater Osteichthyes from the Cenomanian to late Campanian of Grand Staircase-Escalante National Monument, Utah. In A. Titus & M. Loewen (Eds.), *At the top of the grand staircase: The Late Cretaceous of southern Utah* (p. 195-236). Indiana University Press.
- Brown, C. M., Evans, D. C., Campione, N. E., O'Brien, L. J., & Eberth, D. A. (2013). Evidence for taphonomic size bias in the Dinosaur Park Formation (Campanian, Alberta), a model Mesozoic terrestrial alluvial-

## References

---

- paralic system. *Palaeogeography, Palaeoclimatology, Palaeoecology*, 372, 108-122. doi.org/10.1016/j.palaeo.2012.06.027
- Burgener, L., Hyland, E., Huntington, K. W., Kelson, J. R., & Sewall, J. O. (2019). Revisiting the equable climate problem during the Late Cretaceous greenhouse using palaeosol carbonate clumped isotope temperatures from the Campanian of the Western Interior Basin, USA. *Palaeogeography, Palaeoclimatology, Palaeoecology*, 516, 244-267. doi.org/10.1016/j.palaeo.2018.12.004
- Burgener, L., Hyland, E., Griffith, E., Mitasova, H., Zanno, L. E., & Gates, T. A. (2021). An extreme climate gradient-induced ecological regionalization in the Upper Cretaceous Western Interior Basin of North America. *Geological Society of America Bulletin*, 133(9-10), 2125-2136. doi.org/10.1130/B35904.1
- Carr, T. D., Williamson, T. E., Britt, B. B., & Stadtman, K. (2011). Evidence for high taxonomic and morphologic tyrannosauroid diversity in the Late Cretaceous (Late Campanian) of the American Southwest and a new short-skulled tyrannosaurid from the Kaiparowits formation of Utah. *Naturwissenschaften*, 98, 241-246. doi.org/10.1007/s00114-011-0762-7
- Cather, S. M. (2004). Laramide orogeny in central and northern New Mexico and southern Colorado. In G. H. Mack & K. A. Giles (Eds.), *The Geology of New Mexico, A Geologic History* (p. 203-248). New Mexico Geological Society Special Publication 11.
- Chiarenza, A. A., Mannion, P. D., Lunt, D. J., Farnsworth, A., Jones, L. A., Kelland, S.-J., & Allison, P. A. (2019). Ecological niche modelling does not support climatically-driven dinosaur diversity decline before the Cretaceous/Palaeogene mass extinction. *Nature Communications*, 10, 1091. doi.org/10.1038/s41467-019-08997-2
- Chupin, S. V., Chupin, V. P., Barton, J. M., Barton, E. S., Cathelineau, M., & Dubessy, J. (1998). Archean melt inclusions in zircon from quartzite and granitic orthogneiss from South Africa; magma compositions and probable sources of protoliths. *European Journal of Mineralogy*, 10(6), 1241-1251. doi.org/10.1127/ejm/10/6/1241
- Cifelli, R. L. (1990a). Cretaceous mammals of southern Utah I. Marsupial mammals from the Kaiparowits Formation (Judithian). *Journal of Vertebrate Paleontology*, 10(3), 295-319. doi.org/10.1080/02724634.1990.10011816
- Cifelli, R. L. (1990b). Cretaceous mammals of southern Utah II. Marsupials and marsupial-like mammals from the Wahweap Formation (early Campanian). *Journal of Vertebrate Paleontology*, 10(3), 320-331. doi.org/10.1080/02724634.1990.10011817
- Cifelli, R. L. (1990c). Cretaceous mammals of southern Utah IV. Eutherian mammals from the Wahweap (Aquilan) and Kaiparowits (Judithian) formations. *Journal of Vertebrate Paleontology*, 10(3), 346-360. doi.org/10.1080/02724634.1990.10011819
- Cifelli, R. L. (1990d). A primitive higher mammal from the Late Cretaceous of southern Utah. *Journal of Mammalogy*, 71(3), 343-350. doi.org/10.2307/1381944

## References

---

- Cifelli, R. L., Eberle, J. J., Lofgren, D. L., Lillegraven, J. A., & Clemens, W. A. (2004). Mammalian Biochronology of the Latest Cretaceous. In M. O. Woodburne (Ed.), *Late Cretaceous and Cenozoic Mammals of North America: Biostratigraphy and Geochronology* (p. 21-42). Columbia University Press.
- Clemens, W. A. (1986). Evolution of the terrestrial vertebrate fauna during the Cretaceous-Tertiary transition. In D. K. Elliott (Ed.), *Dynamics of Extinction* (p. 63-85). John Wiley and Sons.
- Cobban, W. A., Walaszczyk, I., Obradovich, J. D., & McKinney, K. C. (2006). A USGS Zonal Table for the Upper Cretaceous Middle Cenomanian–Maastrichtian of the Western Interior of the United States Based on Ammonites, Inoceramids, and Radiometric Ages. U.S. Geological Survey Open-File Report 2006-1250.
- Condamine, F. L., Guinot, G., Benton, M. J., & Currie, P. J. (2021). Dinosaur biodiversity declined well before the asteroid impact, influenced by ecological and environmental pressures. *Nature Communications*, *12*, 3833. doi.org/10.1038/s41467-021-23754-0
- Condon, D. J., Schoene, B., McLean, N. M., Bowring, S. A., & Parrish, R. R. (2015). Metrology and traceability of U-Pb isotope dilution geochronology (EARTHTIME Tracer Calibration Part I). *Geochimica et Cosmochimica Acta*, *164*, 464-480. doi.org/10.1016/j.gca.2015.05.026
- Coney, P. J., & Reynolds, S. J. (1977). Cordilleran Benioff zones. *Nature*, *270*(5636), 403-406. doi.org/10.1038/270403a0
- Corbett, M. J., Fielding, C. R., & Birgenheier, L. P. (2011). Stratigraphy of a Cretaceous coastal-plain fluvial succession; the Campanian Masuk Formation, Henry Mountains Syncline, Utah, U.S.A. *Journal of Sedimentary Research*, *81*(2), 80-96. doi.org/10.2110/jsr.2011.12
- Corfu, F., Hanchar, J. M., Hoskin, P. W. O., & Kinny, P. D. (2003). Atlas of zircon textures. *Reviews in Mineralogy and Geochemistry*, *53*(1), 469-500. doi.org/10.2113/0530469
- Cross, T. A., & Pilger, R. H. (1978). Tectonic controls of Late Cretaceous sedimentation, Western Interior, USA. *Nature*, *274*, 653-657. doi.org/10.1038/274653a0
- Cross, T. A. (1986). Tectonic controls of foreland basin subsidence and Laramide style deformation, western United States. *Special Publications of the International Association of Sedimentologists*, *8*, 15-39.
- Crystal, V. F., Evans, E. S. J., Fricke, H., Miller, I. M., & Sertich, J. J. W. (2019). Late Cretaceous fluvial hydrology and dinosaur behavior in southern Utah, USA; insights from stable isotopes of biogenic carbonate. *Palaeogeography, Palaeoclimatology, Palaeoecology*, *516*, 152-165. doi.org/10.1016/j.palaeo.2018.11.022
- Cullen, T. M., Fanti, F., Capobianco, C., Ryan, M. J., & Evans, D. C. (2016). A vertebrate microsite from a marine-terrestrial transition in the Foremost Formation (Campanian) of Alberta, Canada and the use of faunal assemblage data as a palaeoenvironmental indicator. *Palaeogeography, Palaeoclimatology, Palaeoecology*, *444*, 101-114. doi.org/10.1016/j.palaeo.2015.12.015



## References

---

- Currie, P. J. & Russell, D. A. (2005). The geographic and stratigraphic distribution of articulated and associated dinosaur remains. In P. J. Currie & E. B. Koppelhus (Eds.), *Dinosaur Provincial Park: A Spectacular Ancient Ecosystem Revealed* (p. 537-569). Indiana University Press.
- Dalman, S. G., Lucas, S. G., Jasinski, S. E., & Longrich, N. R. (2022). *Sierraceratops turneri*, a new chasmosaurine ceratopsid from the Hall Lake Formation (Upper Cretaceous) of south-central New Mexico. *Cretaceous Research*, 130, 105034. doi.org/10.1016/j.cretres.2021.105034
- Davis, D. W., Williams, I. S., & Krogh, T. E. (2003). Historical development of zircon geochronology. *Reviews in Mineralogy and Geochemistry*, 53(1), 145-181. doi.org/10.2113/0530145
- De Vleeschouwer, D. & Parnell, A. C. (2014). Reducing time-scale uncertainty for the Devonian by integrating astrochronology and Bayesian statistics. *Geology*, 42(6), 491-494. doi.org/10.1130/G35618.1
- Dean, C. D., Chiarenza, A. A., & Maidment, S. C. R. (2020). Formation binning; a new method for increased temporal resolution in regional studies, applied to the Late Cretaceous dinosaur fossil record of North America. *Paleontology*, 63(6), 881-901. doi.org/10.1111/pala.12492
- DeBlieux, D. D., Kirkland, J. I., Gates, T. A., Eaton, J. G., Getty, M. A., Sampson, S. D., Loewen, M. A., & Hayden, M. C. (2013). Paleontological overview and taphonomy of the middle Campanian Wahweap Formation in Grand Staircase – Escalante National Monument. In A. Titus & M. Loewen (Eds.), *At the top of the grand staircase: The Late Cretaceous of southern Utah* (p. 563-587). Indiana University Press.
- DeCelles, P. G. & Giles, K. A. (1996). Foreland basin systems. *Basin Research*, 8(2), 105-123. doi.org/10.1046/j.1365-2117.1996.01491.x
- DeCelles, P. G. (2004). Late Jurassic to Eocene evolution of the Cordilleran thrust belt and foreland basin system, western U.S.A. *American Journal of Science*, 304(2), 105-168. doi.org/10.2475/ajs.304.2.105
- DeCelles, P. G., Ducea, M. N., Kapp, P., & Zandt, G. (2009). Cyclicity in Cordilleran orogenic systems. *Nature Geoscience*, 2, 251-257. doi.org/10.1038/NGEO469
- Deino, A. & Potts, R. (1990). Single-crystal  $^{40}\text{Ar}/^{39}\text{Ar}$  dating of the Ologesailie Formation, Southern Kenya Rift. *Journal of Geophysical Research: Solid Earth*, 95(B6), 8453-8470. doi.org/10.1029/JB095iB06p08453
- Delano, J. W., Tice, S. J., Mitchell, C. E., & Goldman, D. (1994). Rhyolitic glass in Ordovician K-bentonites; a new stratigraphic tool. *Geology*, 22(2), 115-118. doi.org/10.1130/0091-7613(1994)022<0115:RGIOKB>2.3.CO;2
- Dickinson, W. R. & Gehrels, G. E. (2008). Sediment delivery to the Cordilleran foreland basin; insights from U-Pb ages of detrital zircons in Upper Jurassic and Cretaceous strata of the Colorado Plateau. *American Journal of Science*, 308(10), 1041-1082.
- Dickinson, W. R., Lawton, T. F., Pecha, M., Davis, S. J., Gehrels, G. E., & Young, R. A. (2012). Provenance of the Palaeogene Colton Formation (Uinta Basin) and Cretaceous-Palaeogene provenance evolution in the Utah foreland: Evidence from U-Pb ages of detrital zircons, palaeocurrent trends, and sandstone petrofacies. *Geosphere*, 8(4), 854-880. doi.org/10.1130/GES00763.1

## References

---

- Dodson, P. (1971). Sedimentology and Taphonomy of Oldman Formation (Campanian), Dinosaur-Provincial-Park, Alberta (Canada). *Palaeogeography, Palaeoclimatology, Palaeoecology*, 10(1), 21-74. doi.org/10.1016/0031-0182(71)90044-7
- Dodson, P. J. (1983). A faunal review of the Judith River (Oldman) Formation, Dinosaur Provincial Park, Alberta. *Mososaur*, 1, 89-118.
- Dodson, P. J. & Tatarinov, L. P. (1990). Dinosaur extinction. In D. B. Weishampel, P. J. Dodson, & H. Osmolska (Eds.), *The Dinosauria* (p. 55-62). University of California Press.
- Doelling, H. H. (1997). Interim geologic map of the Smoky Mountain 30' x 60' quadrangle, Kane and San Juan Counties, Utah and Coconino County, Arizona: Utah Geological Survey, Open-File Report 359, scale 1:100,000.
- Doelling, H. H. & Willis, G. C. (2006). Geologic map of the Smoky Mountain 30' x 60' Quadrangle, Kane and San Juan Counties, Utah and Coconino County, Arizona. Utah Geological Survey, Map 213, scale 1:100,000.
- Doelling, H. H. & Willis, G. C. (2018). Interim geologic map of the Escalante 30' x 60' quadrangle, Garfield and Kane Counties, Utah. Utah Geological Survey, Open-file Report 690DM, scale 1:100,000.
- Dumitru, T. A. (1990). Subnormal Cenozoic geothermal gradients in the extinct Sierra Nevada magmatic arc; consequences of Laramide and post-Laramide shallow-angle subduction. *Journal of Geophysical Research*, 95(B4), 4925-4941. doi.org/10.1029/JB095iB04p04925
- Eaton, J. G. & Cifelli, R. L. (1988). Preliminary report on Late Cretaceous mammals of the Kaiparowits Plateau, southern Utah. *Contributions to Geology*, 26(2), 45-55.
- Eaton, J. G. (1990). Stratigraphic Revision of Campanian (Upper Cretaceous) Rocks in the Henry Basin, Utah. *The Mountain Geologist*, 27(1), 27-38.
- Eaton, J. G. (1991). Biostratigraphic framework for the Upper Cretaceous rocks of the Kaiparowits Plateau, southern Utah. In J. Nations & J. Eaton (Eds.), *Stratigraphy, depositional environments, and sedimentary tectonics of the western margin, Cretaceous Western Interior Seaway* (p. 47-63). Geological Society of America Special Paper 260.
- Eaton, J. G. (1999). Vertebrate paleontology of the Paunsaugunt Plateau, Upper Cretaceous, southwestern Utah. In D. D. Gillette (Ed.), *Vertebrate Paleontology in Utah* (p. 335-338). Utah Geological Survey Miscellaneous Publication 99(1).
- Eaton, J. G., Diem, S., Archibald, J. D., Schierup, C., & Munk, H. (1999a). Vertebrate paleontology of the Upper Cretaceous rocks of the Markagunt Plateau, southwestern Utah. In D. D. Gillette (Ed.), *Vertebrate Paleontology in Utah* (p. 323-333). Utah Geological Survey Miscellaneous Publication 99(1).
- Eaton, J. G., Cifelli, R. L., Hutchison, J. H., Kirkland, J. I., & Parrish, J. M. (1999b). Cretaceous vertebrate faunas from the Kaiparowits Plateau, south-central Utah. In D. D. Gillette (Ed.), *Vertebrate Paleontology in Utah* (p. 345-353). Utah Geological Survey Miscellaneous Publication 99(1).

## References

---

- Eaton, J. G., Laurin, J., Kirkland, J. I., Tibert, N. E., Leckie, R. M., Sageman, B. B., Goldstrand, P. M., Moore, D. W., Straub, A. W., Cobban, W. A., & Dalebout, J. D. (2001). Cretaceous and Early Tertiary geology of the Cedar and Parowan canyons, western Markagunt Plateau, Utah. In M. C. Erskine, J. E. Faulds, J. M. Bartley, & P. D. Rowley (Eds.), *The Geologic Transition, High Plateaus to Great Basin: A Symposium and Field Guide* (p. 337-363). Utah Geological Association Publication 30.
- Eaton, J. G. (2002). Multituberculate mammals from the Wahweap (Campanian, Aquilan) and Kaiparowits (Campanian, Judithian) formations, within and near Grand Staircase-Escalante National Monument, southern Utah. *Utah Geological Survey Miscellaneous Publication 02-4*, 1-73.
- Eaton, J. G. & Cifelli, R. L. (2013). Review of Late Cretaceous mammalian faunas of the Kaiparowits and Paunsaugunt plateaus, southwestern Utah. In A. Titus & M. Loewen (Eds.), *At the top of the grand staircase: The Late Cretaceous of southern Utah* (p. 319-328). Indiana University Press.
- Eberth, D. A. (1990). Stratigraphy and sedimentology of vertebrate microfossil sites in the uppermost Judith River Formation (Campanian), Dinosaur Provincial Park, Alberta, Canada. *Palaeogeography, Palaeoclimatology, Palaeoecology*, 78(1-2), 1-36. doi.org/10.1016/0031-0182(90)90202-I
- Eberth, D. A., Thomas, R. G., & Deino, A. (1992). Preliminary K-Ar dates from bentonites in the Judith River and Bearpaw formations (Upper Cretaceous) of Dinosaur Provincial Park, southern Alberta, Canada. In N. J. Mateer & P. J. Chen (Eds.), *Aspects of nonmarine Cretaceous geology* (p. 296-304). China Ocean Press.
- Eberth, D. A. & Deino, A. L. (1992). A geochronology of the nonmarine Judith River Formation of Southern Alberta [abstract]. *Society for Sedimentary Geology Theme Meeting; Mesozoic of the Western Interior*, 24-25.
- Eberth, D. A. & Hamblin, A., P. (1993). Tectonic, stratigraphic, and sedimentologic significance of a regional discontinuity in the upper Judith River Group (Belly River wedge) of southern Alberta, Saskatchewan, and northern Montana. *Canadian Journal of Earth Sciences*, 30(1), 174-200. doi.org/10.1139/e93-016
- Eberth, D. A., Delgado de Jesus, C. R., Lerbekmo, J. F., Brinkman, D. B., Rodriguez de la Rosa, R. A., & Sampson, S. D. (2004). Cerro del Pueblo Fm (Difunta Group, Upper Cretaceous) Parras Basin, southern Coahuila, Mexico; reference sections, age, and correlation. *Revista Mexicana de Ciencias Geologicas*, 21(3), 335-352.
- Eberth, D. A. (2005). The geology. In P. J. Currie & E. B. Koppelhus (Eds.), *Dinosaur Provincial Park: A Spectacular Ancient Ecosystem Revealed* (p. 54-82). Indiana University Press.
- Eberth, D. A. (2015). Origins of dinosaur bonebeds in the Cretaceous of Alberta, Canada. *Canadian Journal of Earth Sciences*, 52(8), 655-681. doi.org/10.1139/cjes-2014-0200
- Eberth, D. A. & Kamo, S. L. (2020). High-precision U-Pb CA-ID-TIMS dating and chronostratigraphy of the dinosaur-rich Horseshoe Canyon Formation (Upper Cretaceous, Campanian-Maastrichtian), Red Deer River valley, Alberta, Canada. *Canadian Journal of Earth Sciences*, 57(10), 1220-1237. doi.org/10.1139/cjes-2019-0019

## References

---

- Evans, D. C., Schott, R. K., Larson, D. W., Brown, C. M., & Ryan, M. J. (2013). The oldest North American pachycephalosaurid and the hidden diversity of small-bodied ornithischian dinosaurs. *Nature Communications*, 4, 1828. doi.org/10.1038/ncomms2749
- Evans, D. C., Williamson, T., Loewen, M. A., & Kirkland, J. I. (2013). Review of pachycephalosaurian dinosaurs from Grand Staircase-Escalante National Monument, southern Utah. In A. Titus & M. Loewen (Eds.), *At the top of the grand staircase: The Late Cretaceous of southern Utah* (p. 482-487). Indiana University Press.
- Ewing, R. C., Meldrum, A., Wang, L. M., Weber, W. J., & Corrales, L. R. (2003). Radiation effects in zircon. *Reviews in Mineralogy and Geochemistry*, 53(1), 387–425. doi.org/10.2113/0530387
- Fanti, F. (2009). Bentonite chemical features as proxy of late Cretaceous provenance changes; a case study from the Western Interior Basin of Canada. *Sedimentary Geology*, 217(1-4), 112-127. doi.org/10.1016/j.sedgeo.2009.03.015
- Fanti, F., & Catuneanu, O. (2010). Fluvial sequence stratigraphy; the Wapiti Formation, west-central Alberta, Canada. *Journal of Sedimentary Research*, 80(4), 320-338. doi.org/10.2110/jsr.2010.033
- Farlow, J. O. (1976). Consideration of Trophic Dynamics of a Late Cretaceous Large Dinosaur Community (Oldman Formation). *Ecology*, 57(5), 841-857. doi.org/10.2307/1941052
- Fassett, J. E. & Steiner, M. B. (1997). Precise age of C33N-C32R magnetic-polarity reversal, San Juan Basin, New Mexico and Colorado. In O. Anderson, B. Kues, & S. Lucas (Eds.), *Mesozoic geology and paleontology of the Four Corners Region: New Mexico Geological Society 48th Annual Fall Field Conference Guidebook* (p. 239-247). New Mexico Geological Society.
- Fassett, J. E., Cobban, W. A., & Obradovich, J. D. (1997). Biostratigraphic and isotopic age of the Huerfanito Bentonite Bed of the Upper Cretaceous Lewis Shale at an outcrop near Regina, New Mexico. In O. Anderson, B. Kues, & S. Lucas (Eds.), *Mesozoic geology and paleontology of the Four Corners Region: New Mexico Geological Society 48th Annual Fall Field Conference Guidebook* (p. 229-232). New Mexico Geological Society.
- Fassett, J. E. & Heizler, M. T. (2017). An improved new age for the C33N-C32R palaeomagnetic reversal, San Juan Basin, NW New Mexico and SW Colorado. In K. Karlstrom, D. Gonzales, M. Zimmerer, M. Heizler, & D. Ulmer-Scholle (Eds.), *The geology of the Ouray-Silverton area: 68th Annual Fall Field Conference Guidebook* (p. 115-121). New Mexico Geological Society.
- Ferguson, A. L., & Tapanila, L. (2022). Rare clutch of Cretaceous turtle eggs preserved in the Kaiparowits Formation of southern Utah. *Cretaceous Research*, 135. doi.org/10.1016/j.cretres.2022.105197
- Fiorillo, A. R., McCarthy, P. J., & Flaig, P. P. (2010). Taphonomic and sedimentologic interpretations of the dinosaur-bearing Upper Cretaceous strata of the Prince Creek Formation, Northern Alaska; insights from an ancient high-latitude terrestrial ecosystem. *Palaeogeography, Palaeoclimatology, Palaeoecology*, 295(3-4), 376-388. doi.org/10.1016/j.palaeo.2010.02.029

## References

---

- Foreman, B. Z., Rogers, R. R., Deino, A. L., Wirth, K. R., & Thole, J. T. (2008). Geochemical characterization of bentonite beds in the Two Medicine Formation (Campanian, Montana), including a new  $^{40}\text{Ar}/^{39}\text{Ar}$  age. *Cretaceous Research*, 29(3), 373-385. doi.org/10.1016/j.cretres.2007.07.001
- Foreman, B. Z., Roberts, E. M., Tapanila, L., Ratigan, D., & Sullivan, P. (2015). Stable isotopic insights into palaeoclimatic conditions and alluvial depositional processes in the Kaiparowits Formation (Campanian, south-central Utah, U.S.A.). *Cretaceous Research*, 56, 180-192. doi.org/10.1016/j.cretres.2015.05.001
- Fricke, H. C., Foreman, B. Z., & Sewall, J. O. (2010). Integrated climate model-oxygen isotope evidence for a North American monsoon during the Late Cretaceous. *Earth and Planetary Science Letters*, 289(1-2), 11-21. doi.org/10.1016/j.epsl.2009.10.018
- Gale, A. S., Mutterlose, J., & Batenburg, S. (2020). The Cretaceous Period. In F. M. Gradstein, J. G. Ogg, M. D. Schmitz, & G. M. Ogg (Eds), *The Geologic Time Scale: Volume 2* (p. 1023-1086). Elsevier. doi.org/10.1016/C2020-1-02369-3
- Gardner, J. D., Eaton, J. G., & Cifelli, R. L. (2013). Preliminary report on salamanders (Lissamphibia; Caudata) from the Late Cretaceous (late Cenomanian – late Campanian) of southern Utah, U.S.A. In A. Titus & M. Loewen (Eds.), *At the top of the grand staircase: The Late Cretaceous of southern Utah* (p. 237-272). Indiana University Press.
- Gates, T. A. & Sampson, S. D. (2007). A new species of Gryposaurus (Dinosauria: Hadrosauridae) from the late Campanian Kaiparowits Formation, southern Utah, USA. *Zoological Journal of the Linnean Society*, 151(2), 351-376. doi.org/10.1111/j.1096-3642.2007.00349.x
- Gates, T. A., Sampson, S. D., Zanno, L. E., Roberts, E. M., Eaton, J. G., Nydam, R. L., Hutchinson, J. H., Smith, J. A., Loewen M. A., & Getty, M. A. (2010). Biogeography of terrestrial and freshwater vertebrates from the late Cretaceous (Campanian) Western Interior of North America. *Palaeogeography, Palaeoclimatology, Palaeoecology*, 291(3-4), 371-387. doi.org/10.1016/j.palaeo.2010.03.008
- Gates, T. A., Horner, J. R., Hanna, R. R., & Nelson, C. R. (2011). New unadorned hadrosaurine hadrosaurid (Dinosauria, Ornithopoda) from the Campanian of North America. *Journal of Vertebrate Paleontology*, 31(4), 798-811. doi.org/10.1080/02724634.2011.577854
- Gates, T. A., Prieto-Marquez, A., & Zanno, L. E. (2012). Mountain building triggered Late Cretaceous North American megaherbivore dinosaur radiation. *PloS One*, 7(8), e42135. doi.org/10.1371/journal.pone.0042135
- Gates, T. A., Lund, E. K., Boyd, C. A., DeBlieux, D. D., Titus, A. L., Evans, D. C., Getty, M. A., Kirkland, J. I., & Eaton, J. G. (2013). Ornithopod dinosaurs from the Grand Staircase-Escalante National Monument region, Utah, and their role in palaeobiogeographic and macroevolutionary studies. In A. Titus & M. Loewen (Eds.), *At the top of the grand staircase: The Late Cretaceous of southern Utah* (p. 463-481). Indiana University Press.



## References

---

- Gates, T. A., Jinnah, Z., Levitt, C., & Getty, M. A. (2014). New hadrosaurid (Dinosauria, Ornithopoda) specimens from the lower-middle Campanian Wahweap Formation of southern Utah. In D. C. Evans (Ed), *Hadrosaurs* (p. 156-173). Indiana University Press.
- Getty, M. A., Loewen, M. A., Roberts, E. M., Titus, A. L., & Sampson, S. D. (2010). Taphonomy of horned dinosaurs (Ornithischia: Ceratopsidae) from the late Campanian Kaiparowits Formation, Grand Staircase - Escalante National Monument, Utah. In M. Ryan, B. Chinnery-Allgeier, & D. Eberth (Eds.), *New Perspectives on Horned Dinosaurs* (p. 478-494). Indiana University Press.
- Goldstrand, P. M. (1992). Evolution of Late Cretaceous and early Tertiary basins of Southwest Utah based on clastic petrology. *Journal of Sedimentary Petrology*, 62(3), 495-507. doi.org/10.1306/D4267933-2B26-11D7-8648000102C1865D
- Gradstein, F. M., Ogg, J. G., Schmitz, M. D., & Ogg, G. M. (2020). *Geologic Time Scale 2020: Volume 2*. Elsevier. doi.org/10.1016/C2020-1-02369-3
- Gregory, H. E. & Moore, R. C. (1931). The Kaiparowits region: Geographic and geologic reconnaissance of parts of Utah and Arizona. *U.S. Geological Survey Professional Paper 164*. 161 p.
- Gudelius, D., Zeh, A., Almeev, R. R., Wilson, A. H., Fischer, L. A., & Schmitt, A. K. (2020). Zircon melt inclusions in mafic and felsic rocks of the Bushveld Complex; constraints for zircon crystallization temperatures and partition coefficients. *Geochimica et Cosmochimica Acta*, 289, 158-181. doi.org/10.1016/j.gca.2020.08.027
- Halliday, A. N., Lee, D.-C., Christensen, J. N., Walder, A. J., Freedman, P. A., Jones, C. E., Hall, C. M., Yi, W., & Teagle, D. (1995). Recent developments in inductively coupled plasma magnetic sector multiple collector mass spectrometry. *International Journal of Mass Spectrometry and Ion Processes*, 146(C), 21-33. doi.org/10.1016/0168-1176(95)04200-5
- Hamblin, A. P. & Abrahamson, B. W. (1996). Stratigraphic architecture of “basal Belly River” cycles, Foremost Formation, Belly River Group, subsurface of southern Alberta and southwestern Saskatchewan. *Bulletin of Canadian Petroleum Geology*, 44(4), 654-673.
- Hamblin, A. H. & Foster, J. R. (2000). Ancient animal footprints and traces in the Grand Staircase – Escalante National Monument. In D. A. Sprinkel, T. C. Chidsey, & P. B. Anderson (Eds.), *Geology of Utah's Parks and Monuments* (12 p.). Utah Geological Association Publication 28.
- Haq, B. U., Hardenbol, J., & Vail, P. R. (1987). Chronology of fluctuating sea levels since the Triassic. *Science*, 235, 1156-1166. doi.org/10.1126/science.235.4793.1156
- Haq, B. U. (2014). Cretaceous eustasy revisited. *Global and Planetary Change*, 113, 44-58. doi.org/10.1016/j.gloplacha.2013.12.007
- Haslett, J. & Parnell, A. (2008). A simple monotone process with application to radiocarbon-dated depth chronologies. *Journal of the Royal Statistical Society Series C*, 57(4), 399-418. doi.org/10.1111/j.1467-9876.2008.00623.x

## References

---

- Haynes, J. T., Melson, W. G., & Kunk, M. J. (1995). Composition of biotite phenocrysts in Ordovician tephra casts doubt on the proposed trans-Atlantic correlation of the Millbrig K-bentonite (United States) and the Kinnekulle K-bentonite (Sweden). *Geology*, 23(9), 847-850. doi.org/10.1130/0091-7613(1995)023<0847:COBPIO>2.3.CO;2
- Herriott, T. M., Crowley, J. L., Schmitz, M. D., Wartes, M. A., & Gillis, R. J. (2019). Exploring the law of detrital zircon: LA-ICP-MS and CA-TIMS geochronology of Jurassic forearc strata, Cook Inlet, Alaska, USA. *Geology*, 47, 1044-1048. doi.org/10.1130/G46312.1
- Hilbert-Wolf, H. L., Simpson, E. L., Simpson, W. S., Tindall, S. E., & Wizevichz, M. C. (2009). Insights into syndepositional fault movement in a foreland basin; Trends in seismites of the Upper Cretaceous, Wahweap Formation, Kaiparowits Basin, Utah, USA. *Basin Research*, 21, 856-871. doi.org/10.1111/j.1365-2117.2009.00398.x
- Hoke, G. D., Schmitz, M. D., & Bowring, S. A. (2014). An ultrasonic method for isolating nonclay components from clay-rich material. *Geochemistry Geophysics Geosystems*, 15(2), 492-498. doi.org/10.1002/2013GC005125
- Holroyd, P. A. & Hutchison, H. (2016). Fauna and setting of the *Adelolophus hutchisoni* type locality in the Upper Cretaceous (Campanian) Wahweap Formation of Utah. *PalaeoBios*, 33, 311-96. doi.org/10.5070/P9331031196
- Horner, J. R. & Makela, R. (1979). Nest of Juveniles Provides Evidence of Family-Structure among Dinosaurs. *Nature*, 282, 296-298. doi.org/10.1038/282296a0
- Horner, J. R. (1989). The Mesozoic terrestrial ecosystems of Montana. In *Montana Centennial Field Conference* (p. 153-162). Montana Geological Society.
- Horner, J. R., Varricchio, D. J., & Goodwin, M. B. (1992). Marine Transgressions and the Evolution of Cretaceous Dinosaurs. *Nature*, 358, 59-61. doi.org/10.1038/358059a0
- Horner, J. R., Schmitt, J. G., Jackson, F., & Hanna, R. (2001). Bones and rocks of the Upper Cretaceous Two Medicine-Judith River clastic wedge complex, Montana. In C. L. Hill (Ed.), *Field Trip Guidebook, Society of Vertebrate Paleontology 61st Annual Meeting: Mesozoic and Cenozoic Paleontology in the Western Plains and Rocky Mountains 3* (p. 3-13). Museum of the Rockies Occasional Paper No. 3.
- Hoskin, P. W. O., & Schaltegger, U. (2003). The composition of zircon and igneous and metamorphic petrogenesis. *Reviews in Mineralogy and Geochemistry*, 53(1), 27-62. doi.org/10.2113/0530027
- Huang, H., Guillong, M., Hu, Y., & Spandler, C. (2021). Fine tuning laser focus for improved reproducibility of U-Pb isotope analysis by LA-ICP-MS. *Journal of Analytical Atomic Spectrometry*, 36, 836-844. doi.org/10.1039/d1ja00044f
- Huff, W. D. (2008). Ordovician K-bentonites; issues in interpreting and correlating ancient tephra. *Quaternary International*, 178(1), 276-287. doi.org/10.1016/j.quaint.2007.04.007

## References

---

- Humphreys, M. C. S., Kearns, S. L., & Blundy, J. D. (2006). SIMS investigation of electron-beam damage to hydrous, rhyolitic glasses; implications for melt inclusion analysis. *The American Mineralogist*, *91*(4), 667-679. doi.org/10.2138/am.2006.1936
- Hunt, A. P. & Lucas, S. G. (1992). Stratigraphy, paleontology and age of the Fruitland and Kirtland Formations (Upper Cretaceous), San Juan Basin, New Mexico. In S. G. Lucas, B. S. Kues, T. E. Williamson, & A. P. Hunt (Eds.), *San Juan Basin IV: New Mexico Geological Society 43rd Annual Fall Field Conference Guidebook* (p. 217-239). New Mexico Geological Society.
- Hunt, A. P. & Lucas, S. G. (2003). Origin and stratigraphy of historic dinosaur quarries in the Upper Cretaceous Fruitland Formation of the Fossil Forest Research Natural Area, northwestern New Mexico. In S. G. Lucas, S. C. Semken, W. Berglof, & D. Ulmer-Scholle (Eds.), *Geology of the Zuni Plateau: New Mexico Geological Society 54th Annual Fall Field Conference Guidebook* (p. 383-388). New Mexico Geological Society.
- Hutchison, J. H., Knell, M. J., & Brinkman, D. B. (2013). Turtles from the Kaiparowits Formation, Utah. In A. Titus & M. Loewen (Eds.), *At the top of the grand staircase: The Late Cretaceous of southern Utah* (p. 295-318). Indiana University Press.
- Ickert, R. B., Mundil, R., Magee, C. W., Jr., & Mulcahy, S. R. (2015). The U-Th-Pb systematics of zircon from the Bishop Tuff: A case study in challenges to high-precision Pb/U geochronology at the millennial scale. *Geochimica et Cosmochimica Acta*, *168*, 88-110. doi.org/10.1016/j.gca.2015.07.018
- Irmis, R. B., Martz, J. W., Parker, W. G., & Nesbitt, S. J. (2010). Re-evaluating the correlation between Late Triassic terrestrial vertebrate biostratigraphy and the GSSP-defined marine stages. *Albertiana*, *38*, 40-52.
- Irmis R. B., Hutchison J. H., Sertich J. J. W., & Titus, A. L. (2013). Crocodyliforms from the Late Cretaceous of Grand Staircase-Escalante National Monument and vicinity, southern Utah, U.S.A. In A. Titus & M. Loewen (Eds.), *At the top of the grand staircase: The Late Cretaceous of southern Utah* (p. 424-444). Indiana University Press.
- Jaffey, A. H., Flynn, K. F., Glendenin, L. E., Bentley, W. C., & Essling, A. M. (1971). Precision measurements of half-lives and specific activities of  $^{235}\text{U}$  and  $^{238}\text{U}$ . *Physical Review C*, *4*(5): 1889-1906. doi.org/10.1103/PhysRevC.4.1889
- Jellinek, A. M., Manga, M., & Saar, M. O. (2004). Did melting glaciers cause volcanic eruptions in eastern California? Probing the mechanics of dike formation. *Journal of Geophysical Research*, *109*(B9), B09206. doi.org/10.1029/2004JB002978
- Jinnah, Z. A., Roberts, E. M., Deino, A. L., Larsen, J. S., Link, P. K., & Fanning, C. M. (2009). New  $^{40}\text{Ar}$ - $^{39}\text{Ar}$  and detrital zircon U-Pb ages for the Upper Cretaceous Wahweap and Kaiparowits formations on the Kaiparowits Plateau, Utah: Implications for regional correlation, provenance and biostratigraphy. *Cretaceous Research*, *30*(2), 287-299. doi.org/10.1016/j.cretres.2008.07.012

## References

---

- Jinnah, Z. A. & Roberts, E. M. (2011). Facies associations, palaeoenvironment, and base-level changes in the Upper Cretaceous Wahweap Formation, Utah, U.S.A. *Journal of Sedimentary Research*, 81(4), 266-283. doi.org/10.2110/jsr.2011.22
- Jinnah, Z. A. (2013). Tectonic and sedimentary controls, age and correlation of the Upper Cretaceous Wahweap Formation, southern Utah. In A. Titus & M. Loewen (Eds.), *At the top of the grand staircase: The Late Cretaceous of southern Utah* (p. 57-73). Indiana University Press.
- Kauffman, E. G. (1985). Cretaceous evolution of the Western Interior Basin of the United States. In L. M. Pratt, E. G. Kauffman, & F. B. Zelt (Eds.), *Fine-Grained Deposits and Biofacies of the Cretaceous Western Interior Seaway: Evidence of Cyclic Sedimentary Processes*. SEPM Society for Sedimentary Geology. doi.org/10.2110/sepmfg.04
- Kauffman, E. G. & Caldwell, W. G. E. (1993). The Western Interior Basin in space and time. In W. G. E. Caldwell & E. G. Kauffman (Eds.), *Evolution of the Western Interior Basin: Geological Association of Canada, Special Paper 39* (p. 1-30). Geological Association of Canada.
- Kemp, A. I. S., Hawkesworth, C. J., Collins, W. J., Gray, C. M., & Blevin, P. L. (2009). Isotopic evidence for rapid continental growth in an extensional accretionary orogen; the Tasmanides, eastern Australia. *Earth and Planetary Science Letters*, 284(3-4), 455-466. doi.org/10.1016/j.epsl.2009.05.011
- Kim, S. T. & O'Neil, J. R. (1997). Equilibrium and nonequilibrium oxygen isotope effects in synthetic carbonates. *Geochimica et Cosmochimica Acta*, 61, 3461-3475. doi.org/10.1016/S0016-7037(97)00169-5
- Kinny, P. D., Compston, W., & Williams, I. S. (1991). A reconnaissance ion-probe study of hafnium isotopes in zircons. *Geochimica et Cosmochimica Acta*, 55(3), 849-859. doi.org/10.1016/0016-7037(91)90346-7
- Kinny, P. D. & Maas, R. (2003). Lu-Hf and Sm-Nd isotope systems in zircon. *Reviews in Mineralogy and Geochemistry*, 53(1), 327-341. doi.org/10.2113/0530327
- Kirkland, J. I. & DeBlieux, D. D. (2010). New basal centrosaurine ceratopsian skulls from the Wahweap Formation (middle Campanian), Grand Staircase – Escalante National Monument, southern Utah. In M. J. Ryan, B. J. Chinnery-Allgeier, & D. A. Eberth (Eds.), *New Perspectives on Horned Dinosaurs* (p. 117-140). Indiana University Press.
- Kirkland, J. I., Eaton, J. G., & Brinkman, D. B. (2013). Elasmobranchs from Upper Cretaceous freshwater facies in southern Utah. In A. Titus & M. Loewen (Eds.), *At the top of the grand staircase: The Late Cretaceous of southern Utah* (p. 153-194). Indiana University Press.
- Krogh, T. E. (1982). Improved accuracy of U-Pb zircon ages by the creation of more concordant systems using an air abrasion technique. *Geochimica et Cosmochimica Acta*, 46(4), 637-649. doi.org/10.1016/0016-7037(82)90165-X
- Kuiper, K. F., Deino, A., Hilgen, F. J., Krijgsman, W., Renne, P. R., & Wijbrans, J. R. (2008). Synchronizing rock clocks of earth history. *Science*, 320(5875), 500-504. doi.org/10.1126/science.1154339

## References

---

- Lageson, D. R., Schmitt, J. G., Horton, B. K., Kalakay, T. J., & Burton, B. R. (2001). Influence of Late Cretaceous magmatism on the Sevier orogenic wedge, western Montana. *Geology*, *29*(8), 723-726. doi.org/10.1130/0091-7613(2001)029<0723:IOLCMO>2.0.CO;2
- Landing, E., Geyer, G., Brasier, M. D., & Bowring, S. A. (2013). Cambrian evolutionary radiation; context, correlation, and chronostratigraphy; overcoming deficiencies of the first appearance datum (FAD) concept. *Earth-Science Reviews*, *123*, 133-172. doi.org/10.1016/j.earscirev.2013.03.008
- Larsen, J. S., Link, P. K., Roberts, E. M., Tapanila, L., & Fanning, C. M. (2010). Cyclic stratigraphy of the Palaeogene Pine Hollow formation and detrital zircon provenance of Campanian to Eocene sandstones of the Kaiparowits and Table Cliffs Basins, south-central Utah. In S. Carney, D. Tabet, & C. Johnson (Eds.), *Geology of South-Central Utah* (p. 194-224). Utah Geological Association Publication 39.
- Laskowski, A. K., DeCelles, P. G., & Gehrels, G. E. (2013). Detrital zircon geochronology of Cordilleran retroarc foreland basin strata, western North America. *Tectonics*, *32*, 1027-1048. doi.org/10.1002/tect.20065
- Lawton, T. F., Pollock, S. L., & Robinson, R. A. J. (2003). Integrating sandstone petrology and nonmarine sequence stratigraphy: Application to the Late Cretaceous fluvial systems of southwestern Utah, U.S.A. *Journal of Sedimentary Research*, *73*(3), 389-406. doi.org/10.1306/100702730389
- Lawton, T. F. & Bradford, B. (2011). Correlation and provenance of Upper Cretaceous (Campanian) fluvial strata, Utah, U.S.A., from zircon U-Pb geochronology and petrography. *Journal of Sedimentary Research*, *81*, 495-512. doi.org/10.2110/jsr.2011.45
- Lawton, T. F., Eaton, J. G., Godfrey, K. N., & Schellenbach, W. L. (2014a). Compositional, paleontological and detrital-zircon data from Cretaceous strata of the Henry Mountains Basin and implications for connections with dispersal systems of Wahweap and Kaiparowits formations in southern Utah, U.S.A. In J. S. MacLean, R. F. Biek, & J. E. Huntoon (Eds.), *Geology of Utah's Far South* (p. 373-396). Utah Geological Association Publication 43.
- Lawton, T. F., Schellenbach, W. L., & Nugent, A. E. (2014b). Late Cretaceous fluvial-megafan and axial river systems in the southern Cordilleran Foreland Basin: Drip Tank Member of the Straight Cliffs Formation and adjacent strata, southern Utah, U.S.A. *Journal of Sedimentary Research*, *84*, 407-434. doi.org/10.2110/jsr.2014.33
- Le Bas, M. J., Le Maitre, R. W., Streckeisen, A., & Zanettin, B. A. (1986). Chemical classification of volcanic rocks based on the total alkali-silica diagram. *Journal of Petrology*, *27*(3), 745-750. doi.org/10.1093/petrology/27.3.745
- Lehman, T. M. (1989). *Chasmosaurus mariscalensis*, sp. nov., a new ceratopsian dinosaur from Texas. *Journal of Vertebrate Paleontology*, *9*(2), 137-162. doi.org/10.1080/02724634.1989.10011749
- Lehman, T. M. (1997). Late Campanian dinosaur biogeography in the Western Interior of North America. In D. Wolberg & E. Stump (Eds.), *Dinofest International Proceedings* (p. 223-240). Philadelphia Academy of Natural Sciences.



## References

---

- Lehman, T. M. (2001). Late Cretaceous dinosaur provinciality. In D. H. Tanke & K. Carpenter (Eds.), *Mesozoic vertebrate life* (p. 310-328). Indiana University Press.
- Lehman, T. M., Wick, S. L., & Barnes, K. R. (2017). New specimens of horned dinosaurs from the Aguja Formation of West Texas, and a revision of Agujaceratops. *Journal of Systematic Paleontology*, *15*, 641-674. doi.org/10.1080/14772019.2016.1210683
- Lehman, T. M., Wick, S. L., Brink, A. A., & Shiller, T. A. (2019). Stratigraphy and vertebrate fauna of the lower shale member of the Aguja Formation (lower Campanian) in West Texas. *Cretaceous Research*, *99*, 291-314. doi.org/10.1016/j.cretres.2019.02.028
- Lerbekmo, J. F. (2002). The Dorothy Bentonite; an extraordinary case of secondary thickening in a late Campanian volcanic ash fall in central Alberta. *Canadian Journal of Earth Sciences*, *39*(12), 1745-1754. doi.org/10.1139/e02-079
- Leslie, C. E., Peppe, D. J., Williamson, T. E., Heizler, M. T., Jackson, M., Atchley, S. C., Nordt, L., & Standhardt, B. (2018). Revised age constraints for Late Cretaceous to early Palaeocene terrestrial strata from the Dawson Creek section, Big Bend National Park, West Texas. *Geological Society of America Bulletin*, *130*(7-8), 1143-1163. doi.org/10.1130/B31785.1
- Lillegraven, J. A. & McKenna, M. C. (1986). Fossil mammals from the "Mesaverde" Formation (Late Cretaceous, Judithian) of the Bighorn and Wind River basins, Wyoming, with definitions of Late Cretaceous North American land-mammal "ages". *American Museum Novitates* 2840, 1-68.
- Little, W. W. (1995). The influence of tectonics and eustasy on alluvial architecture, Middle Coniacian through Campanian strata of the Kaiparowits Basin, Utah. Unpublished Ph.D. Dissertation (328 p.). University of Colorado, Boulder.
- Liu, L., Gurnis, M., Seton, M., Saleeby, J., Muller, R. D., & Jackson, J. M. (2010). The role of oceanic plateau subduction in the Laramide Orogeny. *Nature Geoscience*, *3*, 533-537. doi.org/10.1038/ngeo829
- Lively, J. R. (2015). A new species of baenid turtle from the Kaiparowits Formation (Upper Cretaceous, Campanian) of southern Utah. *Journal of Vertebrate Paleontology*, *35*(6), e1009084. doi.org/10.1080/02724634.2015.1009084
- Loewen, M. A., Irmis, R. B., Sertich, J. J. W., Currie, P. J., & Sampson, S. D. (2013a). Tyrant dinosaur evolution tracks the rise and fall of Late Cretaceous oceans. *PLoS ONE*, *8*(11), e79420. doi.org/10.1371/journal.pone.0079420
- Loewen, M. A., Burns, M. E., Getty, M. A., Kirkland, J. I., & Vickaryous, M. K. (2013b). Review of Late Cretaceous ankylosaurian dinosaurs from the Grand Staircase region, southern Utah. In A. Titus & M. Loewen (Eds.), *At the top of the grand staircase: The Late Cretaceous of southern Utah* (p. 445-462). Indiana University Press.

## References

---

- Loewen, M. A., Farke, A. A., Sampson, S. D., Getty, M. A., Lund, E. K., & O'Connor, P. M. (2013c). Ceratopsid dinosaurs from the Grand Staircase of southern Utah. In A. Titus & M. Loewen (Eds.), *At the top of the grand staircase: The Late Cretaceous of southern Utah* (p. 488-503). Indiana University Press.
- Lohrengel, C. F. (1969). Palynology of Kaiparowits Formation, Garfield County, Utah. *The American Association of Petroleum Geologists Bulletin*, 53(3), 729-729.
- Longrich, N. R. (2014). The horned dinosaurs Pentaceratops and Kosmocerotops from the upper Campanian of Alberta and implications for dinosaur biogeography. *Cretaceous Research*, 51, 292-308. doi.org/10.1016/j.cretres.2014.06.011
- Lorenz, J. C. (1981). Sedimentary and tectonic history of the Two Medicine Formation, Late Cretaceous (Campanian), northwestern Montana. Unpublished Ph.D. Dissertation (215 p.). Princeton University.
- Lowe, D. J. (2011). Tephrochronology and its application; a review. *Quaternary Geochronology*, 6(2), 107-153. doi.org/10.1016/j.quageo.2010.08.003
- Lowi-Merri, T. M. & Evans, D. C. (2020). Cranial variation in Gryposaurus and biostratigraphy of hadrosaurines (Ornithischia, Hadrosauridae) from the Dinosaur Park Formation of Alberta, Canada. *Canadian Journal of Earth Sciences*, 57(6), 765-779. doi.org/10.1139/cjes-2019-0073
- Lucas, S. G., Spielmann, J. A., Braman, D. R., Brister, B. S., Peters, L., & McIntosh, W. C. (2005). Age of the Cretaceous Menefee Formation, Gallina Hogback, Rio Arriba County, New Mexico. In, *New Mexico Geological Society, 56th Field Conference Guidebook: Geology of the Chama Basin* (p. 231-235). New Mexico Geological Society.
- Lucas, S. G., Hunt, A. P., & Sullivan, R. M. (2006). Stratigraphy and age of the Upper Cretaceous Fruitland Formation, west-central San Juan Basin, New Mexico. In S. G. Lucas & R. M. Sullivan (Eds.), *Late Cretaceous vertebrates from the Western Interior: New Mexico Museum of Natural History and Science Bulletin 35* (p. 1-6). New Mexico Museum of Natural History and Science.
- Lucas, S. G., Sullivan, R. M., Lichtig, A. J., Dalman, S. G., & Jasinski, S. E. (2016). Late Cretaceous dinosaur biogeography and endemism in the Western Interior basin, North America: A critical re-evaluation. In A. Khosla & S. G. Lucas (Eds.), *Cretaceous Period Biotic Diversity and Biogeography: New Mexico Museum of Natural History and Science Bulletin 71* (p. 195-213). New Mexico Museum of Natural History and Science.
- Ludwig, J. R. (2012). User's manual for Isoplot 3.75: a geochronological toolkit for Microsoft Excel. Berkeley Geochronology Centre Special Publication 5. Online version at: [bgc.org/isoplot\\_etc/isoplot/Isoplot3\\_75-4\\_15manual.pdf](http://bgc.org/isoplot_etc/isoplot/Isoplot3_75-4_15manual.pdf).
- Lund, E. K., O'Connor, P. M., Loewen, M. A., & Jinnah, Z. A. (2016a). A new centrosaurine ceratopsid, *Machairoceratops cronusi* gen et sp. nov., from the upper sand member of the Wahweap Formation (middle Campanian), southern Utah. *PLoS ONE*, 11(5), e0154403. doi.org/10.1371/journal.pone.0154403

## References

---

- Lund, E. K., Sampson, S. D., & Loewen, M. A. (2016b). *Nasutoceratops titusi* (Ornithischia, Ceratopsidae), a basal centrosaurine ceratopsid from the Kaiparowits Formation, southern Utah. *Journal of Vertebrate Paleontology*, *36*(2), e1054936. doi.org/10.1080/02724634.2015.1054936
- Maccracken, S. A., Miller, I. M., & Labandeira, C. C. (2019). Late Cretaceous domatia reveal the antiquity of plant-mite mutualisms in flowering plants. *Biology Letters*, *15*(11), 20190657. doi.org/10.1098/rsbl.2019.0657
- Maccracken, S. A., Sohn, J.-C., Miller, I. M., & Labandeira, C. C. (2021). A new Late Cretaceous leaf mine *Leucopterosa spiralae* gen. et sp. nov. (Lepidoptera: Lyonetiidae) represents the first confirmed fossil evidence of the Cemiostominae. *Journal of Systematic Paleontology*, *19*(2), 131-144. doi.org/10.1080/14772019.2021.1881177
- Maccracken, S. A., Miller, I. M., Johnson, K. R., Sertich, J. M., & Labandeira, C. C. (2022). Insect herbivory on *Catula gettyi* gen. et sp. nov. (Lauraceae) from the Kaiparowits Formation (Late Cretaceous, Utah, USA). *PloS One*, *17*(1), e0261397. doi.org/10.1371/journal.pone.0261397
- MacDonald, M., Currie, P. J., & Spencer, W. A. (2005). Precise mapping of fossil sites in the Park using survey grade GPS technology. In P. J. Currie & E. B. Koppelhus (Eds.), *Dinosaur Provincial Park: A Spectacular Ancient Ecosystem Revealed* (p. 478-485). Indiana University Press.
- Maidment, S. C. R., Dean, C. D., Mansergh, R. I., & Butler, R. J. (2021). Deep-time biodiversity patterns and the dinosaurian fossil record of the Late Cretaceous Western Interior, North America. *Proceedings of the Royal Society. B, Biological Sciences*, *288*(1953), 20210692. doi.org/10.1098/rspb.2021.0692
- Mallon, J. C., Evans, D. C., Ryan, M. J., & Anderson, J. S. (2012). Megaherbivorous dinosaur turnover in the Dinosaur Park Formation (upper Campanian) of Alberta, Canada. *Palaeogeography, Palaeoclimatology, Palaeoecology*, *350-352*, 124-138. doi.org/10.1016/j.palaeo.2012.06.024
- Mallon, J. C., Ott, C. J., Larson, P. L., Iuliano, E. M., & Evans, D. C. (2016). *Spiclypeus shipporum* gen. et sp. nov., a boldly audacious new chasmosaurine ceratopsid (Dinosauria: Ornithischia) from the Judith River Formation (Upper Cretaceous: Campanian) of Montana, USA. *PLoS ONE*, *11*, e0154218. doi.org/10.1371/journal.pone.0154218
- Martinez-Ardila, A. M., Paterson, S. R., Memeti, V., Parada, M. A., & Molina, P. G. (2019). Mantle driven Cretaceous flare-ups in Cordilleran arcs. *Lithos*, *326-327*, 19-27. doi.org/10.1016/j.lithos.2018.12.007
- Mattinson, J. M. (2005). Zircon U-Pb chemical abrasion ("CA-TIMS") method: Combined annealing and multi-step partial dissolution analysis for improved precision and accuracy of zircon ages. *Chemical Geology*, *220*(1-2), 47-66. doi.org/10.1016/j.chemgeo.2005.03.011
- McDonald, A. T. & Wolfe, D. G. (2018). A new nodosaurid ankylosaur (Dinosauria: Thyreophora) from the Upper Cretaceous Menefee Formation of New Mexico. *PeerJ*, *6*, e5435. doi.org/10.7717/peerj.5435
- McDonald, A. T., Wolfe, D. G., & Dooley, A. C. (2018). A new tyrannosaurid (Dinosauria: Theropoda) from the Upper Cretaceous Menefee Formation of New Mexico. *PeerJ*, *6*, e5749. doi.org/10.7717/peerj.5749

## References

---

- McDonald, A. T., Wolfe, D. G., Freedman-Fowler, E. A., & Gates, T. A. (2021). A new brachylophosaurin (Dinosauria: Hadrosauridae) from the Upper Cretaceous Menefee Formation of New Mexico. *PeerJ*, 9, e11084. doi.org/10.7717/peerj.11084
- McLean, J. R. (1977). Lithostratigraphic nomenclature of the Upper Cretaceous Judith River Formation in southern Alberta; philosophy and practice. *Bulletin of Canadian Petroleum Geology*, 25(6), 1105-1114.
- McLean, N. M., Bowring, J. F., & Bowring, S. A. (2011). An algorithm for U-Pb isotope dilution data reduction and uncertainty propagation. *Geochemistry Geophysics Geosystems*, 12(6). doi.org/10.1029/2010GC003478
- McLean, N. M., Condon, D. J., Schoene, B., & Bowring, S. A. (2015). Evaluating uncertainties in the calibration of isotopic reference materials and multi-element isotopic tracers (EARTHTIME Tracer Calibration Part II). *Geochimica et Cosmochimica Acta*, 164, 481-501. doi.org/10.1016/j.gca.2015.02.040
- Miall, A. D., Catuneanu, O., Vakarelov, B. K., & Post, R. (2008). Chapter 9 The Western Interior Basin. In A. D. Miall (Ed.), *Basins of the World: Volume 5* (p. 329-362). Elsevier. 329-362. doi.org/10.1016/S1874-5997(08)00009-9
- Miller, I. M., Johnson, K. R., Kline, D. E., Nichols, D. J., & Barclay, R. S. (2013). A late Campanian flora from the Kaiparowits Formation, southern Utah, and a brief overview of the widely sampled but little-known Campanian vegetation of the Western Interior of North America. In A. Titus & M. Loewen (Eds.), *At the top of the grand staircase: The Late Cretaceous of southern Utah* (p. 107-131). Indiana University Press.
- Molenaar, C. M. & Rice, D. D. (1988). Cretaceous rocks of the Western Interior Basin. In L. L. Sloss (Ed.), *Sedimentary Cover – North American Craton. Geological Society of America D-2*. doi.org/10.1130/DNAG-GNA-D2.77
- Morgan, G. B. & London, D. (1996). Optimizing the electron microprobe analysis of hydrous alkali aluminosilicate glasses. *The American Mineralogist*, 81(9-10), 1176-1185. doi.org/10.2138/am-1996-9-1016
- Nairn, I. A., Shane, P. R., Cole, J. W., Leonard, G. J., Self, S., & Pearson, N. (2004). Rhyolite magma processes of the ~AD 1315 Kaharoa eruption episode, Tarawera volcano, New Zealand. *Journal of Volcanology and Geothermal Research*, 131(3), 265-294. doi.org/10.1016/S0377-0273(03)00381-0
- Newhall, C. G. & Self, S. (1982). The volcanic explosivity index (VEI) an estimate of explosive magnitude for historical volcanism. *Journal of Geophysical Research*, 87(C2), 1231-1238. doi.org/10.1029/JC087iC02p01231
- Nydam, R. L. (2013). Lizards and snakes from the Cenomanian through Campanian of southern Utah: Filling the gap in the fossil record of Squamata from the Late Cretaceous of the Western Interior of North America. In A. Titus & M. Loewen (Eds.), *At the top of the grand staircase: The Late Cretaceous of southern Utah* (p. 370-423). Indiana University Press.

## References

---

- Ogg, J. G. (2012). Geomagnetic polarity time scale. In F. M. Gradstein, J. G. Ogg, M. D. Schmitz, & G. M. Ogg (Eds.), *The Geologic Time Scale 2012: Volume 2* (p. 85-113). Elsevier BV.
- Oriel, S. S., Gabrielse, H., Hay, W. W., Kottlowski, F. E., & Patton, J. B. (2005). North American Stratigraphic Code: North American Commission on Stratigraphic Nomenclature. *AAPG Bulletin*, *89*(11), 1547-1591. doi.org/10.1306/07050504129
- Parnell, A. C., Haslett, J., Allen, J. R. M., Buck, C. E., & Huntley, B. (2008). A flexible approach to assessing synchronicity of past events using Bayesian reconstructions of sedimentation history. *Quaternary Science Reviews*, *27*(19-20), 1872-1885. doi.org/10.1016/j.quascirev.2008.07.009
- Parnell, A. C., Buck, C. E., & Doan, T. K. (2011). A review of statistical chronology models for high-resolution, proxy-based Holocene palaeoenvironmental reconstruction. *Quaternary Science Reviews*, *30*(21-22), 2948-2960. doi.org/10.1016/j.quascirev.2011.07.024
- Parrish, R. R., & Noble, S. R. (2003). Zircon U-Th-Pb geochronology by isotope dilution; thermal ionization mass spectrometry (ID-TIMS). *Reviews in Mineralogy and Geochemistry*, *53*(1), 183-213. doi.org/10.2113/0530183
- Patchett, P. J. & Tatsumoto, M. (1981). A routine high-precision method for Lu-Hf isotope geochemistry and chronology. *Contributions to Mineralogy and Petrology*, *75*(3), 263-267. doi.org/10.1007/BF01166766
- Paterson, S. R. & Ducea, M. N. (2015). Arc magmatic tempos; gathering the evidence. *Elements*, *11*(2), 91-98. doi.org/10.2113/gselements.11.2.91
- Payenberg, T. H. D., Braman, D. R., Davis, D. W., & Miall, A. D. (2002). Litho- and chronostratigraphic relationships of the Santonian-Campanian Milk River Formation in southern Alberta and Eagle Formation in Montana utilising stratigraphy, U-Pb geochronology, and palynology. *Canadian Journal of Earth Sciences*, *39*(10), 1553-1577. doi.org/10.1139/E02-050
- Pecha, M. E., Gehrels, G. E., Karlstrom, K. E., Dickinson, W. R., Donahue, M. S., Gonzales, D. A., & Blum, M. D. (2018). Provenance of Cretaceous through Eocene strata of the Four Corners region: Insights from detrital zircons in the San Juan Basin, New Mexico and Colorado. *Geosphere*, *14*(2), 785-811. doi.org/10.1130/GES01485.1
- Peterson, F. & Waldrop, H. A. (1965). Jurassic and Cretaceous stratigraphy of south-central Kaiparowits Plateau, Utah. In H. D. Goode & R. A. Robison (Eds.), *Geology and resources of south-central Utah: Utah Geological Society and Intermountain Association of Petroleum Geologists Guidebook to the Geology of Utah 19* (p. 47-69). Utah Geological Association.
- Peterson, F. (1969). Cretaceous sedimentation and tectonism in the southeastern Kaiparowits region, Utah. *U.S. Geological Survey Open-file report 69-202*. doi.org/10.3133/ofr69202
- Phillips, D., Matchan, E. L., Dalton, H., & Kuiper, K. F. (2022). Revised astronomically calibrated  $^{40}\text{Ar}/^{39}\text{Ar}$  ages for the Fish Canyon Tuff sanidine – Closing the interlaboratory gap. *Chemical Geology*, *597*, 120815. doi.org/10.1016/j.chemgeo.2022.120815



## References

---

- Pollock, S. L. (1999). Provenance, geometry, lithofacies, and age of the Upper Cretaceous Wahweap Formation, Cordilleran foreland basin, southern Utah. Unpublished MSc Thesis (111 p.). New Mexico State University.
- Prieto-Márquez, A., Wagner, J. R., & Lehman, T. (2019). An unusual 'shovel-billed' dinosaur with trophic specializations from the early Campanian of Trans-Pecos Texas, and the ancestral hadrosaurian crest. *Journal of Systematic Paleontology*, 18(6), 461-498. doi.org/10.1080/14772019.2019.1625078
- Pupin, J. P. (1980). Zircon and granite petrology. *Contributions to Mineralogy and Petrology*, 73(3), 207-220. doi.org/10.1007/BF00381441
- Ramezani, J., Hoke, G. D., Fastovsky, D. E., Bowring, S. A., Therrien, F., Dworkin, S. I., Atchley, S. C., & Nordt, L. C. (2011). High-precision U-Pb zircon geochronology of the Late Triassic Chinle Formation, Petrified Forest National Park (Arizona, USA): Temporal constraints on the early evolution of dinosaurs. *GSA Bulletin*, 123(11-12), 2142-2159. doi.org/10.1130/B30433.1
- Rasmussen, C., Mundil, R., Irmis, R. B., Giesler, D., Gehrels, G. E., Olsen, P. E., Kent, D. V., Lepre, C., Kinney, S. T., Geissman, J. W., & Parker, W. G. (2021). U-Pb zircon geochronology and depositional age models for the Upper Triassic Chinle Formation (Petrified Forest National Park, Arizona, USA): Implications for Late Triassic palaeoecological and palaeoenvironmental change. *Geological Society of America Bulletin*, 133(3-4), 539-558. doi.org/10.1130/B35485.1
- Renne, P. R., Swisher, C. C., Deino, A. L., Karner, D. B., Owens, T. L., & DePaolo, D. J. (1998). Intercalibration of standards, absolute ages and uncertainties in  $^{40}\text{Ar}/^{39}\text{Ar}$  dating. *Chemical Geology*, 145(1-2), 117-152. doi.org/10.1016/S0009-2541(97)00159-9
- Rivera-Sylva, H. E., Hedrick, B. P., & Dodson, P. (2016). A centrosaurine (Dinosauria, Ceratopsia) from the Aguja Formation (late Campanian) of northern Coahuila, Mexico. *PLoS ONE*, 11(4), e0150529. doi.org/10.1371/journal.pone.0150529
- Roberts, L. N. R. & Kirschbaum, M. A. (1995). Palaeogeography of the Late Cretaceous of the Western Interior of middle North America – Coal distribution and sediment accumulation. *U.S. Geological Survey Professional Paper 1561*, 116 p. doi.org/10.3133/pp1561
- Roberts, E. M. & Hendrix, M. S. (2000). Taphonomy of a petrified forest in the Two Medicine Formation (Campanian), Northwest Montana; implications for palinspastic restoration of the Boulder Batholith and Elkhorn Mountains volcanics. *Palaios*, 15(5), 476-482. doi.org/10.2307/3515516
- Roberts, E. M., Deino, A. L., & Chan, M. A. (2005).  $^{40}\text{Ar}/^{39}\text{Ar}$  age of the Kaiparowits Formation, southern Utah, and correlation of contemporaneous Campanian strata and vertebrate faunas along the margin of the Western Interior Basin. *Cretaceous Research*, 26(2), 307-318. doi.org/10.1016/j.cretres.2005.01.002
- Roberts, E. M., & Tapanila, L. (2006). A new social insect nest from the Upper Cretaceous Kaiparowits Formation of southern Utah. *Journal of Paleontology*, 80(4), 768-774. doi.org/10.1666/0022-3360(2006)80[768:ANSINF]2.0.CO;2

## References

---

- Roberts, E. M. (2007). Facies architecture and depositional environments of the Upper Cretaceous Kaiparowits Formation, southern Utah. *Sedimentary Geology*, 197(3-4), 207-233. doi.org/10.1016/j.sedgeo.2006.10.001
- Roberts, E. M., Tapanila, L., & Mijal, B. (2008). Taphonomy and sedimentology of storm-generated continental shell beds: A case example from the Cretaceous Western Interior Basin. *The Journal of Geology*, 116(5), 462-479. doi.org/10.1086/590134
- Roberts, E. M. & Chan, M. A. (2010). Variation in iron oxide, iron sulphide, and carbonate concretions and their distributions in fluvio-deltaic and nearshore sandstones: Cretaceous examples from the Kaiparowits Plateau, Utah and San Juan Basin, New Mexico. In S. Carney, D. Tabet & C. Johnson (Eds.), *Geology of South-Central Utah* (p. 151-177). Utah Geological Association Publication 39.
- Roberts, E. M., Sampson, S. D., Deino, A. L., Bowring, S. A., & Buchwaldt, R. (2013). The Kaiparowits Formation: A remarkable record of Late Cretaceous terrestrial environments, ecosystems, and evolution in western North America. In A. Titus & M. Loewen (Eds.), *At the top of the grand staircase: The Late Cretaceous of southern Utah* (p. 85-106). Indiana University Press.
- Roček, Z., Gardner, J. D., Eaton, J. G., & Příkryl, T. (2013). Anuran ilia from the Upper Cretaceous of Utah – Diversity and stratigraphic patterns. In A. Titus & M. Loewen (Eds.), *At the top of the grand staircase: The Late Cretaceous of southern Utah* (p. 273-294). Indiana University Press.
- Rogers, R. R. (1990). Taphonomy of three dinosaur bone beds in the Upper Cretaceous Two Medicine Formation of northwestern Montana; evidence for drought-related mortality. *Palaios*, 5(5), 394-413. doi.org/10.2307/3514834
- Rogers, R. R., Swisher, C. C., & Horner, J. R. (1993).  $^{40}\text{Ar}/^{39}\text{Ar}$  age and correlation of the nonmarine Two Medicine Formation (Upper Cretaceous), northwestern Montana, U.S.A. *Canadian Journal of Earth Sciences*, 30(5), 1066-1075. doi.org/10.1139/e93-090
- Rogers, R. R. (1998). Sequence analysis of the Upper Cretaceous Two Medicine and Judith River formations, Montana; nonmarine response to the Claggett and Bearpaw marine cycles. *Journal of Sedimentary Research*, 68(4), 615-631. doi.org/10.2110/jsr.68.604
- Rogers, R. R., Kidwell, S. M., Deino, A. L., Mitchell, J. P., Nelson, K., & Thole, J. T. (2016). Age, correlation, and lithostratigraphic revision of the Upper Cretaceous (Campanian) Judith River Formation in its type area (north-central Montana), with a comparison of low- and high-accommodation alluvial records. *The Journal of Geology*, 124(1), 99-135. doi.org/10.1086/684289
- Rowe, T. Cifelli, R. L., Lehman, T. M., & Weil, A. (1992). The Campanian Terlingua local fauna, with a summary of other vertebrates from the Aguja Formation, Trans-Pecos Texas. *Journal of Vertebrate Paleontology*, 12(4), 472-493. doi.org/10.1080/02724634.1992.10011475
- Russell, D. A. (1967). A census of dinosaur specimens collected in western Canada. *National Museum of Canada Natural History Papers* 36, 1-13.

## References

---

- Russell, D. A. (1969). A new specimen of *Stenonychosaurus* from the Oldman Formation (Cretaceous) of Alberta. *Canadian Journal of Earth Sciences*, 6(4), 595-612. doi.org/10.1139/e69-059
- Sahni, A. (1972). The vertebrate fauna of the Judith River Formation, Montana. *Bulletin of the American Museum of Natural History*, 147(6), 323-412.
- Samson, S. D., Matthews, S., Mitchell, C. E., & Goldman, D. (1995). Tephrochronology of highly altered ash beds; the use of trace element and strontium isotope geochemistry of apatite phenocrysts to correlate K-bentonites. *Geochimica et Cosmochimica Acta*, 59(12), 2527-2536. doi.org/10.1016/0016-7037(95)00147-6
- Sampson, S. D., Loewen, M. A., Farke, A. A., Roberts, E. M., Forster, C. A., Smith, J. A., & Titus, A. L. (2010). New horned dinosaurs from Utah provide evidence for intracontinental dinosaur endemism. *PLoS ONE*, 5(9), e12292. doi.org/10.1371/journal.pone.0012292
- Sampson, S. D., Lund, E. K., Loewen, M. A., Farke, A. A., & Clayton, K. E. (2013a). A remarkable short-snouted horned dinosaur from the Late Cretaceous (late Campanian) of southern Laramidia. *Proceedings of the Royal Society. B, Biological Sciences*, 280(1766), 20131186. doi.org/10.1098/rspb.2013.1186
- Sampson, S. D., Loewen, M. A., Roberts, E. M., & Getty, M. A. (2013b). A new macrovertebrate assemblage from the Late Cretaceous (Campanian) of southern Utah. In A. Titus & M. Loewen (Eds.), *At the top of the grand staircase: The Late Cretaceous of southern Utah* (p. 599-622). Indiana University Press.
- Sankey, J. T. (2001). Late Campanian southern dinosaurs, Aguja Formation, Big Bend, Texas. *Journal of Paleontology*, 75(1), 208-215. doi.org/10.1017/S0022336000031991
- Schärer. (1984). The effect of initial <sup>230</sup>Th disequilibrium on young U Pb ages: the Makalu case, Himalaya. *Earth and Planetary Science Letters*, 67(2), 191-204. doi.org/10.1016/0012-821X(84)90114-6
- Schindlbeck, J. C., Jegen, M., Freundt, A., Kutterolf, S., Straub, S. M., Mleneck-Vautravers, M. J., & McManus, J. F. (2018). 100-kyr cyclicity in volcanic ash emplacement; evidence from a 1.1 Myr tephra record from the NW Pacific. *Scientific Reports*, 8, 4440. doi.org/10.1038/s41598-018-22595-0
- Schmitt, J. G., Jones, D. A., & Goldstrand, P. M. (1991). Braided stream deposition and provenance of the Upper Cretaceous-Palaeocene Canaan Peak Formation, Sevier foreland basin, southwestern Utah. In J. Nations & J. Eaton (Eds.), *Stratigraphy, depositional environments, and sedimentary tectonics of the western margin, Cretaceous Western Interior Seaway* (p. 27-45). Geological Society of America Special Paper 260.
- Schmitz, M. D., & Bowring, S. A. (2001). U-Pb zircon and titanite systematics of the Fish Canyon Tuff; an assessment of high-precision U-Pb geochronology and its application to young volcanic rocks. *Geochimica et Cosmochimica Acta*, 65(15), 2571-2587. doi.org/10.1016/S0016-7037(01)00616-0
- Schoene, B., Crowley, J. L., Condon, D. J., Schmitz, M. D., & Bowring, S. A. (2006). Reassessing the uranium decay constants for geochronology using ID-TIMS U/Pb data. *Geochimica et Cosmochimica Acta*, 70(2), 426-445. doi.org/10.1016/j.gca.2005.09.007

## References

---

- Sewall, J. O. & Fricke, H. C. (2013). Andean-scale highlands in the Late Cretaceous Cordillera of the North American western margin. *Earth and Planetary Science Letters*, 362, 88-98. doi.org/10.1016/j.epsl.2012.12.002
- Seymour, D. L. & Fielding, C. R. (2013). High resolution correlation of the Upper Cretaceous stratigraphy between the Book Cliffs and the western Henry Mountains Syncline, Utah, U.S.A. *Journal of Sedimentary Research*, 83(6), 475-494. doi.org/10.2110/jsr.2013.37
- Shanley, K. W. & McCabe, P. J. (1995). Sequence Stratigraphy of Turonian-Santonian Strata, Kaiparowits Plateau, Southern Utah, U.S.A.: Implications for Regional Correlation and Foreland Basin Evolution. In J.C. Van Wagoner & G.T. Bertram (Eds.), *Sequence Stratigraphy of Foreland Basin Deposits: Outcrop and Subsurface Examples from the Cretaceous of North America* (p.103-136). American Association of Petroleum Geologists. doi.org/10.1306/M64594C6
- Simpson, E. L., Hilbert-Wolf, H. L., Simpson, W. S., Tindall, S. E., Bernard, J. J., Jenesky, T. A., & Wizevich, M. C. (2008). The interaction of aeolian and fluvial processes during deposition of the Upper Cretaceous capping sandstone member, Wahweap Formation, Kaiparowits Basin, Utah, U.S.A. *Palaeogeography, Palaeoclimatology, Palaeoecology*, 270, 19-28. doi.org/10.1016/j.palaeo.2008.08.009
- Simpson, E. L., Koch, R., Heness, E. A., Wizevich, M. C., Tindall, S. E., Hilbert-Wolf, H. L., Golder, K., & Steullet, A. K. (2014). Sedimentology and paleontology of the Upper Cretaceous Wahweap Formation sag ponds adjacent to syndepositional normal faults, Grand Staircase-Escalante National Monument, Utah. *Cretaceous Research*, 50, 332-343. doi.org/10.1016/j.cretres.2014.05.001
- Sloan, R. E. (1969). Cretaceous and Palaeocene terrestrial communities of western North America. *North American Paleontological Convention, Chicago (Proc. E)*, 427-453.
- Sloan, R. E. (1976). The ecology of dinosaur extinction. In C. S. Churcher (Ed.), *Essays on Paleontology in Honour of Loris Shano Russell* (p. 134-155). University of Toronto Press.
- Sobolev, A. V. (1996). Melt inclusions in minerals as a source of principle petrological information. *Petrology*, 4(3), 209-220.
- Söderlund, U., Patchett, P. J., Vervoort, J. D., & Isachsen, C. E. (2004). The  $^{176}\text{Lu}$  decay constant determined by Lu–Hf and U–Pb isotope systematics of Precambrian mafic intrusions. *Earth and Planetary Science Letters*, 219(3-4), 311-324. doi.org/10.1016/S0012-821X(04)00012-3
- Spandler, C. J., Eggins, S. M., Arculus, R. J., & Mavrogenes, J. A. (2000). Using melt inclusions to determine parent-magma compositions of layered intrusions; application to the Greenhills Complex (New Zealand), a platinum group minerals-bearing, island-arc intrusion. *Geology*, 28(11), 991-994. doi.org/10.1130/0091-7613(2000)28<991:UMITDP>2.0.CO;2
- Stanton, T. W. & Hatcher, J. B. (1905). Geology and paleontology of the Judith River beds. United States *Geological Survey Bulletin* 257, 1-128.

## References

---

- Sullivan, R. M. & Lucas, S. G. (2003). The Kirtlandian, a new land-vertebrate “age” for the Late Cretaceous of Western North America. In S. G. Lucas, S. C. Semken, W. Berglof, & D. Ulmer-Scholle (Eds.), *Geology of the Zuni Plateau: New Mexico Geological Society 54th Annual Fall Field Conference Guidebook* (p. 369-377). New Mexico Geological Society.
- Sullivan, R. M. & Lucas, S. G. (2006). The Kirtlandian Land-Vertebrate “Age” – faunal composition, temporal position and biostratigraphic correlation in the nonmarine Upper Cretaceous of Western North America. In S. G. Lucas & R. M. Sullivan (Eds.), *Late Cretaceous vertebrates from the Western Interior: New Mexico Museum of Natural History and Science Bulletin 35* (p. 7-29). New Mexico Museum of Natural History and Science.
- Szwarc, T. S., Johnson, C. L., Stright, L. E., & McFarlane, C. M. (2015). Interactions between axial and transverse drainage systems in the Late Cretaceous Cordilleran foreland basin: Evidence from detrital zircons in the Straight Cliffs Formation, southern Utah, USA. *Geological Society of America Bulletin*, 127(3/4), 372-392. doi.org/10.1130/B31039.1
- Tapanila, L. & Roberts, E. M. (2013). Continental invertebrates and trace fossils from the Campanian Kaiparowits Formation, Utah. In A. Titus & M. Loewen (Eds.), *At the top of the grand staircase: The Late Cretaceous of southern Utah* (p. 132-152). Indiana University Press.
- Thomas, R. G., Eberth, D. A., Deino, A. L., & Robinson, D. (1990). Composition, radioisotopic ages, and potential significance of an altered volcanic ash (bentonite) from the Upper Cretaceous Judith River Formation, Dinosaur Provincial Park, southern Alberta, Canada. *Cretaceous Research*, 11(2), 125-162. doi.org/10.1016/S0195-6671(05)80030-8
- Thomas, J. B., Bodnar, R. J., Shimizu, N., & Chesner, C. A. (2003). Melt inclusions in zircon. *Reviews in Mineralogy and Geochemistry*, 53(1), 63-87. doi.org/10.2113/0530063
- Tilton, G. R., Brown, H. S., Hayden, R. J., Hess, D. C., Larsen, E. S., & Patterson, C. C. (1955). Isotopic composition and distribution of lead, uranium, and thorium in a Precambrian granite. *Bulletin of the Geological Society of America*, 66(9), 1131-1148. doi.org/10.1130/0016-7606(1955)66[1131:ICADOL]2.0.CO;2
- Tindall, S. E., Storm, L. P., Jenesky, T. A., & Simpson, E. L. (2010). Growth faults in the Kaiparowits Basin, Utah, pinpoint initial Laramide deformation in the western Colorado Plateau. *Lithosphere*, 2(4), 221-231. doi.org/10.1130/L79.1
- Titus, A. L., Powell, J. D., Roberts, E. M., Sampson, S. D., Pollock, S. L., Kirkland, J. I., & Albright, L. B. (2005). Late Cretaceous stratigraphy, depositional environments, and macrovertebrate paleontology of the Kaiparowits Plateau, Grand Staircase - Escalante National Monument, Utah. In J. Pederson & C. M. Dehler (Eds.), *Interior Western United States; Geological Society of America Field Guide 6* (p. 101-128). Geological Society of America. doi.org/10.1130/2005.fld006(05)
- Titus, A. L. & Loewen, M. A. (2013). *At the top of the grand staircase: The Late Cretaceous of southern Utah*. Indiana University Press, 634 p.



## References

---

- Titus, A. L., Roberts, E. M., & Albright, L. B. (2013). Geologic Overview. In A. Titus & M. Loewen (Eds.), *At the top of the grand staircase: The Late Cretaceous of southern Utah* (p. 13-41). Indiana University Press.
- Titus, A. L., Eaton, J. G., & Sertich, J. (2016). Late Cretaceous stratigraphy and vertebrate faunas of the Markagunt, Paunsaugunt, and Kaiparowits plateaus, southern Utah. *Geology of the Intermountain West*, 3, 229-291. doi.org/10.31711/giw.v3.pp229-291
- Titus, A. L., Knoll, K., Sertich, J. J. W., Yamamura, D., Suarez, C. A., Glasspool, I. J., Ginouves, J. E., Lukacic, A. K., & Roberts, E. M. (2021). Geology and taphonomy of a unique tyrannosaurid bonebed from the upper Campanian Kaiparowits Formation of southern Utah: implications for tyrannosaurid gregariousness. *PeerJ*, 9, e11013. doi.org/10.7717/peerj.11013
- Todd, C. N., Roberts, E. M., Knutsen, E. M., Rozefelds, A. C., Huang, H., & Spandler, C. (2019). Refined age and geological context of two of Australia's most important Jurassic vertebrate taxa (*Rhoetosaurus brownei* and *Siderops kehli*), Queensland. *Gondwana Research*, 76, 19-25. doi.org/10.1016/j.gr.2019.05.008
- Trayler, R. B., Schmitz, M. D., Cuitiño, J. I., Kohn, M. J., Bargo, M. S., Kay, R. F., Strömberg, C. A. E., & Vizcaíno, S. F. (2020). An improved approach to age-modeling in deep time: Implication for the Santa Cruz Formation, Argentina. *GSA Bulletin*, 132(1/2), 233-244. doi.org/10.1130/B35203.1
- Trexler, D. (2001). Two Medicine Formation, Montana: Geology and fauna. In D. H. Tanke & K. Carpenter (Eds.), *Mesozoic vertebrate life* (p. 298-309). Indiana University Press.
- Tucker, R.T., Roberts, E. M., Henderson, R. A., & Kemp, A. I. S. (2016). Large igneous province or long-lived magmatic arc along the eastern margin of Australia during the Cretaceous? Insights from the sedimentary record. *Geological Society of America Bulletin*, 128(9-10), 1461-1480. doi.org/10.1130/B31337.1
- van der Reest, A. J. & Currie, P. J. (2017). Troodontids (Theropoda) from the Dinosaur Park Formation, Alberta, with a description of a unique new taxon; implications for deinonychosaur diversity in North America. *Canadian Journal of Earth Sciences*, 54(9), 919-935. doi.org/10.1139/cjes-2017-0031
- van Wagoner, J. C. & Bertram, G. T. (1995). Sequence stratigraphy of foreland basin deposits: Outcrop and subsurface examples from the Cretaceous of North America. *American Associate of Petroleum Geologists Memoir*, 64, 490 p. doi.org/10.1306/M64594
- Vavra, G. (1990). On the kinematics of zircon growth and its petrogenetic significance; a cathodoluminescence study. *Contributions to Mineralogy and Petrology*, 106(1), 90-99. doi.org/10.1007/BF00306410
- Vavrek, M. J. & Larsson, H. C. E. (2010). Low beta diversity of Maastrichtian dinosaurs of North America. *Proceedings of the National Academy of Sciences*, 107(18), 8265-8268. doi.org/10.1073/pnas.0913645107
- von Quadt, A., Gallhofer, D., Guillong, M., Peytcheva, I., Waelle, M., & Sakata, S. (2014). U-Pb dating of CA/non-CA treated zircons obtained by LA-ICP-MS and CA-TIMS techniques: Impact for their geological interpretation. *Journal of Analytical Atomic Spectrometry*, 29, 1618-1629. doi.org/10.1039/C4JA00102H

## References

---

- Voris, J. T., Therrien, F., Zelenitsky, D. K., & Brown, C. M. (2020). A new tyrannosaurine (Theropoda:Tyrannosauridae) from the Campanian Foremost Formation of Alberta, Canada, provides insight into the evolution and biogeography of tyrannosaurids. *Cretaceous Research*, *110*, 104388. doi.org/10.1016/j.cretres.2020.104388
- Wernicke, B. (2011). The California River and its role in carving Grand Canyon. *Geological Society of America Bulletin*, *123*(7-8), 1288-1316. doi.org/10.1130/B30274.1
- Wiersma, J. P. & Loewen, M. A. (2013). Taphonomy of a Subadult *Teratophoneus curriei* (Tyrannosauridae) from the Upper Campanian Kaiparowits Formation of Utah. In A. Titus & M. Loewen (Eds.), *At the top of the grand staircase: The Late Cretaceous of southern Utah* (p. 588-598). Indiana University Press.
- Wiersma, J. P. & Irmis, R. B. (2018). A new southern Laramidian ankylosaurid, *Akainacephalus johnsoni* gen. et sp. nov., from the upper Campanian Kaiparowits Formation of southern Utah, USA. *PeerJ*, *6*, e5016. doi.org/10.7717/peerj.5016
- Williamson, T. E. & Brusatte, S. L. (2014). Small theropod teeth from the Late Cretaceous of the San Juan Basin, northwestern New Mexico and their implications for understanding latest Cretaceous dinosaur evolution. *PloS One*, *9*(4), e93190. doi.org/10.1371/journal.pone.0093190
- Wilson, J. P., Ryan, M. J., & Evans, D. C. (2020). A new, transitional centrosaurine ceratopsid from the Upper Cretaceous Two Medicine Formation of Montana and the evolution of the “Styracosaurus-line” dinosaurs. *Royal Society Open Science*, *7*(4), 200284. doi.org/10.1098/rsos.200284
- Yamamura, D., Suarez, C. A., Titus, A. L., Manlove, H. M., & Jackson, T. (2021). Multiproxy approaches to investigating palaeoecology and palaeohydrology in the Upper Cretaceous Kaiparowits Formation, USA. *Geological Society Special Publication*, *507*(1), 293-311. doi.org/10.1144/SP507-2020-52
- Zanno, L. E. & Sampson, S. D. (2005). A new Oviraptorosaur (Theropoda, Maniraptora) from the Late Cretaceous (Campanian) of Utah. *Journal of Vertebrate Paleontology*, *25*(4), 897-904. doi.org/10.1671/0272-4634(2005)025[0897:ANOTMF]2.0.CO;2
- Zanno, L. E., Varricchio, D. J., O'Connor, P. M., Titus, A. L., & Knell, M. J. (2011). A new troodontid theropod, *Talos sampsoni* gen. et sp. nov., from the Upper Cretaceous Western Interior Basin of North America. *PloS One*, *6*(9), e24487. doi.org/10.1371/journal.pone.0024487
- Zanno, L. E., Loewen, M. A., Farke, A. A., Kim, G. S., Claessens, L. P. A. M., & McGarrity, C. T. (2013). Late Cretaceous theropod dinosaurs of southern Utah. In A. Titus & M. Loewen (Eds.), *At the top of the grand staircase: The Late Cretaceous of southern Utah* (p. 504-525). Indiana University Press.



# Appendix A

## Collaborative Works

**Conference Abstract – Poster Presentation**

*Society of Vertebrate Paleontology 77th Annual Meeting, Calgary 2017*

A new approach to correlating vertebrate faunas by combining high precision U-Pb geochronology with geochemical tephrostratigraphy: A case example from the Campanian Western Interior Basin.

Beveridge, T.L., Roberts, E.M., Ramezani, J., Eberth, D., Rogers, R.R., & Bowring, S.

Over the last decade, advances in high-precision U-Pb zircon geochronology of terrestrial rocks have led to unprecedented opportunities for resolving the temporal context of vertebrate fossil records. The Late Cretaceous has frequently been referred to as the ‘zenith’ of dinosaur evolution, and few continental settings are better suited for applying these new geochronological approaches as the Upper Cretaceous Western Interior Basin of North America. Our team has focused on systematic dating of interbedded bentonites from three presumed correlative, fossil-rich and geographically distinct stratigraphic units (as far as 1500 km apart), namely the Dinosaur Park Formation in Alberta, the Judith River-Two Medicine formations in Montana, and the Kaiparowits Formation in Utah. Preliminary U-Pb zircon dating by the CA-ID-TIMS method has been successful in identifying individual correlative bentonite marker beds with a precision of  $\pm 25$  kyr. However, geochemical fingerprinting of bentonites remains an invaluable correlation tool, if combined (and tested) by independent radioisotopic dating techniques. Here we present a complimentary new approach to tephrostratigraphy, which does not rely on traditional whole rock or mineral geochemistry of bentonites; it involves chemical and isotopic fingerprinting of minute, melt inclusions preserved as glass within the dated zircon populations. This approach combines trace element geochemistry and Hf-isotope analysis of the glass inclusions and host zircons, thus providing up to four discrete geochemical fingerprints for correlation purposes. Ten volcanic ash beds from the most vertebrate fossil-rich intervals of the Dinosaur Park, Two Medicine and Kaiparowits formations have been examined. Results exceed expectations and demonstrate that this approach can allow us to correlate single ash beds throughout and even between formations via fine-scale fingerprinting. In some cases, distant bentonites with practically identical U-Pb ages have yielded distinct chemical/isotopic fingerprints, which demonstrates for the first time that multiple volcanic systems were synchronously eruptive during the late Campanian. This approach has wide ranging application to other formations and basins, and promises to be a valuable and practical tool in evolutionary and ecological studies.





# A New Approach to Correlating Vertebrate Faunas by Combining High Precision U-Pb Geochronology with Geochemical Tephrostratigraphy: A Case Example from the Campanian Western Interior Basin

Beveridge, T.<sup>1</sup>, Roberts, E. M.<sup>1</sup>, Ramezani, J.<sup>2</sup>, Eberth, D. A.<sup>3</sup>, Rogers, R. R.<sup>4</sup> & Bowring, S. A.<sup>2</sup>

College of Science and Engineering, James Cook University, Townsville AUSTRALIA,<sup>1</sup> Department of Earth, Atmospheric and Planetary Science, Massachusetts Institute of Technology, Cambridge USA,<sup>2</sup> Royal Tyrrell Museum of Paleontology, Drumheller CANADA,<sup>3</sup> Department of Geology, Macalester College, St Paul USA

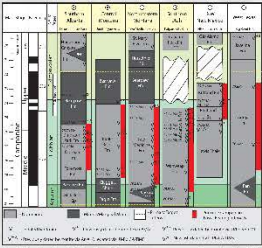


### Project Summary

Over the last decade, advances in high-precision U-Pb zircon geochronology of terrestrial rocks have led to unprecedented opportunities for resolving the temporal context of vertebrate faunal records. Few places offer as good an opportunity for this as the Late Cretaceous of Western North America, which has frequently been referred to as the 'crucible' of dinosaur evolution. Our team has focused on systematic dating of interbedded bentonites from three geographically discrete, fossil-rich and geographically distant stratigraphic units (as far as 1500 km), namely the Dinosaur Park Formation in Alberta, the Judith River Two Medicine Formations in Montana, and the Kaiparowits Formation in Utah (Fig. 1). The primary U-Pb zircon dating by the (CA-ID)-TIMS method has been successful in identifying individual correlative bentonite marker beds with a precision of ±25 kyr. However, geochemical fingerprinting of bentonites remains an invaluable correlation tool. If combined (and tested) by independent radioisotopic dating techniques. Here we present a complementary new approach to tephrostratigraphy, which does not rely on traditional whole rock or mineral geochemistry of bentonites; it involves chemical and isotopic fingerprinting of mica, zircon inclusions preserved as glass within the distal zircon populations (Fig. 2). This approach combines trace element geochemistry and HF-isotope analysis of the glass inclusions and host zircon, thus providing up to four discrete geochemical fingerprints for correlation purposes. Ten volcanic ash beds from the most vertebrate fossil-rich intervals of the Dinosaur Park, Two Medicine and Kaiparowits formations have been examined. Remarkable concordances and demonstrate that this approach can allow us to correlate single ash beds throughout and even between formations via fine-scale fingerprinting. In some cases, distal bentonites with practically identical U-Pb ages have yielded distinct geochemical fingerprints, which demonstrates for the first time that multiple volcanic systems were synchronously active during the late Campanian. This approach has wide ranging application to other formations and basins, and promises to be a valuable and practical tool in evolutionary and ecological studies.



Fig. 1. Three distal volcanic provinces across the Western Interior basin, Canada and the USA. The geographic relationship of the Campanian basin is shown.



**Geological Context**  
The Western Interior was a Mesozoic foreland basin that formed adjacent to the Sevier Orogen and had a complex history of tectono-sedimentary cycles, reaching maximum extension during the Albian to Campanian stages of the Late Cretaceous. Thick clastic sedimentary successions deposited along the western margin of the basin from Alberta to Mexico (Fig. 1 & 3) preserve a remarkably rich record of faunal and floral life that make the 'crucible' of dinosaur diversity. Absolute interbedded volcanic ash preserved in the form of bentonites provide the means for radioisotopic geochronology.



Fig. 3. Fossiliferous bentonite preserved in the Kaiparowits Formation, Utah, USA.

### Dinosaur Provincial Park, Alberta, Canada

The Campanian Red River Group of Alberta, Canada preserves one of the most diverse and best studied Cretaceous terrestrial fossil assemblages in the world and consists of, in ascending order, the predominantly terrestrial Foremost (FF), Oldman (OMF) and Dinosaur Park (DPP) Formations. It is overlain by the marine Bearpaw Formation (BPF). Seven stratigraphically discrete bentonite horizons have been documented encompassing the fossil-rich interval from the upper OMF to the lower BPF (Fig. 5), which have been the subject of our high-precision U-Pb geochronological study.

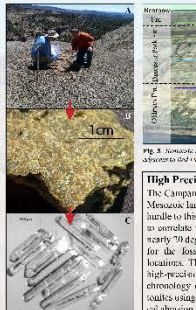


Fig. 5. Photomicrographs of bentonite horizons showing zircon inclusions. Scale bars are 100 micrometers.

### North-central Montana, USA

The fossil-rich Two Medicine (TMF) and Judith River (JR) Formations of Montana form an eastward thinning clastic wedge of alluvial, coastal plain, and shallow marine sands deposited during the Campanian (Fig. 9). More than a century of fossil collection from the TMF and JR has produced one of the best studied Cretaceous vertebrate assemblages in the world, including especially preserved dinosaur bones and mammal remains. Twenty bentonite horizons sampled from both units (5 analysed so far) span their entire stratigraphy.

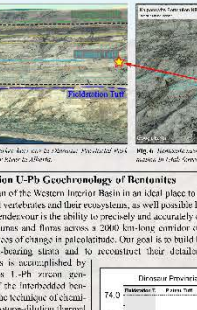


Fig. 9. Photomicrographs of bentonite horizons showing zircon inclusions. Scale bars are 100 micrometers.

### Kaiparowits Plateau, Southern Utah, USA

Accelerated investigations over the past 17 years in the area of the Grand Staircase-Escalante National Monument in Utah has revealed numerous new taxa of dinosaurs, other reptiles, invertebrates, and plant macrofossils from the Campanian Wahweap (WF) and Kaiparowits (KI) formations. The thick and predominantly fluvial, fluvio-deltaic and pond deposits of these formations (Fig. 4) contain in excess of 10 distinct bentonite horizons (Fig. 6), most of which have so far been successfully sampled and analysed.

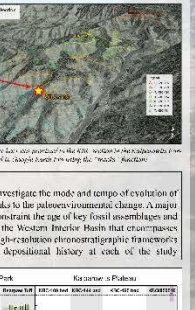


Fig. 6. High Precision U-Pb Geochronology of Bentonites plot showing age ranges for various formations.

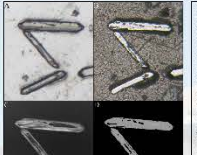


Fig. 10. Photomicrographs of bentonite horizons showing zircon inclusions. Scale bars are 100 micrometers.

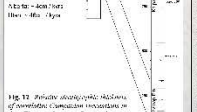


Fig. 11. Substance Ratio plot showing HF isotope ratios for various bentonite horizons.

### Long-distance Tephrostratigraphy

Our high-precision geochronology has identified individual bentonite layers that are separated by nearly 3000 km (e.g., Three Falls in Alberta and the KDC-109 bentonite in Utah; among others), but have yielded strikingly indistinguishable U-Pb ages within 25,000 years. It is possible that the two distal units originated from the same eruptive centre or possibly just the same eruptive cone? To address these questions we applied a multistep geochemical approach to characterize the tails using major element data from glass inclusions in zircon (Fig. 11A), as well as HF isotopic composition of the host zircon (Fig. 11B). The impermeousness of zircon to physical and chemical alteration makes it a suitable carrier of geochemical signatures. In addition, glass inclusions in zircon represent trapped melt at the time of crystallization. Unlike glass in the groundmass of volcanic rocks, melt inclusions encased in ancient zircon are protected from rapid devolatilization and compositional change. Major element compositions of glass inclusions are determined by electron microprobe analysis (EMPA-WDS), whereas HF isotopes are measured using a sensitive laser ablation inductively coupled plasma mass spectrometry (LA-ICP-MS). Our preliminary results indicate that the Phoenix Tuff (DPP) and KDC-109 bentonite (KP) formed out of geochemically distinct magmas and thus are likely to have originated from separate eruptive centres, implying potentially widespread syn-basaltic volcanism at this time. Continuing research will focus on correlating other bentonite horizons within and between formations in the basin.

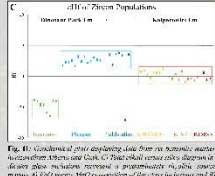
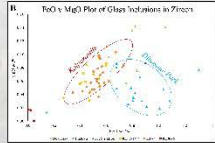
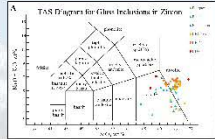


Fig. 12. TAS Diagram, TbO3 Mg# Plot, and Zircon U-Pb Zircon Populations plot showing major element compositions and HF isotope ratios for various bentonite horizons.

### Summary of Outcomes

- High-resolution chronostratigraphic frameworks are built for key Campanian fossil-rich successions across the Western Interior Basin of North America
- High-precision U-Pb geochronology (CA-ID)-TIMS method of interbedded bentonites allow correlation of individual beds to within 25 thousand years over a 1500 km geographic distance
- Refined depositional history of distant successions reveal highly variable sediment accumulation rates across the basin
- Chemical and isotopic fingerprinting of zircon and its glass inclusions from coeval ash beds across the basin point to simultaneous eruptions from geographically distinct volcanic centres

**Conference Abstract – Poster Presentation***Goldschmidt, Boston 2018*

High-resolution correlation and bentonite tephrochronology in the Campanian Western Interior Basin.

Beveridge, T.L., Roberts, E.M., & Ramezani, J.

The Late Cretaceous of the North American Western Interior Basin is world-renowned for preserving a rich fossil and paleoenvironmental history during the ‘zenith’ of dinosaur diversity. Along with abundant volcanic ash horizons throughout the basin, it is a perfect setting to exemplify the application of state-of-the-art U-Pb dating by chemical abrasion ID-TIMS method to the stratigraphic record. The key fossil-bearing units that are examined here comprise a variety of distinct Campanian terrestrial sedimentary units deposited along the basin’s western margin from Alberta to Utah. This study aims to broaden the reach and effectiveness of high-precision geochronology through refined stratigraphic correlations using a multifaceted geochemical approach to characterising bentonite marker horizons. Geochemical characterisation of volcanic material, a process called tephrostratigraphy, is often hampered in pre-Quaternary deposits due to chemical alteration during ash devitrification. Here we present major element characterisation of the Campanian bentonites through the novel use of glass (melt) inclusions that are encased within the same volcanic zircon crystals used for geochronology, and thus are protected from alteration. Several independent geochemical signatures are employed to support fingerprinting of bentonites including trace element composition and Lu-Hf isotopic systematics. Preliminary findings have shown promise in correlating bentonites within and even between formations. Selected bentonite horizons with statistically indistinguishable mean  $^{206}\text{Pb}/^{238}\text{U}$  ages that are spatially separated by >1000km have yielded geochemically distinct fingerprints, implying synchronously eruptive volcanic centres in the northern and southern parts of the basin during the late Campanian. This multifaceted approach will facilitate the construction of a high-resolution chronostratigraphic framework for the basin by relatively inexpensive and accessible means and is entirely transferable to other basins and time periods.



# High-Resolution Correlation and Bentonite Tephrochronology in the Campanian Western Interior Basin



BEVERIDGE, T. L.<sup>1\*</sup>, ROBERTS, E.<sup>1</sup>, RAMEZANI, J.<sup>2</sup>



<sup>1</sup>James Cook University, James Cook Drive, Townsville 4811 QLD Australia; <sup>2</sup>Massachusetts Institute of Technology, 77 Massachusetts Avenue, Cambridge 02139 MA USA

**Abstract:** The Late Cretaceous of the North American Western Interior Basin is world-renowned for preserving a rich fossil and paleoenvironmental history during the 'zenith' of dinosaur diversity. Along with abundant volcanic ash horizons throughout the basin, it is a perfect setting to exemplify the application of state-of-the-art U-Pb dating by chemical abrasion ID-TIMS method to the stratigraphic record. The key fossil-bearing units that are examined here comprise a variety of distinct Campanian terrestrial sedimentary units deposited along the basin's western margin from Alberta to Utah.

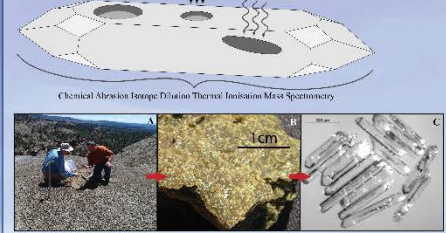
This study aims to broaden the reach and effectiveness of high-precision geochronology through refined stratigraphic correlations using a multifaceted geochemical approach to characterising bentonite marker horizons. Geochemical characterisation of volcanic material, a process called tephrostratigraphy, is often hampered in pre-Quaternary deposits due to chemical alteration during ash devitrification. Here we present major element characterisation of the Campanian bentonites through the novel use of glass (melt) inclusions that are encased within the same volcanic zircon crystals used

for geochronology, and thus are protected from alteration. Several independent geochemical signatures are employed to support fingerprinting of bentonites including trace element composition and Lu-Hf isotopic systematics. Preliminary findings have shown promise in correlating bentonites within and even between formations. Selected bentonite horizons with statistically indistinguishable mean <sup>206</sup>Pb / <sup>238</sup>U ages that are spatially separated by >1000km have yielded geochemically distinct fingerprints, implying synchronously eruptive volcanic centers in the northern and southern parts of the basin during the late Campanian. This multifaceted approach will facilitate the construction of a high-resolution chronostratigraphic framework for the basin by relatively inexpensive and accessible means and is entirely transferable to other basins and time periods.

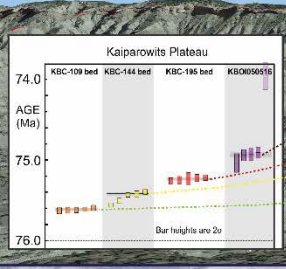
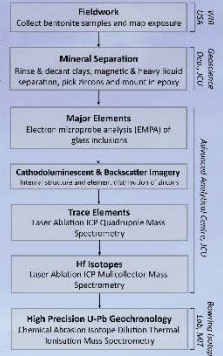


SEM backscatter image of a volcanic zircon with a fresh and a devitrified glass melt inclusion.

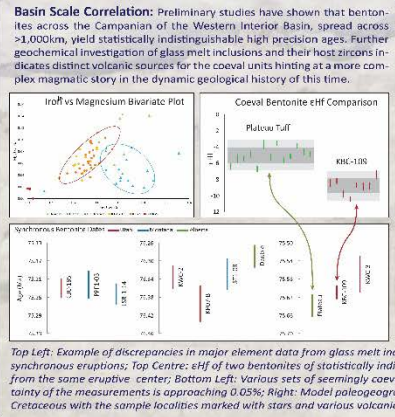
**Multifaceted Geochemical Approach:** Volcanic zircons and the glass melt inclusions hosted within them contain a trove of geochemical information that can be used like a barcode to distinguish between different eruptive events and to reconstruct the magmatic evolution of highly explosive Cretaceous volcanism that occurred during the zenith of dinosaur diversity in the richly fossiliferous Western Interior Basin.



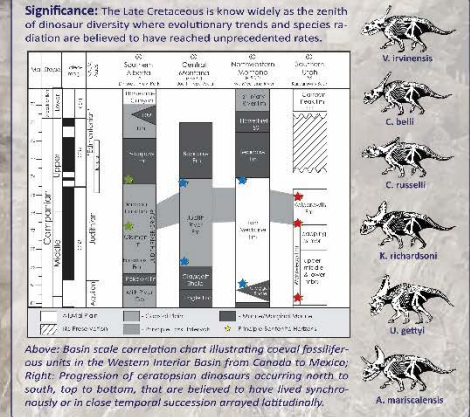
Top Left: Illustration of various geochemical analyses performed on volcanic zircons in this study. Right: Flow chart demonstrating the sequence of analyses. The order is significant due to the sensitivity of the glass inclusions to exposure damage. Bottom Left: Progression of locating bentonite horizons, collecting the most pure samples and selecting the youngest zircon population representative of the main eruptive phase.



Kaiparowits Formation in southern Utah as seen using Google Earth Pro with trace lines indicating the lateral extent of key bentonites. Four of these units have been dated using CA-ID-TIMS at the Massachusetts Institute of Technology where the ages of each closely spaced unit can be clearly distinguished for the first time.



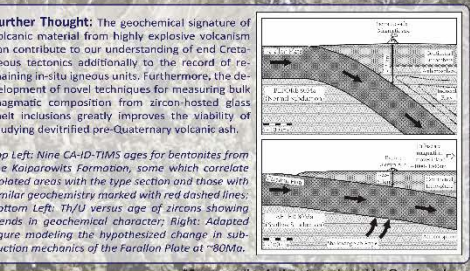
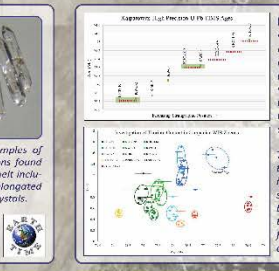
Top Left: Example of discrepancies in major element data from glass melt inclusions from various bentonites including those from synchronous eruptions; Top Centre: eHF of two bentonites of statistically indistinguishable age that were previously thought to be from the same eruptive center; Bottom Left: Various sets of seemingly coeval bentonites from across the basin where the uncertainty of the measurements is approaching 0.05%; Right: Model paleogeography of the North American continent during the Late Cretaceous with the sample localities marked with stars and various volcanic centers listed.



**Concluding Remarks:** High precision geochronology paired with geochemical fingerprinting of bentonite horizons shows significant promise for:

- Correlating isolated fossil localities with a precisely calibrated type section
- Tracing bentonite marker horizons over long distances including across the basin
- Investigating the magmatic evolution of highly explosive Cretaceous volcanism
- Exploring latitudinal change on the western landmass of Cretaceous North America

Thanks To: James Cook University, Massachusetts Institute of Technology, Smithsonian Institution, and other institutions.



Corresponding Author: teagan.beveridge@my.jcu.edu.au

**Conference Abstract – Oral Presentation**

*Society of Vertebrate Paleontology 79th Annual Meeting, Brisbane 2019*

New high-precision U-Pb geochronology for the Wahweap Formation, southern Utah, and implications for Late Cretaceous dinosaur evolution in North America

Beveridge, T.L., Roberts, E.M., Ramezani, J., & Titus, A.L.

High precision temporal calibration of terrestrial vertebrate faunas by the U-Pb geochronology method has advanced significantly in the last decade. Bentonite marker horizons can be dated at 95% confidence level precision that now approaches 0.02%. This improved temporal constraint has significant implications for Late Cretaceous fossil localities that represent the height of dinosaur diversity in North America. The Kaiparowits Plateau in southern Utah has yielded plentiful new vertebrate taxa in the last two decades with a high concentration of discoveries coming from the Wahweap Formation in the Grand Staircase – Escalante National Monument. Important discoveries include early members of Tyrannosauridae and Ceratopsidae. In this study, we systematically contextualised key taxa from the Wahweap Formation using high-precision geochronology and improved intraformational correlations.

Here we present the first high precision U-Pb ages for the Campanian Wahweap Formation using the chemical abrasion isotope dilution thermal ionisation mass spectrometry (CA ID TIMS) method. The findings of this study provide the basis for a revised temporal framework of the Wahweap Formation and taxa within. The Star Seep Bentonite (one of two Wahweap Fm. bentonites with published Ar-Ar geochronology [CF05-B]) was used as a distinctive horizon traceable across the formation. A northern and southern sample of the Star Seep Bentonite (B2-07B and WLS-R respectively) were collected and volcanic zircons from each were analysed using the CA ID TIMS approach. The two samples yielded statistically indistinguishable U-Pb dates thus confirming the correlation across 38 km and, most significantly, the results indicate a U-Pb date nearly 1.5 million years older than the previously published Ar-Ar date. This shift in the temporal framework has substantial implications for taxa from the Wahweap Formation. The type locality for the oldest known tyrannosaurid in North America, *Lythronax argestes*, is two metres below the southern Star Seep Bentonite sample locality. Another basal ancestor of significance is the oldest known ceratopsian *Diabloceratops eatoni*, identified from its type locality approx. 50 m stratigraphically higher than the newly dated bentonite. The new early Campanian age for the lower Wahweap Formation is considerably older than previously thought and has significant implications for understanding the timing and drivers of a major dinosaur diversification interval in the Santonian to early Campanian of the Western Interior Basin.

**Conference Abstract – Oral Presentation**

*GSA Earth Sciences Student Symposium, Brisbane 2019*

Multifaceted geochemical characterisation for pre-Quaternary bentonite tephrostratigraphy

Beveridge, T.

Correlating devitrified volcanic ash horizons (bentonites or tuffs) is a fundamental stratigraphic tool but can be exceedingly difficult to use reliably. Bentonite horizons in terrestrial strata typically exhibit poor lateral continuity over large distances; units are usually preserved in isolated pond or lake deposits. As well as patchy preservation, rapid devitrification of volcanic material after deposition hinders correlation using field observations.

Here we present a new multifaceted approach to bentonite characterisation using geochemical analyses of volcanic zircon and glass (melt) inclusions within. Zircon is an ideal mineral to target for characterisation of devitrified volcanic material as its physical and chemical stability facilitates preservation of primary geochemical information. Zircons for analysis were selected from bentonite heavy mineral separates using criteria including high aspect ratio (1:5) and presence of elongate glass inclusions. Major element composition of the glass inclusions was determined using WDS electron microprobe analysis and the host zircons were subject to laser ablation ICP-MS to determine the trace element and Lu-Hf isotope composition. Finally, high precision chemical abrasion ID-TIMS was conducted on the remaining crystal to determine the U-Pb age. This approach is designed to work in tandem with high precision ages in volcanic-rich strata to correlate understudied, isolate areas to a well constrained stratotype. Improved stratigraphic correlation using bentonite characterisation will help to refine the temporal framework of significant strata and the fossil faunas and floras within. Detailed geochemical information of bentonite horizons can also be used to infer large-scale tectonic and magmatic character of ancient sedimentary basins.

[Note: I was awarded Best Presentation for this work].





Contents lists available at ScienceDirect

Cretaceous Research

journal homepage: [www.elsevier.com/locate/CretRes](http://www.elsevier.com/locate/CretRes)

## Volcaniclastic member of the richly fossiliferous Kaiparowits Formation reveals new insights for regional correlation and tectonics in southern Utah during the latest Campanian

Tegan L. Beveridge<sup>a,\*</sup>, Eric M. Roberts<sup>a</sup>, Alan L. Titus<sup>b</sup><sup>a</sup> Department of Earth and Environmental Sciences, James Cook University, Townsville, QLD, 4811, Australia<sup>b</sup> Grand Staircase – Escalante National Monument, Bureau of Land Management, Kanab, UT, 84741, USA

## ARTICLE INFO

## Article history:

Received 31 March 2020

Received in revised form

15 May 2020

Accepted in revised form 21 May 2020

Available online 30 May 2020

## Keywords:

Upper Valley Member

Detrital zircons

Lithostratigraphy

Provenance

Cordilleran foreland basin

## ABSTRACT

Lithostratigraphic investigation of the richly fossiliferous Kaiparowits Formation in southern Utah reveals the presence of a previously unidentified stratigraphic unit herein named the Upper Valley Member. The 255-m-thick Upper Valley Member is latest Campanian to earliest Maastrichtian in age and records a significant sedimentological change in the Kaiparowits Formation. This change is illustrated in the member by a significant increase in near syn-sedimentary aged zircons, coincident with the introduction of white, volcaniclastic sandstones, as well as a paucity of Jurassic grains, which dominate the provenance of the rest of the formation. The source of the late Campanian volcaniclastic material, including near syn-sedimentary zircons, is most likely from nearby volcanic centers within the Laramide porphyry copper province to the south of the Kaiparowits Plateau in the Mogollon region. Measured sections reported here stratigraphically expand the Kaiparowits Formation to a total of 1005 m and find that the upper boundary of the formation is largely gradational with the overlying Canaan Peak Formation. Lithological changes documented in this study are interpreted to signify a sedimentological response to proximal magmatism and emerging uplifts within the Cordilleran foreland basin during early Laramide orogenesis, which resulted in paleo-drainage rearrangement in southern Laramidia in the latest Campanian. The fossil-bearing Upper Valley Member can be correlated regionally to the Kirtland, Tuscher and Bearpaw formations and other latest Campanian – and possibly early Maastrichtian – units across western North America and represents the capping member one of the most continuous terrestrial records of the Campanian biosphere found anywhere in the world.

© 2020 Elsevier Ltd. All rights reserved.

## 1. Introduction

The richly fossiliferous Kaiparowits Formation in southern Utah preserves a highly resolved temporal and stratigraphic record of mid-to-late Campanian strata of the proximal Cordilleran Foreland Basin in southern Laramidia. Although the reportedly 860-m-thick succession is renowned for its diverse and abundant assemblages of fossil vertebrates, plants, invertebrates and trace fossils, recent advances in understanding the sedimentary architecture, mineralogy, age and depositional settings of the formation highlight its importance as a keystone for paleoenvironmental reconstruction of the southern Cordilleran foreland basin. The Kaiparowits Formation

conformably overlies the early to middle Campanian age Wahweap Formation (Eaton, 1991; Jinnah and Roberts, 2011), and continues a remarkably complete terrestrial sedimentary record throughout the Campanian. The upper contact of the Kaiparowits Formation is a truncating low angle unconformity with the overlying Canaan Peak Formation (Bowers, 1972; Eaton, 1991; Roberts, 2007). Previous dating of Kaiparowits bentonite beds (devitrified volcanic ash) indicate the formation is mid-to late Campanian in age (Roberts et al., 2005, 2013). Several studies including Lohrengel (1969) and Eaton (1991) describe the thickness of the Kaiparowits Formation to be greatest in the vicinity of Canaan Peak, close to the axis of the Table Cliff syncline; however, the lectostratotype section reported by Roberts (2007) was measured in The Blues area below Powell Point, located northwest of Canaan Peak. This section terminates in a covered interval and Roberts (2007) inferred the contact with the overlying Canaan Peak Formation to lie 70 m above the uppermost

\* Corresponding author.

E-mail addresses: [tegan.beveridge@myjcu.edu.au](mailto:tegan.beveridge@myjcu.edu.au) (T.L. Beveridge), [eric.roberts@jcu.edu.au](mailto:eric.roberts@jcu.edu.au) (E.M. Roberts), [atitus@blm.gov](mailto:atitus@blm.gov) (A.L. Titus).<https://doi.org/10.1016/j.cretres.2020.104527>

0195-6671/© 2020 Elsevier Ltd. All rights reserved.



Contents lists available at ScienceDirect

Palaeogeography, Palaeoclimatology, Palaeoecology

journal homepage: [www.elsevier.com/locate/palaeo](http://www.elsevier.com/locate/palaeo)

## Refined geochronology and revised stratigraphic nomenclature of the Upper Cretaceous Wahweap Formation, Utah, U.S.A. and the age of early Campanian vertebrates from southern Laramidia

Tegan L. Beveridge<sup>a,\*</sup>, Eric M. Roberts<sup>a</sup>, Jahandar Ramezani<sup>b</sup>, Alan L. Titus<sup>c</sup>,  
Jeffrey G. Eaton<sup>d,e</sup>, Randall B. Irmis<sup>e,f</sup>, Joseph J.W. Sertich<sup>g,h</sup>

<sup>a</sup> Department of Earth and Environmental Science, James Cook University, Townsville, QLD 4811, Australia

<sup>b</sup> Department of Earth, Atmospheric and Planetary Science, Massachusetts Institute of Technology, Cambridge, MA 02139, USA

<sup>c</sup> Paria River District, Bureau of Land Management, Kanab, UT 84741, USA

<sup>d</sup> P.O. Box 231, Tropic, UT 84776, USA

<sup>e</sup> Natural History Museum of Utah, University of Utah, Salt Lake City, UT 84108-1214, USA

<sup>f</sup> Department of Geology & Geophysics, University of Utah, Salt Lake City, UT 84112-0102, USA

<sup>g</sup> Department of Earth Sciences, Denver Museum of Nature and Science, Denver, CO 80205, USA

<sup>h</sup> Department of Geosciences, Warner College of Natural Resources, Colorado State University, Fort Collins, CO 80523, USA

### ARTICLE INFO

Editor: Howard Falcon-Lang

#### Keywords:

Stratigraphy

Member

High-precision

CA-ID-TIMS

Age-stratigraphic model

Paleontology

### ABSTRACT

The Western Interior of North America preserves one of the most complete successions of Upper Cretaceous marine and non-marine strata in the world; among these, the Cenomanian-Campanian units of the Kaiparowits Plateau in southern Utah are a critical archive of terrestrial environments and biotas. Here we present new radioisotopic ages for the Campanian Wahweap Formation, along with lithostratigraphic revision, to improve the geological context of its fossil biota. The widely accepted informal stratigraphic subdivisions of the Wahweap Formation on the Kaiparowits Plateau are herein formalized and named the Last Chance Creek Member, Reynolds Point Member, Coyote Point Member, and Pardon Canyon Member (formerly the lower, middle, upper, and capping sandstone members respectively). Two high-precision U-Pb zircon ages were obtained from bentonites using CA-ID-TIMS, supported by five additional bentonite and detrital zircon LA-ICP-MS ages. Improved geochronology of the Star Seep bentonite from the base of the Reynolds Point Member via CA-ID-TIMS demonstrates that this important marker horizon is over a million years older than previously thought. A Bayesian age-stratigraphic model was constructed for the Wahweap Formation using the new geochronologic data, yielding statistically robust ages and associated uncertainties that quantifiably account for potential variations in sediment accumulation rate. The new chronostratigraphic framework places the lower and upper formation boundaries at 82.17 ± 1.47/-10.63 Ma and 77.29 ± 0.72/-0.62 Ma, respectively, thus constraining its age to the first half of the Campanian. Additionally, a holistic review of known vertebrate fossil localities from the Wahweap Formation was conducted to better understand their spatio-temporal distribution including revised ages for early members of iconic dinosaur lineages such as Tyrannosauridae, Hadrosauridae, and Centrosaurinae. Chrono- and lithostratigraphic refinement of the Wahweap Formation and its constituent biotic assemblages establishes an important reference for addressing questions of Campanian terrestrial paleoecology and macroevolution, including dinosaur endemism and diversification throughout western North America.

### 1. Introduction

The Western Interior of North America preserves near-continuous successions of Upper Cretaceous strata deposited in a variety of

settings ranging from alluvial and lacustrine to epicontinental marine (e.g., Molenaar and Rice, 1988; Kauffman, 1985; Roberts and Kirschbaum, 1995; Miall et al., 2008). These world-famous strata have been instrumental in developing global concepts of Cretaceous geochronology,

\* Corresponding author at: C.O. EGRU, 1 James Cook Drive, Douglas, QLD 4811, Australia.  
E-mail address: [tegan.beveridge@my.jcu.edu.au](mailto:tegan.beveridge@my.jcu.edu.au) (T.L. Beveridge).

<https://doi.org/10.1016/j.palaeo.2022.110876>

Received 5 July 2021; Received in revised form 3 February 2022; Accepted 6 February 2022

Available online 10 February 2022

0031-0182/© 2022 Elsevier B.V. All rights reserved.



# Appendix B

## Extended Methods



## **Appendix B.1 Mineral separation and zircon mount preparation methodology**

### *Appendix B.1.1 Bentonite collection*

Bentonite horizons were identified as weather-resistant benches with characteristic popcorn swelling textures. The colour of bentonite exposures varied depending on recent wetting and other factors but were generally grey to greenish-grey and exceptionally slick when wet. Pure bentonite beneath the weathered surface material was commonly rich pistachio green with a waxy lustre with visible black flecks interpreted as fresh biotite mica. Hand samples were checked for detrital material such as rounded quartz using a hand lens to ensure the material was not reworked.

A trench was excavated through the bentonite horizon to identify the best level from which to collect material. The most reliable level was deemed to be close to the base of the bentonite unit due to an upwards increasing likelihood of fluvial reworking, although each outcrop was inspected for unique depositional characteristics. The basal few centimetres were also avoided due to increased likelihood of contamination, in this instance from coarser volcanic detritus entrained during eruption. In most instances, roughly the first centimetre of the bentonite horizon was avoided, and sample material was collected from the next 20% of the horizon's total thickness.

Once the optimal interval of the bentonite horizon from which to collect material was identified, overburden was removed to form a bench above this level. Where this was not possible due to local terrain (e.g., steep hills, cliffs), loose sediment around the collection site was cleared and the targeted material was collected by digging into the cut-face making sure not to dislodge undesired material. One to four kilograms of bentonite were collected for each sample. Care was taken to avoid collection of unintended materials including soils or organic material. Samples were double bagged in Ziplock plastic bags secured with heavy duty tape and clearly labelled. Details of the sample and location were recorded including GPS co-ordinates, photographs, rock description / depositional environment interpretation, stratigraphic height, bounding lithofacies and lateral extent.

### *Appendix B.1.2 Bentonite washing*

At MIT, bentonite sample preparation followed the procedure of Hoke et al. (2014). First, approximately 1 kg of material was rehydrated overnight in a large beaker to form a thick paste. This was then homogenised using a sediment blender and diluted with water until the viscosity resembled that of pouring cream. The slurry was gradually added to the Ultrasonic Clay Separator apparatus of Hoke et al. (2014) (see reference for details) in small batches roughly every 45 minutes. This process decanted the clay fraction in a highly controlled manner so that, after a day or two, only the crystalline fraction remained. This resulted in a volume reduction of >90% for most samples.

At JCU, bentonites were decanted manually. Similar to the above approach, samples were rehydrated overnight then pulsed to form a slurry. Following this homogenisation, the slurry was manually decanted



in a large (>4 L) plastic beaker or container by repeatedly adding water, allowing larger particles to settle, then pouring off the suspended clays. This process was performed over the course of a day or two until the remaining portion constituted clean phenocrysts.

#### *Appendix B.1.3 Sandstone collection*

Sandstone units were targeted in various studies during this project primarily for detrital zircon geochronology and provenance, but also for lithological descriptions and petrography. Samples were collected from stratigraphically well-constrained outcrops preferably from an interval of 30 cm or less but occasionally across a broader range to encompass a variety of grain sizes. Samples for detrital zircon geochronology and provenance studies were between one and four kilograms and those for lithological descriptions and petrography constituted representative hand samples. Care was taken to avoid collection of unintended materials including soils or organic material. Samples were double bagged in Ziplock plastic bags secured with heavy duty tape and clearly labelled. Details of the sample and location were recoded including GPS co-ordinates, photographs, rock description / depositional environment interpretation, stratigraphic height, bounding lithofacies and lateral extent. This approach was also applied to the collection of nodules and other material.

#### *Appendix B.1.4 Sandstone cutting, crushing, and milling*

Samples for sandstone petrography were cut using a table trim (lapidary) saw to roughly 1 x 2.5 x 5 cm blocks and shipped to Adelaide Petrographic Laboratories for thin section preparation (30 µm thickness w/ cover slips). Two bentonite samples were prepared similarly (dry cut, no slip) as were three nodules.

Sandstone samples for detrital zircon studies were crushed using a jaw crusher and hydraulic press down to chips of less than 1 cm. These chips were then fed into a disc mill reducing to a maximum grain size of ca 500 µm. Samples were often triple processed to ensure a homogenous output grain size and complete disaggregation. All equipment was thoroughly cleaned via air hose and ethanol between samples.

#### *Appendix B.1.5 Sandstone washing and density separation*

Crushed and milled sandstone samples were cleaned and volumetrically reduced using a Wilfley table. The table inclination and water pressure were adapted for each sample to optimize separation of less dense mineral (quartz, feldspars) from the zircon-bearing fraction. All fractions other than clays were retained. Fractions were transferred to beakers and dried in a laboratory oven at ~80°C. Care was taken to ensure beakers and storage containers were labelled and unlikely to be contaminated. All equipment was thoroughly cleaned and visually inspected between samples. Depending on the yield, the densest one or two fractions were progressed to the next stages of mineral separation.

#### *Appendix B.1.6 Magnetic separation*

A strong hand-magnet was used on the dried heavy Wilfley fraction to remove magnetite, which was abundant in some samples and would cause issues in later steps if not removed. A Frantz Isodynamic magnetic separator set to a consistent slope angle of 15° was used to remove other magnetically susceptible minerals. In most instances, a first pass at 0.5 A was used to remove moderate to strongly magnetic minerals followed by a second pass at 1.15 A. The non-magnetic fraction was progressed to the next stages of mineral separation.

#### *Appendix B.1.7 High density liquid separation*

At MIT, high density liquid separation was conducted using methylene iodide (MEI); an ethanol-soluble liquid with a density of 3.32 g·mL<sup>-1</sup>. The non-magnetic fraction from previous steps was added to ~150 mL MEI in a 250 mL separating funnel (pear-shaped) within a hazardous materials fume hood using appropriate personal protective equipment. After stirring and a period of settling, the heavy fraction was tapped off and cleaned via repeated rinsing with ethanol through high-grade filter paper.

At JCU, high density liquid separation was conducted using a small volume supersaturated lithium heteropolytungstate (LST) approach. LST is water soluble (distilled water was used) and typically supplied at a density of 2.85 g·mL<sup>-1</sup>; thus, additional refinement was required to improve separation of zircon (~4.7 g·cm<sup>-3</sup>) from apatite (~3.2 g·cm<sup>-3</sup>) and other common accessory minerals.

1. Small volumes of LST were supersaturated by evaporation in a 40°C laboratory oven until crystals began to form (~30 mL remaining), indicating minimal H<sub>2</sub>O dilution and thus a density of ~3.1 g·cm<sup>-3</sup>.
2. Each vial was weighed to check the density of the remaining liquid.
3. If the density was satisfactory, a few grams of the non-magnetic fraction from previous steps was added and stirred, then the LST vial was capped and returned to the 40°C oven for ~10 minutes.
4. After this time, the lighter mineral layer that formed at the top was re-agitated with care not to disrupt the bottom-most layer, then the vial was again returned to the oven for ten minutes.
5. Following this, the unopened vial was placed in a beaker with iced water such that only the lower portion of the vial was submerged (lighter fraction layer was not submerged). After a few minutes in the ice bath, the LST crystalized around the heavy mineral fraction in the bottom of the vial.
6. The top layer was scooped out and washed from the vial and placed in a funnel with high-grade filter paper to collect the light mineral separates. (Diluted LST was collected for reuse). As much of the top layer and light minerals was removed as possible without disrupting the frozen bottom layer.
7. A few millilitres of water were added to the vial now containing only the bottom portion and the vial was returned to the oven for a few minutes to liquify the LST.

8. Thereafter, the heavy fraction was washed from the vial and separated from the LST using high-grade filter paper.
9. After three rinses in the filter paper, the separates were washed into labelled petri dishes. Water was gently sprayed over the grains to wash them further then removed via pipette. This was done twice before drying the separates down in a 60°C oven overnight.

#### *Appendix B.1.8 Zircon selection*

Zircons were picked in ethanol using fine laboratory-grade tweezers (sharpened further for precision) under a binocular microscope. Petri dishes were flushed with compressed air and inspected for cross-contaminated zircon grains prior to adding the heavy separates. Carefully cleaned glass dishes were used at JCU and single-use plastic dishes were used at MIT (since there are greater consequences to inclusion of foreign zircons in CA-ID-TIMS weighed means that may constitute only a few analyses). The workstation was prepared by wiping down all surfaces including the microscope with an ethanol-dampened paper towel and fresh paper was placed adjacent to the microscope on both sides. Samples and utensils were arranged on the paper prior to commencement.

Grain morphology was observed to influence distribution within the petri dish, thus consistent methods were considered important. Sample tubes were filled to the brim with ethanol, then the petri dish was placed over the top. Both were inverted and the tube removed. Ethanol was added to the petri dish to ~2 mm depth, then the dish was swirled gently to spread the material. More ethanol was thereafter added as required.

The targeted population was picked using the fine laboratory tweezers and collected in a clear portion of the dish to facilitate comparison with other grains. Once a suitable quantity had been selected, they were transferred using the tweezers to a second, clean petri dish containing ~2 ml ethanol. (Criteria for the target population is outlined in the main thesis text).

At MIT, microphotographs were taken of the selected population and then the grains were transferred to a prepared quartz crucible via fine-tipped pipette (see annealing method). At JCU, the petri dish was dried down in a 40°C oven overnight then water was added, and the drying process repeated.

#### *Appendix B.1.9 Mounts preparation*

Zircon mounts were prepared via dry picking using a binocular microscope. The workstation was prepared the same as for zircon selection. A glass plate (10 x 10 x 0.5 cm) was cleaned using ethanol and thoroughly dried, then a strip of wide double-sided tape (min. 3 x 3 cm) was applied to the smoothest portion of the plate. Care was taken to reduce bubbles in the tape and laboratory-grade brands with a small amount of homogeneous glue was preferred. Before removing the top of the tape, guidelines were drawn on the underside of the glass plate to help with puck alignment and grain positioning.

Once the workbench and glass plate were prepared, the dried petri dish containing selected grains was removed from the oven and transferred to the workbench. The cover was removed from the double-sided tape and zircons were transferred from the petri dish to the tape using tweezers. Typically, I would use the tweezers in my right hand to pick up a grain then my left hand to move the petri dish and replace it with the glass plate, then position the grain on the tape with the aid of the binocular microscope.

This process was continued until all selected grains had been transferred. A small petri dish cover was placed over the tape when not in use for extended periods to reduce the likelihood of rouge grains falling on the tape. For this project, four samples were typically mounted together, and care was taken to mount dissimilar samples together to reduce the likelihood of confusion. Standards were not mounted with the unknowns as per the analytical protocol of the Advanced Analytical Centre at James Cook University.

Once all samples were mounted, a 2.5 cm diameter cylindrical Teflon mould (cleaned and lubricated with a small amount of silicone gel with care not to get gel on the basal surface) was placed over the area and pressed firmly into the tape. In a fume hood, epoxy resin was combined with chemical hardener as per laboratory instructions and held under vacuum for five minutes to remove air bubbles. The epoxy was then carefully poured into the mould from the edge and allowed to spread across the samples (again, with the intention of reducing air bubbles). Roughly 2 cm depth of epoxy was added, and small weights were placed on top of the mould to reduce the likelihood of seepage. The puck was left on the flat surface for at least two days to cure. This period can be accelerated by placing the puck in a 40°C laboratory oven for ~24 hrs, although this approach was avoided herein because it can cause amber discolouration of the epoxy.

#### *Appendix B.1.10 Mount polishing*

Fully cured epoxy pucks were removed from the moulds and the thickness was reduced to ~ 1 cm using a trim saw. Two styles of polishing were conducted; zircons for geochemical characterisation were polished in the first instance such that most grains were just exposed. This helped preserve melt inclusions and the overall zircon volume to facilitate many destructive analyses. Later, these mounts were polished the same as for mounts purely for U-Pb microbeam analysis, which was to expose grains approximately equatorially. Polishing was conducted using silicon carbide (P 600 - P 2400), nylon and velure lap pads with 5, 3, and 1 µm diamond suspension. Mounts were polished in ~60 second bursts and checked with a petrographic microscope to reduce the likelihood of grain plucking.

## Appendix B.2 Zircon mount maps and measurements

### Appendix B.2.1 Maps

Scale-calibrated zircon microphotographs (transmitted and reflected light, and cathodoluminescent imagery) were imported into Adobe Illustrator (versions up to and including Illustrator 2020) to produce maps for each sample with internally consistent scales. Images were manually aligned and cropped to size, and grains were completely visible within the selected images (i.e., no grains overlapped photo boundaries) to ensure later measurements were accurate. Outlines were produced using Illustrator tools (Image trace → Silhouette → Expand) and manually refined. Grains were labelled on the outline maps from one end to the other.

### Appendix B.2.2 Zircon proportion measurements

The complete and labelled grain maps were exported as a .PNG file and opened in ImageJ one at a time. The following procedure was used:

1. Calibrate the scale within ImageJ:
  - a) Use the 'line tool' to draw a line over the scale bar on the grain map (Note: hold shift to snap the line to horizontal)
  - b) Click the Analyse dropdown, then 'Set scale'
  - c) Adjust 'Known distance' and 'Unit of length' (and tick global if necessary) → 'Ok'
  - d) Check measurement using the key shortcut 'm' or 'Analyse' → 'Measure'
2. Beginning with grain #1, Use the 'line tool' to draw a line matching the length of the grain then record the measurement with key shortcut 'm' or 'Analyse' → 'Measure'
3. Repeat for all grains and finish by checking the scale bar and exporting the data
4. Repeat for the width of all grains, again finishing with the scale bar then exporting the data

### Appendix B.2.3 Zircon cross-sectional area measurements

Outline only grain maps were also exported from Illustrator as .PNG files and opened in ImageJ one at a time. The following procedure was used:

1. Calibrate the scale (as above)
2. Prepare the image:
  - a) Use the 'rectangle tool' to crop the boarder but make sure all grain outlines are within the perimeter
  - b) Click the 'Image' dropdown, then 'Duplicate'
  - c) 'Image' → 'Type' → '8-bit'
  - d) 'Image' → 'Adjust' → 'Threshold' → 'Apply'
3. Measure the grain areas:



- a. 'Analyze' → 'Analyze Particles'
  - b. Size thresholds can be adjusted if needed (e.g., to exclude small, non-grain object like bubbles); from 'Show', select outlines; inspect tick boxes for other parameters (if desired)
4. Check that all grains were identified as separate objects and export results (Note: the order may not match grain numbers)

### Appendix B.3 Hafnium anion exchange column chemistry

#### Appendix B.3.1 Sample chemistry conversion

Following column chemistry for the elution of U and Pb, the ‘wash’ portion will be in a HCl chemical state; however, the resin used for Hf elution operates in a HF state. As such, the sample washes must be converted, similar to the procedure used in the U-Pb methodology.

15. At the start of the chemistry day, preheat a hotplate in the laminar flow workbench to 30°C
16. Within the workbench area, remove the caps of wash tubes containing the selected sample aliquots and place the caps on parafilm beside the hotplate
17. Place the wash tubes on the hotplate and cover with a plastic container to reduce the likelihood of contamination  
**Note:** be aware that the plastic wash tubes are easy to knock over and can partly melt or stick to the hotplate
18. Once all (or most) of the condensation droplets have evaporated, add 8 drops of 1 M HCl – 0.1 M HF solution to each tube
19. Replace the caps, ensuring the caps and tubes are matched correctly, and leave the tubes on the hotplate to flux for a further 5 to 10 minutes
20. Remove from the hotplate and allow the tubes to cool before loading

#### Appendix B.3.2 Equipment preparation

As with U and Pb elution, purification of hafnium from the zircon washes is conducted in small (<1mL) plastic polymer funnels referred to as columns. Like all other containers that come into contact with the samples, these columns and the resin that fills their tips should be carefully cleaned to reduce contamination.

12. In the Pb clean lab, use plastic forceps to retrieve a column from the HNO<sub>3</sub> storage baths, handling it using the column board on which it is fitted  
**Note:** Don't use the same set of columns for Hf as for U-Pb
13. Rinse the column and board with MQ water twice, tapping gently between each wash
14. Transfer the rinsed column to the laminar flow workbench with the mouth of the column facing down
15. Over a collection dish, use a specific column cleaning MQ water bottle and touch the tip of the squirt bottle to the tip of the column and flush water back through the column neck to remove any contaminants (count five drops then repeat) and leave a small amount of water in the column to ensure no air bubbles remain in the neck

16. Add ~8 drops of homogenised resin solution (AG 50W-X8 resin, H<sup>+</sup> form 200-400 dry mesh size) so that the neck of the column is completely filled but the reservoir has no more than 1mm depth of resin  
**Note:** If too much resin is added, use a clean mechanical pipette (prepared as previously) to remobilise the resin and remove the excess.
17. Hang the column by the board on the purpose-made column stand ensuring the tip does not interact with anything (be careful not to reach over the columns)
18. Repeat steps 1-6 for at least 15 columns (preparing extra columns is recommended)
19. Once the resin has settled and all water has drained through the columns, half fill each column with MQ water again, then cover the column stand and let it drain through
20. Add 13 drops of 6 M HCl, then cover the column stand and let the acid drain through entirely
21. Add 13 drops of 8 M HF, then cover the column stand and let the acid drain through entirely
22. Add a full column of MQ water (from the dropper bottle so the resin isn't disturbed too much), then cover the column stand and let the acid drain through entirely  
**Note:** this is to make sure no cleaning acid remains in the resin
23. Using a clean durex square, carefully soak up any droplets on the column boards and on the outside of the columns but take care not to reach over the open columns or touch the tips
24. Finally, add 15 drops of 1 M HCl – 0.1 M HF solution to equilibrate the resin ready for the samples

#### *Appendix B.3.3 Anion exchange column chemistry (hafnium)*

1. Prepare two sets of plastic wash tubes by filling each tube and cap to the brim with MQ water, then dispose of water and label each tube and cap pair
2. Set up the column board carousel by wiping it down with a damp durex to remove dust and place parafilm strips around the collection area to help stabilize the sample tubes
3. Once the pre-conditioning solution has completely drained from the columns, carefully transfer the columns from the stand to the carousel with the circle end of the column board facing inwards (ensure the tip of the column does not come into contact with anything and be careful not to reach over open containers)  
**Note:** The boards should be firmly inserted into the carousel with the hole end inwards. This is not the same as the U-Pb approach because sample loading is conducted differently.
4. Place the tubes designated for collection of the Hf-bearing aliquot beneath the columns without touching the tip of the columns and press the tube firmly into the parafilm for stability
5. Place the caps beside the carousel on clean parafilm and bring the tubes designated for the 'unrefined' wash (for trace element measurements) to the side of the workbench, uncapped
6. Reposition the column board, if necessary, so that the tip is directly over the collection tube

7. Prepare a mechanical pipette (set to 100  $\mu\text{L}$ ) by rinsing the disposable plastic tip with MQ water and 6 M HCl, then place the pipette to the side
8. One at a time, uncap the chemically converted and cooled wash sample tubes, draw up 30  $\mu\text{L}$  of solution, transfer it to the 'unrefined' wash tubes, and replace the latter tube's cap
9. Change the pipette volume back to 100  $\mu\text{L}$  and transfer the remaining liquid to a column reservoir with care not to disturb the resin upon injection
10. Dispose of the plastic pipette tip and repeat steps #7-9 for each sample
11. Once the initial solution has completely run through the columns, add 4 drops of 1 M HCl – 0.1 M HF solution to each reservoir to elute Hf
12. Repeat step 11 twice more then finish by adding 10 drops of 1 M HCl – 0.1 M HF solution
13. While this is draining, preheat a hotplate in the laminar flow fume hood to 30°C
14. Once the solution has completely drained from the columns, gently tap the column board to liberate the last drop
15. Carefully transfer the sample tubes to the 30°C hotplate without reaching over the open containers and cover the beakers with a plastic cover to reduce the likelihood of contamination
16. Dry down the samples for approximately one hour, checking for condensation on the tube sides
17. While the samples are drying down, rinse the now empty columns in the same manner as for set up and return the clean columns to their nitric acid storage bath
18. Once the samples are completely dry, add 1 mL of 2%  $\text{HNO}_3$  solution to prepare the aliquot for MC-ICP-MS analysis
19. Replace the caps, ensuring the caps and tubes are matched correctly, and leave the tubes on the hotplate to flux for a further 5 to 10 minutes
20. Remove from the hotplate and allow the tubes to cool

### Appendix B.4 Melt inclusion major element data reduction

Following major element analysis of zircon hosted melt inclusions via quantitative electron dispersive spectroscopy (EDS) SEM (see Chapter 6), data were exported as oxide weight percent .csv data tables (one file per sample per session). Raw data were first formatted and arranged for ease of use. Individual analyses were grouped into five categories:

- Probable glass inclusion analyses
- Low total oxide weight percent (< 85%)
- High ZrO<sub>2</sub> weight percent (> 10%)
- Apatite mineral inclusions (~52% CaO and ~ 42% P<sub>2</sub>O<sub>5</sub>)
- Other mineral inclusions or anomalies:
  - Quartz (very high SiO<sub>2</sub>)
  - Feldspars (higher Al<sub>2</sub>O<sub>3</sub> and K<sub>2</sub>O, Na<sub>2</sub>O, or CaO)
  - Iron oxide minerals or staining (high FeO ± MgO)
  - Devitrified glass (lower than average SiO<sub>2</sub>, very low Na<sub>2</sub>O and K<sub>2</sub>O, high Al<sub>2</sub>O<sub>3</sub> [ $> 15\%$ , often ~20%], higher than average FeO and MgO [several percent])

These criteria (dot points above other than the first) were used to reduce the dataset to represent only probable glass melt inclusions. A total weight cut-off of 85% is generous considering the volatile content is expected to compose only a few weight percent and it is unlikely that the EDS approach failed to identify whole percentages of element oxides. The specific cause of low totals remains under investigation (see Ch.6). Most of the omitted data represent analyses with low total weight percent, high zirconium content, or analyses of apatite inclusions. Very few are attributed to other minerals or unidentified anomalies.

Data representing probable glass inclusions were progressed to the next stage of data reduction wherein the composition was corrected to exclude the portion of analysis that overlapped the host zircon. This was achieved using a purpose-made approach based on the measured ZrO<sub>2</sub> content and stoichiometric calculations. Firstly, the weight percent of zircon included in the analysis (Zirc.) was calculated using:

$$Zirc. = \frac{(ZrO_2)_m}{Z^*} \times 100$$

where (ZrO<sub>2</sub>)<sub>m</sub> is the weight percent of zirconium oxide measured (raw data) and Z\* is the proportion of ZrO<sub>2</sub> in zircon (ZrSiO<sub>4</sub>) when also considering 2% Hf substituted for Zr typical of zircon (thus, Z\* = 65.2%). The weight proportion of Hf included in the analysis (Hf%) was calculated using:

$$Hf\% = \frac{(Zirc.)}{100} \times 2$$



The weight percent SiO<sub>2</sub> within the zircon component (*Silica<sub>Zirc.</sub>*) was calculated using:

$$Silica_{Zirc.} = \frac{(Zirc.)}{100} \times S^*$$

where  $S^*$  is the proportion of SiO<sub>2</sub> in zircon (32.8 wt.%). Oxide weight percent compositions without the zircon component were calculated for Na<sub>2</sub>O, MgO, Al<sub>2</sub>O<sub>3</sub>, K<sub>2</sub>O, CaO, MnO, and FeO using:

$$X_c = \frac{X_m}{(Tot_m - Zirc.)} \times (Tot_m + Hf\%)$$

where X is the weight percent of each oxide, subscripts c and m refer to the corrected and measured values, and Tot is the total weight percent. Due to the component of silica in zircon, correction of the SiO<sub>2</sub> weight percent of the glass measurements required an additional step using:

$$(SiO_2)_c = \frac{((SiO_2)_m - Silica_{Zirc.})}{(Tot_m - Zirc.)} \times (Tot_m + Hf\%)$$

Analyses where ZrO<sub>2</sub> was below detection limits were not affected by the correction. Trials demonstrated that correction of analyses with more than ~10 wt.% ZrO<sub>2</sub> produced seemingly irregular results and were not used in this study. Data produced after this ‘zircon component correction’ are included in Appendix C.6.8.

Investigation showed a consistent trend in the data scatter as plotted on a TAS diagram (conducted after ‘zircon component correction’ but regardless of those adjustments) pertaining to variable total oxide weight percent. Several methods of recalculation to standardize the total oxide weight percent were investigated using:

$$X_r = X_c \times \frac{Tot_n}{(Tot_c)}$$

where X is the weight percent of each oxide, Tot is the total weight percent, and subscripts r, c, and n refer to the recalculated and ‘zircon component corrected’ values, and desired new Tot. The primary approach, as used in Chapter 6, was to recalculate values to a total of 100 wt.% according to the recommendations of Le Bas et al. (1986) (data included in Appendix C.6.9). Other approaches investigated included recalculation to 1) an arbitrary value given a typical percentage of volatiles (e.g., 96% Tot), 2) the average of the entire dataset, 3) the average for each sample, and 4) the highest total for each sample that was within two standard deviations of the median value. These other forms of recalculation may be considered in future work concerning detailed parent magma classification.

## **Appendix B.5 Bayesian age-stratigraphic model construction and testing**

### *Appendix B.5.1 General approach*

The age-stratigraphic models produced in this thesis were constructed using the Bchronology package (version 4.7.1) after Haslett and Parnell (2008) and Parnell et al. (2008) in the free and open-source R Studio software (version 3.5.3). Details of basic functions for the Bchronology package were provided at The R Manual:

<https://cran.r-project.org/web/packages/Bchron/vignettes/Bchron.html>

Additional functions including the iteration and extractDate components were highlighted in the supplementary materials of Baressel et al. (2017) and further refinements were indicated via personal communication with J. Ramezani.

Several tests were conducted for the purpose of 1) familiarising myself with the Bchronology package and script, and 2) investigating the application of several controlled variables. During familiarisation, it became apparent that the package is designed for use in radiocarbon ages over short stratigraphic intervals. As such, the input data was restricted to kyrs rather than Myrs, and the use of centimetres rather than metres only changed the displayed size of the data point representative markers. The centimetre input was preferred due to the simpler appearance of the output, although ages were always generated a one-meter increments. Next, the extractDate parameter was tested by estimated an approximate top age for the section in use (ca 72 Ma for KBC/KBU type section model) versus the date of “extraction” interpreted to mean collection of the radiocarbon dated core in the original studies (0 Ma for the purpose of this study). Given the parameters in use here, the extractDate function did not appear to impact the model output. For the following testing, the “extractDate” component was retained with a value of 0; however, it was deemed unnecessary for work in this thesis.

The number of iterations was investigated starting with a script that does not specify the number of iterations, followed by specifically 10,000 iterations, then 100,000 iterations. Three outputs were calculated for each. This testing showed that without a specified number of iterations, the model appears to use 10,000 (consistent with brief information found in help(Bchronology)). At 10,000 iterations (<1 min run time), variations between the three outputs were noted. At 100,000 iterations (several minutes run time), the three outputs were considerably more consistent. Although Haslett and Parnell (2008) mention that the program may run 1 million iterations, the version used was specified as modified “to converge quicker and require fewer iterations” (see help(Bchronology)).

*Appendix B.5.2 Investigating Data for the Kaiparowits Model*

Following this initial familiarisation and basic testing, a specific investigation was conducted into the most appropriate data to use for construction of age-stratigraphic models for the Kaiparowits Formation using the script:

```
>library(Bchron)

>KaiparowitsFm <- read.csv(file.choose())

>KaiparowitsFmModel=Bchronology(ages=KaiparowitsFm$ages,
                                ageSds=KaiparowitsFm$ageSds,
                                calCurves=KaiparowitsFm$calCurves,
                                positions=KaiparowitsFm$position,
                                positionThicknesses=KaiparowitsFm$thickness,
                                ids=KaiparowitsFm$id,
                                predictPositions=seq(0,101100,by=100),
                                iterations=100000,extractDate=0)

>library(ggplot2)

>plot(KaiparowitsFmModel)+labs(x='Age (ka)',y='Depth (cm)',title='Kaiparowits Fm Bchron Model')

> KaiparowitsFmModelAges <- matrix(nrow=1011, ncol=3)

for(i in 1:1011){ KaiparowitsFmModelAges [i,]=quantile(KaiparowitsFmModel$thetaPredict[i],probs
= c(0.025,0.5,0.975))}

>write.csv(KaiparowitsFmModelAges, "Kaiparowits Fm Model Output.csv")
```

Testing of input parameters for the Kaiparowits Fm model included variations in stratigraphic thickness (bottom three members, Upper Valley Member, all four member), types of uncertainty (internal [X] vs internal plus tracer calibration [Y]), and types of data (CA-ID-TIMS only, added detrital zircon MDAs, top Wahweap Fm model age, selected Upper Valley Member ages). The tested combinations are summarised as:

1. 0-750 m with type-section bentonites (X uncertainty)
2. 0-750 m with type-section bentonites (Y uncertainty)
3. 0-750 m with type section bentonites (X uncertainty) plus top Wahweap Fm model age
4. 0-750 m with type section bentonites (Y uncertainty) plus top Wahweap Fm model age

5. 0-750 m with type-section bentonites (Y uncertainty) plus basal Kaiparowits Fm MDA and KBU-S MDA
6. 0-750 m with type-section bentonites (Y uncertainty) plus top Wahweap Fm MDA, basal Kaiparowits Fm MDA and KBU-S MDA
7. 750-1010 m with UVM MDAs
8. 750-1010 m with UVM MDAs plus KBO-37 single grain age
9. 750-1010 m with UVM MDAs plus KBU-S MDA
10. 750-1010 m with UVM MDAs plus top output from #4
11. 750-1010 m with UVM MDAs plus top output from #5
12. 750-1010 m with UVM MDAs plus top output from #6
13. 0-1010 m with type-section bentonites (Y uncertainty) plus all MDAs
14. 0-1010 m with type-section bentonites (Y uncertainty) plus top Wahweap Fm model age, KBU-S and UVM MDAs

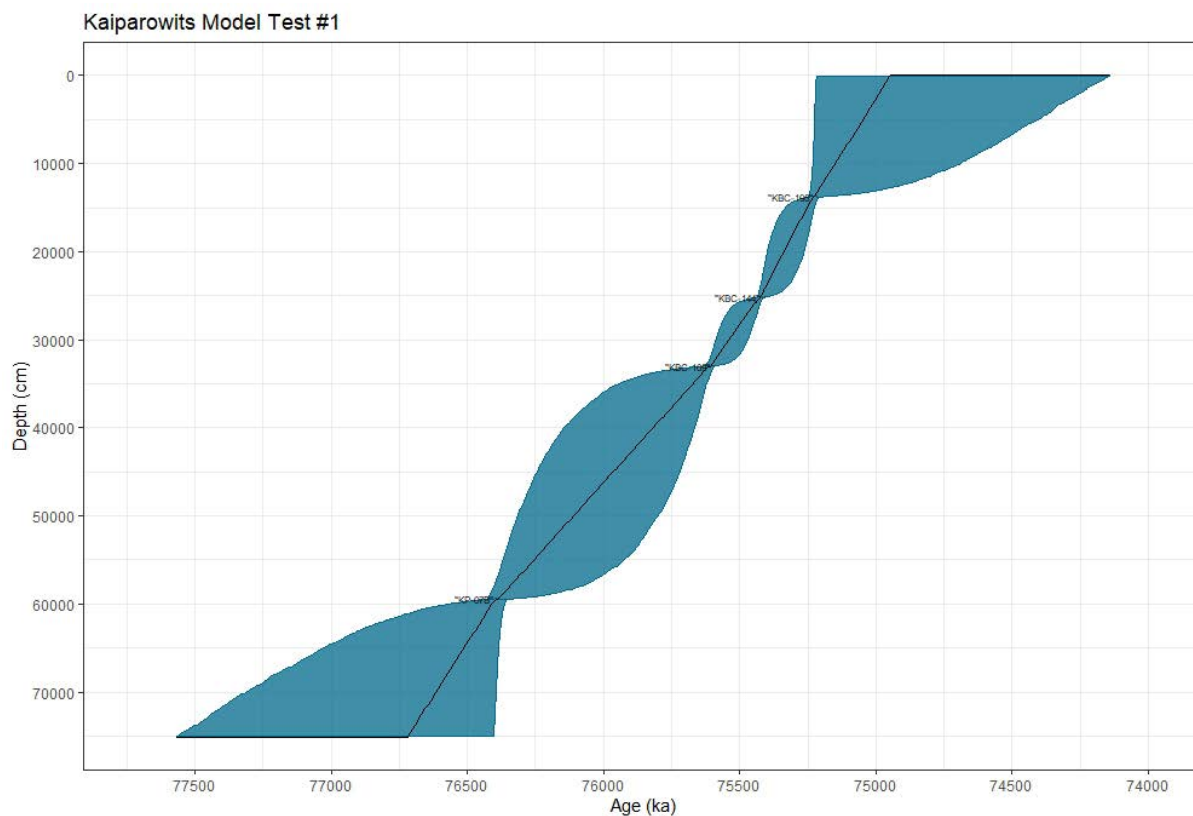
Input data are summarised below:

Sample Number	Published Source	Age (ka)	Uncertainty (1 $\sigma$ , ka)	Stratigraphic Level (cm)*	Used in test number:
KBU-W	Beveridge et al. (2020)	73100	600	0	7 to 14
KBU-O	Beveridge et al. (2020)	73200	700	8000	7 to 14
KBU-F	Beveridge et al. (2020)	73680	405	21000	7 to 14
KBO-37	Beveridge et al. (Ch.4)	73900	85	22000	8 to 14
KBU-V	Beveridge et al. (2020)	73680	330	24500	7 to 14
KBU-S	Beveridge et al. (2020)	75200	700	28000	5, 6, 9, 13, 14
KBC-195 (X)	Ramezani et al. (in prep)	75231	10.5	39800	1, 3
KBC-195 (Y)	Ramezani et al. (in prep)	75231	19	39800	2, 4, 5, 6, 13, 14
KBC-144 (X)	Ramezani et al. (in prep)	75427	6	51200	1, 3
KBC-144 (Y)	Ramezani et al. (in prep)	75427	11.5	51200	2, 4, 5, 6, 13, 14
KBC-109 (X)	Ramezani et al. (in prep)	75609	7.5	59000	1, 3
KBC-109 (Y)	Ramezani et al. (in prep)	75609	12.5	59000	2, 4, 5, 6, 13, 14
KP-07A (X)	Ramezani et al. (in prep)	76394	20	85500	1, 3
KP-07A (Y)	Ramezani et al. (in prep)	76394	22.5	85500	2, 4, 5, 6, 13, 14
WKC-3	Beveridge et al. (2022)	76540	475	100500	5, 6, 13
WKC-1&2	Beveridge et al. (2022)	77800	500	101500	6, 13
Top Wahweap Model Age	Beveridge et al. (2022)	77290	360	101000	3, 4, 14

\* Stratigraphic level is below a datum of 1010 m above the base of the Kaiparowits Formation relative to the KBC/KBU type section.

Three outputs were generated for each of the 14 tests and basic statistics were calculated from the top and basal ages to investigate variance (at 100,000 iterations). In the tables below, mean refers to that of each value (column) from the three tests, average variance refers to the average difference between the mean value and the values from each test, and maximum variance refers to the maximum difference

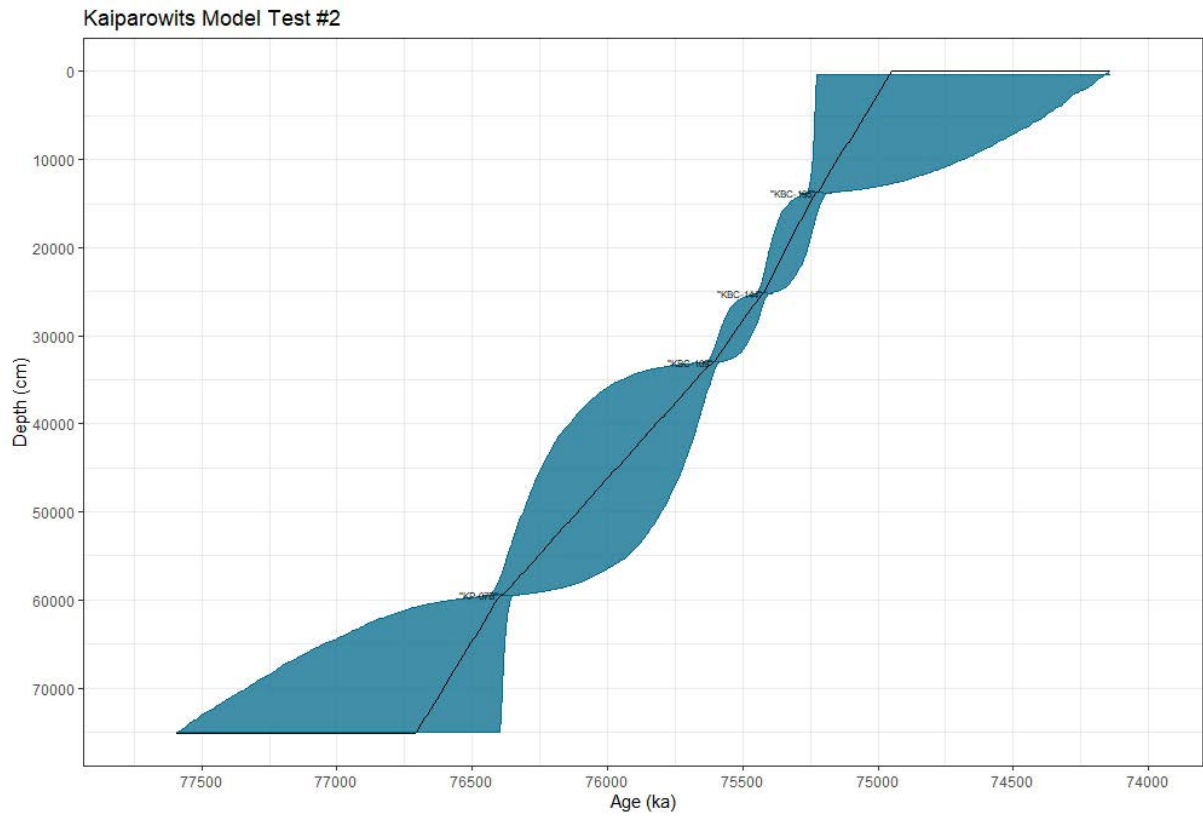
between the mean value and the values from each test as a percentage of the mean. Greater variance was taken to mean the model was less well constrained and differences in the top and basal ages were used to interpret how the addition or exclusion of certain data impacted the boundary ages and their precision.



Test 1: 0-750 m with type-section bentonites (X uncertainty)

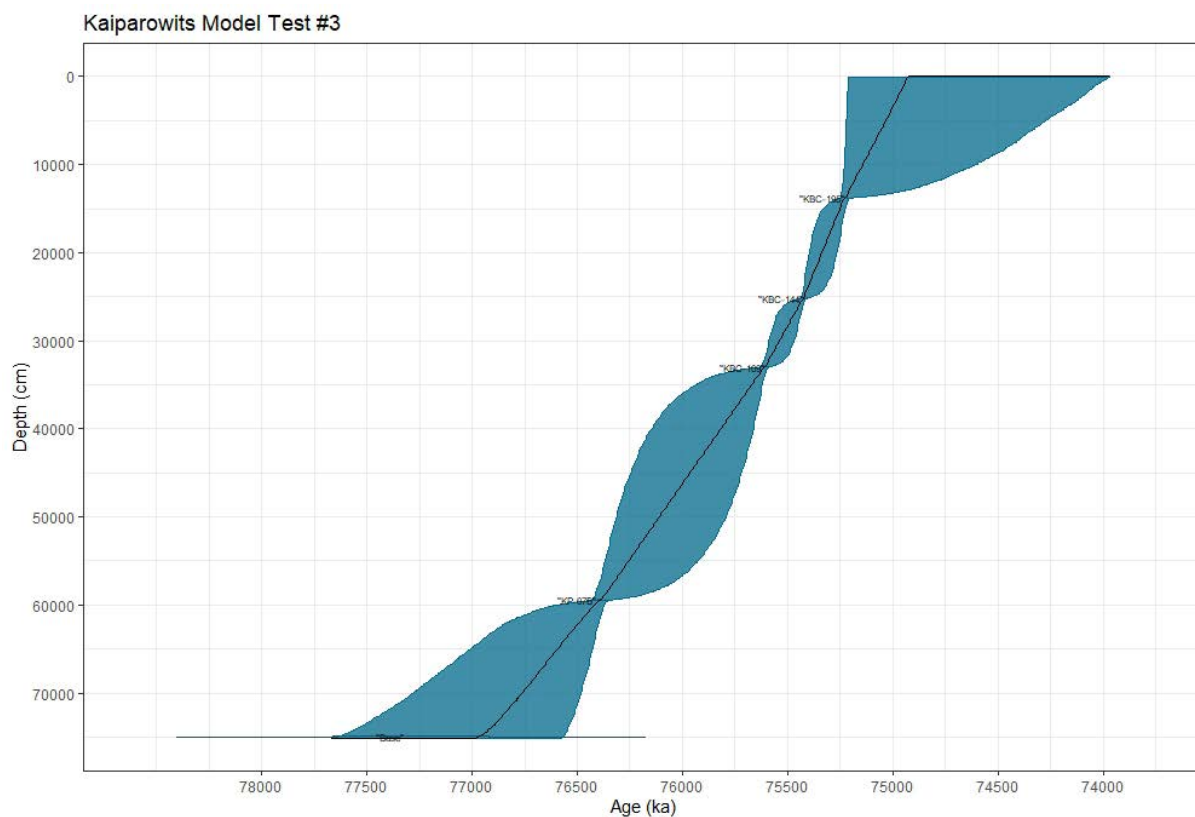
		Median	+	-	Max	Min	Range
Output 1 (Ma)	Top	74.94	0.28	0.81	75.22	74.13	1.09
	Base	76.71	0.87	0.31	77.59	76.40	1.19
Output 2 (Ma)	Top	74.94	0.28	0.80	75.22	74.14	1.08
	Base	76.71	0.84	0.31	77.55	76.40	1.15
Output 3 (Ma)	Top	74.94	0.28	0.79	75.22	74.15	1.07
	Base	76.72	0.85	0.31	77.57	76.40	1.17
Mean (Ma)	Top	74.94	0.28	0.80	75.22	74.14	1.08
	Base	76.71	0.86	0.31	77.57	76.40	1.17
Average	Top	0.002	0.002	0.009	0.000	0.008	0.008
Variance (Ma)	Base	0.001	0.012	0.002	0.012	0.001	0.012
Maximum	Top	0.00	0.96	1.64	0.00	0.02	1.09
Variance (%) (%)	Base	0.00	2.03	1.15	0.02	0.00	1.59





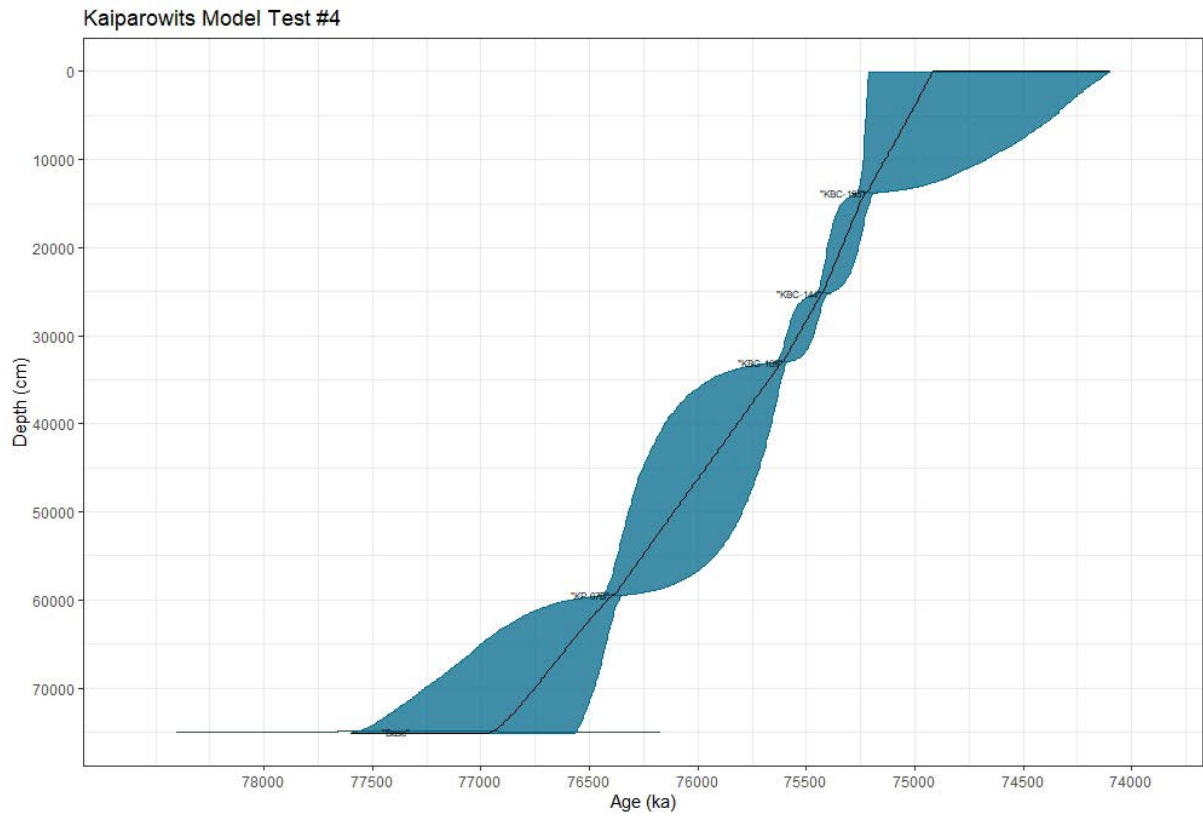
**Test 2: 0-750 m with type-section bentonites (Y uncertainty)**

		Median	+	-	Max	Min	Range
Output 1 (Ma)	Top	74.95	0.27	0.74	75.22	74.21	1.01
	Base	76.70	0.81	0.30	77.51	76.40	1.11
Output 2 (Ma)	Top	74.95	0.27	0.73	75.22	74.21	1.01
	Base	76.72	0.80	0.31	77.52	76.40	1.11
Output 3 (Ma)	Top	74.93	0.29	0.83	75.22	74.10	1.11
	Base	76.73	0.88	0.32	77.61	76.40	1.20
Mean (Ma)	Top	74.94	0.28	0.77	75.22	74.18	1.04
	Base	76.72	0.83	0.31	77.55	76.40	1.14
Average	Top	0.007	0.006	0.041	0.001	0.048	0.047
Variance (Ma)	Base	0.009	0.033	0.007	0.040	0.002	0.039
Maximum	Top	0.01	3.12	8.07	0.00	0.10	6.75
Variance (%)	Base	0.02	5.99	3.51	0.08	0.00	5.14



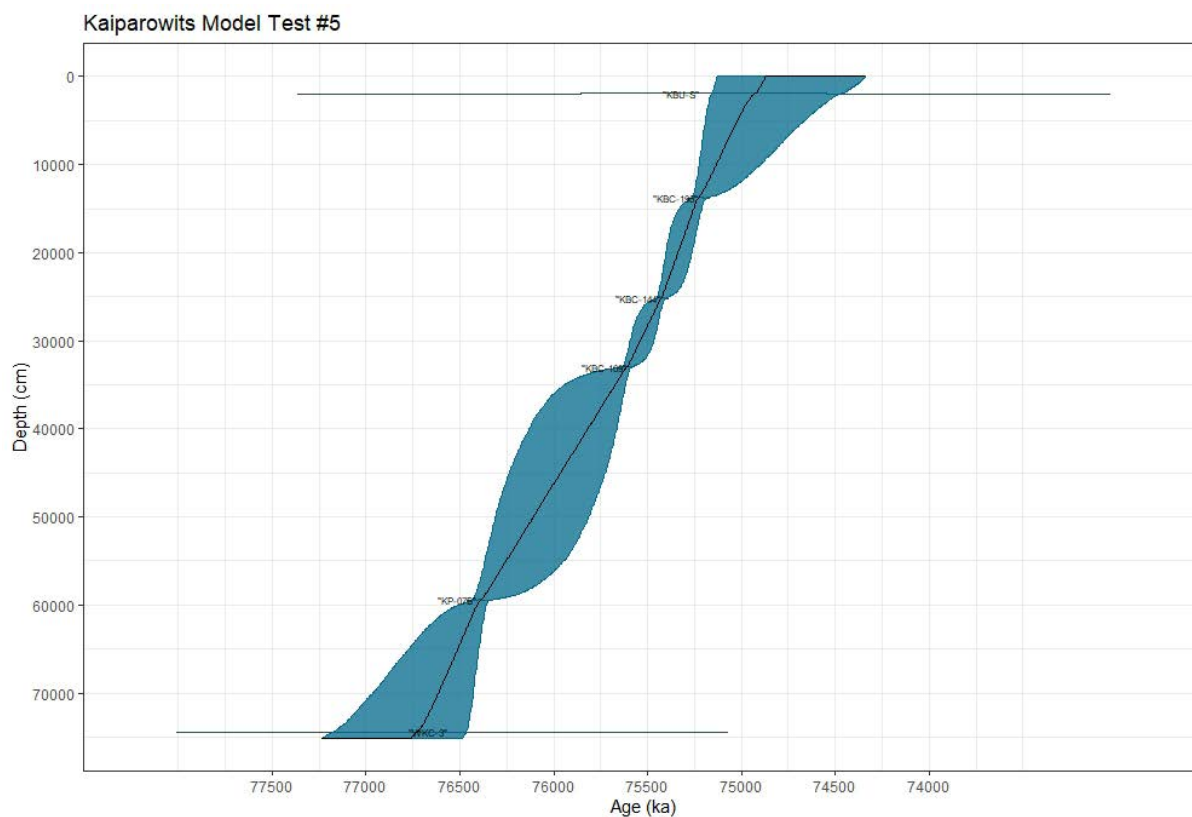
**Test 3: 0-750 m with type section bentonites (X uncertainty) plus top Wahweap Fm model age**

		Median	+	-	Max	Min	Range
Output 1 (Ma)	Top	74.93	0.29	0.83	75.22	74.11	1.11
	Base	76.96	0.66	0.39	77.62	76.57	1.05
Output 2 (Ma)	Top	74.92	0.30	0.80	75.22	74.12	1.10
	Base	76.96	0.64	0.39	77.60	76.57	1.03
Output 3 (Ma)	Top	74.93	0.29	0.78	75.22	74.15	1.07
	Base	76.96	0.64	0.38	77.61	76.58	1.03
Mean (Ma)	Top	74.93	0.29	0.80	75.22	74.12	1.09
	Base	76.96	0.65	0.39	77.61	76.57	1.03
Average	Top	0.003	0.003	0.015	0.001	0.014	0.016
Variance (Ma)	Base	0.001	0.006	0.003	0.007	0.004	0.009
Maximum	Top	0.01	1.66	2.79	0.00	0.03	2.15
Variance (%)	Base	0.00	1.51	1.24	0.01	0.01	1.27



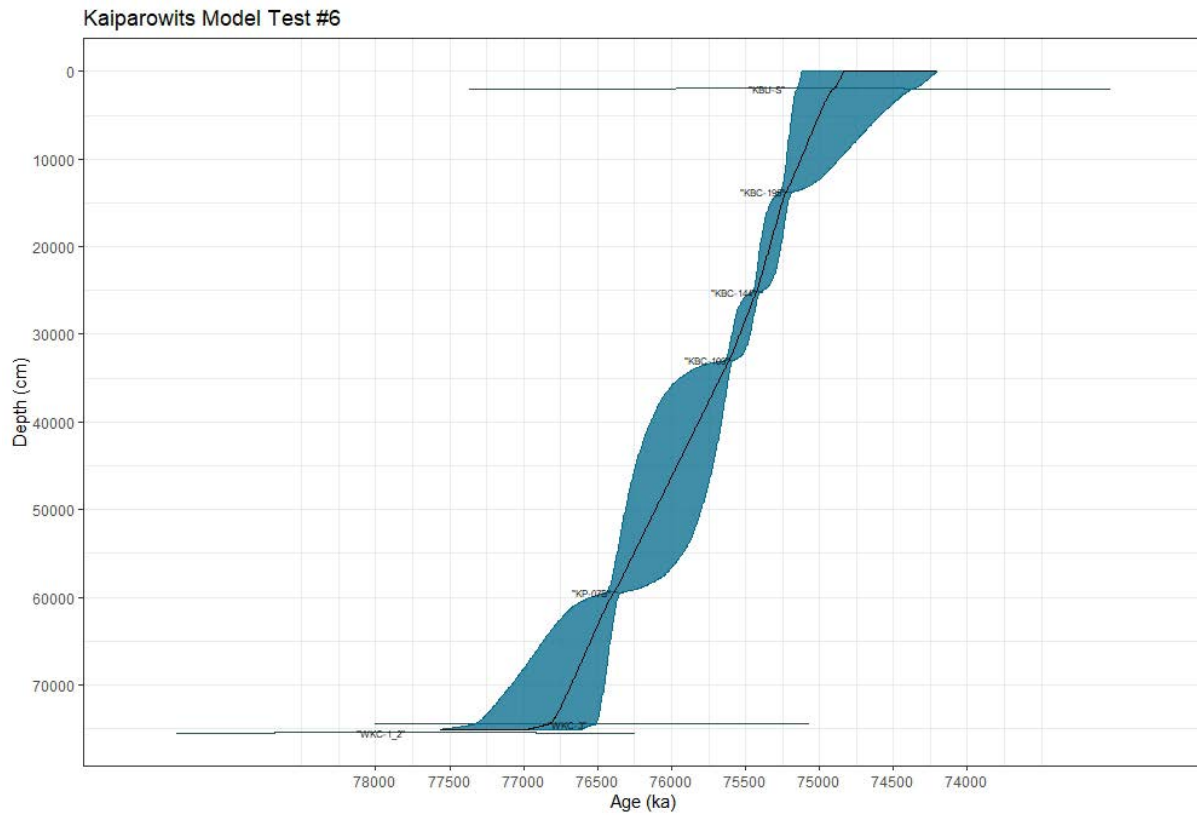
**Test 4: 0-750 m with type section bentonites (Y uncertainty) plus top Wahweap Fm model age**

		Median	+	-	Max	Min	Range
Output 1 (Ma)	Top	74.92	0.31	0.82	75.22	74.10	1.13
	Base	76.97	0.65	0.40	77.63	76.58	1.05
Output 2 (Ma)	Top	74.92	0.30	0.82	75.22	74.09	1.12
	Base	76.97	0.64	0.39	77.62	76.58	1.04
Output 3 (Ma)	Top	74.91	0.31	0.84	75.22	74.07	1.15
	Base	76.98	0.64	0.40	77.62	76.58	1.05
Mean (Ma)	Top	74.91	0.31	0.83	75.22	74.09	1.13
	Base	76.97	0.65	0.40	77.62	76.58	1.04
Average	Top	0.004	0.004	0.006	0.003	0.010	0.009
Variance (Ma)	Base	0.004	0.004	0.004	0.004	0.002	0.006
Maximum	Top	0.01	1.97	1.08	0.01	0.02	1.23
Variance (%)	Base	0.01	0.93	1.64	0.01	0.00	0.89



Test 5: 0-750 m with type-section bentonites (Y uncertainty) plus basal Kaiparowits Fm MDA and KBU-S MDA

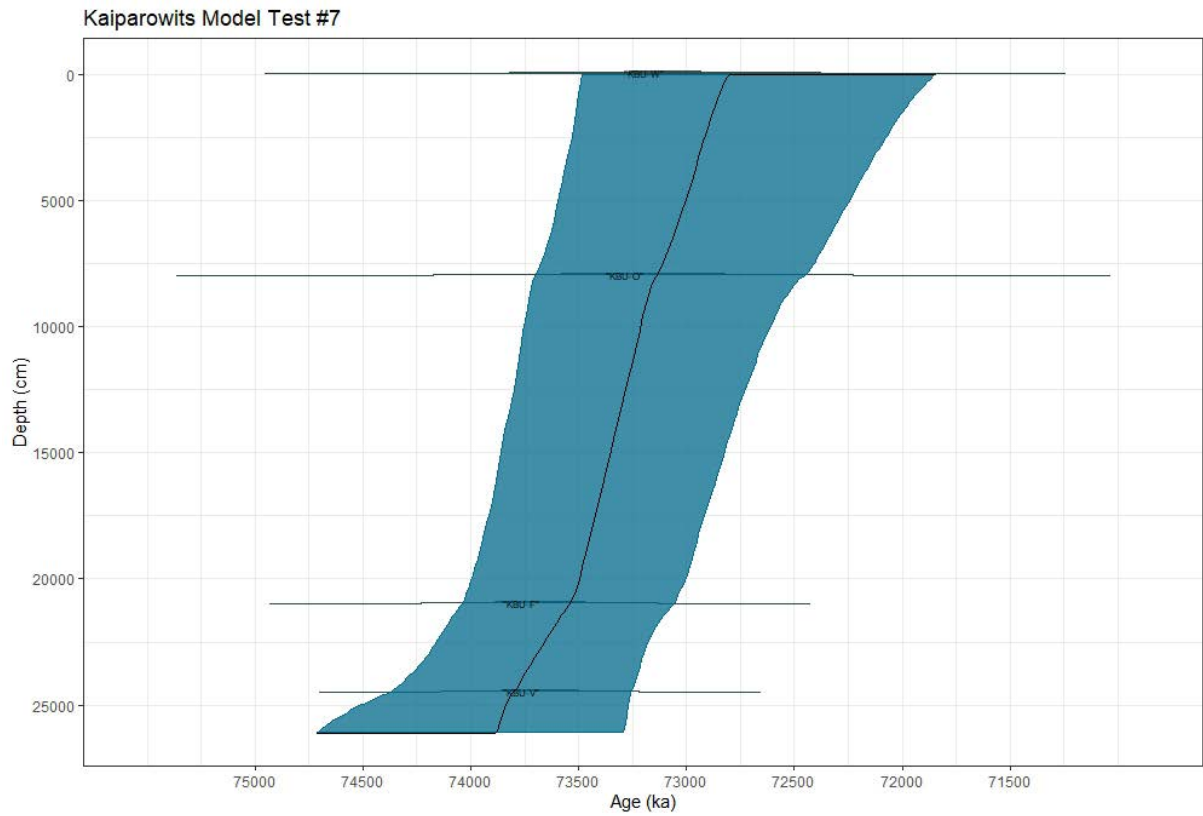
		Median	+	-	Max	Min	Range
Output 1 (Ma)	Top	74.87	0.26	0.55	75.13	74.32	0.81
	Base	76.75	0.47	0.27	77.23	76.48	0.74
Output 2 (Ma)	Top	74.87	0.26	0.53	75.13	74.34	0.78
	Base	76.75	0.48	0.27	77.23	76.48	0.75
Output 3 (Ma)	Top	74.87	0.26	0.54	75.13	74.33	0.80
	Base	76.75	0.48	0.27	77.23	76.48	0.75
Mean (Ma)	Top	74.87	0.26	0.54	75.13	74.33	0.80
	Base	76.75	0.48	0.27	77.23	76.48	0.75
Average	Top	0.000	0.001	0.007	0.001	0.007	0.008
Variance (Ma)	Base	0.001	0.002	0.001	0.001	0.001	0.002
Maximum	Top	0.00	0.39	2.08	0.00	0.01	1.53
Variance (%)	Base	0.00	0.66	0.74	0.00	0.00	0.38



**Test 6: 0-750 m with type-section bentonites (Y uncertainty) plus top Wahweap Fm MDA, basal Kaiparowits Dm MDA and KBU-S MDA**

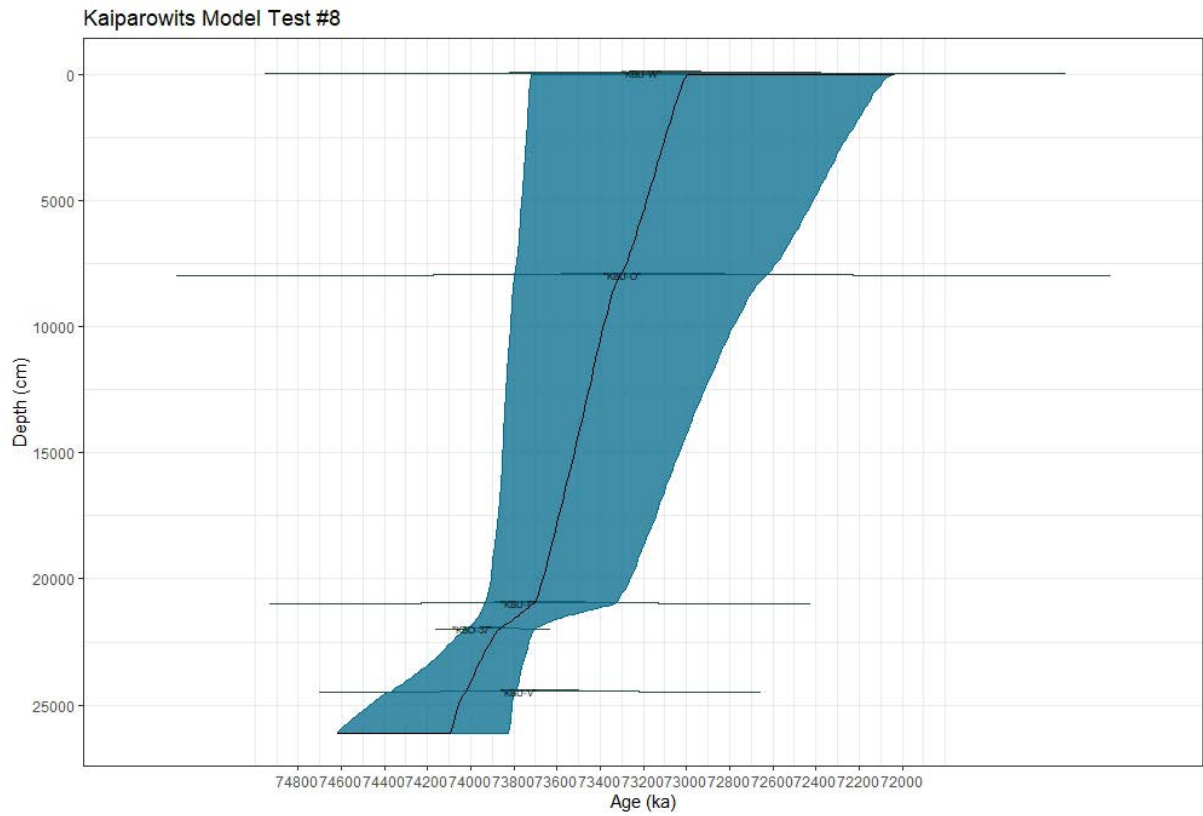
		Median	+	-	Max	Min	Range
Output 1 (Ma)	Top	74.84	0.28	0.62	75.12	74.22	0.89
	Base	76.95	0.56	0.34	77.51	76.61	0.90
Output 2 (Ma)	Top	74.84	0.28	0.64	75.12	74.20	0.92
	Base	76.95	0.57	0.35	77.52	76.60	0.92
Output 3 (Ma)	Top	74.84	0.28	0.63	75.12	74.21	0.91
	Base	76.96	0.57	0.35	77.53	76.61	0.92
Mean (Ma)	Top	74.84	0.28	0.63	75.12	74.21	0.91
	Base	76.95	0.57	0.35	77.52	76.60	0.91
Average	Top	0.000	0.002	0.008	0.002	0.008	0.010
Variance (Ma)	Base	0.003	0.003	0.006	0.006	0.004	0.008
Maximum	Top	0.00	0.84	2.00	0.00	0.02	1.60
Variance (%)	Base	0.01	0.87	2.50	0.01	0.01	1.39





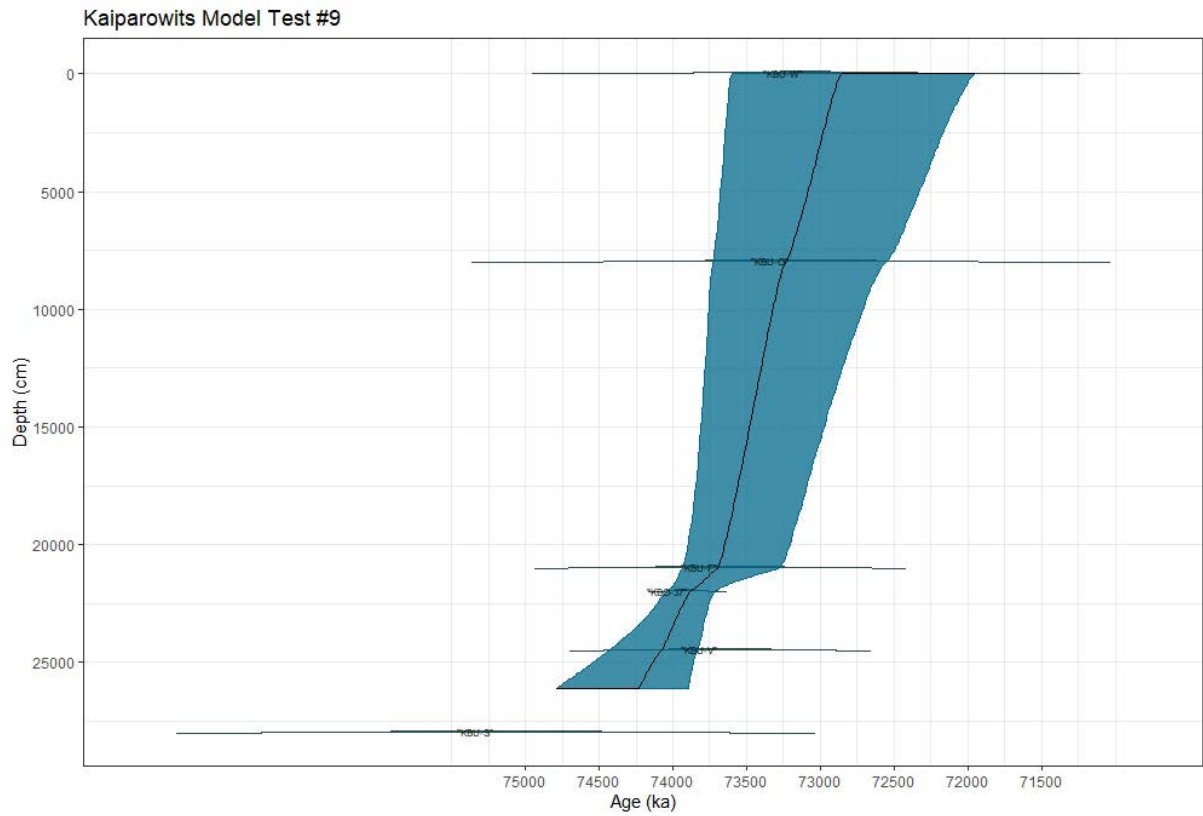
**Test 7: 750-1010 m with UVM MDAs**

		Median	+	-	Max	Min	Range
Output 1 (Ma)	Top	72.85	0.74	0.91	73.60	71.95	1.65
	Base	73.89	0.71	0.53	74.60	73.36	1.24
Output 2 (Ma)	Top	72.82	0.81	0.92	73.63	71.90	1.73
	Base	73.89	0.74	0.57	74.63	73.32	1.31
Output 3 (Ma)	Top	72.81	0.72	0.91	73.54	71.90	1.63
	Base	73.87	0.72	0.55	74.60	73.32	1.28
Mean (Ma)	Top	72.83	0.76	0.91	73.59	71.92	1.67
	Base	73.88	0.73	0.55	74.61	73.33	1.28
Average	Top	0.016	0.035	0.005	0.035	0.020	0.040
Variance (Ma)	Base	0.007	0.011	0.015	0.013	0.019	0.024
Maximum	Top	0.03	6.86	0.81	0.07	0.04	3.56
Variance (%)	Base	0.01	2.18	4.07	0.03	0.04	2.79



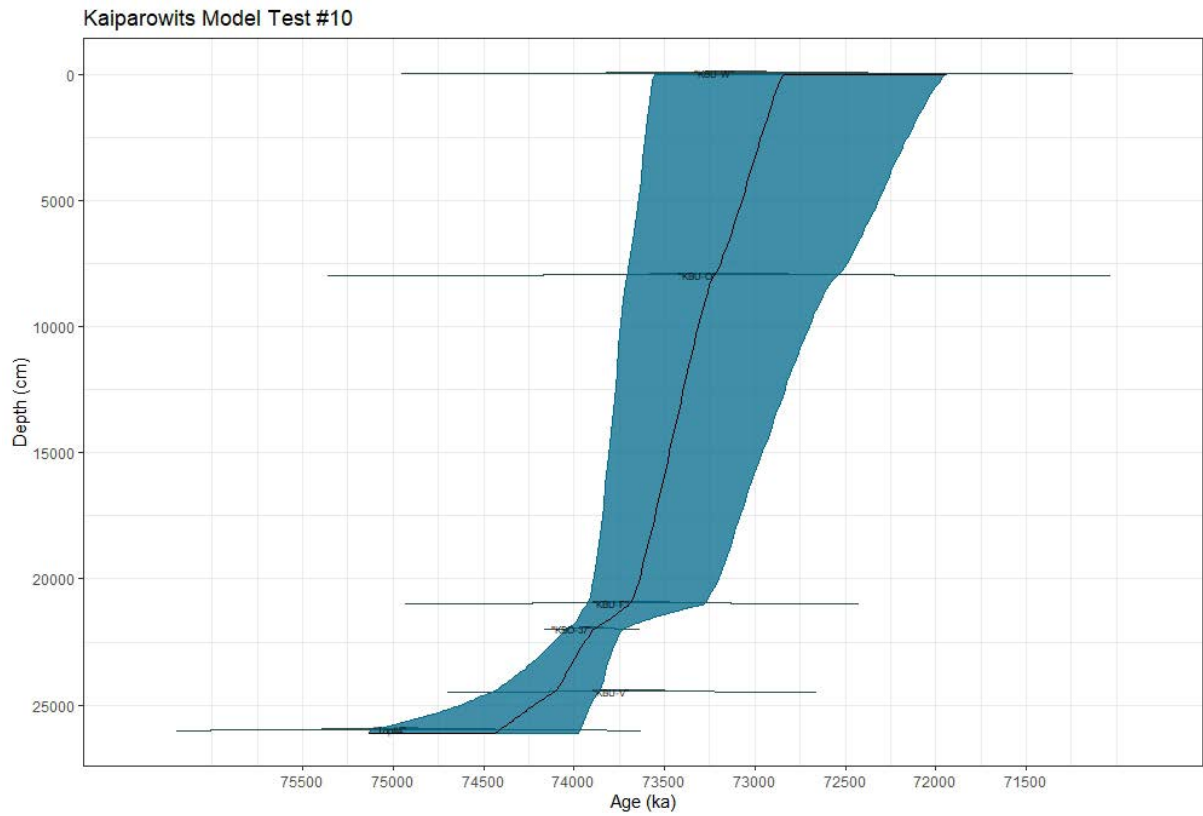
**Test 8: 750-1010 m with UVM MDAs plus KBO-37 single grain age**

		Median	+	-	Max	Min	Range
Output 1 (Ma)	Top	72.94	0.71	0.95	73.65	71.99	1.66
	Base	74.10	0.50	0.27	74.60	73.83	0.77
Output 2 (Ma)	Top	72.99	0.69	0.95	73.68	72.03	1.64
	Base	74.09	0.52	0.28	74.61	73.81	0.80
Output 3 (Ma)	Top	73.01	0.70	0.94	73.71	72.07	1.63
	Base	74.08	0.48	0.26	74.56	73.82	0.74
Mean (Ma)	Top	72.98	0.70	0.94	73.68	72.03	1.64
	Base	74.09	0.50	0.27	74.59	73.82	0.77
Average Variance (Ma)	Top	0.026	0.007	0.006	0.019	0.027	0.008
	Base	0.007	0.015	0.005	0.019	0.005	0.019
Maximum Variance (%)	Top	0.05	1.51	0.91	0.04	0.06	0.72
	Base	0.01	4.46	2.71	0.04	0.01	3.78



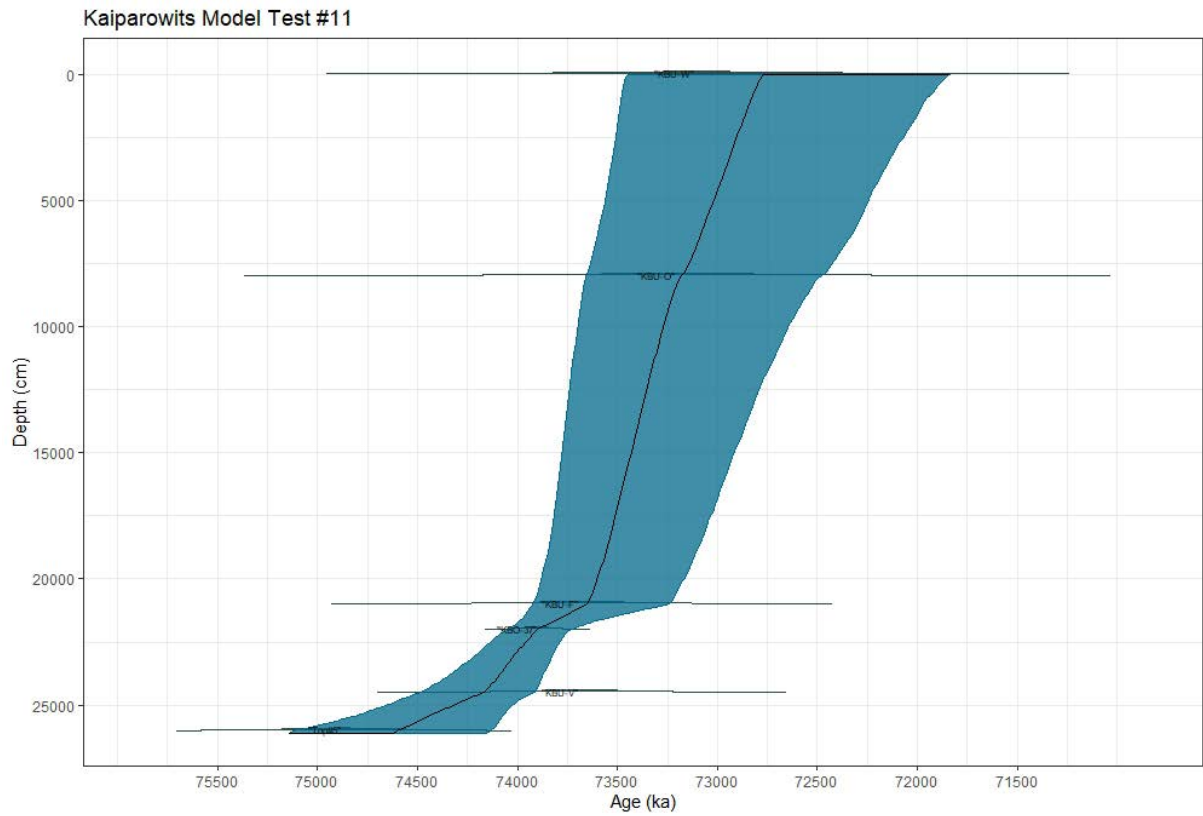
**Test 9: 750-1010 m with UVM MDAs plus KBU-S MDA**

		Median	+	-	Max	Min	Range
Output 1 (Ma)	Top	72.89	0.73	0.98	73.62	71.92	1.71
	Base	74.21	0.55	0.33	74.75	73.87	0.88
Output 2 (Ma)	Top	72.89	0.81	0.92	73.70	71.97	1.73
	Base	74.21	0.54	0.37	74.75	73.84	0.90
Output 3 (Ma)	Top	72.93	0.70	0.92	73.63	72.01	1.62
	Base	74.20	0.52	0.34	74.72	73.86	0.86
Mean (Ma)	Top	72.90	0.75	0.94	73.65	71.97	1.69
	Base	74.20	0.54	0.35	74.74	73.86	0.88
Average Variance (Ma)	Top	0.016	0.042	0.026	0.034	0.033	0.043
	Base	0.005	0.008	0.014	0.012	0.009	0.014
Maximum Variance (%)	Top	0.03	8.47	4.24	0.07	0.07	3.83
	Base	0.01	2.18	5.90	0.02	0.02	2.39



**Test 10: 750-1010 m with UVM MDAs plus top output from Test 4**

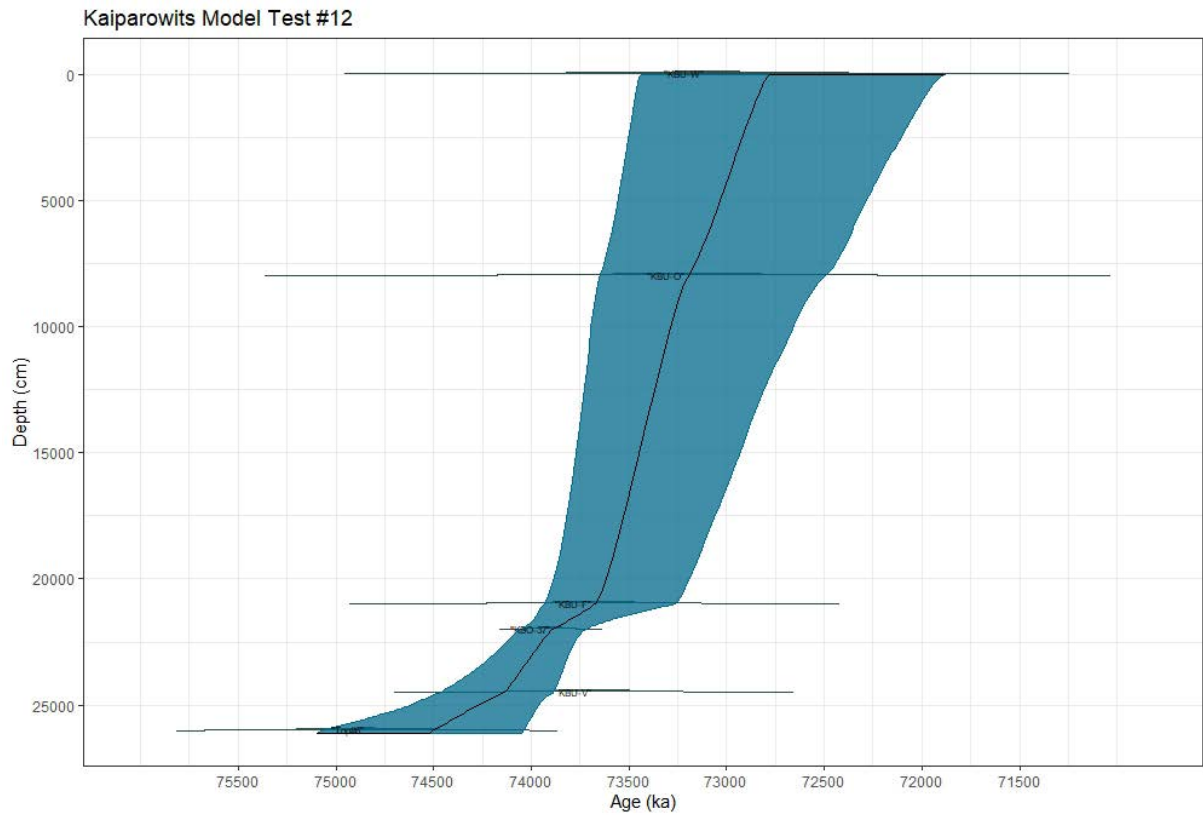
		Median	+	-	Max	Min	Range
Output 1 (Ma)	Top	72.86	0.73	0.93	73.59	71.92	1.67
	Base	74.40	0.69	0.46	75.09	73.95	1.15
Output 2 (Ma)	Top	72.85	0.70	0.96	73.55	71.89	1.66
	Base	74.41	0.68	0.47	75.10	73.94	1.16
Output 3 (Ma)	Top	72.84	0.72	0.88	73.56	71.96	1.60
	Base	74.43	0.67	0.45	75.11	73.98	1.12
Mean (Ma)	Top	72.85	0.72	0.92	73.57	71.93	1.64
	Base	74.42	0.68	0.46	75.10	73.96	1.14
Average	Top	0.007	0.013	0.033	0.014	0.026	0.029
Variance (Ma)	Base	0.010	0.005	0.009	0.005	0.018	0.013
Maximum	Top	0.01	2.65	5.30	0.03	0.05	2.68
Variance (%)	Base	0.02	1.12	3.06	0.01	0.04	1.72



**Test 11: 750-1010 m with UVM MDAs plus top output from Test 5**

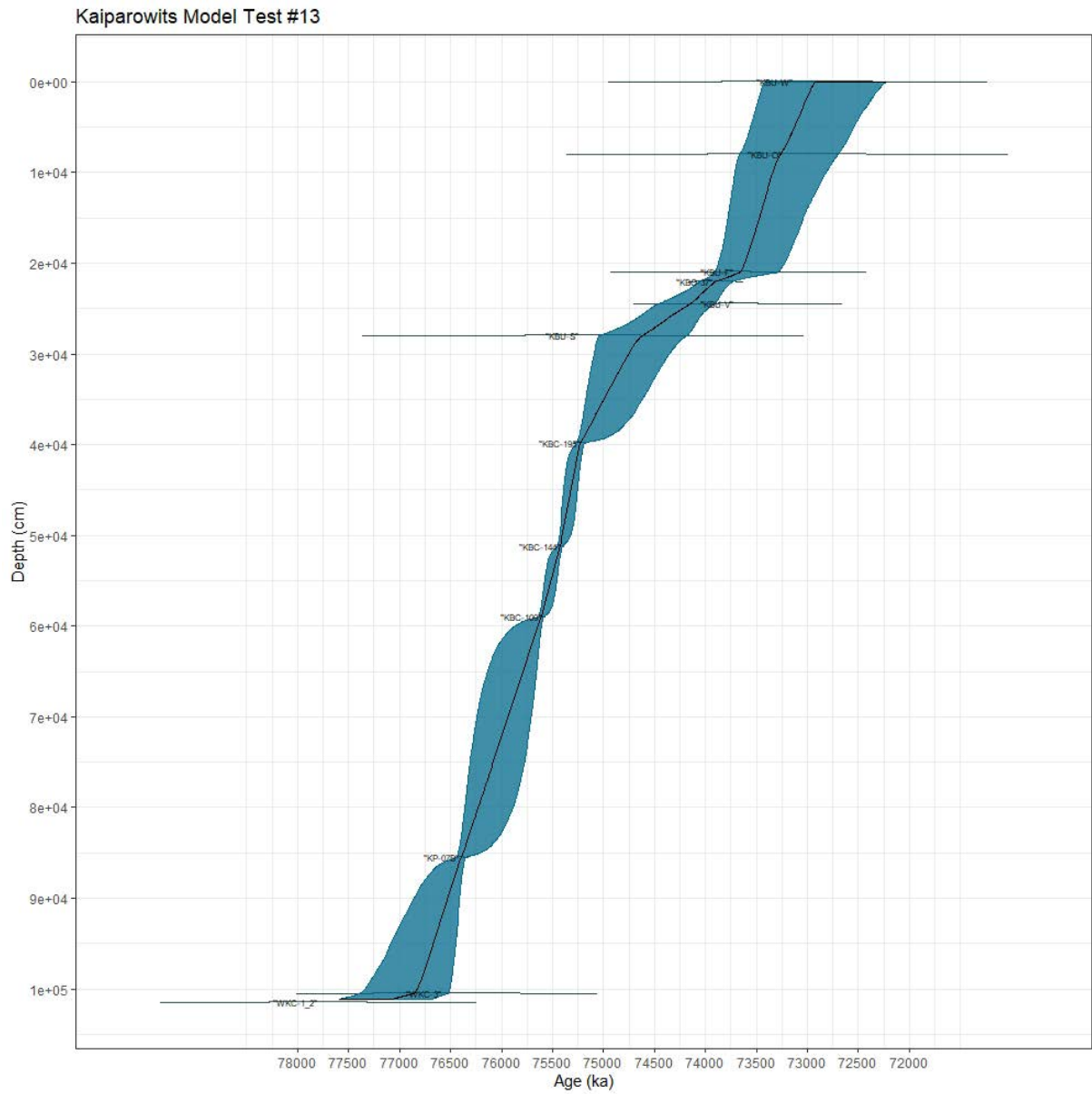
		Median	+	-	Max	Min	Range
Output 1 (Ma)	Top	72.78	0.65	0.90	73.43	71.88	1.55
	Base	74.59	0.50	0.47	75.10	74.12	0.97
Output 2 (Ma)	Top	72.77	0.67	0.91	73.45	71.87	1.58
	Base	74.59	0.51	0.47	75.10	74.12	0.98
Output 3 (Ma)	Top	72.75	0.68	0.92	73.44	71.84	1.60
	Base	74.60	0.50	0.49	75.10	74.11	0.99
Mean (Ma)	Top	72.77	0.67	0.91	73.44	71.86	1.58
	Base	74.60	0.50	0.48	75.10	74.12	0.98
Average	Top	0.009	0.011	0.008	0.005	0.017	0.017
Variance (Ma)	Base	0.004	0.005	0.007	0.003	0.003	0.006
Maximum	Top	0.02	2.49	1.25	0.01	0.03	1.62
Variance (%)	Base	0.01	1.36	2.20	0.01	0.01	0.99





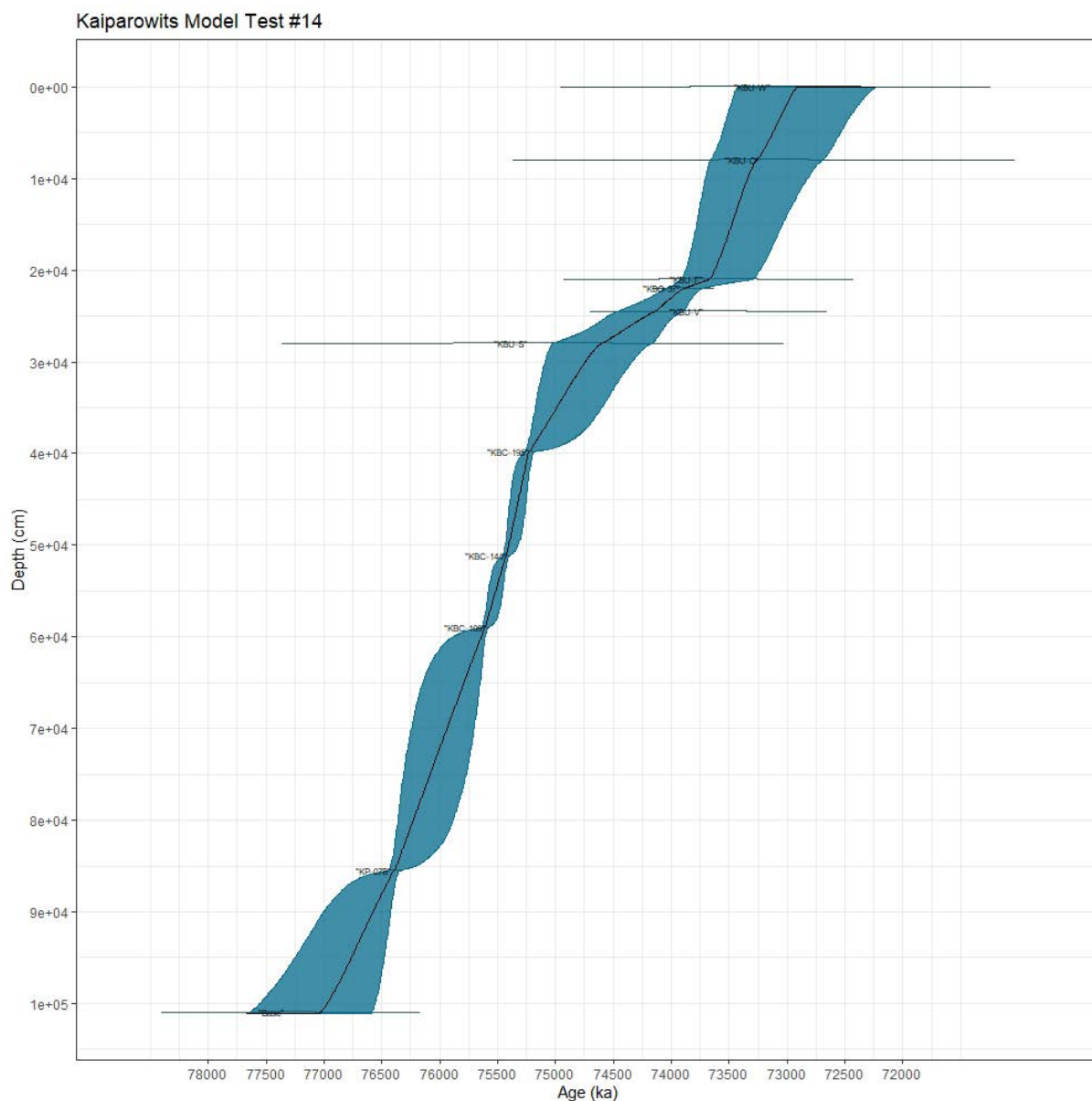
**Test 12: 750-1010 m with UVM MDAs plus top output from Test 6**

		Median	+	-	Max	Min	Range
Output 1 (Ma)	Top	72.82	0.67	0.91	73.48	71.91	1.58
	Base	74.50	0.57	0.46	75.07	74.04	1.03
Output 2 (Ma)	Top	72.83	0.70	0.85	73.53	71.97	1.56
	Base	74.50	0.56	0.46	75.05	74.04	1.02
Output 3 (Ma)	Top	72.81	0.68	0.88	73.49	71.93	1.55
	Base	74.51	0.58	0.45	75.09	74.06	1.03
Mean (Ma)	Top	72.82	0.68	0.88	73.50	71.94	1.56
	Base	74.50	0.57	0.46	75.07	74.05	1.03
Average	Top	0.006	0.013	0.019	0.019	0.023	0.009
Variance (Ma)	Base	0.005	0.006	0.002	0.011	0.007	0.005
Maximum	Top	0.01	2.92	3.22	0.04	0.05	0.87
Variance (%)	Base	0.01	1.65	0.80	0.02	0.01	0.79



**Test 13: 0-1010 m with type-section bentonites (Y uncertainty) plus all MDAs**

		Median	+	-	Max	Min	Range
Output 1 (Ma)	Top	72.91	0.50	0.71	73.41	72.20	1.21
	Base	77.05	0.54	0.39	77.59	76.66	0.93
Output 2 (Ma)	Top	72.90	0.51	0.69	73.41	72.22	1.20
	Base	77.04	0.52	0.39	77.56	76.65	0.91
Output 3 (Ma)	Top	72.91	0.51	0.69	73.42	72.22	1.20
	Base	77.04	0.54	0.38	77.58	76.66	0.92
Mean (Ma)	Top	72.90	0.51	0.70	73.41	72.21	1.20
	Base	77.04	0.53	0.39	77.58	76.66	0.92
Average	Top	0.002	0.003	0.009	0.004	0.009	0.007
Variance (Ma)	Base	0.003	0.010	0.002	0.011	0.003	0.008
Maximum	Top	0.00	0.82	2.01	0.01	0.02	0.82
Variance (%)	Base	0.01	2.68	0.76	0.02	0.01	1.33



**Test 14: 0-1010 m with type-section bentonites (Y uncert.) plus top Wah. Fm model age, KBU-S and UVM MDAs**

		Median	+	-	Max	Min	Range
Output 1 (Ma)	Top	72.91	0.51	0.70	73.42	72.21	1.21
	Base	77.05	0.60	0.46	77.65	76.59	1.06
Output 2 (Ma)	Top	72.91	0.52	0.69	73.44	72.22	1.21
	Base	77.04	0.60	0.46	77.65	76.58	1.07
Output 3 (Ma)	Top	72.90	0.51	0.68	73.41	72.22	1.19
	Base	77.05	0.59	0.46	77.64	76.59	1.05
Mean (Ma)	Top	72.91	0.51	0.69	73.42	72.22	1.20
	Base	77.05	0.60	0.46	77.65	76.58	1.06
Average	Top	0.004	0.006	0.004	0.010	0.004	0.009
	Base	0.003	0.007	0.002	0.004	0.003	0.006
Maximum	Top	0.01	1.76	0.97	0.02	0.01	1.06
	Base	0.01	1.84	0.58	0.01	0.01	0.82

*Appendix B.5.3 Summary of observations*

This informal investigation showed that differences between outputs with the same input data and variables are typically minimal and certainly represents precision finer than stratigraphic resolution dictates. The basal Kaiparowits Fm boundary median age across all tests was shown to vary by ca 0.3 Myrs, which falls well within the 0.75 to 1.28 Myr modelled confidence window. Distinctions between outputs for the lower three members modelled separately to the Upper Valley Member were more notable. Although the differences in median ages for the Powell Point Mbr – Upper Valley Mbr boundary across the relevant tests fell within the modelled uncertainty windows, this offset may suggest a possible depositional hiatus or meaningful change in depositional rate or character at or across the member boundary. The top Kaiparowits Fm boundary median age was found to be (surprisingly) consistent across all relevant tests with only ca 0.2 Myrs variation within uncertainty windows ranging from 1.20 to 1.69 Myrs. This uncertainty range remains larger than in the lower three members of the formation, which suggests more geochronologic constraint is required in the Upper Valley Member to reduce the uncertainty of the model in that portion of the formation. The relatively large uncertainty should account for possible sedimentological complications such as depositional hiatuses or sudden changes in depositional rate or character, although future geochronologic constraint (e.g., magnetostratigraphy? See Ch.5) may aid in more explicit identification of these features.

This testing confirmed that the inclusion of as much data as possible is the most appropriate course of action. One modification to this statement is that the top Wahweap Fm model age is preferred over the inclusion of the two bracketing MDAs because these MDAs were included in the Wahweap model, and the use of the model age facilitates consistent age reporting between the two conformable units. Until such time that a depositional hiatus of (inferred) significant duration is identified from field relationships between the Powell Point and Upper Valley members, it is recommended that the four subdivisions are modelled together. As such, the data input parameters from Test #14 will be applied for age-stratigraphic modelling of the Kaiparowits Formation.

*Appendix B.5.4 References*

Baresel, B., Bucher, H., Brosse, M., Cordey, F., Kuang Guodun, & Schaltegger, U. (2017). Precise age for the Permian-Triassic boundary in south China from high-precision U-Pb geochronology and Bayesian age-depth modeling. *Solid Earth (Göttingen)*, 8(2), 361-378. doi.org/10.5194/se-8-361-2017

Haslett, J. & Parnell, A. (2008). A simple monotone process with application to radiocarbon-dated depth chronologies. *Journal of the Royal Statistical Society Series C*, 57(4), 399-418. doi.org/10.1111/j.1467-9876.2008.00623.x

Parnell, A. C., Haslett, J., Allen, J. R. M., Buck, C. E., & Huntley, B. (2008). A flexible approach to assessing synchronicity of past events using Bayesian reconstructions of sedimentation history. *Quaternary Science Reviews*, 27(19-20), 1872-1885. doi.org/10.1016/j.quascirev.2008.07.009





# Appendix C

Data Repository

## Appendix C.1 No Data Statement

No appended data are included for Chapters One and Seven.

## Appendix C.2 Chapter Two Data

Preliminary CA-ID-TIMS data (current upon completion of the candidate's work at MIT in 2018) are included here for samples included in Chapter Two except for those intended for future publications not yet confirmed at the time of thesis submission (PR082917-1, NF082917-1). See journal publications or the relevant chapters for finalized age data.

IL082717-1

Fraction	Composition			Isotopic Ratios					Dates (Ma)									
	Pbc (pg)	Pb*/Pbc <sup>a</sup>	Th/U	<sup>206</sup> Pb/ <sup>204</sup> Pb <sup>d</sup>	<sup>208</sup> Pb/ <sup>206</sup> Pb <sup>e</sup>	<sup>206</sup> Pb/ <sup>238</sup> U <sup>f</sup>	±2σ %	<sup>207</sup> Pb/ <sup>235</sup> U <sup>g</sup>	±2σ %	<sup>207</sup> Pb/ <sup>206</sup> Pb <sup>h</sup>	±2σ %	<sup>206</sup> Pb/ <sup>238</sup> U <sup>f</sup>	±2σ abs	<sup>207</sup> Pb/ <sup>235</sup> U <sup>g</sup>	±2σ abs	<sup>207</sup> Pb/ <sup>206</sup> Pb <sup>h</sup>	±2σ abs	Corr. coef.
Sort																		
Zircon																		
N z1	0.36	51.61	0.47	3118	0.149	0.0115816	0.047	0.07618	0.42	0.04773	0.41	74.231	0.034	74.55	0.30	84.7	9.7	0.329
N z2	0.30	53.78	0.48	3239	0.152	0.0115717	0.037	0.07602	0.40	0.04767	0.39	74.168	0.027	74.39	0.29	81.7	9.4	0.238
N z3	0.55	24.06	0.55	1433	0.175	0.0115763	0.079	0.07645	0.90	0.04792	0.88	74.197	0.058	74.81	0.65	94	21	0.306
N z5	0.31	42.02	0.51	2511	0.164	0.0115832	0.065	0.07615	0.57	0.04770	0.55	74.241	0.048	74.52	0.41	83	13	0.314
N z6	0.36	39.94	0.53	2379	0.168	0.0115725	0.053	0.07618	0.54	0.04777	0.53	74.173	0.039	74.55	0.39	87	13	0.313
N z9	0.40	36.10	0.52	2154	0.167	0.0115837	0.056	0.07627	0.60	0.04777	0.59	74.244	0.041	74.63	0.43	87	14	0.282
N z10	0.47	27.49	0.55	1633	0.176	0.0115770	0.066	0.07624	0.78	0.04778	0.76	74.201	0.049	74.60	0.56	88	18	0.315

KBO-37/KBO05056-1

Fraction	Composition			Isotopic Ratios					Dates (Ma)									
	Pbc (pg)	Pb*/Pbc <sup>a</sup>	Th/U	<sup>206</sup> Pb/ <sup>204</sup> Pb <sup>d</sup>	<sup>208</sup> Pb/ <sup>206</sup> Pb <sup>e</sup>	<sup>206</sup> Pb/ <sup>238</sup> U <sup>f</sup>	±2σ %	<sup>207</sup> Pb/ <sup>235</sup> U <sup>g</sup>	±2σ %	<sup>207</sup> Pb/ <sup>206</sup> Pb <sup>h</sup>	±2σ %	<sup>206</sup> Pb/ <sup>238</sup> U <sup>f</sup>	±2σ abs	<sup>207</sup> Pb/ <sup>235</sup> U <sup>g</sup>	±2σ abs	<sup>207</sup> Pb/ <sup>206</sup> Pb <sup>h</sup>	±2σ abs	Corr. coef.
Sort																		
Zircon																		
N z1	0.33	13.30	0.77	757	0.247	0.011691	0.12	0.0768	1.8	0.04765	1.8	74.927	0.091	75.1	1.3	81	42	0.228
N z2	0.63	5.63	0.95	317	0.302	0.011720	0.32	0.0779	4.2	0.0482	4.1	75.11	0.24	76.1	3.0	108	96	0.330
N z3	0.28	5.71	1.23	303	0.391	0.011706	0.36	0.0775	4.5	0.0481	4.4	75.02	0.27	75.8	3.3	101	100	0.379
N z4	0.23	115.10	2.22	4678	0.685	0.113375	0.047	1.3397	0.17	0.08574	0.16	692.32	0.31	863.08	0.98	1331.4	3.1	0.316

Fraction	Composition			Isotopic Ratios					Dates (Ma)									
	Pbc (pg)	Pb*/Pbc <sup>a</sup>	Th/U	<sup>206</sup> Pb/ <sup>204</sup> Pb <sup>d</sup>	<sup>208</sup> Pb/ <sup>206</sup> Pb <sup>e</sup>	<sup>206</sup> Pb/ <sup>238</sup> U <sup>f</sup>	±2σ %	<sup>207</sup> Pb/ <sup>235</sup> U <sup>g</sup>	±2σ %	<sup>207</sup> Pb/ <sup>206</sup> Pb <sup>h</sup>	±2σ %	<sup>206</sup> Pb/ <sup>238</sup> U <sup>f</sup>	±2σ abs	<sup>207</sup> Pb/ <sup>235</sup> U <sup>g</sup>	±2σ abs	<sup>207</sup> Pb/ <sup>206</sup> Pb <sup>h</sup>	±2σ abs	Corr. coef.
Sort																		
Zircon																		
N z1	0.17	12.56	0.73	722	0.232	0.011700	0.16	0.0785	1.8	0.04869	1.8	74.98	0.12	76.7	1.3	132	42	0.351
N z2	0.20	125.82	0.79	6753	0.247	0.083218	0.053	1.0933	0.14	0.09533	0.11	515.30	0.26	750.09	0.73	1533.7	2.1	0.651
N z3	0.24	26.01	0.79	1454	0.253	0.011685	0.091	0.07715	0.92	0.04791	0.89	74.890	0.067	75.46	0.67	94	21	0.367
N z4	0.24	22.67	0.70	1300	0.222	0.011679	0.093	0.07745	0.99	0.04812	0.96	74.852	0.069	75.75	0.72	104	23	0.335
N z5	0.23	25.33	0.79	1416	0.254	0.011682	0.10	0.07656	0.98	0.04755	0.95	74.873	0.077	74.90	0.71	76	23	0.318
N z6	0.20	8.10	0.87	456	0.279	0.011530	0.23	0.0773	2.9	0.0487	2.8	73.90	0.17	75.6	2.1	131	66	0.344
N z7	0.32	3.16	0.95	186	0.302	0.011677	0.67	0.0780	7.7	0.0485	7.5	74.84	0.50	76.3	5.7	123	180	0.341
N z8	0.28	5.44	0.80	317	0.256	0.011715	0.33	0.0787	4.1	0.0487	4.0	75.08	0.25	76.9	3.1	133	95	0.335
N z9	0.31	2.75	0.95	164	0.304	0.011713	0.67	0.0785	8.5	0.0486	8.3	75.07	0.50	76.7	6.3	129	200	0.338

KBC-195

Fraction	Composition			Isotopic Ratios					Dates (Ma)									
	Pbc (pg)	Pb*/Pbc <sup>a</sup>	Th/U	<sup>206</sup> Pb/ <sup>204</sup> Pb <sup>d</sup>	<sup>208</sup> Pb/ <sup>206</sup> Pb <sup>e</sup>	<sup>206</sup> Pb/ <sup>238</sup> U <sup>f</sup>	±2σ %	<sup>207</sup> Pb/ <sup>235</sup> U <sup>g</sup>	±2σ %	<sup>207</sup> Pb/ <sup>206</sup> Pb <sup>h</sup>	±2σ %	<sup>206</sup> Pb/ <sup>238</sup> U <sup>f</sup>	±2σ abs	<sup>207</sup> Pb/ <sup>235</sup> U <sup>g</sup>	±2σ abs	<sup>207</sup> Pb/ <sup>206</sup> Pb <sup>h</sup>	±2σ abs	Corr. coef.
Sort																		
Zircon																		
N z1	0.22	84.40	0.62	4889	0.197	0.0117227	0.053	0.07708	0.28	0.04771	0.26	75.130	0.039	75.39	0.21	83.8	6.3	0.423
N z3	1.18	16.08	0.56	960	0.179	0.011722	0.11	0.0775	1.3	0.04796	1.3	75.127	0.085	75.77	0.97	96	31	0.332
N z4	0.23	91.67	0.55	5402	0.176	0.0117275	0.065	0.07703	0.30	0.04766	0.28	75.160	0.048	75.35	0.22	81.4	6.7	0.362
N z5	0.19	61.77	0.54	3653	0.174	0.0117221	0.059	0.07697	0.39	0.04764	0.37	75.126	0.044	75.29	0.28	80.6	8.9	0.348
N z8	0.23	55.15	0.60	3218	0.191	0.0117283	0.058	0.07712	0.43	0.04771	0.41	75.166	0.043	75.44	0.31	84.0	9.8	0.279
N z9	1.01	3.68	0.62	230	0.198	0.011746	0.45	0.0806	5.6	0.0498	5.5	75.28	0.34	78.7	4.3	184	130	0.325
N z10	0.33	9.01	0.84	510	0.268	0.011750	0.20	0.0786	2.5	0.0485	2.5	75.31	0.15	76.8	1.9	124	59	0.301
N z11	0.34	16.40	0.71	942	0.228	0.011732	0.11	0.0772	1.4	0.04777	1.3	75.190	0.086	75.5	1.0	87	32	0.317

KBC-144

Fraction	Composition			Isotopic Ratios						Dates (Ma)						Corr. coef.		
	Pbc (pg) <sup>a</sup>	Pb*/Pbc <sup>b</sup>	Th/U <sup>c</sup>	<sup>206</sup> Pb/ <sup>204</sup> Pb <sup>d</sup>	<sup>208</sup> Pb/ <sup>206</sup> Pb <sup>e</sup>	<sup>206</sup> Pb/ <sup>238</sup> U <sup>f</sup>	±2σ %	<sup>207</sup> Pb/ <sup>235</sup> U <sup>g</sup>	±2σ %	<sup>207</sup> Pb/ <sup>206</sup> Pb <sup>h</sup>	±2σ %	<sup>206</sup> Pb/ <sup>238</sup> U <sup>i</sup>	±2σ abs	<sup>207</sup> Pb/ <sup>235</sup> U <sup>j</sup>	±2σ abs		<sup>207</sup> Pb/ <sup>206</sup> Pb <sup>k</sup>	±2σ abs
Sort	▲▼	▲▼	▲▼	▲▼	▲▼	▲▼	▲▼	▲▼	▲▼	▲▼	▲▼	▲▼	▲▼	▲▼	▲▼	▲▼	▲▼	
Zircon																		
N z1	0.29	127.53	0.71	7204	0.227	0.0117568	0.032	0.07717	0.19	0.047628	0.19	75.347	0.024	75.48	0.14	79.8	4.5	0.259
N z2	0.39	78.07	0.53	4632	0.169	0.0117523	0.041	0.07713	0.29	0.04762	0.28	75.319	0.031	75.44	0.21	79.4	6.7	0.292
N z3	0.36	131.90	0.44	7994	0.141	0.0117751	0.035	0.07735	0.17	0.047667	0.16	75.464	0.026	75.65	0.12	81.7	3.8	0.316
N z4	0.33	75.91	0.57	4456	0.181	0.0117539	0.048	0.07714	0.32	0.04762	0.31	75.329	0.036	75.45	0.23	79.3	7.4	0.327
N z5	0.26	144.46	0.52	8578	0.165	0.0117669	0.046	0.07737	0.22	0.047708	0.20	75.412	0.034	75.67	0.16	83.7	4.8	0.492
N z6	0.32	92.32	0.52	5486	0.166	0.0117630	0.045	0.07724	0.25	0.04764	0.24	75.387	0.034	75.54	0.18	80.5	5.6	0.249
N z7	0.25	110.32	0.55	6504	0.175	0.0117604	0.036	0.07728	0.21	0.047682	0.20	75.370	0.027	75.59	0.15	82.4	4.7	0.303
N z8	0.35	81.23	0.43	4942	0.138	0.0117572	0.034	0.07740	0.26	0.04777	0.25	75.350	0.026	75.70	0.19	86.8	6.1	0.264
N z9	0.40	242.43	0.50	14468	0.158	0.0117622	0.031	0.077250	0.11	0.047654	0.093	75.382	0.023	75.556	0.078	81.1	2.3	0.390
N z10	0.41	91.79	0.43	5582	0.138	0.0117723	0.066	0.07733	0.25	0.04766	0.23	75.446	0.050	75.63	0.18	81.5	5.5	0.391
N z11	0.35	48.15	0.42	2944	0.135	0.0117515	0.052	0.07706	0.45	0.04758	0.44	75.314	0.039	75.38	0.33	77	10	0.305
N z12	0.29	38.42	0.46	2331	0.146	0.0117512	0.053	0.07730	0.56	0.04773	0.54	75.311	0.040	75.61	0.41	85	13	0.348

KWC050316-3

Fraction	Composition			Isotopic Ratios						Dates (Ma)						Corr. coef.		
	Pbc (pg) <sup>a</sup>	Pb*/Pbc <sup>b</sup>	Th/U <sup>c</sup>	<sup>206</sup> Pb/ <sup>204</sup> Pb <sup>d</sup>	<sup>208</sup> Pb/ <sup>206</sup> Pb <sup>e</sup>	<sup>206</sup> Pb/ <sup>238</sup> U <sup>f</sup>	±2σ %	<sup>207</sup> Pb/ <sup>235</sup> U <sup>g</sup>	±2σ %	<sup>207</sup> Pb/ <sup>206</sup> Pb <sup>h</sup>	±2σ %	<sup>206</sup> Pb/ <sup>238</sup> U <sup>i</sup>	±2σ abs	<sup>207</sup> Pb/ <sup>235</sup> U <sup>j</sup>	±2σ abs		<sup>207</sup> Pb/ <sup>206</sup> Pb <sup>k</sup>	±2σ abs
Sort	▲▼	▲▼	▲▼	▲▼	▲▼	▲▼	▲▼	▲▼	▲▼	▲▼	▲▼	▲▼	▲▼	▲▼	▲▼	▲▼	▲▼	
Zircon																		
N z2	0.46	22.97	0.92	1247	0.294	0.011781	0.095	0.07769	1.0	0.04785	1.0	75.500	0.071	75.97	0.75	91	24	0.332
N z3	0.45	8.09	1.06	438	0.337	0.011800	0.24	0.0785	3.0	0.0483	2.9	75.62	0.18	76.7	2.2	111	69	0.332
N z4	0.30	7.82	0.76	453	0.244	0.011766	0.23	0.0782	2.9	0.0482	2.9	75.40	0.18	76.4	2.2	108	68	0.356
N z5	0.50	9.38	1.00	511	0.319	0.011758	0.35	0.0790	2.8	0.0488	2.6	75.36	0.26	77.2	2.1	136	62	0.508
N z6	0.37	5.12	1.06	283	0.339	0.011785	0.38	0.0785	5.3	0.0483	5.2	75.53	0.29	76.7	3.9	113	120	0.416
N z7	0.86	4.34	1.06	242	0.338	0.011767	0.44	0.0814	5.4	0.0502	5.3	75.41	0.33	79.4	4.1	203	120	0.354
N z8	0.30	30.67	0.78	1718	0.248	0.0117754	0.081	0.07768	0.78	0.04787	0.76	75.466	0.061	75.97	0.57	92	18	0.317
N z11	0.30	12.08	1.08	641	0.345	0.011799	0.17	0.0781	2.0	0.04801	2.0	75.62	0.13	76.3	1.5	99	47	0.354

KBC-109

Fraction	Composition			Isotopic Ratios						Dates (Ma)						Corr. coef.		
	Pbc (pg) <sup>a</sup>	Pb*/Pbc <sup>b</sup>	Th/U <sup>c</sup>	<sup>206</sup> Pb/ <sup>204</sup> Pb <sup>d</sup>	<sup>208</sup> Pb/ <sup>206</sup> Pb <sup>e</sup>	<sup>206</sup> Pb/ <sup>238</sup> U <sup>f</sup>	±2σ %	<sup>207</sup> Pb/ <sup>235</sup> U <sup>g</sup>	±2σ %	<sup>207</sup> Pb/ <sup>206</sup> Pb <sup>h</sup>	±2σ %	<sup>206</sup> Pb/ <sup>238</sup> U <sup>i</sup>	±2σ abs	<sup>207</sup> Pb/ <sup>235</sup> U <sup>j</sup>	±2σ abs		<sup>207</sup> Pb/ <sup>206</sup> Pb <sup>k</sup>	±2σ abs
Sort	▲▼	▲▼	▲▼	▲▼	▲▼	▲▼	▲▼	▲▼	▲▼	▲▼	▲▼	▲▼	▲▼	▲▼	▲▼	▲▼	▲▼	
Zircon																		
N z1	0.36	98.41	0.82	5410	0.263	0.0117855	0.034	0.07753	0.24	0.04773	0.23	75.530	0.025	75.82	0.18	85.1	5.6	0.246
N z2	0.55	52.92	0.85	2902	0.270	0.0117874	0.046	0.07760	0.44	0.04777	0.43	75.542	0.035	75.89	0.32	87	10	0.293
N z3	0.42	62.32	0.94	3336	0.301	0.0117829	0.046	0.07753	0.39	0.04774	0.38	75.513	0.035	75.82	0.28	85.4	9.0	0.190
N z4	0.37	77.95	0.89	4224	0.283	0.0117876	0.041	0.07758	0.32	0.04776	0.30	75.544	0.030	75.87	0.23	86.1	7.2	0.405
N z5	1.21	4.94	1.08	273	0.345	0.011806	0.39	0.0791	4.9	0.0486	4.7	75.66	0.29	77.3	3.6	128	110	0.333
N z6	0.35	36.20	0.74	2046	0.235	0.0117872	0.059	0.07759	0.63	0.04776	0.62	75.541	0.044	75.88	0.46	87	15	0.308
N z7	0.27	17.35	0.66	1009	0.210	0.011792	0.11	0.0780	1.3	0.04800	1.2	75.574	0.086	76.27	0.95	98	29	0.416
N z8	0.29	12.70	0.90	702	0.286	0.011819	0.15	0.0786	1.9	0.04828	1.9	75.75	0.11	76.9	1.4	112	44	0.274
N z9	0.82	5.87	0.95	329	0.305	0.011807	0.32	0.0789	4.1	0.0485	4.0	75.67	0.24	77.1	3.0	122	93	0.349

KWC050316-1

Fraction	Composition			Isotopic Ratios						Dates (Ma)						Correlation Co		
	Pbc (pg) <sup>a</sup>	Pb*/Pbc <sup>b</sup>	Th/U <sup>c</sup>	<sup>206</sup> Pb/ <sup>204</sup> Pb <sup>d</sup>	<sup>208</sup> Pb/ <sup>206</sup> Pb <sup>e</sup>	<sup>206</sup> Pb/ <sup>238</sup> U <sup>f</sup>	±2σ %	<sup>207</sup> Pb/ <sup>235</sup> U <sup>g</sup>	±2σ %	<sup>207</sup> Pb/ <sup>206</sup> Pb <sup>h</sup>	±2σ %	<sup>206</sup> Pb/ <sup>238</sup> U <sup>i</sup>	±2σ abs	<sup>207</sup> Pb/ <sup>235</sup> U <sup>j</sup>	±2σ abs		<sup>207</sup> Pb/ <sup>206</sup> Pb <sup>k</sup>	±2σ abs
Sort	▲▼	▲▼	▲▼	▲▼	▲▼	▲▼	▲▼	▲▼	▲▼	▲▼	▲▼	▲▼	▲▼	▲▼	▲▼	▲▼	▲▼	
Zircon																		
N z1	0.32	37.59	0.56	2222	0.178	0.011844	0.066	0.07806	0.58	0.047821	0.56	75.900	0.050	76.32	0.43	89	13	0.34
N z2	0.35	10.57	0.49	648	0.158	0.011864	0.17	0.0796	2.2	0.048705	2.1	76.03	0.12	77.8	1.6	133	50	0.33
N z3	0.37	14.52	0.45	894	0.144	0.011874	0.13	0.0775	1.5	0.047361	1.5	76.09	0.10	75.8	1.1	66	35	0.38
N z4	0.27	86.97	0.40	5332	0.129	0.011871	0.065	0.07803	0.28	0.047692	0.25	76.074	0.049	76.29	0.21	83.0	6.1	0.48
N z5	0.23	8.69	0.81	496	0.258	0.011860	0.22	0.0791	2.7	0.048407	2.6	76.00	0.17	77.3	2.0	118	61	0.34
N z6	0.26	46.83	0.42	2868	0.133	0.011840	0.060	0.07793	0.47	0.047756	0.45	75.879	0.045	76.19	0.34	86	11	0.32
N z7	0.25	6.68	0.62	403	0.199	0.011854	0.26	0.0785	3.2	0.048074	3.1	75.97	0.20	76.8	2.3	102	73	0.33



KDR-5B/KDR050416-1

Fraction	Composition			Isotopic Ratios					Dates (Ma)								Correlation Coef. 206Pb/238U 207Pb/235U		
	Pbc (pg)	Pb*/Pbc <sup>a</sup>	Th/UF	206Pb/204Pb <sup>a</sup>	208Pb/206Pb <sup>a</sup>	206Pb/238U <sup>a</sup>	±2σ %	207Pb/235U <sup>a</sup>	±2σ %	207Pb/206Pb <sup>a</sup>	±2σ %	206Pb/238U <sup>b</sup>	±2σ abs	207Pb/235U <sup>b</sup>	±2σ abs	207Pb/206Pb <sup>b</sup>		±2σ abs	% disc
Zircon																			
N Lz12	0.24	34	1.26	1706	0.402	0.0119118	0.065	0.07866	0.75	0.04792	0.73	76.335	0.050	76.89	0.56	94	17	18.88	0.34
N Lz13	0.25	90	1.12	4614	0.358	0.0118884	0.035	0.07827	0.29	0.04777	0.28	76.185	0.026	76.52	0.21	86.8	6.6	12.26	0.26
N Lz14	0.25	19	1.35	916	0.432	0.011906	0.12	0.0790	1.4	0.04816	1.4	76.300	0.088	77.2	1.1	106	33	27.91	0.33
N z1	0.25	52	1.34	2554	0.426	0.0118953	0.050	0.07837	0.52	0.04781	0.50	76.229	0.038	76.61	0.38	89	12	14.02	0.31
N z3	0.32	18	1.34	889	0.428	0.012128	0.14	0.0798	1.5	0.04776	1.5	77.71	0.10	78.0	1.1	86	35	9.91	0.36
N z4	0.27	80	1.05	4148	0.336	0.0118870	0.045	0.07831	0.32	0.04780	0.31	76.177	0.034	76.55	0.23	88.4	7.4	13.78	0.20
N z5	0.42	52	1.08	2690	0.343	0.0118921	0.073	0.07836	0.57	0.04781	0.55	76.209	0.055	76.60	0.42	89	13	14.19	0.34
N z6	0.83	7	1.66	327	0.530	0.012067	0.31	0.0808	4.0	0.0486	3.9	77.32	0.24	78.9	3.0	126	91	38.65	0.33
N z7	0.46	4	1.52	188	0.484	0.012087	0.60	0.0830	7.7	0.0498	7.6	77.45	0.46	81.0	6.0	186	180	58.37	0.34
N z8	0.29	19	0.94	1050	0.299	0.011977	0.10	0.07930	1.2	0.04804	1.2	76.748	0.079	77.48	0.92	100	28	23.46	0.35
N z9	0.45	7	1.57	362	0.501	0.012045	0.28	0.0801	3.6	0.0482	3.5	77.18	0.22	78.2	2.7	110	84	29.75	0.33
N z10	0.47	15	2.27	626	0.725	0.012071	0.17	0.0793	2.1	0.04766	2.0	77.35	0.13	77.5	1.5	81	48	4.92	0.33

KWC050316-2

Fraction	Composition			Isotopic Ratios					Dates (Ma)								Corr. coef.	
	Pbc (pg)	Pb*/Pbc <sup>a</sup>	Th/UF	206Pb/204Pb <sup>a</sup>	208Pb/206Pb <sup>a</sup>	206Pb/238U <sup>a</sup>	±2σ %	207Pb/235U <sup>a</sup>	±2σ %	207Pb/206Pb <sup>a</sup>	±2σ %	206Pb/238U <sup>b</sup>	±2σ abs	207Pb/235U <sup>b</sup>	±2σ abs	207Pb/206Pb <sup>b</sup>		±2σ abs
Zircon																		
N z1	0.37	19.87	1.71	913	0.546	0.011904	0.12	0.0777	1.4	0.04736	1.4	76.284	0.094	76.0	1.1	66	34	0.337
N z2	0.29	42.63	1.46	2037	0.468	0.0119005	0.073	0.07843	0.64	0.04782	0.62	76.263	0.055	76.66	0.47	89	15	0.341
N z3	0.32	25.15	1.25	1265	0.399	0.011908	0.10	0.07884	1.0	0.04804	1.0	76.311	0.078	77.05	0.76	100	24	0.335
N z4	0.31	19.56	1.51	935	0.483	0.011898	0.12	0.0785	1.4	0.04789	1.4	76.244	0.090	76.8	1.0	93	33	0.336
N z5	0.27	14.60	1.62	688	0.517	0.011890	0.15	0.0780	1.9	0.04759	1.9	76.19	0.12	76.3	1.4	78	44	0.337
N z6	0.35	23.39	1.31	1163	0.418	0.011912	0.10	0.07865	1.1	0.04791	1.1	76.333	0.077	76.88	0.82	94	26	0.327
N z7	0.33	33.85	1.32	1671	0.422	0.0119049	0.076	0.07847	0.77	0.04783	0.75	76.291	0.058	76.71	0.57	90	18	0.341
N z8	0.24	47.74	1.38	2318	0.442	0.0119052	0.064	0.07835	0.56	0.04775	0.54	76.293	0.049	76.60	0.42	86	13	0.350
N z9	0.52	17.90	1.02	954	0.325	0.011898	0.11	0.0785	1.3	0.04788	1.3	76.245	0.087	76.74	0.99	92	31	0.332

KP-07A

Fraction	Composition			Isotopic Ratios					Dates (Ma)								Corr. coef.	
	Pbc (pg)	Pb*/Pbc <sup>a</sup>	Th/UF	206Pb/204Pb <sup>a</sup>	208Pb/206Pb <sup>a</sup>	206Pb/238U <sup>a</sup>	±2σ %	207Pb/235U <sup>a</sup>	±2σ %	207Pb/206Pb <sup>a</sup>	±2σ %	206Pb/238U <sup>b</sup>	±2σ abs	207Pb/235U <sup>b</sup>	±2σ abs	207Pb/206Pb <sup>b</sup>		±2σ abs
Zircon																		
N Lz1	0.39	9.20	1.22	477	0.391	0.011915	0.22	0.0803	2.7	0.0489	2.6	76.35	0.16	78.4	2.0	142	62	0.340
N Lz2	0.43	11.20	1.32	565	0.422	0.011919	0.19	0.0787	2.4	0.0479	2.4	76.38	0.15	76.9	1.8	94	56	0.334
N Lz3	0.27	21.40	1.15	1104	0.366	0.011916	0.11	0.07862	1.2	0.04787	1.2	76.363	0.084	76.85	0.92	92	29	0.348
N Lz4	0.30	29.61	1.04	1558	0.333	0.0119057	0.072	0.07866	0.83	0.04794	0.80	76.296	0.055	76.89	0.61	95	19	0.333
N Lz5	0.26	17.11	1.46	829	0.466	0.011916	0.12	0.0789	1.6	0.04804	1.5	76.364	0.094	77.1	1.2	100	36	0.322

KC061517-1

Fraction	Composition			Isotopic Ratios					Dates (Ma)								Corr. coef.	
	Pbc (pg)	Pb*/Pbc <sup>a</sup>	Th/UF	206Pb/204Pb <sup>a</sup>	208Pb/206Pb <sup>a</sup>	206Pb/238U <sup>a</sup>	±2σ %	207Pb/235U <sup>a</sup>	±2σ %	207Pb/206Pb <sup>a</sup>	±2σ %	206Pb/238U <sup>b</sup>	±2σ abs	207Pb/235U <sup>b</sup>	±2σ abs	207Pb/206Pb <sup>b</sup>		±2σ abs
Zircon																		
N z1	0.42	34.54	0.69	1975	0.220	0.0122536	0.057	0.08057	0.65	0.04771	0.64	78.511	0.044	78.68	0.50	84	15	0.268
N z2	0.45	20.49	0.81	1145	0.258	0.012267	0.092	0.08081	1.1	0.04780	1.1	78.595	0.072	78.91	0.85	88	26	0.331
N z3	0.27	18.37	0.57	1091	0.183	0.012250	0.099	0.08101	1.2	0.04798	1.2	78.489	0.077	79.09	0.92	97	28	0.323
N z4	0.34	21.80	0.59	1287	0.187	0.012255	0.084	0.08068	1.0	0.04777	0.97	78.524	0.066	78.78	0.76	87	23	0.320
N z5	0.47	14.18	0.59	843	0.188	0.012257	0.12	0.0810	1.5	0.04797	1.5	78.534	0.097	79.1	1.2	97	35	0.329
N z6	0.75	5.85	0.65	353	0.207	0.012266	0.29	0.0823	3.7	0.0487	3.6	78.59	0.23	80.3	2.8	132	85	0.329
N z7	0.40	37.84	0.65	2183	0.208	0.0122491	0.052	0.08070	0.58	0.04780	0.57	78.483	0.041	78.80	0.44	88	14	0.282

## B2-07B

Fraction	Composition			Isotopic Ratios						Dates (Ma)								
	Pbc (pg)	Pb*/Pbc <sup>c</sup>	Th/U	206Pb/204Pb <sup>a</sup>	208Pb/206Pb <sup>a</sup>	206Pb/238U <sup>a</sup>	±2σ %	207Pb/235U <sup>a</sup>	±2σ %	207Pb/206Pb <sup>a</sup>	±2σ %	206Pb/238U <sup>f</sup>	±2σ abs	207Pb/235U <sup>f</sup>	±2σ abs	207Pb/206Pb <sup>f</sup>	±2σ abs	Corr. coef.
Sort																		
Zircon																		
z1	0.44	28.75	0.79	1606	0.253	0.0127071	0.072	0.08417	0.81	0.04806	0.78	81.399	0.058	82.06	0.64	101	19	0.334
z2	0.29	56.17	0.89	3044	0.285	0.0127040	0.036	0.08359	0.43	0.04774	0.41	81.379	0.029	81.51	0.33	85.4	9.9	0.318
z3	0.33	43.99	0.56	2597	0.178	0.0127139	0.053	0.08398	0.52	0.04793	0.50	81.442	0.043	81.88	0.41	95	12	0.345
z4	0.31	9.74	0.54	592	0.171	0.012722	0.18	0.0849	2.2	0.0484	2.1	81.49	0.14	82.8	1.7	119	50	0.333
z5	0.32	13.92	0.38	875	0.120	0.012723	0.12	0.0838	1.5	0.04776	1.5	81.503	0.098	81.7	1.2	86	34	0.266
z6	0.35	17.81	0.33	1127	0.107	0.012735	0.097	0.08405	1.2	0.04789	1.1	81.579	0.079	81.95	0.91	93	27	0.329
z7	0.43	33.54	0.65	1936	0.208	0.0127034	0.059	0.08389	0.66	0.04792	0.64	81.376	0.048	81.79	0.52	94	15	0.300
z8	0.33	22.36	0.52	1342	0.166	0.012721	0.080	0.08422	0.95	0.04804	0.93	81.490	0.065	82.10	0.75	100	22	0.331
z10	0.33	16.28	0.47	995	0.150	0.012741	0.10	0.0841	1.3	0.04790	1.3	81.615	0.084	82.0	1.0	93	30	0.328

## WLS-R-070818

Toggle Measured																		
Fraction	Composition			Isotopic Ratios						Dates (Ma)								
	Pbc (pg)	Pb*/Pbc <sup>c</sup>	Th/U	206Pb/204Pb <sup>a</sup>	208Pb/206Pb <sup>a</sup>	206Pb/238U <sup>a</sup>	±2σ %	207Pb/235U <sup>a</sup>	±2σ %	207Pb/206Pb <sup>a</sup>	±2σ %	206Pb/238U <sup>f</sup>	±2σ abs	207Pb/235U <sup>f</sup>	±2σ abs	207Pb/206Pb <sup>f</sup>	±2σ abs	Corr. coef.
Sort																		
Zircon																		
z1	0.36	21.2	0.59	1249.7	0.188	0.012709	0.11	0.08467	1.0	0.04834	1.0	81.409	0.091	82.52	0.82	115	24	0.28
z2	0.38	39.1	0.44	2385.1	0.141	0.0127001	0.060	0.08357	0.54	0.04774	0.53	81.355	0.048	81.49	0.42	86	13	0.28
z3	0.72	6.7	0.54	410.3	0.170	0.012719	0.26	0.0853	3.2	0.0487	3.1	81.48	0.21	83.1	2.5	130	73	0.34
z4	0.97	3.9	0.53	250.0	0.168	0.012713	0.41	0.0856	5.3	0.0488	5.1	81.44	0.33	83.4	4.2	139	120	0.32
z5	0.34	10.1	0.33	647.2	0.106	0.012708	0.16	0.0841	2.0	0.04802	2.0	81.40	0.13	82.0	1.6	99	46	0.33
z6	0.35	12.0	0.33	766.6	0.104	0.012706	0.13	0.0838	1.7	0.04788	1.6	81.39	0.11	81.8	1.3	92	39	0.24
z8	0.33	11.4	0.51	696.0	0.164	0.012698	0.18	0.0838	2.0	0.04787	2.0	81.34	0.15	81.7	1.6	92	47	0.37

Notes: Corr. coef. = correlation coefficient. Ages calculated using the decay constants  $\lambda_{238} = 1.55125E-10$  y<sup>-1</sup> and  $\lambda_{235} = 9.8485E-10$  y<sup>-1</sup> (Jaffey et al. 1971).

†All analyses are single zircon grains and pre-treated by the thermal annealing and acid leaching (CA-TIMS) technique. Data used in date calculation are in bold.

§Pbc(c) is total common-Pb in analysis. Pb\* is radiogenic Pb concentration. Total sample U content in pg.

#Th content is calculated from radiogenic 208Pb assuming concordance between U-Pb and Th-U systems.

\*\*Measured ratio corrected for spike and fractionation only.

‡Radiogenic Pb ratio.

§§Corrected for fractionation, spike and blank. Also corrected for initial Th/U disequilibrium using radiogenic 208Pb and Th/U[magma] = 2.8

All common Pb assumed to be laboratory blank. Total procedural blank less than 0.1 pg for U.

Blank isotopic composition: 206Pb/204Pb = 18.20 ± 0.45, 207Pb/204Pb = 15.29 ± 0.24, 208Pb/204Pb = 37.16 ± 0.77.



### Appendix C.3 Chapter Three Data

Supplementary data are included in the publication of this work in *Palaeogeography, Palaeoclimatology, Palaeoecology* (2022) and reproduced here with permission. See:

Beveridge, T. L., Roberts, E. M., Ramezani, J., Titus, A. L., Eaton, J. G., Irmis, R. B., & Sertich, J. J. W. (2022).

Refined geochronology and revised stratigraphic nomenclature of the Upper Cretaceous Wahweap Formation, Utah, U.S.A. and the age of early Campanian vertebrates from southern Laramidia. *Palaeogeography, Palaeoclimatology, Palaeoecology*, 591, 110876. doi.org/10.1016/j.palaeo.2022.110876

**Appendix C.3.1** *Compilation of in situ (plus some surface) Wahweap Formation fossil localities (n ~ 60 excl. those in Table 3.3) collated from records at the Bureau of Land Management, Denver Museum of Nature and Science (DMNH), and Natural History Museum of Utah (UMNH).*

Museum Locality	Taxa Present (Specimen Numbers)	Area	Member	Approx. Height*	Model Age (Ma)**	2 $\sigma$ uncertainty		Distance from Road (m)
						+	-	
DMNH Locality 6866	Turtle shell	Brigham Plains	Last Chance Creek Member	lower	82.17 to 81.98	1.47	0.46	Moderately Close
DMNH Locality 12432	<i>Naomichelys</i> shell	Nipple Butte	Last Chance Creek Member	lower	82.17 to 81.98	1.47	0.46	Close
DMNH Locality 12433	Crocodylia, Testudines, Dinosauria various	Nipple Butte	Last Chance Creek Member	lower	82.17 to 81.98	1.47	0.46	Far
DMNH Locality 12453	Crocodyliformes partial skeleton	Brigham Plains	Last Chance Creek Member	lower	82.17 to 81.98	1.47	0.46	Moderately Far
UMNH VP Loc. 562	Baenid turtle (UMNH VP 20645)	Tibbet Springs	Last Chance Creek Member	lower	82.17 to 81.98	1.47	0.46	Close
UMNH VP Loc. 1253	Hadrosaurid partial postcranial skeleton	Nipple Butte	Last Chance Creek Member	lower	82.17 to 81.98	1.47	0.46	Close
UMNH VP Loc. 1263	Hadrosaurid articulated postcranial skeleton (UMNH VP 20616)	Nipple Butte	Last Chance Creek Member	lower	82.17 to 81.98	1.47	0.46	Close

Museum Locality	Taxa Present (Specimen Numbers)	Area	Member	Approx. Height*	Model Age (Ma)**	2 $\sigma$ uncertainty		Distance from Road (m)
						+	-	
UMNH VP Loc. 2020	Hadrosaurid partial skeleton	Nipple Butte	Last Chance Creek Member	lower	82.17 to 81.98	1.47	0.46	Close
UMNH VP Loc. 2587	<i>cf. Deinosuchus</i> crocodylian partial skeleton	Tibbet Springs	Last Chance Creek Member	lower	82.17 to 81.98	1.47	0.46	Close
UMNH VP Loc. 2923	Hadrosaurid partial skull	Nipple Butte	Last Chance Creek Member	lower	82.17 to 81.98	1.47	0.46	Close
UMNH VP Loc 2999	<i>cf. Deinosuchus</i> crocodylian partial skeleton	Nipple Butte	Last Chance Creek Member	lower	82.17 to 81.98	1.47	0.46	Close
DMNH Locality 12443	Testudines phalanx	Nipple Butte	Last Chance Creek Member	middle	81.98 to 81.64	1.33	0.16	Close
DMNH Locality 5997	Turtle plastron	Clints Cove	Last Chance Creek Member	upper	81.64 to 81.44	0.92	0.11	Moderately Close
DMNH Locality 6003	Hadrosaur limb element	Clints Cove	Last Chance Creek Member	upper	81.64 to 81.44	0.92	0.11	Moderately Close
DMNH Locality 6005	Turtle plastron	Clints Cove	Last Chance Creek Member	upper	81.64 to 81.44	0.92	0.11	Moderately Close
DMNH Locality 6007	Various	Clints Cove	Last Chance Creek Member	upper	81.64 to 81.44	0.92	0.11	Moderately Close
DMNH Locality 6008	Various	Clints Cove	Last Chance Creek Member	upper	81.64 to 81.44	0.92	0.11	Moderately Close
DMNH Locality 6011	Turtle shell	Ship Mountain Point	Reynolds Point Member	lower	81.64 to 81.44	0.92	0.11	Moderately Far

Museum Locality	Taxa Present (Specimen Numbers)	Area	Member	Approx. Height*	Model Age (Ma)**	2 $\sigma$ uncertainty		Distance from Road (m)
						+	-	
DMNH Locality 5984	Microsite	Clints Cove	Reynolds Point Member	lower	81.64 to 81.44	0.92	0.11	Moderately Close
UMNH VP Loc. 1210	Hadrosaurid proximal humerus, scapula (UMNH VP 20215), and dentary (UMNH VP 20216)	Wesses Cove	Reynolds Point Member	lower	81.64 to 81.44	0.92	0.11	Moderately Close
UMNH VP Loc. 1502	<i>Neurankylus</i> partial carapace and plastron	Star Seep	Reynolds Point Member	lower	81.64 to 81.44	0.92	0.11	Distal
UMNH VP Loc. 2404	Crocodylia and <i>Neurankylus</i> partial skeletons	Brigham Plains	Reynolds Point Member	lower	81.64 to 81.44	0.92	0.11	Close
UMNH VP Loc. 2405	Hadrosauoidea partial skeleton	Brigham Plains	Reynolds Point Member	lower	81.64 to 81.44	0.92	0.11	Moderately Close
UMNH VP Loc. 2847	<i>cf. Deinosuchus</i> crocodylian partial skeleton	Brigham Plains	Reynolds Point Member	lower	81.64 to 81.44	0.92	0.11	Close
DMNH Locality 12462	Hadrosauridae caudal vertebra	Coyote Canyon	Reynolds Point Member	middle	81.44 to 80.69	0.05	0.5	Far
DMNH Locality 8655	Hadrosauridae, turtle, crocodylian vertebra, plastron, osteoderm	Coyote Canyon	Reynolds Point Member	middle	81.44 to 80.69	0.05	0.5	Far
DMNH Locality 8665	Turtle shell	Coyote Canyon	Reynolds Point Member	middle	81.44 to 80.69	0.05	0.5	Far
DMNH Locality 6773	Microsite	Clinton Canyon	Reynolds Point Member	middle	81.44 to 80.69	0.05	0.5	Far
DMNH Locality 12451	Various	Brigham Plains	Reynolds Point Member	middle	81.44 to 80.69	0.05	0.5	Moderately Close
UMNH VP Loc. 1266	Baenid turtle including carapace, plastron, and forelimbs (UMNH VP 20643)	Wesses Cove	Reynolds Point Member	middle	81.44 to 80.69	0.05	0.5	Moderately Close
UMNH VP Loc. 1676	Nodosauridae gen. et sp. nov., partial skull and skeleton (UMNH VP 22080)	Right Hand Collet Canyon	Reynolds Point Member	middle	81.44 to 80.69	0.05	0.5	Moderately Far

Museum Locality	Taxa Present (Specimen Numbers)	Area	Member	Approx. Height*	Model Age (Ma)**	2 $\sigma$ uncertainty		Distance from Road (m)
						+	-	
UMNH VP Loc. 2628	cf. <i>Deinosuchus</i> crocodylian partial skeleton; trionychid turtle shell	The Gut	Reynolds Point Member ?	middle	81.44 to 80.69	0.05	0.5	Close
UMNH VP Loc. 2995	Amiidae maxilla (UMNH VP 19464); cf. <i>Brachylophosaurus</i> saurolophine jugal (UMNH VP 19465)	Wesses Canyon	Reynolds Point Member	middle	81.44 to 80.69	0.05	0.5	Close
DMNH Locality 6010	Turtle shell	Wesses Cove	Reynolds Point Member	middle or upper	81.44 to 80.69	0.05	0.5	Moderately Far
UMNH VP Loc 2998	Hadrosaurid partial skeleton	Brigham Plains	Reynolds Point Member	middle or upper	81.44 to 80.69	0.05	0.5	Moderately Far
DMNH Locality 6004	Turtle shell	Clints Cove	Reynolds Point Member	upper	80.69 to 80.58	0.36	0.52	Far
DMNH Locality 6772	Vertebrata element	Clints Cove	Coyote Point Member	lower	80.69 to 80.58	0.36	0.52	Far
DMNH Locality 12456	Theropoda tooth	Coyote Point	Coyote Point Member	lower	80.69 to 80.58	0.36	0.52	Moderately Far
DMNH Locality 12464	Hadrosauridae limb elements	Coyote Point	Coyote Point Member	lower	80.69 to 80.58	0.36	0.52	Moderately Far
UMNH VP Loc. 147	cf. <i>Brachylophosaurus</i> maxilla and partial limb bones (UMNH VP 9548)	Death Ridge	Coyote Point Member	upper (v)	79	0.9	1.07	Distal
UMNH VP Loc. 324	Saurolophine hadrosaurid bonebed	Camp Flat	???	???	???	???	???	Moderately Close

\* Relative to Reynolds Point lectostratotype section of Eaton (1991)

\*\* Bayesian model age for stratigraphic level or age range for stratigraphic intervals

^ direct map distance (m): Close = 0-249, Moderately Close = 250-499, Moderately Far = 500-749, Far = 750-999, Distal  $\geq$  1000.

Appendix C.3.2 Complete U-Pb data for Waldweap Formation CA-ID-TIMS analyses. LA-ICP-MS data is available online via Palaeogeography, Palaeoclimatology, Palaeoecology (doi.org/10.1016/j.palaeo.2022.110876) or on request to the author.

B2-07B																	
Sample	Pb <sub>c</sub> <sup>§</sup>	Pb* <sup>§</sup>	U <sup>§</sup>	Th <sup>#</sup>	Ratios								Ages (Ma)				
					<b><sup>206</sup>Pb**</b>	<b><sup>208</sup>Pb†</b>	<b><sup>206</sup>Pb<sup>§</sup></b>	err	<b><sup>207</sup>Pb<sup>§</sup></b>	err	<b><sup>207</sup>Pb<sup>§</sup></b>	err	<b><sup>206</sup>Pb</b>	Err	<b><sup>207</sup>Pb</b>	<b><sup>207</sup>Pb</b>	corr.
Frac. <sup>†</sup>	(pg)	Pb <sub>c</sub>	(pg)	U	<sup>204</sup> Pb	<sup>206</sup> Pb	<sup>238</sup> U	(2σ%)	<sup>235</sup> U	(2σ%)	<sup>206</sup> Pb	(2σ%)	<sup>238</sup> U	(2σ)	<sup>235</sup> U	<sup>206</sup> Pb	coef
z10	0.33	16.3	411	0.47	995	0.15	0.01	-0.1	0.08	-1.3	0.05	-1.3	81.7	0.08	82	91	0.33
z6	0.35	17.8	487	0.33	1127	0.11	0.01	-0.1	0.08	-1.2	0.05	-1.1	81.7	0.08	82	90	0.33
z5	0.32	14	350	0.38	878	0.12	0.01	-0.1	0.08	-1.5	0.05	-1.5	81.6	0.1	81.9	90	0.34
z4	0.31	9.7	230	0.54	592	0.17	0.01	-0.2	0.08	-2.2	0.05	-2.1	81.6	0.14	82.8	117	0.33
z8	0.33	22.4	547	0.52	1342	0.17	0.01	-0.1	0.08	-1	0.05	-0.9	81.6	0.07	82.1	97	0.33
z3	0.33	44	1074	0.56	2597	0.18	0.01	-0.1	0.08	-0.5	0.05	-0.5	81.5	0.04	81.9	92	0.34
z1	0.44	28.8	896	0.79	1606	0.25	0.01	-0.1	0.08	-0.8	0.05	-0.8	81.5	0.06	82.1	99	0.33
z7	0.43	33.5	1050	0.65	1936	0.21	0.01	-0.1	0.08	-0.7	0.05	-0.6	81.5	0.05	81.8	92	0.29
z2	0.29	56.2	1127	0.89	3044	0.29	0.01	-0	0.08	-0.4	0.05	-0.4	81.5	0.04	81.5	83	0.28

Notes: Corr. coef. = correlation coefficient. Ages calculated using the decay constants  $\lambda_{238} = 1.55125E-10 \text{ y}^{-1}$  and  $\lambda_{235} = 9.8485E-10 \text{ y}^{-1}$  (Jaffey et al. 1971).

<sup>†</sup> All analyses are single zircon grains and pre-treated by the thermal annealing and acid leaching (CA-TIMS) technique. Data used in date calculation are in bold.

<sup>§</sup> Pb(c) is total common-Pb in analysis. Pb\* is radiogenic Pb concentration. Total sample U content in pg.

<sup>#</sup>Th content is calculated from radiogenic <sup>208</sup>Pb assuming concordance between U-Pb and Th-U systems.

\*\*Measured ratio corrected for spike and fractionation only.

† Radiogenic Pb ratio.

<sup>§</sup> <sup>§</sup> Corrected for fractionation, spike and blank. Also corrected for initial Th/U disequilibrium using radiogenic <sup>208</sup>Pb and Th/U<sub>[magma]</sub> = 2.8

All common Pb assumed to be laboratory blank. Total procedural blank less than 0.1 pg for U.

Blank isotopic composition: <sup>206</sup>Pb/<sup>204</sup>Pb = 18.20 ± 0.45, <sup>207</sup>Pb/<sup>204</sup>Pb = 15.29 ± 0.24, <sup>208</sup>Pb/<sup>204</sup>Pb = 37.16 ± 0.77.



## WLS-R-070818

Sample	Pb <sub>c</sub> <sup>§</sup>	Pb* <sup>§</sup>	U <sup>§</sup>	Th <sup>#</sup>	<u><sup>206</sup>Pb</u> **	<u><sup>208</sup>Pb</u> †	Ratios						Ages (Ma)				
							<u><sup>206</sup>Pb</u> <sup>§</sup>	err	<u><sup>207</sup>Pb</u> <sup>§</sup>	err	<u><sup>207</sup>Pb</u> <sup>§</sup>	err	<u><sup>206</sup>Pb</u>	Err	<u><sup>207</sup>Pb</u>	<u><sup>207</sup>Pb</u>	corr.
Frac. <sup>†</sup>	(pg)	Pb <sub>c</sub>	(pg)	U	<sup>204</sup> Pb	<sup>206</sup> Pb	<sup>238</sup> U	(2σ%)	<sup>235</sup> U	(2σ%)	<sup>206</sup> Pb	(2σ%)	<sup>238</sup> U	(2σ)	<sup>235</sup> U	<sup>206</sup> Pb	coef
z3	0.72	6.7	358	0.53	410	0.17	0.01	-0.3	0.09	-3.2	0.05	-3.1	81.6	0.21	83.1	128	0.34
z4	0.97	3.9	287	0.53	250	0.17	0.01	-0.4	0.09	-5.3	0.05	-5.1	81.5	0.33	83.4	137	0.32
z5	0.34	10.1	273	0.33	647	0.11	0.01	-0.2	0.08	-2	0.05	-2	81.5	0.13	82	96	0.33
z1	0.36	21.2	570	0.59	1250	0.19	0.01	-0.1	0.08	-1	0.05	-1	81.5	0.09	82.5	112	0.28
z6	0.35	12	333	0.33	767	0.1	0.01	-0.1	0.08	-1.7	0.05	-1.6	81.5	0.11	81.8	90	0.24
z2	0.38	39.1	1141	0.44	2385	0.14	0.01	-0.1	0.08	-0.5	0.05	-0.5	81.4	0.05	81.5	83	0.27
z8	0.33	11.4	287	0.51	696	0.16	0.01	-0.2	0.08	-2	0.05	-2	81.4	0.15	81.7	89	0.37

Notes: Corr. coef. = correlation coefficient. Ages calculated using the decay constants  $\lambda_{238} = 1.55125E-10 \text{ y}^{-1}$  and  $\lambda_{235} = 9.8485E-10 \text{ y}^{-1}$  (Jaffey et al. 1971).

<sup>†</sup> All analyses are single zircon grains and pre-treated by the thermal annealing and acid leaching (CA-TIMS) technique. Data used in date calculation are in bold.

<sup>§</sup> Pb(c) is total common-Pb in analysis. Pb\* is radiogenic Pb concentration. Total sample U content in pg.

<sup>#</sup>Th content is calculated from radiogenic <sup>208</sup>Pb assuming concordance between U-Pb and Th-U systems.

\*\*Measured ratio corrected for spike and fractionation only.

† Radiogenic Pb ratio.

<sup>§</sup> <sup>§</sup> Corrected for fractionation, spike and blank. Also corrected for initial Th/U disequilibrium using radiogenic <sup>208</sup>Pb and Th/U<sub>[magma]} = 2.8</sub>

All common Pb assumed to be laboratory blank. Total procedural blank less than 0.1 pg for U.

Blank isotopic composition: <sup>206</sup>Pb/<sup>204</sup>Pb = 18.20 ± 0.45, <sup>207</sup>Pb/<sup>204</sup>Pb = 15.29 ± 0.24, <sup>208</sup>Pb/<sup>204</sup>Pb = 37.16 ± 0.77.

**Appendix C.3.3 Wahweap Formation Bayesian age-stratigraphic model input data.**

id	ages	ageSds	position	thickness	calCurves
"WKC-3"	76540	475	500	0	normal
"WKC-1_2"	77800	500	1500	0	normal
"WHC"	80610	450	17500	1000	normal
"LYASH-19.2"	81330	405	27200	0	normal
"LYASH-19.1"	81210	290	30300	0	normal
"WLS-R"	81465	21	34800	0	normal

Notes: *id* = samples name, *ages* = kyrs, *ageSds* = uncertainty ( $Y$ ) at  $1\sigma$  in kyrs, *position* = stratigraphic height (cm) as “depth” beginning at 10 m above the Wahweap Fm, *thickness* = thickness of sampled horizon (null=0). Sample WHC is a detrital zircon sample that was collected over ~10 m stratigraphically.

**Appendix C.3.4 Wahweap Formation Bayesian age-stratigraphic model script.**

```
>library(Bchron)

>WahweapFm <- read.csv(file.choose())

>WahweapFmModel=Bchronology(ages=WahweapFm$ages,
                             ageSds=WahweapFm$ageSds,
                             calCurves=WahweapFm$calCurves,
                             positions=WahweapFm$position,
                             positionThicknesses=WahweapFm$thickness,
                             ids=WahweapFm$id,
                             predictPositions=seq(0,42100,by=100),
                             iterations=100000)

>library(ggplot2)

>plot(WahweapFmModel)+labs(x='Age (ka)',y='Depth (cm)',title='Wahweap Fm Bchron Model')

> WahweapFmModelAges <- matrix(nrow=421, ncol=3)

for(i in 1:421){ WahweapFmModelAges [i,]=quantile(WahweapFmModel$thetaPredict[,i],probs =
c(0.025,0.5,0.975))}

>write.csv(WahweapFmModelAges, "Wahweap
Fm Model Output.csv")
```

*Appendix C.3.5 Wahweap Formation Bayesian age-stratigraphic model numerical output.*

Strat. Level* (m)	Model Age (Ma)	+	-	(Max)	(Min)	Range	Strat. Level* (m)	Model Age (Ma)	+	-	(Max)	(Min)	Range
410	77.29	0.72	0.62	78.01	76.67	1.34	362	78.32	1.12	0.89	79.44	77.43	2.01
409	77.34	0.72	0.63	78.06	76.71	1.35	361	78.34	1.11	0.89	79.45	77.45	2.00
408	77.40	0.70	0.67	78.10	76.73	1.37	360	78.35	1.13	0.89	79.48	77.46	2.02
407	77.45	0.74	0.69	78.19	76.76	1.43	359	78.36	1.14	0.89	79.50	77.47	2.03
406	77.51	0.73	0.71	78.24	76.80	1.44	358	78.37	1.14	0.88	79.51	77.49	2.02
405	77.58	0.77	0.72	78.35	76.86	1.49	357	78.38	1.14	0.88	79.52	77.50	2.02
404	77.63	0.85	0.73	78.48	76.90	1.58	356	78.40	1.14	0.88	79.54	77.52	2.02
403	77.66	0.85	0.74	78.51	76.92	1.59	355	78.41	1.14	0.87	79.55	77.54	2.01
402	77.69	0.86	0.74	78.55	76.95	1.60	354	78.42	1.14	0.86	79.56	77.56	2.00
401	77.71	0.90	0.74	78.61	76.97	1.64	353	78.43	1.16	0.86	79.59	77.57	2.02
400	77.72	0.93	0.73	78.65	76.99	1.66	352	78.45	1.16	0.87	79.61	77.58	2.03
399	77.75	0.94	0.74	78.69	77.01	1.68	351	78.46	1.16	0.86	79.62	77.60	2.02
398	77.77	0.94	0.74	78.71	77.03	1.68	350	78.48	1.15	0.87	79.63	77.61	2.02
397	77.78	0.97	0.74	78.75	77.04	1.71	349	78.49	1.17	0.87	79.66	77.62	2.04
396	77.80	0.98	0.74	78.78	77.06	1.72	348	78.51	1.16	0.89	79.67	77.62	2.05
395	77.83	0.98	0.76	78.81	77.07	1.74	347	78.52	1.16	0.89	79.68	77.63	2.05
394	77.84	1.00	0.76	78.84	77.08	1.76	346	78.54	1.14	0.90	79.68	77.64	2.04
393	77.86	1.02	0.77	78.88	77.09	1.79	345	78.55	1.14	0.90	79.69	77.65	2.04
392	77.87	1.02	0.76	78.89	77.11	1.78	344	78.56	1.14	0.90	79.70	77.66	2.04
391	77.89	1.04	0.77	78.93	77.12	1.81	343	78.57	1.13	0.90	79.70	77.67	2.03
390	77.91	1.06	0.77	78.97	77.14	1.83	342	78.59	1.12	0.91	79.71	77.68	2.03
389	77.93	1.06	0.76	78.99	77.17	1.82	341	78.60	1.12	0.91	79.72	77.69	2.03
388	77.94	1.07	0.76	79.01	77.18	1.83	340	78.62	1.10	0.92	79.72	77.70	2.02
387	77.96	1.13	0.76	79.09	77.20	1.89	339	78.63	1.10	0.92	79.73	77.71	2.02
386	77.97	1.14	0.77	79.11	77.20	1.91	338	78.64	1.10	0.92	79.74	77.72	2.02
385	78.00	1.12	0.79	79.12	77.21	1.91	337	78.65	1.10	0.92	79.75	77.73	2.02
384	78.02	1.12	0.79	79.14	77.23	1.91	336	78.67	1.08	0.93	79.75	77.74	2.01
383	78.04	1.11	0.79	79.15	77.25	1.90	335	78.68	1.08	0.92	79.76	77.76	2.00
382	78.06	1.10	0.80	79.16	77.26	1.90	334	78.70	1.07	0.93	79.77	77.77	2.00
381	78.07	1.11	0.81	79.18	77.26	1.92	333	78.71	1.08	0.93	79.79	77.78	2.01
380	78.08	1.12	0.81	79.20	77.27	1.93	332	78.73	1.08	0.94	79.81	77.79	2.02
379	78.09	1.13	0.81	79.22	77.28	1.94	331	78.75	1.07	0.94	79.82	77.81	2.01
378	78.11	1.13	0.82	79.24	77.29	1.95	330	78.76	1.08	0.95	79.84	77.81	2.03
377	78.12	1.12	0.83	79.24	77.29	1.95	329	78.77	1.08	0.95	79.85	77.82	2.03
376	78.13	1.12	0.82	79.25	77.31	1.94	328	78.79	1.07	0.94	79.86	77.85	2.01
375	78.15	1.11	0.83	79.26	77.32	1.94	327	78.80	1.08	0.94	79.88	77.86	2.02
374	78.16	1.11	0.84	79.27	77.32	1.95	326	78.81	1.08	0.94	79.89	77.87	2.02
373	78.17	1.13	0.84	79.30	77.33	1.97	325	78.83	1.07	0.95	79.90	77.88	2.02
372	78.19	1.12	0.86	79.31	77.33	1.98	324	78.85	1.05	0.96	79.90	77.89	2.01
371	78.20	1.11	0.86	79.31	77.34	1.97	323	78.86	1.04	0.96	79.90	77.90	2.00
370	78.21	1.11	0.87	79.32	77.34	1.98	322	78.87	1.04	0.96	79.91	77.91	2.00
369	78.22	1.11	0.87	79.33	77.35	1.98	321	78.88	1.04	0.96	79.92	77.92	2.00
368	78.24	1.11	0.88	79.35	77.36	1.99	320	78.90	1.03	0.98	79.93	77.92	2.01
367	78.25	1.11	0.87	79.36	77.38	1.98	319	78.91	1.03	0.98	79.94	77.93	2.01
366	78.26	1.11	0.87	79.37	77.39	1.98	318	78.92	1.03	0.99	79.95	77.93	2.02
365	78.28	1.11	0.89	79.39	77.39	2.00	317	78.94	1.01	1.00	79.95	77.94	2.01
364	78.29	1.11	0.88	79.40	77.41	1.99	316	78.96	1.00	1.01	79.96	77.95	2.01
363	78.31	1.10	0.89	79.41	77.42	1.99	315	78.97	0.99	0.99	79.96	77.98	1.98

Strat. Level* (m)	Model Age (Ma)	+	-	(Max)	(Min)	Range	Strat. Level* (m)	Model Age (Ma)	+	-	(Max)	(Min)	Range
314	78.99	0.98	1.01	79.97	77.98	1.99	264	79.71	0.70	0.96	80.41	78.75	1.66
313	79.00	0.98	0.99	79.98	78.01	1.97	263	79.73	0.69	0.96	80.42	78.77	1.65
312	79.02	0.96	1.00	79.98	78.02	1.96	262	79.75	0.69	0.98	80.44	78.77	1.67
311	79.03	0.96	1.00	79.99	78.03	1.96	261	79.77	0.68	0.97	80.45	78.80	1.65
310	79.05	0.94	1.01	79.99	78.04	1.95	260	79.78	0.68	0.97	80.46	78.81	1.65
309	79.07	0.93	1.03	80.00	78.04	1.96	259	79.79	0.68	0.97	80.47	78.82	1.65
308	79.08	0.93	1.03	80.01	78.05	1.96	258	79.81	0.67	0.98	80.48	78.83	1.65
307	79.10	0.93	1.04	80.03	78.06	1.97	257	79.83	0.67	0.98	80.50	78.85	1.65
306	79.11	0.93	1.05	80.04	78.06	1.98	256	79.84	0.68	0.96	80.52	78.88	1.64
305	79.12	0.92	1.05	80.04	78.07	1.97	255	79.87	0.66	0.95	80.53	78.92	1.61
304	79.14	0.91	1.07	80.05	78.07	1.98	254	79.89	0.65	0.93	80.54	78.96	1.58
303	79.15	0.90	1.07	80.05	78.08	1.97	253	79.91	0.65	0.93	80.56	78.98	1.58
302	79.17	0.89	1.07	80.06	78.10	1.96	252	79.93	0.64	0.92	80.57	79.01	1.56
301	79.19	0.87	1.06	80.06	78.13	1.93	251	79.95	0.64	0.90	80.59	79.05	1.54
300	79.20	0.87	1.06	80.07	78.14	1.93	250	79.97	0.64	0.88	80.61	79.09	1.52
299	79.21	0.87	1.06	80.08	78.15	1.93	249	79.99	0.64	0.88	80.63	79.11	1.52
298	79.23	0.85	1.05	80.08	78.18	1.90	248	80.01	0.64	0.86	80.65	79.15	1.50
297	79.24	0.84	1.05	80.08	78.19	1.89	247	80.04	0.62	0.82	80.66	79.22	1.44
296	79.26	0.83	1.07	80.09	78.19	1.90	246	80.06	0.62	0.80	80.68	79.26	1.42
295	79.27	0.82	1.04	80.09	78.23	1.86	245	80.08	0.62	0.78	80.70	79.30	1.40
294	79.29	0.83	1.05	80.12	78.24	1.88	244	80.09	0.62	0.76	80.71	79.33	1.38
293	79.30	0.83	1.05	80.13	78.25	1.88	243	80.12	0.61	0.74	80.73	79.38	1.35
292	79.31	0.82	1.04	80.13	78.27	1.86	242	80.13	0.62	0.70	80.75	79.43	1.32
291	79.32	0.81	1.04	80.13	78.28	1.85	241	80.15	0.60	0.70	80.75	79.45	1.30
290	79.34	0.80	1.06	80.14	78.28	1.86	240	80.17	0.59	0.69	80.76	79.48	1.28
289	79.36	0.78	1.05	80.14	78.31	1.83	239	80.17	0.61	0.68	80.78	79.49	1.29
288	79.37	0.78	1.05	80.15	78.32	1.83	238	80.19	0.61	0.69	80.80	79.50	1.30
287	79.38	0.79	1.04	80.17	78.34	1.83	237	80.19	0.62	0.67	80.81	79.52	1.29
286	79.40	0.78	1.05	80.18	78.35	1.83	236	80.21	0.61	0.67	80.82	79.54	1.28
285	79.41	0.77	1.06	80.18	78.35	1.83	235	80.22	0.60	0.66	80.82	79.56	1.26
284	79.43	0.76	1.06	80.19	78.37	1.82	234	80.22	0.60	0.64	80.82	79.58	1.24
283	79.44	0.77	1.05	80.21	78.39	1.82	233	80.23	0.60	0.63	80.83	79.60	1.23
282	79.45	0.77	1.05	80.22	78.40	1.82	232	80.24	0.60	0.63	80.84	79.61	1.23
281	79.47	0.75	1.06	80.22	78.41	1.81	231	80.24	0.60	0.61	80.84	79.63	1.21
280	79.48	0.75	1.06	80.23	78.42	1.81	230	80.25	0.59	0.62	80.84	79.63	1.21
279	79.50	0.75	1.06	80.25	78.44	1.81	229	80.26	0.58	0.62	80.84	79.64	1.20
278	79.51	0.75	1.06	80.26	78.45	1.81	228	80.27	0.57	0.63	80.84	79.64	1.20
277	79.53	0.75	1.07	80.28	78.46	1.82	227	80.27	0.57	0.61	80.84	79.66	1.18
276	79.55	0.74	1.08	80.29	78.47	1.82	226	80.28	0.57	0.62	80.85	79.66	1.19
275	79.56	0.73	1.08	80.29	78.48	1.81	225	80.29	0.56	0.62	80.85	79.67	1.18
274	79.57	0.73	1.08	80.30	78.49	1.81	224	80.30	0.55	0.62	80.85	79.68	1.17
273	79.59	0.72	1.08	80.31	78.51	1.80	223	80.30	0.56	0.61	80.86	79.69	1.17
272	79.60	0.72	1.07	80.32	78.53	1.79	222	80.31	0.55	0.61	80.86	79.70	1.16
271	79.61	0.72	1.06	80.33	78.55	1.78	221	80.32	0.54	0.60	80.86	79.72	1.14
270	79.62	0.72	1.06	80.34	78.56	1.78	220	80.32	0.54	0.60	80.86	79.72	1.14
269	79.64	0.71	1.04	80.35	78.60	1.75	219	80.33	0.53	0.59	80.86	79.74	1.12
268	79.66	0.69	1.04	80.35	78.62	1.73	218	80.33	0.53	0.58	80.86	79.75	1.11
267	79.67	0.69	1.03	80.36	78.64	1.72	217	80.34	0.52	0.58	80.86	79.76	1.10
266	79.69	0.68	1.02	80.37	78.67	1.70	216	80.35	0.52	0.58	80.87	79.77	1.10
265	79.70	0.70	0.98	80.40	78.72	1.68	215	80.35	0.52	0.56	80.87	79.79	1.08

Strat. Level* (m)	Model Age (Ma)	+	-	(Max)	(Min)	Range	Strat. Level* (m)	Model Age (Ma)	+	-	(Max)	(Min)	Range
214	80.36	0.51	0.56	80.87	79.80	1.07	164	80.70	0.35	0.50	81.05	80.20	0.85
213	80.37	0.50	0.56	80.87	79.81	1.06	163	80.71	0.35	0.50	81.06	80.21	0.85
212	80.38	0.50	0.57	80.88	79.81	1.07	162	80.72	0.35	0.50	81.07	80.22	0.85
211	80.38	0.50	0.56	80.88	79.82	1.06	161	80.73	0.34	0.51	81.07	80.22	0.85
210	80.39	0.49	0.56	80.88	79.83	1.05	160	80.74	0.34	0.50	81.08	80.24	0.84
209	80.39	0.49	0.56	80.88	79.83	1.05	159	80.75	0.34	0.49	81.09	80.26	0.83
208	80.40	0.49	0.56	80.89	79.84	1.05	158	80.75	0.35	0.48	81.10	80.27	0.83
207	80.40	0.49	0.55	80.89	79.85	1.04	157	80.76	0.35	0.49	81.11	80.27	0.84
206	80.41	0.49	0.55	80.90	79.86	1.04	156	80.77	0.34	0.47	81.11	80.30	0.81
205	80.42	0.48	0.55	80.90	79.87	1.03	155	80.78	0.34	0.47	81.12	80.31	0.81
204	80.43	0.48	0.55	80.91	79.88	1.03	154	80.78	0.35	0.45	81.13	80.33	0.80
203	80.43	0.48	0.54	80.91	79.89	1.02	153	80.79	0.35	0.43	81.14	80.36	0.78
202	80.44	0.47	0.54	80.91	79.90	1.01	152	80.80	0.35	0.43	81.15	80.37	0.78
201	80.45	0.46	0.54	80.91	79.91	1.00	151	80.81	0.34	0.43	81.15	80.38	0.77
200	80.45	0.46	0.54	80.91	79.91	1.00	150	80.83	0.33	0.43	81.16	80.40	0.76
199	80.46	0.45	0.54	80.91	79.92	0.99	149	80.84	0.33	0.42	81.17	80.42	0.75
198	80.47	0.45	0.54	80.92	79.93	0.99	148	80.86	0.34	0.41	81.20	80.45	0.75
197	80.47	0.45	0.52	80.92	79.95	0.97	147	80.87	0.33	0.40	81.20	80.47	0.73
196	80.48	0.44	0.52	80.92	79.96	0.96	146	80.89	0.32	0.41	81.21	80.48	0.73
195	80.49	0.44	0.52	80.93	79.97	0.96	145	80.90	0.32	0.40	81.22	80.50	0.72
194	80.49	0.44	0.51	80.93	79.98	0.95	144	80.91	0.31	0.40	81.22	80.51	0.71
193	80.50	0.43	0.51	80.93	79.99	0.94	143	80.92	0.31	0.39	81.23	80.53	0.70
192	80.51	0.43	0.51	80.94	80.00	0.94	142	80.93	0.31	0.39	81.24	80.54	0.70
191	80.51	0.43	0.50	80.94	80.01	0.93	141	80.94	0.30	0.38	81.24	80.56	0.68
190	80.52	0.42	0.51	80.94	80.01	0.93	140	80.95	0.30	0.37	81.25	80.58	0.67
189	80.52	0.43	0.50	80.95	80.02	0.93	139	80.95	0.30	0.37	81.25	80.58	0.67
188	80.53	0.42	0.50	80.95	80.03	0.92	138	80.96	0.29	0.37	81.25	80.59	0.66
187	80.54	0.41	0.51	80.95	80.03	0.92	137	80.97	0.29	0.36	81.26	80.61	0.65
186	80.54	0.42	0.50	80.96	80.04	0.92	136	80.98	0.28	0.35	81.26	80.63	0.63
185	80.55	0.41	0.51	80.96	80.04	0.92	135	80.99	0.28	0.35	81.27	80.64	0.63
184	80.56	0.41	0.51	80.97	80.05	0.92	134	80.99	0.28	0.34	81.27	80.65	0.62
183	80.57	0.41	0.51	80.98	80.06	0.92	133	81.00	0.28	0.35	81.28	80.65	0.63
182	80.57	0.41	0.51	80.98	80.06	0.92	132	81.01	0.27	0.35	81.28	80.66	0.62
181	80.58	0.40	0.52	80.98	80.06	0.92	131	81.02	0.27	0.35	81.29	80.67	0.62
180	80.58	0.41	0.51	80.99	80.07	0.92	130	81.03	0.26	0.34	81.29	80.69	0.60
179	80.59	0.40	0.51	80.99	80.08	0.91	129	81.04	0.26	0.33	81.30	80.71	0.59
178	80.60	0.39	0.52	80.99	80.08	0.91	128	81.05	0.25	0.33	81.30	80.72	0.58
177	80.60	0.40	0.51	81.00	80.09	0.91	127	81.06	0.25	0.33	81.31	80.73	0.58
176	80.61	0.39	0.51	81.00	80.10	0.90	126	81.07	0.24	0.33	81.31	80.74	0.57
175	80.62	0.39	0.51	81.01	80.11	0.90	125	81.08	0.24	0.33	81.32	80.75	0.57
174	80.63	0.38	0.51	81.01	80.12	0.89	124	81.09	0.23	0.33	81.32	80.76	0.56
173	80.63	0.38	0.51	81.01	80.12	0.89	123	81.10	0.23	0.32	81.33	80.78	0.55
172	80.64	0.38	0.51	81.02	80.13	0.89	122	81.11	0.22	0.32	81.33	80.79	0.54
171	80.65	0.37	0.52	81.02	80.13	0.89	121	81.12	0.22	0.32	81.34	80.80	0.54
170	80.66	0.37	0.52	81.03	80.14	0.89	120	81.13	0.22	0.32	81.35	80.81	0.54
169	80.67	0.36	0.51	81.03	80.16	0.87	119	81.14	0.22	0.31	81.36	80.83	0.53
168	80.68	0.36	0.52	81.04	80.16	0.88	118	81.16	0.21	0.32	81.37	80.84	0.53
167	80.68	0.36	0.50	81.04	80.18	0.86	117	81.18	0.20	0.32	81.38	80.86	0.52
166	80.69	0.36	0.50	81.05	80.19	0.86	116	81.19	0.19	0.31	81.38	80.88	0.50
165	80.70	0.35	0.51	81.05	80.19	0.86	115	81.20	0.19	0.31	81.39	80.89	0.50



Strat. Level* (m)	Model Age (Ma)	+	-	(Max)	(Min)	Range	Strat. Level* (m)	Model Age (Ma)	+	-	(Max)	(Min)	Range
114	81.21	0.18	0.31	81.39	80.90	0.49	64	81.55	0.65	0.08	82.20	81.47	0.73
113	81.21	0.18	0.29	81.39	80.92	0.47	63	81.57	0.71	0.10	82.28	81.47	0.81
112	81.22	0.18	0.29	81.40	80.93	0.47	62	81.57	0.76	0.10	82.33	81.47	0.86
111	81.23	0.17	0.29	81.40	80.94	0.46	61	81.58	0.76	0.11	82.34	81.47	0.87
110	81.24	0.16	0.29	81.40	80.95	0.45	60	81.59	0.79	0.12	82.38	81.47	0.91
109	81.24	0.17	0.27	81.41	80.97	0.44	59	81.60	0.83	0.13	82.43	81.47	0.96
108	81.25	0.16	0.27	81.41	80.98	0.43	58	81.61	0.86	0.13	82.47	81.48	0.99
107	81.26	0.15	0.27	81.41	80.99	0.42	57	81.62	0.86	0.14	82.48	81.48	1.00
106	81.26	0.15	0.26	81.41	81.00	0.41	56	81.63	0.88	0.15	82.51	81.48	1.03
105	81.27	0.15	0.26	81.42	81.01	0.41	55	81.64	0.92	0.16	82.56	81.48	1.08
104	81.27	0.15	0.25	81.42	81.02	0.40	54	81.65	0.93	0.17	82.58	81.48	1.10
103	81.28	0.14	0.25	81.42	81.03	0.39	53	81.66	0.94	0.18	82.60	81.48	1.12
102	81.28	0.15	0.24	81.43	81.04	0.39	52	81.67	0.94	0.19	82.61	81.48	1.13
101	81.29	0.14	0.24	81.43	81.05	0.38	51	81.68	0.95	0.20	82.63	81.48	1.15
100	81.30	0.13	0.24	81.43	81.06	0.37	50	81.69	0.94	0.20	82.63	81.49	1.14
99	81.30	0.13	0.24	81.43	81.06	0.37	49	81.70	0.97	0.21	82.67	81.49	1.18
98	81.31	0.12	0.24	81.43	81.07	0.36	48	81.71	0.98	0.22	82.69	81.49	1.20
97	81.31	0.12	0.23	81.43	81.08	0.35	47	81.72	1.04	0.23	82.76	81.49	1.27
96	81.32	0.12	0.23	81.44	81.09	0.35	46	81.73	1.04	0.24	82.77	81.49	1.28
95	81.32	0.12	0.22	81.44	81.10	0.34	45	81.74	1.04	0.25	82.78	81.49	1.29
94	81.33	0.11	0.22	81.44	81.11	0.33	44	81.75	1.10	0.26	82.85	81.49	1.36
93	81.33	0.11	0.21	81.44	81.12	0.32	43	81.76	1.11	0.27	82.87	81.49	1.38
92	81.34	0.11	0.21	81.45	81.13	0.32	42	81.77	1.13	0.27	82.90	81.50	1.40
91	81.35	0.10	0.20	81.45	81.15	0.30	41	81.78	1.15	0.28	82.93	81.50	1.43
90	81.35	0.10	0.19	81.45	81.16	0.29	40	81.79	1.16	0.29	82.95	81.50	1.45
89	81.36	0.09	0.19	81.45	81.17	0.28	39	81.79	1.18	0.29	82.97	81.50	1.47
88	81.36	0.09	0.18	81.45	81.18	0.27	38	81.81	1.21	0.31	83.02	81.50	1.52
87	81.37	0.08	0.19	81.45	81.18	0.27	37	81.82	1.21	0.32	83.03	81.50	1.53
86	81.38	0.08	0.19	81.46	81.19	0.27	36	81.82	1.25	0.32	83.07	81.50	1.57
85	81.38	0.08	0.18	81.46	81.20	0.26	35	81.84	1.24	0.34	83.08	81.50	1.58
84	81.39	0.07	0.18	81.46	81.21	0.25	34	81.85	1.24	0.35	83.09	81.50	1.59
83	81.39	0.07	0.17	81.46	81.22	0.24	33	81.86	1.25	0.36	83.11	81.50	1.61
82	81.40	0.07	0.17	81.47	81.23	0.24	32	81.87	1.26	0.36	83.13	81.51	1.62
81	81.41	0.06	0.17	81.47	81.24	0.23	31	81.88	1.25	0.37	83.13	81.51	1.62
80	81.41	0.06	0.17	81.47	81.24	0.23	30	81.89	1.26	0.38	83.15	81.51	1.64
79	81.42	0.05	0.16	81.47	81.26	0.21	29	81.90	1.25	0.39	83.15	81.51	1.64
78	81.42	0.06	0.15	81.48	81.27	0.21	28	81.91	1.25	0.40	83.16	81.51	1.65
77	81.43	0.05	0.14	81.48	81.29	0.19	27	81.92	1.24	0.41	83.16	81.51	1.65
76	81.44	0.04	0.13	81.48	81.31	0.17	26	81.93	1.24	0.42	83.17	81.51	1.66
75	81.44	0.05	0.11	81.49	81.33	0.16	25	81.94	1.25	0.42	83.19	81.52	1.67
74	81.45	0.04	0.09	81.49	81.36	0.13	24	81.95	1.28	0.43	83.23	81.52	1.71
73	81.46	0.04	0.07	81.50	81.39	0.11	23	81.95	1.30	0.43	83.25	81.52	1.73
72	81.47	0.03	0.04	81.50	81.43	0.07	22	81.96	1.34	0.44	83.30	81.52	1.78
71	81.48	0.23	0.04	81.71	81.44	0.27	21	81.97	1.34	0.45	83.31	81.52	1.79
70	81.49	0.37	0.04	81.86	81.45	0.41	20	81.98	1.33	0.46	83.31	81.52	1.79
69	81.51	0.45	0.06	81.96	81.45	0.51	19	81.99	1.37	0.47	83.36	81.52	1.84
68	81.52	0.52	0.07	82.04	81.45	0.59	18	82.00	1.37	0.48	83.37	81.52	1.85
67	81.53	0.60	0.07	82.13	81.46	0.67	17	82.01	1.37	0.49	83.38	81.52	1.86
66	81.54	0.60	0.08	82.14	81.46	0.68	16	82.03	1.36	0.51	83.39	81.52	1.87
65	81.55	0.62	0.09	82.17	81.46	0.71	15	82.03	1.37	0.50	83.40	81.53	1.87

Strat. Level* (m)	Model Age (Ma)	+	-	(Max)	(Min)	Range
14	82.05	1.38	0.52	83.43	81.53	1.90
13	82.05	1.38	0.52	83.43	81.53	1.90
12	82.06	1.38	0.53	83.44	81.53	1.91
11	82.08	1.37	0.55	83.45	81.53	1.92
10	82.08	1.40	0.55	83.48	81.53	1.95
9	82.10	1.40	0.57	83.50	81.53	1.97
8	82.11	1.40	0.58	83.51	81.53	1.98
7	82.11	1.42	0.58	83.53	81.53	2.00

Strat. Level* (m)	Model Age (Ma)	+	-	(Max)	(Min)	Range
6	82.12	1.43	0.59	83.55	81.53	2.02
5	82.13	1.42	0.59	83.55	81.54	2.01
4	82.14	1.42	0.60	83.56	81.54	2.02
3	82.15	1.43	0.61	83.58	81.54	2.04
2	82.16	1.44	0.62	83.60	81.54	2.06
1	82.17	1.46	0.63	83.63	81.54	2.09
0	82.17	1.47	0.63	83.64	81.54	2.10

\* Relative to the Reynolds Point lectostratotype section of Eaton (1991)

## Appendix C.4 Chapter Four Data

Appendix C.4.1 Complete U-Pb data for new Kaiparowits Formation CA-ID-TIMS analyses.

KWC050316-3																			
Samp.	Pb <sub>c</sub> <sup>§</sup>	Pb* <sup>§</sup>	U <sup>§</sup>	Th <sup>#</sup>	Ratios								Ages (Ma)						
					<u><sup>206</sup>Pb</u> **	<u><sup>208</sup>Pb</u> †	<u><sup>206</sup>Pb</u> § §	err	<u><sup>207</sup>Pb</u> § §	err	<u><sup>207</sup>Pb</u> § §	err	<u><sup>206</sup>Pb</u>	Err	<u><sup>207</sup>Pb</u>	Err	<u><sup>207</sup>Pb</u>	Err	corr.
Frac. †	(pg)	Pb <sub>c</sub>	(pg)	U	<sup>206</sup> Pb	<sup>206</sup> Pb	<sup>238</sup> U	(2σ%)	<sup>235</sup> U	(2σ%)	<sup>206</sup> Pb	(2σ%)	<sup>238</sup> U	(2σ)	<sup>235</sup> U	(2σ)	<sup>206</sup> Pb	(2σ)	coef.
z3	0.45	8.1	256	1.06	437.6	0.337	0.011810	(.24)	0.07847	(2.98)	0.04821	(2.91)	75.69	0.18	76.7	2.2	109	69	0.33
z11	0.30	12.1	260	1.08	640.5	0.345	0.011810	(.17)	0.07808	(2.04)	0.04797	(1.99)	75.69	0.13	76.3	1.5	97	47	0.35
z6	0.37	5.1	134	1.06	282.8	0.339	0.011796	(.38)	0.07846	(5.33)	0.04826	(5.18)	75.59	0.29	76.7	3.9	111	122	0.41
z2	0.46	23.0	776	0.92	1247.4	0.294	0.011792	(.10)	0.07769	(1.03)	0.04780	(1.00)	75.573	0.072	75.97	0.75	88	24	0.33
z8	0.30	30.7	704	0.78	1718.0	0.248	0.011788	(.08)	0.07768	(.78)	0.04782	(.76)	75.544	0.062	75.97	0.57	89	18	0.31
z4	0.30	7.8	178	0.76	453.1	0.244	0.011778	(.23)	0.07816	(2.95)	0.04815	(2.87)	75.48	0.18	76.4	2.2	106	68	0.35
z7	0.86	4.3	264	1.06	242.4	0.338	0.011778	(.44)	0.08139	(5.42)	0.05014	(5.28)	75.48	0.33	79.4	4.1	200	123	0.35
z5	0.50	9.4	341	1.00	510.6	0.319	0.011769	(.35)	0.07903	(2.79)	0.04872	(2.63)	75.43	0.26	77.2	2.1	133	62	0.51

Notes: Corr. coef. = correlation coefficient. Ages calculated using the decay constants  $\lambda_{238} = 1.55125E-10$  y<sup>-1</sup> and  $\lambda_{235} = 9.8485E-10$  y<sup>-1</sup> (Jaffey et al. 1971).

† All analyses are single zircon grains and pre-treated by the thermal annealing and acid leaching (CA-TIMS) technique. Data used in date calculation are in bold.

§ Pb(c) is total common-Pb in analysis. Pb\* is radiogenic Pb concentration. Total sample U content in pg.

#Th content is calculated from radiogenic <sup>208</sup>Pb assuming concordance between U-Pb and Th-U systems.

\*\*Measured ratio corrected for spike and fractionation only.

‡ Radiogenic Pb ratio.

§ § Corrected for fractionation, spike and blank. Also corrected for initial Th/U disequilibrium using radiogenic <sup>208</sup>Pb and Th/U[magma] = 2.8

Mass fractionation based on <sup>202</sup>Pb/<sup>205</sup>Pb ratio of tracer (~0.18% ± 0.04% /amu) was applied to single-collector Daly analyses.

All common Pb assumed to be laboratory blank. Total procedural blank less than 0.1 pg for U.

Blank isotopic composition: <sup>206</sup>Pb/<sup>204</sup>Pb = 18.20 ± 0.45, <sup>207</sup>Pb/<sup>204</sup>Pb = 15.29 ± 0.24, <sup>208</sup>Pb/<sup>204</sup>Pb = 37.16 ± 0.77.

IM1442																			
Samp.	Pb <sub>c</sub> <sup>§</sup>	Pb* <sup>§</sup>	U <sup>§</sup>	Th <sup>#</sup>	Ratios								Ages (Ma)						
					<u><sup>206</sup>Pb</u> **	<u><sup>208</sup>Pb</u> †	<u><sup>206</sup>Pb</u> <sup>§</sup>	err	<u><sup>207</sup>Pb</u> <sup>§</sup>	err	<u><sup>207</sup>Pb</u> <sup>§</sup>	err	<u><sup>206</sup>Pb</u>	Err	<u><sup>207</sup>Pb</u>	Err	<u><sup>207</sup>Pb</u>	Err	corr.
Frac <sup>†</sup>	(pg)	Pb <sub>c</sub>	(pg)	U	<sup>204</sup> Pb	<sup>206</sup> Pb	<sup>238</sup> U	(2σ%)	<sup>235</sup> U	(2σ%)	<sup>206</sup> Pb	(2σ%)	<sup>238</sup> U	(2σ)	<sup>235</sup> U	(2σ)	<sup>206</sup> Pb	(2σ)	coef.
z1	0.29	34.0	735	0.90	1850.0	0.286	0.011812	(.09)	0.07764	(.72)	0.04769	(.70)	75.701	0.064	75.92	0.52	83	17	0.29
z3	0.27	17.1	331	1.06	905.2	0.337	0.011810	(.13)	0.07763	(1.45)	0.04769	(1.42)	75.69	0.10	75.9	1.1	83	34	0.32
z5	0.24	16.4	274	1.12	855.4	0.358	0.011806	(.14)	0.07741	(1.59)	0.04758	(1.54)	75.66	0.11	75.7	1.2	77	37	0.34
z4	0.28	14.0	294	0.84	779.7	0.270	0.011803	(.16)	0.07768	(1.76)	0.04776	(1.71)	75.64	0.12	76.0	1.3	86	41	0.33
z2	0.41	19.7	595	0.91	1076.5	0.290	0.011800	(.11)	0.07762	(1.23)	0.04773	(1.19)	75.621	0.084	75.90	0.90	85	28	0.36
z6	0.23	20.3	361	0.68	1171.9	0.218	0.011798	(.11)	0.07796	(1.14)	0.04795	(1.10)	75.609	0.085	76.22	0.84	96	26	0.35

Notes: Corr. coef. = correlation coefficient. Ages calculated using the decay constants  $\lambda_{238} = 1.55125E-10$  y<sup>-1</sup> and  $\lambda_{235} = 9.8485E-10$  y<sup>-1</sup> (Jaffey et al. 1971).

† All analyses are single zircon grains and pre-treated by the thermal annealing and acid leaching (CA-TIMS) technique. Data used in date calculation are in bold.

§ Pb(c) is total common-Pb in analysis. Pb\* is radiogenic Pb concentration. Total sample U content in pg.

#Th content is calculated from radiogenic <sup>208</sup>Pb assuming concordance between U-Pb and Th-U systems.

\*\*Measured ratio corrected for spike and fractionation only.

‡ Radiogenic Pb ratio.

§ § Corrected for fractionation, spike and blank. Also corrected for initial Th/U disequilibrium using radiogenic <sup>208</sup>Pb and Th/U[magma] = 2.8

Mass fractionation based on <sup>202</sup>Pb/<sup>205</sup>Pb ratio of tracer (~0.18% ± 0.04% /amu) was applied to single-collector Daly analyses.

All common Pb assumed to be laboratory blank. Total procedural blank less than 0.1 pg for U.

Blank isotopic composition: <sup>206</sup>Pb/<sup>204</sup>Pb = 18.20 ± 0.45, <sup>207</sup>Pb/<sup>204</sup>Pb = 15.29 ± 0.24, <sup>208</sup>Pb/<sup>204</sup>Pb = 37.16 ± 0.77.

KWC050316-1																			
Samp.	Pb <sub>c</sub> <sup>§</sup>	Pb* <sup>§</sup>	U <sup>§</sup>	Th <sup>#</sup>	Ratios								Ages (Ma)						
					<u><sup>206</sup>Pb</u> **	<u><sup>208</sup>Pb</u> ‡	<u><sup>206</sup>Pb</u> <sup>§</sup> §	err	<u><sup>207</sup>Pb</u> <sup>§</sup> §	err	<u><sup>207</sup>Pb</u> <sup>§</sup> §	err	<u><sup>206</sup>Pb</u>	Err	<u><sup>207</sup>Pb</u>	Err	<u><sup>207</sup>Pb</u>	Err	<u><sup>206</sup>Pb</u>
Frac <sup>†</sup>	(pg)	Pb <sub>c</sub>	(pg)	U	<sup>204</sup> Pb	<sup>206</sup> Pb	<sup>238</sup> U	(2σ%)	<sup>235</sup> U	(2σ%)	<sup>206</sup> Pb	(2σ%)	<sup>238</sup> U	(2σ)	<sup>235</sup> U	(2σ)	<sup>206</sup> Pb	(2σ)	coef.
z3	0.37	14.5	437	0.45	894.2	0.144	0.011874	(.13)	0.07751	(1.50)	0.04736	(1.45)	76.09	0.10	75.8	1.1	66	35	0.38
z4	0.27	87.0	1977	0.40	5332.1	0.129	0.011871	(.06)	0.07803	(.28)	0.04769	(.25)	76.074	0.049	76.29	0.21	83.0	6.1	0.48
z2	0.35	10.6	304	0.49	647.9	0.158	0.011864	(.17)	0.07964	(2.16)	0.04870	(2.11)	76.03	0.12	77.8	1.6	133	50	0.33
z5	0.23	8.7	151	0.81	496.3	0.258	0.011860	(.22)	0.07912	(2.67)	0.04841	(2.60)	76.00	0.17	77.3	2.0	118	61	0.34
z7	0.25	6.7	130	0.62	402.8	0.199	0.011854	(.26)	0.07854	(3.15)	0.04807	(3.07)	75.97	0.20	76.8	2.3	102	73	0.33
z1	0.32	37.6	955	0.56	2222.2	0.178	0.011844	(.07)	0.07806	(.58)	0.04782	(.56)	75.900	0.050	76.32	0.43	89	13	0.34
z6	0.26	46.8	1003	0.42	2868.5	0.133	0.011840	(.06)	0.07793	(.47)	0.04776	(.45)	75.879	0.045	76.19	0.34	86	11	0.32

Notes: Corr. coef. = correlation coefficient. Ages calculated using the decay constants  $\lambda_{238} = 1.55125E-10$  y<sup>-1</sup> and  $\lambda_{235} = 9.8485E-10$  y<sup>-1</sup> (Jaffey et al. 1971).

† All analyses are single zircon grains and pre-treated by the thermal annealing and acid leaching (CA-TIMS) technique. Data used in date calculation are in bold.

§ Pb(c) is total common-Pb in analysis. Pb\* is radiogenic Pb concentration. Total sample U content in pg.

#Th content is calculated from radiogenic <sup>208</sup>Pb assuming concordance between U-Pb and Th-U systems.

\*\*Measured ratio corrected for spike and fractionation only.

‡ Radiogenic Pb ratio.

§ § Corrected for fractionation, spike and blank. Also corrected for initial Th/U disequilibrium using radiogenic <sup>208</sup>Pb and Th/U[magma] = 2.8

Mass fractionation based on <sup>202</sup>Pb/<sup>205</sup>Pb ratio of tracer (~0.18% ± 0.04% /amu) was applied to single-collector Daly analyses.

All common Pb assumed to be laboratory blank. Total procedural blank less than 0.1 pg for U.

Blank isotopic composition: <sup>206</sup>Pb/<sup>204</sup>Pb = 18.20 ± 0.45, <sup>207</sup>Pb/<sup>204</sup>Pb = 15.29 ± 0.24, <sup>208</sup>Pb/<sup>204</sup>Pb = 37.16 ± 0.77.

KDR050416-1																			
Samp.	Pb <sub>c</sub> <sup>§</sup>	Pb* <sup>§</sup>	U <sup>§</sup>	Th <sup>#</sup>	Ratios								Ages (Ma)						
					<u><sup>206</sup>Pb</u> **	<u><sup>208</sup>Pb</u> ‡	<u><sup>206</sup>Pb</u> <sup>§</sup> §	err	<u><sup>207</sup>Pb</u> <sup>§</sup> §	err	<u><sup>207</sup>Pb</u> <sup>§</sup> §	err	<u><sup>206</sup>Pb</u>	Err	<u><sup>207</sup>Pb</u>	Err	<u><sup>207</sup>Pb</u>	Err	corr.
Frac <sup>†</sup>	(pg)	Pb <sub>c</sub>	(pg)	U	<sup>204</sup> Pb	<sup>206</sup> Pb	<sup>238</sup> U	(2σ%)	<sup>235</sup> U	(2σ%)	<sup>206</sup> Pb	(2σ%)	<sup>238</sup> U	(2σ)	<sup>235</sup> U	(2σ)	<sup>206</sup> Pb	(2σ)	coef.
z11	0.81	28.5	759	1.02	1507.2	0.324	0.025731	(.08)	0.17508	(.82)	0.04937	(.80)	163.78	0.12	163.8	1.2	164	19	0.37
z3	0.32	17.9	367	1.34	889.2	0.428	0.012137	(.14)	0.07983	(1.52)	0.04772	(1.47)	77.77	0.11	78.0	1.1	85	35	0.35
z7	0.46	3.6	105	1.52	187.5	0.484	0.012095	(.60)	0.08301	(7.74)	0.04980	(7.56)	77.50	0.46	81.0	6.0	185	176	0.34
z6	0.83	6.8	345	1.66	327.3	0.530	0.012074	(.31)	0.08077	(3.97)	0.04854	(3.88)	77.37	0.24	78.9	3.0	125	91	0.32
z10	0.47	15.0	379	2.27	625.5	0.725	0.012074	(.17)	0.07928	(2.07)	0.04765	(2.02)	77.37	0.13	77.5	1.5	81	48	0.32
z9	0.45	7.4	206	1.57	362.4	0.501	0.012053	(.28)	0.08008	(3.62)	0.04821	(3.54)	77.23	0.22	78.2	2.7	108	84	0.33
z8	0.29	19.4	407	0.94	1050.1	0.299	0.011988	(.11)	0.07930	(1.23)	0.04800	(1.20)	76.819	0.080	77.48	0.92	98	28	0.35
Lz12	0.24	34.1	559	1.26	1705.9	0.402	0.011921	(.07)	0.07866	(.75)	0.04788	(.73)	76.394	0.052	76.89	0.56	92	17	0.32
Lz14	0.25	18.5	306	1.35	916.4	0.432	0.011915	(.12)	0.07902	(1.42)	0.04812	(1.39)	76.356	0.090	77.2	1.1	104	33	0.33
z1	0.25	52.1	874	1.34	2554.2	0.426	0.011904	(.06)	0.07837	(.52)	0.04777	(.50)	76.286	0.042	76.61	0.38	87	12	0.28
z5	0.42	51.8	1541	1.08	2690.3	0.343	0.011903	(.08)	0.07836	(.57)	0.04777	(.55)	76.276	0.057	76.60	0.42	87	13	0.33
Lz13	0.25	90.0	1571	1.12	4613.8	0.358	0.011899	(.04)	0.07827	(.29)	0.04773	(.28)	76.250	0.030	76.52	0.21	84.8	6.6	0.22
z4	0.27	79.6	1525	1.05	4147.6	0.336	0.011898	(.05)	0.07831	(.32)	0.04776	(.31)	76.244	0.037	76.55	0.23	86.2	7.4	0.18

Notes: Corr. coef. = correlation coefficient. Ages calculated using the decay constants  $\lambda_{238} = 1.55125E-10$  y<sup>-1</sup> and  $\lambda_{235} = 9.8485E-10$  y<sup>-1</sup> (Jaffey et al. 1971).

† All analyses are single zircon grains and pre-treated by the thermal annealing and acid leaching (CA-TIMS) technique. Data used in date calculation are in bold.

§ Pb(c) is total common-Pb in analysis. Pb\* is radiogenic Pb concentration. Total sample U content in pg.

#Th content is calculated from radiogenic <sup>208</sup>Pb assuming concordance between U-Pb and Th-U systems.

\*\*Measured ratio corrected for spike and fractionation only.

‡ Radiogenic Pb ratio.

§ § Corrected for fractionation, spike and blank. Also corrected for initial Th/U disequilibrium using radiogenic <sup>208</sup>Pb and Th/U[magma] = 2.8

Mass fractionation based on <sup>202</sup>Pb/<sup>205</sup>Pb ratio of tracer (~0.18% ± 0.04% /amu) was applied to single-collector Daly analyses.

All common Pb assumed to be laboratory blank. Total procedural blank less than 0.1 pg for U.

Blank isotopic composition: <sup>206</sup>Pb/<sup>204</sup>Pb = 18.20 ± 0.45, <sup>207</sup>Pb/<sup>204</sup>Pb = 15.29 ± 0.24, <sup>208</sup>Pb/<sup>204</sup>Pb = 37.16 ± 0.77.



KWC050316-2																			
Samp.	Pb <sub>c</sub> <sup>§</sup>	Pb* <sup>§</sup>	U <sup>§</sup>	Th <sup>#</sup>	Ratios								Ages (Ma)						
					<u><sup>206</sup>Pb</u> **	<u><sup>208</sup>Pb</u> ‡	<u><sup>206</sup>Pb</u> <sup>§</sup> §	err	<u><sup>207</sup>Pb</u> <sup>§</sup> §	err	<u><sup>207</sup>Pb</u> <sup>§</sup> §	err	<u><sup>206</sup>Pb</u>	Err	<u><sup>207</sup>Pb</u>	Err	<u><sup>207</sup>Pb</u>	Err	corr.
Frac <sup>†</sup>	(pg)	Pb <sub>c</sub>	(pg)	U	<sup>204</sup> Pb	<sup>206</sup> Pb	<sup>238</sup> U	(2σ%)	<sup>235</sup> U	(2σ%)	<sup>206</sup> Pb	(2σ%)	<sup>238</sup> U	(2σ)	<sup>235</sup> U	(2σ)	<sup>206</sup> Pb	(2σ)	coef.
z6	0.35	23.4	538	1.31	1163.1	0.418	0.011921	(.10)	0.07865	(1.11)	0.04787	(1.08)	76.391	0.079	76.88	0.82	92	26	0.32
z3	0.32	25.1	539	1.25	1265.1	0.399	0.011918	(.11)	0.07884	(1.03)	0.04800	(1.00)	76.371	0.080	77.05	0.76	98	24	0.33
z7	0.33	33.9	744	1.32	1671.4	0.422	0.011914	(.08)	0.07847	(.77)	0.04779	(.75)	76.348	0.060	76.71	0.57	88	18	0.32
z8	0.24	47.7	753	1.38	2318.4	0.442	0.011914	(.07)	0.07835	(.56)	0.04772	(.54)	76.347	0.052	76.60	0.42	84	13	0.33
z1	0.37	19.9	447	1.71	912.8	0.546	0.011910	(.13)	0.07770	(1.45)	0.04734	(1.41)	76.326	0.097	76.0	1.1	65	34	0.33
z2	0.29	42.6	789	1.46	2036.8	0.468	0.011909	(.08)	0.07843	(.64)	0.04778	(.62)	76.314	0.059	76.66	0.47	88	15	0.32
z9	0.52	17.9	663	1.02	954.3	0.325	0.011908	(.12)	0.07851	(1.34)	0.04784	(1.31)	76.313	0.088	76.74	0.99	90	31	0.33
z4	0.31	19.6	383	1.51	935.0	0.483	0.011905	(.12)	0.07853	(1.41)	0.04786	(1.38)	76.293	0.092	76.8	1.0	91	33	0.33
z5	0.27	14.6	249	1.62	687.8	0.517	0.011897	(.16)	0.07799	(1.90)	0.04757	(1.86)	76.24	0.12	76.3	1.4	77	44	0.33

Notes: Corr. coef. = correlation coefficient. Ages calculated using the decay constants  $\lambda_{238} = 1.55125E-10$  y<sup>-1</sup> and  $\lambda_{235} = 9.8485E-10$  y<sup>-1</sup> (Jaffey et al. 1971).

† All analyses are single zircon grains and pre-treated by the thermal annealing and acid leaching (CA-TIMS) technique. Data used in date calculation are in bold.

§ Pb(c) is total common-Pb in analysis. Pb\* is radiogenic Pb concentration. Total sample U content in pg.

#Th content is calculated from radiogenic <sup>208</sup>Pb assuming concordance between U-Pb and Th-U systems.

\*\*Measured ratio corrected for spike and fractionation only.

‡ Radiogenic Pb ratio.

§ § Corrected for fractionation, spike and blank. Also corrected for initial Th/U disequilibrium using radiogenic <sup>208</sup>Pb and Th/U[magma] = 2.8

Mass fractionation based on <sup>202</sup>Pb/<sup>205</sup>Pb ratio of tracer (~0.18% ± 0.04% /amu) was applied to single-collector Daly analyses.

All common Pb assumed to be laboratory blank. Total procedural blank less than 0.1 pg for U.

Blank isotopic composition: <sup>206</sup>Pb/<sup>204</sup>Pb = 18.20 ± 0.45, <sup>207</sup>Pb/<sup>204</sup>Pb = 15.29 ± 0.24, <sup>208</sup>Pb/<sup>204</sup>Pb = 37.16 ± 0.77.

**Appendix C.4.2** Kaiparowits Formation Bayesian age-stratigraphic model (KBC/KBU stratotype section) input data.

id	ages	ageSds	position	thickness	calCurves
"KBU-W"	73100	600	0	0	normal
"KBU-O"	73200	700	8000	0	normal
"KBU-F"	73680	405	21000	0	normal
"KBO-37"	73900	85	22000	0	normal
"KBU-V"	73680	330	24500	0	normal
"KBU-S"	75200	700	28000	0	normal
"KBC-195"	75231	19	39800	0	normal
"KBC-144"	75427	11.5	51200	0	normal
"KBC-109"	75609	12.5	59000	0	normal
"KP-07A"	76394	22.5	83000	0	normal
"Base"	77290	360	101000	0	normal

Notes: *id* = samples name, *ages* = kyrs, *ageSds* = uncertainty (*Y*) at  $1\sigma$  in kyrs, *position* = stratigraphic height (cm) as “depth” beginning at 5 m above the Kaiparowits Fm, *thickness* = thickness of sampled horizon (null=0).

**Appendix C.4.3** Kaiparowits Formation Bayesian age-stratigraphic model (KBC/KBU stratotype section) script.

```
>library(Bchron)

>KBC_Stratotype <- read.csv(file.choose())

>KBC_StratotypeModel=Bchronology(ages=KBC_Stratotype$ages,
                                ageSds=KBC_Stratotype$ageSds,
                                calCurves=KBC_Stratotype$calCurves,
                                positions=KBC_Stratotype$position,
                                positionThicknesses=KBC_Stratotype$thickness,
                                ids=KBC_Stratotype$id,
                                predictPositions=seq(0,101100,by=100),
                                iterations=100000)

>library(ggplot2)

>plot(KBC_StratotypeModel)+labs(x='Age (ka)',y='Depth (cm)',title='KBC Stratotype Bchron Model')

> KBC_StratotypeModelAges <- matrix(nrow=1011, ncol=3)

for(i in 1:1011){ KBC_StratotypeModelAges [i,]=quantile(KBC_StratotypeModel$thetaPredict[,i],probs =
c(0.025,0.5,0.975))}

>write.csv(KBC_StratotypeModelAges, "KBC Stratotype Model Output.csv")
```

**Appendix C.4.4** *Kaiparowits Formation Bayesian age-stratigraphic model (KBC/KBU stratotype section) numerical output.*

Strat. Level* (m)	Model Age (Ma)	+	-	(Max)	(Min)	Range	Strat. Level* (m)	Model Age (Ma)	+	-	(Max)	(Min)	Range
1010	72.91	0.51	0.67	73.42	72.24	1.18	963	73.11	0.43	0.58	73.54	72.53	1.01
1009	72.92	0.50	0.67	73.42	72.25	1.17	962	73.11	0.43	0.58	73.54	72.53	1.01
1008	72.92	0.50	0.67	73.42	72.26	1.17	961	73.12	0.43	0.58	73.54	72.53	1.01
1007	72.93	0.50	0.67	73.43	72.26	1.17	960	73.12	0.43	0.58	73.55	72.54	1.01
1006	72.94	0.50	0.66	73.43	72.27	1.16	959	73.12	0.43	0.58	73.55	72.54	1.00
1005	72.94	0.49	0.66	73.44	72.28	1.16	958	73.13	0.42	0.58	73.55	72.55	1.00
1004	72.95	0.49	0.66	73.44	72.29	1.15	957	73.13	0.42	0.58	73.55	72.55	1.00
1003	72.95	0.49	0.66	73.44	72.29	1.15	956	73.14	0.42	0.58	73.56	72.56	1.00
1002	72.96	0.49	0.66	73.44	72.30	1.14	955	73.14	0.42	0.58	73.56	72.56	1.00
1001	72.96	0.49	0.65	73.45	72.31	1.14	954	73.14	0.42	0.58	73.56	72.57	1.00
1000	72.97	0.49	0.65	73.45	72.32	1.14	953	73.15	0.42	0.58	73.57	72.57	0.99
999	72.97	0.48	0.64	73.45	72.32	1.13	952	73.15	0.41	0.58	73.57	72.58	0.99
998	72.97	0.48	0.64	73.46	72.33	1.13	951	73.16	0.41	0.58	73.57	72.58	0.99
997	72.98	0.48	0.64	73.46	72.34	1.12	950	73.16	0.41	0.58	73.58	72.59	0.99
996	72.98	0.48	0.64	73.46	72.34	1.12	949	73.17	0.41	0.58	73.58	72.59	0.99
995	72.99	0.48	0.64	73.47	72.35	1.12	948	73.17	0.41	0.58	73.58	72.59	0.99
994	72.99	0.48	0.63	73.47	72.36	1.11	947	73.17	0.41	0.57	73.58	72.60	0.99
993	72.99	0.48	0.63	73.47	72.36	1.11	946	73.18	0.41	0.57	73.59	72.60	0.98
992	73.00	0.48	0.63	73.47	72.37	1.10	945	73.18	0.41	0.57	73.59	72.61	0.98
991	73.00	0.48	0.63	73.48	72.37	1.10	944	73.19	0.41	0.57	73.59	72.61	0.98
990	73.01	0.48	0.62	73.48	72.38	1.10	943	73.19	0.41	0.57	73.60	72.62	0.98
989	73.01	0.47	0.62	73.48	72.39	1.10	942	73.19	0.41	0.57	73.60	72.62	0.98
988	73.01	0.47	0.62	73.48	72.39	1.09	941	73.20	0.41	0.57	73.60	72.63	0.98
987	73.02	0.47	0.62	73.49	72.40	1.09	940	73.20	0.41	0.57	73.61	72.63	0.98
986	73.02	0.47	0.62	73.49	72.41	1.08	939	73.21	0.41	0.57	73.61	72.64	0.98
985	73.03	0.47	0.62	73.49	72.41	1.08	938	73.21	0.41	0.57	73.62	72.64	0.97
984	73.03	0.46	0.61	73.49	72.42	1.08	937	73.22	0.40	0.57	73.62	72.65	0.97
983	73.03	0.46	0.61	73.50	72.42	1.07	936	73.22	0.40	0.57	73.62	72.65	0.97
982	73.04	0.46	0.61	73.50	72.43	1.07	935	73.23	0.40	0.56	73.63	72.66	0.97
981	73.04	0.46	0.61	73.50	72.43	1.07	934	73.23	0.40	0.56	73.63	72.67	0.96
980	73.04	0.46	0.61	73.50	72.44	1.06	933	73.24	0.40	0.56	73.64	72.68	0.96
979	73.05	0.46	0.60	73.50	72.44	1.06	932	73.25	0.40	0.56	73.64	72.68	0.96
978	73.05	0.46	0.60	73.51	72.45	1.06	931	73.25	0.39	0.56	73.65	72.69	0.95
977	73.06	0.45	0.60	73.51	72.45	1.05	930	73.26	0.39	0.56	73.65	72.70	0.95
976	73.06	0.45	0.60	73.51	72.46	1.05	929	73.27	0.39	0.56	73.66	72.71	0.95
975	73.06	0.45	0.60	73.51	72.46	1.05	928	73.27	0.39	0.55	73.66	72.72	0.94
974	73.07	0.45	0.60	73.51	72.47	1.04	927	73.28	0.39	0.55	73.66	72.72	0.94
973	73.07	0.45	0.60	73.52	72.47	1.04	926	73.28	0.39	0.55	73.67	72.73	0.94
972	73.07	0.44	0.59	73.52	72.48	1.04	925	73.28	0.39	0.55	73.67	72.74	0.93
971	73.08	0.44	0.59	73.52	72.49	1.03	924	73.29	0.39	0.54	73.68	72.74	0.93
970	73.08	0.44	0.59	73.52	72.49	1.03	923	73.29	0.39	0.54	73.68	72.75	0.93
969	73.09	0.44	0.59	73.52	72.50	1.03	922	73.29	0.39	0.54	73.68	72.76	0.92
968	73.09	0.44	0.59	73.53	72.50	1.02	921	73.30	0.39	0.53	73.68	72.76	0.92
967	73.09	0.44	0.58	73.53	72.51	1.02	920	73.30	0.38	0.53	73.69	72.77	0.92
966	73.10	0.43	0.58	73.53	72.51	1.02	919	73.31	0.38	0.53	73.69	72.77	0.91
965	73.10	0.43	0.58	73.53	72.52	1.01	918	73.31	0.38	0.53	73.69	72.78	0.91
964	73.10	0.43	0.58	73.54	72.52	1.01	917	73.31	0.38	0.53	73.69	72.78	0.91

Strat. Level* (m)	Model Age (Ma)	+	-	(Max)	(Min)	Range	Strat. Level* (m)	Model Age (Ma)	+	-	(Max)	(Min)	Range
916	73.32	0.38	0.52	73.69	72.79	0.90	866	73.46	0.31	0.45	73.77	73.01	0.77
915	73.32	0.38	0.52	73.70	72.80	0.90	865	73.46	0.31	0.45	73.77	73.01	0.76
914	73.32	0.38	0.52	73.70	72.80	0.90	864	73.46	0.31	0.45	73.77	73.01	0.76
913	73.33	0.37	0.52	73.70	72.81	0.89	863	73.47	0.31	0.45	73.77	73.02	0.76
912	73.33	0.37	0.52	73.70	72.81	0.89	862	73.47	0.31	0.45	73.78	73.02	0.76
911	73.33	0.37	0.52	73.70	72.82	0.89	861	73.47	0.31	0.44	73.78	73.03	0.75
910	73.34	0.37	0.52	73.70	72.82	0.88	860	73.47	0.31	0.44	73.78	73.03	0.75
909	73.34	0.37	0.52	73.71	72.82	0.88	859	73.48	0.31	0.44	73.78	73.04	0.75
908	73.34	0.37	0.51	73.71	72.83	0.88	858	73.48	0.31	0.44	73.79	73.04	0.75
907	73.34	0.37	0.51	73.71	72.83	0.88	857	73.48	0.31	0.44	73.79	73.05	0.74
906	73.35	0.37	0.51	73.71	72.83	0.88	856	73.48	0.31	0.43	73.79	73.05	0.74
905	73.35	0.36	0.51	73.71	72.84	0.87	855	73.49	0.30	0.43	73.79	73.05	0.74
904	73.35	0.36	0.51	73.72	72.85	0.87	854	73.49	0.30	0.43	73.79	73.06	0.74
903	73.36	0.36	0.50	73.72	72.85	0.87	853	73.49	0.30	0.43	73.79	73.06	0.73
902	73.36	0.36	0.50	73.72	72.86	0.86	852	73.49	0.30	0.43	73.79	73.06	0.73
901	73.36	0.36	0.50	73.72	72.86	0.86	851	73.50	0.30	0.43	73.80	73.07	0.73
900	73.36	0.36	0.50	73.72	72.87	0.86	850	73.50	0.30	0.43	73.80	73.07	0.72
899	73.37	0.36	0.50	73.72	72.87	0.85	849	73.50	0.30	0.43	73.80	73.08	0.72
898	73.37	0.35	0.50	73.73	72.87	0.85	848	73.50	0.30	0.43	73.80	73.08	0.72
897	73.37	0.35	0.49	73.73	72.88	0.85	847	73.51	0.30	0.42	73.80	73.08	0.72
896	73.38	0.35	0.49	73.73	72.88	0.84	846	73.51	0.29	0.42	73.80	73.09	0.72
895	73.38	0.35	0.49	73.73	72.89	0.84	845	73.51	0.29	0.42	73.81	73.09	0.71
894	73.38	0.35	0.49	73.73	72.89	0.84	844	73.52	0.29	0.42	73.81	73.10	0.71
893	73.38	0.35	0.49	73.73	72.90	0.83	843	73.52	0.29	0.42	73.81	73.10	0.71
892	73.39	0.35	0.48	73.73	72.90	0.83	842	73.52	0.29	0.42	73.81	73.10	0.71
891	73.39	0.35	0.48	73.73	72.91	0.83	841	73.52	0.29	0.42	73.81	73.11	0.70
890	73.39	0.34	0.48	73.74	72.91	0.83	840	73.53	0.29	0.42	73.81	73.11	0.70
889	73.40	0.34	0.48	73.74	72.92	0.82	839	73.53	0.29	0.42	73.81	73.11	0.70
888	73.40	0.34	0.48	73.74	72.92	0.82	838	73.53	0.28	0.41	73.82	73.12	0.70
887	73.40	0.34	0.48	73.74	72.92	0.82	837	73.54	0.28	0.41	73.82	73.12	0.70
886	73.40	0.34	0.48	73.74	72.93	0.82	836	73.54	0.28	0.41	73.82	73.13	0.69
885	73.41	0.34	0.47	73.74	72.93	0.81	835	73.54	0.28	0.41	73.82	73.13	0.69
884	73.41	0.34	0.47	73.75	72.94	0.81	834	73.54	0.28	0.41	73.82	73.13	0.69
883	73.41	0.34	0.47	73.75	72.94	0.81	833	73.55	0.28	0.41	73.83	73.14	0.69
882	73.41	0.33	0.47	73.75	72.94	0.81	832	73.55	0.28	0.41	73.83	73.14	0.68
881	73.42	0.33	0.47	73.75	72.95	0.80	831	73.55	0.28	0.40	73.83	73.15	0.68
880	73.42	0.33	0.47	73.75	72.95	0.80	830	73.56	0.28	0.40	73.83	73.15	0.68
879	73.42	0.33	0.47	73.75	72.95	0.80	829	73.56	0.28	0.40	73.84	73.16	0.68
878	73.43	0.33	0.47	73.75	72.96	0.80	828	73.56	0.27	0.40	73.84	73.16	0.68
877	73.43	0.33	0.47	73.76	72.96	0.79	827	73.56	0.27	0.40	73.84	73.16	0.68
876	73.43	0.33	0.46	73.76	72.97	0.79	826	73.57	0.27	0.40	73.84	73.17	0.68
875	73.43	0.32	0.46	73.76	72.97	0.79	825	73.57	0.27	0.40	73.84	73.17	0.67
874	73.44	0.32	0.46	73.76	72.97	0.78	824	73.57	0.27	0.40	73.85	73.18	0.67
873	73.44	0.32	0.46	73.76	72.98	0.78	823	73.58	0.27	0.40	73.85	73.18	0.67
872	73.44	0.32	0.46	73.76	72.98	0.78	822	73.58	0.27	0.40	73.85	73.18	0.67
871	73.44	0.32	0.46	73.76	72.98	0.78	821	73.58	0.27	0.40	73.85	73.19	0.67
870	73.45	0.32	0.46	73.77	72.99	0.78	820	73.59	0.27	0.40	73.85	73.19	0.66
869	73.45	0.32	0.45	73.77	72.99	0.77	819	73.59	0.27	0.40	73.86	73.19	0.66
868	73.45	0.32	0.45	73.77	73.00	0.77	818	73.59	0.27	0.40	73.86	73.20	0.66
867	73.45	0.32	0.45	73.77	73.00	0.77	817	73.60	0.26	0.39	73.86	73.20	0.66

Strat. Level* (m)	Model Age (Ma)	+	-	(Max)	(Min)	Range	Strat. Level* (m)	Model Age (Ma)	+	-	(Max)	(Min)	Range
816	73.60	0.26	0.40	73.86	73.20	0.66	766	74.13	0.30	0.24	74.43	73.90	0.54
815	73.60	0.26	0.40	73.87	73.21	0.66	765	74.14	0.31	0.24	74.46	73.90	0.55
814	73.61	0.26	0.39	73.87	73.21	0.65	764	74.16	0.32	0.24	74.48	73.92	0.56
813	73.61	0.26	0.39	73.87	73.22	0.65	763	74.18	0.31	0.24	74.49	73.93	0.56
812	73.61	0.26	0.39	73.87	73.22	0.65	762	74.19	0.31	0.24	74.50	73.95	0.56
811	73.62	0.26	0.39	73.88	73.23	0.65	761	74.20	0.31	0.25	74.52	73.96	0.56
810	73.62	0.26	0.39	73.88	73.23	0.65	760	74.22	0.31	0.25	74.53	73.97	0.56
809	73.62	0.26	0.38	73.88	73.24	0.64	759	74.23	0.31	0.25	74.54	73.98	0.56
808	73.63	0.26	0.39	73.89	73.24	0.64	758	74.25	0.31	0.26	74.56	73.99	0.57
807	73.63	0.26	0.38	73.89	73.25	0.64	757	74.26	0.31	0.26	74.57	74.00	0.57
806	73.64	0.26	0.38	73.89	73.26	0.63	756	74.27	0.31	0.27	74.58	74.01	0.57
805	73.64	0.26	0.38	73.90	73.26	0.63	755	74.29	0.31	0.27	74.59	74.01	0.58
804	73.64	0.25	0.38	73.90	73.27	0.63	754	74.30	0.31	0.28	74.60	74.02	0.58
803	73.65	0.25	0.37	73.90	73.27	0.63	753	74.31	0.31	0.28	74.62	74.03	0.59
802	73.65	0.25	0.37	73.91	73.28	0.63	752	74.32	0.31	0.29	74.63	74.04	0.59
801	73.66	0.25	0.37	73.91	73.29	0.62	751	74.34	0.31	0.30	74.64	74.04	0.60
800	73.67	0.25	0.37	73.92	73.30	0.62	750	74.35	0.31	0.30	74.65	74.05	0.61
799	73.69	0.24	0.34	73.93	73.35	0.58	749	74.36	0.30	0.31	74.67	74.05	0.61
798	73.71	0.23	0.30	73.94	73.41	0.53	748	74.38	0.30	0.32	74.68	74.06	0.62
797	73.73	0.22	0.28	73.95	73.46	0.49	747	74.39	0.31	0.32	74.69	74.07	0.63
796	73.76	0.20	0.25	73.96	73.51	0.45	746	74.40	0.31	0.33	74.71	74.07	0.64
795	73.78	0.19	0.22	73.97	73.55	0.42	745	74.41	0.31	0.33	74.73	74.08	0.65
794	73.80	0.18	0.20	73.98	73.60	0.38	744	74.43	0.31	0.34	74.74	74.09	0.66
793	73.82	0.17	0.18	74.00	73.64	0.36	743	74.44	0.32	0.35	74.76	74.09	0.67
792	73.85	0.17	0.17	74.01	73.67	0.34	742	74.45	0.33	0.35	74.78	74.10	0.68
791	73.87	0.16	0.17	74.03	73.71	0.33	741	74.46	0.33	0.36	74.79	74.10	0.69
790	73.90	0.16	0.16	74.05	73.74	0.32	740	74.48	0.34	0.37	74.81	74.11	0.71
789	73.91	0.16	0.16	74.07	73.75	0.32	739	74.49	0.35	0.38	74.83	74.11	0.72
788	73.92	0.16	0.16	74.08	73.76	0.32	738	74.50	0.35	0.38	74.85	74.12	0.74
787	73.93	0.16	0.16	74.09	73.77	0.32	737	74.51	0.36	0.39	74.87	74.12	0.75
786	73.94	0.16	0.16	74.11	73.78	0.33	736	74.52	0.37	0.40	74.89	74.13	0.76
785	73.95	0.17	0.17	74.12	73.79	0.33	735	74.54	0.38	0.40	74.91	74.13	0.78
784	73.96	0.17	0.17	74.13	73.79	0.34	734	74.55	0.38	0.41	74.93	74.14	0.79
783	73.97	0.17	0.17	74.14	73.80	0.34	733	74.56	0.39	0.42	74.96	74.15	0.81
782	73.98	0.17	0.17	74.16	73.81	0.35	732	74.58	0.41	0.42	74.98	74.15	0.83
781	73.99	0.18	0.18	74.17	73.81	0.35	731	74.59	0.42	0.43	75.00	74.16	0.84
780	74.00	0.18	0.18	74.18	73.82	0.36	730	74.61	0.42	0.43	75.03	74.18	0.85
779	74.01	0.19	0.18	74.20	73.83	0.37	729	74.62	0.42	0.42	75.04	74.20	0.84
778	74.02	0.19	0.19	74.21	73.83	0.38	728	74.63	0.41	0.42	75.04	74.21	0.83
777	74.03	0.20	0.19	74.23	73.84	0.39	727	74.64	0.41	0.42	75.04	74.22	0.82
776	74.04	0.21	0.19	74.24	73.84	0.40	726	74.64	0.40	0.42	75.05	74.23	0.82
775	74.05	0.22	0.20	74.26	73.85	0.41	725	74.65	0.40	0.41	75.05	74.24	0.81
774	74.06	0.22	0.20	74.28	73.85	0.43	724	74.66	0.40	0.41	75.05	74.25	0.81
773	74.07	0.23	0.21	74.30	73.86	0.44	723	74.67	0.39	0.41	75.06	74.25	0.80
772	74.07	0.24	0.21	74.32	73.86	0.45	722	74.67	0.39	0.41	75.06	74.26	0.80
771	74.08	0.25	0.22	74.34	73.87	0.47	721	74.68	0.38	0.41	75.06	74.27	0.79
770	74.09	0.26	0.22	74.35	73.87	0.48	720	74.69	0.38	0.41	75.07	74.28	0.79
769	74.10	0.27	0.22	74.37	73.88	0.50	719	74.69	0.38	0.41	75.07	74.29	0.78
768	74.11	0.28	0.23	74.39	73.88	0.51	718	74.70	0.37	0.40	75.07	74.29	0.78
767	74.12	0.29	0.23	74.41	73.89	0.53	717	74.70	0.37	0.41	75.07	74.30	0.77

Strat. Level* (m)	Model Age (Ma)	+	-	(Max)	(Min)	Range	Strat. Level* (m)	Model Age (Ma)	+	-	(Max)	(Min)	Range
716	74.71	0.37	0.40	75.08	74.31	0.77	666	74.96	0.20	0.38	75.17	74.58	0.59
715	74.71	0.36	0.40	75.08	74.31	0.76	665	74.97	0.20	0.38	75.17	74.58	0.59
714	74.72	0.36	0.40	75.08	74.32	0.76	664	74.97	0.20	0.38	75.17	74.59	0.58
713	74.73	0.36	0.40	75.08	74.33	0.75	663	74.98	0.20	0.38	75.17	74.59	0.58
712	74.73	0.35	0.40	75.09	74.33	0.75	662	74.98	0.19	0.38	75.17	74.60	0.58
711	74.74	0.35	0.40	75.09	74.34	0.75	661	74.99	0.19	0.38	75.17	74.60	0.57
710	74.74	0.35	0.40	75.09	74.35	0.74	660	74.99	0.19	0.38	75.18	74.61	0.57
709	74.75	0.34	0.40	75.09	74.35	0.74	659	75.00	0.18	0.38	75.18	74.61	0.56
708	74.75	0.34	0.39	75.10	74.36	0.74	658	75.00	0.18	0.38	75.18	74.62	0.56
707	74.76	0.34	0.39	75.10	74.36	0.73	657	75.00	0.17	0.38	75.18	74.63	0.55
706	74.76	0.34	0.39	75.10	74.37	0.73	656	75.01	0.17	0.38	75.18	74.63	0.55
705	74.77	0.33	0.39	75.10	74.38	0.73	655	75.01	0.17	0.38	75.18	74.64	0.55
704	74.77	0.33	0.39	75.10	74.38	0.72	654	75.02	0.16	0.38	75.18	74.64	0.54
703	74.78	0.33	0.39	75.11	74.39	0.72	653	75.02	0.16	0.38	75.18	74.65	0.54
702	74.79	0.32	0.39	75.11	74.40	0.71	652	75.03	0.16	0.38	75.19	74.65	0.53
701	74.79	0.32	0.39	75.11	74.40	0.71	651	75.03	0.15	0.38	75.19	74.65	0.53
700	74.80	0.32	0.39	75.11	74.41	0.70	650	75.04	0.15	0.38	75.19	74.66	0.53
699	74.80	0.31	0.39	75.11	74.41	0.70	649	75.04	0.15	0.38	75.19	74.66	0.52
698	74.81	0.31	0.39	75.12	74.42	0.70	648	75.05	0.14	0.38	75.19	74.67	0.52
697	74.81	0.31	0.39	75.12	74.42	0.69	647	75.05	0.14	0.38	75.19	74.67	0.52
696	74.82	0.30	0.39	75.12	74.43	0.69	646	75.06	0.13	0.38	75.19	74.68	0.51
695	74.82	0.30	0.39	75.12	74.43	0.69	645	75.06	0.13	0.38	75.20	74.68	0.51
694	74.83	0.30	0.39	75.12	74.44	0.69	644	75.07	0.13	0.38	75.20	74.69	0.51
693	74.83	0.29	0.39	75.12	74.44	0.68	643	75.07	0.13	0.37	75.20	74.70	0.50
692	74.84	0.29	0.39	75.13	74.45	0.68	642	75.08	0.12	0.37	75.20	74.70	0.50
691	74.84	0.29	0.39	75.13	74.45	0.67	641	75.08	0.12	0.37	75.20	74.71	0.49
690	74.85	0.28	0.39	75.13	74.46	0.67	640	75.09	0.11	0.37	75.20	74.72	0.49
689	74.85	0.28	0.39	75.13	74.46	0.67	639	75.09	0.11	0.37	75.20	74.72	0.48
688	74.86	0.28	0.39	75.13	74.47	0.66	638	75.10	0.11	0.37	75.21	74.73	0.48
687	74.86	0.27	0.39	75.13	74.47	0.66	637	75.10	0.10	0.36	75.21	74.74	0.47
686	74.87	0.27	0.39	75.14	74.48	0.66	636	75.11	0.10	0.36	75.21	74.75	0.46
685	74.87	0.27	0.38	75.14	74.49	0.65	635	75.11	0.10	0.36	75.21	74.75	0.46
684	74.87	0.27	0.38	75.14	74.49	0.65	634	75.12	0.09	0.36	75.21	74.76	0.45
683	74.88	0.26	0.38	75.14	74.49	0.65	633	75.12	0.09	0.35	75.21	74.77	0.44
682	74.88	0.26	0.39	75.14	74.50	0.64	632	75.13	0.09	0.35	75.21	74.78	0.44
681	74.89	0.26	0.38	75.14	74.50	0.64	631	75.13	0.08	0.35	75.22	74.78	0.43
680	74.89	0.25	0.39	75.15	74.51	0.64	630	75.14	0.08	0.34	75.22	74.80	0.42
679	74.90	0.25	0.39	75.15	74.51	0.63	629	75.14	0.08	0.34	75.22	74.80	0.41
678	74.90	0.24	0.39	75.15	74.52	0.63	628	75.15	0.08	0.33	75.22	74.82	0.40
677	74.91	0.24	0.39	75.15	74.52	0.63	627	75.15	0.07	0.32	75.22	74.83	0.39
676	74.91	0.24	0.39	75.15	74.53	0.62	626	75.16	0.07	0.32	75.22	74.84	0.39
675	74.92	0.23	0.39	75.15	74.53	0.62	625	75.16	0.06	0.31	75.23	74.85	0.37
674	74.92	0.23	0.39	75.15	74.54	0.62	624	75.17	0.06	0.30	75.23	74.87	0.36
673	74.93	0.23	0.39	75.16	74.54	0.62	623	75.17	0.06	0.29	75.23	74.88	0.35
672	74.93	0.22	0.39	75.16	74.55	0.61	622	75.18	0.06	0.29	75.23	74.89	0.34
671	74.94	0.22	0.39	75.16	74.55	0.61	621	75.18	0.05	0.28	75.23	74.90	0.33
670	74.94	0.22	0.39	75.16	74.55	0.61	620	75.19	0.05	0.27	75.24	74.92	0.32
669	74.95	0.21	0.39	75.16	74.56	0.60	619	75.19	0.05	0.26	75.24	74.93	0.31
668	74.95	0.21	0.39	75.16	74.56	0.60	618	75.20	0.05	0.24	75.24	74.95	0.29
667	74.96	0.21	0.38	75.17	74.57	0.59	617	75.20	0.04	0.22	75.24	74.98	0.27



Strat. Level* (m)	Model Age (Ma)	+	-	(Max)	(Min)	Range	Strat. Level* (m)	Model Age (Ma)	+	-	(Max)	(Min)	Range
616	75.21	0.04	0.20	75.25	75.01	0.24	566	75.31	0.08	0.06	75.39	75.25	0.14
615	75.21	0.04	0.17	75.25	75.04	0.21	565	75.31	0.08	0.06	75.39	75.25	0.14
614	75.22	0.04	0.13	75.26	75.08	0.17	564	75.31	0.08	0.06	75.39	75.25	0.14
613	75.22	0.04	0.08	75.26	75.14	0.12	563	75.31	0.08	0.06	75.39	75.25	0.14
612	75.23	0.04	0.04	75.27	75.19	0.07	562	75.32	0.08	0.07	75.39	75.25	0.14
611	75.23	0.04	0.04	75.27	75.19	0.08	561	75.32	0.07	0.07	75.39	75.25	0.14
610	75.23	0.05	0.04	75.28	75.20	0.09	560	75.32	0.07	0.07	75.39	75.25	0.14
609	75.24	0.05	0.04	75.29	75.20	0.09	559	75.32	0.07	0.07	75.39	75.25	0.14
608	75.24	0.06	0.04	75.30	75.20	0.10	558	75.32	0.07	0.07	75.39	75.25	0.14
607	75.24	0.07	0.04	75.31	75.20	0.10	557	75.33	0.07	0.07	75.40	75.25	0.14
606	75.24	0.07	0.04	75.31	75.20	0.11	556	75.33	0.07	0.07	75.40	75.26	0.14
605	75.24	0.07	0.04	75.32	75.21	0.11	555	75.33	0.07	0.07	75.40	75.26	0.14
604	75.25	0.08	0.04	75.32	75.21	0.11	554	75.33	0.07	0.07	75.40	75.26	0.14
603	75.25	0.08	0.04	75.33	75.21	0.12	553	75.33	0.07	0.07	75.40	75.26	0.14
602	75.25	0.08	0.04	75.33	75.21	0.12	552	75.33	0.07	0.07	75.40	75.26	0.14
601	75.25	0.08	0.04	75.33	75.21	0.12	551	75.34	0.07	0.07	75.40	75.26	0.14
600	75.25	0.08	0.04	75.34	75.21	0.12	550	75.34	0.06	0.08	75.40	75.26	0.14
599	75.25	0.09	0.04	75.34	75.21	0.13	549	75.34	0.06	0.08	75.40	75.26	0.14
598	75.26	0.09	0.04	75.34	75.22	0.13	548	75.34	0.06	0.08	75.40	75.26	0.14
597	75.26	0.09	0.04	75.35	75.22	0.13	547	75.34	0.06	0.08	75.40	75.26	0.14
596	75.26	0.09	0.04	75.35	75.22	0.13	546	75.34	0.06	0.08	75.40	75.26	0.14
595	75.26	0.09	0.04	75.35	75.22	0.13	545	75.35	0.06	0.08	75.40	75.27	0.14
594	75.26	0.09	0.04	75.35	75.22	0.13	544	75.35	0.06	0.08	75.41	75.27	0.14
593	75.26	0.09	0.04	75.35	75.22	0.13	543	75.35	0.06	0.08	75.41	75.27	0.14
592	75.27	0.09	0.04	75.36	75.22	0.13	542	75.35	0.06	0.08	75.41	75.27	0.14
591	75.27	0.09	0.04	75.36	75.22	0.13	541	75.35	0.06	0.08	75.41	75.27	0.14
590	75.27	0.09	0.04	75.36	75.23	0.14	540	75.35	0.05	0.08	75.41	75.27	0.14
589	75.27	0.09	0.04	75.36	75.23	0.14	539	75.36	0.05	0.08	75.41	75.27	0.14
588	75.27	0.09	0.05	75.36	75.23	0.14	538	75.36	0.05	0.08	75.41	75.27	0.14
587	75.27	0.09	0.05	75.36	75.23	0.14	537	75.36	0.05	0.08	75.41	75.28	0.13
586	75.28	0.09	0.05	75.37	75.23	0.14	536	75.36	0.05	0.09	75.41	75.28	0.14
585	75.28	0.09	0.05	75.37	75.23	0.14	535	75.36	0.05	0.08	75.41	75.28	0.14
584	75.28	0.09	0.05	75.37	75.23	0.14	534	75.36	0.05	0.09	75.41	75.28	0.14
583	75.28	0.09	0.05	75.37	75.23	0.14	533	75.37	0.05	0.09	75.41	75.28	0.13
582	75.28	0.09	0.05	75.37	75.23	0.14	532	75.37	0.05	0.09	75.41	75.28	0.13
581	75.28	0.09	0.05	75.37	75.23	0.14	531	75.37	0.05	0.09	75.42	75.28	0.13
580	75.29	0.09	0.05	75.37	75.24	0.14	530	75.37	0.04	0.09	75.42	75.28	0.13
579	75.29	0.09	0.05	75.37	75.24	0.14	529	75.37	0.04	0.09	75.42	75.28	0.13
578	75.29	0.09	0.05	75.38	75.24	0.14	528	75.37	0.04	0.09	75.42	75.29	0.13
577	75.29	0.09	0.05	75.38	75.24	0.14	527	75.38	0.04	0.09	75.42	75.29	0.13
576	75.29	0.08	0.05	75.38	75.24	0.14	526	75.38	0.04	0.09	75.42	75.29	0.13
575	75.29	0.08	0.05	75.38	75.24	0.14	525	75.38	0.04	0.09	75.42	75.29	0.13
574	75.30	0.08	0.06	75.38	75.24	0.14	524	75.38	0.04	0.09	75.42	75.29	0.13
573	75.30	0.08	0.06	75.38	75.24	0.14	523	75.38	0.04	0.09	75.42	75.29	0.13
572	75.30	0.08	0.06	75.38	75.24	0.14	522	75.38	0.04	0.09	75.42	75.29	0.13
571	75.30	0.08	0.06	75.38	75.24	0.14	521	75.39	0.04	0.09	75.42	75.30	0.13
570	75.30	0.08	0.06	75.38	75.24	0.14	520	75.39	0.03	0.09	75.42	75.30	0.13
569	75.30	0.08	0.06	75.38	75.24	0.14	519	75.39	0.03	0.09	75.42	75.30	0.13
568	75.31	0.08	0.06	75.39	75.25	0.14	518	75.39	0.03	0.09	75.42	75.30	0.12
567	75.31	0.08	0.06	75.39	75.25	0.14	517	75.39	0.03	0.09	75.43	75.30	0.12

Strat. Level* (m)	Model Age (Ma)	+	-	(Max)	(Min)	Range	Strat. Level* (m)	Model Age (Ma)	+	-	(Max)	(Min)	Range
516	75.39	0.03	0.09	75.43	75.31	0.12	466	75.50	0.07	0.05	75.57	75.45	0.12
515	75.40	0.03	0.09	75.43	75.31	0.12	465	75.51	0.07	0.05	75.57	75.45	0.12
514	75.40	0.03	0.09	75.43	75.31	0.12	464	75.51	0.07	0.06	75.57	75.45	0.12
513	75.40	0.03	0.09	75.43	75.31	0.12	463	75.51	0.06	0.06	75.57	75.45	0.12
512	75.40	0.03	0.09	75.43	75.31	0.12	462	75.51	0.06	0.06	75.58	75.45	0.12
511	75.40	0.03	0.09	75.43	75.32	0.12	461	75.51	0.06	0.06	75.58	75.46	0.12
510	75.41	0.03	0.09	75.43	75.32	0.11	460	75.52	0.06	0.06	75.58	75.46	0.12
509	75.41	0.03	0.08	75.43	75.32	0.11	459	75.52	0.06	0.06	75.58	75.46	0.12
508	75.41	0.03	0.08	75.44	75.33	0.11	458	75.52	0.06	0.06	75.58	75.46	0.12
507	75.41	0.03	0.08	75.44	75.33	0.11	457	75.52	0.06	0.06	75.58	75.46	0.12
506	75.41	0.03	0.08	75.44	75.33	0.10	456	75.53	0.06	0.06	75.58	75.46	0.12
505	75.41	0.03	0.07	75.44	75.34	0.10	455	75.53	0.05	0.07	75.58	75.46	0.12
504	75.42	0.02	0.07	75.44	75.35	0.09	454	75.53	0.05	0.07	75.58	75.46	0.12
503	75.42	0.03	0.06	75.44	75.35	0.09	453	75.53	0.05	0.07	75.59	75.46	0.12
502	75.42	0.02	0.06	75.44	75.36	0.08	452	75.54	0.05	0.07	75.59	75.47	0.12
501	75.42	0.02	0.05	75.45	75.37	0.08	451	75.54	0.05	0.07	75.59	75.47	0.12
500	75.42	0.02	0.04	75.45	75.38	0.07	450	75.54	0.05	0.07	75.59	75.47	0.12
499	75.42	0.02	0.03	75.45	75.39	0.06	449	75.54	0.05	0.07	75.59	75.47	0.12
498	75.43	0.02	0.03	75.45	75.40	0.05	448	75.54	0.05	0.07	75.59	75.47	0.12
497	75.43	0.03	0.02	75.46	75.41	0.05	447	75.55	0.04	0.07	75.59	75.47	0.12
496	75.43	0.04	0.03	75.47	75.41	0.07	446	75.55	0.04	0.08	75.59	75.47	0.12
495	75.44	0.05	0.03	75.49	75.41	0.08	445	75.55	0.04	0.08	75.59	75.48	0.12
494	75.44	0.06	0.03	75.50	75.41	0.08	444	75.55	0.04	0.08	75.59	75.48	0.12
493	75.44	0.06	0.02	75.50	75.42	0.09	443	75.56	0.04	0.08	75.60	75.48	0.12
492	75.44	0.07	0.03	75.51	75.42	0.09	442	75.56	0.04	0.08	75.60	75.48	0.12
491	75.45	0.07	0.03	75.51	75.42	0.09	441	75.56	0.04	0.08	75.60	75.48	0.11
490	75.45	0.07	0.03	75.52	75.42	0.10	440	75.56	0.03	0.08	75.60	75.48	0.11
489	75.45	0.07	0.03	75.52	75.42	0.10	439	75.57	0.03	0.08	75.60	75.49	0.11
488	75.45	0.08	0.03	75.53	75.42	0.10	438	75.57	0.03	0.08	75.60	75.49	0.11
487	75.45	0.08	0.03	75.53	75.43	0.11	437	75.57	0.03	0.08	75.60	75.49	0.11
486	75.46	0.08	0.03	75.53	75.43	0.11	436	75.57	0.03	0.08	75.60	75.49	0.11
485	75.46	0.08	0.03	75.54	75.43	0.11	435	75.57	0.03	0.08	75.61	75.50	0.11
484	75.46	0.08	0.03	75.54	75.43	0.11	434	75.58	0.03	0.08	75.61	75.50	0.11
483	75.46	0.08	0.03	75.54	75.43	0.11	433	75.58	0.03	0.08	75.61	75.50	0.11
482	75.47	0.08	0.03	75.55	75.43	0.11	432	75.58	0.03	0.08	75.61	75.50	0.11
481	75.47	0.08	0.03	75.55	75.43	0.11	431	75.58	0.03	0.08	75.61	75.50	0.11
480	75.47	0.08	0.03	75.55	75.44	0.11	430	75.59	0.03	0.08	75.61	75.51	0.10
479	75.47	0.08	0.03	75.55	75.44	0.11	429	75.59	0.03	0.08	75.61	75.51	0.10
478	75.47	0.08	0.04	75.55	75.44	0.11	428	75.59	0.02	0.08	75.62	75.52	0.10
477	75.48	0.08	0.04	75.56	75.44	0.12	427	75.59	0.03	0.07	75.62	75.52	0.10
476	75.48	0.08	0.04	75.56	75.44	0.12	426	75.59	0.03	0.07	75.62	75.53	0.09
475	75.48	0.08	0.04	75.56	75.44	0.12	425	75.60	0.03	0.06	75.62	75.53	0.09
474	75.48	0.08	0.04	75.56	75.44	0.12	424	75.60	0.02	0.06	75.62	75.54	0.08
473	75.49	0.08	0.04	75.56	75.44	0.12	423	75.60	0.03	0.05	75.63	75.55	0.08
472	75.49	0.07	0.04	75.56	75.44	0.12	422	75.60	0.02	0.04	75.63	75.56	0.07
471	75.49	0.07	0.05	75.56	75.45	0.12	421	75.61	0.02	0.03	75.63	75.58	0.05
470	75.49	0.07	0.05	75.57	75.45	0.12	420	75.61	0.02	0.03	75.63	75.59	0.05
469	75.50	0.07	0.05	75.57	75.45	0.12	419	75.62	0.06	0.02	75.68	75.59	0.09
468	75.50	0.07	0.05	75.57	75.45	0.12	418	75.62	0.11	0.03	75.73	75.59	0.13
467	75.50	0.07	0.05	75.57	75.45	0.12	417	75.62	0.14	0.03	75.76	75.59	0.16

Strat. Level* (m)	Model Age (Ma)	+	-	(Max)	(Min)	Range	Strat. Level* (m)	Model Age (Ma)	+	-	(Max)	(Min)	Range
416	75.63	0.16	0.03	75.79	75.60	0.19	366	75.79	0.35	0.13	76.14	75.66	0.49
415	75.63	0.18	0.03	75.81	75.60	0.21	365	75.79	0.35	0.14	76.14	75.66	0.49
414	75.63	0.20	0.03	75.84	75.60	0.23	364	75.80	0.35	0.14	76.15	75.66	0.49
413	75.64	0.22	0.03	75.85	75.60	0.25	363	75.80	0.35	0.14	76.15	75.66	0.49
412	75.64	0.23	0.03	75.87	75.61	0.27	362	75.80	0.35	0.14	76.15	75.66	0.49
411	75.64	0.24	0.04	75.88	75.61	0.28	361	75.81	0.35	0.15	76.15	75.66	0.49
410	75.65	0.25	0.04	75.90	75.61	0.29	360	75.81	0.35	0.15	76.16	75.66	0.50
409	75.65	0.27	0.04	75.91	75.61	0.31	359	75.81	0.35	0.15	76.16	75.66	0.50
408	75.65	0.27	0.04	75.92	75.61	0.31	358	75.82	0.34	0.15	76.16	75.66	0.50
407	75.66	0.28	0.04	75.93	75.61	0.32	357	75.82	0.35	0.15	76.16	75.66	0.50
406	75.66	0.28	0.05	75.94	75.61	0.32	356	75.82	0.34	0.16	76.17	75.67	0.50
405	75.66	0.29	0.05	75.95	75.62	0.34	355	75.82	0.34	0.16	76.17	75.67	0.50
404	75.67	0.29	0.05	75.96	75.62	0.34	354	75.83	0.34	0.16	76.17	75.67	0.50
403	75.67	0.30	0.05	75.97	75.62	0.35	353	75.83	0.34	0.16	76.17	75.67	0.50
402	75.67	0.30	0.05	75.98	75.62	0.36	352	75.83	0.34	0.17	76.17	75.67	0.51
401	75.68	0.31	0.06	75.99	75.62	0.37	351	75.84	0.34	0.17	76.18	75.67	0.51
400	75.68	0.32	0.06	76.00	75.62	0.38	350	75.84	0.34	0.17	76.18	75.67	0.51
399	75.68	0.32	0.06	76.00	75.62	0.38	349	75.84	0.34	0.17	76.18	75.67	0.51
398	75.69	0.32	0.06	76.01	75.62	0.38	348	75.85	0.34	0.17	76.19	75.67	0.51
397	75.69	0.33	0.06	76.01	75.62	0.39	347	75.85	0.34	0.18	76.19	75.67	0.51
396	75.69	0.33	0.07	76.02	75.63	0.39	346	75.85	0.34	0.18	76.19	75.68	0.51
395	75.70	0.33	0.07	76.03	75.63	0.40	345	75.86	0.34	0.18	76.19	75.68	0.52
394	75.70	0.33	0.07	76.03	75.63	0.40	344	75.86	0.33	0.18	76.19	75.68	0.52
393	75.70	0.34	0.07	76.04	75.63	0.41	343	75.86	0.33	0.18	76.20	75.68	0.52
392	75.70	0.34	0.07	76.04	75.63	0.41	342	75.87	0.33	0.19	76.20	75.68	0.52
391	75.71	0.34	0.08	76.05	75.63	0.42	341	75.87	0.33	0.19	76.20	75.68	0.52
390	75.71	0.35	0.08	76.06	75.63	0.43	340	75.87	0.33	0.19	76.20	75.68	0.52
389	75.71	0.35	0.08	76.06	75.63	0.43	339	75.88	0.33	0.19	76.21	75.68	0.52
388	75.72	0.35	0.08	76.06	75.63	0.43	338	75.88	0.33	0.20	76.21	75.68	0.52
387	75.72	0.35	0.09	76.07	75.63	0.43	337	75.88	0.33	0.20	76.21	75.69	0.52
386	75.72	0.35	0.09	76.07	75.64	0.44	336	75.89	0.33	0.20	76.21	75.69	0.52
385	75.73	0.35	0.09	76.08	75.64	0.44	335	75.89	0.33	0.20	76.21	75.69	0.53
384	75.73	0.35	0.09	76.08	75.64	0.44	334	75.89	0.32	0.20	76.22	75.69	0.53
383	75.73	0.35	0.10	76.08	75.64	0.45	333	75.90	0.32	0.21	76.22	75.69	0.53
382	75.74	0.35	0.10	76.09	75.64	0.45	332	75.90	0.32	0.21	76.22	75.69	0.53
381	75.74	0.35	0.10	76.09	75.64	0.45	331	75.90	0.32	0.21	76.22	75.69	0.53
380	75.74	0.35	0.10	76.10	75.64	0.45	330	75.91	0.32	0.21	76.22	75.69	0.53
379	75.75	0.35	0.11	76.10	75.64	0.46	329	75.91	0.32	0.21	76.23	75.70	0.53
378	75.75	0.35	0.11	76.10	75.64	0.46	328	75.91	0.31	0.22	76.23	75.70	0.53
377	75.75	0.36	0.11	76.11	75.64	0.46	327	75.92	0.31	0.22	76.23	75.70	0.53
376	75.76	0.36	0.11	76.11	75.64	0.47	326	75.92	0.31	0.22	76.23	75.70	0.53
375	75.76	0.36	0.12	76.12	75.65	0.47	325	75.92	0.31	0.22	76.23	75.70	0.53
374	75.76	0.36	0.12	76.12	75.65	0.47	324	75.93	0.31	0.22	76.24	75.70	0.54
373	75.77	0.36	0.12	76.12	75.65	0.47	323	75.93	0.31	0.23	76.24	75.70	0.53
372	75.77	0.35	0.12	76.12	75.65	0.47	322	75.93	0.31	0.23	76.24	75.70	0.54
371	75.77	0.36	0.12	76.13	75.65	0.48	321	75.94	0.30	0.23	76.24	75.70	0.54
370	75.78	0.35	0.13	76.13	75.65	0.48	320	75.94	0.30	0.23	76.24	75.71	0.54
369	75.78	0.36	0.13	76.13	75.65	0.48	319	75.94	0.30	0.23	76.24	75.71	0.53
368	75.78	0.35	0.13	76.14	75.65	0.48	318	75.95	0.30	0.24	76.25	75.71	0.54
367	75.79	0.35	0.13	76.14	75.65	0.49	317	75.95	0.30	0.24	76.25	75.71	0.54

Strat. Level* (m)	Model Age (Ma)	+	-	(Max)	(Min)	Range
316	75.95	0.30	0.24	76.25	75.71	0.54
315	75.95	0.30	0.24	76.25	75.71	0.54
314	75.96	0.30	0.24	76.25	75.71	0.54
313	75.96	0.29	0.25	76.25	75.72	0.54
312	75.96	0.29	0.25	76.26	75.72	0.54
311	75.97	0.29	0.25	76.26	75.72	0.54
310	75.97	0.29	0.25	76.26	75.72	0.54
309	75.97	0.29	0.25	76.26	75.72	0.54
308	75.98	0.29	0.26	76.26	75.72	0.54
307	75.98	0.28	0.26	76.27	75.72	0.54
306	75.98	0.28	0.26	76.27	75.72	0.54
305	75.99	0.28	0.26	76.27	75.73	0.54
304	75.99	0.28	0.26	76.27	75.73	0.54
303	75.99	0.28	0.27	76.27	75.73	0.54
302	76.00	0.28	0.27	76.27	75.73	0.54
301	76.00	0.27	0.27	76.27	75.73	0.54
300	76.00	0.27	0.27	76.28	75.73	0.54
299	76.01	0.27	0.27	76.28	75.73	0.54
298	76.01	0.27	0.28	76.28	75.73	0.54
297	76.01	0.27	0.28	76.28	75.74	0.54
296	76.02	0.27	0.28	76.28	75.74	0.54
295	76.02	0.26	0.28	76.28	75.74	0.54
294	76.02	0.26	0.28	76.28	75.74	0.54
293	76.03	0.26	0.28	76.29	75.74	0.55
292	76.03	0.26	0.29	76.29	75.74	0.54
291	76.03	0.26	0.29	76.29	75.74	0.54
290	76.04	0.26	0.29	76.29	75.75	0.54
289	76.04	0.25	0.29	76.29	75.75	0.54
288	76.04	0.25	0.29	76.29	75.75	0.54
287	76.05	0.25	0.29	76.29	75.75	0.54
286	76.05	0.25	0.30	76.30	75.75	0.54
285	76.05	0.25	0.30	76.30	75.75	0.54
284	76.05	0.24	0.30	76.30	75.76	0.54
283	76.06	0.24	0.30	76.30	75.76	0.54
282	76.06	0.24	0.30	76.30	75.76	0.54
281	76.06	0.24	0.30	76.30	75.76	0.54
280	76.07	0.24	0.31	76.30	75.76	0.54
279	76.07	0.23	0.31	76.30	75.76	0.54
278	76.07	0.23	0.31	76.31	75.76	0.54
277	76.08	0.23	0.31	76.31	75.77	0.54
276	76.08	0.23	0.31	76.31	75.77	0.54
275	76.08	0.23	0.31	76.31	75.77	0.54
274	76.09	0.22	0.32	76.31	75.77	0.54
273	76.09	0.22	0.32	76.31	75.77	0.54
272	76.09	0.22	0.32	76.31	75.78	0.54
271	76.10	0.22	0.32	76.31	75.78	0.54
270	76.10	0.22	0.32	76.32	75.78	0.54
269	76.10	0.21	0.32	76.32	75.78	0.54
268	76.11	0.21	0.32	76.32	75.78	0.54
267	76.11	0.21	0.32	76.32	75.78	0.53
266	76.11	0.21	0.33	76.32	75.79	0.53
265	76.12	0.21	0.33	76.32	75.79	0.53
264	76.12	0.20	0.33	76.32	75.79	0.53
263	76.12	0.20	0.33	76.32	75.79	0.53
262	76.13	0.20	0.33	76.33	75.79	0.53
261	76.13	0.20	0.33	76.33	75.80	0.53
260	76.13	0.20	0.33	76.33	75.80	0.53
259	76.13	0.19	0.33	76.33	75.80	0.53
258	76.14	0.19	0.34	76.33	75.80	0.53
257	76.14	0.19	0.34	76.33	75.80	0.53
256	76.14	0.19	0.34	76.33	75.81	0.53
255	76.15	0.19	0.34	76.33	75.81	0.53
254	76.15	0.18	0.34	76.33	75.81	0.52
253	76.15	0.18	0.34	76.34	75.81	0.52
252	76.16	0.18	0.34	76.34	75.81	0.52
251	76.16	0.18	0.34	76.34	75.82	0.52
250	76.16	0.17	0.34	76.34	75.82	0.52
249	76.17	0.17	0.35	76.34	75.82	0.52
248	76.17	0.17	0.35	76.34	75.82	0.52
247	76.17	0.17	0.35	76.34	75.83	0.52
246	76.18	0.17	0.35	76.34	75.83	0.51
245	76.18	0.16	0.35	76.34	75.83	0.51
244	76.18	0.16	0.35	76.35	75.83	0.51
243	76.19	0.16	0.35	76.35	75.84	0.51
242	76.19	0.16	0.35	76.35	75.84	0.51
241	76.19	0.16	0.35	76.35	75.84	0.51
240	76.20	0.15	0.35	76.35	75.85	0.50
239	76.20	0.15	0.35	76.35	75.85	0.50
238	76.20	0.15	0.35	76.35	75.85	0.50
237	76.21	0.15	0.35	76.35	75.86	0.50
236	76.21	0.15	0.35	76.36	75.86	0.50
235	76.21	0.14	0.35	76.36	75.86	0.50
234	76.22	0.14	0.35	76.36	75.87	0.49
233	76.22	0.14	0.35	76.36	75.87	0.49
232	76.22	0.14	0.35	76.36	75.87	0.49
231	76.22	0.14	0.35	76.36	75.87	0.49
230	76.23	0.13	0.35	76.36	75.88	0.48
229	76.23	0.13	0.35	76.36	75.88	0.48
228	76.23	0.13	0.35	76.36	75.88	0.48
227	76.24	0.13	0.35	76.36	75.89	0.48
226	76.24	0.13	0.35	76.37	75.89	0.47
225	76.24	0.12	0.35	76.37	75.89	0.47
224	76.25	0.12	0.35	76.37	75.90	0.47
223	76.25	0.12	0.35	76.37	75.90	0.46
222	76.25	0.11	0.35	76.37	75.91	0.46
221	76.26	0.11	0.34	76.37	75.91	0.46
220	76.26	0.11	0.34	76.37	75.92	0.46
219	76.26	0.11	0.34	76.37	75.92	0.45
218	76.27	0.11	0.34	76.37	75.93	0.45
217	76.27	0.10	0.34	76.37	75.93	0.44

Strat. Level* (m)	Model Age (Ma)	+	-	(Max)	(Min)	Range	Strat. Level* (m)	Model Age (Ma)	+	-	(Max)	(Min)	Range
216	76.27	0.10	0.34	76.38	75.93	0.44	166	76.45	0.30	0.07	76.75	76.38	0.36
215	76.28	0.10	0.34	76.38	75.94	0.44	165	76.45	0.30	0.07	76.75	76.39	0.37
214	76.28	0.10	0.33	76.38	75.95	0.43	164	76.46	0.31	0.07	76.76	76.39	0.38
213	76.28	0.10	0.33	76.38	75.95	0.43	163	76.46	0.31	0.07	76.77	76.39	0.39
212	76.29	0.09	0.33	76.38	75.96	0.42	162	76.46	0.32	0.08	76.78	76.39	0.39
211	76.29	0.09	0.33	76.38	75.96	0.42	161	76.47	0.32	0.08	76.79	76.39	0.40
210	76.29	0.09	0.33	76.38	75.96	0.42	160	76.47	0.33	0.08	76.80	76.39	0.41
209	76.30	0.09	0.33	76.38	75.97	0.42	159	76.48	0.34	0.08	76.81	76.39	0.42
208	76.30	0.09	0.33	76.38	75.97	0.41	158	76.48	0.34	0.08	76.82	76.39	0.43
207	76.30	0.08	0.32	76.39	75.98	0.41	157	76.48	0.35	0.09	76.83	76.39	0.44
206	76.30	0.08	0.32	76.39	75.98	0.41	156	76.49	0.35	0.09	76.84	76.40	0.44
205	76.31	0.08	0.32	76.39	75.99	0.40	155	76.49	0.35	0.09	76.84	76.40	0.45
204	76.31	0.08	0.32	76.39	75.99	0.40	154	76.49	0.36	0.09	76.85	76.40	0.45
203	76.31	0.08	0.31	76.39	76.00	0.39	153	76.50	0.36	0.10	76.86	76.40	0.46
202	76.32	0.08	0.31	76.39	76.01	0.39	152	76.50	0.37	0.10	76.87	76.40	0.47
201	76.32	0.07	0.30	76.39	76.02	0.38	151	76.50	0.37	0.10	76.87	76.40	0.47
200	76.32	0.07	0.30	76.39	76.02	0.37	150	76.51	0.37	0.10	76.88	76.40	0.47
199	76.33	0.07	0.30	76.40	76.03	0.37	149	76.51	0.38	0.11	76.89	76.40	0.48
198	76.33	0.07	0.29	76.40	76.04	0.36	148	76.51	0.38	0.11	76.89	76.41	0.49
197	76.33	0.07	0.29	76.40	76.04	0.35	147	76.52	0.38	0.11	76.90	76.41	0.49
196	76.34	0.06	0.28	76.40	76.06	0.34	146	76.52	0.38	0.11	76.91	76.41	0.50
195	76.34	0.06	0.27	76.40	76.07	0.34	145	76.52	0.39	0.12	76.91	76.41	0.50
194	76.34	0.06	0.27	76.40	76.07	0.33	144	76.53	0.39	0.12	76.92	76.41	0.51
193	76.35	0.06	0.26	76.41	76.08	0.32	143	76.53	0.39	0.12	76.93	76.41	0.52
192	76.35	0.06	0.26	76.41	76.09	0.31	142	76.54	0.40	0.12	76.93	76.41	0.52
191	76.35	0.06	0.25	76.41	76.11	0.30	141	76.54	0.40	0.13	76.94	76.41	0.53
190	76.36	0.05	0.24	76.41	76.12	0.29	140	76.54	0.40	0.13	76.95	76.41	0.53
189	76.36	0.05	0.23	76.41	76.13	0.29	139	76.55	0.41	0.13	76.95	76.41	0.54
188	76.36	0.05	0.22	76.41	76.14	0.27	138	76.55	0.41	0.13	76.96	76.42	0.54
187	76.37	0.05	0.21	76.42	76.16	0.26	137	76.55	0.41	0.14	76.96	76.42	0.55
186	76.37	0.05	0.19	76.42	76.17	0.24	136	76.56	0.41	0.14	76.97	76.42	0.55
185	76.37	0.05	0.17	76.42	76.20	0.22	135	76.56	0.41	0.14	76.97	76.42	0.56
184	76.38	0.05	0.16	76.42	76.22	0.21	134	76.56	0.42	0.14	76.98	76.42	0.56
183	76.38	0.05	0.13	76.43	76.25	0.18	133	76.57	0.42	0.15	76.98	76.42	0.56
182	76.38	0.05	0.10	76.43	76.28	0.15	132	76.57	0.42	0.15	76.99	76.42	0.57
181	76.39	0.05	0.07	76.43	76.32	0.11	131	76.57	0.42	0.15	77.00	76.42	0.58
180	76.39	0.04	0.05	76.44	76.35	0.09	130	76.58	0.43	0.15	77.00	76.42	0.58
179	76.40	0.06	0.05	76.46	76.35	0.11	129	76.58	0.43	0.16	77.01	76.42	0.58
178	76.41	0.10	0.05	76.51	76.36	0.15	128	76.58	0.43	0.16	77.01	76.43	0.59
177	76.41	0.13	0.05	76.54	76.36	0.18	127	76.59	0.43	0.16	77.02	76.43	0.59
176	76.41	0.16	0.05	76.57	76.36	0.20	126	76.59	0.43	0.16	77.02	76.43	0.60
175	76.42	0.18	0.05	76.60	76.37	0.23	125	76.59	0.43	0.17	77.03	76.43	0.60
174	76.42	0.20	0.05	76.62	76.37	0.25	124	76.60	0.44	0.17	77.03	76.43	0.60
173	76.43	0.21	0.05	76.64	76.37	0.26	123	76.60	0.44	0.17	77.04	76.43	0.61
172	76.43	0.22	0.06	76.65	76.37	0.28	122	76.60	0.44	0.17	77.04	76.43	0.61
171	76.43	0.24	0.06	76.67	76.38	0.30	121	76.61	0.44	0.18	77.05	76.43	0.62
170	76.44	0.25	0.06	76.69	76.38	0.31	120	76.61	0.44	0.18	77.05	76.43	0.62
169	76.44	0.26	0.06	76.70	76.38	0.32	119	76.61	0.44	0.18	77.06	76.43	0.62
168	76.44	0.28	0.06	76.72	76.38	0.34	118	76.62	0.44	0.18	77.06	76.43	0.63
167	76.45	0.28	0.06	76.73	76.38	0.35	117	76.62	0.44	0.19	77.07	76.44	0.63

Strat. Level* (m)	Model Age (Ma)	+	-	(Max)	(Min)	Range
116	76.62	0.44	0.19	77.07	76.44	0.63
115	76.63	0.44	0.19	77.07	76.44	0.64
114	76.63	0.45	0.19	77.08	76.44	0.64
113	76.63	0.45	0.20	77.08	76.44	0.64
112	76.64	0.45	0.20	77.08	76.44	0.64
111	76.64	0.45	0.20	77.09	76.44	0.65
110	76.64	0.45	0.20	77.09	76.44	0.65
109	76.65	0.45	0.21	77.09	76.44	0.65
108	76.65	0.45	0.21	77.10	76.44	0.66
107	76.65	0.45	0.21	77.10	76.44	0.66
106	76.66	0.45	0.21	77.11	76.45	0.66
105	76.66	0.45	0.22	77.11	76.45	0.67
104	76.66	0.45	0.22	77.12	76.45	0.67
103	76.67	0.45	0.22	77.12	76.45	0.67
102	76.67	0.46	0.22	77.13	76.45	0.68
101	76.67	0.46	0.22	77.13	76.45	0.68
100	76.68	0.46	0.23	77.14	76.45	0.69
99	76.68	0.46	0.23	77.14	76.45	0.69
98	76.68	0.46	0.23	77.14	76.45	0.69
97	76.69	0.46	0.23	77.15	76.45	0.70
96	76.69	0.46	0.24	77.15	76.45	0.70
95	76.69	0.46	0.24	77.16	76.45	0.70
94	76.70	0.46	0.24	77.16	76.46	0.70
93	76.70	0.46	0.24	77.17	76.46	0.71
92	76.70	0.47	0.25	77.17	76.46	0.71
91	76.71	0.47	0.25	77.18	76.46	0.72
90	76.71	0.47	0.25	77.18	76.46	0.72
89	76.71	0.47	0.25	77.18	76.46	0.72
88	76.72	0.47	0.26	77.19	76.46	0.73
87	76.72	0.47	0.26	77.19	76.46	0.73
86	76.72	0.47	0.26	77.20	76.46	0.74
85	76.73	0.48	0.26	77.20	76.46	0.74
84	76.73	0.48	0.27	77.21	76.46	0.74
83	76.73	0.48	0.27	77.21	76.47	0.75
82	76.74	0.48	0.27	77.22	76.47	0.75
81	76.74	0.48	0.27	77.22	76.47	0.75
80	76.75	0.48	0.28	77.22	76.47	0.75
79	76.75	0.48	0.28	77.23	76.47	0.76
78	76.75	0.48	0.28	77.23	76.47	0.76
77	76.76	0.48	0.28	77.24	76.47	0.77
76	76.76	0.48	0.29	77.24	76.47	0.77
75	76.76	0.48	0.29	77.25	76.47	0.77
74	76.77	0.49	0.29	77.25	76.47	0.78
73	76.77	0.49	0.29	77.26	76.48	0.78
72	76.77	0.49	0.30	77.26	76.48	0.78
71	76.78	0.49	0.30	77.27	76.48	0.79
70	76.78	0.49	0.30	77.27	76.48	0.79
69	76.78	0.49	0.30	77.27	76.48	0.79
68	76.79	0.49	0.30	77.28	76.48	0.80
67	76.79	0.49	0.31	77.28	76.48	0.80
66	76.79	0.50	0.31	77.29	76.48	0.80
65	76.80	0.50	0.31	77.29	76.49	0.81
64	76.80	0.50	0.31	77.30	76.49	0.81
63	76.80	0.50	0.32	77.30	76.49	0.82
62	76.81	0.50	0.32	77.31	76.49	0.82
61	76.81	0.50	0.32	77.31	76.49	0.82
60	76.81	0.50	0.32	77.32	76.49	0.83
59	76.82	0.51	0.32	77.32	76.49	0.83
58	76.82	0.51	0.33	77.33	76.49	0.83
57	76.82	0.51	0.33	77.33	76.49	0.84
56	76.83	0.51	0.33	77.34	76.49	0.84
55	76.83	0.51	0.33	77.34	76.50	0.85
54	76.83	0.52	0.34	77.35	76.50	0.85
53	76.84	0.52	0.34	77.35	76.50	0.86
52	76.84	0.52	0.34	77.36	76.50	0.86
51	76.84	0.52	0.34	77.36	76.50	0.86
50	76.85	0.52	0.34	77.37	76.50	0.87
49	76.85	0.52	0.35	77.37	76.50	0.87
48	76.85	0.52	0.35	77.38	76.50	0.87
47	76.86	0.53	0.35	77.38	76.51	0.88
46	76.86	0.53	0.35	77.39	76.51	0.88
45	76.86	0.53	0.35	77.39	76.51	0.88
44	76.87	0.53	0.36	77.39	76.51	0.88
43	76.87	0.53	0.36	77.40	76.51	0.89
42	76.87	0.53	0.36	77.41	76.51	0.89
41	76.88	0.53	0.36	77.41	76.52	0.89
40	76.88	0.54	0.36	77.42	76.52	0.90
39	76.88	0.54	0.37	77.42	76.52	0.90
38	76.89	0.54	0.37	77.42	76.52	0.91
37	76.89	0.54	0.37	77.43	76.52	0.91
36	76.89	0.54	0.37	77.43	76.52	0.91
35	76.90	0.54	0.37	77.43	76.52	0.91
34	76.90	0.54	0.38	77.44	76.53	0.91
33	76.91	0.54	0.38	77.44	76.53	0.92
32	76.91	0.54	0.38	77.45	76.53	0.92
31	76.91	0.54	0.38	77.46	76.53	0.92
30	76.92	0.54	0.39	77.46	76.53	0.93
29	76.92	0.54	0.39	77.47	76.53	0.93
28	76.93	0.55	0.39	77.47	76.54	0.94
27	76.93	0.55	0.39	77.48	76.54	0.94
26	76.93	0.55	0.40	77.48	76.54	0.94
25	76.94	0.55	0.40	77.49	76.54	0.95
24	76.94	0.55	0.40	77.50	76.54	0.95
23	76.95	0.55	0.40	77.50	76.55	0.95
22	76.95	0.56	0.40	77.51	76.55	0.96
21	76.95	0.56	0.40	77.51	76.55	0.96
20	76.96	0.56	0.41	77.52	76.55	0.96
19	76.96	0.56	0.41	77.52	76.55	0.97
18	76.97	0.56	0.41	77.53	76.56	0.97
17	76.97	0.56	0.41	77.53	76.56	0.98



Strat. Level* (m)	Model Age (Ma)	+	-	(Max)	(Min)	Range	Strat. Level* (m)	Model Age (Ma)	+	-	(Max)	(Min)	Range
16	76.97	0.57	0.42	77.54	76.56	0.98	7	77.02	0.59	0.44	77.60	76.58	1.03
15	76.98	0.57	0.42	77.55	76.56	0.99	6	77.02	0.59	0.44	77.61	76.58	1.03
14	76.98	0.57	0.42	77.55	76.56	0.99	5	77.03	0.59	0.44	77.62	76.58	1.04
13	76.99	0.58	0.42	77.56	76.56	1.00	4	77.03	0.60	0.45	77.63	76.58	1.05
12	76.99	0.58	0.42	77.57	76.57	1.00	3	77.04	0.60	0.45	77.64	76.59	1.06
11	77.00	0.58	0.43	77.57	76.57	1.01	2	77.05	0.60	0.46	77.65	76.59	1.06
10	77.00	0.58	0.43	77.58	76.57	1.01	1	77.05	0.61	0.46	77.66	76.59	1.07
9	77.01	0.58	0.43	77.59	76.57	1.02	0	77.06	0.62	0.47	77.68	76.60	1.08
8	77.01	0.59	0.44	77.60	76.57	1.02							

\* Relative to the KBC/KBU stratotype section (see also Roberts, 2007; Beveridge et al., 2020 [Ch.5])

**Appendix C.4.5** Kaiparowits Formation Bayesian age-stratigraphic model (KBC/KBU stratotype section) input data.

id	ages	ageSds	position	thickness	calCurves
"KWC-3"	75569	22	6000	0	normal
"KWC-1"	75903	24	19000	0	normal
"KWC-2"	76336	28	29800	0	normal

Notes: *id* = samples name, *ages* = kyrs, *ageSds* = uncertainty (*Y*) at  $1\sigma$  in kyrs, *position* = stratigraphic height (cm) as “depth” beginning at the top of the KWC section, *thickness* = thickness of sampled horizon (null=0).

**Appendix C.4.6** *Kaiparowits Formation Bayesian age-stratigraphic model (KBC/KBU stratotype section) script.*

```
>library(Bchron)

>KWC_Section <- read.csv(file.choose())

>KWC_SectionModel=Bchronology(ages=KWC_Section$ages,
                               ageSds=KWC_Section$ageSds,
                               calCurves=KWC_Section$calCurves,
                               positions=KWC_Section$position,
                               positionThicknesses=KWC_Section$thickness,
                               ids=KWC_Section$id,
                               predictPositions=seq(0,36100,by=100),
                               iterations=100000)

>library(ggplot2)

>plot(KWC_SectionModel)+labs(x='Age (ka)',y='Depth (cm)',title='KWC Section Bchron Model')

> KWC_SectionModelAges <- matrix(nrow=361, ncol=3)

for(i in 1:361){ KWC_SectionModelAges [i,]=quantile(KWC_SectionModel$thetaPredict[,i],probs =
c(0.025,0.5,0.975))}

>write.csv(KWC_SectionModelAges, "KWC Section Model Output.csv")
```

*Appendix C.4.7 Kaiparowits Formation Bayesian age-stratigraphic model (KBC/KBU stratotype section) numerical output.*

Strat. Level* (m)	Model Age (Ma)	+	-	(Max)	(Min)	Range	Strat. Level* (m)	Model Age (Ma)	+	-	(Max)	(Min)	Range
360	75.41	0.17	1.25	75.58	74.16	1.42	313	75.53	0.07	0.57	75.60	74.96	0.64
359	75.42	0.17	1.25	75.58	74.16	1.42	312	75.53	0.07	0.55	75.60	74.98	0.62
358	75.42	0.17	1.24	75.58	74.18	1.40	311	75.53	0.06	0.52	75.60	75.01	0.59
357	75.42	0.16	1.22	75.58	74.20	1.39	310	75.54	0.06	0.49	75.60	75.04	0.55
356	75.42	0.16	1.22	75.58	74.20	1.38	309	75.54	0.06	0.47	75.60	75.07	0.53
355	75.43	0.16	1.21	75.58	74.22	1.36	308	75.54	0.06	0.43	75.60	75.11	0.49
354	75.43	0.16	1.19	75.58	74.24	1.34	307	75.54	0.06	0.39	75.60	75.15	0.45
353	75.43	0.15	1.17	75.58	74.26	1.32	306	75.55	0.06	0.35	75.60	75.20	0.40
352	75.43	0.15	1.16	75.58	74.27	1.32	305	75.55	0.06	0.30	75.60	75.24	0.36
351	75.44	0.15	1.16	75.58	74.28	1.31	304	75.55	0.05	0.26	75.60	75.29	0.31
350	75.44	0.15	1.14	75.58	74.30	1.29	303	75.55	0.05	0.22	75.60	75.34	0.27
349	75.44	0.14	1.12	75.58	74.32	1.27	302	75.56	0.05	0.16	75.61	75.40	0.21
348	75.44	0.14	1.11	75.59	74.33	1.26	301	75.56	0.05	0.10	75.61	75.46	0.15
347	75.45	0.14	1.10	75.59	74.35	1.23	300	75.57	0.05	0.04	75.61	75.53	0.09
346	75.45	0.14	1.08	75.59	74.37	1.22	299	75.57	0.05	0.04	75.62	75.53	0.09
345	75.45	0.13	1.07	75.59	74.38	1.20	298	75.58	0.06	0.04	75.64	75.53	0.10
344	75.45	0.13	1.05	75.59	74.40	1.18	297	75.58	0.07	0.04	75.65	75.53	0.12
343	75.46	0.13	1.04	75.59	74.42	1.17	296	75.58	0.08	0.04	75.67	75.54	0.13
342	75.46	0.13	1.03	75.59	74.43	1.15	295	75.58	0.09	0.05	75.68	75.54	0.14
341	75.46	0.13	1.01	75.59	74.45	1.13	294	75.59	0.10	0.05	75.69	75.54	0.14
340	75.46	0.12	1.00	75.59	74.46	1.12	293	75.59	0.11	0.05	75.70	75.54	0.15
339	75.47	0.12	0.99	75.59	74.48	1.11	292	75.59	0.11	0.05	75.70	75.55	0.16
338	75.47	0.12	0.98	75.59	74.49	1.10	291	75.59	0.12	0.05	75.71	75.55	0.16
337	75.47	0.12	0.97	75.59	74.50	1.08	290	75.60	0.12	0.05	75.72	75.55	0.17
336	75.47	0.11	0.96	75.59	74.52	1.07	289	75.60	0.12	0.05	75.72	75.55	0.17
335	75.48	0.11	0.95	75.59	74.53	1.06	288	75.60	0.13	0.05	75.73	75.55	0.17
334	75.48	0.11	0.93	75.59	74.54	1.04	287	75.60	0.13	0.05	75.73	75.56	0.18
333	75.48	0.11	0.92	75.59	74.56	1.03	286	75.61	0.13	0.05	75.74	75.56	0.18
332	75.48	0.10	0.92	75.59	74.57	1.02	285	75.61	0.14	0.05	75.74	75.56	0.19
331	75.49	0.10	0.90	75.59	74.59	1.00	284	75.61	0.14	0.05	75.75	75.56	0.19
330	75.49	0.10	0.88	75.59	74.61	0.98	283	75.62	0.14	0.05	75.75	75.56	0.19
329	75.49	0.10	0.86	75.59	74.63	0.96	282	75.62	0.14	0.06	75.76	75.56	0.19
328	75.49	0.10	0.84	75.59	74.65	0.94	281	75.62	0.14	0.06	75.76	75.56	0.20
327	75.50	0.09	0.84	75.59	74.66	0.93	280	75.62	0.14	0.06	75.76	75.57	0.20
326	75.50	0.09	0.82	75.59	74.68	0.91	279	75.63	0.14	0.06	75.77	75.57	0.20
325	75.50	0.09	0.81	75.59	74.69	0.90	278	75.63	0.14	0.06	75.77	75.57	0.20
324	75.50	0.09	0.79	75.59	74.71	0.88	277	75.63	0.14	0.06	75.77	75.57	0.20
323	75.51	0.08	0.77	75.59	74.74	0.85	276	75.63	0.14	0.06	75.78	75.57	0.20
322	75.51	0.08	0.74	75.59	74.76	0.83	275	75.63	0.14	0.06	75.78	75.57	0.21
321	75.51	0.08	0.72	75.59	74.79	0.81	274	75.64	0.14	0.06	75.78	75.57	0.21
320	75.51	0.08	0.71	75.59	74.81	0.79	273	75.64	0.15	0.06	75.79	75.58	0.21
319	75.52	0.08	0.69	75.59	74.82	0.77	272	75.64	0.15	0.07	75.79	75.58	0.21
318	75.52	0.08	0.67	75.59	74.84	0.75	271	75.65	0.15	0.07	75.79	75.58	0.21
317	75.52	0.07	0.66	75.59	74.86	0.73	270	75.65	0.15	0.07	75.79	75.58	0.21
316	75.52	0.07	0.63	75.59	74.89	0.71	269	75.65	0.14	0.07	75.80	75.58	0.22
315	75.52	0.07	0.62	75.60	74.91	0.69	268	75.65	0.14	0.07	75.80	75.58	0.22
314	75.53	0.07	0.60	75.60	74.93	0.67	267	75.66	0.14	0.07	75.80	75.58	0.22

Strat. Level* (m)	Model Age (Ma)	+	-	(Max)	(Min)	Range	Strat. Level* (m)	Model Age (Ma)	+	-	(Max)	(Min)	Range
266	75.66	0.14	0.07	75.80	75.58	0.22	216	75.79	0.09	0.14	75.87	75.65	0.22
265	75.66	0.14	0.08	75.80	75.59	0.22	215	75.79	0.09	0.14	75.87	75.65	0.22
264	75.66	0.14	0.08	75.80	75.59	0.22	214	75.79	0.08	0.14	75.88	75.65	0.22
263	75.67	0.14	0.08	75.81	75.59	0.22	213	75.79	0.08	0.14	75.88	75.65	0.22
262	75.67	0.14	0.08	75.81	75.59	0.22	212	75.80	0.08	0.14	75.88	75.66	0.22
261	75.67	0.14	0.08	75.81	75.59	0.22	211	75.80	0.08	0.14	75.88	75.66	0.22
260	75.67	0.14	0.08	75.81	75.59	0.22	210	75.80	0.08	0.14	75.88	75.66	0.22
259	75.68	0.14	0.08	75.82	75.59	0.22	209	75.80	0.08	0.14	75.88	75.66	0.22
258	75.68	0.14	0.08	75.82	75.59	0.22	208	75.81	0.08	0.14	75.88	75.67	0.22
257	75.68	0.14	0.09	75.82	75.59	0.22	207	75.81	0.08	0.14	75.88	75.67	0.22
256	75.68	0.14	0.09	75.82	75.60	0.22	206	75.81	0.08	0.14	75.89	75.67	0.22
255	75.69	0.13	0.09	75.82	75.60	0.22	205	75.81	0.07	0.14	75.89	75.67	0.21
254	75.69	0.13	0.09	75.82	75.60	0.23	204	75.82	0.07	0.14	75.89	75.68	0.21
253	75.69	0.13	0.09	75.82	75.60	0.22	203	75.82	0.07	0.14	75.89	75.68	0.21
252	75.69	0.13	0.09	75.83	75.60	0.23	202	75.82	0.07	0.14	75.89	75.68	0.21
251	75.70	0.13	0.09	75.83	75.60	0.23	201	75.82	0.07	0.14	75.89	75.68	0.21
250	75.70	0.13	0.10	75.83	75.60	0.23	200	75.83	0.07	0.14	75.89	75.68	0.21
249	75.70	0.13	0.10	75.83	75.60	0.23	199	75.83	0.07	0.14	75.90	75.69	0.21
248	75.70	0.13	0.10	75.83	75.60	0.23	198	75.83	0.07	0.14	75.90	75.69	0.21
247	75.71	0.13	0.10	75.83	75.61	0.23	197	75.83	0.06	0.14	75.90	75.69	0.21
246	75.71	0.13	0.10	75.83	75.61	0.23	196	75.84	0.06	0.14	75.90	75.69	0.21
245	75.71	0.13	0.10	75.84	75.61	0.23	195	75.84	0.06	0.14	75.90	75.69	0.21
244	75.71	0.12	0.10	75.84	75.61	0.23	194	75.84	0.06	0.14	75.90	75.70	0.21
243	75.72	0.12	0.10	75.84	75.61	0.23	193	75.84	0.06	0.14	75.90	75.70	0.20
242	75.72	0.12	0.11	75.84	75.61	0.23	192	75.85	0.06	0.14	75.91	75.70	0.20
241	75.72	0.12	0.11	75.84	75.61	0.23	191	75.85	0.06	0.14	75.91	75.71	0.20
240	75.72	0.12	0.11	75.84	75.62	0.23	190	75.85	0.06	0.14	75.91	75.71	0.20
239	75.73	0.12	0.11	75.85	75.62	0.23	189	75.85	0.06	0.14	75.91	75.71	0.20
238	75.73	0.12	0.11	75.85	75.62	0.23	188	75.86	0.06	0.14	75.91	75.72	0.19
237	75.73	0.12	0.11	75.85	75.62	0.23	187	75.86	0.06	0.14	75.91	75.72	0.19
236	75.73	0.12	0.11	75.85	75.62	0.23	186	75.86	0.06	0.14	75.92	75.73	0.19
235	75.74	0.11	0.12	75.85	75.62	0.23	185	75.86	0.05	0.13	75.92	75.73	0.19
234	75.74	0.11	0.12	75.85	75.62	0.23	184	75.87	0.05	0.13	75.92	75.74	0.18
233	75.74	0.11	0.12	75.85	75.63	0.23	183	75.87	0.05	0.13	75.92	75.74	0.18
232	75.74	0.11	0.12	75.85	75.63	0.23	182	75.87	0.05	0.13	75.92	75.74	0.18
231	75.75	0.11	0.12	75.86	75.63	0.23	181	75.87	0.05	0.13	75.93	75.75	0.18
230	75.75	0.11	0.12	75.86	75.63	0.23	180	75.88	0.05	0.12	75.93	75.75	0.17
229	75.75	0.11	0.12	75.86	75.63	0.23	179	75.88	0.05	0.12	75.93	75.76	0.17
228	75.75	0.10	0.12	75.86	75.63	0.23	178	75.88	0.05	0.11	75.93	75.77	0.16
227	75.76	0.10	0.12	75.86	75.63	0.23	177	75.88	0.05	0.11	75.93	75.78	0.16
226	75.76	0.10	0.12	75.86	75.64	0.23	176	75.89	0.05	0.10	75.94	75.79	0.15
225	75.76	0.10	0.13	75.86	75.64	0.23	175	75.89	0.05	0.10	75.94	75.79	0.15
224	75.76	0.10	0.13	75.86	75.64	0.23	174	75.89	0.05	0.09	75.94	75.81	0.14
223	75.77	0.10	0.13	75.86	75.64	0.23	173	75.89	0.05	0.08	75.94	75.82	0.12
222	75.77	0.10	0.13	75.87	75.64	0.23	172	75.90	0.05	0.06	75.95	75.83	0.11
221	75.77	0.09	0.13	75.87	75.64	0.22	171	75.90	0.05	0.05	75.95	75.85	0.10
220	75.77	0.09	0.13	75.87	75.64	0.23	170	75.90	0.05	0.05	75.95	75.86	0.10
219	75.78	0.09	0.13	75.87	75.64	0.22	169	75.91	0.06	0.05	75.97	75.86	0.11
218	75.78	0.09	0.13	75.87	75.65	0.22	168	75.92	0.08	0.05	75.99	75.87	0.13
217	75.78	0.09	0.13	75.87	75.65	0.22	167	75.92	0.09	0.05	76.01	75.87	0.14

Strat. Level* (m)	Model Age (Ma)	+	-	(Max)	(Min)	Range	Strat. Level* (m)	Model Age (Ma)	+	-	(Max)	(Min)	Range
166	75.92	0.11	0.05	76.03	75.87	0.16	116	76.12	0.14	0.14	76.26	75.98	0.28
165	75.93	0.12	0.05	76.05	75.88	0.17	115	76.12	0.14	0.14	76.26	75.98	0.28
164	75.93	0.13	0.05	76.06	75.88	0.18	114	76.13	0.14	0.14	76.26	75.98	0.28
163	75.94	0.14	0.05	76.08	75.88	0.19	113	76.13	0.13	0.15	76.27	75.98	0.28
162	75.94	0.15	0.05	76.09	75.89	0.20	112	76.14	0.13	0.15	76.27	75.99	0.28
161	75.94	0.15	0.05	76.10	75.89	0.20	111	76.14	0.13	0.15	76.27	75.99	0.28
160	75.95	0.16	0.05	76.11	75.89	0.21	110	76.14	0.13	0.15	76.27	75.99	0.28
159	75.95	0.16	0.05	76.11	75.90	0.21	109	76.15	0.13	0.16	76.27	75.99	0.28
158	75.96	0.17	0.05	76.12	75.90	0.22	108	76.15	0.12	0.16	76.28	75.99	0.28
157	75.96	0.17	0.06	76.13	75.90	0.22	107	76.16	0.12	0.16	76.28	76.00	0.28
156	75.96	0.17	0.06	76.13	75.91	0.23	106	76.16	0.12	0.16	76.28	76.00	0.28
155	75.97	0.17	0.06	76.14	75.91	0.23	105	76.16	0.12	0.16	76.28	76.00	0.28
154	75.97	0.17	0.06	76.14	75.91	0.24	104	76.17	0.12	0.16	76.28	76.00	0.28
153	75.98	0.18	0.06	76.15	75.91	0.24	103	76.17	0.11	0.16	76.29	76.01	0.28
152	75.98	0.18	0.06	76.16	75.91	0.24	102	76.17	0.11	0.17	76.29	76.01	0.28
151	75.98	0.18	0.07	76.16	75.92	0.25	101	76.18	0.11	0.17	76.29	76.01	0.28
150	75.99	0.18	0.07	76.17	75.92	0.25	100	76.18	0.11	0.17	76.29	76.01	0.28
149	75.99	0.18	0.07	76.17	75.92	0.25	99	76.19	0.11	0.17	76.29	76.02	0.28
148	75.99	0.18	0.07	76.17	75.92	0.25	98	76.19	0.10	0.17	76.29	76.02	0.28
147	76.00	0.18	0.08	76.18	75.92	0.25	97	76.19	0.10	0.17	76.30	76.02	0.27
146	76.00	0.18	0.08	76.18	75.93	0.26	96	76.20	0.10	0.17	76.30	76.02	0.27
145	76.01	0.18	0.08	76.18	75.93	0.26	95	76.20	0.10	0.17	76.30	76.03	0.27
144	76.01	0.18	0.08	76.19	75.93	0.26	94	76.21	0.09	0.18	76.30	76.03	0.27
143	76.01	0.18	0.08	76.19	75.93	0.26	93	76.21	0.09	0.18	76.30	76.03	0.27
142	76.02	0.18	0.09	76.19	75.93	0.26	92	76.21	0.09	0.18	76.31	76.04	0.27
141	76.02	0.18	0.09	76.20	75.93	0.26	91	76.22	0.09	0.18	76.31	76.04	0.27
140	76.03	0.18	0.09	76.20	75.94	0.27	90	76.22	0.09	0.18	76.31	76.04	0.27
139	76.03	0.18	0.09	76.21	75.94	0.27	89	76.23	0.09	0.18	76.31	76.05	0.27
138	76.03	0.17	0.09	76.21	75.94	0.27	88	76.23	0.08	0.18	76.31	76.05	0.26
137	76.04	0.17	0.10	76.21	75.94	0.27	87	76.23	0.08	0.18	76.32	76.05	0.26
136	76.04	0.17	0.10	76.21	75.94	0.27	86	76.24	0.08	0.18	76.32	76.06	0.26
135	76.05	0.17	0.10	76.22	75.94	0.27	85	76.24	0.08	0.18	76.32	76.06	0.26
134	76.05	0.17	0.10	76.22	75.95	0.27	84	76.25	0.08	0.18	76.32	76.06	0.26
133	76.05	0.17	0.11	76.22	75.95	0.27	83	76.25	0.07	0.18	76.32	76.07	0.26
132	76.06	0.17	0.11	76.22	75.95	0.27	82	76.25	0.07	0.18	76.33	76.07	0.25
131	76.06	0.16	0.11	76.23	75.95	0.28	81	76.26	0.07	0.18	76.33	76.08	0.25
130	76.07	0.16	0.11	76.23	75.95	0.28	80	76.26	0.07	0.18	76.33	76.08	0.25
129	76.07	0.16	0.12	76.23	75.95	0.28	79	76.26	0.07	0.18	76.33	76.09	0.24
128	76.07	0.16	0.12	76.23	75.96	0.28	78	76.27	0.07	0.17	76.34	76.09	0.24
127	76.08	0.16	0.12	76.24	75.96	0.28	77	76.27	0.06	0.17	76.34	76.10	0.24
126	76.08	0.16	0.12	76.24	75.96	0.28	76	76.28	0.06	0.17	76.34	76.11	0.23
125	76.08	0.16	0.12	76.24	75.96	0.28	75	76.28	0.06	0.17	76.34	76.11	0.23
124	76.09	0.16	0.13	76.24	75.96	0.28	74	76.28	0.06	0.16	76.35	76.12	0.22
123	76.09	0.15	0.13	76.25	75.97	0.28	73	76.29	0.06	0.16	76.35	76.13	0.22
122	76.10	0.15	0.13	76.25	75.97	0.28	72	76.29	0.06	0.16	76.35	76.13	0.22
121	76.10	0.15	0.13	76.25	75.97	0.28	71	76.30	0.06	0.15	76.36	76.14	0.21
120	76.10	0.15	0.13	76.25	75.97	0.28	70	76.30	0.06	0.15	76.36	76.15	0.21
119	76.11	0.15	0.14	76.25	75.97	0.28	69	76.30	0.06	0.14	76.36	76.16	0.20
118	76.11	0.14	0.14	76.26	75.97	0.28	68	76.31	0.06	0.13	76.37	76.17	0.19
117	76.12	0.14	0.14	76.26	75.98	0.28	67	76.31	0.06	0.12	76.37	76.19	0.18

Strat. Level* (m)	Model Age (Ma)	+	-	(Max)	(Min)	Range	Strat. Level* (m)	Model Age (Ma)	+	-	(Max)	(Min)	Range
66	76.32	0.06	0.11	76.37	76.20	0.17	32	76.42	0.91	0.11	77.33	76.31	1.02
65	76.32	0.06	0.10	76.38	76.22	0.15	31	76.42	0.93	0.11	77.35	76.31	1.04
64	76.32	0.06	0.08	76.38	76.24	0.14	30	76.42	0.94	0.11	77.36	76.31	1.05
63	76.33	0.06	0.07	76.39	76.26	0.12	29	76.42	0.95	0.12	77.38	76.31	1.07
62	76.34	0.06	0.05	76.39	76.28	0.11	28	76.43	0.97	0.12	77.40	76.31	1.09
61	76.34	0.10	0.06	76.44	76.29	0.15	27	76.43	0.98	0.12	77.41	76.31	1.10
60	76.35	0.16	0.06	76.51	76.29	0.22	26	76.43	1.00	0.12	77.43	76.31	1.12
59	76.35	0.22	0.06	76.57	76.29	0.28	25	76.43	1.01	0.12	77.45	76.31	1.14
58	76.35	0.27	0.06	76.63	76.29	0.33	24	76.44	1.03	0.13	77.46	76.31	1.15
57	76.36	0.32	0.06	76.68	76.29	0.39	23	76.44	1.04	0.13	77.47	76.31	1.16
56	76.36	0.36	0.07	76.72	76.29	0.43	22	76.44	1.04	0.13	77.48	76.31	1.17
55	76.36	0.40	0.07	76.77	76.30	0.47	21	76.44	1.05	0.13	77.49	76.31	1.18
54	76.37	0.44	0.07	76.80	76.30	0.51	20	76.45	1.06	0.13	77.51	76.31	1.20
53	76.37	0.47	0.07	76.84	76.30	0.54	19	76.45	1.07	0.14	77.52	76.31	1.21
52	76.37	0.50	0.07	76.86	76.30	0.57	18	76.45	1.08	0.14	77.53	76.31	1.22
51	76.37	0.52	0.07	76.90	76.30	0.60	17	76.45	1.09	0.14	77.55	76.31	1.23
50	76.37	0.55	0.07	76.93	76.30	0.63	16	76.46	1.10	0.14	77.56	76.31	1.25
49	76.38	0.58	0.08	76.96	76.30	0.66	15	76.46	1.11	0.14	77.57	76.31	1.26
48	76.38	0.61	0.08	76.99	76.30	0.69	14	76.46	1.13	0.15	77.59	76.31	1.28
47	76.38	0.64	0.08	77.02	76.30	0.72	13	76.46	1.14	0.15	77.60	76.31	1.29
46	76.38	0.66	0.08	77.05	76.30	0.74	12	76.47	1.15	0.15	77.62	76.31	1.31
45	76.39	0.68	0.08	77.07	76.30	0.76	11	76.47	1.16	0.15	77.63	76.31	1.31
44	76.39	0.71	0.09	77.10	76.30	0.80	10	76.47	1.16	0.16	77.63	76.31	1.32
43	76.39	0.73	0.09	77.12	76.30	0.82	9	76.47	1.17	0.16	77.64	76.31	1.32
42	76.39	0.74	0.09	77.14	76.30	0.83	8	76.48	1.17	0.16	77.65	76.32	1.33
41	76.40	0.77	0.09	77.17	76.30	0.86	7	76.48	1.18	0.16	77.66	76.32	1.35
40	76.40	0.79	0.09	77.19	76.31	0.88	6	76.48	1.20	0.17	77.68	76.32	1.36
39	76.40	0.81	0.09	77.21	76.31	0.90	5	76.49	1.20	0.17	77.69	76.32	1.37
38	76.40	0.82	0.10	77.23	76.31	0.92	4	76.49	1.21	0.17	77.70	76.32	1.38
37	76.41	0.85	0.10	77.25	76.31	0.95	3	76.49	1.22	0.17	77.71	76.32	1.39
36	76.41	0.86	0.10	77.27	76.31	0.96	2	76.49	1.23	0.18	77.72	76.32	1.41
35	76.41	0.87	0.10	77.28	76.31	0.97	1	76.50	1.23	0.18	77.73	76.32	1.41
34	76.41	0.88	0.11	77.29	76.31	0.99	0	76.50	1.24	0.18	77.74	76.32	1.42
33	76.41	0.89	0.11	77.31	76.31	1.00							

\* Relative to the KWC section (Beveridge et al., in prep [Ch.4])



**Appendix C.5 Chapter Five Data**

Supplementary data are included in the publication of this work in *Cretaceous Research* (2020) and reproduced here with permission. See:

Beveridge, T. L., Roberts, E. M., & Titus, A. L. (2020). Volcaniclastic member of the richly fossiliferous Kaiparowits Formation reveals new insights for regional correlation and tectonics in southern Utah during the latest Campanian. *Cretaceous Research*, 114, 104527. doi.org/10.1016/j.cretres.2020.104527

**Appendix C.5.1** *U-Pb detrital zircon data (LA-ICP-MS) is available online via Cretaceous Research (doi.org/10.1016/j.cretres.2020.104527) or on request to the author.*

**Appendix C.5.2** Summary of sandstone, mudstone and concretion samples used in this study. All GPS location are in WGS84.

Sample Name	Strat. Height	Location		Description	Use
		Latitude	Longitude		
KBU-W	1010	37°37'51.10"N	111°48'51.40"W	Sandstone from the basal Canaan Peak Fm. collected from interval below pebble conglomerate	Detrital zircon geochronology
CPT-Y	950	37°40'39.50"N	111°48'4.60"W	Tan sandstone collected from the Canaan Peak Trail area in the Upper Valley	Thin section petrography
KBU-O	930	37°37'58.80"N	111°49'27.30"W	Sandstone from high in the Upper Valley Member type area	Detrital zircon geochronology and thin section petrography
KBU-M	910	37°37'57.22"N	111°49'26.67"W	Septarian nodule with abundant veins collected in the Upper Valley Member type area	Stable isotopes and cation geochemistry
Carbonaceous Mudstone	890	37°40'38.90"N	111°48'18.60"W	Mudstone with carbonised leaf traces from the Canaan Peak Trail area	Clay mineralogy
KBU-F	800	37°37'41.81"N	111°49'32.21"W	White volcanoclastic sandstone (Sv) from thin lens (best example of Sv)	Detrital zircon geochronology and thin section petrography
Bentonitic Mudstone	790	37°37'43.12"N	111°49'34.40"W	Richly bentonitic mudstone from directly above one of the rare airfall tuff horizons	Clay mineralogy
KBU-V	765	37°37'53.40"N	111°49'41.60"W	First white volcanoclastic sandstone (Sv) in the UVM	Detrital zircon geochronology and thin section petrography
Green Mudstone	755	37°37'52.70"N	111°49'41.60"W	First mudstone above the basal contact of the UVM	Clay mineralogy
KBU-S	730	37°37'52.10"N	111°49'44.10"W	Litharenite from the amalgamated sandstone channel complex	Detrital zircon geochronology and thin section petrography

**Appendix C.5.3** Sandstone point-count data as a percentage of total. Abbreviations are as per. Lawton et al. (2003).

Sample:	CPT-Y	KBU-O	KBU-F	KBU-V	KBU-S
Height:	950 m	930 m	800 m	785 m	730 m
FA:	FA 11	FA 5	FA 10	FA 10	FA 3
Qm	53	22	29	35	18
Qpq	8	14	6	10	5
Cht	9	5	16	10	14
Qp	16	20	22	21	19
Qt	70	42	51	56	38
K	11	11	14	10	7
P	2	3	14	8	2
F	13	14	28	18	9
Lvm	5	30	12	11	23
Lss	1	13	4	5	20
Lsc	6	0	0	1	7
L	12	43	16	17	50
Lt	28	62	38	38	69
Lsm	7	13	4	6	26
Bt	4	1	5	5	1
Other	2	1	0	4	2

**Appendix C.5.4** Element proportions for calcite domains within septarian nodules. Groundmass sample contained a high proportion of detrital material and were not used in this study.

Domain	ID Number	wt. %					wt. % Total
		Ca	O	Fe	Mn	Mg	
Purple zone	22	70.14	28.57	ND	0.74	0.55	100.0
Purple zone	24	70.17	28.55	ND	0.82	0.46	100.0
Purple zone	25	70.2	28.59	ND	0.63	0.58	100.0
Purple zone	26	70.34	28.58	ND	0.58	0.5	100.0
Purple zone	28	69.67	28.92	ND	ND	1.21	99.8
Purple zone	3	70.94	28.48	ND	0.58	ND	100.0
Major veins (amber)	1	62.99	28.02	5.03	3.2	0.76	100.0
Major veins (amber)	5	61.43	27.79	4.94	5.43	0.4	100.0
Major veins (amber)	7	62.46	27.98	4.89	3.87	0.8	100.0
Major veins (amber)	10	62.88	27.95	4.35	4.28	0.54	100.0
Major veins (amber)	11	63.52	27.98	4.17	3.87	0.45	100.0
Major veins (amber)	16	61.21	27.88	5.54	4.57	0.8	100.0
Major veins (amber)	21	61.95	27.93	5.27	4.11	0.74	100.0
Major veins (amber)	36	63.71	28.07	4	3.51	0.72	100.0
Major veins (amber)	39	61.29	27.91	5.96	3.94	0.9	100.0
Major veins (amber)	40	61.44	27.93	5.4	4.33	0.9	100.0
Major veins (amber)	42	59.78	27.72	6.44	5.4	0.66	100.0
Major veins (amber)	43	60.77	27.81	5.91	4.83	0.68	100.0
Major veins (amber)	44	61.11	27.84	5.64	4.74	0.68	100.0
Major veins (amber)	45	61.09	27.82	5.49	4.94	0.65	100.0
Secondary veins (milky)	4	68.27	28.26	ND	3.47	ND	100.0
Secondary veins (milky)	23	67.7	28.21	ND	4.09	ND	100.0
Secondary veins (milky)	31	67.04	28.16	ND	4.8	ND	100.0
Secondary veins (milky)	32	68.2	28.26	ND	3.54	ND	100.0
Secondary veins (milky)	33	68.69	28.3	ND	3.01	ND	100.0
Secondary veins (milky)	34	68.81	28.31	ND	2.88	ND	100.0
Secondary veins (milky)	35	67.84	28.23	ND	3.93	ND	100.0

**Appendix C.5.5** Stable isotope values for carbonate domains in septarian nodules.  $\delta^{18}\text{O}$  ‰ VSMOW was calculated using the calcite fractionation equation of Kim and O'Neil (1997).

Sample Number	Domain	$\delta^{13}\text{C}$ ‰ VPDB	$\delta^{18}\text{O}$ ‰ VPDB	$\delta^{18}\text{O}$ ‰ VSMOW
1	Groundmass	-4.99	-7.81	-5.93
2	Groundmass	-12.83	-8.66	-6.77
3	Groundmass	-12.02	-8.33	-6.44
4	Groundmass	-11.79	-8.15	-6.26
5	Purple zone	-9.78	-8.24	-6.35
6	Purple zone	-10.28	-8.05	-6.16
7	Secondary veins (milky)	-12.02	-8.70	-6.81
8	Secondary veins (milky)	-12.13	-8.34	-6.45
9	Major veins (amber)	-12.22	-8.16	-6.27
10	Major veins (amber)	-12.23	-8.30	-6.41

**Appendix C.5.6** *Difference between YCP weighted mean ages calculated using 10% and 5% discordance and analytical uncertainty criteria. The “percentage of grains excluded” reflects the total number of analysis rejected at each criteria level. Note that ages for samples KBU-S, KBU-O and KBU-W are only subtly affected by stricter criteria; however, samples KBU-V and KBU-F are different by as much as a million years. The unusually high exclusion rate of grains from sample KBU-F at both 5 and 10% criteria is attributed to the abundance of small (< 30  $\mu\text{m}$  width) zircons in that particular sample.*

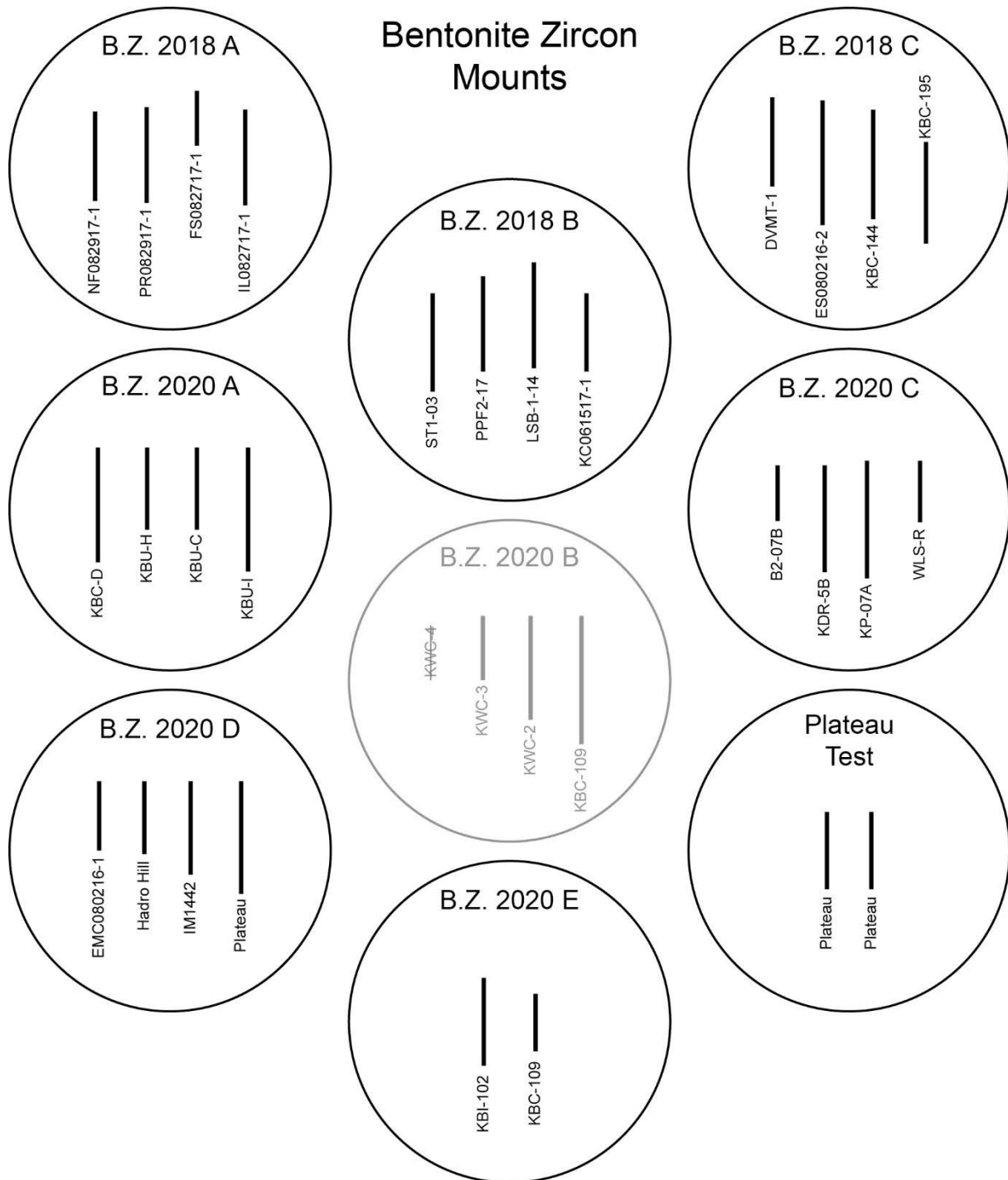
Sample	10% discordance and 2 $\sigma$ uncertainty				5% discordance and 2 $\sigma$ uncertainty			
	Ages excl. (%)	YCP Age	n	MSWD	Ages excl. (%)	YCP Age	n	MSWD
KBU-W	11.3	72.9 $\pm$ 1.3	3	0.32	21.8	73.1 $\pm$ 1.2	4	0.43
KBU-O	19.5	73.2 $\pm$ 1.4	3	0.51	29.9	73.2 $\pm$ 1.4	3	0.51
KBU-F	40.1	72.94 $\pm$ 0.97	10	0.18	58.5	73.68 $\pm$ 0.81	10	0.3
KBU-V	18.3	72.7 $\pm$ 1.0	10	0.056	35.5	73.68 $\pm$ 0.66	10	0.19
KBU-S	4	75.1 $\pm$ 1.3	5	0.12	13	75.2 $\pm$ 1.4	4	0.15

**Appendix C.5.7** *Kolmogorov-Smirnov statistical comparison of detrital zircon spectra for sandstones from the Upper Valley Member type area showing no statistical similarity between the age suites for any sample herein.*

	KBU-W2	KBU-O	KBU-F	KBU-V	KBU-S
KBU-W2		0.000	0.000	0.000	0.033
KBU-O	0.000		0.000	0.009	0.000
KBU-F	0.000	0.000		0.001	0.000
KBU-V	0.000	0.009	0.001		0.000
KBU-S	0.033	0.000	0.000	0.000	

**Appendix C.6 Chapter Six Data**

*Appendix C.6.1 Zircon mount names and samples. B. Z. abbreviated from 'bentonite zircon'.*

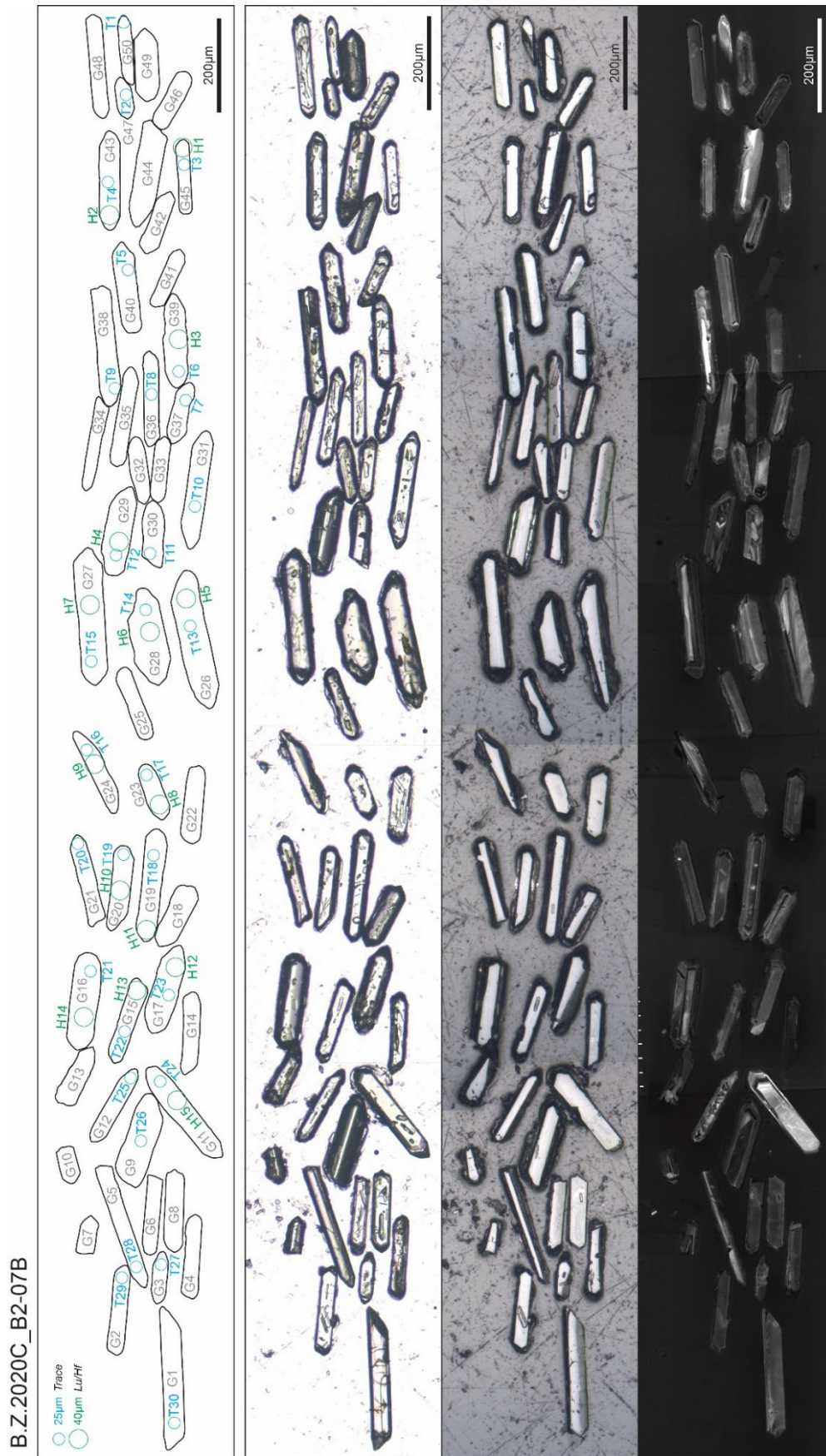




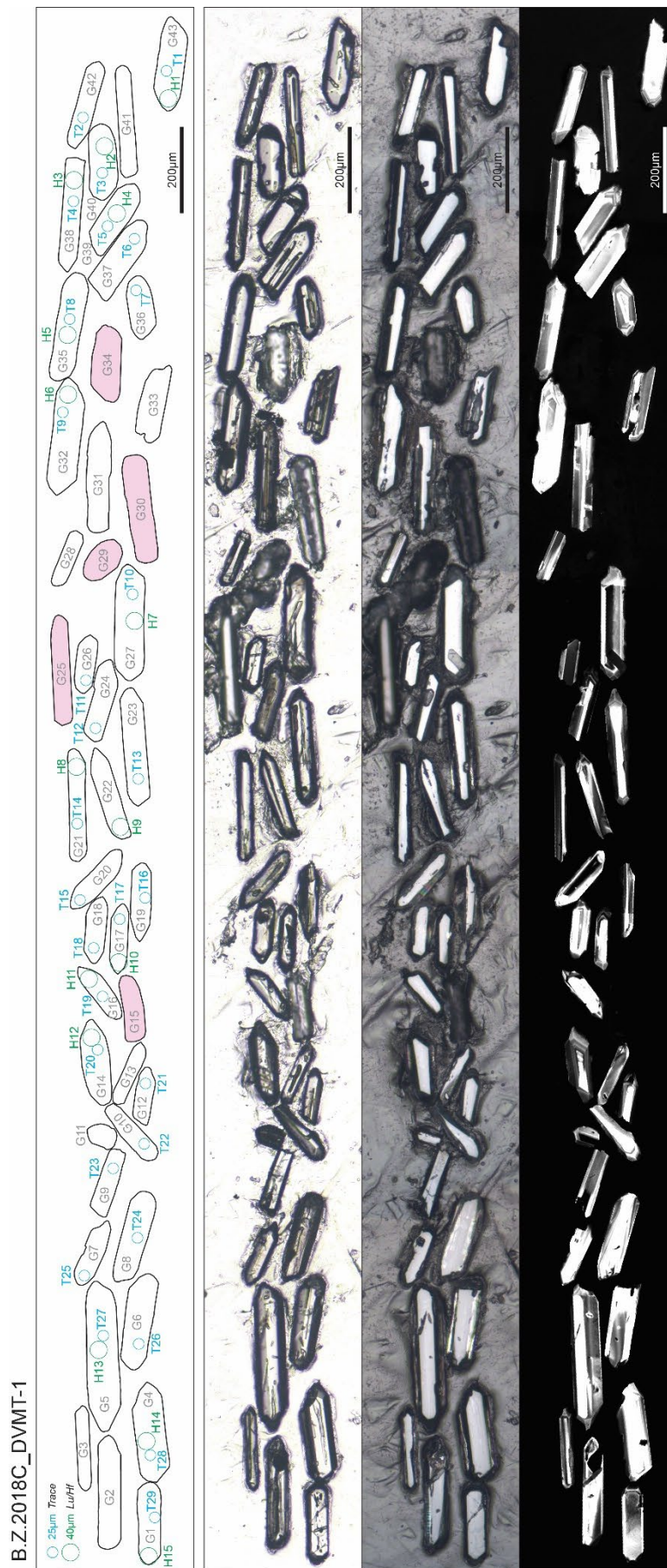
*Appendix C.6.2 List of samples and their details as used in Chapter 6. Ages for PR, LSB, EMC, and HH are treated as confidential pending development of a manuscript for publication.*

Zircon Mount	Sample Name	Abbrev. Name	Stratigraphic Unit	Location	N° Zircons	N° of Analyses			Age (Ma)	Uncertainty (Ma)			Publication / Chapter
						MI	TE	Hf		X	Y	Z	
B.Z. 2018 A	FS082717-1	FS	Dinosaur Park Fm	Alberta	20	4	17	16	76.718	0.02	0.029	0.087	Ramezani et al.
	IL082717-1	IL	Dinosaur Park Fm	Alberta	26	20	25	15	74.27	0.017	0.026	0.084	Ramezani et al.
	NF082917-1	NF	Oldman Fm	Alberta	24	13	24	15	76.3ish	-	-	-	N/A
	PR082917-1	PR	Oldman Fm	Alberta	29	17	26	18	ca 76.3	(0.03%)	-	-	N/A
B.Z. 2018 B	KC061517-1	KC	Judith River Fm	Montana	24	9	22	15	78.594	0.024	0.032	0.09	Ramezani et al.
	LSB-1-14	LSB	Two Medicine Fm	Montana	34	38	30	15	ca 75.2	(0.03%)	-	-	N/A
	PPF2-17	PPF	Judith River Fm	Montana	21	13	19	15	~75.22	-	-	-	N/A
	ST1-03	ST1	Judith River Fm	Montana	44	13	30	15	76.329	0.035	0.043	0.092	Ramezani et al.
B.Z. 2018 C	DVMT-1	DVMT-1	Two Medicine Fm	Montana	43	14	29	15	~74.5	-	-	-	N/A
	ES080216-2	ES	Two Medicine Fm	Montana	27	13	26	15	74.43	0.015	0.025	0.083	Ramezani et al.
	KBC-144	KBC-144	Kaiparowits Fm	Utah	25	18	25	15	75.427	0.012	0.023	0.084	Ramezani et al.
	KBC-195	KBC-195	Kaiparowits Fm	Utah	26	1	20	15	75.231	0.021	0.038	0.089	Ramezani et al.
B.Z. 2020 A	KBC-D-030818	KBC-D	Kaiparowits Fm	Utah	75	4	30	15	~75.23	-	-	-	Chapter 5/6
	KBU-C-310718	KBU-C	Kaiparowits Fm	Utah	61	4	30	12	~75.23	-	-	-	Chapter 5/6
	KBU-H-050818	KBU-H	Kaiparowits Fm	Utah	65	3	30	15	~73.9	-	-	-	Chapter 5/6
	KBU-I-050818	KBU-I	Kaiparowits Fm	Utah	62	0	30	15	~73.9	-	-	-	Chapter 5/6
B.Z. 2020 C	B2-07B	B2-07B	Wahweap Fm	Utah	50	25	30	15	81.458	0.024	0.032	0.093	Chapter 3
	KDR-5B	KDR-5B	Kaiparowits Fm	Utah	56	18	30	15	76.259	0.019	0.028	0.066	Chapter 4
	KP-07A	KP-07A	Kaiparowits Fm	Utah	59	32	30	15	76.394	0.04	0.045	0.093	Ramezani et al.
B.Z. 2020 D	WLS-R-070818	WLS-R	Wahweap Fm	Utah	50	14	27	7	81.465	0.036	0.042	0.097	Chapter 3
	EMC080216-1	EMC	Two Medicine Fm	Montana	33	14	29	15	ca 78.0	(0.03%)	-	-	N/A
	Hadro Hill	HH	Two Medicine Fm	Montana	37	25	30	15	ca 78.6	(0.03%)	-	-	N/A
	IM1442	IM1442	Kaiparowits Fm	Utah	30	30	28	15	75.659	0.036	0.054	0.097	Chapter 4
B.Z. 2020 E / Plateau Test	Plateau	Plateau	Dinosaur Park Fm	Alberta	65	17	30	15	75.639	0.025	0.032	0.087	Ramezani et al.
	KBI-102	KBI-102	Kaiparowits Fm	Utah	51	41	30	13	75.609	0.015	0.025	0.085	Ramezani et al.
	KBC-109	KBC-109	Kaiparowits Fm	Utah	29	22	20	9	75.609	0.015	0.025	0.085	Ramezani et al.
	Plateau(EMR)	Plateau/	Dinosaur Park Fm	Alberta	44	12	0	0	75.639	0.025	0.032	0.087	Ramezani et al.
	Plateau(EMR)	Plateau/	Dinosaur Park Fm	Alberta	41	12	0	0	75.639	0.025	0.032	0.087	Ramezani et al.

**Appendix C.6.3 Zircon microphotography and mount maps (28 samples arranged alphabetically by sample name).**

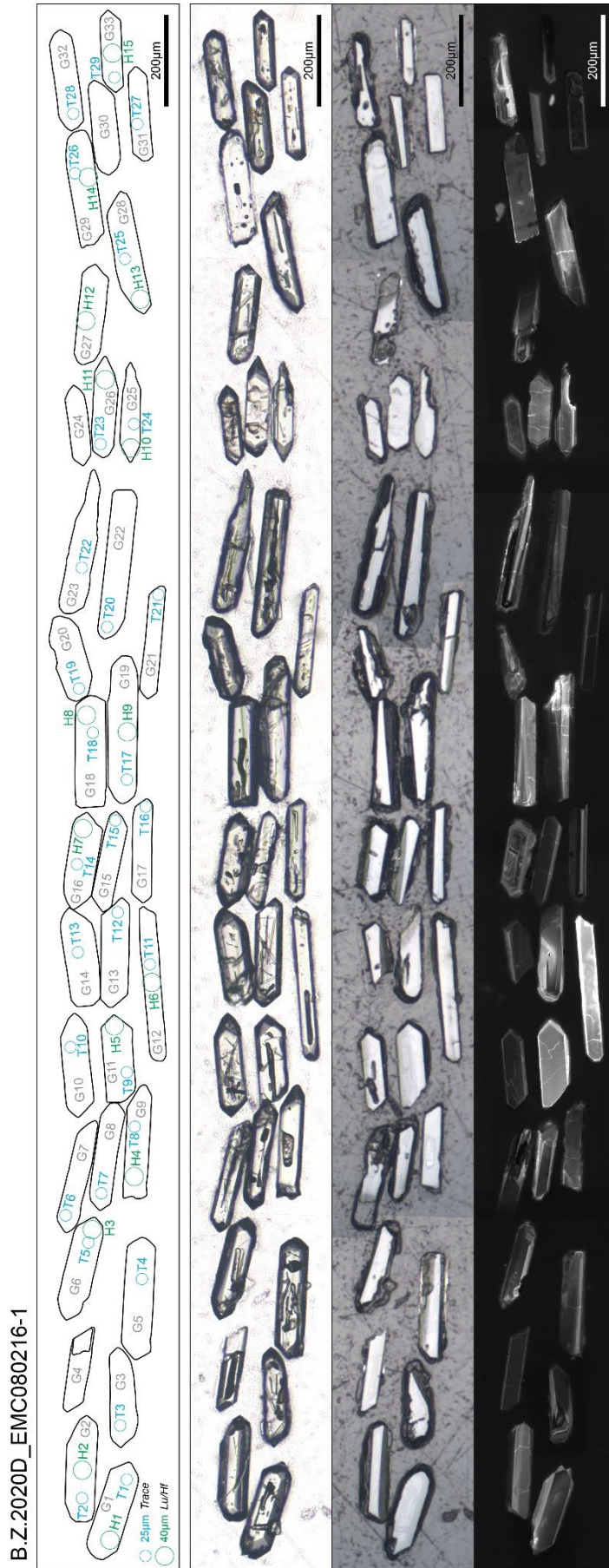


B2-07B (B.Z.2020C) from the Wahweap Formation, Utah U.S.A.



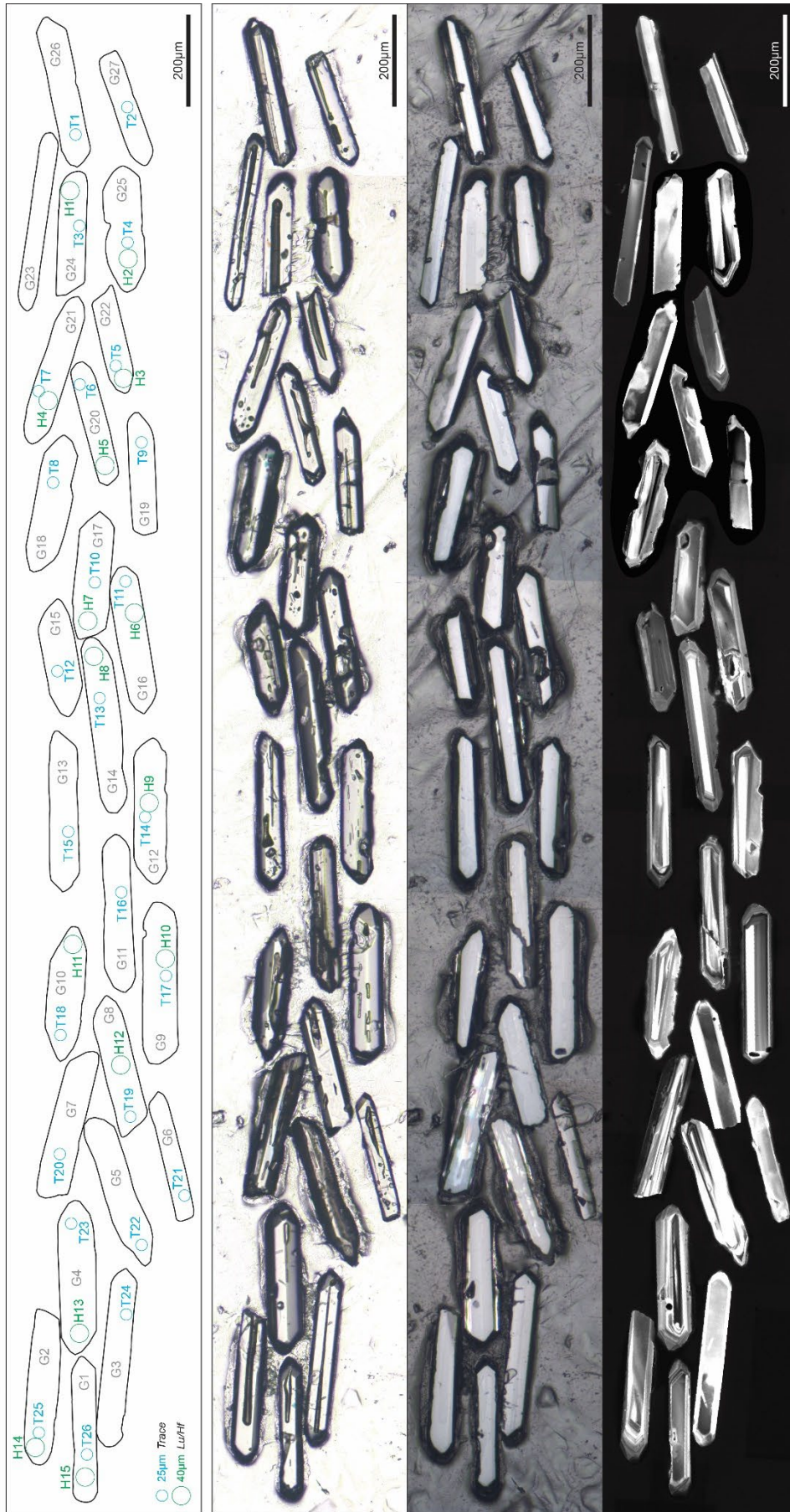
DVMT-1 (B.Z.2018C) from the Two Medicine Formation, Montana U.S.A.





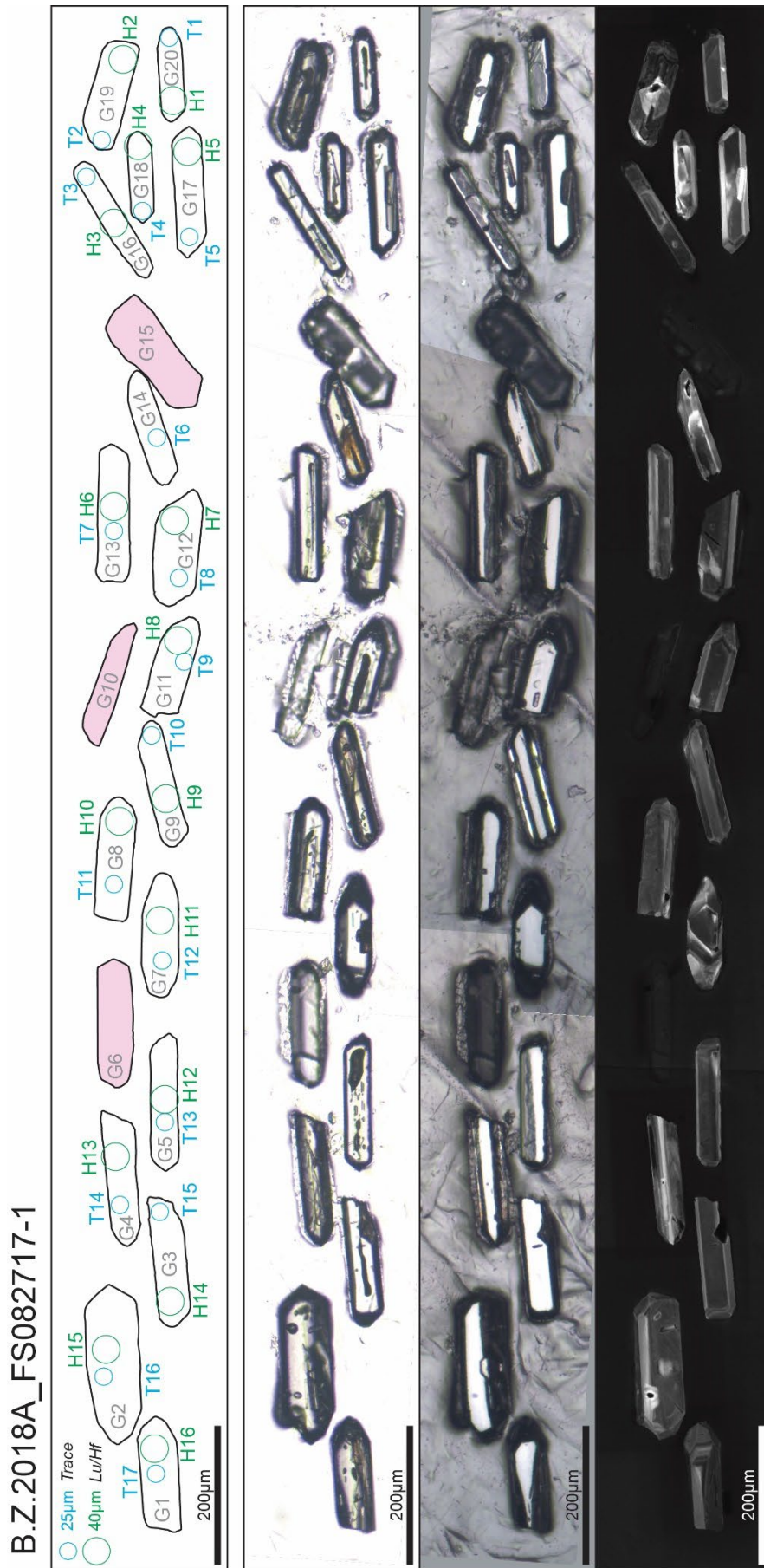
EMC080216-1 (B.Z.2020D) from the Two Medicine Formation, Montana U.S.A.

B.Z.2018C\_ES080216



ES080216-2 (B.Z.2018C) from the Two Medicine Formation, Montana U.S.A.

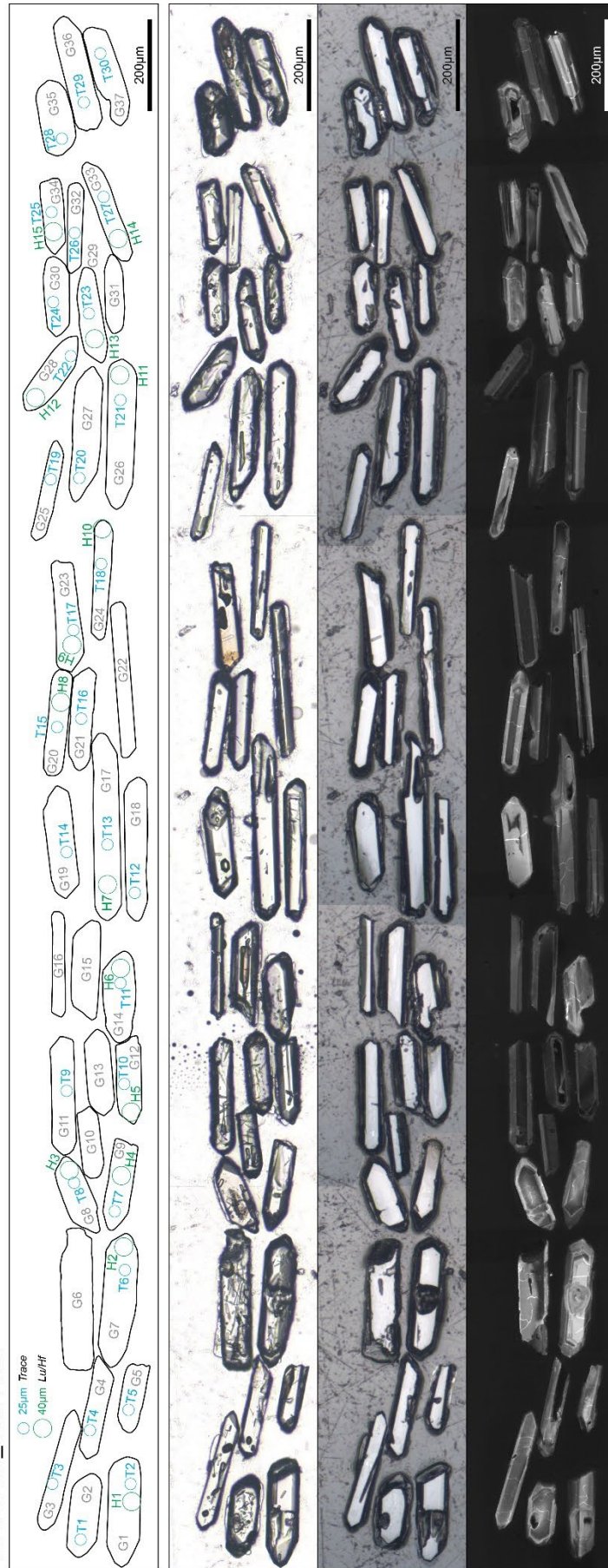




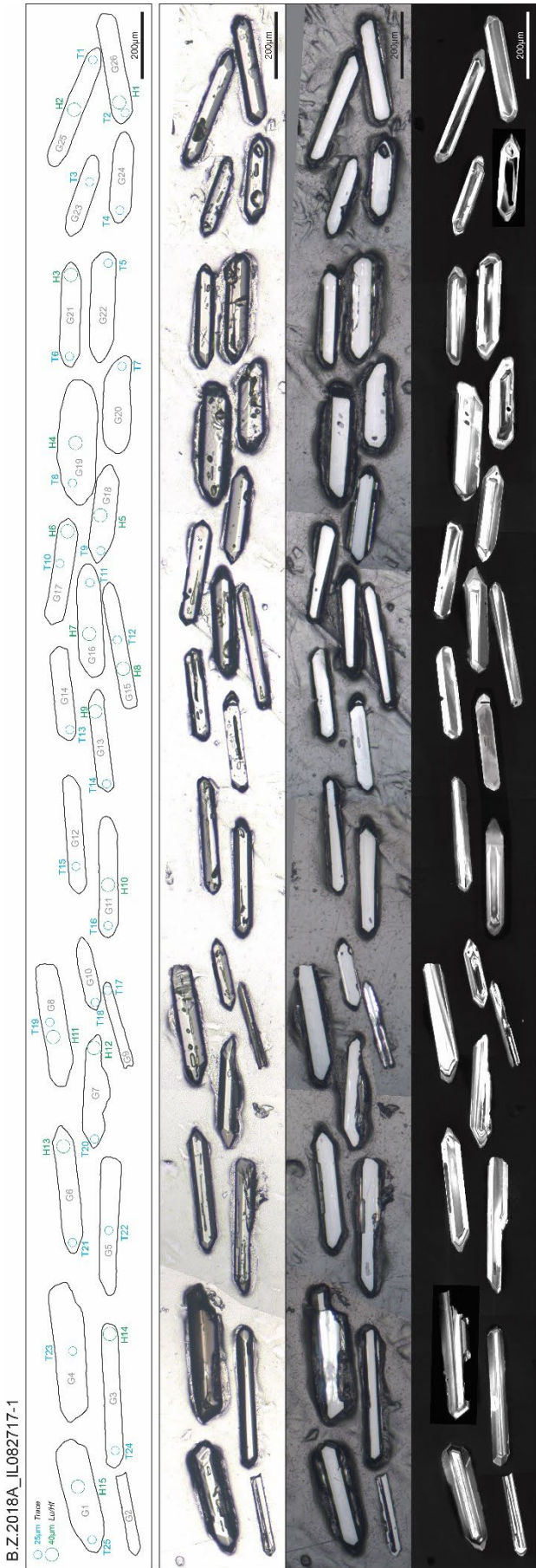
FS082717-1 (B.Z.2018A) from the Dinosaur Park Formation, Alberta Canada.



B.Z.2020D\_Hadro Hill

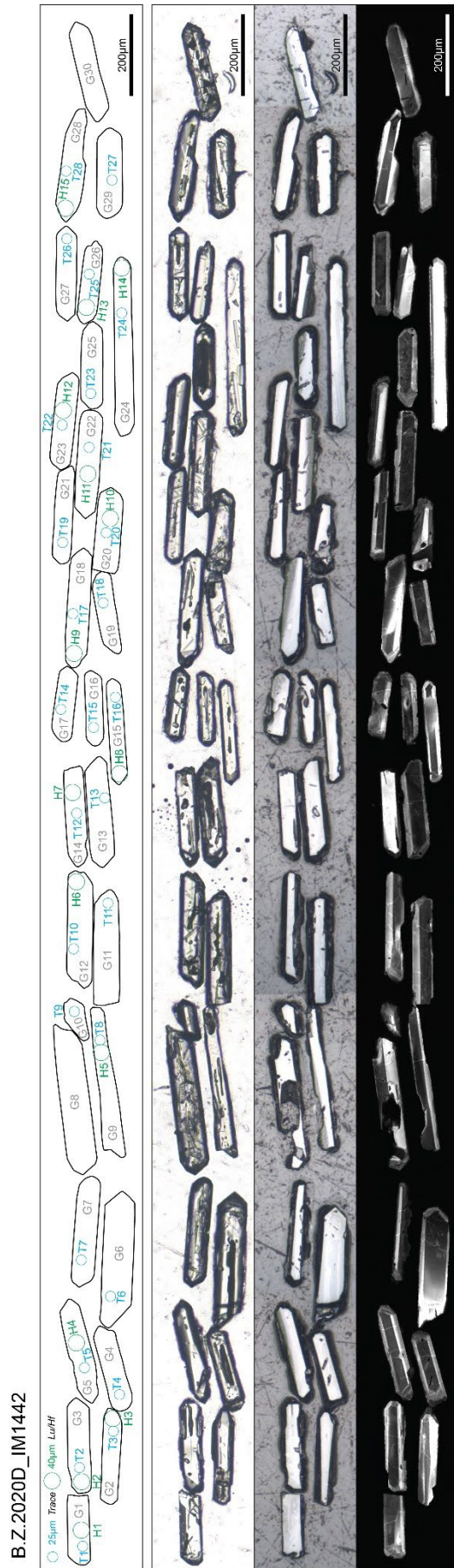


Hadro Hill (B.Z.2020D) from the Two Medicine Formation, Montana U.S.A.

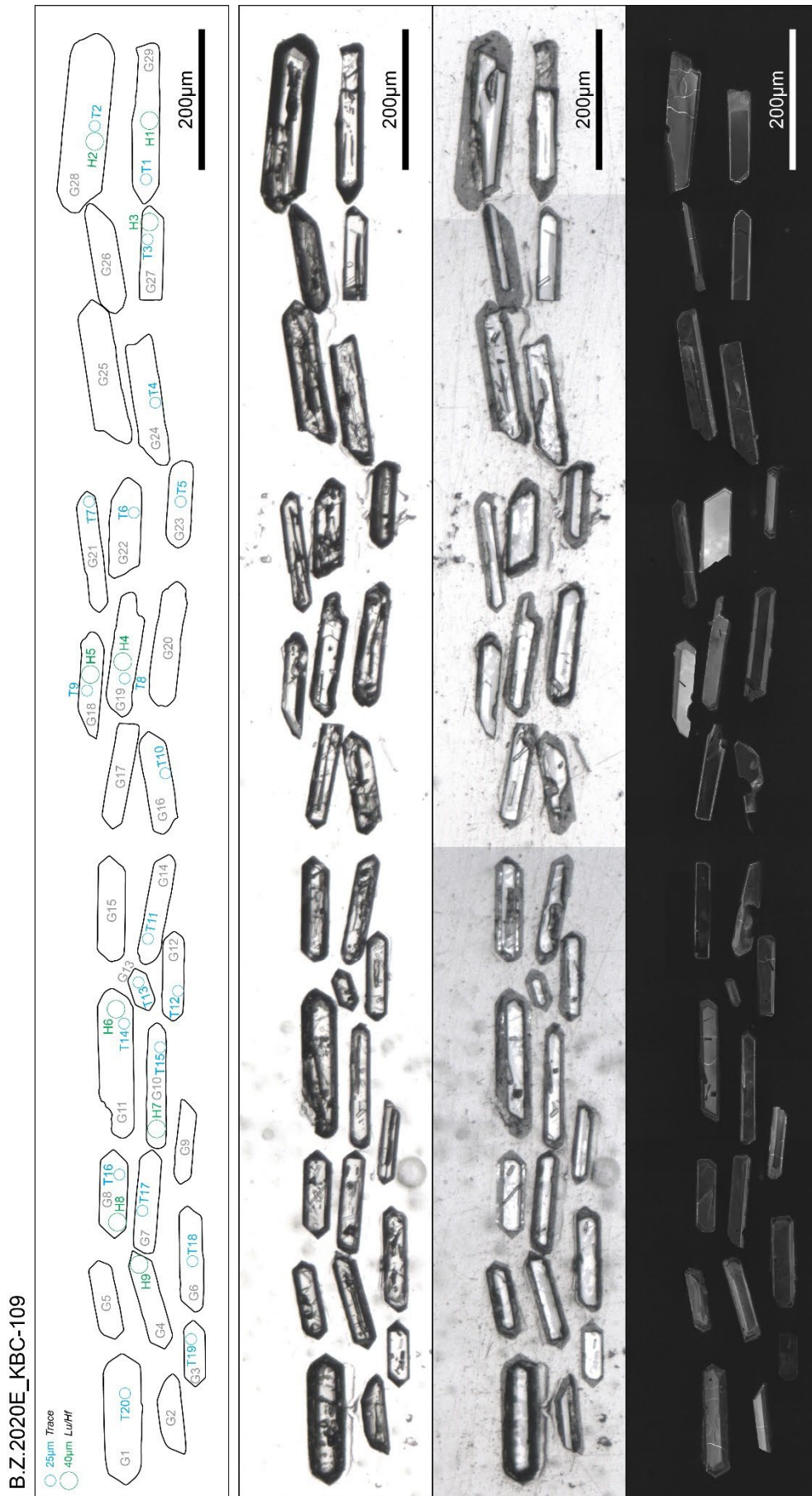


IL082717-1 (B.Z.2018A) from the Bearpaw Formation, Alberta Canada.



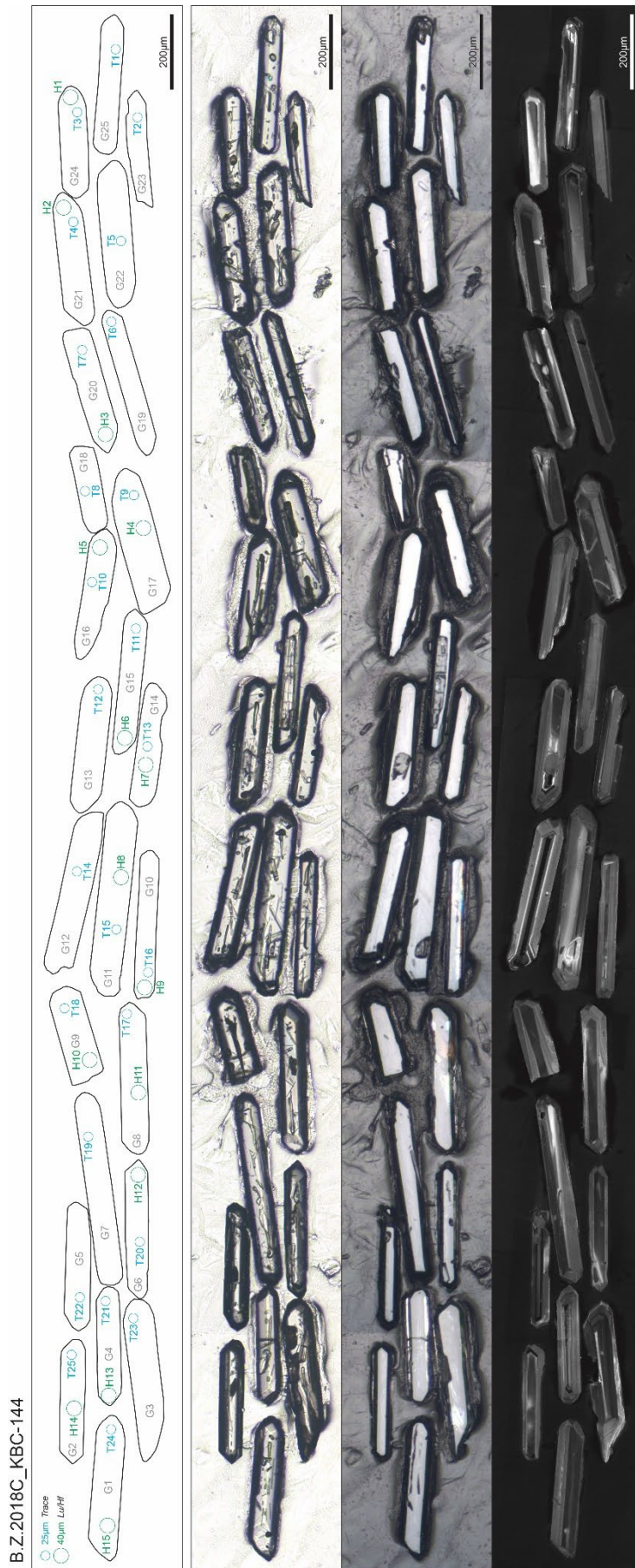


IM1442 (B.Z.2020D) from the Kaiparowits Formation, Utah U.S.A.



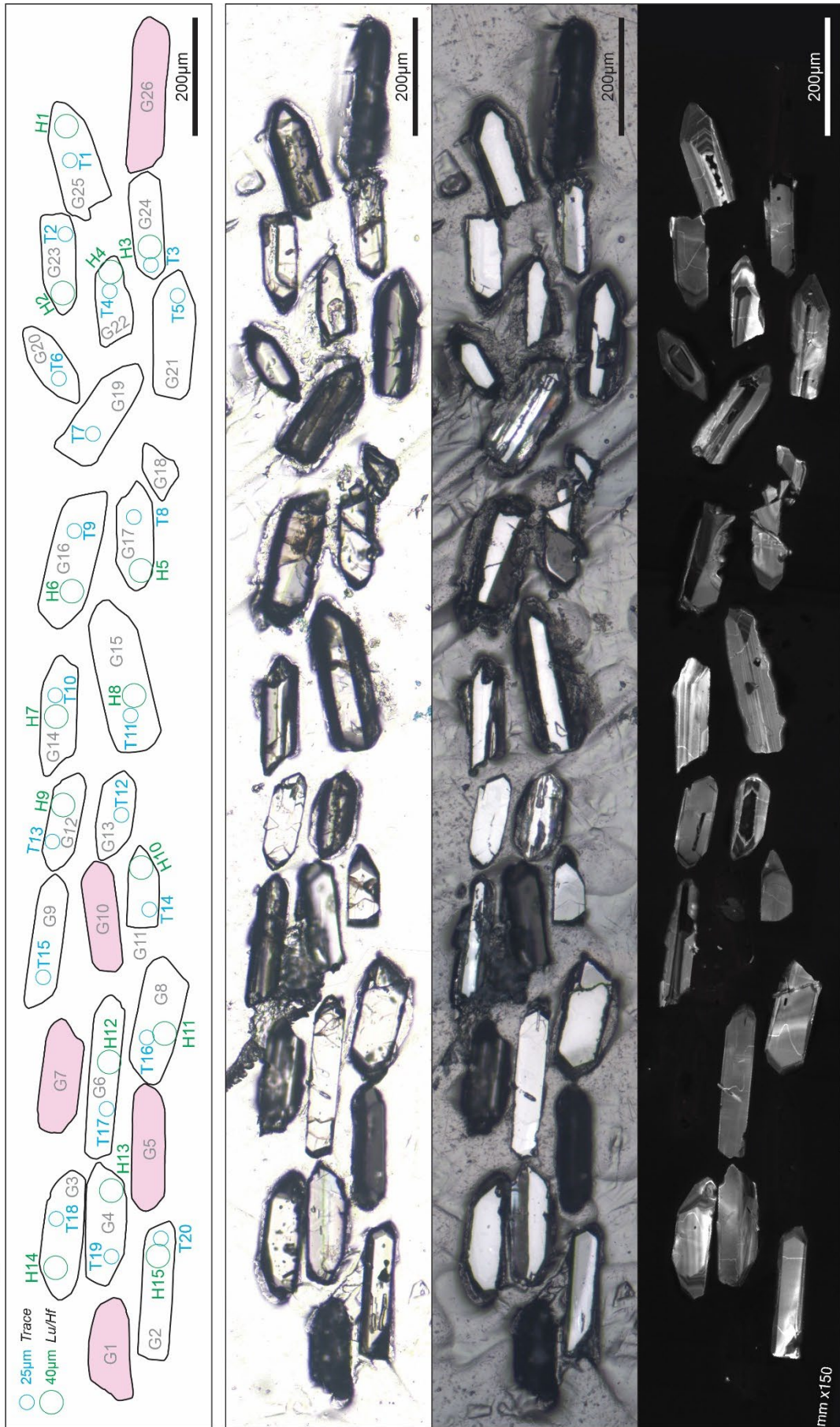
KBC-109 (B.Z.2020E) from the Kaiparowits Formation, Utah U.S.A.





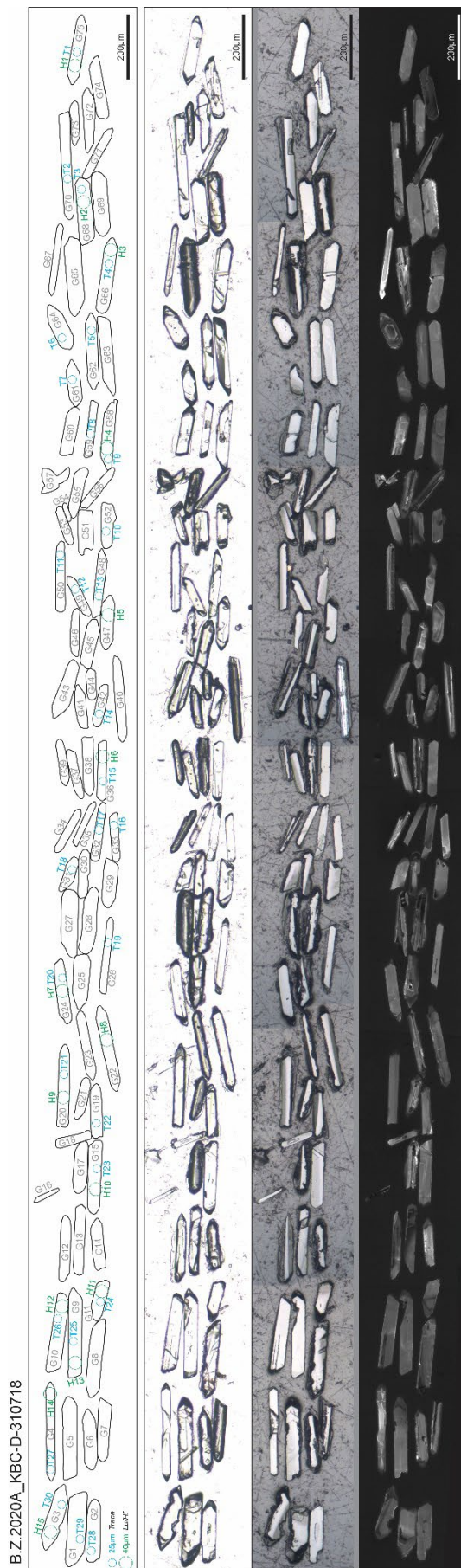
KBC-144 (B.Z.2018C) from the Kaiparowits Formation, Utah U.S.A.

B.Z.2018C\_KBC-195

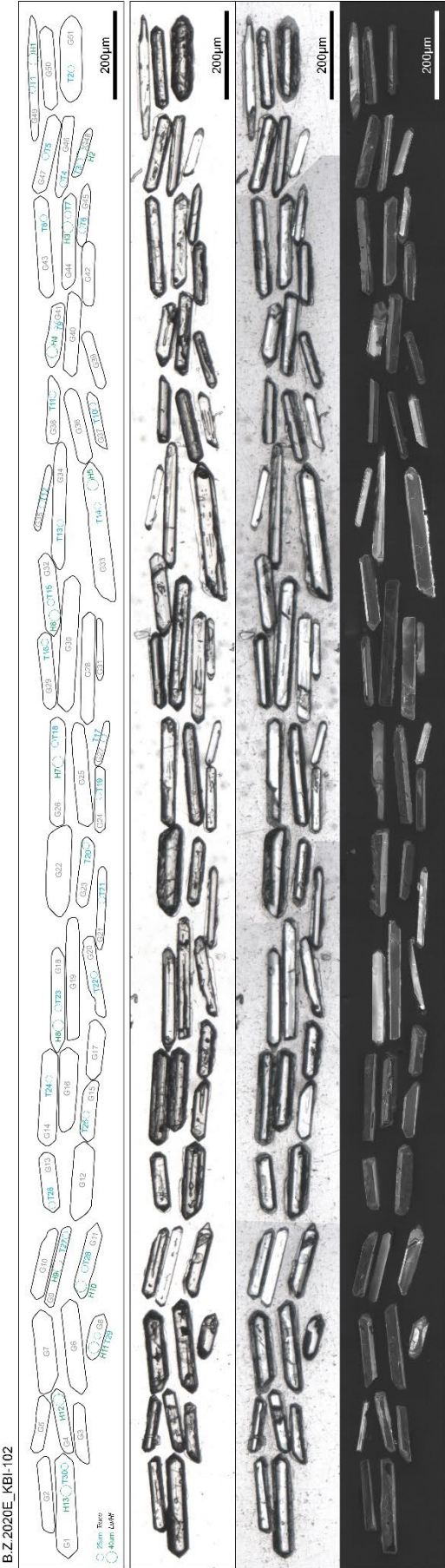


KBC-195 (B.Z.2018C) from the Kaiparowits Formation, Utah U.S.A.

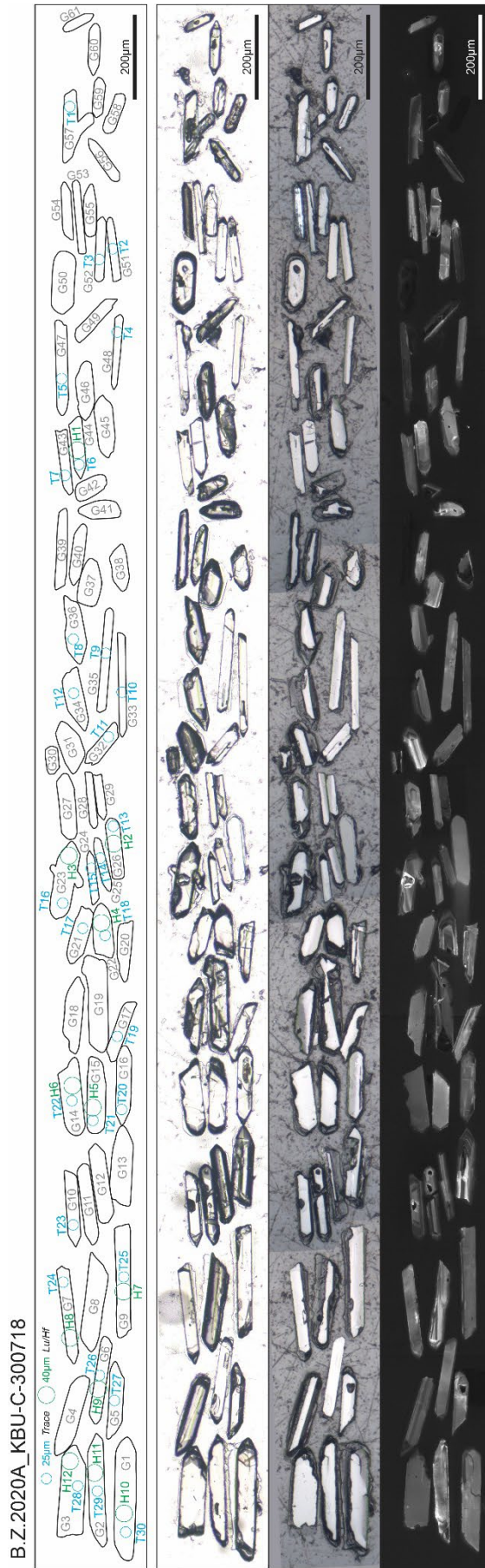




KBC-D-030818 (B.Z.2020A) from the Kaiparowits Formation, Utah U.S.A.



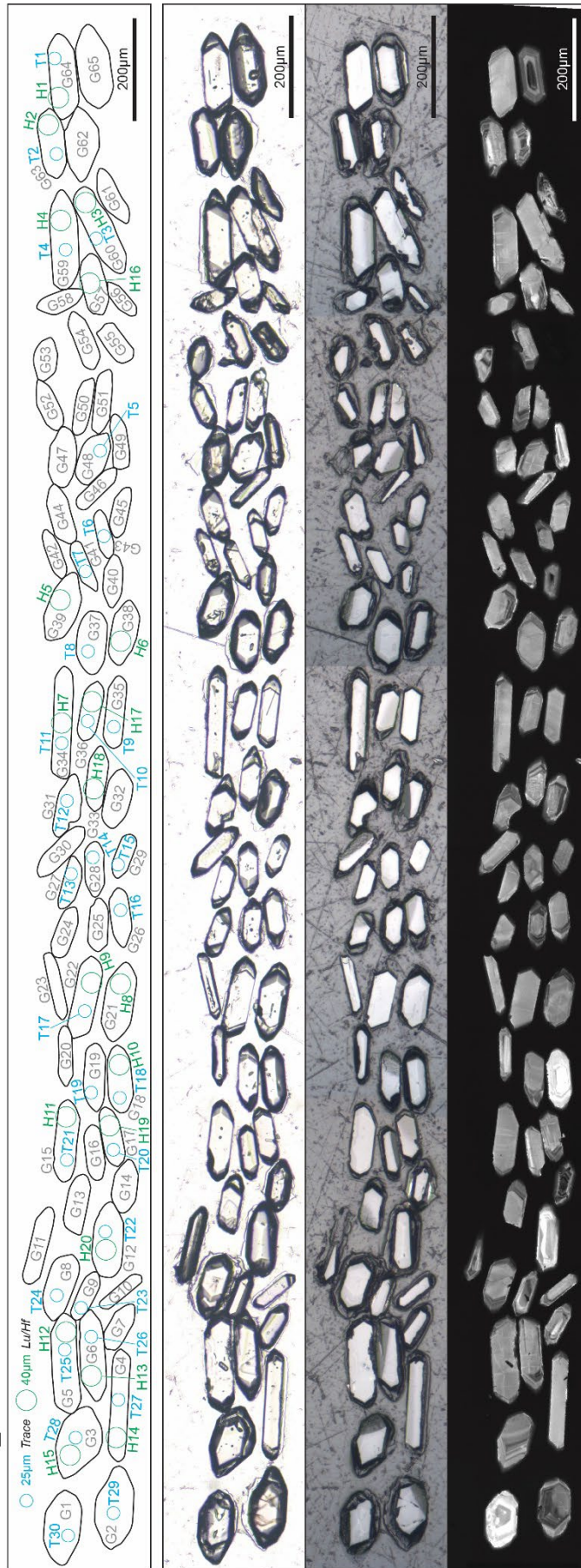
KBI-102 (B.Z.2020E) from the Kaiparowits Formation, Utah U.S.A.



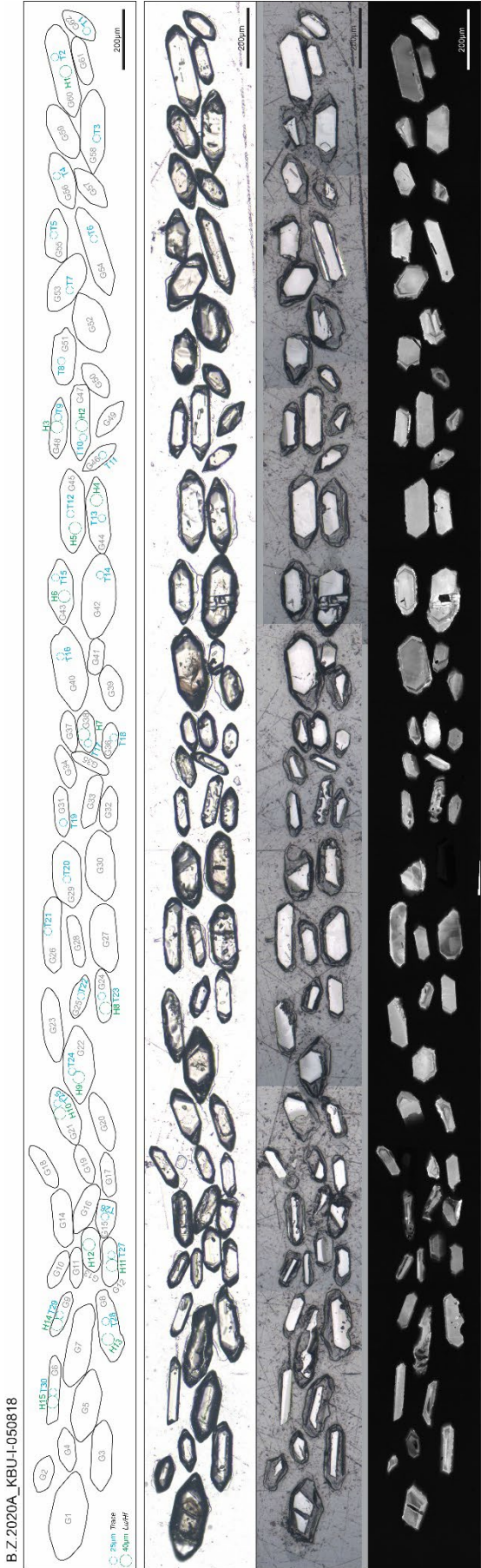
KBU-C-310718 (B.Z.2020A) from the Kaiparowits Formation, Utah U.S.A.



B.Z.2020A\_KBU-H-050818

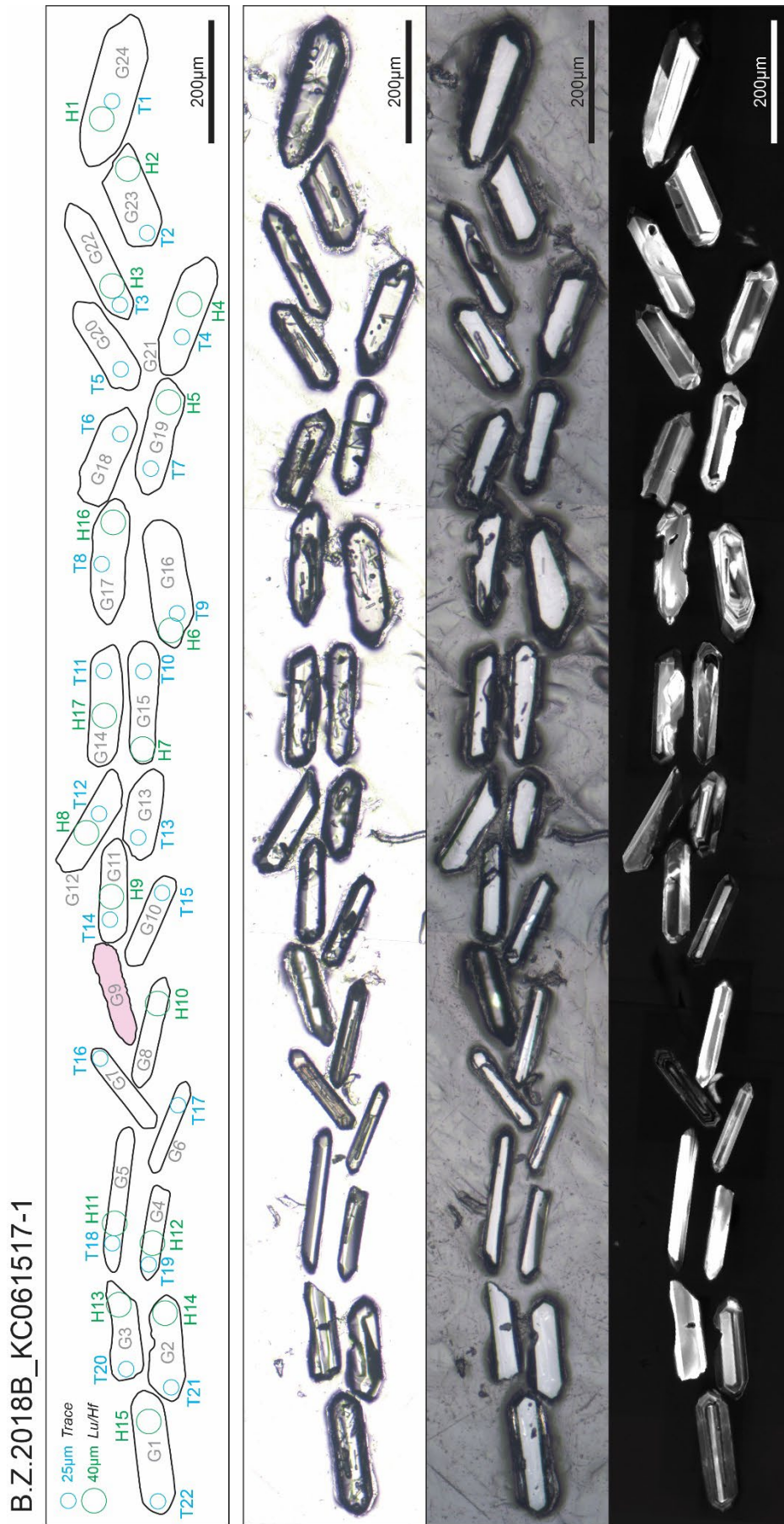


KBU-H-050818 (B.Z.2020A) from the Kaiparowits Formation, Utah U.S.A.



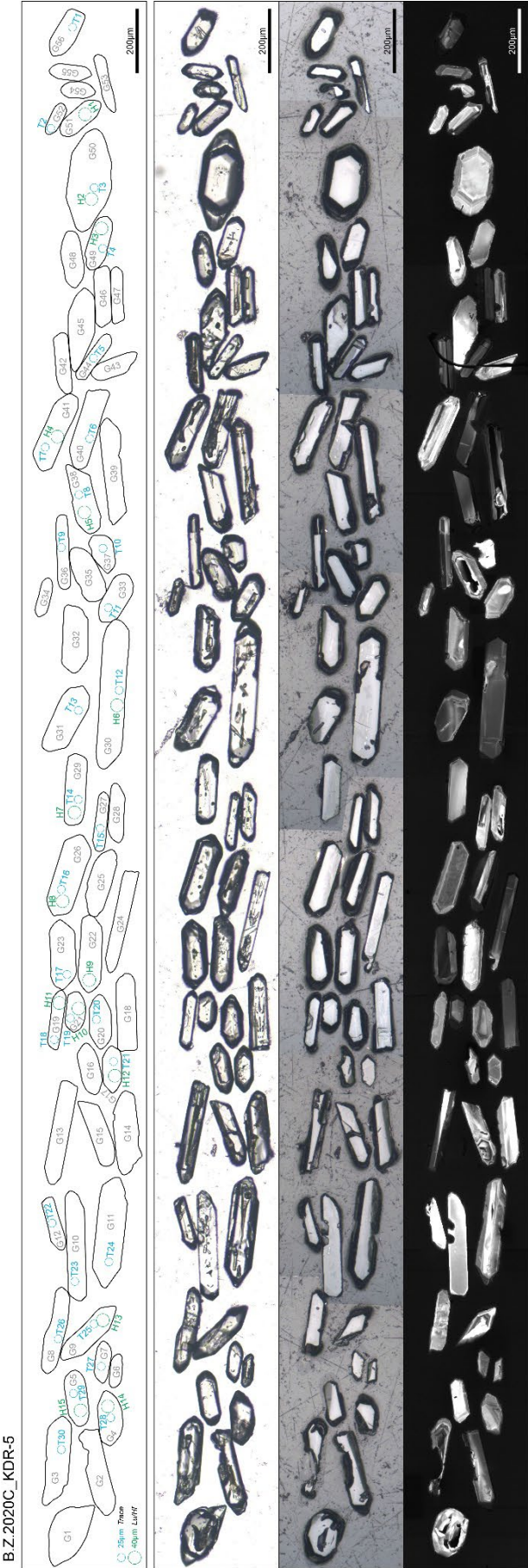
KBU-I-050818 (B.Z.2020A) from the Kaiparowits Formation, Utah U.S.A.



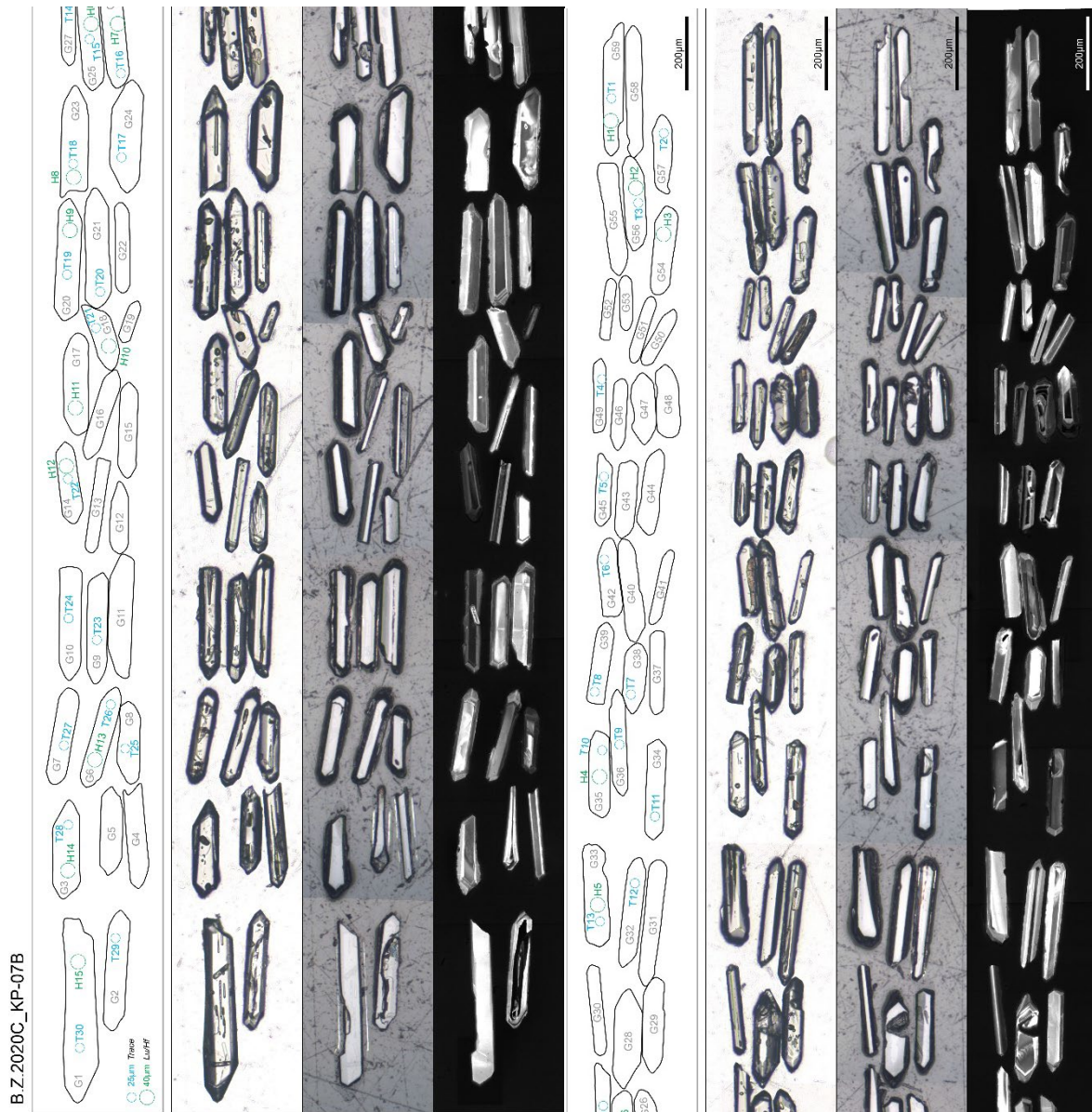


KC061517-1 (B.Z.2018B) from the Judith River Formation, Montana U.S.A.



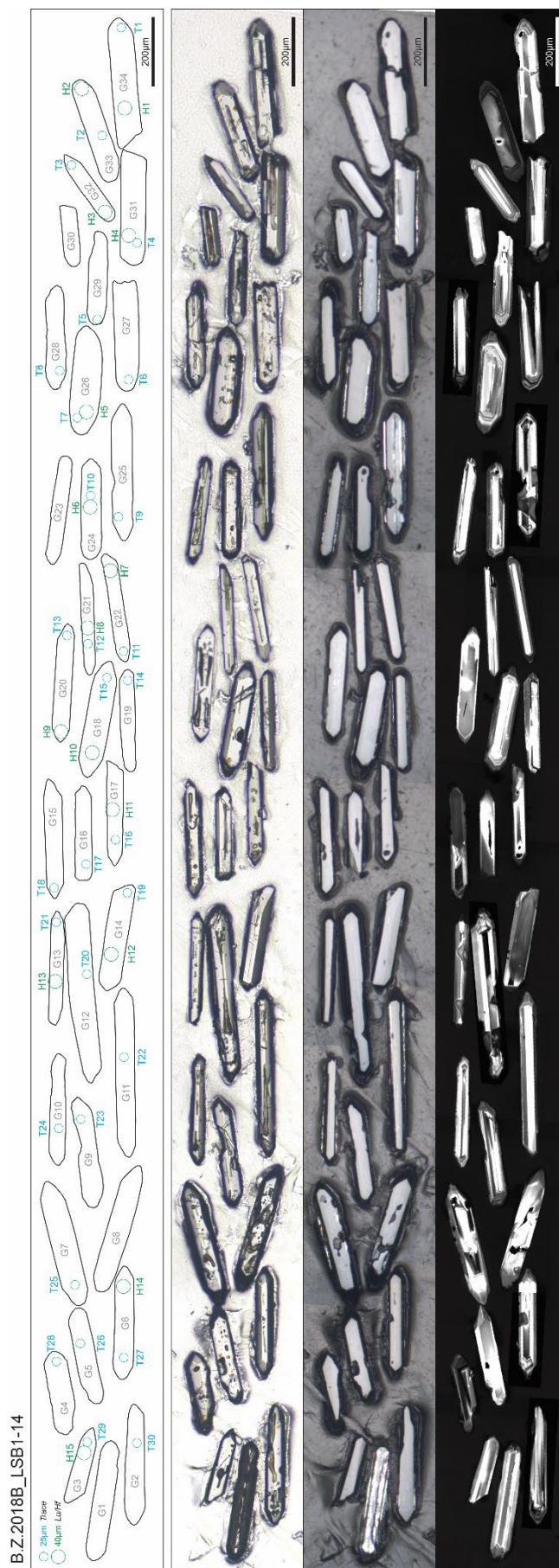


KDR-5B (B.Z.2020C) from the Kaiparowits Formation, Utah U.S.A.

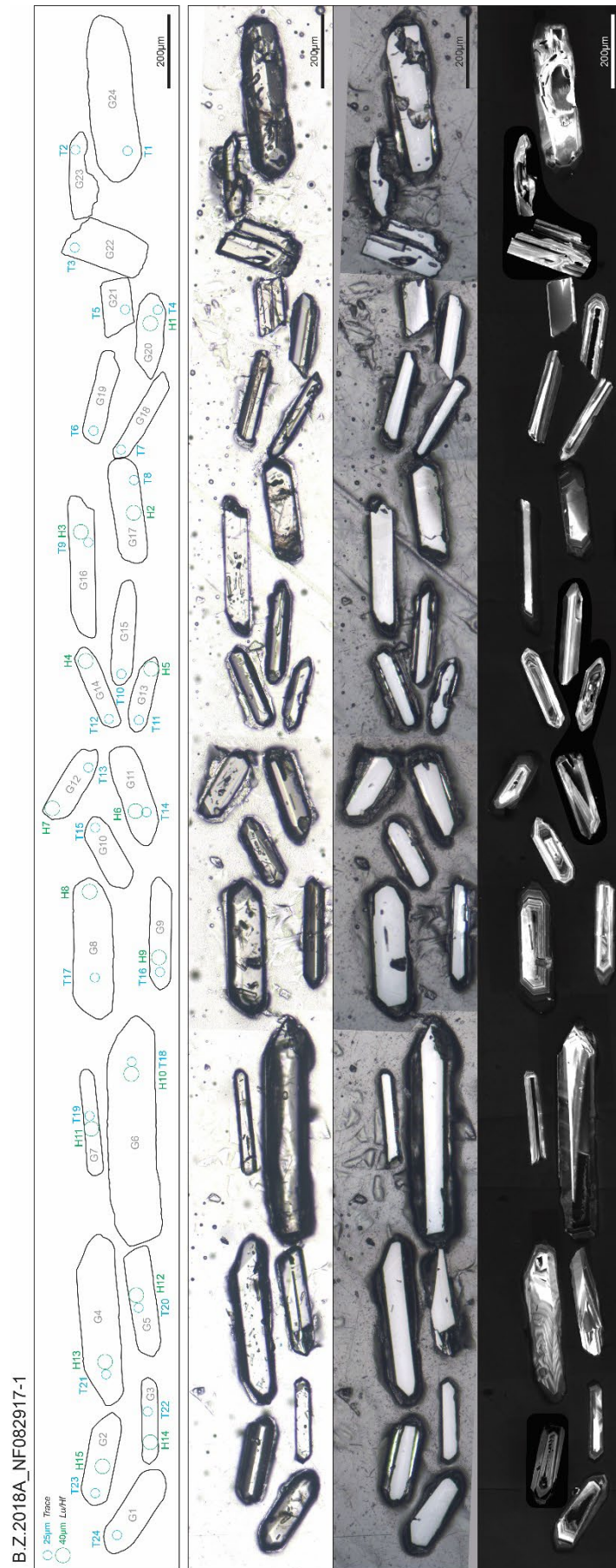


KP-07A (B.Z.2020C) from the Kaiparowits Formation, Utah U.S.A.



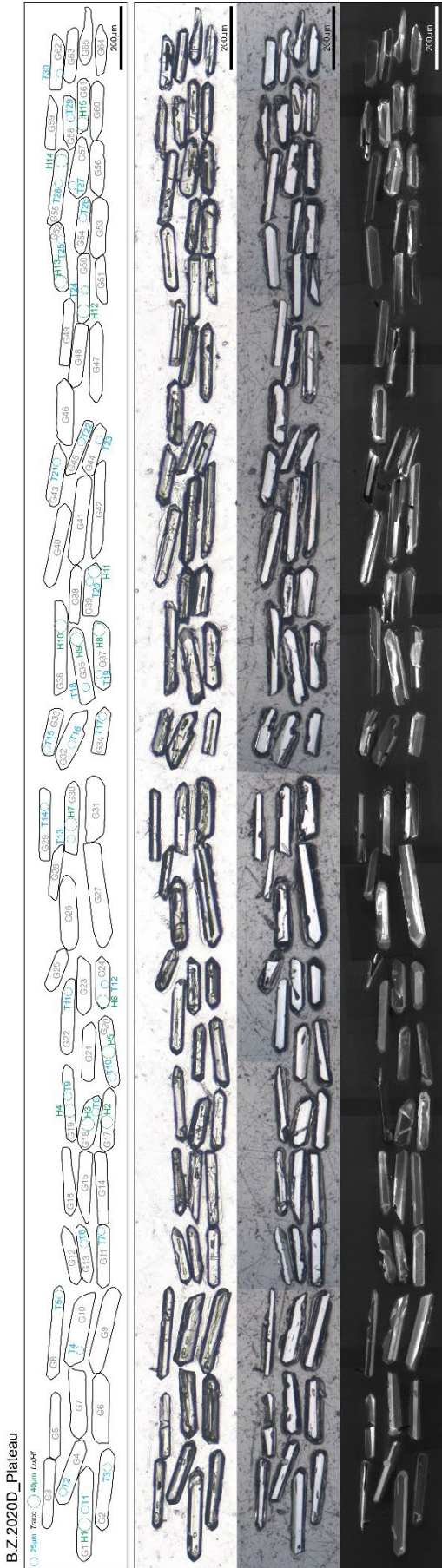


LSB-1-14 (B.Z.2018B) from the Two Medicine Formation, Montana U.S.A.

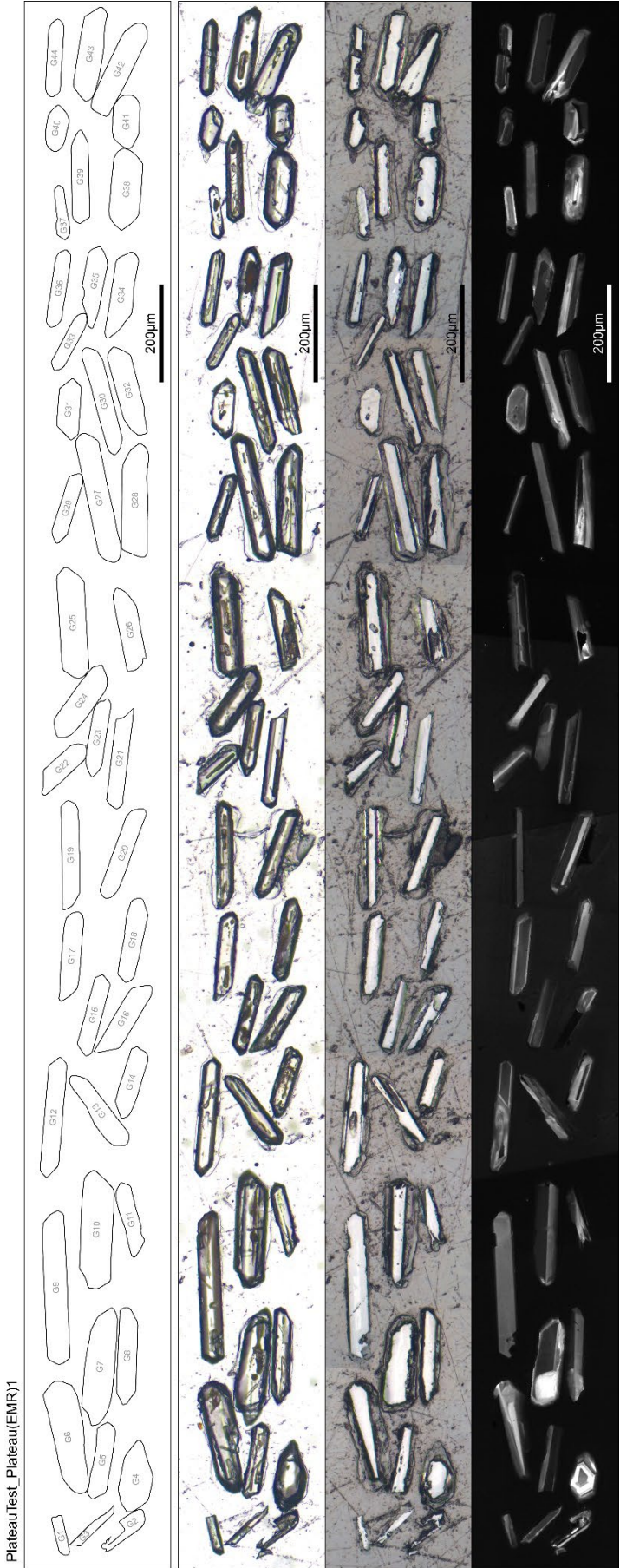


NF082917-1 (B.Z.2018A) from the Oldman Formation, Alberta Canada.



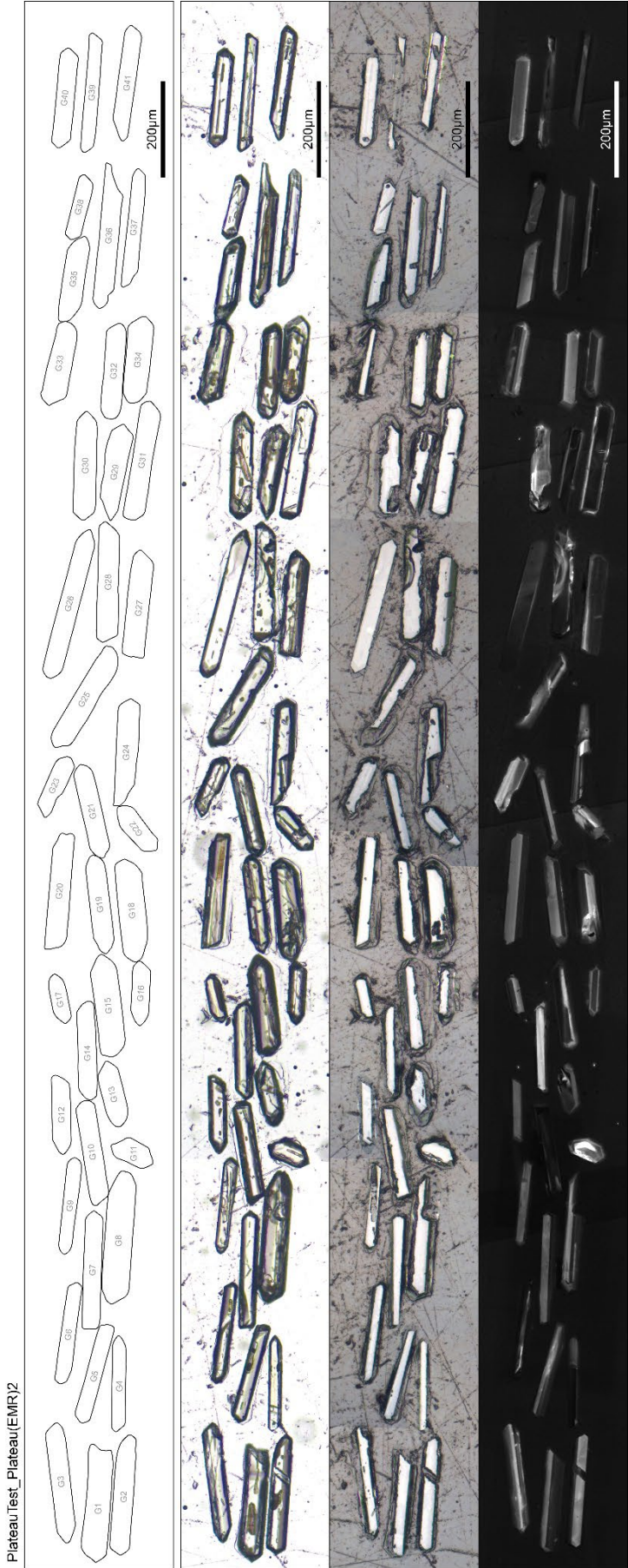


Plateau (B.Z.2020D) from the Dinosaur Park Formation, Alberta Canada.

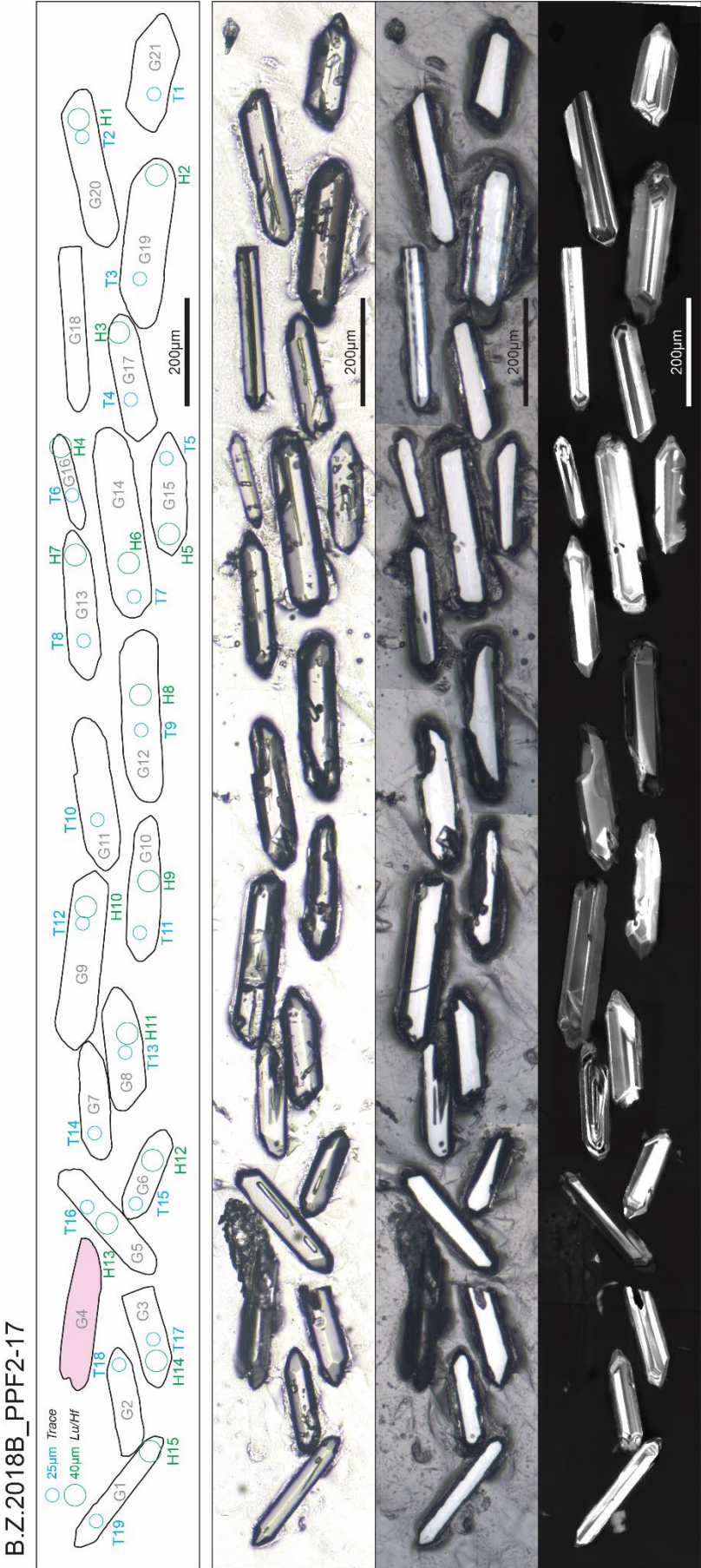


Plateau (EMR)1 (Plateau Test) from the Dinosaur Park Formation, Alberta Canada.



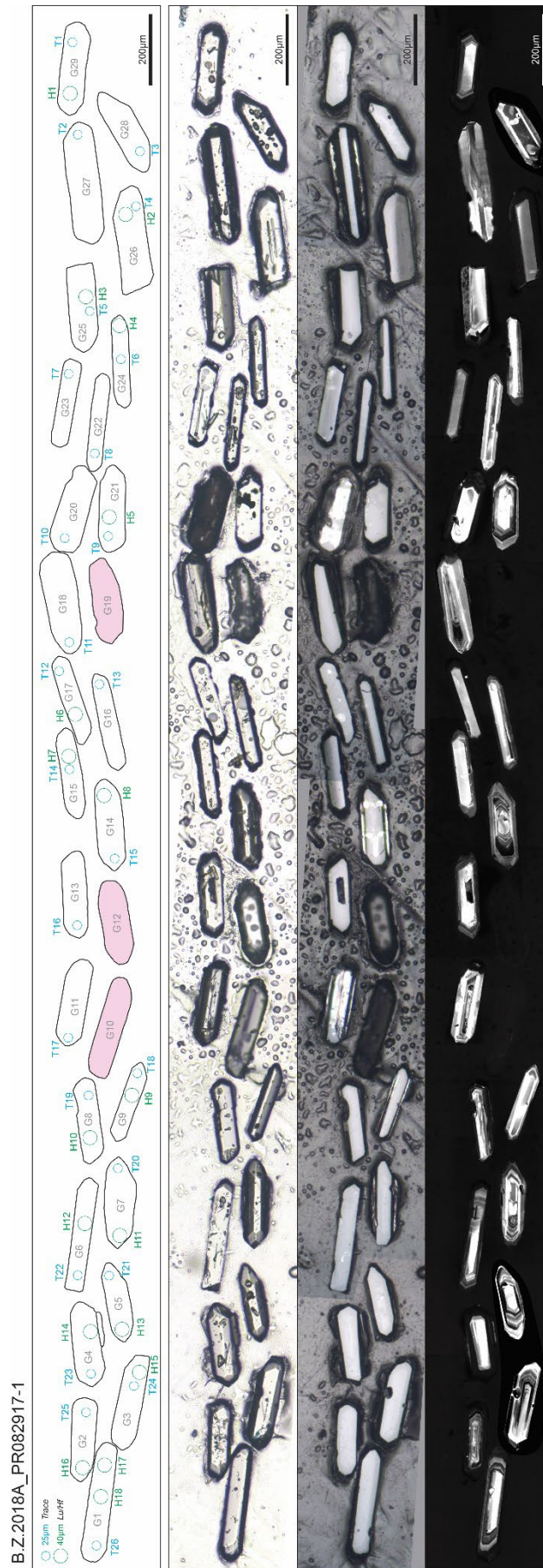


Plateau (EMR)2 (Plateau Test) from the Dinosaur Park Formation, Alberta Canada.

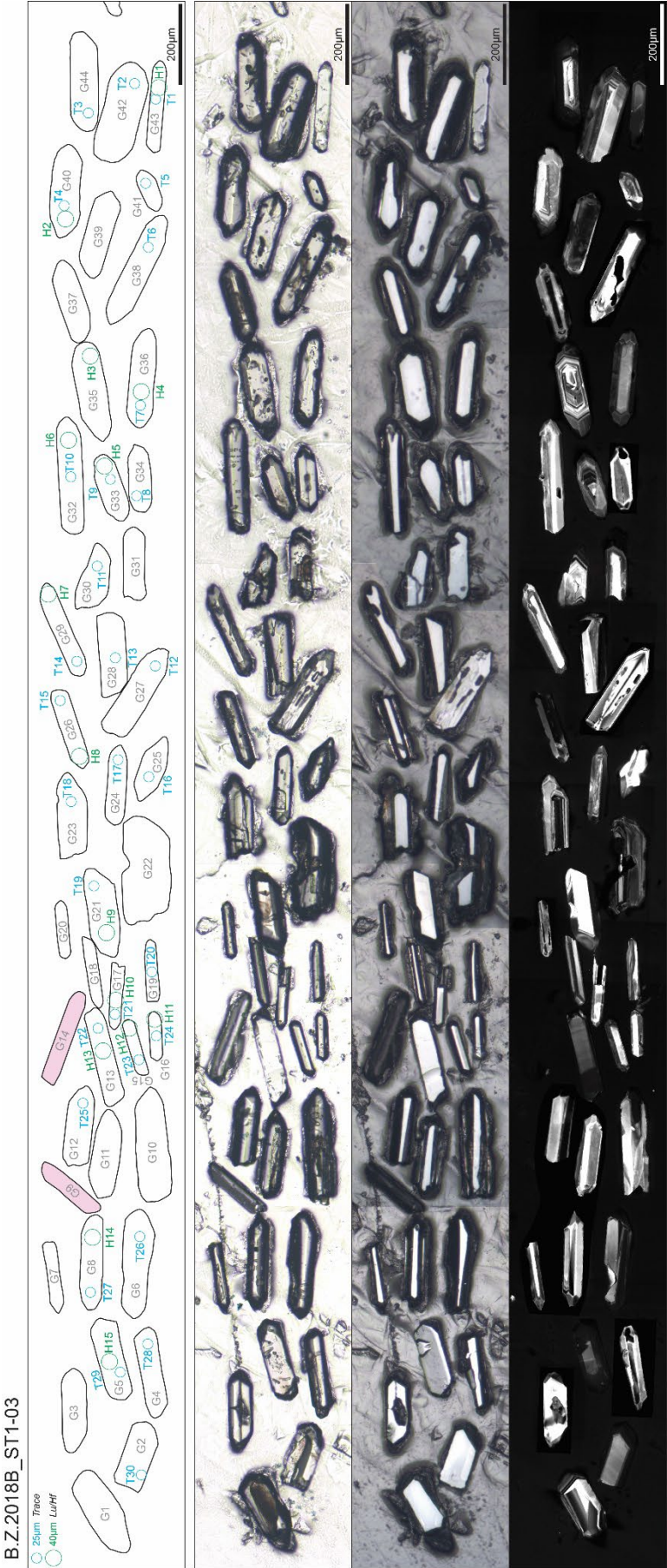


PPF2-17 (B.Z.2018B) from the Judith River Formation, Montana U.S.A.



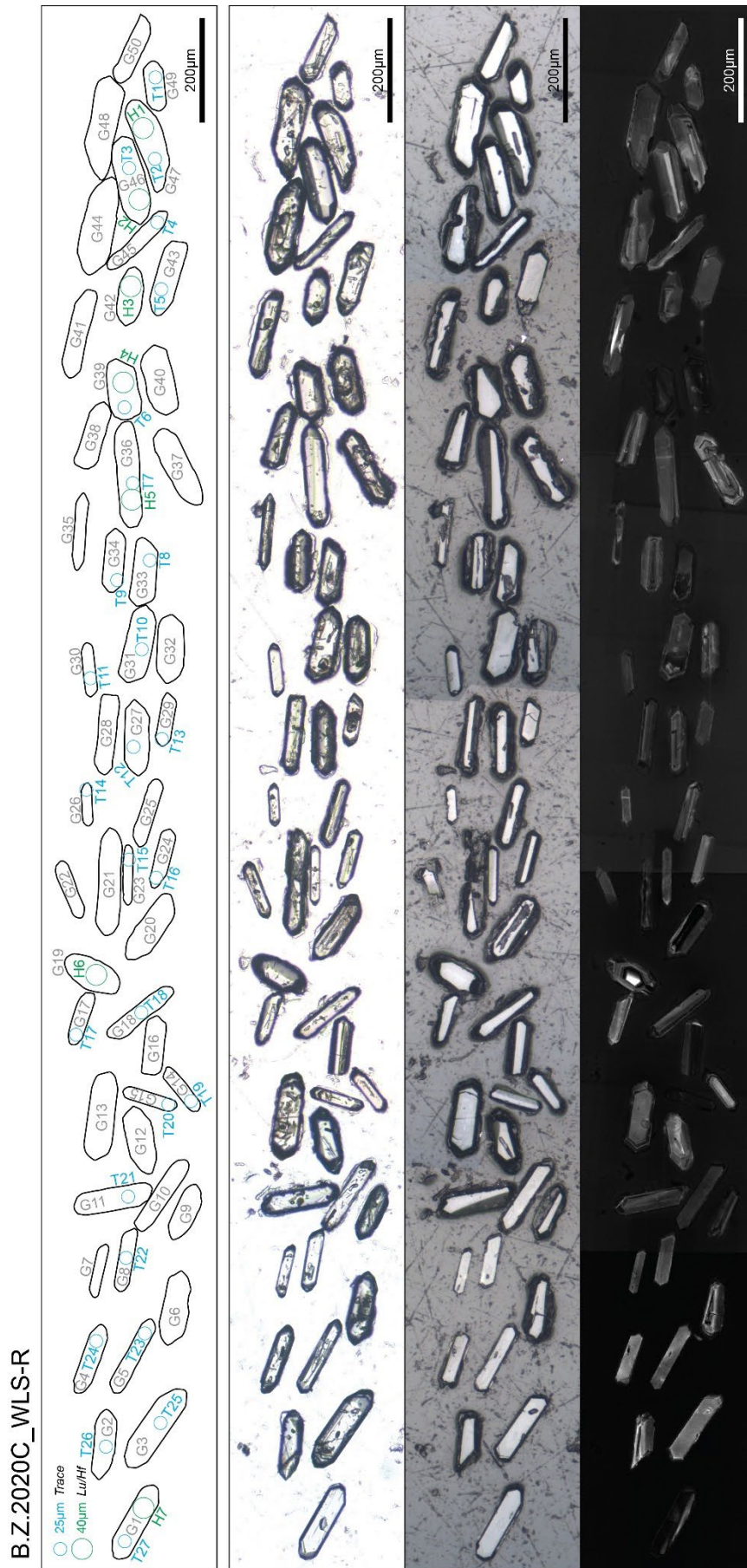


PR082917-1 (B.Z.2018A) from the Oldman Formation, Alberta Canada.



ST1-03 (B.Z.2018B) from the Judith River Formation, Montana U.S.A.





WLS-R-070818 (B.Z.2020C) from the Wahweap Formation, Utah U.S.A.



**Appendix C.6.4** *Qualitative zircon descriptions (28 samples arranged alphabetically by sample name).*

Investigation of zircon morphology in this study was intended as a general comparison between Campanian bentonites from western North America. Grains included in this study were purposefully selected from heavy mineral separates based on a set of morphological criteria (see Chapters 2, 3, 4, 6); thus, they represent only a portion of the possible population of zircon from any given sample. The purpose of selecting grains based on criteria such as long aspect ratio, clean crystal faces, and the presence of glass melt inclusions, was to target the grains that most likely represent those formed at or immediately before the eruption event that led to their dispersal. It is therefore noted that the following qualitative descriptions inherently portray bias towards these desired characteristics and further investigation is required to determine whether the selected grains genuinely represent the youngest zircons. Nevertheless, broad differences in morphology of the best available grains (relative to the selection criteria) may yield some insight into similarities and differences between samples. Grain morphology may be influenced by several factors both natural (e.g., reworking, distance of aerial transport, magmatic conditions) and anthropogenic (e.g., pre-selection of grains from a batch, systematic limitations in mineral separation, selection bias). The descriptions below serve as a starting point for the investigation of these factors. Observations were made primarily based on transmitted light microphotographs and internal textures were described from cathodoluminescent imagery (see methods in Chapter 6).

**B2-07B:** Zircons from this sample are consistently elongate and euhedral to subhedral with slightly rounded terminations. Grains are clear and vitreous. Clear to brownish-grey elongate inclusions are abundant and represent both melt and apatite. Uniform sectors and heterogenous internal textures are common, as seen in cathodoluminescent imagery, as well as feint oscillatory patches and uncommon Maltese cross textures.

**DVMT-1:** Zircons from this sample show significant morphological variation with common subhedral grains, broken ends, and significant variation in size and proportion. Some grains are clear and even adamantine in lustre, but others are murky to brownish grey and clouded. Elongate to non-uniform morphotype melt inclusions are common. Some of these are clean and dark, while others are heterogeneous and brown. Occasional apatite inclusions were observed. Most grains show uniform internal zoning, as seen in cathodoluminescent imagery, and some contain oscillatory sectors.

**EMC080216-1:** Zircons from this sample are generally morphologically consistent, characterised by elongate euhedral grains. These are generally clear, although some grains with broken facets or impurities appear clouded. Clear to brown to black melt inclusions are common, particularly of non-uniform morphotypes, and apatite inclusions are also common. Internal textures dominantly show uniform contrast.

**ES080216-2:** Zircons from this sample are morphologically consistent, composed of elongated euhedral to slightly subhedral forms commonly with pointed terminations. The grains are mostly clear/vitreous to adamantine in lustre, with one or two clouded examples. Striking grey to translucent, elongate to non-uniform morphotype melt inclusions are abundant and apatite inclusions are also present. Internal textures identified in cathodoluminescent imagery are characterised by sectors of uniform contrast with less common oscillatory and heterogenous textures.

**FS082717-1:** Zircons from the sample are characterised by elongate euhedral to subhedral grains that are dominantly clear with vitreous lustre although some show staining around inclusions. Dark, non-uniform shaped melt inclusions are common, and apatite inclusions are present in comparably rarer abundance.

Cathodoluminescent imagery dominantly show zones of uniform contrast with limited to absent oscillatory banding.

**Hadro Hill:** Zircons from this sample are moderately consistent in morphology, featuring euhedral to mildly subhedral grains that are occasionally broken. The grains are clear and vitreous with rare orange staining and some with abundant impurities. Bevelled/grey to black melt inclusions are common, as are apatite inclusions. Cathodoluminescence shows common sector zoning with uniform zones and feint oscillatory bands.

**IL082717-1:** Zircons from this sample are generally morphologically homogeneous, dominated by elongate, euhedral forms commonly with pointed double terminations. The grains are clear with vitreous to adamantine lustre. Melt inclusions are common (various morphotypes) and may be dark, clear, or bevelled/high relief. Apatite inclusions are rare. Internal morphologies are shown by cathodoluminescent imagery to commonly have uniform cores with sectors of oscillatory banding at the grain terminations, and heterogeneous internal textures were common.

**IM1442:** Zircons from this sample represent a consistent morphological population that is dominantly euhedral with commonly broken ends. Some grains are vitreous and glassy, while others have abundant impurities that give a murky appearance. Apatite inclusions are abundant, especially in some grains, and dark, ovoid morphotype melt inclusions are common. Internal textures are characterised by uniform sector zoning as seen in cathodoluminescent imagery.

**KBC-102:** Zircons from this sample generally show consistent morphological characteristics and are typically elongate and euhedral with some rounded ends and some pointed tips. Grains are mostly clear, although some appear clouded (it is noted that the optical microphotographs are of poorer quality than those for other samples). Small melt inclusions are common and apatite inclusions are uncommon. Cathodoluminescence reveals common uniform and less common heterogeneous internal textures.

**KBC-109:** The morphology of zircons from this sample is generally consistent with elongate, euhedral grains with some slightly rounded ends. Most grains are clear, although some have abundant impurities that give grains a murky appearance. Elongate morphotype melt inclusions are common, as are apatite inclusions. Internal textures generally show uniform and sector zoning with some feint banding.

**KBC-144:** The morphology of zircons from this sample are generally consistent, characterised by elongated euhedral to mildly subhedral forms with common vitreous to adamantine lustres. Apatite inclusions are exceedingly abundant in grains from this sample, while melt inclusions are common but generally small and clear. Cathodoluminescent imagery shows sectors of uniform contrast with some feint oscillatory areas.

**KBC-195:** Zircons from this sample are typically stubby, subhedral, and fractured. The broken grains are generally clear although often slightly clouded with some staining around fractures. Small dark unidentified inclusions are noted but rare. Internal textures as seen in cathodoluminescent imagery are inconsistent and poorly visible with uniform and oscillatory sectors, Maltese cross textures, and other odd heterogeneities.

**KBC-D-030818:** Zircons from this sample are consistently elongate and euhedral, commonly with excellent pointed double terminations. Most grains are clear, although several are clouded and cracked. Inclusions of any

kind are very rare; those noted are small melt inclusions. Internal zoning is dominantly uniform with some Maltese cross textures.

**KBU-C-310718:** Zircons from this sample depict a morphological duality where most grains are elongate and euhedral, while some are distinctly stubby. Most grains are clear but some, often the stubby ones, are clouded and cracked. Inclusions of any kind are very rare; those noted are small melt inclusions. Cathodoluminescent imagery shows internal features that are dominantly uniform with some Maltese cross textures and feint oscillatory sectors.

**KBU-H-050818:** Zircons from this sample are consistently stubby and euhedral in form and are dominantly clear and vitreous. Inclusions of any kind are very rare; those noted are small, ovoid melt inclusions. Internally, the grains dominantly show uniform sectors with occasional oscillatory patches and common Maltese cross textures (intensely so in some grains).

**KBU-I-050818:** Zircons from this sample show moderately consistent morphologies, described as characteristically stubby and euhedral with abundant pointed double terminations; some with perfect tips, others are comparably more rounded. The grains are generally clear and vitreous, although some are frosted or clouded, and rare orange staining was noted. Small melt inclusions are present but rare. Cathodoluminescence commonly shows uniform sectors with occasional Maltese cross textures.

**KC061517-1:** Zircons from this sample show a moderate spread of elongate morphologies from euhedral to slightly subhedral, with occasional broken ends. The grains are clear with vitreous to adamantine lustre. Some apatite inclusions were observed, along with melt inclusions of various colours and morphotypes. Cathodoluminescent imagery commonly shows a uniform response, while some grains have some oscillatory zones.

**KDR-5B:** Zircons from this sample represent a moderate spread of morphologies from stubby to elongate and euhedral to subhedral. Grains are mostly clear and vitreous. Small brown to grey non-uniform and ovoid shaped melt inclusions and small elongate apatite inclusions are present. Internal textures most commonly display as uniform zones with some heterogeneities and feint banding.

**KP-07A:** Zircons from this sample are characterised by consistently elongate, euhedral grains with clear/vitreous to adamantine lustre. Melt inclusion of various morphotypes are common and apatite inclusions are small and uncommon. Internal textures dominantly display uniform sectors with some internal heterogeneities and rare Maltese cross textures.

**LSB-1-14:** The morphology zircons from this sample shows a high degree of consistency. The grains are characterised by elongate, euhedral forms with good double termination although some slightly rounded tips are noted. Grains are clear/vitreous and rarely adamantine in lustre. Non-uniform and small blebby melt inclusions are common with brown to dark colouration. Apatite inclusions are present but rare. Unlike the external morphology, internal textures are more varied. Sector zoning is common, which shows patches of uniform response and zones of oscillatory banding. Heterogeneous internal textures are also common.

**NF082917-1:** Zircons from this sample show a range of morphologies from subhedral to less commonly euhedral, sometimes with broken ends. Grains are generally clear, although some have concentrations of impurities and busy textures that make the grain(s) appear murky. Apatite inclusions are common and small non-uniform melt

inclusions were also observed. Common heterogeneous internal textures are shown in cathodoluminescent imagery, while some grains show tight, high-contrast oscillatory zoning.

**Plateau:** The morphology of zircons from this sample is moderately consistent with elongate and generally euhedral grains. These are clear and vitreous to adamantine in lustre. Elongate and non-uniform morphotype melt inclusions are common and appear in plane polar light as bevelled/grey with heterogeneous internal textures and occasionally dark. Apatite is noted in some grains. Cathodoluminescent imagery shows dominantly uniform sector internal zoning.

**Plateau(EMR)1:** The morphologies of zircons from this sample are not particularly consistent. Grains are generally clear/vitreous, elongate and euhedral with some broken ends and some rounded ends. Melt inclusions are uncommon and generally of the non-uniform and elongate morphotypes. Apatite inclusions are uncommon to rare. Cathodoluminescence shows a common uniform response zoning with some feint banding and odd internal textures.

**Plateau(EMR)2:** The morphologies of selected zircons for this sample are not particularly consistent. Grains are generally elongate and euhedral with some broken ends and some rounded ends. Although mostly clear/vitreous, some grains are clouded. Melt inclusions are common and are often brown and occasionally grey. Apatite inclusions are uncommon. Internal textures generally shows a uniform response.

**PPF2-17:** Zircons from this sample show moderately consistent external morphologies characterised as elongate euhedral to subhedral forms that are clear and vitreous to adamantine in lustre. Melt inclusions are common, especially clear/bevelled to greenish-brown coloured elongate morphotypes. Internal textures show both oscillatory and sector zoning.

**PR082917-1:** Zircons from this sample show generally consistent morphologies characterised by elongate euhedral to subhedral forms that are generally clear with vitreous and rarely adamantine lustre. Very small, clear to bevelled/high relief melt inclusions are abundant and small apatite inclusions are also common. Cathodoluminescent imagery illustrates two dominant populations, one with zones of uniform contrast, and another characterised by oscillatory zoning. Rare grains display heterogeneous internal textures.

**ST1-03:** Zircons from this sample show significant morphological variation. The size and proportion of grains varies significantly and subhedral grains and broken ends are common. Colour and lustre range from clear and vitreous to clouded. Melt inclusions are uncommon; larger ones are typically brown with murky textures, although small, blebby clear/bevelled inclusions and very small unidentified impurities are also present. Internal textures also show a high degree of variation with common heterogeneous textures, areas of uniform response, feint sector and oscillatory zoning, and rare tight high-contrast oscillatory zoning with feint sector tips.

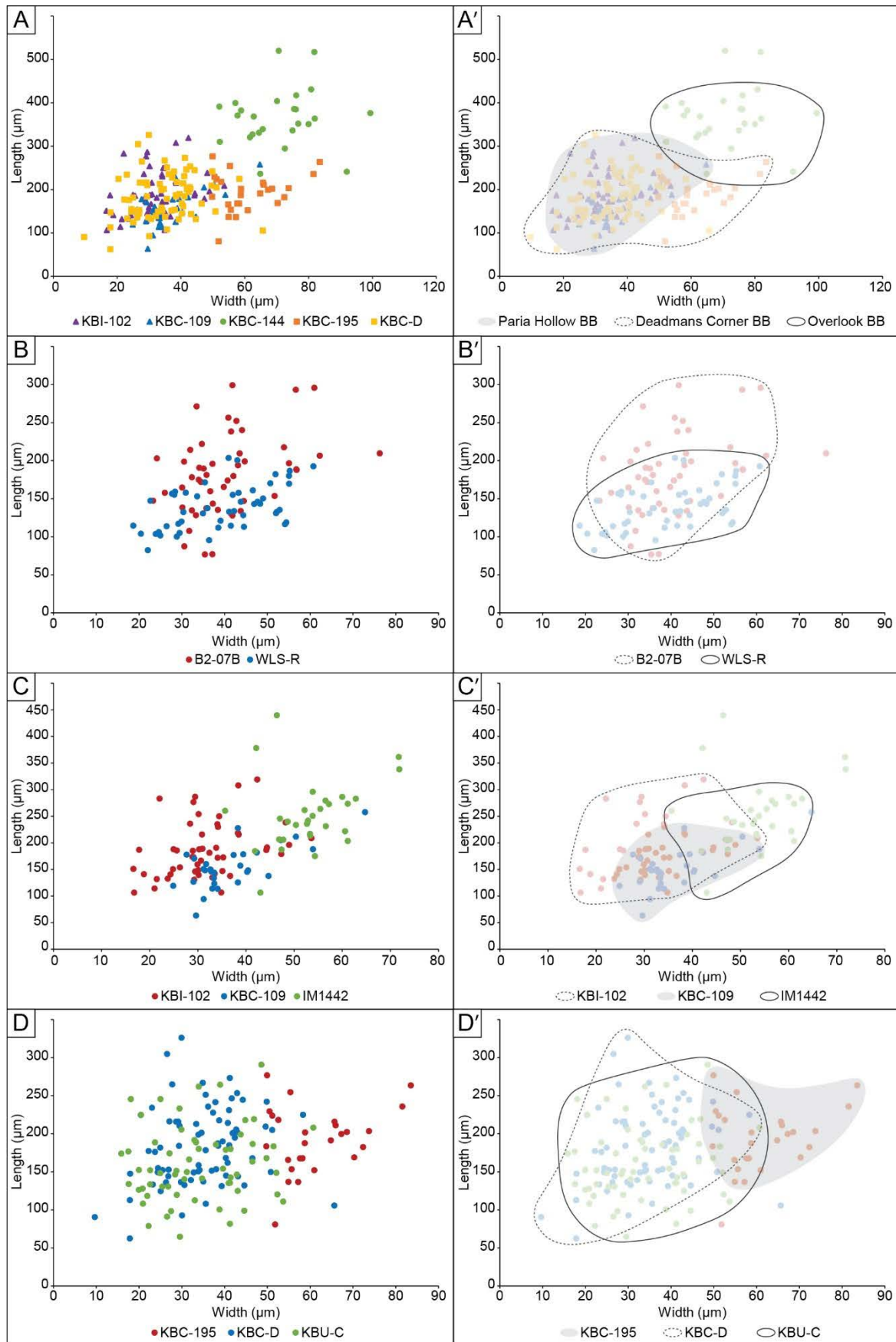
**WLS-R-070818:** The morphology of zircons from this sample is moderately consistent, showing generally elongate euhedral to somewhat subhedral grains. These are mostly clear and vitreous, although some grains are slightly murky. Small melt inclusions are common and apatite inclusions are abundant. Cathodoluminescent imagery shows variable internal textures including soft uniform zones and banding with some heterogeneous textures.

Mount Name	Sample Name	Length ( $\mu\text{m}$ )					Width ( $\mu\text{m}$ )					Average	Cross-sectional Area ( $\mu\text{m}^2$ )				
		av	med	max	min	st.dev	av	med	max	min	st.dev	Ratio	av	med	max	min	st.dev
B.Z.2018A	FS082717-1	173	178	229	128	23	46	43	76	26	13	4.1	7711	7781	14681	4054	2312
	IL082717-1	327	331	427	221	54	60	58	93	28	16	5.7	19170	18866	36572	7731	6927
	NF082917-1	282	255	605	143	101	70	66	111	37	22	4.2	21313	15532	74068	9385	15151
B.Z.2018B	PR082917-1	258	251	339	222	30	65	66	88	39	13	4.2	16450	16428	28032	10138	4007
	KC061517-1	181	175	248	146	27	47	47	75	27	12	4.1	7993	8047	16538	3655	2740
	LSB-1-14	320	317	517	174	65	54	53	84	34	11	6.1	16887	15632	33704	7829	5588
B.Z.2018C	PPF2-17	252	253	342	175	52	59	59	78	30	12	4.4	13948	13044	24231	5065	5109
	ST1-03	205	203	284	104	43	56	59	96	28	17	3.9	11397	11613	27202	3481	5113
	DVMT-1	197	191	344	70	56	50	49	72	28	11	4.1	9526	9249	22625	3011	3904
B.Z.2020A	ES080216-2	310	318	391	219	44	61	62	75	37	10	5.2	18220	19199	24504	11428	3618
	KBC-144	366	368	520	236	66	71	71	99	52	12	5.3	24610	22222	41737	14434	6575
	KBC-195	193	195	277	81	43	61	58	84	50	9	3.2	10875	10801	20020	3582	3467
B.Z.2020C	KBC-D-030818	183	182	326	62	51	35	35	66	10	10	5.6	6007	5792	11903	832	2381
	KBU-C-310718	160	151	291	65	49	34	33	61	16	11	5.2	5053	4843	13108	1533	2462
	KBU-H-050818	128	120	218	80	31	42	39	85	22	13	3.2	4783	4257	9015	1992	2018
B.Z.2020D	KBU-I-050818	193	181	310	118	54	66	63	113	36	19	3	11096	8793	26563	4821	5603
	B2-07B	182	181	299	77	52	40	38	76	23	11	4.7	7147	6449	16482	2600	3145
	KDR-5B	208	189	464	103	71	61	60	127	29	19	3.6	12503	10727	35552	3708	6604
B.Z.2020E / Plateau Test	KP-07A	255	257	498	120	62	52	54	85	30	12	5	13216	12591	39561	3883	5497
	WLS-R-070818	139	135	204	83	29	39	41	61	19	11	3.8	5381	5340	10292	1682	2110
	EMC080216-1	235	224	332	175	41	54	55	72	35	10	4.5	12211	12067	19593	7169	3015
B.Z.2020E / Plateau Test	Hadro Hill	231	222	409	151	58	52	51	74	28	12	4.7	11654	10548	22787	6608	4000
	IM1442	253	244	440	106	65	53	53	72	36	8	4.8	13227	12606	25200	4448	4391
	Plateau	212	211	335	144	42	43	42	63	32	7	5	9079	8674	18595	4973	2612
B.Z.2020E / Plateau Test	KBC-102	186	181	319	106	51	32	30	54	17	8	6.1	5871	5366	13467	1859	2508
	KBC-109	154	148	258	63	40	37	33	65	25	9	4.2	5597	4782	15351	1585	2691
	Plateau(EMR)1	174	168	312	81	49	41	40	64	17	11	4.4	7056	6735	14275	1820	3168
	Plateau(EMR)2	206	211	316	94	50	41	40	57	27	8	5.3	8201	8144	14824	3265	2589

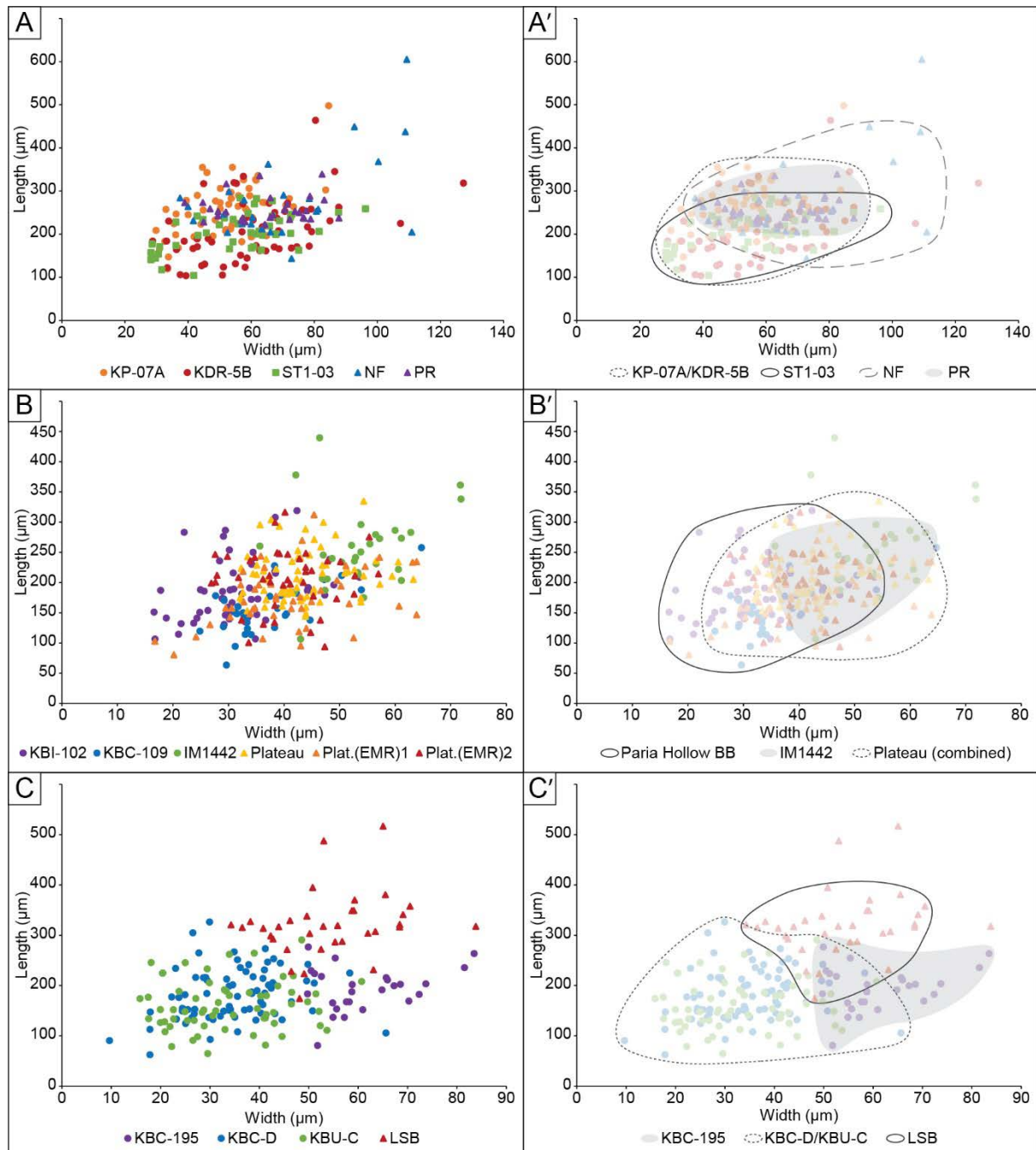
*Appendix C.6.5 Summary of zircon morphological measurements. Average ratio refers to length over width.*



**Appendix C.6.6** Graphical comparison of groups of samples representing outcrops known to be unique (A) and those known or suspected to be correlatives (B-D).



**Appendix C.6.7** Graphical comparison of groups of samples representing bentonites with statistically indistinguishable high-precision ages from across Laramidia.



**Appendix C.6.8** Melt inclusion data for all analysis remaining after data reduction described in Appendix B.4 prior to recalculation to 100 wt. % totals.

Spot Name	Spot No.	Na <sub>2</sub> O	MgO	Al <sub>2</sub> O <sub>3</sub>	SiO <sub>2</sub>	K <sub>2</sub> O	CaO	MnO	FeO	Total
KBU-H-050818										
KBU-H_08	S. 18	1.11	0.57	12.55	66.83	5.10	0.77	0.00	0.96	87.70
KBU-H_10, 11	Av. S. 20, 21	2.64	0.00	12.19	70.08	3.42	1.41	0.00	0.78	90.27
KBU-H_12-14	Av. S. 22-24	2.83	0.00	12.31	70.87	3.41	1.37	0.00	0.00	90.74

Spot Name	Spot No.	Na <sub>2</sub> O	MgO	Al <sub>2</sub> O <sub>3</sub>	SiO <sub>2</sub>	K <sub>2</sub> O	CaO	MnO	FeO	Total
KBC-195										
KBC-195_12-14	Av. S. 332-334	3.15	0.25	13.67	64.05	2.47	2.17	0.12	0.94	86.79
KBC-D-030818										
KBC-D_02, 03	Av. S. 2, 3	1.89	0.00	12.65	70.62	3.87	0.88	0.00	0.55	90.45
KBC-D_06	S. 6	3.07	0.00	12.80	72.32	3.99	0.90	0.00	0.52	93.49
KBC-D_07	S. 7	3.24	0.00	12.55	75.27	5.67	0.63	0.00	0.00	97.24
KBC-D_10	S. 10	2.00	0.00	12.68	68.89	3.62	1.09	0.00	0.82	89.01
KBU-C-310718										
KBU-C_05	S. 29	2.50	0.00	12.16	67.33	3.70	1.03	0.00	0.73	87.12
KBU-C_07	S. 31	1.80	0.00	13.01	69.76	3.47	1.28	0.00	0.68	89.71
KBU-C_09	S. 33	1.96	0.00	12.38	69.00	4.34	1.02	0.00	0.00	88.46
KBU-C_10	S. 34	2.36	0.00	13.54	64.93	2.79	1.67	0.00	0.53	85.74
KBC-144										
KBC-144_01	S. 291	3.35	0.12	12.58	71.49	3.96	1.05	0.01	0.92	93.25
KBC-144_02	S. 292	3.21	0.02	12.68	67.14	3.67	1.38	0.09	1.17	89.13
KBC-144_04	[1] S. 294	2.83	0.09	11.20	71.55	4.58	1.63	0.03	0.67	93.37
KBC-144_15	S. 305	3.51	0.10	13.46	67.39	3.85	1.33	0.21	0.70	90.51
KBC-144_16	S. 306	2.67	0.07	11.42	72.54	4.77	0.72	0.04	0.86	92.97
KBC-144_17	S. 307	2.42	0.07	11.59	71.41	4.09	0.83	0.08	0.79	91.25
KBC-144_18	S. 308	3.01	0.02	11.36	72.69	4.80	0.70	0.08	0.51	93.16
KBC-144_19	S. 309	2.57	0.01	10.96	69.53	4.04	0.78	0.02	1.03	88.87
KBC-144_20	S. 310	2.85	0.04	11.78	72.75	4.90	0.72	0.04	0.69	93.75
KBC-144_22	S. 312	3.19	0.05	11.98	71.97	4.29	0.85	0.23	0.57	93.08
KBC-144_23	S. 313	2.80	0.09	11.60	71.80	4.68	0.75	0.11	0.76	92.58
KBC-144_24	S. 314	2.92	0.04	11.64	71.60	4.89	0.57	0.16	0.83	92.64
KBC-144_25	S. 315	3.23	0.06	11.92	73.39	4.40	0.73	0.05	0.88	94.60
KBC-144_26	S. 316	3.14	0.11	11.53	71.90	4.33	0.73	0.23	0.82	92.76
KBC-144_27	S. 317	3.19	0.06	12.65	68.53	3.50	1.79	0.14	1.25	91.08
KBC-144_28	S. 318	2.89	0.02	11.71	72.16	4.90	0.49	0.01	0.64	92.77
KBC-144_29	S. 319	2.89	0.11	11.53	71.77	4.52	0.54	0.07	0.48	91.90
KBC-144_30	S. 320	2.58	0.06	11.35	72.85	4.67	0.69	0.02	0.55	92.67
KBC-109										
KBC-109_03-05	Av. S. 3-5	3.25	0.14	13.53	69.42	4.11	1.14	0.08	0.60	92.20
KBC-109_09,10	Av. S. 9, 10	2.75	0.11	11.93	74.15	5.05	0.71	0.08	0.39	95.13
KBC-109_16	S. 16	2.01	0.14	11.79	65.92	3.70	1.19	0.05	0.85	85.38
KBC-109_19-21	Av. S. 19-21	2.90	0.09	11.79	73.08	4.98	0.53	0.09	0.35	93.42
KBC-109_23-25	Av. S. 23-25	3.01	0.23	12.36	72.35	4.64	0.87	0.14	0.63	94.22
KBC-109_29-31	Av. S. 29-31	2.91	0.23	12.25	71.06	3.86	1.08	0.07	0.83	92.21
KBC-109_32	S. 32	2.90	0.20	12.01	70.56	4.30	0.97	0.02	0.78	91.54
KBC-109_35	[1] S. 35	3.79	0.10	13.65	69.96	4.46	1.21	0.02	0.41	93.57
KBC-109_46	S. 46	2.84	0.11	11.76	74.06	5.13	0.71	0.03	0.62	95.20
KBC-109_48	S. 48	2.53	0.10	11.20	72.61	4.78	0.71	0.14	0.47	92.51
KBC-109_49	S. 49	2.35	0.08	11.55	73.80	4.91	0.71	0.14	0.56	93.91
KBC-109_52, 63,64	[1]+Av. S. 52, 63,64	3.54	0.14	13.48	70.73	4.16	1.16	0.10	0.60	93.88
KBC-109_68-70	Av. S. 68-70	2.84	0.05	11.41	73.77	4.88	0.56	0.20	0.38	93.98
KBC-109_71	S. 71	2.42	0.08	11.44	72.37	4.96	0.55	0.02	0.56	92.23
KBC-109_73	[1] S. 73	3.01	0.06	11.53	73.66	5.00	0.65	0.05	0.43	94.23
KBC-109_84	S. 84	3.17	0.02	11.85	74.82	5.11	0.52	0.27	0.53	96.21
KBC-109_85	S. 85	3.38	0.15	12.60	70.27	4.30	1.02	0.14	0.81	92.58
KBC-109_88,99	[1]+Av. S. 88,99	2.91	0.06	11.34	73.55	4.89	0.64	0.01	0.58	93.97
KBC-109_100,101	Av. S. 100, 101	2.92	0.01	11.66	73.77	4.95	0.53	0.21	0.40	94.13
KBC-109_102	S. 102	2.68	0.12	11.85	74.29	5.12	0.54	0.00	0.65	95.22

Spot Name	Spot No.	Na <sub>2</sub> O	MgO	Al <sub>2</sub> O <sub>3</sub>	SiO <sub>2</sub>	K <sub>2</sub> O	CaO	MnO	FeO	Total
KBC-109_103,104	Av. S. 103, 104	2.65	0.04	11.41	72.85	4.82	0.66	0.05	0.44	92.76
KBC-109_108	S. 108	3.65	0.13	13.89	71.05	4.33	1.78	0.14	0.26	95.18
KBI-102										
KBI-102_01-03	Av. S. 112-114	2.91	0.03	11.92	73.94	5.11	0.65	0.15	0.59	95.25
KBI-102_04	S. 115	2.70	0.00	11.59	75.20	5.09	0.69	0.13	0.60	95.52
KBI-102_05	S. 116	2.86	0.08	11.93	72.44	4.93	0.71	0.14	0.54	93.60
KBI-102_06	[1] S. 117	3.11	0.02	11.57	73.43	4.88	0.62	0.05	0.29	93.91
KBI-102_18	S. 129	3.04	0.03	11.53	73.05	4.96	0.68	0.08	0.51	93.78
KBI-102_19	[1] S. 130	2.76	0.16	11.84	73.87	4.98	0.65	0.11	0.47	94.57
KBI-102_31	S. 142	2.39	0.06	11.44	72.68	4.83	0.79	0.13	0.60	92.62
KBI-102_33	S. 144	2.70	0.04	11.62	73.52	4.91	0.74	0.04	0.40	93.84
KBI-102_35	S. 146	2.20	0.03	10.93	68.62	4.79	0.65	0.05	0.64	87.58
KBI-102_37	S. 148	2.72	0.08	11.63	70.86	3.38	1.03	0.18	0.63	90.41
KBI-102_38	S. 149	2.55	0.06	12.36	70.57	3.57	0.89	0.16	0.56	90.67
KBI-102_39	S. 150	2.56	0.04	10.84	71.61	4.99	0.71	0.13	0.39	91.06
KBI-102_40	S. 151	3.14	0.03	13.53	67.06	4.99	0.92	0.02	0.43	90.07
KBI-102_42	S. 153	3.66	0.11	12.41	70.70	3.49	1.19	0.01	0.92	92.29
KBI-102_43	S. 154	3.05	0.21	12.11	71.26	3.88	0.69	0.14	0.90	92.10
KBI-102_44	S. 155	2.53	0.21	12.33	67.11	3.94	1.19	0.06	0.52	87.57
KBI-102_48	S. 159	2.98	0.05	11.97	66.45	4.13	1.14	0.06	0.54	86.97
KBI-102_50	[1] S. 161	3.21	0.06	12.70	72.41	4.53	0.92	0.28	0.55	94.61
KBI-102_61	[1] S. 172	3.67	0.14	12.93	71.31	4.21	1.15	0.07	0.52	93.98
KBI-102_72	S. 183	2.97	0.10	11.27	68.85	3.98	0.87	0.14	0.67	88.72
KBI-102_73-75	Av. S. 184-186	3.38	0.01	13.09	70.65	5.30	0.80	0.06	0.55	93.66
KBI-102_78	[1] S. 189	2.90	0.11	11.50	73.87	5.13	0.58	0.01	0.21	94.27
KBI-102_89	S. 200	2.90	0.04	11.44	71.97	5.02	0.61	0.20	0.44	92.53
KBI-102_90	S. 201	2.90	0.01	11.84	73.96	5.09	0.58	0.00	0.48	94.83
KBI-102_91	S. 202	3.37	0.02	12.77	69.16	4.06	1.09	0.14	0.60	91.14
KBI-102_92	S. 203	3.82	0.03	13.09	71.18	4.24	1.06	0.01	0.44	93.85
KBI-102_93	S. 204	2.23	0.17	10.69	67.96	3.70	0.78	0.05	0.66	86.01
KBI-102_94	S. 205	2.62	0.12	12.18	72.21	4.92	0.83	0.17	0.45	93.40
KBI-102_95	S. 206	3.50	0.19	12.55	72.44	3.54	1.03	0.11	0.49	93.86
KBI-102_96	S. 207	2.40	0.12	11.52	73.07	5.15	0.78	0.06	0.39	93.35
KBI-102_97	S. 208	2.92	0.04	11.41	73.15	5.08	0.68	0.14	0.39	93.77
KBI-102_98	S. 209	3.71	0.08	13.42	69.27	4.03	1.07	0.29	0.52	92.29
KBI-102_100,101	Av. S. 211, 212	2.89	0.03	11.47	74.18	5.02	0.61	0.06	0.54	94.65
KBI-102_102	S. 213	3.96	0.06	13.70	71.37	4.16	1.20	0.05	0.62	94.99
KBI-102_104	S. 215	3.00	0.10	12.71	73.18	3.85	0.92	0.22	0.68	94.43
KBI-102_105	S. 216	3.28	0.22	12.52	72.27	3.72	0.83	0.05	0.71	93.51
KBI-102_106	S. 217	3.94	0.13	13.85	66.79	3.01	1.69	0.27	0.73	90.08
KBI-102_107	S. 218	2.87	0.01	11.99	74.53	5.02	0.73	0.07	0.75	95.77
KBI-102_109	S. 220	2.77	0.04	11.79	73.88	5.02	0.68	0.02	0.46	94.63
KBI-102_110	S. 221	3.01	0.18	11.61	73.24	5.07	0.67	0.11	0.59	94.48
KBI-102_111	S. 222	3.52	0.14	13.51	70.82	4.14	1.15	0.08	0.57	93.87
IM1442										
IM1442_04	S. 366	2.58	0.02	12.24	70.56	5.26	0.87	0.05	0.64	92.06
IM1442_08	S. 370	3.24	0.07	12.23	70.77	3.77	0.89	0.02	0.60	91.56
IM1442_14	S. 376	3.21	0.00	12.52	67.94	3.66	1.32	0.01	0.21	88.77
IM1442_02 (R2)	S. 85	2.60	0.00	11.47	72.31	4.95	0.73	0.00	0.65	92.72
IM1442_03, 04 (R2)	Av. S. 86, 87	2.33	0.00	10.83	69.57	4.68	0.67	0.00	0.00	88.02
IM1442_05 (R2)	S. 88	2.32	0.00	11.01	71.11	4.81	0.60	0.00	0.58	90.39
IM1442_06 (R2)	S. 89	2.75	0.00	11.59	72.68	5.03	0.61	0.00	0.53	93.16

Spot Name	Spot No.	Na <sub>2</sub> O	MgO	Al <sub>2</sub> O <sub>3</sub>	SiO <sub>2</sub>	K <sub>2</sub> O	CaO	MnO	FeO	Total
IM1442_07 (R2)	S. 90	2.68	0.00	11.34	72.24	4.98	0.63	0.00	0.00	91.82
IM1442_08 (R2)	S. 91	2.70	0.00	11.26	72.64	4.99	0.64	0.00	0.61	92.82
IM1442_06	S. 368	1.84	0.08	10.81	68.59	4.72	0.62	0.01	0.53	87.02
IM1442_09 (R2)	S. 92	2.70	0.00	11.29	70.95	4.84	0.63	0.00	0.00	90.38
IM1442_10 (R2)	S. 93	2.92	0.00	11.84	73.34	5.21	0.63	0.00	0.67	94.55
IM1442_11 (R2)	S. 94	3.75	0.00	13.40	68.96	3.91	1.24	0.00	0.72	91.97
IM1442_12 (R2)	S. 95	3.56	0.00	13.11	68.38	4.10	0.96	0.00	0.00	90.01
IM1442_13 (R2)	S. 96	2.13	0.00	11.87	68.01	3.78	1.00	0.00	0.74	87.39
IM1442_14,15 (R2)	Av. S. 97, 98 (R2)	3.22	0.00	12.83	69.88	4.21	0.98	0.00	0.61	91.68
IM1442_16 (R2)	S. 99	3.54	0.00	13.46	69.11	4.38	1.35	0.00	0.76	92.59
IM1442_17 (R2)	S. 100	2.58	0.00	11.41	72.69	5.30	0.59	0.00	0.00	92.37
IM1442_18 (R2)	S. 101	2.62	0.00	11.63	67.61	3.96	1.00	0.00	0.54	87.31
IM1442_12	S. 374	3.09	0.34	12.27	69.88	3.99	0.95	0.23	0.99	91.47
IM1442_19,20 (R2)	Av. S. 102, 103	3.27	0.00	11.86	69.39	3.86	0.94	0.00	0.67	89.97
IM1442_22 (R2)	S. 105	2.81	0.00	11.48	72.77	5.02	0.60	0.00	0.63	93.26
IM1442_23 (R2)	S. 106	2.78	0.00	11.52	73.05	4.92	0.61	0.00	0.64	93.46
IM1442_24,26 (R2)	Av. S. 107, 109	4.03	0.00	13.60	69.74	3.89	1.13	0.00	1.00	92.86
IM1442_27 (R2)	S. 110	3.90	0.00	13.56	71.10	4.37	1.08	0.00	0.54	94.52
IM1442_15,16	Av. S. 377, 378	3.69	0.03	13.20	70.33	4.16	1.01	0.03	0.32	92.75
IM1442_28 (R2)	S. 111	2.92	0.00	11.36	72.63	5.01	0.70	0.00	0.00	92.59
IM1442_30 (R2)	S. 113	2.76	0.00	11.60	72.27	4.79	0.52	0.00	0.51	92.41
IM1442_31 (R2)	S. 114	2.67	0.00	11.43	73.49	5.11	0.56	0.00	0.00	93.22
IM1442_32 (R2)	S. 115	3.84	0.00	10.93	71.03	1.12	0.60	0.00	0.00	87.50
KDR-5B										
KDR-5_03	S. 760	2.34	0.14	11.19	68.18	4.66	1.36	0.07	0.58	88.27
KDR-5_04	S. 761	3.09	0.18	12.48	72.58	4.94	1.31	0.04	0.07	94.67
KDR-5_05	S. 762	3.07	0.03	11.43	71.30	4.50	0.61	0.08	0.58	91.41
KDR-5_06	S. 763	2.88	0.14	11.83	64.63	3.72	1.18	0.03	0.99	85.22
KDR-5_09	S. 766	2.41	0.14	10.96	67.57	4.34	0.81	0.20	0.73	87.11
KDR-5_10	S. 767	2.80	0.04	13.09	65.43	4.33	1.15	0.09	0.61	87.45
KDR-5_11	S. 768	2.24	0.02	11.00	68.38	4.64	0.65	0.03	0.20	86.95
KDR-5_13	S. 770	3.23	0.01	10.57	71.20	2.28	1.12	0.09	1.51	89.78
KDR-5_14	S. 771	3.36	0.08	11.12	70.35	2.70	1.04	0.01	0.06	88.68
KDR-5_16	S. 773	2.80	0.06	11.77	66.83	4.30	1.23	0.06	0.91	87.86
KDR-5_17	S. 774	2.12	0.18	10.62	72.83	3.07	1.99	0.04	0.22	91.05
KDR-5_19	S. 776	3.89	0.04	12.16	74.85	4.93	0.00	0.03	0.33	96.14
KDR-5_20	S. 777	3.71	0.09	9.96	79.97	2.51	0.00	0.17	0.44	96.81
KDR-5_21	S. 778	3.06	0.01	12.19	74.95	5.87	0.00	0.14	0.33	96.06
KDR-5_24-26	Av. S. 781-783	3.44	0.11	12.83	69.13	4.13	1.02	0.08	0.83	91.30
KDR-5_27	S. 784	2.59	0.00	10.11	69.33	3.90	0.68	0.20	0.06	86.10
KDR-5_30	S. 787	2.75	0.08	12.49	65.55	3.92	0.97	0.05	1.00	86.59
KDR-5_31	S. 788	3.19	0.11	11.54	69.58	4.45	0.59	0.05	0.99	90.16
KP-07A										
KP-07A_06	S. 795	2.74	0.04	11.29	69.14	4.48	0.65	0.14	0.51	88.65
KP-07A_07	S. 796	2.37	0.04	11.06	67.68	4.41	0.75	0.02	0.69	86.85
KP-07A_09	S. 798	2.22	0.16	11.44	70.80	4.19	1.10	0.02	0.58	90.42
KP-07A_10	S. 799	2.41	0.01	11.33	68.13	4.56	0.77	0.01	0.54	87.53
KP-07A_12, 13	Av. S. 801, 802	3.43	0.05	12.64	68.14	4.58	0.68	0.05	0.51	89.91
KP-07A_15, 16	Av. S. 804, 805	2.41	0.08	11.26	68.75	4.58	0.78	0.15	0.52	88.41
KP-07A_17	S. 806	2.36	0.08	10.93	68.80	4.55	0.81	0.14	0.52	88.04
KP-07A_18	S. 807	2.23	0.02	10.62	67.20	4.50	0.80	0.02	0.18	85.46
KP-07A_19	S. 808	2.38	0.15	11.39	70.16	4.82	0.82	0.30	0.60	90.58



Spot Name	Spot No.	Na <sub>2</sub> O	MgO	Al <sub>2</sub> O <sub>3</sub>	SiO <sub>2</sub>	K <sub>2</sub> O	CaO	MnO	FeO	Total
KP-07A_20-22	Av. S. 809-811	2.90	0.05	11.86	70.31	4.05	0.85	0.01	0.53	90.56
KP-07A_24	S. 813	2.85	0.04	11.63	69.93	4.69	0.79	0.24	0.51	90.33
KP-07A_25	S. 814	2.38	0.06	11.76	65.66	3.89	1.24	0.05	0.52	85.49
KP-07A_26	S. 815	2.66	0.11	11.35	69.18	4.71	0.90	0.07	0.52	89.38
KP-07A_27	S. 816	3.06	0.10	11.92	72.27	4.84	0.75	0.10	0.62	93.43
KP-07A_28	S. 817	3.09	0.02	11.27	70.77	4.33	0.55	0.03	0.60	90.62
KP-07A_29	S. 818	2.92	0.03	11.30	68.71	3.96	0.92	0.00	0.41	88.21
KP-07A_30	S. 819	3.57	0.05	13.70	65.89	3.52	1.65	0.09	0.77	89.05
KP-07A_31	S. 820	3.46	0.15	11.63	70.31	1.70	0.99	0.01	0.47	88.57
KP-07A_32	S. 821	3.09	0.00	11.22	69.14	1.67	0.74	0.05	0.43	86.22
KP-07A_35	S. 824	2.37	0.11	10.65	66.33	4.60	0.75	0.07	0.65	85.36
KP-07A_37	S. 826	2.83	0.06	11.28	70.02	4.64	0.79	0.03	0.72	90.35
KP-07A_38	S. 827	2.78	0.09	11.45	70.02	4.63	0.64	0.06	0.37	91.29
KP-07A_39	S. 828	2.69	0.01	10.73	68.64	4.45	0.61	0.02	0.71	87.63
KP-07A_40	S. 829	2.38	0.00	11.01	69.02	4.54	0.55	0.29	0.42	88.16
KP-07A_41	S. 830	3.46	0.05	12.93	63.24	3.14	1.86	0.08	0.80	85.49
KP-07A_42	S. 831	2.80	0.07	11.10	70.09	4.57	0.54	0.15	0.30	89.13
KP-07A_43	S. 832	2.35	0.07	10.84	67.90	4.49	0.00	0.06	0.42	85.78
KP-07A_44	S. 833	2.99	0.11	11.45	69.83	4.54	0.90	0.04	0.49	90.30
KP-07A_46	S. 835	2.39	0.02	11.02	68.03	4.57	0.82	0.07	0.35	86.87
KP-07A_47	S. 836	3.00	0.05	11.30	69.95	4.41	0.87	0.07	0.41	90.03
KP-07A_48	S. 837	3.18	0.01	11.58	68.06	4.10	0.78	0.14	0.31	87.88
KP-07A_50	S. 839	2.89	0.05	11.43	68.93	4.45	0.80	0.19	0.39	88.79
B2-07B										
B2-07B_02-05	Av. S. 709-712	2.50	0.07	11.19	67.69	4.41	1.10	0.04	0.57	87.54
B2-07B_06-08	Av. S. 713-715	2.58	0.06	11.47	68.46	4.40	1.13	0.03	0.47	88.48
B2-07B_11	S. 718	2.41	0.08	11.31	69.04	4.47	1.16	0.01	0.44	88.86
B2-07B_12	S. 719	2.54	0.05	11.14	69.64	4.49	1.06	0.07	0.58	89.09
B2-07B_13	S. 720	2.43	0.02	11.25	68.65	4.71	1.07	0.12	0.41	88.46
B2-07B_15	S. 722	1.55	0.10	10.65	67.60	4.30	1.13	0.01	0.64	85.79
B2-07B_16	S. 723	2.33	0.08	11.24	70.30	4.72	1.04	0.10	0.36	90.13
B2-07B_17	S. 724	1.71	0.01	11.13	68.30	4.37	1.22	0.07	0.70	87.05
B2-07B_19	S. 726	2.46	0.06	11.78	68.63	4.79	1.11	0.11	0.59	89.51
B2-07B_20	S. 727	2.50	0.08	11.19	68.90	4.52	1.12	0.02	0.38	88.65
B2-07B_24	S. 731	2.51	0.13	11.34	68.86	4.62	1.21	0.05	0.66	89.24
B2-07B_25	S. 732	2.11	0.07	11.10	68.44	4.14	0.80	0.01	0.55	87.15
B2-07B_26	S. 733	2.19	0.08	11.21	67.18	4.44	1.11	0.08	0.52	86.64
B2-07B_29, 30	Av. S. 736, 737	2.48	0.01	11.60	69.09	4.66	0.97	0.14	0.51	89.42
B2-07B_32	S. 739	2.10	0.10	10.85	67.62	4.47	1.06	0.02	0.61	86.56
B2-07B_34	S. 741	2.09	0.07	11.20	66.59	3.43	1.11	0.01	0.66	85.10
B2-07B_35	S. 742	2.09	0.01	10.86	67.02	4.70	1.20	0.14	0.23	86.14
B2-07B_36	S. 743	1.80	0.02	11.14	67.33	4.38	1.23	0.18	0.57	86.30
B2-07B_38	S. 745	2.60	0.07	11.35	69.60	4.32	0.94	0.20	0.57	89.61
B2-07B_39	S. 746	1.93	0.03	10.66	66.60	4.36	1.03	0.19	0.70	85.41
B2-07B_40	S. 747	1.78	0.01	11.03	68.37	4.19	1.20	0.08	0.46	87.08
B2-07B_41	S. 748	2.08	0.04	10.41	66.99	4.25	1.02	0.11	0.71	85.25
B2-07B_43-46	Av. S. 750-753	2.59	0.07	10.92	71.42	4.29	0.92	0.00	0.54	90.74
B2-07B_48, 49	Av. S. 755, 756	2.24	0.06	11.60	66.31	4.13	1.18	0.01	0.75	85.97
B2-07B_50	S. 757	2.26	0.03	11.00	69.37	4.12	0.94	0.11	0.47	88.19
WLS-R-070818										
WLS-R_03, 04	Av. S. 843, 844	2.59	0.04	11.21	68.77	4.04	1.01	0.02	0.45	87.97
WLS-R_06	S. 846	2.56	0.05	11.37	68.92	4.70	1.10	0.02	0.49	89.06

Spot Name	Spot No.	Na <sub>2</sub> O	MgO	Al <sub>2</sub> O <sub>3</sub>	SiO <sub>2</sub>	K <sub>2</sub> O	CaO	MnO	FeO	Total
WLS-R_10	S. 850	2.49	0.03	11.64	69.56	4.70	0.93	0.01	0.60	89.80
WLS-R_11	S. 851	2.10	0.00	10.77	69.57	4.71	0.92	0.09	0.56	88.55
WLS-R_13	S. 853	2.36	0.05	11.39	70.74	4.65	1.19	0.12	0.47	90.65
WLS-R_14	S. 854	2.02	0.05	10.74	68.53	3.94	1.22	0.04	0.39	86.71
WLS-R_15	S. 855	2.03	0.00	10.70	69.24	4.37	0.97	0.03	0.46	87.74
WLS-R_19	S. 859	2.45	0.02	11.15	67.48	4.87	1.04	0.08	0.47	87.15
WLS-R_21, 22	Av. S. 861, 862	2.31	0.07	11.17	70.24	4.31	1.14	0.16	0.46	89.70
WLS-R_23	S. 863	1.90	0.02	10.52	67.52	4.51	1.03	0.05	0.34	85.74
WLS-R_25	S. 865	2.88	0.15	13.73	65.63	3.22	2.18	0.11	0.36	88.25
WLS-R_26	S. 866	2.50	0.05	12.06	68.86	4.71	1.24	0.03	0.54	89.89
WLS-R_27	S. 867	2.16	0.01	11.11	69.81	4.87	0.80	0.16	0.52	89.40
WLS-R_28	S. 868	1.91	0.10	10.44	67.93	4.15	0.93	0.16	0.43	85.46
DVMT-1										
DVMT-1_01	S. 224	3.17	0.07	12.43	71.72	3.89	1.15	0.00	0.77	93.15
DVMT-1_02	S. 225	3.39	0.14	12.84	71.19	3.67	0.97	0.07	0.81	92.92
DVMT-1_04	S. 227	2.31	0.17	11.38	67.90	3.82	1.03	0.11	0.76	87.36
DVMT-1_05,06	Av. S. 228, 229	2.72	0.13	11.47	70.61	4.33	0.79	0.03	0.66	90.48
DVMT-1_10-12	Av. S. 233-235	3.52	0.07	12.45	72.06	4.14	0.93	0.05	0.91	94.13
DVMT-1_13	S. 236	3.27	0.33	13.07	65.61	3.56	1.85	0.01	0.88	88.23
DVMT-1_18	S. 241	2.96	0.17	12.25	69.36	3.74	1.28	0.06	0.86	90.57
DVMT-1_19	S. 242	2.82	0.13	12.13	70.55	4.28	1.08	0.07	0.68	92.12
DVMT-1_21	S. 244	2.56	0.08	12.64	69.70	3.78	1.27	0.02	1.00	90.81
DVMT-1_24	S. 247	2.96	0.10	11.97	67.70	3.74	1.07	0.01	0.80	88.29
DVMT-1_27	S. 250	2.48	0.11	12.21	69.94	3.77	1.49	0.11	0.77	91.32
DVMT-1_30	S. 253	3.07	0.10	12.33	73.37	3.88	1.04	0.08	0.60	94.28
DVMT-1_31,32	Av. S. 254, 255	3.45	0.08	11.52	73.20	3.59	0.90	0.02	0.81	93.50
DVMT-1_33	S. 256	2.67	0.19	12.46	66.18	3.95	1.29	0.09	1.23	87.93
ES080216-2										
ES_05	S. 262	2.35	0.18	11.85	71.33	4.84	1.01	0.01	1.26	92.75
ES_06	S. 263	2.87	0.09	11.32	71.52	3.93	0.82	0.09	0.98	91.37
ES_09	S. 266	2.99	0.24	13.22	67.76	3.93	1.51	0.01	1.92	91.47
ES_11	S. 268	2.78	0.21	11.59	69.45	4.10	0.85	0.04	1.45	90.33
ES_12	S. 269	3.01	0.19	12.28	71.58	3.99	1.31	0.20	0.99	93.50
ES_13-14	Av. S. 270, 271	2.78	0.05	11.24	71.65	4.42	0.71	0.08	0.80	91.72
ES_15	S. 272	2.58	0.09	11.26	71.29	4.58	0.85	0.05	0.77	91.48
ES_16	S. 273	2.60	0.11	11.87	71.37	4.32	1.20	0.01	0.93	92.35
ES_17	S. 274	2.83	0.05	11.37	71.49	4.51	0.85	0.02	0.52	91.45
ES_25	S. 282	3.33	0.13	12.64	71.04	4.15	0.95	0.07	1.26	93.54
ES_30	S. 287	2.15	0.19	11.91	66.66	3.69	1.23	0.12	1.33	87.15
ES_31	S. 288	3.34	0.09	12.73	68.98	3.85	1.32	0.11	0.93	91.10
ES_32	S. 289	3.11	0.13	11.99	71.26	4.30	0.84	0.07	0.86	92.57
LSB1-14										
LSB1-14_01	S. 583	3.05	0.15	12.37	70.68	3.89	1.09	0.04	0.56	91.72
LSB1-14_02-04	Av. S. 584-586	3.21	0.06	11.55	72.27	4.71	0.57	0.13	0.62	92.91
LSB1-14_09-11	Av. S. 591-593	3.27	0.12	12.65	67.75	3.58	1.28	0.06	0.64	89.32
LSB1-14_12	S. 594	3.25	0.13	13.01	69.01	3.64	1.39	0.12	0.74	91.25
LSB1-14_13	S. 595	3.32	0.04	13.04	69.87	3.92	1.60	0.07	0.74	92.57
LSB1-14_14	S. 596	3.23	0.05	11.44	71.85	4.35	0.88	0.11	0.50	92.84
LSB1-14_16	S. 598	3.22	0.10	10.93	69.62	3.64	0.77	0.01	0.81	88.94
LSB1-14_17	S. 599	2.92	0.02	11.29	70.15	4.69	0.51	0.14	0.39	90.12
LSB1-14_18	S. 600	2.41	0.13	11.39	69.04	3.72	0.85	0.00	0.35	87.60
LSB1-14_19, 20	Av. S. 601, 602	4.35	0.03	11.42	71.92	1.75	0.43	0.15	0.75	90.78

Spot Name	Spot No.	Na <sub>2</sub> O	MgO	Al <sub>2</sub> O <sub>3</sub>	SiO <sub>2</sub>	K <sub>2</sub> O	CaO	MnO	FeO	Total
LSB1-14_23-25	Av. S. 605-607	3.30	0.06	11.43	72.39	3.74	0.78	0.06	0.53	92.13
LSB1-14_27	S. 609	2.45	0.20	11.53	66.27	3.47	1.33	0.11	0.58	85.78
LSB1-14_28	S. 610	2.81	0.13	11.66	67.42	3.55	1.02	0.25	0.78	87.36
LSB1-14_29	S. 611	3.34	0.11	13.59	71.76	3.61	1.57	0.01	0.59	94.53
LSB1-14_30	S. 612	3.36	0.14	11.87	70.57	3.60	1.11	0.07	0.50	91.17
LSB1-14_32, 33	Av. S. 614, 615	4.46	0.04	11.41	72.50	0.90	0.63	0.00	0.17	90.10
LSB1-14_35	S. 617	2.93	0.17	11.37	73.00	4.39	0.91	0.11	0.45	93.33
LSB1-14_37	S. 619	3.19	0.07	11.50	71.90	3.99	0.94	0.14	0.64	92.28
LSB1-14_38	S. 620	2.94	0.06	12.07	71.45	4.03	0.78	0.02	0.54	91.83
LSB1-14_41	S. 623	2.39	0.10	11.24	68.04	3.65	0.92	0.07	0.66	86.91
LSB1-14_42	S. 624	3.02	0.11	12.36	71.19	3.90	0.90	0.18	0.72	92.34
LSB1-14_43	S. 625	3.01	0.06	11.31	71.52	3.90	0.85	0.06	0.58	91.20
LSB1-14_44	S. 626	3.32	0.04	12.79	68.68	3.57	1.47	0.03	0.75	90.52
LSB1-14_45	S. 627	3.46	0.04	12.38	70.84	3.52	1.08	0.06	0.73	92.12
LSB1-14_46	S. 628	3.55	0.09	13.59	73.41	3.58	1.29	0.30	0.75	96.52
LSB1-14_47	S. 629	2.93	0.17	11.79	67.74	0.95	1.57	0.07	0.63	85.68
LSB1-14_48	S. 630	3.15	0.03	12.15	66.75	3.39	1.37	0.05	0.82	87.52
LSB1-14_49	S. 631	3.30	0.12	11.25	70.35	3.41	0.98	0.01	0.80	90.16
LSB1-14_50	S. 632	2.46	0.01	10.77	68.75	3.66	0.80	0.17	0.64	87.17
LSB1-14_52	S. 634	2.87	0.04	11.21	70.54	4.58	0.54	0.03	0.56	90.30
LSB1-14_53	S. 635	2.95	0.16	11.36	71.43	3.71	0.77	0.04	0.65	91.00
LSB1-14_54	S. 636	2.83	0.08	11.49	71.85	4.18	0.59	0.10	0.76	91.85
LSB1-14_55	S. 637	3.01	0.14	12.42	68.11	3.50	1.43	0.09	0.57	89.21
LSB1-14_56	S. 638	2.91	0.20	11.44	68.74	3.65	1.02	0.01	0.72	88.64
LSB1-14_58	S. 640	2.85	0.14	11.41	71.81	4.65	0.41	0.12	0.54	91.90
LSB1-14_60, 61	Av. S. 642, 643	3.18	0.07	11.24	69.08	3.69	0.83	0.02	0.59	88.69
LSB1-14_63-65	Av. S. 645-647	3.02	0.08	11.70	72.18	3.97	0.90	0.11	0.67	92.60
LSB1-14_66	S. 648	2.79	0.08	11.75	71.19	3.99	0.95	0.16	0.53	91.41
PPF2-17										
PPF2-17_02	S. 650	3.11	0.07	11.87	71.88	4.52	0.88	0.11	0.48	92.65
PPF2-17_04	S. 652	2.45	0.05	12.12	66.81	3.79	1.11	0.10	0.83	86.97
PPF2-17_07-09	Av. S. 655-657	2.85	0.08	11.34	71.20	3.74	0.86	0.14	0.61	90.79
PPF2-17_13	S. 661	3.24	0.08	12.19	70.35	3.83	1.04	0.00	0.51	91.19
PPF2-17_04 (R2)	S. 55	3.08	0.00	11.10	70.61	4.55	0.64	0.00	0.62	90.53
PPF2-17_14-16	Av. S. 662-664	2.99	0.06	11.40	70.87	4.09	0.83	0.06	0.56	90.83
PPF2-17_19,20	Av. S. 667, 668	3.22	0.06	12.16	71.58	4.37	0.83	0.00	0.63	92.83
PPF2-17_21, 22	Av. S. 669, 670	3.07	0.04	11.08	71.28	4.71	0.60	0.02	0.74	91.46
PPF2-17_23	S. 671	3.17	0.14	11.37	70.70	3.67	0.86	0.04	0.35	90.22
PPF2-17_25, 26	Av. S. 673, 674	3.04	0.09	11.30	70.95	3.68	0.85	0.03	0.48	90.30
PPF2-17_02,03 (R2)	Av. S. 53, 54	2.58	0.00	11.21	69.78	4.30	0.81	0.00	0.49	88.89
PPF2-17_05 (R2)	S. 56	2.64	0.00	12.29	68.77	3.54	0.80	0.00	0.00	87.77
PPF2-17_07 (R2)	S. 58	3.23	0.00	11.72	73.33	3.93	0.89	0.00	0.00	93.07
ST1-03										
ST1-03_07, 08	Av. S. 681, 682	2.57	0.02	11.89	69.91	4.34	0.66	0.02	0.44	89.82
ST1-03_12	S. 686	2.30	0.03	11.46	68.09	4.63	0.98	0.05	0.26	87.74
ST1-03_15-17	Av. S. 689-691	2.84	0.03	11.39	69.74	2.72	1.70	0.09	0.01	88.47
ST1-03_19	S. 693	3.50	0.00	12.21	75.06	2.63	1.73	0.02	0.03	94.90
ST1-03_21	S. 695	2.30	0.29	12.33	68.81	4.65	1.39	0.11	1.15	90.86
ST1-03_10 (R2)	S. 68	2.51	0.00	12.87	70.79	4.84	1.23	0.00	0.81	92.93
ST1-03_22	S. 696	2.02	0.05	11.28	66.40	4.66	0.96	0.14	0.46	85.74
ST1-03_09 (R2)	S. 67	2.82	0.00	12.22	69.93	4.72	1.27	0.00	0.00	90.94
ST1-03_28	S. 702	2.13	0.13	11.75	69.21	4.95	1.05	0.20	0.57	89.84

Spot Name	Spot No.	Na <sub>2</sub> O	MgO	Al <sub>2</sub> O <sub>3</sub>	SiO <sub>2</sub>	K <sub>2</sub> O	CaO	MnO	FeO	Total
ST1-03_02 (R2)	S. 60	2.07	0.00	10.91	71.69	5.60	0.57	0.00	0.00	90.59
ST1-03_05,06 (R2)	Av. S. 63, 64	2.57	0.00	12.53	69.79	4.37	1.58	0.00	1.53	92.46
ST1-03_08 (R2)	S. 66	2.36	0.00	11.56	70.14	4.53	0.96	0.00	0.53	90.02
ST1-03_11 (R2)	S. 69	2.81	0.00	13.16	69.54	3.97	1.47	0.00	1.30	92.24
EMC080216-1										
EMC_01	S. 399	3.47	0.13	11.42	71.05	4.31	0.00	0.06	0.79	91.20
EMC_06	S. 404	3.61	0.81	14.22	65.98	5.65	0.97	0.25	3.47	94.90
EMC_06 (R2)	S. 146	4.79	0.00	13.51	70.15	2.47	1.61	0.00	0.00	92.53
EMC_11	S. 409	3.54	0.01	11.65	65.68	3.95	0.00	0.14	3.01	87.65
EMC_12-14	Av. S. 410-412	2.97	0.08	12.17	72.86	3.08	0.83	0.00	0.12	92.03
EMC_02 (R2)	S. 142	3.50	0.00	12.87	70.93	4.17	0.59	0.00	0.69	92.70
EMC_03 (R2)	S. 143	3.81	0.00	13.60	70.22	5.09	0.64	0.00	0.00	93.32
EMC_04 (R2)	S. 144	3.29	0.00	12.84	68.11	4.70	0.79	0.00	0.00	89.66
EMC_05 (R2)	S. 145	1.96	0.00	14.15	65.89	9.00	0.48	0.00	0.86	92.32
EMC_07 (R2)	S. 147	2.54	0.00	11.05	69.89	4.90	0.53	0.00	0.00	88.77
EMC_08 (R2)	S. 148	3.13	0.00	11.50	73.68	4.68	0.53	0.00	0.00	93.48
EMC_09 (R2)	S. 149	2.01	0.00	11.06	68.82	4.93	0.86	0.00	0.00	87.49
EMC_10 (R2)	S. 150	2.68	0.00	11.38	71.50	4.70	1.02	0.00	0.73	92.00
EMC_11 (R2)	S. 151	3.12	0.00	12.10	75.23	4.99	0.45	0.00	0.00	95.81
KC061517-1										
KC_01-06	Av. S. 560-565	2.33	0.05	11.76	73.19	5.38	1.02	0.02	0.47	94.19
KC_07	S. 566	2.36	0.01	12.14	72.21	5.68	1.13	0.13	0.62	94.24
KC061517-1_02 (R2)	S. 47	2.53	0.00	11.49	71.60	5.44	0.69	0.00	1.08	92.75
KC_08	S. 567	2.72	0.15	11.18	72.37	4.45	0.71	0.06	0.51	92.11
KC_16, 19	Av. S. 575, 578	4.06	0.06	11.03	70.19	2.01	0.63	0.03	0.59	88.55
KC061517-1_04 (R2)	S. 49	2.69	0.00	12.06	73.19	5.15	0.93	0.00	0.00	94.37
KC_22	S. 581	3.20	0.11	12.59	73.75	4.57	1.09	0.03	0.82	96.06
KC_23	S. 582	2.63	0.04	10.95	71.13	4.73	0.52	0.18	0.63	90.80
KC061517-1_06 (R2)	S. 51	2.92	0.00	11.84	69.64	4.51	0.98	0.00	0.00	89.65
Hadro Hill										
HH_03	S. 381	2.82	0.09	11.80	73.56	5.07	0.89	0.28	0.94	95.43
HH_04	S. 382	2.66	0.15	11.49	70.96	4.78	0.75	0.06	1.07	92.10
HH_06	S. 384	2.63	0.15	11.20	71.64	4.82	0.89	0.02	1.17	92.51
HH_07	S. 385	2.38	0.01	10.36	68.45	4.32	0.00	0.18	0.69	85.77
HH_08	S. 386	2.73	0.03	11.16	71.77	4.96	0.62	0.06	0.69	91.74
HH_09,10	Av. S. 387, 388	3.04	-0.01	11.60	72.82	4.78	0.56	0.01	0.64	93.40
HH_11	S. 389	3.30	0.04	11.62	74.00	4.98	0.53	0.07	0.48	94.86
HadroHill_02 (R2)	S. 117	2.44	0.00	10.71	70.94	4.38	0.73	0.00	0.76	89.90
HadroHill_04 (R2)	S. 119	2.37	0.00	10.93	71.03	4.77	0.70	0.00	1.27	90.96
HadroHill_05 (R2)	S. 120	2.33	0.00	11.11	74.50	5.48	0.59	0.00	0.00	93.96
HadroHill_06 (R2)	S. 121	2.61	0.00	11.50	74.25	5.64	0.62	0.00	0.67	95.27
HadroHill_07 (R2)	S. 122	2.51	0.26	11.80	70.67	5.44	1.03	0.00	1.17	92.86
HadroHill_09,10 (R2)	Av. S. 124, 125	3.02	0.00	11.94	71.76	4.76	0.71	0.00	0.72	92.87
HadroHill_12-14 (R2)	Av. S. 127-129	2.65	0.23	12.22	72.86	5.77	0.76	0.00	0.60	94.94
HadroHill_15 (R2)	S. 130	2.99	0.00	12.34	72.55	4.98	0.72	0.00	0.63	94.19
HadroHill_16 (R2)	S. 131	3.01	0.00	11.23	72.72	4.93	0.47	0.00	0.00	92.32
HadroHill_17 (R2)	S. 132	2.49	0.00	11.28	73.11	5.40	0.75	0.00	0.00	93.02
HadroHill_18 (R2)	S. 133	3.23	0.00	11.49	73.54	5.02	0.48	0.00	0.64	94.36
HadroHill_19 (R2)	S. 134	2.76	0.00	11.92	70.96	4.82	0.95	0.00	0.00	91.40
HadroHill_20 (R2)	S. 135	2.76	0.23	12.63	70.16	4.44	1.24	0.00	1.19	92.61
HadroHill_21 (R2)	S. 136	2.82	0.00	12.63	70.60	4.63	1.41	0.00	1.42	93.45
HadroHill_22 (R2)	S. 137	2.79	0.00	10.91	72.73	4.82	0.47	0.00	0.67	92.32

Spot Name	Spot No.	Na <sub>2</sub> O	MgO	Al <sub>2</sub> O <sub>3</sub>	SiO <sub>2</sub>	K <sub>2</sub> O	CaO	MnO	FeO	Total
HadroHill_23 (R2)	S. 138	2.44	0.00	10.68	70.96	4.72	0.69	0.00	0.74	90.09
HadroHill_24 (R2)	S. 139	2.71	0.00	12.09	73.08	5.36	0.95	0.00	0.88	95.05
HadroHill_25 (R2)	S. 140	2.38	0.00	11.58	72.99	4.54	0.66	0.00	0.64	92.53
IL082717-1										
IL_05	S. 511	2.62	0.11	11.42	74.47	5.17	0.62	0.04	0.73	95.08
IL_06	[1] S. 512	3.84	0.23	13.21	72.63	4.28	1.28	0.04	1.20	96.61
IL_20	S. 526	2.30	0.08	11.84	74.35	5.36	1.07	0.01	1.00	95.94
IL_22	S. 528	2.67	0.20	11.48	74.93	4.58	0.93	0.09	0.96	95.81
IL_25	S. 531	3.42	0.15	12.97	70.90	4.33	1.17	0.07	1.07	93.88
IL_26-28	Av. S. 532-534	3.84	0.09	11.75	72.18	1.75	0.92	0.05	0.96	91.51
IL_30	S. 536	2.86	-0.05	11.49	72.62	4.18	0.73	0.23	0.69	92.75
IL_31	S. 537	2.64	0.19	11.52	71.56	4.03	0.89	0.09	0.77	91.62
IL_32, 33	Av. S. 538, 539	2.81	0.10	11.53	73.67	4.29	0.84	0.14	0.73	94.09
IL_34-36	Av. S. 540-542	3.00	0.11	11.79	74.35	4.43	0.95	0.07	0.53	95.19
IL_37-39	Av. S. 543-545	3.42	0.13	12.80	71.68	4.37	1.17	0.05	0.77	94.37
IL_40	S. 546	3.26	0.03	13.15	71.32	4.17	1.06	0.13	0.75	93.82
IL_41	S. 547	3.53	0.20	13.13	70.73	3.89	1.43	0.03	0.93	93.86
IL_42,43	Av. S. 548, 549	2.93	0.08	12.13	71.72	4.64	1.06	0.08	0.81	93.31
IL_44-46	Av. S. 550-552	3.50	0.17	13.36	70.62	4.06	1.54	0.06	0.89	94.24
IL_47	S. 553	3.27	0.03	12.81	73.67	4.02	1.01	0.07	0.94	95.81
IL_48	S. 554	3.13	0.18	13.62	70.29	3.86	1.55	0.05	0.99	93.59
IL_49	S. 555	2.78	0.16	12.04	68.62	3.86	1.04	0.09	0.98	89.44
IL_50	S. 556	3.53	0.16	12.77	72.69	4.10	1.06	0.15	0.92	95.32
IL_51	S. 557	3.06	0.12	12.91	69.12	4.00	1.29	0.05	1.09	91.57
Plateau										
Plateau_02,03	Av. S. 336, 337	2.52	-0.01	11.35	71.75	4.38	0.74	0.04	0.34	90.95
Plateau_02 (R2)	S. 71	3.13	0.00	12.22	68.04	3.81	1.26	0.00	1.08	89.45
Plateau_06	S. 340	2.81	0.00	12.37	67.77	3.80	1.21	0.23	0.80	88.93
Plateau_09,10	Av. S. 343, 344	3.79	0.02	14.24	67.38	1.75	1.70	0.04	0.48	89.31
Plateau_11,12	Av. S. 345, 346	3.32	0.06	14.00	66.54	1.66	1.32	0.11	1.38	88.33
Plateau_13	S. 347	2.18	0.03	10.80	68.24	4.25	0.87	0.11	1.09	87.21
Plateau_14	S. 348	2.92	-0.02	11.26	70.92	1.13	0.55	0.05	0.81	87.56
Plateau_18	S. 352	2.82	0.05	11.20	71.17	4.09	0.92	0.06	0.83	91.10
Plateau_24	S. 358	3.07	0.05	11.50	71.66	4.37	0.75	0.07	0.62	92.04
Plateau_26	S. 360	3.41	-0.01	12.20	73.09	4.48	0.79	0.19	1.18	95.31
Plateau_03 (R2)	S. 72	3.10	0.00	11.48	70.00	4.20	0.74	0.00	0.00	89.48
Plateau_07 (R2)	S. 76	3.55	0.00	12.46	70.28	4.21	0.99	0.00	0.88	92.14
Plateau_08 (R2)	S. 77	3.23	0.00	12.33	70.89	4.51	0.69	0.00	1.09	92.71
Plateau_09 (R2)	S. 78	3.02	0.00	12.03	68.13	4.30	0.75	0.00	0.84	88.88
Plateau_10 (R2)	S. 79	2.95	0.00	11.73	72.00	4.49	0.63	0.00	0.65	92.42
Plateau_11 (R2)	S. 80	2.82	0.00	11.31	71.07	4.55	0.00	0.00	0.77	90.45
Plateau_13 (R2)	S. 82	3.39	0.00	11.94	69.36	3.96	0.81	0.00	0.87	90.27
PlateauPuck_02 (R2)	S. 153	3.21	0.00	11.99	70.55	4.44	0.76	0.00	0.83	91.79
PlateauPuck_03 (R2)	S. 154	2.47	0.00	10.96	67.68	4.26	0.74	0.00	1.34	87.12
PlateauPuck_04 (R2)	S. 155	3.38	0.00	12.19	76.40	4.69	0.00	0.00	0.75	97.35
PlateauPuck_05 (R2)	S. 156	2.58	0.00	11.36	71.42	4.63	0.68	0.00	0.76	91.40
PlateauPuck_07 (R2)	S. 158	2.51	0.00	11.75	67.08	4.07	1.01	0.00	0.95	87.33
PlateauPuck_08 (R2)	S. 159	2.72	0.00	12.42	68.97	4.32	1.10	0.00	0.98	90.51
PlateauPuck_09 (R2)	S. 160	3.34	0.00	11.54	71.19	1.41	0.62	0.00	0.81	88.90
PlateauPuck_10 (R2)	S. 161	2.69	0.00	11.38	70.19	4.35	0.70	0.00	0.99	90.08
PlateauPuck_11 (R2)	S. 162	3.41	0.00	11.62	70.06	2.00	0.82	0.00	1.02	88.89
PlateauPuck_14 (R2)	S. 165	3.64	0.00	13.75	72.15	4.19	1.21	0.00	0.00	94.91



Spot Name	Spot No.	Na <sub>2</sub> O	MgO	Al <sub>2</sub> O <sub>3</sub>	SiO <sub>2</sub>	K <sub>2</sub> O	CaO	MnO	FeO	Total
PlateauPuck_15 (R2)	S. 166	3.07	0.00	12.07	70.49	4.21	0.88	0.00	1.18	91.80
PlateauPuck_18 (R2)	S. 169	2.41	0.00	12.53	67.83	4.14	1.18	0.00	1.07	89.03
PlateauPuck_19 (R2)	S. 170	2.87	0.00	11.41	71.36	4.82	0.52	0.00	0.69	91.43
PlateauPuck_20 (R2)	S. 171	2.57	0.00	11.14	70.74	4.72	0.56	0.00	1.02	90.73
PlateauPuck_21 (R2)	S. 172	2.77	0.00	11.32	70.71	4.06	1.39	0.00	0.94	92.29
PlateauPuck_23 (R2)	S. 174	3.04	0.00	13.20	67.71	1.49	1.10	0.00	1.37	87.87
PlateauPuck_24 (R2)	S. 175	3.24	0.00	11.92	72.96	4.37	0.82	0.00	0.90	94.20
PlateauPuck_25,26 (R2)	Av. S. 176, 177	3.00	0.00	11.41	71.37	4.57	0.79	0.00	0.87	91.99
PlateauPuck_27 (R2)	S. 178	3.06	0.00	11.36	71.12	3.00	0.79	0.00	0.73	90.05
PlateauPuck_28 (R2)	S. 179	2.63	0.00	11.10	70.98	4.51	0.60	0.00	0.95	90.77
PlateauPuck_29 (R2)	S. 180	2.14	0.00	11.04	68.25	3.94	0.68	0.00	0.99	86.88
PlateauPuck_30 (R2)	S. 181	2.72	0.00	11.50	72.57	4.55	0.64	0.00	0.57	92.53
PlateauPuck_32 (R2)	S. 183	3.06	0.00	12.16	70.78	4.43	1.43	0.00	0.89	93.51
PlateauPuck_34 (R2)	S. 185	3.56	0.00	13.38	71.47	4.29	1.21	0.00	1.34	94.99
FS082717-1										
FS_08-11	Av. S. 498-501	3.71	0.02	12.35	71.04	4.44	0.67	0.15	0.92	93.26
FS_12	S. 502	3.18	-0.07	11.72	72.97	4.48	0.44	0.02	0.70	93.40
FS_15	S. 505	3.54	0.05	12.76	71.45	4.29	0.60	0.10	1.04	93.81
FS_16	S. 506	2.89	0.02	11.04	71.74	4.24	0.45	0.05	0.74	91.08
NF082917-1										
NF_03	S. 416	2.90	0.15	12.22	70.55	4.78	1.14	0.02	0.44	91.97
NF_04	S. 417	2.61	-0.08	12.39	71.74	4.73	0.94	0.04	0.27	92.42
NF_05-07	Av. S. 418-420	2.62	0.09	11.94	71.13	4.15	1.08	0.12	0.50	91.53
NF_08	S. 421	3.18	0.12	12.09	70.54	2.12	0.65	0.12	0.51	89.32
NF_09-11	Av. S. 422-424	3.02	0.22	13.07	71.29	3.78	1.73	0.13	0.47	93.70
NF_12	S. 425	2.95	0.27	12.85	70.93	3.09	1.73	0.13	0.50	92.39
NF_13	S. 426	2.59	0.07	12.36	72.14	4.72	0.77	0.03	0.45	93.04
NF_18	S. 431	2.70	0.02	11.43	72.47	4.59	0.98	0.02	0.47	92.56
NF_20	S. 433	2.90	0.22	12.01	71.75	4.35	0.00	0.25	0.45	91.87
NF_21	S. 434	3.22	0.01	12.37	72.68	4.52	0.62	0.31	0.42	93.91
NF_22	S. 435	2.53	0.09	12.00	69.08	4.27	0.73	0.12	0.22	88.86
NF_24-26	Av. S. 437-439	2.77	0.05	11.79	71.09	4.59	0.72	0.01	0.45	91.40
NF_28	S. 441	2.85	0.04	12.36	71.26	4.66	1.32	0.19	0.19	92.82
PR082917-1										
PR_01	S. 442	2.22	0.13	12.44	70.76	4.42	0.90	0.10	0.56	91.38
PR_07	S. 448	2.55	0.02	12.54	70.73	3.45	1.54	0.26	0.50	91.51
PR_08	S. 449	2.48	0.19	11.71	69.09	3.72	1.50	0.04	0.51	89.08
PR_09	S. 450	2.21	0.13	11.75	68.81	4.42	0.66	0.08	0.45	88.32
PR_10, 11	Av. S. 451, 452	2.62	0.07	12.20	69.91	4.82	1.16	0.07	0.43	91.06
PR_12	S. 453	3.32	0.04	12.48	71.69	3.89	1.24	0.03	0.59	93.29
PR_16	S. 457	2.25	0.11	12.79	69.34	3.72	1.95	0.01	0.36	90.43
PR_17	S. 458	3.37	0.03	12.84	70.37	3.85	1.93	0.06	0.44	92.53
PR_18	S. 459	3.05	0.07	11.91	71.42	4.70	1.09	0.05	0.78	92.70
PR_19	S. 460	2.97	0.14	12.21	71.67	4.36	0.66	0.17	0.42	92.53
PR_21	S. 462	2.10	0.13	11.23	69.49	4.15	1.00	0.05	0.67	88.66
PR_30	S. 471	2.82	0.18	12.47	71.62	5.16	0.56	0.19	1.02	93.65
PR_31	S. 472	3.00	0.02	13.13	69.62	4.01	2.20	0.17	0.77	92.54
PR_32	S. 473	2.35	0.08	11.71	71.42	4.16	0.00	0.06	0.29	89.95
PR_36	S. 477	3.11	0.04	12.98	73.78	4.32	1.02	0.24	0.31	95.65
PR_37	S. 478	3.17	0.10	12.32	69.24	4.20	1.05	0.09	0.65	90.57
PR_38	S. 479	2.99	0.15	12.64	71.56	4.78	0.93	0.04	0.69	93.76

**Appendix C.6.9** Melt inclusion data for all analysis remaining after data reduction described in Appendix B.4 and also after recalculation to 100 wt. % totals.

Spot Name	Spot No.	Na <sub>2</sub> O	MgO	Al <sub>2</sub> O <sub>3</sub>	SiO <sub>2</sub>	K <sub>2</sub> O	CaO	MnO	FeO	Total
KBU-H-050818										
KBU-H_08	S. 18	1.27	0.65	14.31	76.20	5.82	0.88	0.00	1.09	100.00
KBU-H_10, 11	Av. S. 20, 21	2.92	0.00	13.50	77.63	3.78	1.57	0.00	0.86	100.00
KBU-H_12-14	Av. S. 22-24	3.12	0.00	13.57	78.10	3.76	1.51	0.00	0.00	100.00
KBC-195										
KBC-195_12-14	Av. S. 332-334	3.63	0.29	15.75	73.79	2.85	2.50	0.14	1.08	100.00
KBC-D-030818										
KBC-D_02, 03	Av. S. 2, 3	2.09	0.00	13.98	78.07	4.28	0.98	0.00	0.61	100.00
KBC-D_06	S. 6	3.28	0.00	13.69	77.36	4.27	0.96	0.00	0.55	100.00
KBC-D_07	S. 7	3.33	0.00	12.91	77.41	5.83	0.65	0.00	0.00	100.00
KBC-D_10	S. 10	2.25	0.00	14.25	77.41	4.06	1.22	0.00	0.93	100.00
KBU-C-310718										
KBU-C_05	S. 29	2.87	0.00	13.96	77.29	4.25	1.19	0.00	0.84	100.00
KBU-C_07	S. 31	2.01	0.00	14.50	77.76	3.87	1.43	0.00	0.75	100.00
KBU-C_09	S. 33	2.22	0.00	13.99	78.01	4.91	1.15	0.00	0.00	100.00
KBU-C_10	S. 34	2.76	0.00	15.79	75.73	3.26	1.95	0.00	0.61	100.00
KBC-144										
KBC-144_01	S. 291	3.59	0.13	13.49	76.66	4.25	1.12	0.01	0.99	100.00
KBC-144_02	S. 292	3.60	0.02	14.22	75.32	4.12	1.55	0.10	1.31	100.00
KBC-144_04	[1] S. 294	3.03	0.10	11.99	76.63	4.91	1.75	0.03	0.72	100.00
KBC-144_15	S. 305	3.88	0.11	14.87	74.46	4.26	1.46	0.23	0.77	100.00
KBC-144_16	S. 306	2.87	0.08	12.29	78.02	5.13	0.78	0.04	0.92	100.00
KBC-144_17	S. 307	2.65	0.08	12.70	78.26	4.48	0.91	0.09	0.87	100.00
KBC-144_18	S. 308	3.23	0.02	12.19	78.03	5.15	0.75	0.09	0.54	100.00
KBC-144_19	S. 309	2.90	0.01	12.33	78.23	4.55	0.88	0.02	1.16	100.00
KBC-144_20	S. 310	3.04	0.04	12.57	77.60	5.23	0.77	0.04	0.74	100.00
KBC-144_22	S. 312	3.43	0.05	12.87	77.31	4.61	0.91	0.25	0.61	100.00
KBC-144_23	S. 313	3.02	0.10	12.53	77.55	5.06	0.81	0.12	0.82	100.00
KBC-144_24	S. 314	3.15	0.04	12.56	77.29	5.28	0.62	0.17	0.90	100.00
KBC-144_25	S. 315	3.42	0.06	12.60	77.57	4.65	0.77	0.05	0.93	100.00
KBC-144_26	S. 316	3.39	0.12	12.43	77.52	4.67	0.79	0.25	0.88	100.00
KBC-144_27	S. 317	3.51	0.07	13.89	75.24	3.84	1.96	0.16	1.38	100.00
KBC-144_28	S. 318	3.11	0.02	12.62	77.78	5.29	0.53	0.01	0.69	100.00
KBC-144_29	S. 319	3.15	0.12	12.54	78.09	4.92	0.59	0.08	0.52	100.00
KBC-144_30	S. 320	2.78	0.07	12.25	78.61	5.04	0.74	0.02	0.60	100.00
KBC-109										
KBC-109_03-05	Av. S. 3-5	3.52	0.15	14.67	75.29	4.46	1.24	0.08	0.65	100.00
KBC-109_09,10	Av. S. 9, 10	2.89	0.11	12.54	77.95	5.31	0.75	0.08	0.41	100.00
KBC-109_16	S. 16	2.35	0.16	13.81	77.20	4.34	1.40	0.05	0.99	100.00
KBC-109_19-21	Av. S. 19-21	3.11	0.10	12.62	78.23	5.33	0.57	0.09	0.37	100.00
KBC-109_23-25	Av. S. 23-25	3.20	0.25	13.12	76.78	4.93	0.92	0.15	0.67	100.00
KBC-109_29-31	Av. S. 29-31	3.15	0.25	13.28	77.06	4.19	1.17	0.08	0.90	100.00
KBC-109_32	S. 32	3.17	0.21	13.12	77.07	4.69	1.06	0.02	0.86	100.00
KBC-109_35	[1] S. 35	4.05	0.11	14.59	74.76	4.77	1.30	0.02	0.44	100.00
KBC-109_46	S. 46	2.98	0.12	12.35	77.80	5.39	0.74	0.03	0.65	100.00
KBC-109_48	S. 48	2.74	0.11	12.11	78.49	5.16	0.77	0.15	0.51	100.00
KBC-109_49	S. 49	2.50	0.09	12.30	78.59	5.23	0.76	0.15	0.60	100.00
KBC-109_52, 63,64	[1]+Av. S. 52, 63,64	3.77	0.14	14.35	75.34	4.43	1.24	0.11	0.64	100.00
KBC-109_68-70	Av. S. 68-70	3.02	0.06	12.14	78.50	5.19	0.59	0.21	0.41	100.00

KBC-109_71	S. 71	2.63	0.08	12.41	78.47	5.37	0.59	0.02	0.60	100.00
KBC-109_73	[1] S. 73	3.19	0.07	12.23	78.16	5.30	0.69	0.05	0.46	100.00
KBC-109_84	S. 84	3.29	0.02	12.32	77.77	5.31	0.54	0.28	0.55	100.00
KBC-109_85	S. 85	3.65	0.16	13.61	75.91	4.64	1.11	0.15	0.88	100.00
KBC-109_88,99	[1]+Av. S. 88,99	3.09	0.06	12.07	78.27	5.20	0.68	0.02	0.62	100.00
KBC-109_100,101	Av. S. 100, 101	3.10	0.01	12.39	78.37	5.26	0.56	0.23	0.43	100.00
KBC-109_102	S. 102	2.82	0.13	12.45	78.02	5.38	0.57	0.00	0.68	100.00
KBC-109_103,104	Av. S. 103, 104	2.86	0.04	12.30	78.53	5.20	0.71	0.06	0.48	100.00
KBC-109_108	S. 108	3.83	0.14	14.59	74.65	4.55	1.87	0.15	0.27	100.00
KBI-102										
KBI-102_01-03	Av. S. 112-114	3.05	0.04	12.52	77.62	5.36	0.68	0.16	0.62	100.00
KBI-102_04	S. 115	2.83	0.00	12.13	78.73	5.33	0.72	0.14	0.63	100.00
KBI-102_05	S. 116	3.06	0.09	12.74	77.40	5.27	0.76	0.15	0.58	100.00
KBI-102_06	[1] S. 117	3.31	0.02	12.32	78.18	5.20	0.66	0.05	0.30	100.00
KBI-102_18	S. 129	3.24	0.03	12.30	77.90	5.29	0.72	0.09	0.54	100.00
KBI-102_19	[1] S. 130	2.91	0.17	12.52	78.11	5.26	0.68	0.12	0.50	100.00
KBI-102_31	S. 142	2.58	0.07	12.35	78.47	5.22	0.85	0.14	0.65	100.00
KBI-102_33	S. 144	2.88	0.04	12.38	78.34	5.23	0.79	0.04	0.43	100.00
KBI-102_35	S. 146	2.51	0.04	12.48	78.35	5.47	0.75	0.05	0.73	100.00
KBI-102_37	S. 148	3.00	0.09	12.86	78.37	3.73	1.14	0.20	0.70	100.00
KBI-102_38	S. 149	2.81	0.07	13.63	77.83	3.94	0.98	0.18	0.62	100.00
KBI-102_39	S. 150	2.81	0.05	11.91	78.64	5.48	0.78	0.15	0.43	100.00
KBI-102_40	S. 151	3.49	0.03	15.02	74.46	5.54	1.02	0.02	0.48	100.00
KBI-102_42	S. 153	3.96	0.12	13.45	76.61	3.78	1.29	0.01	1.00	100.00
KBI-102_43	S. 154	3.31	0.23	13.15	77.37	4.21	0.74	0.15	0.98	100.00
KBI-102_44	S. 155	2.89	0.24	14.08	76.63	4.50	1.36	0.07	0.60	100.00
KBI-102_48	S. 159	3.43	0.06	13.76	76.41	4.75	1.31	0.07	0.62	100.00
KBI-102_50	[1] S. 161	3.39	0.06	13.42	76.53	4.78	0.97	0.29	0.58	100.00
KBI-102_61	[1] S. 172	3.91	0.15	13.76	75.87	4.48	1.22	0.08	0.55	100.00
KBI-102_72	S. 183	3.34	0.11	12.71	77.60	4.49	0.98	0.16	0.76	100.00
KBI-102_73-75	Av. S. 184-186	3.61	0.01	13.97	75.43	5.66	0.85	0.06	0.59	100.00
KBI-102_78	[1] S. 189	3.07	0.12	12.20	78.36	5.45	0.61	0.01	0.23	100.00
KBI-102_89	S. 200	3.14	0.05	12.36	77.78	5.43	0.66	0.22	0.48	100.00
KBI-102_90	S. 201	3.06	0.01	12.48	77.99	5.37	0.61	0.00	0.50	100.00
KBI-102_91	S. 202	3.70	0.02	14.01	75.88	4.45	1.19	0.16	0.66	100.00
KBI-102_92	S. 203	4.07	0.03	13.95	75.85	4.52	1.13	0.01	0.46	100.00
KBI-102_93	S. 204	2.59	0.20	12.43	79.01	4.30	0.90	0.05	0.77	100.00
KBI-102_94	S. 205	2.81	0.12	13.04	77.31	5.26	0.89	0.18	0.48	100.00
KBI-102_95	S. 206	3.73	0.20	13.37	77.18	3.77	1.10	0.12	0.52	100.00
KBI-102_96	S. 207	2.58	0.13	12.34	78.27	5.51	0.84	0.07	0.41	100.00
KBI-102_97	S. 208	3.11	0.04	12.17	78.01	5.42	0.72	0.15	0.42	100.00
KBI-102_98	S. 209	4.02	0.09	14.54	75.06	4.36	1.16	0.31	0.56	100.00
KBI-102_100,101	Av. S. 211, 212	3.06	0.03	12.12	78.38	5.31	0.64	0.06	0.57	100.00
KBI-102_102	S. 213	4.17	0.06	14.42	75.13	4.38	1.26	0.05	0.65	100.00
KBI-102_104	S. 215	3.18	0.11	13.46	77.49	4.08	0.97	0.24	0.72	100.00
KBI-102_105	S. 216	3.50	0.24	13.39	77.28	3.98	0.88	0.06	0.76	100.00
KBI-102_106	S. 217	4.37	0.15	15.37	74.14	3.34	1.88	0.30	0.81	100.00
KBI-102_107	S. 218	3.00	0.01	12.51	77.82	5.24	0.76	0.07	0.79	100.00
KBI-102_109	S. 220	2.93	0.04	12.46	78.07	5.30	0.72	0.02	0.48	100.00
KBI-102_110	S. 221	3.19	0.19	12.29	77.53	5.37	0.71	0.12	0.62	100.00
KBI-102_111	S. 222	3.75	0.14	14.39	75.45	4.41	1.23	0.09	0.61	100.00
IM1442										
IM1442_04	S. 366	2.80	0.02	13.29	76.65	5.72	0.94	0.06	0.69	100.00

IM1442_08	S. 370	3.54	0.08	13.36	77.29	4.12	0.98	0.02	0.65	100.00
IM1442_14	S. 376	3.62	0.00	14.10	76.54	4.13	1.48	0.01	0.24	100.00
IM1442_02 (R2)	S. 85	2.80	0.00	12.37	77.99	5.34	0.79	0.00	0.70	100.00
IM1442_03, 04 (R2)	Av. S. 86, 87	2.64	0.00	12.31	79.03	5.32	0.76	0.00	0.00	100.00
IM1442_05 (R2)	S. 88	2.57	0.00	12.18	78.67	5.32	0.67	0.00	0.65	100.00
IM1442_06 (R2)	S. 89	2.95	0.00	12.44	78.02	5.40	0.65	0.00	0.57	100.00
IM1442_07 (R2)	S. 90	2.92	0.00	12.35	78.67	5.42	0.69	0.00	0.00	100.00
IM1442_08 (R2)	S. 91	2.91	0.00	12.13	78.26	5.37	0.69	0.00	0.66	100.00
IM1442_06	S. 368	2.12	0.09	12.42	78.81	5.42	0.71	0.01	0.61	100.00
IM1442_09 (R2)	S. 92	2.98	0.00	12.49	78.50	5.35	0.70	0.00	0.00	100.00
IM1442_10 (R2)	S. 93	3.09	0.00	12.53	77.57	5.51	0.67	0.00	0.71	100.00
IM1442_11 (R2)	S. 94	4.08	0.00	14.57	74.98	4.25	1.35	0.00	0.78	100.00
IM1442_12 (R2)	S. 95	3.96	0.00	14.57	75.97	4.56	1.07	0.00	0.00	100.00
IM1442_13 (R2)	S. 96	2.44	0.00	13.58	77.82	4.32	1.15	0.00	0.85	100.00
IM1442_14,15 (R2)	Av. S. 97, 98 (R2)	3.51	0.00	14.00	76.22	4.59	1.07	0.00	0.67	100.00
IM1442_16 (R2)	S. 99	3.82	0.00	14.54	74.65	4.73	1.46	0.00	0.82	100.00
IM1442_17 (R2)	S. 100	2.79	0.00	12.35	78.70	5.73	0.64	0.00	0.00	100.00
IM1442_18 (R2)	S. 101	3.00	0.00	13.32	77.44	4.54	1.15	0.00	0.61	100.00
IM1442_12	S. 374	3.38	0.37	13.41	76.40	4.36	1.04	0.25	1.09	100.00
IM1442_19,20 (R2)	Av. S. 102, 103	3.63	0.00	13.18	77.12	4.29	1.05	0.00	0.75	100.00
IM1442_22 (R2)	S. 105	3.01	0.00	12.31	78.03	5.39	0.64	0.00	0.68	100.00
IM1442_23 (R2)	S. 106	2.97	0.00	12.32	78.16	5.26	0.66	0.00	0.69	100.00
IM1442_24,26 (R2)	Av. S. 107, 109	4.34	0.00	14.64	75.11	4.19	1.22	0.00	1.08	100.00
IM1442_27 (R2)	S. 110	4.12	0.00	14.34	75.23	4.63	1.14	0.00	0.57	100.00
IM1442_15,16	Av. S. 377, 378	3.97	0.03	14.23	75.83	4.48	1.09	0.03	0.34	100.00
IM1442_28 (R2)	S. 111	3.15	0.00	12.27	78.44	5.41	0.75	0.00	0.00	100.00
IM1442_30 (R2)	S. 113	2.99	0.00	12.56	78.20	5.18	0.56	0.00	0.55	100.00
IM1442_31 (R2)	S. 114	2.87	0.00	12.27	78.84	5.48	0.60	0.00	0.00	100.00
IM1442_32 (R2)	S. 115	4.38	0.00	12.49	81.18	1.28	0.69	0.00	0.00	100.00
KDR-5B										
KDR-5_03	S. 760	2.65	0.15	12.68	77.24	5.28	1.54	0.08	0.66	100.00
KDR-5_04	S. 761	3.26	0.19	13.19	76.67	5.22	1.39	0.04	0.08	100.00
KDR-5_05	S. 762	3.36	0.03	12.50	78.00	4.93	0.67	0.09	0.63	100.00
KDR-5_06	S. 763	3.38	0.17	13.88	75.84	4.36	1.38	0.04	1.16	100.00
KDR-5_09	S. 766	2.77	0.17	12.58	77.57	4.99	0.93	0.23	0.84	100.00
KDR-5_10	S. 767	3.20	0.05	14.97	74.82	4.95	1.31	0.11	0.69	100.00
KDR-5_11	S. 768	2.58	0.03	12.65	78.65	5.34	0.75	0.04	0.23	100.00
KDR-5_13	S. 770	3.60	0.01	11.77	79.30	2.54	1.25	0.10	1.68	100.00
KDR-5_14	S. 771	3.79	0.09	12.54	79.33	3.04	1.17	0.01	0.07	100.00
KDR-5_16	S. 773	3.19	0.07	13.40	76.06	4.90	1.40	0.07	1.04	100.00
KDR-5_17	S. 774	2.33	0.20	11.66	79.99	3.37	2.19	0.04	0.25	100.00
KDR-5_19	S. 776	4.05	0.04	12.65	77.86	5.13	0.00	0.03	0.34	100.00
KDR-5_20	S. 777	3.83	0.09	10.29	82.60	2.59	0.00	0.18	0.45	100.00
KDR-5_21	S. 778	3.19	0.01	12.69	78.03	6.11	0.00	0.15	0.35	100.00
KDR-5_24-26	Av. S. 781-783	3.77	0.12	14.05	75.72	4.52	1.11	0.09	0.91	100.00
KDR-5_27	S. 784	3.01	0.00	11.74	80.53	4.53	0.79	0.24	0.07	100.00
KDR-5_30	S. 787	3.17	0.09	14.43	75.71	4.52	1.12	0.05	1.15	100.00
KDR-5_31	S. 788	3.53	0.12	12.80	77.17	4.93	0.65	0.06	1.10	100.00
KP-07A										
KP-07A_06	S. 795	3.09	0.05	12.73	77.99	5.06	0.73	0.16	0.57	100.00
KP-07A_07	S. 796	2.73	0.05	12.74	77.94	5.07	0.87	0.03	0.79	100.00
KP-07A_09	S. 798	2.46	0.18	12.65	78.30	4.64	1.21	0.02	0.65	100.00
KP-07A_10	S. 799	2.76	0.01	12.94	77.84	5.21	0.89	0.01	0.62	100.00

KP-07A_12, 13	Av. S. 801, 802	3.82	0.06	14.05	75.79	5.09	0.75	0.05	0.57	100.00
KP-07A_15, 16	Av. S. 804, 805	2.73	0.09	12.73	77.77	5.18	0.88	0.17	0.59	100.00
KP-07A_17	S. 806	2.68	0.09	12.42	78.15	5.17	0.92	0.16	0.59	100.00
KP-07A_18	S. 807	2.61	0.02	12.43	78.64	5.26	0.94	0.02	0.21	100.00
KP-07A_19	S. 808	2.63	0.17	12.57	77.46	5.32	0.90	0.33	0.66	100.00
KP-07A_20-22	Av. S. 809-811	3.20	0.06	13.09	77.64	4.48	0.94	0.01	0.58	100.00
KP-07A_24	S. 813	3.15	0.04	12.87	77.42	5.19	0.88	0.27	0.56	100.00
KP-07A_25	S. 814	2.78	0.07	13.75	76.81	4.56	1.45	0.06	0.61	100.00
KP-07A_26	S. 815	2.98	0.12	12.70	77.40	5.27	1.01	0.08	0.59	100.00
KP-07A_27	S. 816	3.28	0.11	12.76	77.35	5.18	0.80	0.11	0.66	100.00
KP-07A_28	S. 817	3.41	0.02	12.44	78.10	4.78	0.61	0.03	0.66	100.00
KP-07A_29	S. 818	3.31	0.03	12.81	77.89	4.49	1.04	0.00	0.46	100.00
KP-07A_30	S. 819	4.01	0.06	15.39	74.00	3.96	1.86	0.10	0.86	100.00
KP-07A_31	S. 820	3.91	0.17	13.13	79.37	1.92	1.12	0.01	0.53	100.00
KP-07A_32	S. 821	3.58	0.00	13.01	80.19	1.93	0.86	0.06	0.50	100.00
KP-07A_35	S. 824	2.78	0.13	12.48	77.71	5.39	0.87	0.08	0.76	100.00
KP-07A_37	S. 826	3.13	0.07	12.49	77.50	5.14	0.88	0.03	0.80	100.00
KP-07A_38	S. 827	3.05	0.10	12.54	76.70	5.07	0.70	0.07	0.41	100.00
KP-07A_39	S. 828	3.06	0.01	12.25	78.33	5.08	0.70	0.02	0.81	100.00
KP-07A_40	S. 829	2.70	0.00	12.49	78.29	5.15	0.62	0.33	0.48	100.00
KP-07A_41	S. 830	4.04	0.06	15.13	73.98	3.68	2.17	0.10	0.94	100.00
KP-07A_42	S. 831	3.14	0.08	12.45	78.64	5.13	0.60	0.17	0.34	100.00
KP-07A_43	S. 832	2.74	0.09	12.64	79.17	5.23	0.00	0.07	0.49	100.00
KP-07A_44	S. 833	3.31	0.12	12.68	77.33	5.03	1.00	0.05	0.54	100.00
KP-07A_46	S. 835	2.75	0.03	12.68	78.32	5.26	0.95	0.08	0.40	100.00
KP-07A_47	S. 836	3.34	0.06	12.56	77.70	4.90	0.96	0.08	0.46	100.00
KP-07A_48	S. 837	3.61	0.01	13.17	77.44	4.66	0.89	0.16	0.36	100.00
KP-07A_50	S. 839	3.25	0.05	12.87	77.63	5.01	0.91	0.21	0.44	100.00
B2-07B										
B2-07B_02-05	Av. S. 709-712	2.86	0.08	12.79	77.32	5.04	1.26	0.05	0.65	100.00
B2-07B_06-08	Av. S. 713-715	2.91	0.07	12.96	77.37	4.97	1.27	0.04	0.53	100.00
B2-07B_11	S. 718	2.72	0.09	12.73	77.70	5.04	1.30	0.01	0.49	100.00
B2-07B_12	S. 719	2.85	0.05	12.51	78.17	5.04	1.19	0.08	0.65	100.00
B2-07B_13	S. 720	2.75	0.02	12.72	77.61	5.33	1.21	0.14	0.46	100.00
B2-07B_15	S. 722	1.81	0.12	12.42	78.79	5.02	1.31	0.01	0.75	100.00
B2-07B_16	S. 723	2.58	0.09	12.47	77.99	5.24	1.15	0.11	0.40	100.00
B2-07B_17	S. 724	1.96	0.01	12.79	78.47	5.02	1.40	0.08	0.80	100.00
B2-07B_19	S. 726	2.75	0.07	13.16	76.67	5.36	1.24	0.13	0.66	100.00
B2-07B_20	S. 727	2.82	0.09	12.62	77.72	5.10	1.26	0.02	0.43	100.00
B2-07B_24	S. 731	2.81	0.15	12.71	77.16	5.18	1.35	0.06	0.74	100.00
B2-07B_25	S. 732	2.43	0.08	12.73	78.54	4.75	0.91	0.01	0.64	100.00
B2-07B_26	S. 733	2.52	0.09	12.94	77.54	5.12	1.28	0.09	0.60	100.00
B2-07B_29, 30	Av. S. 736, 737	2.77	0.01	12.97	77.27	5.21	1.09	0.15	0.57	100.00
B2-07B_32	S. 739	2.42	0.12	12.53	78.11	5.16	1.22	0.03	0.71	100.00
B2-07B_34	S. 741	2.46	0.08	13.16	78.25	4.03	1.30	0.01	0.77	100.00
B2-07B_35	S. 742	2.43	0.01	12.61	77.80	5.46	1.39	0.16	0.27	100.00
B2-07B_36	S. 743	2.09	0.03	12.91	78.01	5.07	1.43	0.21	0.66	100.00
B2-07B_38	S. 745	2.90	0.08	12.66	77.67	4.82	1.05	0.22	0.64	100.00
B2-07B_39	S. 746	2.26	0.04	12.48	77.98	5.11	1.21	0.22	0.81	100.00
B2-07B_40	S. 747	2.04	0.01	12.67	78.52	4.81	1.38	0.09	0.53	100.00
B2-07B_41	S. 748	2.43	0.05	12.21	78.58	4.98	1.19	0.13	0.83	100.00
B2-07B_43-46	Av. S. 750-753	2.86	0.08	12.04	78.71	4.73	1.01	0.00	0.60	100.00
B2-07B_48, 49	Av. S. 755, 756	2.60	0.07	13.50	77.13	4.81	1.37	0.01	0.87	100.00



B2-07B_50	S. 757	2.56	0.04	12.48	78.66	4.68	1.07	0.12	0.53	100.00
WLS-R-070818										
WLS-R_03,04	Av. S. 843, 844	2.94	0.05	12.75	78.18	4.59	1.15	0.02	0.51	100.00
WLS-R_06	S. 846	2.88	0.06	12.77	77.38	5.28	1.24	0.02	0.55	100.00
WLS-R_10	S. 850	2.78	0.04	12.97	77.46	5.23	1.04	0.01	0.67	100.00
WLS-R_11	S. 851	2.37	0.00	12.16	78.57	5.32	1.04	0.10	0.63	100.00
WLS-R_13	S. 853	2.61	0.06	12.57	78.04	5.12	1.31	0.13	0.52	100.00
WLS-R_14	S. 854	2.33	0.06	12.39	79.03	4.54	1.40	0.05	0.45	100.00
WLS-R_15	S. 855	2.32	0.00	12.19	78.92	4.98	1.11	0.04	0.53	100.00
WLS-R_19	S. 859	2.81	0.03	12.80	77.44	5.59	1.19	0.09	0.54	100.00
WLS-R_21,22	Av. S. 861, 862	2.57	0.08	12.45	78.31	4.81	1.27	0.17	0.51	100.00
WLS-R_23	S. 863	2.22	0.02	12.27	78.75	5.26	1.20	0.06	0.40	100.00
WLS-R_25	S. 865	3.26	0.17	15.56	74.37	3.65	2.47	0.13	0.40	100.00
WLS-R_26	S. 866	2.78	0.06	13.41	76.60	5.24	1.38	0.03	0.60	100.00
WLS-R_27	S. 867	2.41	0.01	12.43	78.09	5.45	0.90	0.18	0.59	100.00
WLS-R_28	S. 868	2.24	0.12	12.21	79.49	4.85	1.08	0.19	0.50	100.00
DVM1-1										
DVM1-1_01	S. 224	3.41	0.08	13.35	77.00	4.18	1.24	0.00	0.82	100.00
DVM1-1_02	S. 225	3.65	0.15	13.82	76.62	3.95	1.05	0.08	0.87	100.00
DVM1-1_04	S. 227	2.64	0.19	13.03	77.72	4.37	1.18	0.12	0.86	100.00
DVM1-1_05,06	Av. S. 228, 229	3.00	0.15	12.68	78.04	4.78	0.88	0.03	0.73	100.00
DVM1-1_10-12	Av. S. 233-235	3.74	0.07	13.22	76.55	4.39	0.99	0.05	0.97	100.00
DVM1-1_13	S. 236	3.71	0.37	14.82	74.37	4.04	2.10	0.01	1.00	100.00
DVM1-1_18	S. 241	3.27	0.19	13.52	76.58	4.12	1.42	0.07	0.95	100.00
DVM1-1_19	S. 242	3.06	0.14	13.16	76.59	4.65	1.17	0.08	0.74	100.00
DVM1-1_21	S. 244	2.82	0.09	13.92	76.76	4.16	1.40	0.02	1.10	100.00
DVM1-1_24	S. 247	3.36	0.12	13.56	76.68	4.23	1.21	0.01	0.90	100.00
DVM1-1_27	S. 250	2.71	0.12	13.37	76.59	4.13	1.64	0.12	0.85	100.00
DVM1-1_30	S. 253	3.26	0.11	13.08	77.82	4.11	1.10	0.09	0.64	100.00
DVM1-1_31,32	Av. S. 254, 255	3.69	0.09	12.32	78.29	3.84	0.97	0.02	0.86	100.00
DVM1-1_33	S. 256	3.04	0.22	14.16	75.26	4.49	1.46	0.10	1.40	100.00
ES080216-2										
ES_05	S. 262	2.53	0.19	12.77	76.90	5.22	1.09	0.01	1.36	100.00
ES_06	S. 263	3.14	0.10	12.38	78.27	4.31	0.90	0.10	1.08	100.00
ES_09	S. 266	3.27	0.27	14.45	74.08	4.30	1.65	0.01	2.10	100.00
ES_11	S. 268	3.08	0.23	12.83	76.89	4.54	0.95	0.05	1.61	100.00
ES_12	S. 269	3.21	0.21	13.13	76.56	4.26	1.40	0.22	1.06	100.00
ES_13-14	Av. S. 270, 271	3.03	0.05	12.26	78.12	4.81	0.77	0.08	0.87	100.00
ES_15	S. 272	2.82	0.10	12.31	77.93	5.01	0.93	0.05	0.84	100.00
ES_16	S. 273	2.81	0.12	12.85	77.28	4.68	1.29	0.01	1.01	100.00
ES_17	S. 274	3.10	0.06	12.44	78.17	4.94	0.93	0.02	0.57	100.00
ES_25	S. 282	3.56	0.14	13.52	75.94	4.43	1.01	0.08	1.35	100.00
ES_30	S. 287	2.47	0.22	13.66	76.48	4.24	1.41	0.14	1.52	100.00
ES_31	S. 288	3.66	0.10	13.97	75.72	4.22	1.45	0.12	1.02	100.00
ES_32	S. 289	3.36	0.14	12.95	76.98	4.65	0.91	0.08	0.93	100.00
LSB1-14										
LSB1-14_01	S. 583	3.32	0.16	13.48	77.07	4.24	1.19	0.05	0.61	100.00
LSB1-14_02-04	Av. S. 584-586	3.45	0.06	12.43	77.79	5.07	0.62	0.13	0.67	100.00
LSB1-14_09-11	Av. S. 591-593	3.66	0.14	14.16	75.84	4.01	1.43	0.07	0.71	100.00
LSB1-14_12	S. 594	3.56	0.15	14.25	75.63	3.98	1.52	0.13	0.81	100.00
LSB1-14_13	S. 595	3.59	0.04	14.09	75.48	4.24	1.73	0.08	0.79	100.00
LSB1-14_14	S. 596	3.48	0.05	12.32	77.39	4.69	0.95	0.12	0.54	100.00
LSB1-14_16	S. 598	3.62	0.11	12.29	78.28	4.10	0.86	0.01	0.91	100.00

LSB1-14_17	S. 599	3.24	0.02	12.53	77.84	5.20	0.57	0.16	0.43	100.00
LSB1-14_18	S. 600	2.75	0.15	13.01	78.81	4.25	0.97	0.00	0.40	100.00
LSB1-14_19, 20	Av. S. 601, 602	4.79	0.03	12.58	79.22	1.92	0.47	0.17	0.82	100.00
LSB1-14_23-25	Av. S. 605-607	3.58	0.06	12.41	78.57	4.06	0.85	0.07	0.58	100.00
LSB1-14_27	S. 609	2.86	0.23	13.44	77.26	4.04	1.55	0.13	0.67	100.00
LSB1-14_28	S. 610	3.21	0.14	13.35	77.17	4.06	1.17	0.29	0.90	100.00
LSB1-14_29	S. 611	3.54	0.12	14.38	75.91	3.82	1.66	0.01	0.62	100.00
LSB1-14_30	S. 612	3.69	0.16	13.02	77.41	3.95	1.22	0.08	0.55	100.00
LSB1-14_32, 33	Av. S. 614, 615	4.95	0.04	12.66	80.46	1.00	0.70	0.00	0.19	100.00
LSB1-14_35	S. 617	3.14	0.18	12.18	78.22	4.70	0.98	0.12	0.48	100.00
LSB1-14_37	S. 619	3.46	0.08	12.46	77.91	4.33	1.02	0.15	0.69	100.00
LSB1-14_38	S. 620	3.20	0.07	13.15	77.80	4.39	0.85	0.02	0.59	100.00
LSB1-14_41	S. 623	2.75	0.11	12.94	78.29	4.20	1.06	0.08	0.76	100.00
LSB1-14_42	S. 624	3.27	0.12	13.39	77.09	4.23	0.97	0.20	0.78	100.00
LSB1-14_43	S. 625	3.30	0.07	12.40	78.42	4.28	0.93	0.07	0.64	100.00
LSB1-14_44	S. 626	3.67	0.05	14.13	75.86	3.94	1.63	0.04	0.83	100.00
LSB1-14_45	S. 627	3.76	0.04	13.44	76.90	3.82	1.17	0.07	0.79	100.00
LSB1-14_46	S. 628	3.67	0.10	14.08	76.06	3.71	1.34	0.31	0.78	100.00
LSB1-14_47	S. 629	3.41	0.20	13.76	79.06	1.11	1.83	0.08	0.74	100.00
LSB1-14_48	S. 630	3.60	0.04	13.88	76.27	3.88	1.56	0.06	0.94	100.00
LSB1-14_49	S. 631	3.66	0.14	12.48	78.03	3.78	1.09	0.01	0.89	100.00
LSB1-14_50	S. 632	2.83	0.01	12.36	78.86	4.20	0.92	0.19	0.74	100.00
LSB1-14_52	S. 634	3.18	0.05	12.41	78.11	5.07	0.60	0.03	0.62	100.00
LSB1-14_53	S. 635	3.24	0.17	12.48	78.50	4.07	0.84	0.05	0.72	100.00
LSB1-14_54	S. 636	3.08	0.09	12.51	78.22	4.55	0.64	0.11	0.83	100.00
LSB1-14_55	S. 637	3.38	0.16	13.92	76.35	3.92	1.60	0.10	0.63	100.00
LSB1-14_56	S. 638	3.28	0.22	12.91	77.56	4.12	1.15	0.01	0.81	100.00
LSB1-14_58	S. 640	3.10	0.16	12.41	78.15	5.06	0.44	0.13	0.59	100.00
LSB1-14_60, 61	Av. S. 642, 643	3.59	0.08	12.68	77.90	4.16	0.93	0.02	0.66	100.00
LSB1-14_63-65	Av. S. 645-647	3.26	0.09	12.64	77.95	4.28	0.97	0.12	0.72	100.00
LSB1-14_66	S. 648	3.05	0.09	12.85	77.87	4.37	1.04	0.18	0.58	100.00
PPF2-17										
PPF2-17_02	S. 650	3.36	0.08	12.81	77.58	4.87	0.95	0.12	0.52	100.00
PPF2-17_04	S. 652	2.82	0.05	13.93	76.82	4.36	1.27	0.12	0.95	100.00
PPF2-17_07-09	Av. S. 655-657	3.14	0.09	12.50	78.43	4.11	0.95	0.15	0.68	100.00
PPF2-17_13	S. 661	3.56	0.09	13.37	77.15	4.20	1.14	0.00	0.55	100.00
PPF2-17_04 (R2)	S. 55	3.40	0.00	12.26	77.99	5.03	0.71	0.00	0.69	100.00
PPF2-17_14-16	Av. S. 662-664	3.29	0.07	12.55	78.02	4.50	0.92	0.07	0.62	100.00
PPF2-17_19,20	Av. S. 667, 668	3.47	0.07	13.10	77.11	4.71	0.89	0.00	0.67	100.00
PPF2-17_21, 22	Av. S. 669, 670	3.36	0.04	12.11	77.94	5.15	0.66	0.02	0.81	100.00
PPF2-17_23	S. 671	3.52	0.15	12.61	78.37	4.07	0.96	0.05	0.38	100.00
PPF2-17_25, 26	Av. S. 673, 674	3.36	0.10	12.51	78.57	4.08	0.94	0.03	0.53	100.00
PPF2-17_02,03 (R2)	Av. S. 53, 54	2.90	0.00	12.61	78.50	4.84	0.91	0.00	0.55	100.00
PPF2-17_05 (R2)	S. 56	3.00	0.00	14.00	78.35	4.03	0.91	0.00	0.00	100.00
PPF2-17_07 (R2)	S. 58	3.47	0.00	12.59	78.79	4.22	0.96	0.00	0.00	100.00
ST1-03										
ST1-03_07, 08	Av. S. 681, 682	2.86	0.02	13.23	77.83	4.83	0.73	0.02	0.49	100.00
ST1-03_12	S. 686	2.63	0.04	13.06	77.61	5.28	1.12	0.06	0.30	100.00
ST1-03_15-17	Av. S. 689-691	3.21	0.03	12.87	78.83	3.08	1.92	0.10	0.02	100.00
ST1-03_19	S. 693	3.69	0.00	12.86	79.09	2.78	1.83	0.02	0.03	100.00
ST1-03_21	S. 695	2.53	0.32	13.56	75.72	5.11	1.53	0.12	1.27	100.00
ST1-03_10 (R2)	S. 68	2.70	0.00	13.84	76.17	5.21	1.33	0.00	0.87	100.00
ST1-03_22	S. 696	2.35	0.05	13.16	77.44	5.43	1.12	0.16	0.54	100.00

ST1-03_09 (R2)	S. 67	3.10	0.00	13.43	76.90	5.19	1.40	0.00	0.00	100.00
ST1-03_28	S. 702	2.37	0.15	13.08	77.04	5.51	1.17	0.22	0.64	100.00
ST1-03_02 (R2)	S. 60	2.29	0.00	12.04	79.14	6.18	0.63	0.00	0.00	100.00
ST1-03_05,06 (R2)	Av. S. 63, 64	2.78	0.00	13.55	75.48	4.73	1.70	0.00	1.66	100.00
ST1-03_08 (R2)	S. 66	2.62	0.00	12.84	77.92	5.03	1.07	0.00	0.59	100.00
ST1-03_11 (R2)	S. 69	3.05	0.00	14.27	75.39	4.31	1.60	0.00	1.41	100.00
EMC080216-1										
EMC_01	S. 399	3.80	0.15	12.52	77.91	4.73	0.00	0.07	0.87	100.00
EMC_06	S. 404	3.80	0.86	14.98	69.52	5.95	1.02	0.26	3.66	100.00
EMC_06 (R2)	S. 146	5.18	0.00	14.60	75.81	2.67	1.74	0.00	0.00	100.00
EMC_11	S. 409	4.03	0.01	13.29	74.93	4.50	0.00	0.16	3.43	100.00
EMC_12-14	Av. S. 410-412	3.23	0.09	13.22	79.16	3.34	0.90	0.00	0.13	100.00
EMC_02 (R2)	S. 142	3.77	0.00	13.88	76.52	4.50	0.64	0.00	0.75	100.00
EMC_03 (R2)	S. 143	4.08	0.00	14.57	75.24	5.45	0.69	0.00	0.00	100.00
EMC_04 (R2)	S. 144	3.67	0.00	14.32	75.97	5.24	0.88	0.00	0.00	100.00
EMC_05 (R2)	S. 145	2.13	0.00	15.33	71.37	9.75	0.52	0.00	0.93	100.00
EMC_07 (R2)	S. 147	2.87	0.00	12.45	78.74	5.51	0.60	0.00	0.00	100.00
EMC_08 (R2)	S. 148	3.34	0.00	12.31	78.82	5.01	0.57	0.00	0.00	100.00
EMC_09 (R2)	S. 149	2.29	0.00	12.64	78.66	5.63	0.98	0.00	0.00	100.00
EMC_10 (R2)	S. 150	2.91	0.00	12.37	77.72	5.11	1.11	0.00	0.79	100.00
EMC_11 (R2)	S. 151	3.26	0.00	12.63	78.52	5.21	0.47	0.00	0.00	100.00
KC061517-1										
KC_01-06	Av. S. 560-565	2.47	0.05	12.48	77.71	5.71	1.09	0.02	0.50	100.00
KC_07	S. 566	2.50	0.01	12.88	76.62	6.02	1.20	0.14	0.66	100.00
KC061517-1_02 (R2)	S. 47	2.73	0.00	12.39	77.20	5.86	0.75	0.00	1.17	100.00
KC_08	S. 567	2.96	0.17	12.13	78.56	4.83	0.77	0.07	0.56	100.00
KC_16, 19	Av. S. 575, 578	4.58	0.06	12.45	79.26	2.27	0.71	0.03	0.66	100.00
KC061517-1_04 (R2)	S. 49	2.85	0.00	12.78	77.56	5.46	0.98	0.00	0.00	100.00
KC_22	S. 581	3.33	0.12	13.11	76.77	4.76	1.14	0.03	0.85	100.00
KC_23	S. 582	2.90	0.04	12.06	78.34	5.21	0.57	0.20	0.69	100.00
KC061517-1_06 (R2)	S. 51	3.26	0.00	13.21	77.69	5.03	1.10	0.00	0.00	100.00
Hadro Hill										
HH_03	S. 381	2.95	0.10	12.36	77.08	5.31	0.93	0.30	0.99	100.00
HH_04	S. 382	2.89	0.17	12.47	77.04	5.19	0.82	0.07	1.16	100.00
HH_06	S. 384	2.84	0.17	12.11	77.45	5.22	0.96	0.02	1.27	100.00
HH_07	S. 385	2.78	0.01	12.08	79.81	5.03	0.00	0.21	0.80	100.00
HH_08	S. 386	2.97	0.04	12.16	78.23	5.40	0.68	0.06	0.75	100.00
HH_09,10	Av. S. 387, 388	3.26	0.01	12.42	77.97	5.12	0.60	0.01	0.69	100.00
HH_11	S. 389	3.48	0.04	12.25	78.01	5.25	0.56	0.07	0.50	100.00
HadroHill_02 (R2)	S. 117	2.72	0.00	11.92	78.91	4.87	0.82	0.00	0.84	100.00
HadroHill_04 (R2)	S. 119	2.61	0.00	12.02	78.09	5.24	0.77	0.00	1.39	100.00
HadroHill_05 (R2)	S. 120	2.48	0.00	11.83	79.29	5.84	0.63	0.00	0.00	100.00
HadroHill_06 (R2)	S. 121	2.74	0.00	12.07	77.94	5.92	0.65	0.00	0.70	100.00
HadroHill_07 (R2)	S. 122	2.70	0.27	12.71	76.11	5.86	1.11	0.00	1.26	100.00
HadroHill_09,10 (R2)	Av. S. 124, 125	3.25	0.00	12.86	77.27	5.12	0.77	0.00	0.77	100.00
HadroHill_12-14 (R2)	Av. S. 127-129	2.80	0.25	12.88	76.74	6.08	0.80	0.00	0.63	100.00
HadroHill_15 (R2)	S. 130	3.18	0.00	13.10	77.03	5.29	0.76	0.00	0.67	100.00
HadroHill_16 (R2)	S. 131	3.26	0.00	12.16	78.77	5.34	0.51	0.00	0.00	100.00
HadroHill_17 (R2)	S. 132	2.68	0.00	12.13	78.60	5.81	0.81	0.00	0.00	100.00
HadroHill_18 (R2)	S. 133	3.42	0.00	12.18	77.93	5.32	0.50	0.00	0.68	100.00
HadroHill_19 (R2)	S. 134	3.02	0.00	13.04	77.64	5.28	1.04	0.00	0.00	100.00
HadroHill_20 (R2)	S. 135	2.98	0.25	13.64	75.75	4.79	1.34	0.00	1.29	100.00
HadroHill_21 (R2)	S. 136	3.02	0.00	13.51	75.54	4.95	1.51	0.00	1.52	100.00

HadroHill_22 (R2)	S. 137	3.02	0.00	11.82	78.79	5.22	0.50	0.00	0.73	100.00
HadroHill_23 (R2)	S. 138	2.70	0.00	11.85	78.76	5.24	0.77	0.00	0.82	100.00
HadroHill_24 (R2)	S. 139	2.85	0.00	12.72	76.89	5.64	1.00	0.00	0.93	100.00
HadroHill_25 (R2)	S. 140	2.57	0.00	12.51	78.88	4.90	0.71	0.00	0.69	100.00
IL082717-1										
IL_05	S. 511	2.76	0.12	12.01	78.32	5.43	0.65	0.04	0.77	100.00
IL_06	[1] S. 512	3.97	0.24	13.68	75.18	4.43	1.32	0.04	1.24	100.00
IL_20	S. 526	2.40	0.08	12.34	77.49	5.59	1.11	0.01	1.04	100.00
IL_22	S. 528	2.79	0.21	11.98	78.20	4.78	0.97	0.10	1.00	100.00
IL_25	S. 531	3.65	0.15	13.82	75.53	4.62	1.25	0.08	1.14	100.00
IL_26-28	Av. S. 532-534	4.20	0.10	12.84	78.87	1.91	1.01	0.05	1.05	100.00
IL_30	S. 536	3.08	0.05	12.39	78.30	4.51	0.79	0.25	0.74	100.00
IL_31	S. 537	2.88	0.20	12.57	78.11	4.39	0.97	0.10	0.84	100.00
IL_32, 33	Av. S. 538, 539	2.98	0.11	12.25	78.30	4.56	0.89	0.14	0.77	100.00
IL_34-36	Av. S. 540-542	3.15	0.12	12.39	78.11	4.65	1.00	0.08	0.56	100.00
IL_37-39	Av. S. 543-545	3.62	0.14	13.56	75.96	4.63	1.24	0.05	0.82	100.00
IL_40	S. 546	3.48	0.03	14.01	76.02	4.45	1.13	0.14	0.80	100.00
IL_41	S. 547	3.76	0.22	13.99	75.36	4.14	1.53	0.03	0.99	100.00
IL_42,43	Av. S. 548, 549	3.14	0.08	13.00	76.86	4.98	1.13	0.08	0.87	100.00
IL_44-46	Av. S. 550-552	3.72	0.19	14.18	74.94	4.30	1.63	0.07	0.95	100.00
IL_47	S. 553	3.41	0.03	13.37	76.89	4.19	1.06	0.07	0.98	100.00
IL_48	S. 554	3.34	0.19	14.55	75.10	4.13	1.66	0.06	1.05	100.00
IL_49	S. 555	3.11	0.18	13.46	76.72	4.32	1.16	0.10	1.10	100.00
IL_50	S. 556	3.70	0.17	13.39	76.26	4.31	1.11	0.16	0.96	100.00
IL_51	S. 557	3.34	0.14	14.10	75.48	4.37	1.40	0.06	1.19	100.00
Plateau										
Plateau_02,03	Av. S. 336, 337	2.77	0.01	12.47	78.89	4.81	0.81	0.05	0.38	100.00
Plateau_02 (R2)	S. 71	3.50	0.00	13.66	76.07	4.26	1.41	0.00	1.21	100.00
Plateau_06	S. 340	3.16	0.00	13.91	76.21	4.28	1.36	0.26	0.90	100.00
Plateau_09,10	Av. S. 343, 344	4.24	0.02	15.95	75.45	1.96	1.90	0.05	0.54	100.00
Plateau_11,12	Av. S. 345, 346	3.75	0.06	15.85	75.33	1.88	1.49	0.12	1.56	100.00
Plateau_13	S. 347	2.50	0.04	12.38	78.24	4.87	1.00	0.12	1.25	100.00
Plateau_14	S. 348	3.33	0.02	12.86	80.99	1.29	0.63	0.06	0.92	100.00
Plateau_18	S. 352	3.09	0.06	12.29	78.12	4.49	1.00	0.07	0.92	100.00
Plateau_24	S. 358	3.33	0.06	12.50	77.86	4.75	0.82	0.08	0.67	100.00
Plateau_26	S. 360	3.58	0.01	12.80	76.68	4.70	0.83	0.20	1.24	100.00
Plateau_03 (R2)	S. 72	3.46	0.00	12.83	78.22	4.69	0.83	0.00	0.00	100.00
Plateau_07 (R2)	S. 76	3.86	0.00	13.53	76.27	4.57	1.08	0.00	0.95	100.00
Plateau_08 (R2)	S. 77	3.48	0.00	13.30	76.47	4.87	0.75	0.00	1.18	100.00
Plateau_09 (R2)	S. 78	3.40	0.00	13.53	76.66	4.84	0.84	0.00	0.94	100.00
Plateau_10 (R2)	S. 79	3.19	0.00	12.69	77.91	4.86	0.68	0.00	0.70	100.00
Plateau_11 (R2)	S. 80	3.12	0.00	12.51	78.57	5.03	0.00	0.00	0.85	100.00
Plateau_13 (R2)	S. 82	3.76	0.00	13.22	76.84	4.39	0.89	0.00	0.96	100.00
PlateauPuck_02 (R2)	S. 153	3.50	0.00	13.06	76.86	4.84	0.83	0.00	0.90	100.00
PlateauPuck_03 (R2)	S. 154	2.84	0.00	12.58	77.69	4.89	0.85	0.00	1.54	100.00
PlateauPuck_04 (R2)	S. 155	3.47	0.00	12.52	78.47	4.82	0.00	0.00	0.77	100.00
PlateauPuck_05 (R2)	S. 156	2.82	0.00	12.42	78.14	5.06	0.74	0.00	0.83	100.00
PlateauPuck_07 (R2)	S. 158	2.87	0.00	13.46	76.81	4.66	1.16	0.00	1.09	100.00
PlateauPuck_08 (R2)	S. 159	3.01	0.00	13.72	76.20	4.77	1.22	0.00	1.08	100.00
PlateauPuck_09 (R2)	S. 160	3.76	0.00	12.98	80.08	1.59	0.70	0.00	0.91	100.00
PlateauPuck_10 (R2)	S. 161	2.99	0.00	12.64	77.91	4.83	0.77	0.00	1.10	100.00
PlateauPuck_11 (R2)	S. 162	3.84	0.00	13.07	78.81	2.25	0.92	0.00	1.15	100.00
PlateauPuck_14 (R2)	S. 165	3.84	0.00	14.49	76.02	4.42	1.28	0.00	0.00	100.00

PlateauPuck_15 (R2)	S. 166	3.34	0.00	13.14	76.79	4.58	0.96	0.00	1.29	100.00
PlateauPuck_18 (R2)	S. 169	2.71	0.00	14.07	76.19	4.65	1.32	0.00	1.20	100.00
PlateauPuck_19 (R2)	S. 170	3.14	0.00	12.48	78.05	5.27	0.57	0.00	0.76	100.00
PlateauPuck_20 (R2)	S. 171	2.83	0.00	12.28	77.97	5.20	0.62	0.00	1.13	100.00
PlateauPuck_21 (R2)	S. 172	3.00	0.00	12.27	76.62	4.40	1.51	0.00	1.01	100.00
PlateauPuck_23 (R2)	S. 174	3.46	0.00	15.03	77.06	1.69	1.25	0.00	1.55	100.00
PlateauPuck_24 (R2)	S. 175	3.44	0.00	12.65	77.46	4.64	0.87	0.00	0.95	100.00
PlateauPuck_25,26 (R2)	Av. S. 176, 177	3.26	0.00	12.40	77.58	4.96	0.86	0.00	0.95	100.00
PlateauPuck_27 (R2)	S. 178	3.39	0.00	12.61	78.98	3.33	0.88	0.00	0.81	100.00
PlateauPuck_28 (R2)	S. 179	2.90	0.00	12.23	78.20	4.97	0.66	0.00	1.05	100.00
PlateauPuck_29 (R2)	S. 180	2.46	0.00	12.71	78.56	4.54	0.78	0.00	1.14	100.00
PlateauPuck_30 (R2)	S. 181	2.94	0.00	12.43	78.44	4.92	0.69	0.00	0.61	100.00
PlateauPuck_32 (R2)	S. 183	3.27	0.00	13.00	75.69	4.74	1.53	0.00	0.95	100.00
PlateauPuck_34 (R2)	S. 185	3.75	0.00	14.09	75.24	4.52	1.27	0.00	1.41	100.00
FS082717-1										
FS_08-11	Av. S. 498-501	3.98	0.02	13.24	76.17	4.76	0.71	0.16	0.99	100.00
FS_12	S. 502	3.40	0.08	12.55	78.14	4.80	0.47	0.02	0.75	100.00
FS_15	S. 505	3.78	0.05	13.60	76.17	4.58	0.64	0.11	1.10	100.00
FS_16	S. 506	3.17	0.02	12.12	78.76	4.66	0.49	0.06	0.81	100.00
NF082917-1										
NF_03	S. 416	3.15	0.16	13.29	76.71	5.20	1.24	0.02	0.48	100.00
NF_04	S. 417	2.83	0.08	13.41	77.62	5.12	1.02	0.05	0.29	100.00
NF_05-07	Av. S. 418-420	2.86	0.10	13.05	77.71	4.54	1.18	0.13	0.55	100.00
NF_08	S. 421	3.56	0.14	13.53	78.97	2.38	0.73	0.14	0.57	100.00
NF_09-11	Av. S. 422-424	3.22	0.24	13.95	76.09	4.03	1.85	0.14	0.50	100.00
NF_12	S. 425	3.19	0.29	13.91	76.77	3.35	1.87	0.15	0.54	100.00
NF_13	S. 426	2.78	0.08	13.28	77.53	5.08	0.83	0.03	0.48	100.00
NF_18	S. 431	2.92	0.02	12.35	78.30	4.96	1.05	0.02	0.50	100.00
NF_20	S. 433	3.16	0.24	13.07	78.10	4.73	0.00	0.27	0.49	100.00
NF_21	S. 434	3.42	0.01	13.17	77.39	4.81	0.66	0.34	0.44	100.00
NF_22	S. 435	2.84	0.10	13.51	77.75	4.81	0.83	0.14	0.25	100.00
NF_24-26	Av. S. 437-439	3.03	0.06	12.90	77.78	5.02	0.79	0.01	0.49	100.00
NF_28	S. 441	3.08	0.04	13.31	76.77	5.02	1.42	0.21	0.21	100.00
PR082917-1										
PR_01	S. 442	2.43	0.14	13.61	77.43	4.84	0.98	0.11	0.62	100.00
PR_07	S. 448	2.78	0.02	13.70	77.29	3.77	1.69	0.28	0.54	100.00
PR_08	S. 449	2.79	0.21	13.15	77.56	4.18	1.68	0.05	0.57	100.00
PR_09	S. 450	2.50	0.15	13.30	77.92	5.01	0.75	0.09	0.51	100.00
PR_10, 11	Av. S. 451, 452	2.87	0.07	13.40	76.78	5.29	1.27	0.07	0.47	100.00
PR_12	S. 453	3.56	0.04	13.38	76.85	4.17	1.33	0.03	0.63	100.00
PR_16	S. 457	2.49	0.13	14.14	76.68	4.12	2.16	0.01	0.40	100.00
PR_17	S. 458	3.65	0.04	13.88	76.05	4.16	2.08	0.06	0.48	100.00
PR_18	S. 459	3.29	0.08	12.85	77.04	5.07	1.18	0.05	0.84	100.00
PR_19	S. 460	3.21	0.15	13.20	77.45	4.71	0.71	0.18	0.45	100.00
PR_21	S. 462	2.36	0.14	12.67	78.38	4.68	1.13	0.06	0.75	100.00
PR_30	S. 471	3.01	0.19	13.32	76.47	5.51	0.60	0.20	1.08	100.00
PR_31	S. 472	3.24	0.03	14.19	75.23	4.33	2.38	0.18	0.83	100.00
PR_32	S. 473	2.61	0.09	13.02	79.40	4.62	0.00	0.07	0.32	100.00
PR_36	S. 477	3.25	0.04	13.57	77.14	4.51	1.06	0.25	0.32	100.00
PR_37	S. 478	3.50	0.11	13.60	76.45	4.63	1.16	0.10	0.72	100.00
PR_38	S. 479	3.19	0.16	13.48	76.32	5.10	1.00	0.04	0.74	100.00

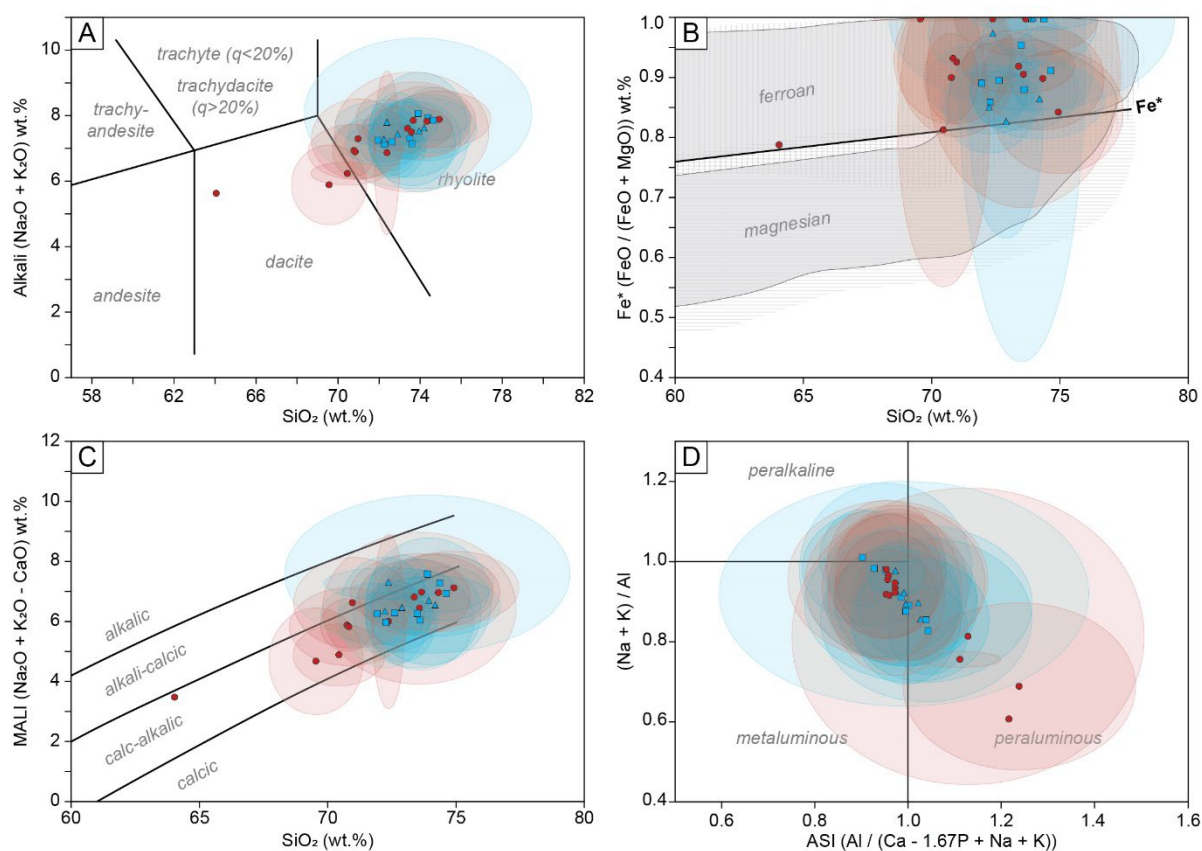


**Appendix C.6.10** Classification of glass inclusion data using the granitoid scheme of Frost et al. (2001).

Sample	SiO <sub>2</sub>	Alkali	Fe*	Fe* Type	MALI	MALI Type	ASI	ASI Type	Rock Type
Utah									
KBU-H	70.15	6.25	0.81	ferroan	5.06	calc-alkalic	1.13	peraluminous	two-mica granite
KBC-D	72.51	6.87	1.00	ferroan	5.98	calc-alkalic	1.13	peraluminous	two-mica granite
KBC-195	64.05	5.63	0.79	ferroan	3.46	calc-alkalic	1.22	peraluminous	two-mica granite
KBU-C	69.25	5.86	1.00	ferroan	4.58	calc-alkalic	1.24	peraluminous	two-mica granite
KBC-144	73.06	7.53	0.92	ferroan	6.60	calc-alkalic	0.97	metaluminous	granite
KBC-109	74.40	7.81	0.85	ferroan	6.94	calc-alkalic	0.97	metaluminous	granite
KBI-102	73.98	7.75	0.87	ferroan	6.86	calc-alkalic	0.98	metaluminous	granite
IM1442	73.25	7.64	0.97	ferroan	6.79	calc-alkalic	0.99	metaluminous	granite
KDR-5B	73.69	7.36	0.86	ferroan	6.43	calc-alkalic	0.99	metaluminous	granite
KP-07A	70.89	7.20	0.94	ferroan	6.35	alkali-calcic	0.99	metaluminous	ferrodiorite, syenite, granite
B2-07B	70.69	6.85	0.92	ferroan	5.73	calc-alkalic	0.97	metaluminous	granite
WLS-R	70.61	6.89	0.94	ferroan	5.74	calc-alkalic	0.97	metaluminous	granite
Montana									
DVMT-1	72.39	7.06	0.86	ferroan	5.86	calc-alkalic	1.04	peraluminous	two-mica granite
ES	71.91	7.17	0.91	ferroan	6.11	calc-alkalic	1.00	peraluminous	two-mica granite
LSB1-14	73.37	7.04	0.87	ferroan	6.02	calc-alkalic	1.05	peraluminous	two-mica granite
PPF2-17	72.57	7.22	0.90	ferroan	6.35	calc-alkalic	1.00	peraluminous	two-mica granite
ST1-03	73.33	7.22	0.94	ferroan	5.96	calc-alkalic	1.00	peraluminous	two-mica granite
EMC	73.15	8.28	0.90	ferroan	7.59	alkali-calcic	0.98	metaluminous	ferrodiorite, syenite, granite
KC	74.68	7.76	0.91	ferroan	6.88	calc-alkalic	0.95	metaluminous	granite
HH	74.22	7.88	0.95	ferroan	7.13	calc-alkalic	0.92	peralkaline	N/A (granite)
Alberta									
IL	74.20	7.50	0.88	ferroan	6.38	calc-alkalic	1.01	peraluminous	two-mica granite
Plateau	73.80	7.19	1.00	ferroan	6.30	calc-alkalic	1.07	peraluminous	two-mica granite
FS	72.52	7.77	1.00	ferroan	7.23	alkali-calcic	0.98	metaluminous	ferrodiorite, syenite, granite
NF	72.78	7.16	0.85	ferroan	6.19	calc-alkalic	1.04	peraluminous	two-mica granite
PR	72.27	7.14	0.85	ferroan	5.97	calc-alkalic	1.03	peraluminous	two-mica granite

Values represent the average for each sample after data recalculation based on the highest weight percent total for each sample within two standard deviations of the median. Samples are listed in general stratigraphic order.

**Appendix C.6.11** Glass inclusion major element data modelled after the granitoid classification scheme of Frost et al. (2001). Samples from northern field areas are shown in blue (Alberta = triangles, Montana = squares) and southern samples in red (circles). Ellipses represent two standard deviations except  $Fe^*$  (=1std).



\*Data for each sample were recalculated to the highest measured total within two standard deviations of the median to best align with the scheme of Frost et al. (2001).

**Appendix C.6.12** Zircon Lu-Hf data for samples from southern Utah after error in quadrature and normalisation procedures (see methods Chapter 6, section 6.7.1).

ID #	$\frac{^{176}\text{Lu}}{^{177}\text{Hf}}$	$\pm$ er.	$\frac{^{176}\text{Hf}}{^{177}\text{Hf}}$	$\pm$ er.	Age (Ma)	$e^{\lambda t} - 1$	Initial $\frac{^{176}\text{Hf}}{^{177}\text{Hf}}$	$\epsilon\text{Hf} (t = \text{now})$	$\epsilon\text{Hf} (t = \text{age})$	$\pm$ in $\epsilon\text{Hf}$ units
KBU-F-050818										
KBU-F_01	1.25E-03	2.63E-05	2.82E-01	3.06E-05	73.68	1.38E-03	2.82E-01	-17.13	-15.56	1.08
KBU-F_02	1.19E-03	9.96E-06	2.82E-01	2.96E-05	73.68	1.38E-03	2.82E-01	-16.31	-14.74	1.05
KBU-F_03	1.08E-03	1.45E-05	2.82E-01	3.08E-05	73.68	1.38E-03	2.82E-01	-15.93	-14.35	1.09
KBU-F_04	1.07E-03	4.71E-05	2.82E-01	2.94E-05	73.68	1.38E-03	2.82E-01	-16.46	-14.88	1.04
KBU-F_05	6.95E-04	3.50E-05	2.82E-01	2.91E-05	73.68	1.38E-03	2.82E-01	-16.78	-15.18	1.03
KBU-F_06	9.25E-04	5.47E-05	2.82E-01	2.95E-05	73.68	1.38E-03	2.82E-01	-17.02	-15.43	1.05
KBU-F_07	9.73E-04	2.45E-05	2.82E-01	2.95E-05	73.68	1.38E-03	2.82E-01	-15.60	-14.01	1.05
KBU-F_08	1.03E-03	2.00E-05	2.82E-01	2.99E-05	73.68	1.38E-03	2.82E-01	-17.62	-16.04	1.06
KBU-F_09	1.23E-03	2.24E-05	2.82E-01	3.08E-05	73.68	1.38E-03	2.82E-01	-17.77	-16.20	1.09
KBU-F_10	1.79E-03	7.13E-05	2.82E-01	3.26E-05	73.68	1.38E-03	2.82E-01	-14.98	-13.43	1.15
KBU-F_11	1.28E-03	1.03E-05	2.82E-01	2.95E-05	73.68	1.38E-03	2.82E-01	-15.79	-14.22	1.05

ID #	$\frac{^{176}\text{Lu}}{^{177}\text{Hf}}$	$\pm$ er.	$\frac{^{176}\text{Hf}}{^{177}\text{Hf}}$	$\pm$ er.	Age (Ma)	$e^{\lambda t} - 1$	Initial $\frac{^{176}\text{Hf}}{^{177}\text{Hf}}$	$\epsilon\text{Hf} (t = \text{now})$	$\epsilon\text{Hf} (t = \text{age})$	$\pm$ in $\epsilon\text{Hf}$ units
KBU-F_12	1.37E-03	1.51E-05	2.82E-01	3.06E-05	73.68	1.38E-03	2.82E-01	-16.68	-15.12	1.09
KBU-F_13	1.42E-03	1.90E-05	2.82E-01	2.91E-05	73.68	1.38E-03	2.82E-01	-17.07	-15.51	1.03
KBU-F_14	1.38E-03	1.47E-05	2.82E-01	2.94E-05	73.68	1.38E-03	2.82E-01	-17.12	-15.56	1.04
KBU-V-090818										
KBU-V_01	9.34E-04	1.86E-05	2.82E-01	2.98E-05	73.68	1.38E-03	2.82E-01	-16.47	-14.88	1.05
KBU-V_02	1.01E-03	2.71E-05	2.82E-01	2.98E-05	73.68	1.38E-03	2.82E-01	-15.29	-13.71	1.06
KBU-V_03	1.03E-03	3.86E-05	2.82E-01	2.99E-05	73.68	1.38E-03	2.82E-01	-17.34	-15.76	1.06
KBU-V_04	7.95E-04	2.52E-05	2.82E-01	2.84E-05	73.68	1.38E-03	2.82E-01	-17.16	-15.56	1.01
KBU-V_05	9.38E-04	1.61E-05	2.82E-01	3.06E-05	73.68	1.38E-03	2.82E-01	-16.77	-15.18	1.08
KBU-V_06	9.27E-04	3.61E-05	2.82E-01	2.95E-05	73.68	1.38E-03	2.82E-01	-16.57	-14.99	1.05
KBU-V_07	1.29E-03	6.18E-06	2.82E-01	3.06E-05	73.68	1.38E-03	2.82E-01	-16.57	-15.00	1.08
KBU-V_08	6.69E-04	2.89E-05	2.82E-01	2.88E-05	73.68	1.38E-03	2.82E-01	-15.48	-13.88	1.02
KBU-V_09	9.14E-04	1.46E-05	2.82E-01	3.06E-05	73.68	1.38E-03	2.82E-01	-19.34	-17.75	1.08
KBU-V_10	7.81E-04	1.82E-05	2.82E-01	3.66E-05	73.68	1.38E-03	2.82E-01	-17.23	-15.64	1.29
KBU-V_11	9.89E-04	2.94E-05	2.82E-01	2.97E-05	73.68	1.38E-03	2.82E-01	-16.46	-14.87	1.05
KBU-H-050818										
KBU-H_01	1.32E-03	1.86E-05	2.82E-01	1.74E-05	73.90	1.38E-03	2.82E-01	-15.89	-14.32	0.62
KBU-H_02	1.43E-03	1.60E-05	2.82E-01	1.63E-05	73.90	1.38E-03	2.82E-01	-16.05	-14.48	0.58
KBU-H_03	1.70E-03	2.10E-05	2.82E-01	1.77E-05	73.90	1.38E-03	2.82E-01	-15.78	-14.22	0.63
KBU-H_04	1.70E-03	2.02E-05	2.82E-01	1.88E-05	73.90	1.38E-03	2.82E-01	-15.96	-14.41	0.67
KBU-H_05	1.10E-03	4.28E-05	2.82E-01	1.51E-05	73.90	1.38E-03	2.82E-01	-15.30	-13.72	0.54
KBU-H_06	1.17E-03	8.89E-06	2.82E-01	1.79E-05	73.90	1.38E-03	2.82E-01	-27.17	-25.59	0.63
KBU-H_07	1.53E-03	1.09E-04	2.82E-01	1.55E-05	73.90	1.38E-03	2.82E-01	-15.79	-14.23	0.55
KBU-H_08	1.12E-03	1.76E-05	2.82E-01	1.62E-05	73.90	1.38E-03	2.82E-01	-17.47	-15.89	0.58
KBU-H_09	1.67E-03	2.70E-05	2.82E-01	1.46E-05	73.90	1.38E-03	2.82E-01	-21.84	-20.29	0.52
KBU-H_10	6.97E-04	9.30E-06	2.82E-01	1.38E-05	73.90	1.38E-03	2.82E-01	-25.09	-23.49	0.49
KBU-H_11	1.80E-03	1.62E-05	2.82E-01	1.90E-05	73.90	1.38E-03	2.82E-01	-26.49	-24.94	0.67
KBU-H_12	1.51E-03	1.77E-05	2.82E-01	1.89E-05	73.90	1.38E-03	2.82E-01	-27.99	-26.43	0.67
KBU-H_13	1.29E-03	1.05E-05	2.82E-01	1.70E-05	73.90	1.38E-03	2.82E-01	-32.30	-30.72	0.60
KBU-H_14	1.29E-03	6.01E-05	2.82E-01	1.96E-05	73.90	1.38E-03	2.82E-01	-33.98	-32.41	0.69
KBU-H_15	7.73E-04	3.14E-05	2.82E-01	1.90E-05	73.90	1.38E-03	2.82E-01	-37.59	-35.99	0.67
KBU-H_16	1.11E-03	1.52E-05	2.82E-01	1.49E-05	73.90	1.38E-03	2.82E-01	-16.27	-14.69	0.53
KBU-H_17	7.48E-04	1.03E-05	2.82E-01	1.40E-05	73.90	1.38E-03	2.82E-01	-15.61	-14.01	0.50
KBU-H_18	1.26E-03	6.86E-06	2.82E-01	1.70E-05	73.90	1.38E-03	2.82E-01	-17.10	-15.52	0.60
KBU-H_19	1.56E-03	2.15E-05	2.82E-01	1.91E-05	73.90	1.38E-03	2.82E-01	-17.40	-15.83	0.68
KBU-H_20	7.69E-04	9.49E-06	2.82E-01	1.60E-05	73.90	1.38E-03	2.82E-01	-15.39	-13.79	0.57
KBU-I-050818										
KBU-I_01	1.00E-03	1.45E-05	2.82E-01	1.78E-05	73.90	1.38E-03	2.82E-01	-15.34	-13.75	0.63
KBU-I_02	1.28E-03	4.72E-05	2.82E-01	1.82E-05	73.90	1.38E-03	2.82E-01	-16.18	-14.60	0.65
KBU-I_03	9.89E-04	2.72E-05	2.82E-01	1.42E-05	73.90	1.38E-03	2.82E-01	-16.70	-15.11	0.50
KBU-I_04	8.12E-04	1.82E-05	2.82E-01	1.64E-05	73.90	1.38E-03	2.82E-01	-16.70	-15.10	0.58
KBU-I_05	9.89E-04	1.91E-05	2.82E-01	1.72E-05	73.90	1.38E-03	2.82E-01	-16.12	-14.53	0.61
KBU-I_06	1.64E-03	8.79E-05	2.82E-01	1.54E-05	73.90	1.38E-03	2.82E-01	-16.39	-14.83	0.54
KBU-I_07	1.01E-03	2.25E-05	2.82E-01	1.70E-05	73.90	1.38E-03	2.82E-01	-17.17	-15.58	0.60
KBU-I_08	1.24E-03	1.88E-05	2.82E-01	2.19E-05	73.90	1.38E-03	2.82E-01	-16.60	-15.03	0.77
KBU-I_09	1.04E-03	1.74E-05	2.82E-01	1.39E-05	73.90	1.38E-03	2.82E-01	-17.65	-16.06	0.49
KBU-I_10	8.97E-04	1.61E-05	2.82E-01	1.68E-05	73.90	1.38E-03	2.82E-01	-17.74	-16.14	0.59
KBU-I_11	1.20E-03	2.06E-05	2.82E-01	1.61E-05	73.90	1.38E-03	2.82E-01	-15.56	-13.98	0.57
KBU-I_12	1.37E-03	9.84E-06	2.82E-01	1.47E-05	73.90	1.38E-03	2.82E-01	-16.43	-14.86	0.52
KBU-I_13	1.04E-03	3.99E-05	2.82E-01	1.63E-05	73.90	1.38E-03	2.82E-01	-16.38	-14.79	0.58

ID #	$\frac{^{176}\text{Lu}}{^{177}\text{Hf}}$	$\pm$ er.	$\frac{^{176}\text{Hf}}{^{177}\text{Hf}}$	$\pm$ er.	Age (Ma)	$e^{\lambda t} - 1$	Initial $\frac{^{176}\text{Hf}}{^{177}\text{Hf}}$	$\epsilon\text{Hf} (t = \text{now})$	$\epsilon\text{Hf} (t = \text{age})$	$\pm$ in $\epsilon\text{Hf}$ units
KBU-I_14	1.49E-03	1.38E-05	2.82E-01	1.67E-05	73.90	1.38E-03	2.82E-01	-17.77	-16.21	0.59
KBU-I_15	6.13E-04	3.60E-05	2.82E-01	1.64E-05	73.90	1.38E-03	2.82E-01	-15.15	-13.54	0.58
KBC-195										
KBC-195_01	2.05E-03	4.28E-05	2.82E-01	2.95E-05	75.23	1.41E-03	2.82E-01	-15.07	-13.51	1.05
KBC-195_02	2.64E-03	2.75E-05	2.82E-01	3.05E-05	75.23	1.41E-03	2.82E-01	-14.03	-12.49	1.08
KBC-195_03	2.59E-03	2.72E-05	2.82E-01	2.95E-05	75.23	1.41E-03	2.82E-01	-15.58	-14.04	1.04
KBC-195_04	2.12E-03	2.69E-05	2.82E-01	3.09E-05	75.23	1.41E-03	2.82E-01	-15.02	-13.45	1.09
KBC-195_05	2.23E-03	1.33E-05	2.82E-01	2.78E-05	75.23	1.41E-03	2.82E-01	-14.51	-12.95	0.98
KBC-195_06	2.89E-03	2.26E-05	2.82E-01	2.82E-05	75.23	1.41E-03	2.82E-01	-14.37	-12.85	1.00
KBC-195_07	3.01E-03	2.21E-04	2.82E-01	3.21E-05	75.23	1.41E-03	2.82E-01	-15.51	-13.99	1.14
KBC-195_08	2.17E-03	2.95E-05	2.82E-01	3.07E-05	75.23	1.41E-03	2.82E-01	-15.37	-13.81	1.09
KBC-195_09	3.30E-03	1.87E-05	2.82E-01	3.04E-05	75.23	1.41E-03	2.82E-01	-15.58	-14.08	1.08
KBC-195_10	2.22E-03	1.89E-05	2.82E-01	3.08E-05	75.23	1.41E-03	2.82E-01	-13.73	-12.17	1.09
KBC-195_11	2.24E-03	9.80E-05	2.82E-01	3.00E-05	75.23	1.41E-03	2.82E-01	-13.96	-12.41	1.06
KBC-195_12	2.77E-03	3.07E-05	2.82E-01	2.96E-05	75.23	1.41E-03	2.82E-01	-13.36	-11.83	1.05
KBC-195_13	3.44E-03	1.72E-05	2.82E-01	2.93E-05	75.23	1.41E-03	2.82E-01	-14.81	-13.31	1.04
KBC-195_14	1.98E-03	5.71E-05	2.82E-01	3.13E-05	75.23	1.41E-03	2.82E-01	-14.06	-12.49	1.11
KBC-195_15	1.82E-03	2.83E-05	2.82E-01	3.08E-05	75.23	1.41E-03	2.82E-01	-13.80	-12.22	1.09
KBC-D-030818										
KBC-D_01	2.07E-03	3.59E-05	2.82E-01	1.72E-05	75.23	1.41E-03	2.82E-01	-16.01	-14.45	0.61
KBC-D_02	2.27E-03	8.29E-05	2.82E-01	1.63E-05	75.23	1.41E-03	2.82E-01	-15.17	-13.61	0.58
KBC-D_03	2.61E-03	3.30E-05	2.82E-01	1.89E-05	75.23	1.41E-03	2.82E-01	-15.03	-13.49	0.67
KBC-D_04	3.71E-03	9.33E-06	2.82E-01	1.69E-05	75.23	1.41E-03	2.82E-01	-15.50	-14.02	0.60
KBC-D_05	1.49E-03	4.90E-05	2.82E-01	1.59E-05	75.23	1.41E-03	2.82E-01	-14.67	-13.08	0.56
KBC-D_06	3.79E-03	4.23E-05	2.82E-01	1.93E-05	75.23	1.41E-03	2.82E-01	-16.06	-14.58	0.68
KBC-D_07	2.07E-03	5.46E-05	2.82E-01	1.81E-05	75.23	1.41E-03	2.82E-01	-16.44	-14.87	0.64
KBC-D_08	2.99E-03	6.68E-05	2.82E-01	1.75E-05	75.23	1.41E-03	2.82E-01	-15.24	-13.72	0.62
KBC-D_09	2.19E-03	6.06E-05	2.82E-01	1.56E-05	75.23	1.41E-03	2.82E-01	-13.83	-12.27	0.55
KBC-D_10	2.10E-03	3.32E-05	2.82E-01	1.52E-05	75.23	1.41E-03	2.82E-01	-15.48	-13.92	0.54
KBC-D_11	2.46E-03	5.97E-05	2.82E-01	1.91E-05	75.23	1.41E-03	2.82E-01	-15.86	-14.31	0.68
KBC-D_12	2.37E-03	4.36E-05	2.82E-01	1.47E-05	75.23	1.41E-03	2.82E-01	-15.96	-14.41	0.52
KBC-D_13	2.36E-03	3.89E-05	2.82E-01	1.73E-05	75.23	1.41E-03	2.82E-01	-15.73	-14.18	0.61
KBC-D_14	1.70E-03	2.39E-05	2.82E-01	1.65E-05	75.23	1.41E-03	2.82E-01	-15.38	-13.79	0.59
KBC-D_15	2.61E-03	1.47E-05	2.82E-01	2.03E-05	75.23	1.41E-03	2.82E-01	-14.92	-13.38	0.72
KBU-C-310718										
KBU-C_01	2.18E-03	5.29E-05	2.82E-01	1.98E-05	75.23	1.41E-03	2.82E-01	-14.61	-13.05	0.70
KBU-C_03	2.31E-03	1.25E-05	2.82E-01	1.65E-05	75.23	1.41E-03	2.82E-01	-16.31	-14.76	0.58
KBU-C_04	2.37E-03	6.46E-06	2.82E-01	1.67E-05	75.23	1.41E-03	2.82E-01	-14.60	-13.05	0.59
KBU-C_05	2.01E-03	7.08E-05	2.82E-01	1.85E-05	75.23	1.41E-03	2.82E-01	-14.91	-13.34	0.65
KBU-C_06	3.02E-03	2.37E-05	2.82E-01	1.76E-05	75.23	1.41E-03	2.82E-01	-15.92	-14.40	0.63
KBU-C_07	2.62E-03	7.51E-05	2.82E-01	1.55E-05	75.23	1.41E-03	2.82E-01	-15.10	-13.56	0.55
KBU-C_08	2.69E-03	4.10E-05	2.82E-01	1.77E-05	75.23	1.41E-03	2.82E-01	-14.75	-13.22	0.63
KBU-C_09	2.24E-03	5.63E-05	2.82E-01	1.62E-05	75.23	1.41E-03	2.82E-01	-15.40	-13.84	0.57
KBU-C_10	1.74E-03	5.55E-05	2.82E-01	1.68E-05	75.23	1.41E-03	2.82E-01	-15.07	-13.49	0.60
KBU-C_11	1.82E-03	4.41E-05	2.82E-01	1.89E-05	75.23	1.41E-03	2.82E-01	-15.04	-13.46	0.67
KBU-C_12	1.75E-03	4.27E-05	2.82E-01	1.74E-05	75.23	1.41E-03	2.82E-01	-14.36	-12.78	0.62
KBC-144										
KBC-144_01	1.02E-03	2.37E-05	2.83E-01	3.00E-05	75.43	1.41E-03	2.83E-01	-3.88	-2.26	1.06
KBC-144_02	1.20E-03	1.12E-05	2.83E-01	2.99E-05	75.43	1.41E-03	2.83E-01	-3.44	-1.83	1.06
KBC-144_03	1.57E-03	3.22E-05	2.83E-01	3.02E-05	75.43	1.41E-03	2.83E-01	-5.10	-3.50	1.07

ID #	$\frac{^{176}\text{Lu}}{^{177}\text{Hf}}$	$\pm$ er.	$\frac{^{176}\text{Hf}}{^{177}\text{Hf}}$	$\pm$ er.	Age (Ma)	$e^{\lambda t} - 1$	Initial $\frac{^{176}\text{Hf}}{^{177}\text{Hf}}$	$\epsilon\text{Hf} (t = \text{now})$	$\epsilon\text{Hf} (t = \text{age})$	$\pm$ in $\epsilon\text{Hf}$ units
KBC-144_04	1.07E-03	1.72E-05	2.83E-01	2.92E-05	75.43	1.41E-03	2.83E-01	-4.39	-2.77	1.03
KBC-144_05	8.40E-04	3.73E-06	2.83E-01	2.96E-05	75.43	1.41E-03	2.83E-01	-4.52	-2.89	1.05
KBC-144_06	1.99E-03	1.08E-04	2.83E-01	3.20E-05	75.43	1.41E-03	2.83E-01	-3.66	-2.08	1.13
KBC-144_07	1.34E-03	7.82E-05	2.83E-01	3.04E-05	75.43	1.41E-03	2.83E-01	-3.16	-1.55	1.07
KBC-144_08	9.97E-04	2.05E-05	2.83E-01	2.99E-05	75.43	1.41E-03	2.83E-01	-3.32	-1.69	1.06
KBC-144_09	2.48E-03	1.07E-04	2.83E-01	3.30E-05	75.43	1.41E-03	2.83E-01	-2.82	-1.27	1.17
KBC-144_10	1.00E-03	1.80E-05	2.83E-01	2.93E-05	75.43	1.41E-03	2.83E-01	-3.25	-1.63	1.03
KBC-144_11	1.09E-03	1.60E-05	2.83E-01	2.86E-05	75.43	1.41E-03	2.83E-01	-3.78	-2.16	1.01
KBC-144_12	1.32E-03	3.46E-05	2.83E-01	2.99E-05	75.43	1.41E-03	2.83E-01	-3.67	-2.06	1.06
KBC-144_13	1.59E-03	1.63E-05	2.83E-01	2.99E-05	75.43	1.41E-03	2.83E-01	-3.66	-2.07	1.06
KBC-144_14	1.40E-03	5.61E-05	2.83E-01	3.09E-05	75.43	1.41E-03	2.83E-01	-2.24	-0.64	1.09
KBC-144_15	1.93E-03	8.33E-05	2.83E-01	3.02E-05	75.43	1.41E-03	2.83E-01	-4.80	-3.23	1.07
KBC-109										
KBC-109_01	1.39E-03	1.80E-05	2.83E-01	1.92E-05	75.61	1.41E-03	2.83E-01	-8.57	-6.96	0.68
KBC-109_02	2.69E-03	1.08E-04	2.83E-01	1.79E-05	75.61	1.41E-03	2.83E-01	-8.99	-7.45	0.63
KBC-109_03	1.56E-03	6.27E-05	2.83E-01	1.74E-05	75.61	1.41E-03	2.83E-01	-8.22	-6.62	0.62
KBC-109_04	1.59E-03	7.81E-05	2.82E-01	1.71E-05	75.61	1.41E-03	2.82E-01	-10.60	-9.00	0.60
KBC-109_05	2.08E-03	9.40E-05	2.83E-01	1.80E-05	75.61	1.41E-03	2.83E-01	-8.68	-7.11	0.64
KBC-109_06	1.40E-03	1.83E-05	2.83E-01	1.63E-05	75.61	1.41E-03	2.83E-01	-8.40	-6.79	0.58
KBC-109_07	1.69E-03	3.96E-05	2.83E-01	1.65E-05	75.61	1.41E-03	2.83E-01	-9.11	-7.52	0.58
KBC-109_08	1.33E-03	2.95E-05	2.83E-01	1.45E-05	75.61	1.41E-03	2.83E-01	-9.76	-8.15	0.51
KBC-109_09	1.25E-03	3.46E-06	2.83E-01	1.68E-05	75.61	1.41E-03	2.83E-01	-9.79	-8.18	0.60
KBI-102										
KBI-102_01	2.13E-03	9.78E-05	2.82E-01	1.78E-05	75.61	1.41E-03	2.82E-01	-10.32	-8.75	0.63
KBI-102_02	5.14E-03	1.81E-04	2.83E-01	2.15E-05	75.61	1.41E-03	2.82E-01	-9.97	-8.55	0.76
KBI-102_03	1.42E-03	1.78E-05	2.83E-01	1.52E-05	75.61	1.41E-03	2.82E-01	-10.03	-8.43	0.54
KBI-102_04	3.49E-03	9.19E-05	2.82E-01	2.20E-05	75.61	1.41E-03	2.82E-01	-11.02	-9.51	0.78
KBI-102_05	2.12E-03	3.93E-05	2.82E-01	2.05E-05	75.61	1.41E-03	2.82E-01	-12.05	-10.48	0.73
KBI-102_06	1.45E-03	6.90E-05	2.83E-01	2.17E-05	75.61	1.41E-03	2.83E-01	-8.68	-7.08	0.77
KBI-102_07	2.20E-03	1.34E-04	2.83E-01	1.83E-05	75.61	1.41E-03	2.83E-01	-6.17	-4.60	0.65
KBI-102_08	3.73E-03	4.59E-04	2.82E-01	2.16E-05	75.61	1.41E-03	2.82E-01	-11.42	-9.93	0.76
KBI-102_09	3.19E-03	1.31E-04	2.83E-01	1.84E-05	75.61	1.41E-03	2.83E-01	-9.57	-8.05	0.65
KBI-102_10	2.47E-03	7.97E-05	2.83E-01	2.30E-05	75.61	1.41E-03	2.83E-01	-8.19	-6.64	0.81
KBI-102_11	3.55E-03	4.52E-05	2.83E-01	2.57E-05	75.61	1.41E-03	2.83E-01	-9.63	-8.13	0.91
KBI-102_12	1.80E-03	2.21E-05	2.83E-01	1.92E-05	75.61	1.41E-03	2.83E-01	-8.39	-6.81	0.68
KBI-102_13	1.56E-03	5.35E-05	2.83E-01	1.90E-05	75.61	1.41E-03	2.83E-01	-8.75	-7.15	0.67
IM1442										
IM1442_01	1.57E-03	8.27E-05	2.83E-01	1.61E-05	75.66	1.41E-03	2.83E-01	-9.39	-7.79	0.57
IM1442_02	1.72E-03	3.72E-05	2.83E-01	2.06E-05	75.66	1.41E-03	2.83E-01	-9.48	-7.89	0.73
IM1442_03	2.58E-03	2.10E-05	2.83E-01	2.11E-05	75.66	1.41E-03	2.83E-01	-9.36	-7.81	0.75
IM1442_04	2.44E-03	9.63E-05	2.83E-01	2.00E-05	75.66	1.41E-03	2.83E-01	-9.53	-7.98	0.71
IM1442_05	3.69E-03	1.47E-04	2.83E-01	2.46E-05	75.66	1.41E-03	2.82E-01	-9.91	-8.42	0.87
IM1442_06	4.15E-03	1.70E-04	2.83E-01	2.24E-05	75.66	1.41E-03	2.83E-01	-8.80	-7.33	0.79
IM1442_07	4.79E-03	2.07E-04	2.83E-01	2.51E-05	75.66	1.41E-03	2.83E-01	-9.52	-8.08	0.89
IM1442_08	1.86E-03	6.21E-05	2.82E-01	1.50E-05	75.66	1.41E-03	2.82E-01	-10.27	-8.69	0.53
IM1442_09	1.93E-03	7.90E-05	2.83E-01	1.95E-05	75.66	1.41E-03	2.83E-01	-9.87	-8.29	0.69
IM1442_10	2.15E-03	7.54E-05	2.83E-01	1.78E-05	75.66	1.41E-03	2.83E-01	-8.61	-7.04	0.63
IM1442_11	1.97E-03	5.24E-05	2.83E-01	2.06E-05	75.66	1.41E-03	2.83E-01	-9.62	-8.04	0.73
IM1442_12	1.73E-03	4.03E-05	2.83E-01	1.84E-05	75.66	1.41E-03	2.82E-01	-10.01	-8.41	0.65
IM1442_13	2.64E-03	4.24E-05	2.83E-01	2.10E-05	75.66	1.41E-03	2.83E-01	-8.82	-7.27	0.74

ID #	$\frac{^{176}\text{Lu}}{^{177}\text{Hf}}$	$\pm$ er.	$\frac{^{176}\text{Hf}}{^{177}\text{Hf}}$	$\pm$ er.	Age (Ma)	$e^{\lambda t} - 1$	Initial $\frac{^{176}\text{Hf}}{^{177}\text{Hf}}$	$\epsilon\text{Hf} (t = \text{now})$	$\epsilon\text{Hf} (t = \text{age})$	$\pm$ in $\epsilon\text{Hf}$ units
IM1442_14	3.00E-03	4.65E-05	2.82E-01	2.22E-05	75.66	1.41E-03	2.82E-01	-10.11	-8.59	0.79
IM1442_15	2.30E-03	6.85E-05	2.83E-01	1.75E-05	75.66	1.41E-03	2.83E-01	-9.12	-7.55	0.62
KDR-5B										
KDR-5_01	5.79E-04	9.09E-06	2.82E-01	1.45E-05	76.26	1.42E-03	2.82E-01	-13.58	-11.92	0.51
KDR-5_02	7.60E-04	1.96E-05	2.82E-01	2.00E-05	76.26	1.42E-03	2.82E-01	-14.56	-12.91	0.71
KDR-5_03	7.21E-04	1.25E-05	2.82E-01	1.44E-05	76.26	1.42E-03	2.82E-01	-13.59	-11.93	0.51
KDR-5_04	6.99E-04	1.45E-05	2.82E-01	1.58E-05	76.26	1.42E-03	2.82E-01	-13.21	-11.55	0.56
KDR-5_05	1.31E-03	6.03E-05	2.82E-01	1.93E-05	76.26	1.42E-03	2.82E-01	-13.32	-11.70	0.68
KDR-5_06	1.06E-03	5.79E-06	2.82E-01	1.78E-05	76.26	1.42E-03	2.82E-01	-13.02	-11.38	0.63
KDR-5_07	9.27E-04	3.82E-05	2.82E-01	1.60E-05	76.26	1.42E-03	2.82E-01	-13.24	-11.59	0.57
KDR-5_08	1.06E-03	6.24E-05	2.82E-01	1.58E-05	76.26	1.42E-03	2.82E-01	-12.87	-11.23	0.56
KDR-5_09	8.66E-04	2.64E-05	2.82E-01	1.50E-05	76.26	1.42E-03	2.82E-01	-13.84	-12.19	0.53
KDR-5_10	1.27E-03	2.99E-05	2.82E-01	1.73E-05	76.26	1.42E-03	2.82E-01	-13.15	-11.52	0.61
KDR-5_11	1.11E-03	8.69E-06	2.82E-01	1.66E-05	76.26	1.42E-03	2.82E-01	-13.34	-11.70	0.59
KDR-5_12	1.00E-03	1.27E-05	2.82E-01	1.68E-05	76.26	1.42E-03	2.82E-01	-13.35	-11.71	0.59
KDR-5_13	9.65E-04	3.55E-05	2.82E-01	1.66E-05	76.26	1.42E-03	2.82E-01	-12.67	-11.03	0.59
KDR-5_14	9.81E-04	2.73E-05	2.82E-01	1.69E-05	76.26	1.42E-03	2.82E-01	-14.34	-12.70	0.60
KDR-5_15	4.91E-04	2.12E-05	2.82E-01	1.81E-05	76.26	1.42E-03	2.82E-01	-14.68	-13.01	0.64
KP-07A										
KP-07A_01	8.59E-04	4.12E-05	2.82E-01	2.07E-05	76.39	1.43E-03	2.82E-01	-11.54	-9.89	0.73
KP-07A_02	9.50E-04	1.83E-05	2.82E-01	1.69E-05	76.39	1.43E-03	2.82E-01	-13.34	-11.70	0.60
KP-07A_03	1.04E-03	3.51E-05	2.82E-01	2.06E-05	76.39	1.43E-03	2.82E-01	-12.03	-10.39	0.73
KP-07A_04	1.15E-03	8.95E-05	2.82E-01	1.54E-05	76.39	1.43E-03	2.82E-01	-11.11	-9.47	0.55
KP-07A_05	1.12E-03	5.11E-05	2.82E-01	1.91E-05	76.39	1.43E-03	2.82E-01	-11.47	-9.83	0.68
KP-07A_06	8.19E-04	1.99E-05	2.82E-01	1.69E-05	76.39	1.43E-03	2.82E-01	-11.84	-10.19	0.60
KP-07A_07	1.97E-03	2.72E-05	2.82E-01	2.05E-05	76.39	1.43E-03	2.82E-01	-11.94	-10.35	0.73
KP-07A_08	3.79E-04	3.45E-05	2.82E-01	1.65E-05	76.39	1.43E-03	2.82E-01	-10.67	-8.99	0.58
KP-07A_09	1.82E-03	6.48E-05	2.82E-01	2.11E-05	76.39	1.43E-03	2.82E-01	-11.79	-10.19	0.75
KP-07A_10	6.52E-04	1.96E-05	2.83E-01	1.79E-05	76.39	1.43E-03	2.83E-01	-9.04	-7.38	0.63
KP-07A_11	1.15E-03	4.47E-05	2.82E-01	1.66E-05	76.39	1.43E-03	2.82E-01	-11.63	-9.99	0.59
KP-07A_12	1.37E-03	5.54E-05	2.82E-01	2.03E-05	76.39	1.43E-03	2.82E-01	-11.52	-9.90	0.72
KP-07A_13	1.09E-03	3.76E-05	2.82E-01	1.90E-05	76.39	1.43E-03	2.82E-01	-11.70	-10.06	0.67
KP-07A_14	1.18E-03	5.46E-05	2.82E-01	1.82E-05	76.39	1.43E-03	2.82E-01	-12.46	-10.83	0.64
KP-07A_15	1.11E-03	7.47E-05	2.82E-01	2.30E-05	76.39	1.43E-03	2.82E-01	-10.91	-9.27	0.81
B2-07B										
B2-07B_01	1.29E-03	1.88E-05	2.83E-01	1.70E-05	81.48	1.52E-03	2.83E-01	-7.81	-6.07	0.60
B2-07B_02	5.70E-04	1.39E-05	2.82E-01	1.55E-05	81.48	1.52E-03	2.82E-01	-12.29	-10.51	0.55
B2-07B_03	7.98E-04	8.89E-06	2.82E-01	1.83E-05	81.48	1.52E-03	2.82E-01	-12.25	-10.49	0.65
B2-07B_04	6.45E-04	3.26E-05	2.83E-01	1.43E-05	81.48	1.52E-03	2.83E-01	-7.85	-6.08	0.51
B2-07B_05	6.59E-04	7.39E-05	2.83E-01	1.56E-05	81.48	1.52E-03	2.83E-01	-7.78	-6.01	0.55
B2-07B_06	5.23E-04	2.02E-05	2.82E-01	1.51E-05	81.48	1.52E-03	2.82E-01	-10.79	-9.01	0.53
B2-07B_07	6.03E-04	1.98E-05	2.83E-01	1.52E-05	81.48	1.52E-03	2.83E-01	-7.60	-5.82	0.54
B2-07B_08	9.00E-04	1.48E-05	2.83E-01	1.60E-05	81.48	1.52E-03	2.83E-01	-7.56	-5.80	0.57
B2-07B_09	5.87E-04	8.85E-06	2.83E-01	1.86E-05	81.48	1.52E-03	2.83E-01	-7.79	-6.02	0.66
B2-07B_10	8.36E-04	3.16E-05	2.83E-01	1.83E-05	81.48	1.52E-03	2.83E-01	-7.97	-6.21	0.65
B2-07B_11	8.52E-04	4.12E-06	2.83E-01	1.55E-05	81.48	1.52E-03	2.83E-01	-8.23	-6.47	0.55
B2-07B_12	7.52E-04	1.59E-05	2.83E-01	1.82E-05	81.48	1.52E-03	2.83E-01	-8.50	-6.73	0.64
B2-07B_13	6.59E-04	1.24E-05	2.82E-01	1.51E-05	81.48	1.52E-03	2.82E-01	-10.67	-8.89	0.53
B2-07B_14	6.42E-04	1.77E-05	2.83E-01	1.41E-05	81.48	1.52E-03	2.83E-01	-8.38	-6.61	0.50
B2-07B_15	8.48E-04	3.19E-05	2.82E-01	2.00E-05	81.48	1.52E-03	2.82E-01	-13.26	-11.49	0.71



ID #	$\frac{^{176}\text{Lu}}{^{177}\text{Hf}}$	$\pm$ er.	$\frac{^{176}\text{Hf}}{^{177}\text{Hf}}$	$\pm$ er.	Age (Ma)	$e^{\lambda t} - 1$	Initial $\frac{^{176}\text{Hf}}{^{177}\text{Hf}}$	$\epsilon\text{Hf} (t = \text{now})$	$\epsilon\text{Hf} (t = \text{age})$	$\pm$ in $\epsilon\text{Hf}$ units
WLS-R-070818										
WLS-R_01	9.06E-04	9.24E-06	2.83E-01	1.81E-05	81.47	1.52E-03	2.83E-01	-8.44	-6.68	0.64
WLS-R_02	5.40E-04	1.61E-05	2.82E-01	1.44E-05	81.47	1.52E-03	2.82E-01	-12.24	-10.46	0.51
WLS-R_03	1.09E-03	6.34E-06	2.83E-01	1.49E-05	81.47	1.52E-03	2.83E-01	-9.39	-7.64	0.53
WLS-R_04	8.26E-04	5.95E-06	2.83E-01	1.65E-05	81.47	1.52E-03	2.83E-01	-8.10	-6.34	0.58
WLS-R_05	8.86E-04	5.01E-05	2.83E-01	1.41E-05	81.47	1.52E-03	2.83E-01	-8.31	-6.55	0.50
WLS-R_06	6.07E-04	1.69E-05	2.83E-01	1.76E-05	81.47	1.52E-03	2.83E-01	-7.56	-5.78	0.62
WLS-R_07	6.61E-04	2.53E-05	2.83E-01	1.82E-05	81.47	1.52E-03	2.83E-01	-7.62	-5.84	0.64

**Appendix C.6.13** Zircon Lu-Hf data for samples from Montana after error in quadrature and normalisation procedures (see methods Chapter 6, section 6.7.1).

ID #	$\frac{^{176}\text{Lu}}{^{177}\text{Hf}}$	$\pm$ er.	$\frac{^{176}\text{Hf}}{^{177}\text{Hf}}$	$\pm$ er.	Age (Ma)	$e^{\lambda t} - 1$	Initial $\frac{^{176}\text{Hf}}{^{177}\text{Hf}}$	$\epsilon\text{Hf} (t = \text{now})$	$\epsilon\text{Hf} (t = \text{age})$	$\pm$ in $\epsilon\text{Hf}$ units
DVMT-1										
DVMT-1_01	1.56E-03	1.86E-05	2.82E-01	3.05E-05	74.50	1.39E-03	2.82E-01	-15.93	-14.35	1.08
DVMT-1_02	1.38E-03	6.96E-06	2.82E-01	2.98E-05	74.50	1.39E-03	2.82E-01	-16.59	-15.01	1.06
DVMT-1_03	2.34E-03	9.30E-05	2.82E-01	3.32E-05	74.50	1.39E-03	2.82E-01	-16.66	-15.12	1.18
DVMT-1_04	1.52E-03	2.57E-05	2.82E-01	3.18E-05	74.50	1.39E-03	2.82E-01	-16.16	-14.59	1.13
DVMT-1_05	9.87E-04	1.41E-05	2.82E-01	2.89E-05	74.50	1.39E-03	2.82E-01	-16.29	-14.68	1.02
DVMT-1_06	1.73E-03	4.88E-06	2.82E-01	3.08E-05	74.50	1.39E-03	2.82E-01	-16.85	-15.29	1.09
DVMT-1_07	1.51E-03	1.69E-05	2.82E-01	2.93E-05	74.50	1.39E-03	2.82E-01	-16.32	-14.75	1.04
DVMT-1_08	1.70E-03	1.60E-05	2.82E-01	3.03E-05	74.50	1.39E-03	2.82E-01	-14.83	-13.26	1.07
DVMT-1_09	1.96E-03	1.03E-04	2.82E-01	3.12E-05	74.50	1.39E-03	2.82E-01	-16.55	-14.99	1.10
DVMT-1_10	2.19E-03	2.55E-05	2.82E-01	3.10E-05	74.50	1.39E-03	2.82E-01	-16.29	-14.75	1.10
DVMT-1_11	1.79E-03	1.27E-05	2.82E-01	3.09E-05	74.50	1.39E-03	2.82E-01	-16.80	-15.24	1.09
DVMT-1_12	1.73E-03	1.00E-05	2.82E-01	3.19E-05	74.50	1.39E-03	2.82E-01	-17.16	-15.59	1.13
DVMT-1_13	1.64E-03	7.11E-05	2.82E-01	3.05E-05	74.50	1.39E-03	2.82E-01	-17.02	-15.45	1.08
DVMT-1_14	2.10E-03	8.87E-05	2.82E-01	3.31E-05	74.50	1.39E-03	2.82E-01	-15.13	-13.58	1.17
DVMT-1_15	3.46E-03	9.28E-05	2.82E-01	3.31E-05	74.50	1.39E-03	2.82E-01	-19.27	-17.79	1.17
ES080216-2										
ES080216-2_01	1.20E-03	2.54E-05	2.82E-01	3.06E-05	74.43	1.39E-03	2.82E-01	-16.79	-15.20	1.08
ES080216-2_02	1.10E-03	6.78E-06	2.82E-01	3.07E-05	74.43	1.39E-03	2.82E-01	-15.43	-13.83	1.09
ES080216-2_03	7.77E-04	6.11E-06	2.82E-01	2.95E-05	74.43	1.39E-03	2.82E-01	-17.84	-16.23	1.05
ES080216-2_04	1.34E-03	5.88E-05	2.82E-01	3.05E-05	74.43	1.39E-03	2.82E-01	-16.22	-14.63	1.08
ES080216-2_05	8.60E-04	2.26E-05	2.82E-01	3.08E-05	74.43	1.39E-03	2.82E-01	-15.69	-14.09	1.09
ES080216-2_06	1.43E-03	5.55E-05	2.82E-01	3.22E-05	74.43	1.39E-03	2.82E-01	-19.39	-17.81	1.14
ES080216-2_07	9.33E-04	1.99E-05	2.82E-01	3.15E-05	74.43	1.39E-03	2.82E-01	-19.90	-18.30	1.12
ES080216-2_08	5.78E-04	2.18E-05	2.82E-01	2.95E-05	74.43	1.39E-03	2.82E-01	-21.09	-19.47	1.04
ES080216-2_09	1.10E-03	2.36E-05	2.82E-01	3.16E-05	74.43	1.39E-03	2.82E-01	-19.04	-17.44	1.12
ES080216-2_10	1.16E-03	1.81E-05	2.82E-01	3.00E-05	74.43	1.39E-03	2.82E-01	-14.83	-13.24	1.06
ES080216-2_11	8.74E-04	9.22E-06	2.82E-01	2.99E-05	74.43	1.39E-03	2.82E-01	-20.80	-19.19	1.06
ES080216-2_12	1.51E-03	5.15E-05	2.82E-01	3.10E-05	74.43	1.39E-03	2.82E-01	-17.28	-15.70	1.10
ES080216-2_13	1.20E-03	1.94E-05	2.82E-01	3.08E-05	74.43	1.39E-03	2.82E-01	-19.80	-18.21	1.09
ES080216-2_14	9.75E-04	1.04E-05	2.82E-01	3.04E-05	74.43	1.39E-03	2.82E-01	-17.22	-15.62	1.08
ES080216-2_15	1.35E-03	3.08E-05	2.82E-01	3.06E-05	74.43	1.39E-03	2.82E-01	-19.52	-17.93	1.09
LSB-1-14										

ID #	$\frac{^{176}\text{Lu}}{^{177}\text{Hf}}$	$\pm$ er.	$\frac{^{176}\text{Hf}}{^{177}\text{Hf}}$	$\pm$ er.	Age (Ma)	$e^{\lambda t} - 1$	Initial $\frac{^{176}\text{Hf}}{^{177}\text{Hf}}$	$\epsilon\text{Hf} (t = \text{now})$	$\epsilon\text{Hf} (t = \text{age})$	$\pm$ in $\epsilon\text{Hf}$ units
LSB-1-14_01	1.92E-03	8.11E-05	2.82E-01	3.20E-05	75.24	1.41E-03	2.82E-01	-18.82	-17.24	1.13
LSB-1-14_02	1.61E-03	1.91E-05	2.82E-01	2.97E-05	75.24	1.41E-03	2.82E-01	-18.20	-16.61	1.05
LSB-1-14_03	1.47E-03	2.29E-05	2.82E-01	2.90E-05	75.24	1.41E-03	2.82E-01	-18.90	-17.30	1.03
LSB-1-14_04	7.87E-04	3.33E-05	2.82E-01	2.89E-05	75.24	1.41E-03	2.82E-01	-18.94	-17.31	1.02
LSB-1-14_05	9.71E-04	2.03E-05	2.82E-01	3.07E-05	75.24	1.41E-03	2.82E-01	-20.16	-18.54	1.09
LSB-1-14_06	1.20E-03	2.44E-05	2.82E-01	3.04E-05	75.24	1.41E-03	2.82E-01	-18.88	-17.28	1.08
LSB-1-14_07	2.41E-03	7.21E-05	2.82E-01	3.14E-05	75.24	1.41E-03	2.82E-01	-17.11	-15.57	1.11
LSB-1-14_08	1.26E-03	2.30E-05	2.82E-01	3.15E-05	75.24	1.41E-03	2.82E-01	-18.91	-17.31	1.12
LSB-1-14_09	1.43E-03	2.50E-05	2.82E-01	2.99E-05	75.24	1.41E-03	2.82E-01	-18.28	-16.68	1.06
LSB-1-14_10	1.29E-03	2.38E-05	2.82E-01	3.01E-05	75.24	1.41E-03	2.82E-01	-18.68	-17.07	1.07
LSB-1-14_11	2.10E-03	1.07E-04	2.82E-01	2.94E-05	75.24	1.41E-03	2.82E-01	-18.64	-17.08	1.04
LSB-1-14_12	2.34E-03	1.47E-04	2.82E-01	3.54E-05	75.24	1.41E-03	2.82E-01	-17.76	-16.21	1.26
LSB-1-14_13	1.82E-03	3.36E-05	2.82E-01	3.07E-05	75.24	1.41E-03	2.82E-01	-19.33	-17.75	1.09
LSB-1-14_14	1.73E-03	4.19E-05	2.82E-01	3.05E-05	75.24	1.41E-03	2.82E-01	-17.95	-16.37	1.08
LSB-1-14_15	1.42E-03	6.28E-05	2.82E-01	2.99E-05	75.24	1.41E-03	2.82E-01	-17.80	-16.20	1.06
PPF2-17										
PPF2-17_01	1.32E-03	4.59E-05	2.82E-01	2.93E-05	75.22	1.41E-03	2.82E-01	-17.27	-15.67	1.04
PPF2-17_02	1.28E-03	1.36E-05	2.82E-01	2.98E-05	75.22	1.41E-03	2.82E-01	-18.01	-16.41	1.05
PPF2-17_03	2.12E-03	2.17E-05	2.82E-01	3.06E-05	75.22	1.41E-03	2.82E-01	-17.15	-15.59	1.08
PPF2-17_04	1.96E-03	2.47E-05	2.82E-01	3.41E-05	75.22	1.41E-03	2.82E-01	-16.79	-15.22	1.21
PPF2-17_05	1.65E-03	1.11E-04	2.82E-01	3.18E-05	75.22	1.41E-03	2.82E-01	-17.02	-15.44	1.12
PPF2-17_06	1.18E-03	8.97E-05	2.82E-01	2.96E-05	75.22	1.41E-03	2.82E-01	-18.96	-17.35	1.05
PPF2-17_07	1.65E-03	2.76E-05	2.82E-01	3.11E-05	75.22	1.41E-03	2.82E-01	-18.86	-17.28	1.10
PPF2-17_08	7.94E-04	2.86E-05	2.82E-01	2.88E-05	75.22	1.41E-03	2.82E-01	-17.22	-15.60	1.02
PPF2-17_09	1.29E-03	4.03E-05	2.82E-01	3.18E-05	75.22	1.41E-03	2.82E-01	-18.14	-16.53	1.13
PPF2-17_10	1.41E-03	2.74E-05	2.82E-01	3.21E-05	75.22	1.41E-03	2.82E-01	-17.83	-16.24	1.14
PPF2-17_11	1.39E-03	1.94E-05	2.82E-01	3.23E-05	75.22	1.41E-03	2.82E-01	-18.39	-16.79	1.15
PPF2-17_12	1.66E-03	8.61E-05	2.82E-01	3.01E-05	75.22	1.41E-03	2.82E-01	-17.79	-16.21	1.07
PPF2-17_13	1.34E-03	4.85E-05	2.82E-01	3.11E-05	75.22	1.41E-03	2.82E-01	-17.21	-15.61	1.10
PPF2-17_14	1.56E-03	4.45E-05	2.82E-01	3.21E-05	75.22	1.41E-03	2.82E-01	-19.05	-17.46	1.14
PPF2-17_15	2.26E-03	2.71E-05	2.82E-01	2.99E-05	75.22	1.41E-03	2.82E-01	-18.49	-16.94	1.06
ST1-03										
ST1-03_01	2.54E-03	2.77E-05	2.82E-01	2.96E-05	76.33	1.43E-03	2.82E-01	-21.46	-19.90	1.05
ST1-03_02	1.42E-03	4.43E-05	2.82E-01	3.01E-05	76.33	1.43E-03	2.82E-01	-21.04	-19.42	1.07
ST1-03_03	1.06E-03	3.74E-05	2.82E-01	2.92E-05	76.33	1.43E-03	2.82E-01	-24.08	-22.44	1.03
ST1-03_04	9.56E-04	3.70E-05	2.82E-01	2.90E-05	76.33	1.43E-03	2.82E-01	-24.51	-22.87	1.03
ST1-03_05	1.19E-03	6.42E-06	2.82E-01	2.89E-05	76.33	1.43E-03	2.82E-01	-23.68	-22.05	1.03
ST1-03_06	1.80E-03	7.51E-05	2.82E-01	2.94E-05	76.33	1.43E-03	2.82E-01	-23.39	-21.79	1.04
ST1-03_07	1.43E-03	1.73E-05	2.82E-01	2.85E-05	76.33	1.43E-03	2.82E-01	-22.18	-20.56	1.01
ST1-03_08	2.03E-03	1.20E-04	2.82E-01	3.02E-05	76.33	1.43E-03	2.82E-01	-22.09	-20.50	1.07
ST1-03_09	8.12E-04	4.68E-05	2.82E-01	2.91E-05	76.33	1.43E-03	2.82E-01	-19.17	-17.51	1.03
ST1-03_10	3.84E-03	2.08E-04	2.82E-01	3.37E-05	76.33	1.43E-03	2.82E-01	-21.50	-20.00	1.19
ST1-03_11	1.88E-03	2.79E-05	2.82E-01	3.41E-05	76.33	1.43E-03	2.82E-01	-25.54	-23.95	1.21
ST1-03_12	2.06E-03	2.90E-05	2.82E-01	3.08E-05	76.33	1.43E-03	2.82E-01	-23.24	-21.65	1.09
ST1-03_13	4.19E-03	2.86E-04	2.82E-01	4.06E-05	76.33	1.43E-03	2.82E-01	-21.86	-20.38	1.44
ST1-03_14	1.48E-03	9.84E-05	2.82E-01	3.15E-05	76.33	1.43E-03	2.82E-01	-17.80	-16.18	1.12
ST1-03_15	1.39E-03	3.44E-05	2.82E-01	3.00E-05	76.33	1.43E-03	2.82E-01	-22.44	-20.81	1.06
EMC080216-1										
EMC080216-1_01	1.10E-03	5.11E-05	2.83E-01	1.68E-05	77.97	1.46E-03	2.83E-01	1.36	3.03	0.59

ID #	$\frac{^{176}\text{Lu}}{^{177}\text{Hf}}$	$\pm$ er.	$\frac{^{176}\text{Hf}}{^{177}\text{Hf}}$	$\pm$ er.	Age (Ma)	$e^{\lambda t} - 1$	Initial $\frac{^{176}\text{Hf}}{^{177}\text{Hf}}$	$\epsilon\text{Hf} (t = \text{now})$	$\epsilon\text{Hf} (t = \text{age})$	$\pm$ in $\epsilon\text{Hf}$ units
EMC080216-1_02	1.89E-03	8.03E-05	2.83E-01	1.76E-05	77.97	1.46E-03	2.83E-01	1.35	2.98	0.62
EMC080216-1_03	1.68E-03	4.90E-05	2.83E-01	1.88E-05	77.97	1.46E-03	2.83E-01	0.66	2.30	0.67
EMC080216-1_04	2.13E-03	9.87E-05	2.82E-01	2.03E-05	77.97	1.46E-03	2.82E-01	-14.02	-12.40	0.72
EMC080216-1_05	1.29E-03	2.73E-05	2.83E-01	1.73E-05	77.97	1.46E-03	2.83E-01	2.11	3.78	0.61
EMC080216-1_06	1.62E-03	6.94E-05	2.83E-01	2.01E-05	77.97	1.46E-03	2.83E-01	0.46	2.11	0.71
EMC080216-1_07	5.43E-04	4.24E-06	2.83E-01	1.60E-05	77.97	1.46E-03	2.83E-01	-9.76	-8.06	0.56
EMC080216-1_08	1.80E-03	1.58E-04	2.83E-01	1.67E-05	77.97	1.46E-03	2.83E-01	0.48	2.12	0.59
EMC080216-1_09	1.45E-03	5.25E-05	2.83E-01	1.88E-05	77.97	1.46E-03	2.83E-01	0.65	2.31	0.67
EMC080216-1_10	2.08E-03	3.24E-05	2.83E-01	1.96E-05	77.97	1.46E-03	2.83E-01	1.14	2.76	0.69
EMC080216-1_11	2.50E-03	5.70E-05	2.82E-01	1.68E-05	77.97	1.46E-03	2.82E-01	-20.12	-18.53	0.59
EMC080216-1_12	1.48E-03	2.51E-05	2.83E-01	2.08E-05	77.97	1.46E-03	2.83E-01	0.88	2.53	0.74
EMC080216-1_13	1.84E-03	3.46E-05	2.83E-01	2.09E-05	77.97	1.46E-03	2.83E-01	1.10	2.73	0.74
EMC080216-1_14	7.16E-04	1.36E-05	2.83E-01	2.10E-05	77.97	1.46E-03	2.83E-01	-8.14	-6.44	0.74
EMC080216-1_15	1.54E-03	6.46E-05	2.83E-01	2.03E-05	77.97	1.46E-03	2.83E-01	-8.00	-6.35	0.72
KC061517-1										
KC061517-1_01	7.87E-04	1.97E-05	2.83E-01	2.92E-05	78.59	1.47E-03	2.83E-01	-1.89	-0.19	1.03
KC061517-1_02	8.12E-04	1.62E-05	2.83E-01	3.05E-05	78.59	1.47E-03	2.83E-01	-3.79	-2.09	1.08
KC061517-1_03	1.02E-03	3.65E-05	2.83E-01	2.90E-05	78.59	1.47E-03	2.83E-01	-6.10	-4.41	1.03
KC061517-1_04	1.15E-03	2.13E-05	2.83E-01	3.09E-05	78.59	1.47E-03	2.83E-01	-4.14	-2.45	1.09
KC061517-1_05	2.00E-03	2.39E-05	2.83E-01	3.08E-05	78.59	1.47E-03	2.83E-01	-3.20	-1.56	1.09
KC061517-1_06	7.42E-04	1.75E-05	2.83E-01	2.92E-05	78.59	1.47E-03	2.83E-01	-4.13	-2.42	1.03
KC061517-1_07	1.72E-03	2.67E-05	2.83E-01	3.03E-05	78.59	1.47E-03	2.83E-01	-4.16	-2.50	1.07
KC061517-1_08	2.64E-03	6.82E-05	2.83E-01	3.19E-05	78.59	1.47E-03	2.83E-01	-6.39	-4.78	1.13
KC061517-1_09	1.36E-03	5.08E-05	2.83E-01	3.00E-05	78.59	1.47E-03	2.83E-01	-5.30	-3.63	1.06
KC061517-1_10	1.60E-03	5.85E-05	2.83E-01	3.20E-05	78.59	1.47E-03	2.83E-01	-4.70	-3.04	1.13
KC061517-1_11	1.17E-03	4.04E-05	2.83E-01	3.36E-05	78.59	1.47E-03	2.83E-01	-4.23	-2.54	1.19
KC061517-1_13	1.74E-03	1.03E-04	2.83E-01	3.48E-05	78.59	1.47E-03	2.83E-01	-4.25	-2.60	1.23
KC061517-1_14	1.11E-03	1.45E-05	2.83E-01	2.91E-05	78.59	1.47E-03	2.83E-01	-5.07	-3.38	1.03
KC061517-1_15	9.72E-04	1.93E-05	2.83E-01	3.02E-05	78.59	1.47E-03	2.83E-01	-5.63	-3.93	1.07
KC061517-1_16	2.44E-03	7.32E-05	2.83E-01	3.10E-05	78.59	1.47E-03	2.83E-01	-3.00	-1.39	1.10
KC061517-1_17	1.36E-03	4.41E-05	2.83E-01	3.13E-05	78.59	1.47E-03	2.83E-01	-3.17	-1.50	1.11
Hadro Hill										
HadroHill_01	7.73E-04	1.48E-05	2.83E-01	1.70E-05	78.60	1.47E-03	2.83E-01	-4.21	-2.50	0.60
HadroHill_02	7.55E-04	1.04E-05	2.83E-01	1.80E-05	78.60	1.47E-03	2.83E-01	-4.33	-2.62	0.64
HadroHill_03	9.26E-04	2.20E-05	2.83E-01	1.64E-05	78.60	1.47E-03	2.83E-01	-5.83	-4.13	0.58
HadroHill_04	9.94E-04	4.74E-05	2.83E-01	1.68E-05	78.60	1.47E-03	2.83E-01	-4.75	-3.06	0.59
HadroHill_05	2.09E-03	4.78E-05	2.83E-01	1.67E-05	78.60	1.47E-03	2.83E-01	-4.64	-3.00	0.59
HadroHill_06	5.43E-04	9.01E-06	2.83E-01	1.58E-05	78.60	1.47E-03	2.83E-01	-4.02	-2.31	0.56
HadroHill_07	1.08E-03	2.09E-05	2.83E-01	1.75E-05	78.60	1.47E-03	2.83E-01	-3.87	-2.19	0.62
HadroHill_08	1.37E-03	6.84E-05	2.83E-01	1.85E-05	78.60	1.47E-03	2.83E-01	-3.87	-2.20	0.66
HadroHill_09	2.54E-03	9.96E-05	2.83E-01	2.05E-05	78.60	1.47E-03	2.83E-01	-6.84	-5.23	0.73
HadroHill_10	2.23E-03	6.12E-05	2.83E-01	2.09E-05	78.60	1.47E-03	2.83E-01	-4.99	-3.36	0.74
HadroHill_11	1.44E-03	2.04E-05	2.83E-01	1.80E-05	78.60	1.47E-03	2.83E-01	-5.04	-3.37	0.64
HadroHill_12	1.53E-03	2.03E-05	2.83E-01	1.82E-05	78.60	1.47E-03	2.83E-01	-4.96	-3.30	0.64
HadroHill_13	1.02E-03	4.37E-05	2.83E-01	1.65E-05	78.60	1.47E-03	2.83E-01	-4.39	-2.70	0.58
HadroHill_14	1.09E-03	1.73E-05	2.83E-01	1.58E-05	78.60	1.47E-03	2.83E-01	-4.91	-3.22	0.56
HadroHill_15	1.78E-03	3.93E-05	2.83E-01	1.80E-05	78.60	1.47E-03	2.83E-01	-4.10	-2.45	0.64

**Appendix C.6.14** Zircon Lu-Hf data for samples from southern Alberta after error in quadrature and normalisation procedures (see methods Chapter 6, section 6.7.1).

ID #	$\frac{^{176}\text{Lu}}{^{177}\text{Hf}}$	$\pm$ er.	$\frac{^{176}\text{Hf}}{^{177}\text{Hf}}$	$\pm$ er.	Age (Ma)	$e^{\lambda t} - 1$	Initial $\frac{^{176}\text{Hf}}{^{177}\text{Hf}}$	$\epsilon\text{Hf}(t = \text{now})$	$\epsilon\text{Hf}(t = \text{age})$	$\pm$ in $\epsilon\text{Hf}$ units
IL082717-1										
IL082717-1_01	1.09E-03	3.35E-05	2.82E-01	1.88E-05	74.27	1.39E-03	2.82E-01	-15.50	-13.91	0.66
IL082717-1_02	1.75E-03	3.56E-05	2.82E-01	1.88E-05	74.27	1.39E-03	2.82E-01	-17.97	-16.41	0.66
IL082717-1_03	1.70E-03	1.32E-05	2.82E-01	1.97E-05	74.27	1.39E-03	2.82E-01	-17.22	-15.66	0.70
IL082717-1_04	1.79E-03	1.21E-04	2.82E-01	1.68E-05	74.27	1.39E-03	2.82E-01	-21.05	-19.49	0.60
IL082717-1_05	1.27E-03	2.90E-05	2.82E-01	1.73E-05	74.27	1.39E-03	2.82E-01	-17.53	-15.94	0.61
IL082717-1_06	1.47E-03	1.40E-05	2.82E-01	1.80E-05	74.27	1.39E-03	2.82E-01	-18.56	-16.99	0.64
IL082717-1_07	1.06E-03	3.12E-05	2.82E-01	1.97E-05	74.27	1.39E-03	2.82E-01	-18.13	-16.54	0.70
IL082717-1_08	1.37E-03	6.11E-05	2.82E-01	1.94E-05	74.27	1.39E-03	2.82E-01	-15.96	-14.38	0.69
IL082717-1_09	5.89E-04	6.94E-06	2.82E-01	1.50E-05	74.27	1.39E-03	2.82E-01	-22.05	-20.43	0.53
IL082717-1_10	1.68E-03	1.27E-04	2.82E-01	2.07E-05	74.27	1.39E-03	2.82E-01	-21.33	-19.76	0.73
IL082717-1_11	1.03E-03	6.42E-05	2.82E-01	1.44E-05	74.27	1.39E-03	2.82E-01	-14.24	-12.65	0.51
IL082717-1_12	1.27E-03	4.55E-05	2.82E-01	2.04E-05	74.27	1.39E-03	2.82E-01	-15.64	-14.06	0.72
IL082717-1_13	1.56E-03	6.32E-05	2.82E-01	1.87E-05	74.27	1.39E-03	2.82E-01	-13.97	-12.40	0.66
IL082717-1_14	1.41E-03	2.32E-05	2.82E-01	2.00E-05	74.27	1.39E-03	2.82E-01	-18.68	-17.10	0.71
IL082717-1_15	1.01E-03	8.53E-06	2.82E-01	1.38E-05	74.27	1.39E-03	2.82E-01	-18.53	-16.93	0.49
Plateau										
Plateau_01	1.88E-03	6.70E-05	2.83E-01	1.87E-05	75.64	1.41E-03	2.83E-01	-4.60	-3.02	0.66
Plateau_02	1.53E-03	6.40E-05	2.83E-01	1.87E-05	75.64	1.41E-03	2.83E-01	-4.98	-3.38	0.66
Plateau_03	2.22E-03	3.04E-05	2.83E-01	2.42E-05	75.64	1.41E-03	2.83E-01	-6.44	-4.87	0.86
Plateau_04	2.71E-03	3.14E-05	2.83E-01	2.05E-05	75.64	1.41E-03	2.83E-01	-5.82	-4.28	0.72
Plateau_05	1.21E-03	2.83E-05	2.83E-01	1.58E-05	75.64	1.41E-03	2.83E-01	-5.45	-3.83	0.56
Plateau_06	1.71E-03	5.46E-05	2.83E-01	1.68E-05	75.64	1.41E-03	2.83E-01	-5.17	-3.57	0.59
Plateau_07	1.65E-03	5.63E-05	2.83E-01	1.71E-05	75.64	1.41E-03	2.83E-01	-6.26	-4.67	0.61
Plateau_08	1.64E-03	2.29E-05	2.83E-01	1.84E-05	75.64	1.41E-03	2.83E-01	-5.52	-3.93	0.65
Plateau_09	1.86E-03	3.02E-05	2.83E-01	1.82E-05	75.64	1.41E-03	2.83E-01	-5.26	-3.68	0.64
Plateau_10	1.50E-03	4.76E-05	2.83E-01	1.62E-05	75.64	1.41E-03	2.83E-01	-6.24	-4.63	0.57
Plateau_11	1.64E-03	7.02E-05	2.83E-01	1.77E-05	75.64	1.41E-03	2.83E-01	-3.73	-2.13	0.63
Plateau_12	1.21E-03	3.82E-05	2.83E-01	1.50E-05	75.64	1.41E-03	2.83E-01	-5.38	-3.76	0.53
Plateau_13	1.20E-03	8.16E-06	2.83E-01	1.77E-05	75.64	1.41E-03	2.83E-01	-6.40	-4.78	0.63
Plateau_14	2.75E-03	8.75E-05	2.83E-01	2.34E-05	75.64	1.41E-03	2.83E-01	-4.64	-3.10	0.83
Plateau_15	2.60E-03	1.21E-04	2.83E-01	2.02E-05	75.64	1.41E-03	2.83E-01	-6.48	-4.93	0.71
FS082717-1										
FS082717-1_01	2.49E-03	1.43E-04	2.83E-01	2.38E-05	76.72	1.43E-03	2.83E-01	-3.14	-1.57	0.84
FS082717-1_02	1.47E-03	2.25E-05	2.83E-01	1.57E-05	76.72	1.43E-03	2.83E-01	-2.93	-1.30	0.56
FS082717-1_03	2.10E-03	6.57E-05	2.83E-01	2.08E-05	76.72	1.43E-03	2.83E-01	-3.84	-2.25	0.74
FS082717-1_04	2.19E-03	4.58E-05	2.83E-01	2.10E-05	76.72	1.43E-03	2.83E-01	-3.59	-2.00	0.74
FS082717-1_05	1.43E-03	4.29E-05	2.83E-01	1.95E-05	76.72	1.43E-03	2.83E-01	-2.91	-1.28	0.69
FS082717-1_06	2.05E-03	5.36E-05	2.83E-01	2.00E-05	76.72	1.43E-03	2.83E-01	-3.11	-1.51	0.71
FS082717-1_07	2.08E-03	1.07E-04	2.83E-01	2.06E-05	76.72	1.43E-03	2.83E-01	-2.94	-1.34	0.73
FS082717-1_08	1.00E-03	1.08E-05	2.83E-01	1.52E-05	76.72	1.43E-03	2.83E-01	-2.93	-1.28	0.54
FS082717-1_09	1.67E-03	9.02E-05	2.83E-01	2.37E-05	76.72	1.43E-03	2.83E-01	-3.80	-2.18	0.84
FS082717-1_10	1.16E-03	5.89E-06	2.83E-01	1.72E-05	76.72	1.43E-03	2.83E-01	-3.21	-1.57	0.61
FS082717-1_11	1.34E-03	2.75E-05	2.83E-01	2.01E-05	76.72	1.43E-03	2.83E-01	-2.84	-1.21	0.71
FS082717-1_12	1.61E-03	2.75E-05	2.83E-01	1.72E-05	76.72	1.43E-03	2.83E-01	-4.82	-3.20	0.61
FS082717-1_13	2.10E-03	6.19E-05	2.83E-01	1.87E-05	76.72	1.43E-03	2.83E-01	-3.73	-2.13	0.66

ID #	$\frac{^{176}\text{Lu}}{^{177}\text{Hf}}$	$\pm$ er.	$\frac{^{176}\text{Hf}}{^{177}\text{Hf}}$	$\pm$ er.	Age (Ma)	$e^{\lambda t} - 1$	Initial $\frac{^{176}\text{Hf}}{^{177}\text{Hf}}$	$\epsilon\text{Hf} (t = \text{now})$	$\epsilon\text{Hf} (t = \text{age})$	$\pm$ in $\epsilon\text{Hf}$ units
FS082717-1_14	1.53E-03	2.34E-05	2.83E-01	1.95E-05	76.72	1.43E-03	2.83E-01	-3.40	-1.78	0.69
FS082717-1_15	1.19E-03	1.92E-05	2.83E-01	2.00E-05	76.72	1.43E-03	2.83E-01	-3.07	-1.43	0.71
FS082717-1_16	1.30E-03	9.55E-05	2.83E-01	1.80E-05	76.72	1.43E-03	2.83E-01	-3.63	-2.00	0.64
NF082917-1										
NF082917-1_01	9.48E-04	7.30E-05	2.82E-01	2.91E-05	76.30	1.43E-03	2.82E-01	-23.70	-22.05	1.03
NF082917-1_02	1.66E-03	3.85E-05	2.82E-01	2.99E-05	76.30	1.43E-03	2.82E-01	-23.30	-21.69	1.06
NF082917-1_03	2.25E-03	3.19E-05	2.82E-01	3.01E-05	76.30	1.43E-03	2.82E-01	-23.82	-22.24	1.07
NF082917-1_04	1.22E-03	1.52E-05	2.82E-01	2.84E-05	76.30	1.43E-03	2.82E-01	-24.20	-22.57	1.01
NF082917-1_05	9.66E-04	8.19E-06	2.82E-01	2.89E-05	76.30	1.43E-03	2.82E-01	-17.76	-16.12	1.02
NF082917-1_06	1.90E-03	4.60E-05	2.82E-01	2.93E-05	76.30	1.43E-03	2.82E-01	-20.35	-18.76	1.04
NF082917-1_07	1.73E-03	2.39E-05	2.82E-01	2.84E-05	76.30	1.43E-03	2.82E-01	-20.78	-19.18	1.01
NF082917-1_08	1.68E-03	6.60E-05	2.82E-01	2.96E-05	76.30	1.43E-03	2.82E-01	-20.11	-18.50	1.05
NF082917-1_09	1.17E-03	3.41E-05	2.82E-01	2.93E-05	76.30	1.43E-03	2.82E-01	-22.42	-20.79	1.04
NF082917-1_10	5.65E-04	3.12E-05	2.82E-01	3.39E-05	76.30	1.43E-03	2.82E-01	-17.91	-16.25	1.20
NF082917-1_11	4.24E-03	2.06E-04	2.82E-01	3.25E-05	76.30	1.43E-03	2.82E-01	-21.21	-19.73	1.15
NF082917-1_12	1.31E-03	1.27E-05	2.82E-01	2.83E-05	76.30	1.43E-03	2.82E-01	-24.96	-23.34	1.00
NF082917-1_13	1.17E-03	2.73E-05	2.82E-01	3.37E-05	76.30	1.43E-03	2.82E-01	-22.45	-20.81	1.19
NF082917-1_14	2.03E-03	4.13E-05	2.82E-01	2.93E-05	76.30	1.43E-03	2.82E-01	-24.29	-22.70	1.04
NF082917-1_15	1.13E-03	7.71E-06	2.82E-01	2.91E-05	76.30	1.43E-03	2.82E-01	-23.54	-21.90	1.03
PR082917-1										
PR082917-1_01	1.83E-03	3.78E-05	2.82E-01	3.02E-05	76.29	1.43E-03	2.82E-01	-22.22	-20.63	1.07
PR082917-1_02	1.17E-03	1.71E-05	2.82E-01	2.84E-05	76.29	1.43E-03	2.82E-01	-23.81	-22.18	1.01
PR082917-1_03	9.44E-04	7.19E-06	2.82E-01	2.82E-05	76.29	1.43E-03	2.82E-01	-23.71	-22.07	1.00
PR082917-1_04	1.17E-03	3.08E-05	2.82E-01	3.03E-05	76.29	1.43E-03	2.82E-01	-26.39	-24.76	1.07
PR082917-1_05	1.09E-03	4.56E-05	2.82E-01	2.82E-05	76.29	1.43E-03	2.82E-01	-18.97	-17.34	1.00
PR082917-1_06	1.37E-03	6.34E-05	2.82E-01	2.94E-05	76.29	1.43E-03	2.82E-01	-21.68	-20.06	1.04
PR082917-1_07	1.73E-03	1.03E-04	2.82E-01	3.03E-05	76.29	1.43E-03	2.82E-01	-27.37	-25.77	1.07
PR082917-1_08	1.46E-03	1.31E-05	2.82E-01	2.97E-05	76.29	1.43E-03	2.82E-01	-23.49	-21.87	1.05
PR082917-1_09	1.30E-03	3.94E-05	2.82E-01	2.91E-05	76.29	1.43E-03	2.82E-01	-26.93	-25.30	1.03
PR082917-1_10	1.68E-03	6.42E-05	2.82E-01	3.13E-05	76.29	1.43E-03	2.82E-01	-25.68	-24.07	1.11
PR082917-1_11	1.43E-03	8.24E-06	2.82E-01	3.01E-05	76.29	1.43E-03	2.82E-01	-23.89	-22.28	1.07
PR082917-1_12	1.99E-03	1.01E-04	2.82E-01	3.13E-05	76.29	1.43E-03	2.82E-01	-20.34	-18.75	1.11
PR082917-1_13	7.98E-04	4.30E-05	2.82E-01	2.87E-05	76.29	1.43E-03	2.82E-01	-19.19	-17.54	1.02
PR082917-1_14	1.26E-03	3.57E-05	2.82E-01	3.19E-05	76.29	1.43E-03	2.82E-01	-21.14	-19.51	1.13
PR082917-1_15	3.80E-04	3.58E-06	2.82E-01	3.18E-05	76.29	1.43E-03	2.82E-01	-19.41	-17.73	1.13
PR082917-1_16	1.28E-03	3.07E-05	2.82E-01	3.08E-05	76.29	1.43E-03	2.82E-01	-23.27	-21.64	1.09
PR082917-1_17	1.72E-03	1.87E-05	2.82E-01	2.98E-05	76.29	1.43E-03	2.82E-01	-22.51	-20.90	1.06
PR082917-1_18	1.51E-03	4.92E-05	2.82E-01	3.12E-05	76.29	1.43E-03	2.82E-01	-20.93	-19.32	1.10